



**HAL**  
open science

# Meteorite impacts on Mars - Seismic observation, source theory and modeling.

Marouchka Froment

► **To cite this version:**

Marouchka Froment. Meteorite impacts on Mars - Seismic observation, source theory and modeling.. Planetology. Université Paris Cité, 2023. English. NNT : . tel-04461927

**HAL Id: tel-04461927**

**<https://hal.science/tel-04461927>**

Submitted on 16 Feb 2024

**HAL** is a multi-disciplinary open access archive for the deposit and dissemination of scientific research documents, whether they are published or not. The documents may come from teaching and research institutions in France or abroad, or from public or private research centers.

L'archive ouverte pluridisciplinaire **HAL**, est destinée au dépôt et à la diffusion de documents scientifiques de niveau recherche, publiés ou non, émanant des établissements d'enseignement et de recherche français ou étrangers, des laboratoires publics ou privés.



Distributed under a Creative Commons Attribution - NonCommercial - NoDerivatives 4.0 International License



Thèse préparée à l'Institut de Physique du Globe de Paris  
Université Paris Cité

en collaboration avec

Los Alamos National Laboratory

École doctorale Sciences de la Terre et de l'Environnement  
et physique de l'Univers STEP'UP n°560

Équipe de Planétologie et Sciences Spatiales - IPGP  
Earth and Environmental Sciences Division - LANL

# Meteorite impacts on Mars

Seismic observation,  
source theory and modeling.

par **Marouchka FROMENT**

Thèse de doctorat de Sciences de la Terre et de l'environnement

dirigée par **Philippe LOGNONNÉ** et **Carène LARMAT**,

présentée et soutenue publiquement le **26 octobre 2023**,

devant un jury composé de:

Mme	<b>Éléonore STUTZMANN</b>	Physicienne - IPGP, France	PRÉSIDENTE
M.	<b>Jeroen TROMP</b>	Professeur - Princeton University, USA	RAPPORTEUR
M.	<b>Kai WÜNNEMANN</b>	Professeur - Museum für Naturkunde, Allemagne	RAPPORTEUR
M.	<b>Gareth COLLINS</b>	Professeur - Imperial College, Royaume-Uni	EXAMINATEUR
Mme	<b>Ingrid DAUBAR</b>	Associate Professor - Brown University, USA	EXAMINATRICE
Mme	<b>Carène LARMAT</b>	Scientist III - LANL, USA	CO-ENCADRANTE
M.	<b>Alexis LE PICHON</b>	Directeur de Recherche - CEA, France	EXAMINATEUR
M.	<b>Philippe LOGNONNÉ</b>	Professeur - Université Paris Cité, IPGP, France	DIRECTEUR





*“Have you wandered in the wilderness, the sagebrush desolation,  
The bunch-grass levels where the cattle graze?  
Have you whistled bits of rag-time at the end of all creation,  
And learned to know the desert’s little ways?  
Have you camped upon the foothills, have you galloped o’er the ranges,  
Have you roamed the arid sun-lands through and through?  
Have you chummed up with the mesa? Do you know its moods and changes?  
Then listen to the Wild – it’s calling you.”*

Robert William Service, *The Call Of The Wild*

# Meteorite impacts on Mars

## Seismic observation, source theory and modelling.

par Marouchka FROMENT

### Résumé

Les impacts de météorite sont des acteurs majeurs de l'évolution du système solaire et des planètes telluriques. Les expériences de sismologie menées sur la Lune durant les missions Apollo ont permis de découvrir que ces impacts sont également une source importante de signal sismique. L'intérêt pour ce type de source s'est accru avec l'atterrissage de la sonde InSight sur Mars en novembre 2018, qui y a placé deux sismomètres large-bande et courtes périodes. Durant les quatre ans de la mission, ces instruments ont détecté huit impacts de météorites. Comme sur la Lune, les signaux d'impacts diffèrent de ceux, plus classiques, d'origine tectonique. Aucun modèle ne permet encore d'expliquer tout à la fois leur spectre en fréquence, leur magnitude, l'amplitude relative de leurs ondes P et S, ainsi que le mécanisme de la source sismique.

La chute et l'impact final des météores produit également des ondes de choc dans l'atmosphère martienne. Sur Mars, ces chocs peuvent être piégés dans un guide d'onde atmosphérique à basse altitude, et se propager ainsi sur de longues distances sous forme d'infrasons. Ces infrasons ont pu être détectés par les sismomètres d'InSight après s'être couplés à la surface. De tels signaux sismo-acoustiques contiennent des informations sur leur milieu de propagation, l'atmosphère martienne, ainsi que sur le milieu de couplage, le sous-sol d'InSight, et peuvent donc permettre d'interroger la structure de Mars.

A travers cette thèse, nous proposons d'analyser ces deux types de signaux. Premièrement, nous modélisons la source sismique liée à la formation d'un cratère d'impact. Nous élaborons un modèle analytique de la source d'un impact à l'aide du Théorème de Représentation sismique et de la notion de "stress glut". L'impact peut ainsi être vu comme un champ étendu de force équivalentes, ou comme une source ponctuelle, combinant un tenseur de moment sismique et une force vectorielle. Nous développons une méthode numérique pour calculer le stress glut d'un impact à grande vitesse à partir de simulations numériques basées sur la méthode des éléments finis-discrets (FDEM). Ce modèle est testé via un système de couplage logiciel : à une certaine distance du cratère, le signal produit par le modèle de stress glut est comparé au "vrai" signal prolongé de la simulation FDEM. Notre modèle parvient ainsi à expliquer le contenu basse-fréquence des signaux d'impacts, mais des termes de source supplémentaires sont nécessaires pour modéliser leur énergie à haute-fréquence. Nous montrons que ce modèle éclaire les différences de mécanisme sismique entre les impacts obliques et verticaux, et reproduit certaines caractéristiques clés des signaux martiens et lunaires.

En parallèle, nous examinons les signaux sismo-acoustiques liés aux impacts martiens. Grâce à un modèle 1D de la propagation et du couplage des infrasons guidés, nous montrons que la vitesse de groupe de ces signaux dépend du profil de vitesse sonore dans l'atmosphère martienne. De même, le ratio des amplitudes sismiques radiales et verticales dépend principalement du profil de vitesse des ondes S sous InSight. Nous dérivons la structure de l'atmosphère et du sous-sol martien via une inversion bayésienne à partir de trois des signaux sismo-acoustiques d'impacts. Les profils de vitesse sonore obtenus sont en accord avec ceux prédits par les simulations climatiques du Mars Climate Database. En revanche, la structure souterraine est dépendante des paramètres de l'inversion. Deux modèles sont ainsi possibles, l'un ayant de fortes vitesses sismiques dans les premiers  $\sim 20$  m sous InSight, l'autre ayant une simple interface vers  $\sim 40$  m de profondeur. Ces solutions s'approchent de celles obtenues par de précédentes études. Ainsi, combiner les signaux d'infrasons à d'autres données pourra permettre de trancher entre différents modèles.

**Mots-Clés :** Impact de météorites, Mars, InSight, Source sismique, Stress glut, Compliance, Infrasons, Ondes de choc.

## Abstract

Meteorite impacts are important actors in the evolution of the solar system and planetary surfaces. With the first seismic exploration of the Moon during the Apollo missions, it was revealed that meteorite impacts can also be a significant source of seismic signal. The interest in this type of source has been renewed since the landing of the InSight mission on Mars in November 2018, which brought a short-period and a very broadband seismometer on the surface. Eight signals of impact origin were detected by InSight seismometers during the four-year mission. As on the Moon, these signals differ from those of more classical tectonic quakes. Today, no model can fully explain, the impact signal spectrum and magnitude, the P- and S- wave relative amplitudes and the seismic source mechanism.

In addition to seismic waves, the fall and final impact of the meteor produces a shock wave in the Martian atmosphere. On Mars, such shock can be trapped in a low-altitude atmospheric waveguide, and can thus propagate over long distances as a guided infrasound wave. Such infrasound was recorded by InSight seismometer after coupling to the ground surface. These seismo-acoustic signals carry information about their propagation medium, the Martian atmosphere, and their coupling medium, the subsurface below InSight. Hence, they can help understand the structure of Mars.

In this work, we propose to investigate both types of seismic signals. First, we model the seismic source related to the impact cratering process. We design a new analytical model of the impact seismic source using the seismic Representation Theorem and the notion of stress glut. The impact can be seen as an extended field of equivalent forces, or as a point source, combining a seismic moment tensor and a vector force. We develop a numerical method to compute the stress glut associated to a hypervelocity impact using numerical simulations based on the Finite-Discrete Element Method (FDEM). We test this numerical model thanks to a coupling method: at some distance from the crater, the signal produced by the stress glut model is compared to the FDEM signal, prolonged by coupling. Our model succeeds in representing the low-frequency amplitude of impact generated signals, but additional terms are needed to explain the signal cutoff-frequency and high-frequency energy content. We show that this model of the impact seismic source brings insight into the difference in source mechanism of vertical and oblique impacts, and reproduces key properties of Lunar and Martian recordings.

In parallel, we investigate Martian impact-generated seismo-acoustic signals. Thanks to a 1D model of the propagation and coupling of guided infrasound, we show that the group velocity of these signals depends on the effective sound speed profile in the Martian atmosphere. On the other hand, the amplitude ratio of horizontal to vertical displacement is shown to depend on the shear wave velocity structure below InSight. With a Bayesian inversion and using three impact-generated seismo-acoustic signals, we infer the Martian atmospheric and subsurface structure. The obtained sound speed profiles are in agreement with simulations of the Martian Climate Database. However, the inversion of the subsurface is shown to be dependent on the choice of inversion priors. Two models are possible: one with high seismic velocities in the first  $\sim 20$  m below InSight, and the other with a single interface at  $\sim 40$  m depth. These solutions are consistent with those obtained by previous near-subsurface studies. Hence, a better discrimination between models can be achieved in the future by combining multiple datasets.

**Keywords:** Meteorite Impacts, Mars, InSight, Seismic Source, Stress Glut, Compliance, Infrasound, Shock waves.



## Remerciements

*Ce projet de thèse a reçu une bourse de l'École Normale Supérieure Paris Saclay, et les financements de l'ANR MAGIS et du Center for Earth and Space Science de Los Alamos. La thèse doit également sa réussite au succès de la mission InSight opérée par la NASA, à laquelle il me fut donné la chance de participer, et qui fournit les premiers enregistrements sismiques d'impacts sur Mars.*

*L'impact d'une météorite est l'histoire d'un long périple dans l'obscurité, auquel met fin une rencontre éblouissante. Au niveau scientifique, le chemin parcouru durant ce doctorat fut pareillement ponctué de périodes d'errances tout comme d'excitantes découvertes. Et sur le plan personnel, ces trois (quatre) années ont apporté leur lot de voyages, quelques secousses, et bien sur de chaleureuses rencontres. C'est à ces acteurs directs ou indirects de mon doctorat que je veux rendre hommage ici.*

*Je voudrais remercier tout d'abord ceux qui m'ont permis de m'engager et m'ont aidé à avancer dans ce projet : mes directeurs de thèse Philippe Lognonné et Carène Larmat. C'est Philippe qui, en 2019, m'a le premier accordé sa confiance en me proposant un passionnant sujet de recherche de Master à l'IPGP ainsi qu'une visite à LANL. C'est Carène qui à son tour m'a ouvert les portes de Los Alamos pour faire de ce premier séjour et des deux suivants une réussite. Auprès de vous, j'ai appris les grands enjeux de la sismologie planétaire, les ressorts de la vie scientifique, et la difficulté du problème de la source sismique. Vous m'avez toujours offert l'opportunité d'élargir le champ de mes recherches, en particulier quand les signaux des premiers impacts martiens nous parvinrent. Les semaines d'excitation qui suivirent ces découvertes resteront gravées dans ma mémoire ! Je suis fier du chemin parcouru à vos côtés.*

*Mes remerciements vont également à mes rapporteurs, Jeroen Tromp et Kai Wünnemann, aux examinateurs Gareth Collins, Ingrid Daubar et Alexis Le Pichon et à la présidente du jury Eléonore Stutzmann pour le temps passé à la lecture de mon manuscrit et leurs commentaires constructifs.*

*La mission InSight fut une source considérable d'ouverture et de rencontres scientifiques, sur tous les fronts de la géophysique, et je souhaite remercier ses acteurs, jeunes et moins jeunes chercheurs, pour le savoir qu'ils y ont construit et partagé. C'est aussi pour moi l'occasion de rendre hommage à mes encadrants de stage et/ou proches collaborateurs de thèse, qui m'ont offert leur savoir et leurs outils. Ainsi, merci à Esteban Rougier et Zhou (Alex) Lei pour m'avoir permis de petit enseigné l'utilisation de HOSS, et pour l'effort investi à déboguer et modifier son code pour mes applications spécifiques. Merci à Zongbo Xu pour avoir mené avec moi ce formidable travail d'analyse des infrasons martiens, et pour ta disponibilité qui a rendu cette collaboration si agréable. Merci à Taichi Kawamura pour m'avoir introduite aux grandes questions de la sismologie des impacts sur la Lune, et même sur les astéroïdes, et de m'avoir suggéré tant de nouveaux chemins de recherches. J'espère les emprunter dans le futur.*

*Je voudrais également remercier mes collègues de France et d'outre Atlantique pour leur soutien matériel et moral. À Lamarck, je pense à Grégory, Anne, Claudine, Stéphane et Taoufik pour leur aide relative à l'informatique l'administratif et l'enseignement. Je remercie également Anne Caignard pour son mentorat et l'ouverture précieuse que m'a offert nos discussions. Merci à mes camarades doctorants, aux postdocs et jeunes personnels de Lamarck pour nos agréables repas et discussions: Zongbo, Josipa, Sreejaya, Keisuke, Baptiste, Chloé, Amande, Dung, Salma, Alice J., Ninh, Maël, Matthieu, Clément P., Wanbo, Jing, Maylis... En particulier merci à Sabrina M., pour avoir été ma camarade depuis le Master jusqu'aux derniers jours de la mission InSight: tu m'as permis de m'y sentir chez moi. Merci à Sébastien de toujours avancer. Ma gratitude va aussi à Boris pour ton soutien moral et ton humour dans les moments difficiles de la thèse, à Ana et Gabrielle pour votre générosité et votre bonne humeur ! Merci à Xiang pour notre aide mutuelle dans le traitement des données Apollo. Et merci à Alice D., pour ton humour, et ces bons moments passés en Corse avec Louis.*

---

*Mes séjours à Los Alamos n'auraient été possible sans l'aide inestimable apportée par Emily et Veronica dans toutes mes démarches administratives américaines. Tout n'a pas été sans heurts, mais vous avez toujours trouvé une solution pour moi. Je voudrais remercier Neala, pour avoir répondu à mes questions sur le laboratoire et sur la recherche aux Etats-Unis, et pour tes nombreux conseils. Merci à Yao et à Yu-Hsuan pour avoir partagé avec moi des repas, des joies et des peines, des cultures. Je vous souhaite à toutes beaucoup de réussite. Merci à Brent pour tes précieux commentaires sur mon travail d'inversion bayésienne, et à Loïc pour ton aide dans la recherche de postdoc. Enfin, mes remerciements vont à Dave, Kevin, Bryan, Damien, Carly et Siobhan pour nos diverses rencontres et discussions de pauses café.*

*De nombreuses personnes, en dehors du laboratoire, ont supporté ce doctorat... Bien souvent, paradoxalement, ce fut en m'en détournant ! Ainsi, merci à Sabrina B., pour ta fidèle amitié, et pour avoir été ma colocataire deux ans de suite et à travers la pandémie de Covid-19, en compagnie de quelques chats et de quantité de fromage. Merci à Lucas pour ton enthousiasme jamais tari et nos discussions sur les inversions de Monte Carlo. Merci à Claire R. pour cette improbable visite au Nouveau Mexique, qui m'a tant fait plaisir. Merci à Elliot, pour toujours me parler de ce qui est beau, du travail créatif et de la persévérance. Merci à mes amies de toujours, Aurore et Claire V. : chacune à sa manière, la vie nous a porté très loin, mais nous nous retrouvons toujours et continuons de grandir ensemble ! Merci aux belles âmes de Los Alamos, Zack, Romain, Diana, Connor, Maharshi, Eric, Greg, Henry, Brandon, Will et Hailey, pour ces nombreuses bières, barbecues et sorties. Merci à Bobbi pour ton amitié et ta vaste culture, que tu transmets passionnément. Mes pensées iront vers toi lorsque je mangerai mon prochain Pozole.*

*A ma famille : merci pour votre soutien constant dans tous mes choix de vie et de carrière, bien qu'ils nous aient malheureusement longtemps tenus éloignés. Mais qui sait ce que le futur nous réserve ?*

*Enfin, merci à Clément. Pendant que les météores embrasaient l'atmosphère de Mars, le ciel du Nouveau Mexique s'est peint de nouvelles couleurs en ta présence. Et alors que nous laissons derrière nous le désert et les mesas, j'ai hâte d'explorer bientôt avec toi de nouveaux paysages.*

## Acknowledgements

*This PhD project received a grant from the École Normale Supérieure Paris Saclay, and fundings from the ANR MAGIS and the Center for Earth and Space Science of Los Alamos. The progress of this thesis also owes much to the success of the InSight mission operated by NASA, in which I became a lucky early-career participant, and which provided the first seismic recordings of impacts on Mars.*

*A meteorite impact is the tale of a long journey ending in a beautiful and bright encounter. Likewise, on a scientific level, the PhD road featured times of aimless wandering as well as exciting discoveries. On the personal level, these three (four) years were shaped by multiples journeys across continents, a couple tremors, and, of course, heart-warming encounters. Through the following words, I wish to pay tribute to many figures who supported this doctorate.*

*I first wish to thank those who allowed me to embark and progress in this project: my PhD advisors Philippe Lognonné and Carène Larmat. Philippe first put his trust in me in 2019, when he offered me a fascinating Master's research project at IPGP, together with a visit at LANL. It was then Carène who opened the doors of Los Alamos for me, and ensured the success of this first stay and the subsequent ones. By your side, I learned about the great questions and stakes of planetary seismology, the mainsprings of scientific life, and the challenges of seismic source studies. You always provided me with opportunities to enlarge the scope of my research, in particular when the first Martian impact signals were received. The exciting weeks which followed these discoveries will forever be in my memory! I am proud of what we have achieved together.*

*My thanks also extend to my reviewers, Jeroen Tromp and Kai Wünnemann, my examiners Gareth Collins, Ingrid Daubar, Alexis Le Pichon, and the president of the jury Eléonore Stutzmann, for the time spent reading my manuscript and their constructive comments.*

*The InSight mission was a mind-opening experiences, through which I met amazing scientists on all fronts of geophysics. I'd like to thank all those involved, young and senior researchers alike, for the knowledge they built up and shared in this endeavour. In the same way, I want to pay tribute to my former internship advisors and/or close thesis collaborators, for offering me their knowledge and tools. Thus, thanks to Esteban Rougier and Zhou (Alex) Lei for teaching me, little by little, how to use HOSS, and for their effort in debugging and modifying the code for my specific applications. Thanks to Zongbo Xu for leading with me this fantastic work of analysis and modeling of Martian impact, infrasound, and for your availability which made this collaboration so pleasant. Thanks to Taichi Kawamura for introducing me to the great questions of impact seismology on the Moon and even on asteroids, at for suggesting me many new research paths. I hope I will follow them in the future.*

*I would also like to thank my colleagues in France and accross the pond, for their material and moral support. At Lamarck, my thoughts extend to Grégory, Anne, Claudine, Stéphane and Taoufik for their help with administrative, teaching and IT matters. I would also like to thank Anne Caignard for her mentorship and precious advice related to life in research. Thanks to my fellow PhD students, to the postdocs and young fellows of Lamarck for our pleasant lunches and discussions: Zongbo, Josipa, Sreejaya, Keisuke, Baptiste, Chloé, Amande, Dung, Salma, Alice J., Ninh, Maël, Matthieu, Clément P., Wanbo, Jing, Maylis... In particular, thanks to Sabrina M., for having been my comrade from the Master's to the last days of the InSight mission: you made me feel at home there. Thanks to Sébastien for always moving forward. My gratitude also goes to Boris, for your moral support and your humour in difficult times, and to Ana and Gabrielle for your generosity and your good mood! Thanks to Xiang for our mutual help with Apollo data, and thanks to Alice D., for your humour and the good time we had in Corsica with Louis.*

---

*My stays in Los Alamos would not have been possible without the invaluable assistance of Emily and Veronica with the lab paperwork. It has not been all smooth sailing, but you've always found a solution for me. I would like to thank Neala, for answering my many questions on the lab and research in the US, and for your great advice. Thanks to Yao and Yu-Hsuan for sharing with me some meals, joys and griefs, and cultures. I wish you three a lot of success. Thanks to Brent for your precious comments on my Bayesian inversion work, and to Loïc for your help in my postdoc applications. And finally, I would like to thank Dave, Kevin, Bryan, Damien, Carly et Siobhan for our meetings and coffee breaks.*

*Many people, outside of the lab, have supported my PhD... Quite often, paradoxically, it was by distracting me from it! Thus, thanks to Sabrina B. for your loyal friendship, and for being my roommate for two years through the Covid-19 pandemic, in the company of a couple of cats and plenty of cheese. Thanks to Lucas for your unfailing enthusiasm and our discussions on Monte Carlo inversions. Thanks to Claire R. for your unexpected visit to New Mexico, which made me so happy ! Thanks to Elliot for always telling me about beautiful things, creative work and perseverance. Thanks also to my lifelong friends, Aurore and Claire V.: life carried each of us a long way, but we always find each other again and continue to grow up together. Thanks to the beautiful souls of Los Alamos: Zack, Romain, Diana, Connor, Maharshi, Eric, Greg, Henry, Brandon Will and Hailey, for our many beers, barbecues and meetings. Thank you Bobbi for your friendship and your vast culture, which you pass on with passion. I'll be thinking of you when I eat my next Pozole.*

*To my family: thank you for your unwavering support in all my life and career choices, even though they unfortunately kept us apart for a long time. But who knows what the future holds?*

*Finally, thank you, Clément. As meteors set the atmosphere of Mars ablaze, the New Mexican sky took on new colours in your presence. And as we leave the deserts and the mesas behind, I look forward to exploring new landscapes with you.*



# Contents

<b>ABSTRACT</b>	<b>i</b>
<b>ACKNOWLEDGEMENTS</b>	<b>iii</b>
<b>LIST OF FIGURES</b>	<b>xi</b>
<b>LIST OF TABLES</b>	<b>xvi</b>
<b>ABBREVIATIONS AND ACRONYMS</b>	<b>xvii</b>
<b>NOMENCLATURE</b>	<b>xix</b>
<b>RÉSUMÉ DE LA THÈSE</b>	<b>xxi</b>
<b>1 INTRODUCTION</b>	<b>1</b>
<b>1.1 Meteorites and Meteors</b>	<b>1</b>
1.1.1 Context and definitions . . . . .	1
1.1.2 The global effect of meteors and meteorites . . . . .	3
<b>1.2 Exploring the solar system using seismology</b>	<b>5</b>
1.2.1 History of Earth seismology and acoustics . . . . .	5
1.2.2 The beginnings of Planetary Seismology: the Apollo missions . . . . .	9
1.2.3 The InSight mission on Mars . . . . .	11
<b>1.3 Meteorite seismic signals</b>	<b>15</b>
1.3.1 Observations on Earth . . . . .	15
1.3.2 Seismic detection of impacts on the Moon . . . . .	17
1.3.3 Seismic detection of impacts on Mars . . . . .	19
<b>1.4 Aim of this work</b>	<b>26</b>
1.4.1 Identified questions of impact seismology . . . . .	26
1.4.2 Structure of this work . . . . .	28

<b>2</b>	<b>THE IMPACT CRATERING SEISMIC SOURCE</b>	<b>31</b>
<b>2.1</b>	<b>General Introduction</b>	<b>33</b>
2.1.1	The notion of seismic source . . . . .	33
2.1.2	Numerical modelling of impacts . . . . .	37
2.1.3	The cratering process . . . . .	39
<b>2.2</b>	<b>Introduction</b>	<b>42</b>
<b>2.3</b>	<b>The Representation Theorem applied to impacts</b>	<b>45</b>
2.3.1	Representation of seismic sources . . . . .	45
2.3.2	Point-source of an impact . . . . .	47
2.3.3	Towards a more detailed source model . . . . .	52
<b>2.4</b>	<b>Numerical method and verification</b>	<b>53</b>
2.4.1	Numerical modeling of meteorite impacts . . . . .	53
2.4.2	Seismic source computation . . . . .	55
2.4.3	Verification - Software coupling . . . . .	58
<b>2.5</b>	<b>Results</b>	<b>61</b>
2.5.1	Source of a vertical and an oblique impact . . . . .	61
2.5.2	Verification of the point-source . . . . .	71
2.5.3	Simulating an extended source . . . . .	73
2.5.4	Towards Lunar and Martian data . . . . .	77
<b>2.6</b>	<b>Discussion</b>	<b>82</b>
<b>2.7</b>	<b>Conclusion</b>	<b>85</b>
<b>2.8</b>	<b>Additional Results</b>	<b>87</b>
	<b>Appendices</b>	<b>89</b>
A1	Equations of motion with surface mass losses . . . . .	89
A2	Representation of a seismic wavefield in a volume with constant mass	90
A3	Representation Theorem for a variable-mass system . . . . .	91
A4	Stress Glut on a self-gravitating, rotating planet . . . . .	93
	<b>Supplementary Information</b>	<b>94</b>
SI-1	HOSS material models . . . . .	95
SI-2	Stress glut computation - single element test . . . . .	95
SI-3	Mesh test for seismic source computation . . . . .	100

SI-4	Fit of HOSS force and moment source time functions . . . . .	105
SI-5	Point source and coupled signals . . . . .	105
<b>Related Articles</b>		<b>113</b>
<b>3</b>	<b>IMPACT-GENERATED SEISMO-ACOUSTIC SIGNALS ON MARS</b>	<b>129</b>
<b>3.1</b>	<b>Introduction</b>	<b>131</b>
3.1.1	Atmospheric shock waves from meteors and meteorites . . . . .	131
3.1.2	Phenomenology of air-to-ground coupling . . . . .	137
3.1.3	Martian chirp signals . . . . .	139
<b>3.2</b>	<b>Seismo-acoustic model of a guided meteorite infrasound</b>	<b>144</b>
3.2.1	Modelling of dispersed infrasound . . . . .	144
3.2.2	Modelling of seismic signals coupled from infrasound . . . . .	145
3.2.3	Characteristics of the model . . . . .	146
<b>3.3</b>	<b>Inversion method</b>	<b>147</b>
3.3.1	Model parametrisation and sensitivity . . . . .	147
3.3.2	The Markov chain Monte Carlo inversion method . . . . .	153
3.3.3	Data selection . . . . .	158
<b>3.4</b>	<b>Inversion of the atmospheric structure</b>	<b>159</b>
3.4.1	Test of the inversion method . . . . .	159
3.4.2	Atmospheric structure inverted for three individual events . . . . .	162
<b>3.5</b>	<b>Inversion of InSight near-surface structure</b>	<b>162</b>
3.5.1	Test of the subsurface inversion . . . . .	162
3.5.2	Subsurface model inverted from event H/V ratio . . . . .	166
<b>3.6</b>	<b>Discussion</b>	<b>168</b>
3.6.1	Interpretation of the atmospheric inversion . . . . .	168
3.6.2	Interpretation of the subsurface inversion . . . . .	169
<b>3.7</b>	<b>Conclusion</b>	<b>171</b>
<b>Appendices</b>		<b>173</b>
A1	The propagator matrix method for compliance . . . . .	173
A2	The propagator matrix method for guided infrasound . . . . .	175
A3	Test of different McMC implementations . . . . .	177

---

<b>Related Articles</b>	180
<b>4 CONCLUSION AND PERSPECTIVES</b>	<b>203</b>
<b>4.1 Exploring the impact seismic source - and other sources</b>	203
4.1.1 An exhaustive source model . . . . .	203
4.1.2 Towards scaling relationships and validation . . . . .	205
<b>4.2 Impact-generated Infrasound</b>	206
4.2.1 Dispersed infrasounds: a unique dataset for InSight . . . . .	206
4.2.2 Possible improvements of the model . . . . .	206
<b>4.3 Towards a multi-physics view of the source</b>	207
4.3.1 The problem of impact blast waves . . . . .	207
4.3.2 Numerical modelling of impact shock waves . . . . .	208
4.3.3 A new view of the source . . . . .	212

# List of Figures

1.1	Terminology of the phenomena associated to meteoroids from their entry to their eventual collision. . . . .	1
1.2	Picture of a fragment of the Zagami meteorite. . . . .	2
1.3	Picture of Meteor Crater, Arizona. . . . .	4
1.4	Schematic representation of the mass-spring system design for two seismometers deployed on the Moon and on Mars. . . . .	6
1.5	Map of the Moon showing major geographic features, the Apollo seismic network and the location of some recorded impact events. . . . .	9
1.6	Comparison of seismograms recorded on the Earth, the Moon and Mars at a similar source-receiver distance. . . . .	10
1.7	View of the InSight lander and its instruments. . . . .	12
1.8	Map of Mars showing major geographic features around InSight, and the location of impact and quality A events recorded by SEIS. . . . .	13
1.9	Comparison between the low frequency seismic signal recorded on a seismic station at Irkutsk, Russia after Tunguska, and a signal recorded after an atmospheric explosion on October 14, 1970, in Lop-Nor, China. . . . .	15
1.10	Spectrogram and time series of the seismic ground velocity recorded during the entry of the Stardust capsule. . . . .	16
1.11	Picture of the S-IVB boosters and LM modules used as artificial impacts on the Moon, with associated craters and seismic signals. . . . .	18
1.12	Comparison of the signals and spectra recorded during a lunar impact and a moonquake. . . . .	18
1.13	Examples of albedo disturbances found around fresh craters by the HiRISE color camera. . . . .	21
1.14	Spectrograms of impact-generated seismic events comprising "chirps" recorded during the InSight mission. . . . .	23
1.15	Map and images of all impacts detected seismically near InSight (~300 km). . . . .	24
1.16	CTX and HiRISE images of the impact craters associated to seismic events S1094b and S1000a. . . . .	25
1.17	Comparison of seismic signals and spectra recorded for impact event S1094b and marsquake S1222a. . . . .	26

2.1	Simplified representation of the earthquake source mechanism. . . . .	33
2.2	Simplified representation of the explosive source mechanism. . . . .	34
2.3	Graphic representation of Eshelby's inclusion problem and associated traction forces. . . . .	35
2.4	Stress glut formed during a fault rupture and relation with the region of inelastic displacement. . . . .	36
2.5	Representation of finite and discrete elements in a FDEM mesh as implemented by HOSS. . . . .	38
2.6	Graphic representation of the different stages of crater formation. . . . .	39
2.7	Graphic showing the computation method for the volumetric stress glut. . . . .	55
2.8	Principle of the verification method proposed for the seismic source computation. . . . .	59
2.9	Stress glut and velocity fields of a vertical impact scenario, at different instants following the impact. . . . .	62
2.10	Stress glut and velocity fields of an oblique impact scenario, at different instants following the impact. . . . .	63
2.11	Crater of the vertical (left) and oblique (right) simulations after 116 ms. . . . .	64
2.12	Force experienced by the target material for the vertical and oblique simulations. . . . .	65
2.13	Components of moment tensor $\mathbf{M}(\boldsymbol{\xi}^*, \tau)$ for the vertical impact. . . . .	66
2.14	Components of moment tensor $\mathbf{M}(\boldsymbol{\xi}^*, \tau)$ for the oblique impact. . . . .	66
2.15	Lune diagram of the focal mechanism calculated for the vertical and oblique impacts. . . . .	69
2.16	Evolution of the Cauchy stress and "angular momentum" components of the seismic source for the vertical and oblique impact. . . . .	70
2.17	Results of the comparison between coupled and combined point-source waveforms. . . . .	74
2.18	Vertical displacement signal (left) and spectra (right) of the P-wave in Fig. 2.17, decomposed to show the contribution of different source mechanisms. . . . .	75
2.19	Comparison between the coupled signal, the point-source signal, and signal modelled with an extended source. . . . .	76
2.20	Effect of source extension on the seismic signal at 400 m distance. . . . .	77
2.21	Spectra of the coupled and point-source signals extrapolated from 400 m distance up to 100 km distance. . . . .	78
2.22	Scaling of different impact seismic moments estimates with their impactor momentum, $(P_i)$ . . . . .	79

2.23	Scaling of the "Source size" estimate, $(\tau v_s)$ , with the impactor momentum $P_i$ and the impactor kinetic energy $E_i$ . . . . .	82
2.24	Lune diagram for the moment tensor of an impact with a $22.5^\circ$ , $45^\circ$ , $67.5^\circ$ and $90^\circ$ incidence angle from the horizontal. . . . .	87
2.25	Evolution of the source characteristics with impact incidence angle. . . . .	88
2.26	Computation of the volumetric stress glut for a single regular tetrahedral element subject to isotropic compression followed by extension. . . . .	97
2.27	Computation of the deviatoric stress glut for a single tetrahedral element subject to compression followed by extension in the vertical direction. . . . .	98
2.28	Computation of the deviatoric stress glut for a single tetrahedral element subject to shear in the horizontal direction. . . . .	99
2.29	Computation of the deviatoric stress glut for a single tetrahedral element subject to shear in the vertical direction followed by a 90-degree rigid-body rotation about the $y$ axis. . . . .	100
2.30	3D Tetrahedral meshes tested for a vertical impact simulation. . . . .	101
2.31	Image of the distribution of elements for each distinct mesh, 2.98 ms after the impact. . . . .	103
2.32	Pressure amplitude decay in three different directions for each distinct mesh. . . . .	104
2.33	Times series and spectra of extrapolated moment and force components. . . . .	107
2.34	Comparison between coupled and combined point-source waveforms at 100 m source-receiver distance. . . . .	109
2.35	Comparison between coupled and combined point-source waveforms at 200 m source-receiver distance. . . . .	110
2.36	Comparison between coupled and combined point-source waveforms at 300 m source-receiver distance. . . . .	111
2.37	Fit of the coupled P- and S- wave spectra. . . . .	112
2.38	Results of the fit of the coupled P-wave and S-wave spectra at 100 km distance. . . . .	112
3.1	Graphic representation of the fireball and airburst phenomena. . . . .	132
3.2	Near field decay of the pressure wavefield of a Mach cone. . . . .	134
3.3	Evolution of a weakly non-linear N-wave under the effect of atmospheric attenuation processes. . . . .	135
3.4	Different models for the blast wave associated to the detonation of a high explosive. . . . .	135
3.5	Schematic representation of the evolution of an explosion blast wave with distance. . . . .	136

3.6	Schematic representation of various types of air-to-ground coupled motion. . . . .	138
3.7	Average effective sound-speed profile from 0 km to 10 km altitude on Mars in four different propagation directions. . . . .	140
3.8	Individual times series and spectrograms of seismo-acoustic signals (chirps) recorded by InSight. . . . .	142
3.9	Schematic representation of the Martian atmospheric waveguide and the dispersion phenomenon. . . . .	144
3.10	Sensitivity of the group velocity calculated with the propagator matrix method to the discretisation of atmospheric profiles. . . . .	148
3.11	Normalised pressure term and pressure eigenfunction calculated for different discretisations of the atmosphere. . . . .	149
3.12	Sensitivity of the group velocity to changes in sound speed and density. . . . .	150
3.13	Sensitivity of the pressure waveform to different types of acoustic source time functions. . . . .	151
3.14	Sensitivity of the HV ratio to changes in the layer thickness, the Poisson's ratio and the S-wave velocity, based on the ZX model. . . . .	153
3.15	Generation of Rayleigh waves by the coupling of a dispersed infrasound with different subsurface models. . . . .	154
3.16	MCD effective and thermodynamic sound speed profiles for the three events S0986c, S0981c and S1034a, with modelled and measured group velocity curves. . . . .	159
3.18	Mean misfit measured in the last portion of Markov chains as a function of the number of atmospheric layers below the halfspace. . . . .	159
3.17	Amplitude spectra and H/V ratio for each selected chirp event. . . . .	160
3.19	PDF of models extracted from the posterior distribution of the synthetic atmosphere inversion. . . . .	161
3.20	Histogram of the altitude of layers in all models produced by the synthetic atmosphere inversion. . . . .	161
3.21	Posterior probability density of atmospheric models inverted from the group velocity measurements of S0986c, S1034a and S0981c. . . . .	163
3.22	Posterior distribution of layer altitude for each atmospheric model inversion. . . . .	164
3.23	PDF of models extracted from the posterior distribution of the synthetic subsurface inversion. . . . .	165
3.24	400 models extracted from the inversions with large and reduced priors. . . . .	165
3.26	Representation of the two families of models obtained from the inversion of chirp HV curves. . . . .	166



3.25	Histogram of interface depths inverted from the chirp data using large prior bounds. . . . .	166
3.28	Compared density of probability inverted with narrow prior bounds and with different Poisson ratios, treated as fixed or as a model variable. . . . .	167
3.27	Histogram of interface depths inverted from the chirp data using reduced prior bounds. . . . .	167
3.29	Histogram of inverted Poisson ratio values. . . . .	168
3.30	Comparison of vertical compliance amplitude and H/V ratios for different subsurface models. . . . .	170
3.31	Comparison of various models of the shear wave velocity in the first 100 m below InSight. . . . .	171
32	Autocorrelation time estimated during the McMC inversion of a synthetic group velocity curve for S0986c, run with three different methods. . . . .	178
33	Autocorrelation time estimated during the McMC inversion of three synthetic H/V ratio curves, run with three different methods. . . . .	178
34	Posterior probability density of atmospheric models inverted from a synthetic group velocity curve compared for three McMC methods. . . . .	179
35	Posterior probability density of subsurface models inverted from synthetic H/V ratio curves compared for three McMC methods. . . . .	179
4.1	Shock wave produced by the impact of a 1 m radius stone meteor with a velocity of $20 \text{ km}\cdot\text{s}^{-1}$ , simulated with the SOVA hydrocode. . . . .	208
4.2	Results of verification tests conducted with HOSS/FSIS. . . . .	209
4.3	HOSS/FSIS simulation of a $12 \text{ km}\cdot\text{s}^{-1}$ flow of $\text{CO}_2$ against a fixed impactor. . . . .	211
4.4	Overpressure recorded behind the fixed meteor, along several lines perpendicular to the trajectory. . . . .	212

# List of Tables

- 2.1 Normalisation and decomposition of the single force and moment tensor, with associated source time functions. . . . . 68
- 2.2 Parameters used for the scaling of seismic moments and source size estimates (Figs. 2.22 and 2.23). . . . . 81
- 2.3 Parameters of impactor and target material models used in HOSS simulations. 96
- 2.4 Parameters of the fit performed on time series of the oblique and vertical point source components. . . . . 106
- 2.5 Misfit between the P- and S- wave spectra at 400 m and the result of the  $\Omega_3$  and  $\Omega_2$  model fits. . . . . 108
- 3.1 Location, date and parameters of each impact event of the InSight mission associated to a chirp signal. . . . . 143
- 3.2 Parameters of a 3-layers model of the subsurface below InSight derived by [Xu et al. \[2022\]](#) (ZX model). . . . . 152
- 3 Computational cost and convergence of a synthetic inversion using the Ensemble Sampler, the Parallel Tempering implementation and an in-house implementation. . . . . 178

# List of Abbreviations and Acronyms

- ALSEP** Apollo Lunar Surface Experiments
- APSS** Auxiliary Payload Sensor Suite
- BB** Broad-Band
- CLPS** Commercial Lunar Payload Services
- CLVD** Compensated Linear Vector Dipole (source mechanism)
- CMBD** Cruise Mass Balance Devices
- CNES** Centre National d'Études Spatiales
- CNSA** Chinese National Space Administration
- CPPR** Cells Per Projectile Radius
- CTBT** Comprehensive Nuclear-Test-Ban Treaty
- CTX** Context Camera (Mars Reconnaissance Orbiter instrument)
- DART** Double Asteroid Redirection Test
- DARTS** Data ARchives and Transmission System
- DC** Double Couple (source mechanism)
- DEM** Discrete Element Method
- EDL** Entry, Descent and Landing
- EEW** Earthquake Early Warning
- EOS** Equation Of State
- ES** Ensemble Sampling
- F1** Family 1 (model)
- F2** Family 2 (model)
- FDEM** Combined Finite-Discrete Element Method
- FEM** Finite Element Method
- FSS** Farside Seismic Suite
- HF** High Frequency
- HOSS** Hybrid Optimization Software Suite
- HP<sup>3</sup>** Heat Flow and Physical Properties Package
- HV** Horizontal to Vertical amplitude ratio
- IAU** International Astronomical Union
- ICC** Instrument Context Camera
- IDA** Instrument Deployment Arm
- IDC** Instrument Deployment Camera

**IMS** International Monitoring System  
**INSU** Institut National des Sciences de l'Univers  
**IPGP** Institut de Physique du Globe de Paris  
**IRIS** Incorporated Research Institutions for Seismology  
**ISO** Isotropic (source mechanism)  
**InSight** Interior Exploration using Seismic Investigations  
**JAXA** Japan Aerospace Exploration Agency  
**LANL** Los Alamos National Laboratory  
**LF** Low Frequency  
**LM** Lunar Module  
**LOLA** Lunar Orbiter Laser Altimeter  
**MAP** Maximum A Posteriori (model)  
**MARCI** Mars Color Imager  
**MCD** Mars Climate Database  
**ML** Maximum Likelihood (model)  
**MOLA** Mars Orbiter Laser Altimeter  
**MQS** MarsQuake Service  
**MRO** Mars Reconnaissance Orbiter  
**McMC** Markov chain Monte Carlo  
**NASA** National Aeronautics and Space Administration  
**PDF** Probability Density Function  
**PDS** Planetary Data System  
**PREOS** Peng-Robinson Equation Of State  
**PSE** Passive Seismic Experiment  
**PT** Parallel Tempering  
**RISE** Rotation and Interior Structure Experiment  
**S-IVB** Saturn IV rocket Booster  
**SEIS** Seismic Experiment for Interior Structure  
**SNC** Shergottites, Nakhilites and Chassignites (types of meteorites)  
**SNR** Signal to Noise Ratio  
**SP** Short Period (seismic instrument)  
**SWEOS** Span & Wagner Equation Of State  
**TGO** Trace Gas Orbiter  
**TNT** 2,4,6-Trinitrotoluene (explosive)  
**USGS** United States Geological Survey  
**VBB** Very BroadBand (seismic instrument)  
**VF** Very high Frequency  
**WTS** Wind and Thermal Shield  
**ZX (model)** Subsurface model proposed by [Xu et al. \[2022\]](#)

# Nomenclature

Except otherwise noted, the International System of Units (SI) is used throughout this manuscript. One notation or symbol may have a different signification in different contexts, listed below. Similarly, different symbols may be used to represent the same variable, such as  $v_x, v_z$  for velocity in section 2.3, and alternatively  $V_x, V_z$  in section 3.2.2.

SYMBOL	SIGNIFICATION
<b>Coordinate Systems</b>	
$e_x, e_y, e_z$	Unit cartesian vectors
$\mathbf{n}, n_j$	Surface normal vector, and projection in direction $j$
$\mathbf{x}, \mathbf{r}, (x, y, z)$	Position vector and its cartesian coordinates
$\boldsymbol{\xi}, \xi_j$	Coordinates of points belonging to the seismic source
$\boldsymbol{\xi}^*, \xi_j^*$	Coordinates chosen for the point-source
<b>Mechanics and Fluid Dynamics</b>	
$\nabla, \partial_t, \partial_j$	Gradient operator, time derivative, space derivative in $j$ direction
$D_t, \frac{d}{dt}$	Material derivative
$t, \tau$	Time and source time
$V, \Delta V$	Volume, Volume change
$S, \Sigma$	Surface
$\mathbf{u}, (u_x, u_y, u_z)$	Displacement vector and cartesian components
$\mathbf{v}, (v_x, v_y, v_z)$	Velocity vector and its cartesian components
$V_x, V_z$	Seismic velocity projected in source azimuth ( $x$ ) and vertical direction ( $z$ )
$\mathbf{f}, (f_x, f_y, f_z)$	Cartesian forces
$\mathbf{f}^V, \mathbf{h}^V, f_i^V, h_i^V$	Cartesian volume forces and projection in direction $i$
$\mathbf{f}^\Sigma, f_i^\Sigma$	Cartesian surface forces
$\boldsymbol{\gamma}^V, \gamma_i^V$	Cartesian volume equivalent forces
$\boldsymbol{\gamma}^\Sigma, \gamma_i^\Sigma$	Cartesian surface equivalent forces
$\boldsymbol{\varepsilon}, \boldsymbol{\varepsilon}^E, \boldsymbol{\varepsilon}^T, \boldsymbol{\varepsilon}^P, \varepsilon_{kl}$	Strain tensor (elastic, stress-free, plastic) and tensor notation.
$P, p, P_{el}$	Pressure, elastic pressure limit
$\boldsymbol{\Psi}, \mathbf{T}, \Psi_{ij}$	Elastic stress tensor and tensor element, Cauchy stress tensor
$\mathbf{S}, S_{ij}$	True non-linear stress tensor and tensor element
$\boldsymbol{\Pi}, \Pi_{ij}$	Stress glut tensor and tensor element
$\mathbf{G}, G_{in}$	Green's function of elasticity
$C_{x/p}, C_{v_x/p}, C_{z/p}, C_{v_z/p}$	Compliance function for displacement, velocity, in two directions
$\varphi_i, \varphi_i^E, \varphi_i^P$	angle of deformation in mode $i$ (total, plastic, elastic)
$F_{ij}$	Shear stress operator
$\mathbf{R}$	Rotation tensor
$\mathbf{F}$	Deformation gradient
$\phi, \phi^0$	Gravitational potential

---

**Impactor and Meteor Properties**


---

$E_i$	Impactor kinetic energy
$P_i$	Impactor momentum
$r_i$	Impactor radius
$v_i$	Impactor velocity
$R_0$	Radius of a meteor highly non-linear shock region

---

**Material Properties**


---

$g$	Gravity acceleration
$G$	Gravitational constant
$\lambda$	Lamé's first parameter
$K, K_{el}$	Bulk modulus, Elastic bulk modulus
$\mu, G$	Lamé's second parameter, shear modulus
$m$	Mass
$\rho, \rho^0$	Density
$v_p, v_s$	Velocity of P-waves and S-waves
$c_s, \alpha, C_{s,T}, c_{s,eff}, c$	Acoustic wave velocity (thermodynamic/ effective), phase velocity
$\mathbf{C}, C_{ijkl}$	Stiffness tensor and elements in a cartesian reference frame
$Q$	Material attenuation

---

**Seismology and Acoustics**


---

$\omega, \omega_c$	Pulsation and corner/cutoff pulsation
$f, f_c$	Frequency and corner/cutoff frequency
$\mathbf{k}, k_x, k$	Wave number, projection in propagation direction
$v_\varphi, v_g$	Signal phase and group velocity
$\mathbf{M}, M_{ij}$	Moment tensor and tensor components
$\mathbf{F}, F_i$	Total seismic force and cartesian components
$M^0$	Seismic moment
$M_w$	Moment magnitude based on work energy
$\delta$	Dirac distribution (impulse function)
$\Omega_2, \Omega_3$	Spectral shape functions
$S(\omega)$	Source spectrum as a function of pulsation
$HV$	Signal horizontal to vertical amplitude ratio

---

**Probabilities**


---

$P$	Distribution of probability (function)
$\mathbf{m}$	Vector of model parameters
$\mathbf{d}$	Vector of data points
$\sigma$	Data uncertainty

---

**Propagator Matrix Method**


---

$\mathbf{f}$	Motion-stress vector
$\mathbf{A}$	Matrix of linearised differential equations
$\mathbf{P}$	Propagator matrix
$\sigma_{xx}, \sigma_{zz}, \sigma_{zx}$	Stress
$\gamma$	Matrix eigenvalues
$r_1, r_2, r_3, r_4$	Amplitude functions for velocity and stress

---

# Résumé de la Thèse

Les météorites sont des acteurs majeurs de l'évolution du système solaire et des planètes telluriques. Sur la Terre, protégée par son atmosphère, les impacts sont rares mais les chutes de météores produisent des ondes de choc destructrices, comme lors des événements de Toungouska et Tcheliabinsk. L'interaction de ces ondes de choc avec l'atmosphère et la surface terrestre génèrent également des ondes infra-sonore et sismiques.

En l'absence d'une atmosphère dense, les surfaces des objets de notre système solaire se couvrent de cratères. Les expériences de sismologie menées sur la Lune durant les missions Apollo ont permis de découvrir que ces impacts sont une source importante de signal sismique. Le catalogue établi suite aux sept ans de missions contient ainsi environ 1750 événements sismiques issus d'impacts. L'intérêt pour ce type de source s'est accru avec l'atterrissage de la sonde InSight sur Mars en novembre 2018. La mission a pour objectif d'étudier l'histoire et la formation de Mars en explorant sa structure interne, grâce entre autres à la sismologie. InSight a déployé dans ce but l'instrument SEIS, composé de deux sismomètres large-bande et courtes périodes. Durant les quatre ans de la mission, ces instruments ont détecté huit impacts de météorites, à des distances allant de 50 à 7500 km d'InSight. Les deux impacts les plus lointains ont formé des cratères de 140 et 150 m de diamètres. Ce sont les plus grands impacts contemporains constatés depuis les débuts de l'exploration spatiale. Quant aux impacts les plus proches, ils présentent une caractéristique unique pour la sismologie martienne : leurs vibrations sismiques sont accompagnées d'un ou plusieurs trains d'onde à basse fréquence, qui correspondent à des ondes de choc atmosphériques couplées avec le sol. Ces signaux mettent donc en évidence la génération d'infrasons et d'ondes sismo-acoustiques par les météores martiens.

Sur la Lune comme sur Mars, ces événements sismiques sont d'une grande importance pour les investigations scientifiques. En effet, leur localisation est dans certains cas connue : celle-ci est obtenue grâce à des impacteurs artificiels sur la Lune, à des images satellites des cratères sur Mars, ou encore en utilisant l'onde de choc associée aux impacts de la planète rouge. Leurs signaux servent alors de calibration pour les modèles sismiques.

Cependant, les signaux d'impacts ne sont pas parfaitement expliqués par les modèles actuels. Un des problèmes majeurs de la sismologie d'impact consiste à relier les caractéristiques d'un cratère ou d'un météore à la magnitude du signal sismique associé. Les modèles existants reposent sur des analogies entre les impacts et les explosions de surface, mais ne prennent pas en compte l'obliquité de l'impact ou son apport de quantité de mouvement. Ainsi, le mécanisme physique décrivant la génération d'ondes sismique par un impact est encore mal compris. De la même manière, les caractéristiques spectrales des signaux d'impacts demeurent inexpliquées. Les spectres en fréquence des événements provenant d'impacts lunaires sont distincts de ceux d'origine tectonique. Les fréquences de coupure diffèrent également entre un impact martien et un impact lunaire. Grâce à la sismologie martienne, de nouvelles études comparatives deviennent possibles. En particulier, des ondes sismo-acoustiques générées par des impacts de météorites ont été observées pour la première fois sur une autre planète. Ces signaux sont le produit de l'interaction d'un choc avec l'atmosphère et le sol de Mars. Ils représentent donc une opportunité unique d'étudier les propriétés de ces deux milieux, et la source des ondes de chocs.

Cette thèse a pour but de mieux comprendre ces signaux d'impacts, et en particulier ceux enregistrés par InSight. Dans une première partie, nous proposons de modéliser la source sismique liée à la formation d'un cratère d'impact. Pour cela, nous élaborons un modèle analytique de la source d'un impact à l'aide du Théorème de Représentation sismique et

de la notion de "stress glut". Un impact est un événement extrême, lors duquel l'impacteur et sa cible subissent une déformation plastique et un transport de masse significatif. Ces phénomènes ne sont pas correctement modélisés par les équations classiques de l'élasticité. Le stress glut est une mesure de la plasticité et de la non-linéarité subie par un matériau se déformant. Ainsi, il permet d'introduire dans les équations élastiques ces effets mécaniques non-linéaires. Suite à nos développements, la source de l'impact peut être vue soit comme un champ étendu de force équivalentes, soit comme une source ponctuelle, combinant un tenseur de moment sismique et une force vectorielle variant dans le temps.

Nous développons une méthode numérique pour calculer le stress glut d'un impact à grande vitesse à partir de simulations numériques basées sur la méthode des éléments finis-discrets (FDEM) implémentée par la Hybrid Optimization Software Suite (HOSS). Cette méthode est appliquée dans le cadre de quatre scénarios d'impacts à  $1000 \text{ m}\cdot\text{s}^{-1}$ , avec différents angles d'incidence. Les résultats de ces simulations permettent de visualiser la région source, c'est-à-dire la région spatiale ayant subi une déformation plastique et un endommagement, et où le stress glut est non nul. Les tenseurs de moment et les forces vectorielles associées sont calculées et décomposées en différents mécanismes de source, comme une explosion, un double-couple ou un dipôle linéaire compensé (CLVD). Nous mettons en évidence une évolution de la source avec l'angle d'incidence : le mécanisme d'un impact vertical est analogue à une explosion, mais celui d'un impact très oblique se rapproche d'un double-couple semblable à une faille sismique.

Nous évaluons ensuite notre modèle de source ponctuelle. De manière générale, un modèle est testé en comparant l'une de ses observables à une solution analytique, numérique ou expérimentale connue. Dans notre cas, le signal sismique simulé par HOSS constitue notre solution numérique, car il incorpore les phénomènes physiques non linéaires de l'impact. Les signaux sismiques générés par notre source ponctuelle, formé d'une force vectorielle et d'un tenseur de moment, constituent donc notre modèle. Afin de pouvoir comparer ces deux signaux à grande distance de la source, nous prolongeons la solution de HOSS via une méthode de couplage avec SPECFEM3D. À 400 m du point d'impact, nous montrons que la source ponctuelle calculée à partir du stress glut reproduit l'amplitude du signal numérique à basse fréquence. Cependant, des différences existent entre les signaux à haute fréquence. Inclure l'extension spatiale de la source dans notre modèle ne suffit pas à expliquer ces divergences. Ainsi, nous postulons que ces différences sont dues à l'approche numérique utilisée : la FDEM introduit des forces non-linéaires supplémentaires et inhabituelles telle que la friction, qui nécessitent d'être incluses dans la définition du stress glut.

Malgré tout, les signaux produits par HOSS et par notre modèle ponctuel présentent des caractéristiques en accord avec les observations lunaires et martiennes. Nous retrouvons ainsi dans les signaux d'impacts martiens et lunaires, et dans nos simulations une relation d'échelle entre le moment sismique et l'impulsion de l'impacteur. De plus, nous mettons en évidence une relation logarithmique entre la taille estimée de la source et l'énergie ou l'impulsion du bolide. Ainsi, notre modèle basé sur le stress glut permet de mieux comprendre les observations d'Apollo et d'InSight.

Dans une seconde partie, nous examinons les signaux sismo-acoustiques observés lors de six impacts martiens. Ces signaux présentent une dispersion normale entre 0.5 et 4 Hz, qui est caractéristique de la propagation d'un infrason dans un guide d'onde atmosphérique. Ce type de guide d'onde est expliqué par les modèles climatiques de la Mars Climate Database (MCD). Il est présent en dessous de 2 km d'altitude à certaines saisons et en particulier la nuit, en raison du refroidissement par radiation de la surface martienne. La source des infrasons est quant à elle moins bien connue, et le blast d'un impact de météorite est comparé dans les études récentes à celui d'une explosion d'énergie équivalente.



Nous proposons d'étudier les propriétés de ces ondes dispersées grâce à un modèle analytique simple. Dans le domaine spectral, l'infrason guidé est le produit d'une source de pression, d'un terme de dispersion, et de termes d'atténuation. La dispersion est calculée à partir d'un modèle discret des vitesses du son et de la densité dans l'atmosphère, via une méthode d'intégration matricielle. L'infrason est ensuite converti en un signal sismique en calculant la compliance élastique du sol en réponse à la pression. Ce modèle est capable de reproduire les caractéristiques principales des signaux sismo-acoustiques martiens. Il possède deux particularités : tout d'abord, les vitesses de groupe du signal dépendent du profil de vitesse sonore dans l'atmosphère. De plus, le rapport des vitesses horizontale et verticales (ratio H/V) du signal sismique est lui sensible au profil de vitesse des ondes S sous InSight. Ces deux propriétés sont mesurables dans les données martiennes.

Par conséquent, nous mettons en place une méthode d'inversion bayésienne afin de dériver le profil atmosphériques et sismiques martiens. Un algorithme d'inversion de Monte Carlo par chaînes de Markov est implémenté et validé sur des données synthétiques. Une première inversion est conduite à partir des mesures de vitesses de groupe martiennes obtenus pour les événements S0981c, S0986c and S1034a. Cette inversion est sensible à la vitesse du son à basse altitude et confirme la présence d'un guide d'onde jusqu'à 500 m d'altitude. Le profil obtenu est en bon accord avec les profils calculés indépendamment par MCD.

Une seconde inversion est menée sur les mesures de ratio H/V combinées de ces trois mêmes événements martiens. L'inversion est sensible aux vitesses des ondes S dans les premiers 50 m de profondeurs, mais est cependant dépendantes des limites a priori choisies pour les paramètres du modèle. Lorsque les limites a priori autorisent de larges variations dans la profondeur des interfaces entre deux couches sismiques, le profil produit par l'inversion présente une transition entre de faibles vitesses sismiques, de 200 à 300  $\text{m}\cdot\text{s}^{-1}$ , vers de plus hautes vitesses sismiques à 40 m de profondeur. En revanche, lorsque les variations de profondeur des interfaces sont restreintes, le modèle le plus probable produit par l'inversion bayésienne présente de hautes vitesses sismiques, près de 2000  $\text{m}\cdot\text{s}^{-1}$  à faible profondeur, suivies d'une diminution des vitesses jusqu'à 150  $\text{m}\cdot\text{s}^{-1}$  to 300  $\text{m}\cdot\text{s}^{-1}$  en dessous de 15 m de profondeur. Ainsi, deux familles principales de modèles apparaissent.

L'existence de deux familles de modèles indique que l'inversion bayésienne manque de contraintes. Les données de ratio H/V mesurée lors de ces trois impacts ne sont pas suffisantes pour trancher entre les deux structures du sous-sol martien. Cependant, les spectres et les ratios H/V correspondant à ces deux familles de modèle diffèrent à haute fréquence. Pour mieux contraindre l'inversion et discriminer entre les deux familles de modèles, il serait nécessaire d'augmenter la plage de fréquence de l'inversion ou de combiner différents types de données de ratio H/V. Alternativement, modéliser le spectre de la source, i.e. le blast d'impact permettrait de déterminer quelle portion du spectre en amplitude est contrôlée par la structure du sous-sol.

En conclusion, notre thèse permet d'éclairer les données sismiques d'impacts martiens et lunaires. Cela est fait dans un premier temps en développant un modèle analytique et numérique de la source sismique d'un cratère d'impact. Dans un deuxième temps, nous étudions un modèle analytique d'infrasons couplés et en déduisons des informations sur la structure de l'atmosphère et du sous-sol de Mars. Pour aller plus loin, nous avons montré la nécessité d'inclure dans nos modèles une physique supplémentaire. Il serait par exemple souhaitable d'inclure l'effet des phénomènes de friction dans le stress glut, et de proposer un modèle numérique de l'ondes de choc et du blast causé par un météore et son impact.





*Pink Hills*, 1937, Georgia O'Keeffe

Private collection.

# Introduction

## 1.1 Meteorites and Meteors

### 1.1.1 Context and definitions

**The fall of a meteor** Meteorites, bolides, meteors, fireballs: these words are often encountered in planetary and Earth sciences. They describe an ensemble of phenomena that follow the approach of a high-velocity object in a colliding course with the surface or atmosphere of a planet or moon. Such objects, whose size ranges from 0.01 mm to tens of meters, are termed *meteoroids* by the International Astronomical Union (IAU), although *meteors* is also often used. We will recall here the definition and origin of various processes related to meteoroids, some of which are illustrated on Fig. 1.1.

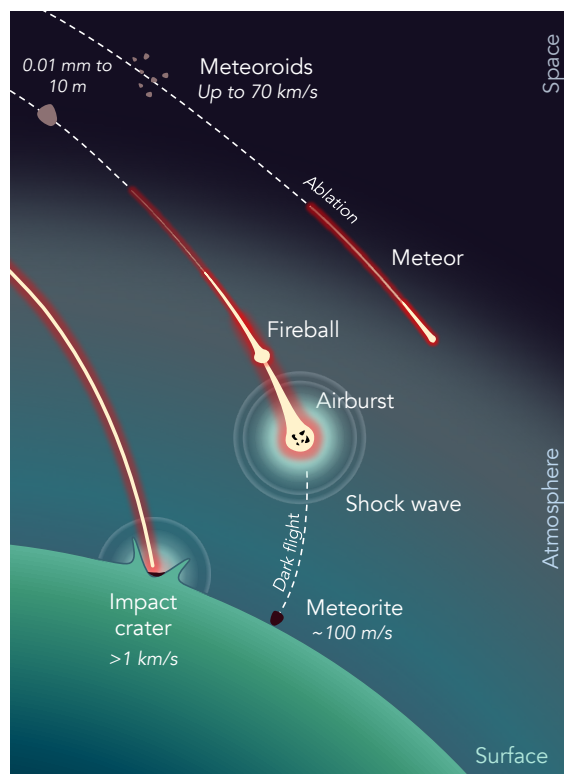


**Figure 1.1:** Terminology of the phenomena associated to meteoroids interacting with Earth, from their entry to their eventual collision if not totally ablated

Meteoroids originate mainly from the asteroid belt, between Mars and Jupiter, and from the trail of comets crossing a planet's orbit. In the solar system, their travel speed is

bounded by the escape velocity from the sun, i.e.  $42 \text{ km}\cdot\text{s}^{-1}$  [Ceplecha et al., 1998]. When considering possible collision geometries, a meteoroid's reaches its maximal velocity relative to a solar system body when travelling in the direction opposite to the impacted body. This maximal velocity is  $72.8 \text{ km}\cdot\text{s}^{-1}$  on the Earth and the Moon [Ceplecha et al., 1998], while it is about  $66 \text{ km}\cdot\text{s}^{-1}$  for Mars. On the other end, collisions at a speed lower than the planet's escape velocity are rare: in such cases, the cosmic object enters into orbit, and might fall only under the effect of atmospheric drag.

On planets with an atmosphere, such as the Earth or Mars, the incoming meteoroid is subject to a phenomenon called *ablation*: due to highly energetic collisions with air molecules in the upper atmosphere, its surface is heated above sublimation temperature, resulting in a loss of mass along its trajectory. The ablated material forms a vapour and plasma cloud in the meteoroid's wake, which radiates visible light and is commonly observed at night: this is the *meteor phenomenon*. Very bright meteors, with apparent magnitude greater than -4, are called *fireballs*, and *bolides* for the brightest ones.

Small meteoroids whose entry velocity exceeds  $30 \text{ km}\cdot\text{s}^{-1}$  lose all of their mass to ablation before they reach the lower atmosphere. Spectacular meteor showers, such as the Perseids in August or the Geminids in December, are composed of such short-lived meteors. However, a meteoroid with a general size between 20 cm and 1 m may pass through the atmosphere while preserving a portion of its initial mass. It is then slowed down progressively by aerodynamic forces until its speed is not sufficient to generate further ablation or heating [Ceplecha et al., 1998].

On Earth, this level of deceleration is reached at a typical altitude of 20 km, when the velocity of a meteoroid drops below 2 to  $4 \text{ km}\cdot\text{s}^{-1}$  [Revelle, 1979]: deceleration continues but light emission stops. During this *dark flight* stage, drag forces eventually bring the meteoroid to a terminal velocity typically lower than  $200 \text{ m}\cdot\text{s}^{-1}$ . At such velocities, it reaches the surface of the Earth without generating a crater and becomes a *meteorite*.

Every year, around 4000 meteorites in the kilogram range are estimated to complete their fall, but only a small portion (10–20) are recovered by meteorite hunters of by chance [Halliday et al., 1984]. This was the case on the night between February 12 and February 13, 2023, when fragments of meteorite 2023 CX1 were found on the coast of Normandy in France, just a few hours after its fireball was observed [Antier & FRIPON/Vigie-ciel, 2023]. In a rare occurrence, the parent body, a near-Earth asteroid, had been detected on its course to Earth before it entered the atmosphere, enabling the organisation of coordinated observation and search campaigns [European Space Agency, 2023].

Most meteorites found on Earth are asteroid fragments. On occasions, material may be ejected from the surface of a large asteroid or planet during a primary impact and become a meteoroid. Hence, meteorites from Mars, the Moon or Vesta [Kelley et al., 2003] have been found on Earth, such as the Zagami meteorite shown on Fig. 1.2.



**Figure 1.2:** Fragment of the  $\sim 18 \text{ kg}$  Zagami meteorite, found in Zagami, Nigeria. This is the largest Martian meteorite (SNC) recovered on Earth. (Picture by the author in 2022).

**The meteorite impact phenomenon** On Mars, terminal velocities are about five times larger than Earth's due to the lower atmospheric density. The kinetic energy of the bolide is thus considerably higher. Similarly, on the Moon and bodies with faint

atmospheres, incoming meteoroids experience little to no deceleration and impact the ground at full speed, with a velocity averaging to  $16.2 \text{ km}\cdot\text{s}^{-1}$  on the Moon [Ivanov, 2001].

The meteoroid and the planet surface are often referred to as the *impactor* and the *target*, respectively. The disruption of the target under impact projects particles at high velocity: this is the *ejecta*. During a hypervelocity impact, the velocity of the impactor is higher than the typical speed of sound in the target : the impacted material enters a shock regime. The stress caused by this shock and the ejection of material below the impactor act together in creating an *impact crater*.

### 1.1.2 The global effect of meteors and meteorites

#### Effects at the solar system scale

Meteorite impacts are a key process in the formation and evolution of the solar system and its bodies. In the late stage of planetary accretion (around 25 Myr to 50 Myr after accretion began), the evolution of planetesimals was dominated by giant collisions [Wetherill, 1985; Agnor, 1999; O'Brien et al., 2006], which induce a significant heating and melting on the planetary surfaces [de Vries et al., 2016] and are also responsible for increasing the eccentricity of planetary orbits and their rotation speed [Dones & Tremaine, 1993]. Today, the dominant theory for the formation of the Moon is the Giant Impact hypothesis, which proposes that the Moon formed from the accretion of debris released during the collision of the proto-Earth with a Mars-size planetesimal, named Theia [Hartmann & Davis, 1975; Cameron & Ward, 1976; Ida et al., 1997]. Long after the formations of planets, impacts are also thought to be responsible for the import of different chemical elements and molecules. Earth and Mars volatile elements such as water may have originated from impacts of comets and water-rich asteroids [Chyba, 1987; Albarède, 2009; Daly & Schultz, 2018].

#### Meteorite impacts as a geologic process

The surfaces of bodies with low tectonic, volcanic and atmospheric activity are covered with craters. This fact was known centuries before Man walked on the Moon, but it took until the middle of the 20<sup>th</sup> century for these craters to finally be attributed to meteorite impacts [Melosh, 1989]. Indeed, large depressions covered by a basaltic floor observed on the lunar surface (called "*maria*") were initially thought to be of volcanic origin [Melosh, 1989].

Although several authors made a link between lunar craters and projectiles during the 19<sup>th</sup> century, the geologist Grove K. Gilbert was the first to propose an explanation of their features (ejecta rays, central mound, variations of morphology with size, etc.) based on the impact process [Gilbert, 1893]. Other authors performed small-scale impact experiments or noted similarities between impact and explosion craters, but the meteoritic origin of lunar craters was not widely accepted until way into the 20<sup>th</sup> century [Shoemaker, 1962].

Similarly, the recognition of the existence of impact cratering on Earth, and its connection with meteor falls was not straightforward. In 1906, Daniel M. Barringer, was interested in the iron deposits found around a 1-mile bowl-shaped crater in Arizona, now named Meteor Crater (Fig. 1.3). The crater had been visited by Gilbert, who dismissed the impact hypothesis, favouring volcanic processes. However, Barringer claimed that Meteor Crater was of impact origin [Barringer, 1905]. Convinced that a large mass of meteoritic iron was still buried below the crater, he invested in the development of a mining company





**Figure 1.3:** Picture of Meteor Crater, Arizona. The crater diameter is approximately 1100 m, with a depth of  $\sim 50$  m below the surrounding plains. The original crater floor was progressively filled with eroded material [Shoemaker, 1963]. The entry to Barringer’s historic mining shafts is visible in the centre (Picture by the author on May 21, 2023).

to exploit the ore. Without success, as it was later understood that the crater had been generated by an impactor whose mass was much smaller than his estimates, most of which was furthermore vaporised and oxidised in the surroundings Meteor Crater. Nevertheless, his effort opened the way for a wider investigation of crater structures around Earth, such that the existence of relatively recent cratering of Earth was progressively accepted. The mechanics of crater formation, both on Earth and on the Moon, was consolidated by Eugene M. Shoemaker, who connected the stratigraphy of craters created by nuclear explosions to the one observed for Meteor Crater, and proposed a scaling of crater dimensions and impact shock parameters based on the impactor energy [Shoemaker, 1959, 1963].

It is now clear that meteorite impacts affect the surface of bodies in the solar system and constitute a unique geologic process. In the absence of atmospheric or subsurface weathering process, craters left by impacts suffer little erosion: this is the case for instance on the Moon or asteroids. On such bodies, surfaces which appear heavily cratered can be considered older than undisturbed ones. Thus, crater counting on solar system bodies constitutes a method for dating their surface, as was applied for example for the Moon and Mars in the works of Hartmann [1965] and Hartmann & Neukum [2001]. This method should however be used with precautions on small bodies with low gravity, where contemporary impactors generate seismic shaking: this effect can destabilise slopes of small craters and be a factor of erosion [Richardson et al., 2020].

Exposed surfaces are progressively damaged by repeated impacts. The successive fracturing of rock and deposit of ejecta forms a porous, unconsolidated layer called *regolith*, that can range from tens of meter to kilometres in depth for *megaregolith*. Very large impacts in the kilometre scale also form vast *basins*, such as the Mare Orientale basin on the Moon, or Hellas Planitia on Mars. Due to the constant resurfacing of material by tectonic and volcanic activity, regolith is not found on Earth. However, meteorite and meteors have affected it long after the accretion and formation of the solar system took place. It is

now accepted that the mass extinction of the Cretaceous-Paleogene, approximately 66 million years ago, followed from a major impact event, which left behind the  $\sim 180$  km wide Chicxulub crater [Schulte et al., 2010] in the gulf of Mexico. Events of such magnitude are of course extremely rare. Still, Earth regularly experiences the effects of small and large meteoroids. Thousands of meteors come across Earth every day, and airburst are common. The shock wave they induce can cause substantial damage if generated sufficiently close to the ground.

Several examples of such recent events exist. The most significant is the Tunguska event, on June 30, 1908 in Siberia. A meteor estimated to be 50 m to 60 m in size disrupted aboveground, causing a major airburst. This explosion was equivalent to 10 megaton to 20 megaton of TNT ( $\sim 5 \times 10^{16}$  J) [Ben-Menahem, 1975; Chyba et al., 1993]. More recently on 15 February 2013, the Chelyabinsk airburst was estimated to be the result of the disruption of a 17 m to 20 m diameter bolide, and is compared to an explosion of  $500 \pm 100$  kilotons of TNT ( $\sim 2 \times 10^{15}$  J) [Brown et al., 2013; Popova et al., 2013]. More precisely, an energy between 1 and 100 kilotons was released continuously from the high atmosphere to about 20 km altitude along the meteor trajectory [Brown et al., 2013]. Fragments of the Chelyabinsk meteorite could be found around its trajectory, but neither the Tunguska nor the Chelyabinsk airburst generated an impact crater. In modern times, a single occurrence of crater formation on Earth was witnessed. This event is known as the Carancas impact, on September 15, 2007 at the border between Bolivia and Peru [Le Pichon et al., 2008; Borovička & Spurný, 2008; Brown et al., 2008]. The collision caused a loud explosion and left a 13.5 m crater in the muddy mountainous terrain.

Coincidentally with the birth of meteor and impact science, the development of seismology and acoustics has led to the recording of multiple meteorite and meteor-generated signals, including during the events mentioned above. This was not only possible on Earth, but also on other bodies with the emergence of planetary exploration. Much is still to be learned on the nature of these signals. In the next section, we will present important concepts of Earth seismology, before introducing planetary seismology on Moon and Mars.

## 1.2 Exploring the solar system using seismology

In the general sense, seismology is the science of perturbations of the solid Earth. Its counterpart, acoustics, focuses on the perturbations propagating in fluids, i.e., ocean, atmospheres, and fluids in industrial or aeronautical settings. We describe here briefly how both sciences can be used to investigate the structure of the Earth and the nature of acoustic and seismic sources, and how their successes lead to the emergence of planetary seismology.

### 1.2.1 History of Earth seismology and acoustics

Seismology was, at its infancy, a science of earthquakes. It became a quantitative discipline in the 19<sup>th</sup> century, in great part thanks to Robert Mallet who attempted to connect seismic motion to the laws of mechanics [Mallet, 1846] developed at this time. Throughout his life, he advocated for the development of instruments to quantify the time history and amplitude of seismic motion. Hence, in 1889, thanks to this continued progress of instrumentation, an earthquake in Japan was recorded for the first time as far as Germany by von Reuber-Paschwitz [Dewey & Byerly, 1969]. This instrumental breakthrough allowed to test the theories of propagation of elastic waves at Earth scale, such as the theory



of surface waves established by Lord Rayleigh [Rayleigh, 1885]. The technology of seismometers, the knowledge of Earth's interior and earthquake mechanisms have progressed continuously since then.

### Technologic and Instrumental progress

A seismometer is, in essence, a mass connected to a solid frame by a system of springs and hinges. Additionally, a damping system prevents the ringing of the mass around the resonance frequency of the spring. In general, this mass is designed to be heavy, so that it stays immobile while the Earth and the seismometer frame move together. The position of the mass then shares a linear relationship with the local displacement of the Earth relative to its inertial reference frame (see e.g., Aki & Richards [2002]). This motion can be recorded by an analog tracing system, for example a stylus attached to the mass and a rolling drum of paper attached to the Earth, although electronic recording systems are now the norm.

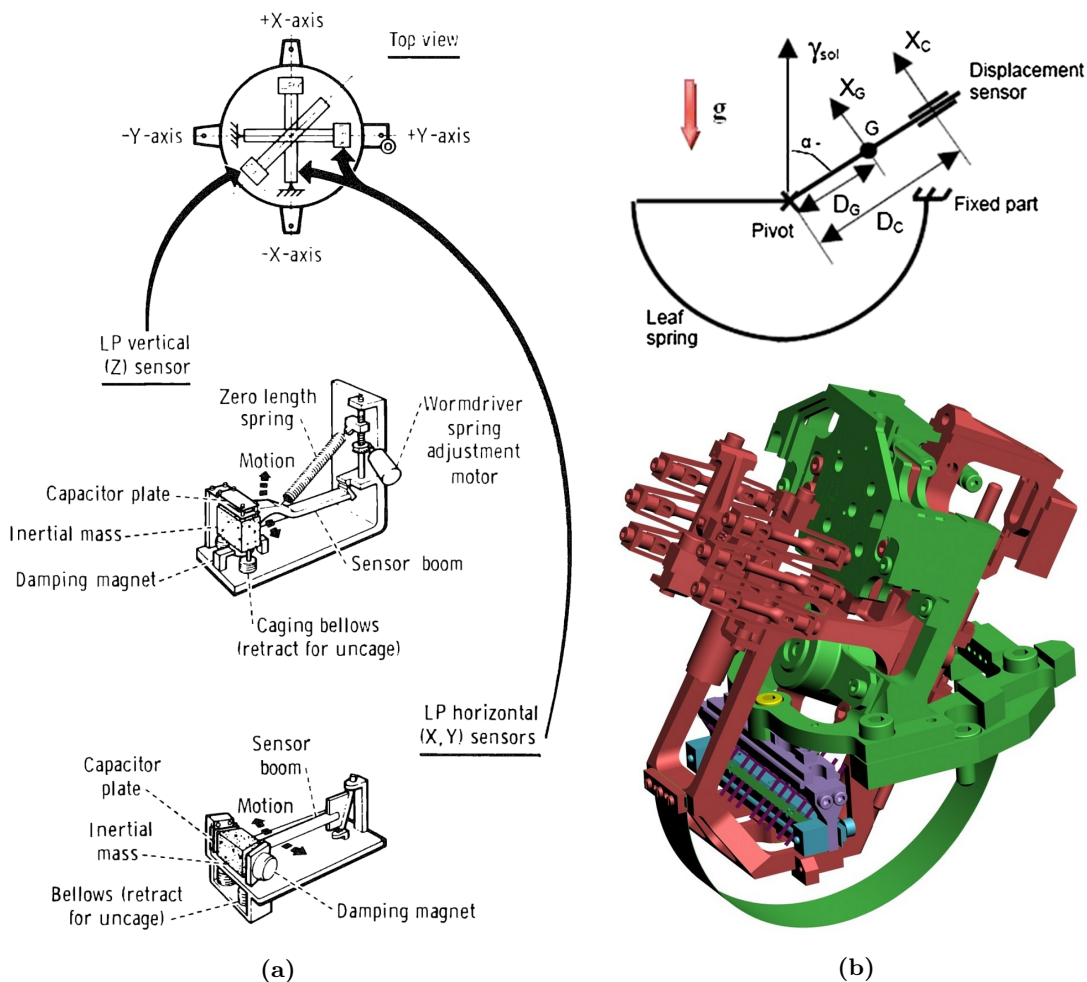


**Figure 1.4:** (a) Schematic representation of a long-period seismometer used on the Moon around 1970 (figure from Latham et al. [1970]). (b, top) Schematic representation of the pendulum and feedback system designed for the VBB seismometer deployed on Mars in 2018 (from Lognonné et al. [2019]). (b, bottom) Computer model of the fixed part (red) and moving part (green) of the VBB inverted pendulum system (from IPGP/David Ducros).

Early seismometers were limited in sensitivity, and their mass was considerable (500 kg to 1000 kg according to Dewey & Byerly [1969]). The recording of long-period seismic motion

in the vertical direction was improved by the zero-length spring invented by LaCoste. His design was implemented in many seismometers of the 20<sup>th</sup> century, including seismometers deployed on the Moon (see section 1.2.2) as schematised on Fig. 1.4a [Latham et al., 1969]. Another system, based on electronic feedback loops, can improve recordings in other directions. The electronic feedback loop maintains the mass fixed with respect to the frame using electromagnetic forces. The voltage output of this feedback loop is then translated into displacements. This technique ensures the linearity of the system and considerably improves the recording of long-period motion. It was for example implemented in the Very Broad-Band (VBB) seismometer of the InSight mission on Mars (see section 1.2.3) [Lognonné et al., 2019], whose pendulum is represented on Fig. 1.4b.

Nowadays, progress in engineering allows to reduce the mass of long-period seismometers to a few kilograms, with a sensitivity of  $10^3$  to  $10^4$  V/(m·s<sup>-1</sup>) between  $10^{-2}$  and 10 Hz achieved for modern broadband instruments (e.g., Franck et al. [2019]). As mentioned above, this enables the transport of seismometer into space. Moreover, seismometers can be rapidly installed to capture aftershock series after major earthquakes, or deployed in the form of arrays to improve source characterisation [Shearer, 2019]. Multiple countries (USA, France, Germany) have funded global networks of seismic sensors in recent decades, and a large part of the world's seismic data is now publicly available through online repositories.

## Seismic investigation of the Earth's interior

Seismology allows to study both the source of seismic waves, and their propagation media. When the characteristics of a seismic source are well known, like its location, amplitude and mechanisms, it is possible to focus on the phenomenon of propagation. Thus, thanks to the deployment of seismometers around the world in the early 20<sup>th</sup>, seismology led to the discovery of the Earth's internal structure. In 1906, British geologist Richard Oldham detected the Earth's fluid outer core from the absence of P- or S- wave in its shadow zone. In 1909, Croatian seismologist Andrija Mohorovičić determined the thickness of the Earth crust by measuring the travel times of direct waves and waves reflected on the crust-mantle discontinuity, now termed "*Moho*". In 1939, Danish geophysicist Inge Lehmann proved the existence of a solid inner core within the liquid core, thus further completing our modern view of the Earth's structure. Further efforts using a combination of surface-wave, normal modes and seismic phase data, have produced the widely-used Preliminary Reference Earth Model (PREM) [Dziewonski & Anderson, 1981], which includes a characterisation of phase transitions and discontinuities in the mantle.

Now, modern seismology enables to investigate the presence of finer 3D structures in the Earth crust and mantle, such as hot convection plumes [Romanowicz & Gung, 2002; Maruyama et al., 2007] and subduction slabs [Fukao et al., 2001]. Controlled sources, such as manmade nuclear explosions whose location is well constrained, can be used to evaluate global seismic models, including the position of the inner core [Wang & Vidale, 2022]. On a smaller scale, explosives or air guns can be positioned around an area of interest to perform exploration seismology experiments. The reflexions of these controlled seismic waves on underground interfaces can be used to draw a profile of the local subsurface, in order to detect anomalies or the presence of specific reservoirs and ores [Sheriff & Geldart, 1995]. Using increasingly large datasets and complex inversion methods, the techniques of seismic tomography and full-waveform inversion allow to determine the origin and ray path of recorded seismic waves and image complex propagation velocity anomalies along their trajectory [Tromp, 2020].

## Source studies

Conversely, if the properties of a region of propagation are sufficiently well known, seismology allows to investigate the characteristics of seismic sources and monitor them. One of the primary goals of seismology is thus to measure seismic hazard, i.e., to determine the potential for earthquakes in a certain area based on its existing faults, and quantify the effects of such earthquakes on human populations and installations. National agencies like the United States Geological Survey (USGS) deploy vast seismometer arrays to continuously monitor seismic activity, and the properties and location of earthquake sources in near real-time (e.g.,s [Herrmann et al., 2011]). This data can then be used to provide earthquake probabilities for a certain region, or inform early-warning systems, such as the Earthquake Early Warning (EEW) provided by the Japan Meteorological Agency [Kamigaichi et al., 2009]. This type of investigation is not limited to classical earthquakes, produced by the rupture of faults in the Earth's interiors. Source seismology may also help investigate the physical processes at play around and below active volcanoes (see e.g. [Kawakatsu & Yamamoto, 2015]).

Finally, constant progress in the technology of seismometers has made possible their deployment on a large scale, allowing for investigation of low-energy sources such as dormant volcanoes, glaciers, geothermal and hydrothermal exploitation areas, and low-yield explosives. In addition, it is used worldwide to monitor human activities and the testing of nuclear weapons in the framework of the Comprehensive Nuclear-Test-Ban Treaty (CTBT) (e.g. [Richards et al., 2021]).

## Acoustics and infrasound waves

The field of acoustics developed in parallel of seismology, initially to understand the propagation of audible sound in the air. By analogy with seismic waves propagating in a solid media, audible sounds are acoustic waves, i.e. pressure perturbations propagating in a fluid media. Their typical frequencies is comprised between 20 Hz and 20 kHz. It was soon understood that *infrasound* waves, a type of acoustic wave with frequency below 20 Hz, are subject to less attenuation in the Earth atmosphere and could propagate over larger distances than waves in the audible frequency range. Indeed, infrasound waves generated by the explosion of the Krakatoa volcano in 1883 [Scott, 1883; Strachey, 1883; Symons, 1888] and the Tunguska meteor in 1908 [Whipple, 1934; Astapowitsch, 1934; Ben-Menahem, 1975] were recorded multiple times on early barometers as they circled the globe. Similar observations were made more recently and with modern instruments during the extreme eruption of the Hunga Tonga-Hunga Ha'apai volcano in the pacific, on January 15, 2022 [Matoza et al., 2022].

Unlike the Earth's interior, the Earth's atmosphere varies on time-scale comparable to the propagation time of infrasounds. Therefore, the ability of acoustic waves to inform on the structure of the atmosphere on the global scale is limited. Instead, infrasonic studies rely on powerful weather data assimilation systems, such as the European Center for Medium-Range Weather Forecasting (ECMWF) in Europe or the National Center for Environmental Prediction (NCEP) in the USA to assess the properties of the media through which acoustic waves propagate. This marks the difference between seismology and acoustics [Le Pichon et al., 2019].

Despite this limitation, the infrasound waves produced by highly energetic events still carry plenty of information. Such sources can be of natural origin, such as storms, lightning, volcanic or meteoritic explosions, and even earthquakes, but also anthropogenic, as

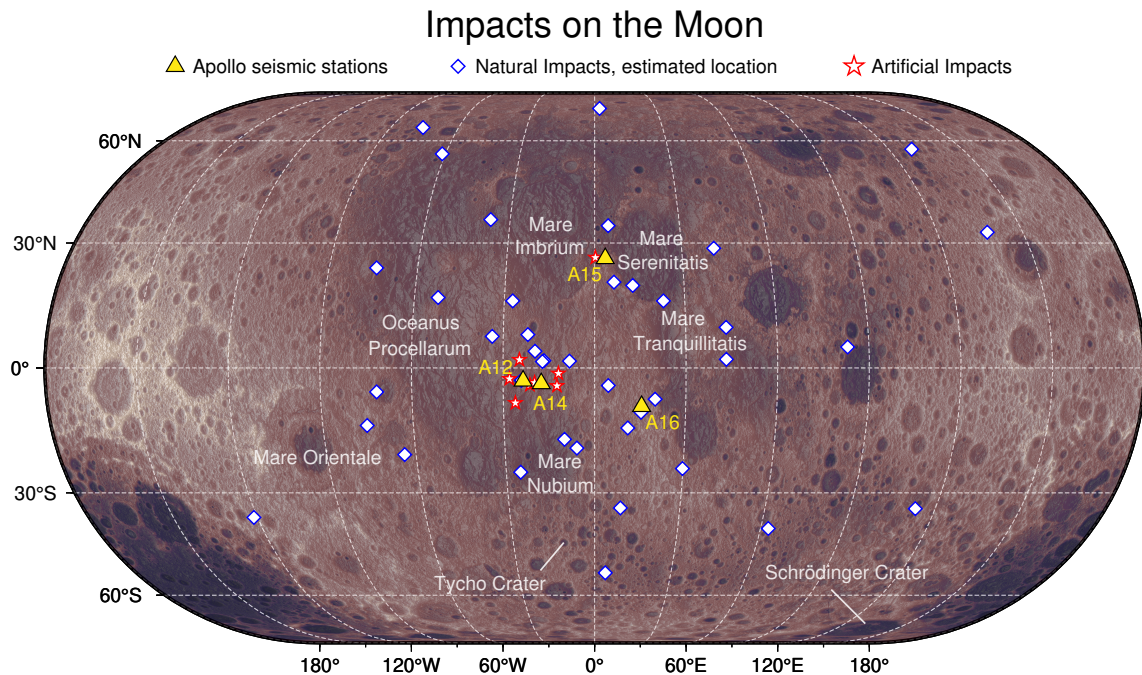


**Figure 1.5:** Map of the Moon showing several major geographic features, its seismic network during the Apollo missions 12 (A12), 14 (A14), 15 (A15) and 16 (A16), and the location (estimated or measured) of some recorded impact events. The map is coloured using the topography produced by the Lunar Orbiter Laser Altimeter (LOLA) [Barker et al., 2016].

for man-made chemical and nuclear explosions, and high speed trains and space vehicle re-entry [Campus & Christie, 2009]. Since the detection of the Krakatoa and Tunguska events, and with the considerable improvement in the understanding of Earth weather evolution and atmospheric dynamics made possible by modern instrumentation and satellites, infrasonic acoustics is now also one of the pillars of explosion monitoring. This effort is supported by an international network of microbarometers, part of the International Monitoring System (IMS) [Christie & Campus, 2009].

### 1.2.2 The beginnings of Planetary Seismology: the Apollo missions

Strengthened by its successes on Earth, seismology was seen as a tool of choice when the exploration of other solar terrestrial solar system bodies became possible. The Moon was the primary objective of such seismic study, with the aim to determine its seismic activity and its internal structure [Press et al., 1960]. In 1969, the Apollo 11 mission of the National Aeronautics and Space Administration (NASA) carried onboard the Passive Seismic Experiment (PSE), composed of a seismometer designed to operate during the lunar day [Latham et al., 1969]. The instrument fulfilled its mission for a duration of 21 days, before its failure on August 27, 1969 [Latham et al., 1970]. Although short, this experiment led to several important discoveries. First, the background seismic noise of the Moon was found to be lower than any site on Earth. In addition, unlike Earth signals which present well-defined arrivals for P and S phases, lunar seismic signals were found to be emergent and longer in duration, with a *coda* of decreasing amplitude following the main arrivals. These distinctions are clear on the seismograms of Fig. 1.6, showing recordings of terrestrial and Lunar quakes with similar source-receiver distances.

Following Apollo 11, 4 other missions carried a seismometer to the Moon. Between 1969 and 1977, a network of four seismometers was active on the lunar surface (Apollo 12



(1969-1977), Apollo 14 (1971 - 1977), Apollo 15 (1971-1977) and Apollo 16 (1972-1977)), represented on Fig. 1.5. A gravimeter was also carried by Apollo 17, whose initial goal was to detect gravitational waves and long period displacements. Even though it suffered from a design issue and could not fulfil this goal, it acted as a one-axis seismometer between March 1, 1976 and September 30, 1977 [Kawamura et al., 2010, 2017]. The data recorded by this network was initially stored on magnetic tapes, before being made available in recent years in a processed digital format on various repositories (the Japan Aerospace Exploration Agency (JAXA) Data ARchives and Transmission System (DARTS), the Incorporated Research Institutions for Seismology (IRIS) and the Planetary Data System (PDS)) [Nagihara et al., 2011; Nunn et al., 2022].

During the period of operation of the Apollo seismometer, a total of 13058 events were recorded [Nakamura et al., 2008]. A significant portion of these events ( $\sim 7100$ ) could be classified as shallow or deep moonquakes of tectonic origin. However, an even larger portion were determined to have impact origin, 9 of them being signals from artificial impacts of man-made spacecrafts, and about 1750 originating from natural meteorite impacts. The estimated location of some of them is shown on Fig. 1.5. We will discuss these important lunar impact signals in more detail in section 1.3.2.

The emergent and scattered nature of lunar seismograms make the identification of P- and S- wave arrival times difficult and limits the number of events that can be used for inversion of subsurface models. Still, the processing of lunar seismic waveforms lead to the possible seismic detection of core phases in studies by Weber et al. [2011] and Garcia et al. [2011], who proposed a preliminary 1D reference model of the Moon. Other studies focused on the crust and mantle of the Moon [Khan & Mosegaard, 2002; Lognonné et al., 2003; Gagnepain-Beyneix et al., 2006], and a recent review of these models by Garcia et al. [2019] reports crustal thickness estimates between 30 and 45 km, consistent mantle

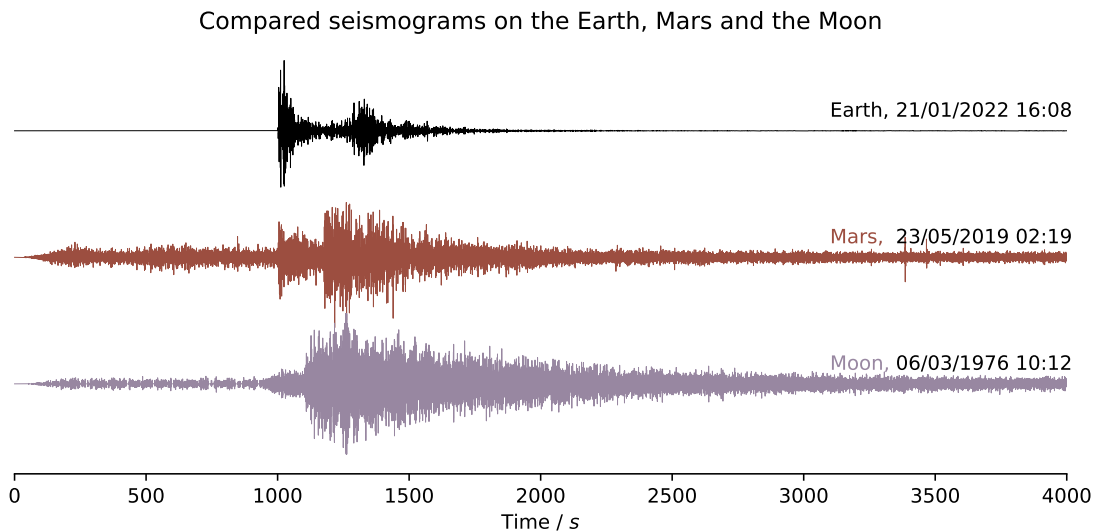


**Figure 1.6:** Comparison of seismograms recorded on the Earth, the Moon and Mars at a similar source-receiver distance of about 1700 km. The Earth event correspond to a magnitude  $M_w = 6.3$  earthquake in the Shikoku region of Japan on January 21, 2022 at 16:08 (UTC), recorded on station BJT in Beijing (1634 km). The represented Martian event is S0173a, a magnitude  $\sim 3.2$  marsquake that occurred in the Cerberus Fossae region (1778 km). The Lunar event correspond to a magnitude  $\sim 2.3$  shallow Moonquake recorded on March 6, 1976 by the Apollo 12 station (1676 km). Seismograms have been corrected for instrument response in velocity. They are aligned on their P-wave arrival, filtered between 0.3 and 1.5 Hz and normalised in amplitude.

velocities of about  $7.7\text{km}\cdot\text{s}^{-1}$  for P waves and  $4.5\text{km}\cdot\text{s}^{-1}$  for S waves up to 1200 m depth. Estimates of the core size are more difficult to achieve and vary between around 330 and 380 km with some uncertainty on the presence and size of a liquid layer [Weber et al., 2011; Garcia et al., 2011]. A recent geophysical study using tidal and thermodynamical constraints finds a solid inner core of radius  $\sim 258$  km [Briaud et al., 2023]. The long-duration, high-frequency coda and emergent phased observed in Lunar seismograms (Fig. 1.6) is itself attributed to the scattering properties of the Lunar crust [Gillet et al., 2017; Onodera et al., 2022] caused by multi-scale heterogeneities of the megaregolith generated by impact fragmentation [Hartmann, 1973; Wiggins et al., 2019].

Further improvement of these lunar seismic models would require events with higher epicentral distance and preferably on the far-side of the Moon. This could not be achieved with the geometry of the Apollo stations, but future missions planned through the NASA Artemis program, the Commercial Lunar Payload Services (CLPS) and the Chinese Lunar Exploration Program might lead to the installation of seismometers on the Lunar South Pole and its far-side. The Farside Seismic Suite (FSS) is planned to land in 2025 in the Lunar Schrödinger crater and deploy a vertical Very BroadBand (VBB) seismometer and three-component Short Period (SP) seismic sensors similar in design to the ones in use by the InSight mission [Panning et al., 2022], which we will now introduce.

### 1.2.3 The InSight mission on Mars

#### Previous seismology missions to Mars

In the years following Apollo, Mars became a high priority target for scientific and geophysical exploration. Indeed, with its thin atmosphere and its 3390 km radius, approximately half of the Earth's, Mars shares more similarity with our planet than the Moon. Its environment is also friendlier to electronic instruments than the Earth's closest cousin, Venus. It therefore makes an ideal target for a comparative the study of terrestrial planets interiors and planetary seismology missions were soon proposed.

In 1976, the Viking missions brought two seismometers to Mars [Anderson et al., 1977]. The instrument onboard Viking 1 failed to deploy after landing, but Viking 2 also carried an SP instrument and operated as intended during 560 martian solar days, known as *sols*. However, the instrument was fixed on the deck of the lander, and imperfectly coupled to the ground by its shock-absorbing legs. This design led to an extreme contamination of the signal by the martian winds, which interacted with the lander and its moving parts. In the absence of independent weather measurements, it was impossible to confirm the seismic origin of some of its recorded events. Note that a very recent re-analysis of Viking data in light of InSight results suggests that two Viking events were in fact marsquakes [Lazarewicz, 2023]. In 1976 however, the study of Viking 2 records led to the important conclusion that if the effect of winds was suppressed, the overall background seismic noise on Mars would be extremely low. In 1996, the Mars 96 mission attempted to follow the steps of Viking 2 [Linkin et al., 1998]. The spacecraft system design was shared between Russia, France and Finland, with instruments from various countries, including a seismometer provided by INSU and IPGP and funded by the French Centre National d'Etudes Spatiales (CNES) [Lognonné et al., 1998]. Unfortunately, the fourth stage of the Proton launcher failed and the probe fell back from Earth orbit.

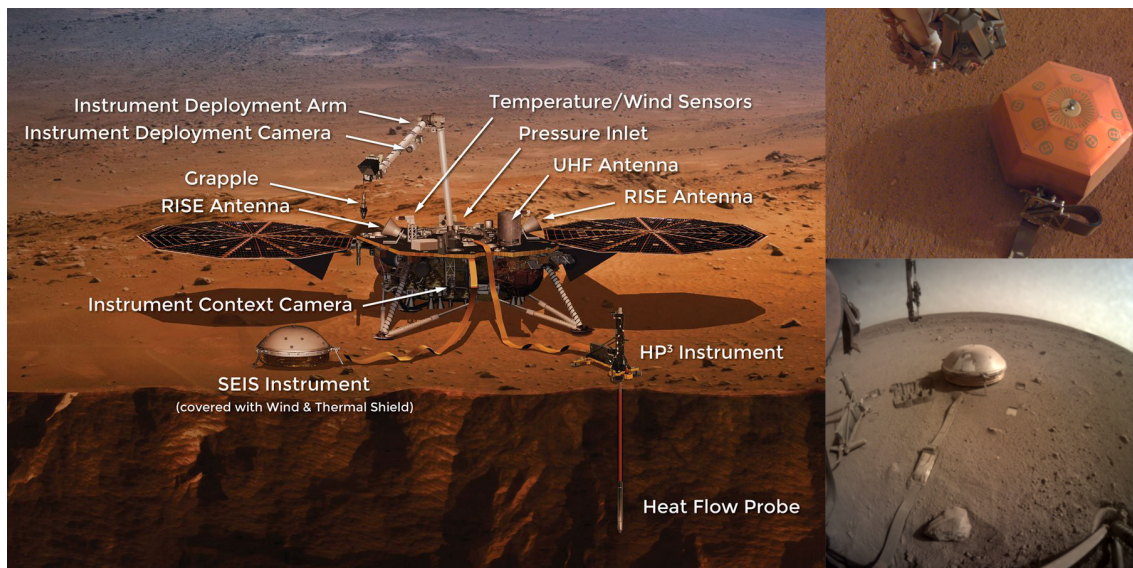


**Figure 1.7:** (Left) Artist view of the InSight lander and its instrument once deployed. (Top right) Picture of the SEIS instrument deployed on the ground on sol 59 of the mission and (bottom right) under its Wind and Thermal Shield (WTS) on sol 1171. The HP<sup>3</sup> probe can be seen on the left of the picture and the robotic arm (IDA) towards the top. All of them are covered with dust. The two images are taken with IDC and ICC cameras of the lander, respectively. Credits: NASA/JPL-Caltech.

### InSight and the SEIS instrument

The NASA Interior Exploration using Seismic Investigations, Geodesy and Heat Transport (InSight) mission landed on Mars on November 26, 2018, in the Elysium Planitia region. InSight carried several geophysics experiments: a heat-flow probe known as the Heat Flow and Physical Properties Package (HP<sup>3</sup>) [Spohn et al., 2018], the Rotation and Interior Structure Experiment (RISE) [Folkner et al., 2018], and the Seismic Experiment for Interior Structure (SEIS) [Lognonné et al., 2019]. The SEIS experiment was composed of a three-component VBB and a three-component SP seismometer, which, for the first time, were deployed directly on the surface of Mars. Building on Viking's experience, the seismometer was also placed below a Wind and Thermal Shield (WTS) to reduce wind interactions. Moreover, its seismic sensors were supported by the Auxiliary Payload Sensor Suite (APSS) [Banfield et al., 2019] which enabled measurement of the environmental seismic noise produced by wind, pressure and magnetic field perturbations. Fig. 1.7 illustrates the mission scientific payload and shows the deployed seismometer.

After a little more than two Martian years of operation, the energy supply of the lander suffered from the accumulation of dust on its solar panels. Scientific instruments were shut down intermittently to save power and prolongate the mission. On December 15, 2022, likely because of battery failure, communications with the probe stopped and the mission officially ended on December 21, 2022.

### Results of the InSight mission

InSight operated on Mars for 1440 sols. It acquired more than 1400 images using two cameras mounted on its robotic arm and below its deck. These cameras and the robotic arm were primarily intended to support the deployment of instruments, but eventually contributed to scientific investigation of the aeolian and mechanical properties of the Mar-



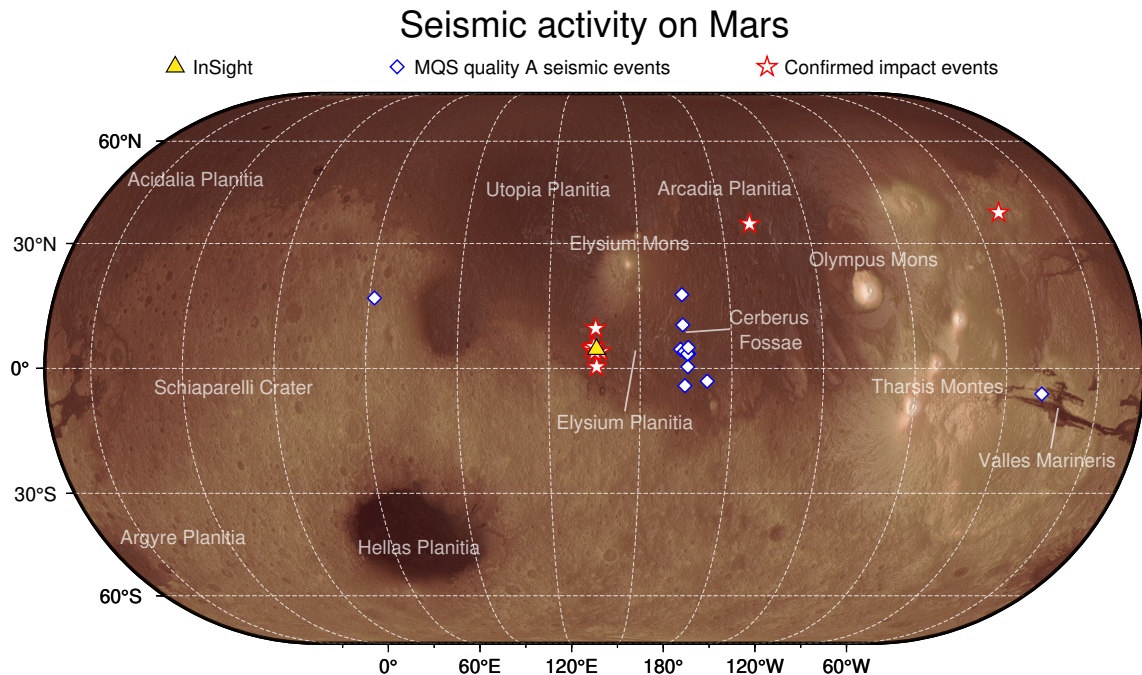


**Figure 1.8:** Map of Mars showing several major geographic features and InSight location in Elysium Planitia. The map is coloured using the topography produced by the Mars Orbiter Laser Altimeter (MOLA) [Neumann et al., 2003]. Impact craters detected seismically by SEIS and with location confirmed by satellite imagery are shown with stars [Garcia et al., 2022; Posiolova et al., 2022]. The estimated epicentres of other significant (MQS quality A) seismic events are shown with diamonds [InSight Marsquake Service, 2023].

tian soil [Golombek et al., 2020, 2023], and to the detection of dust devil tracks in the vicinity of the lander [Perrin et al., 2020; Banerdt et al., 2020]. The APSS instruments proved to be the most complete weather station established on the surface of Mars until now, capturing local as well as regional atmospheric phenomena [Banfield et al., 2020]. In particular, pressure vortices were observed both on APSS pressure sensor and on the SEIS instrument: in fact, atmospheric pressure perturbations between  $\sim 0.1$  Pa to 10 Pa in amplitude coupled to the ground and produced ground displacements above the sensitivity of the seismometer [Lognonné et al., 2020; Kenda et al., 2020; Murdoch et al., 2021].

The HP<sup>3</sup> heat probe failed to penetrate the surface of Mars. However, its dedicated hammering device provided a controlled source of seismic signal for the nearby SEIS instrument. Combined with the seismic recordings of pressure vortices, this data led to the first inversion of InSight near-surface properties [Lognonné et al., 2020]. The P-wave seismic velocity in the first meter from the surface was found to be  $\sim 118 \text{ m}\cdot\text{s}^{-1}$ , consistent with a loose regolith cover.

SEIS recordings confirmed the reduced background seismic noise level evaluated by Viking 2, with values as low as  $2 \times 10^{-10} \text{ m}\cdot\text{s}^{-1}\cdot\text{Hz}^{-1/2}$  at 0.5 Hz [Lognonné et al., 2020]. This noise level varies significantly with the time of day and season, as the seismometer still remains sensitive to winds picking up during the day [Stutzmann et al., 2021]. The best period for marsquake detection turned out to be in the evening of the Martian spring and summer. Resonances are also present in the high-frequency SEIS record, some of which are caused by the excitation of the lander structure by its environment. A particular resonance is present at 2.4 Hz and is excited by seismic events and marsquakes [Dahmen et al., 2021]. It has been proposed that this resonance is a site effect due to the local subsurface structure below InSight [Hobiger et al., 2021].



The first seismic events recorded by SEIS caused surprise once again, due to their differences with typical Earth seismograms. As seen on Fig. 1.6, typical strong Martian events present features found in earthquakes, such as well-defined P and S arrivals, and characteristics of moonquakes, i.e. a strong scattering leading to a long coda [Banerdt et al., 2020]. For distant events, the P and S arrival times can be identified and an estimate of epicentral distance can be provided. However, smaller events show a less clear distinction between ballistic P- and S- phases, and scattering makes difficult the identification of horizontal polarisation, and hence event back-azimuth. This identification was possible so far for 14 events, which were ranked of "quality A": their epicentres is shown on the map of Fig. 1.8 [Giardini et al., 2022]. Among them, 9 were located in Cerberus Fossae, a region about 1700 km east of InSight which was suspected to be tectonically active before landing [Taylor et al., 2013].

Martian events were further classified in families depending on their frequency content. High-Frequency (HF) events present energy predominantly above 2.4 Hz, and Very high Frequency (VF) events exhibit seismic energy beyond 10 Hz. Low Frequency (LF) event on the contrary have most of their energy below 2.4 Hz, while the energy of Broad Band (BB) events spans above and below the 2.4 Hz resonance. The MarsQuake Service (MQS) [InSight Marsquake Service, 2021] assigns a family to events detected in SEIS continuous records and publishes a catalog of arrival picks and location and origin time estimations [Ceylan et al., 2022]. SEIS data are made available through IRIS, the PDS and the IPGP data service.

Analysis of Cerberus Fossae events via the receiver function and autocorrelation methods allowed to derive properties of the Martian crust below the lander. Lognonné et al. [2020] and Knapmeyer-Endrun et al. [2021] found S-wave velocities of  $1.7 \text{ m}\cdot\text{s}^{-1}$  to  $2.1 \text{ m}\cdot\text{s}^{-1}$  in the first two kilometres of the crust, with a first discontinuity in the first 8 km to 11 km of depth and a second one at  $20 \pm 5$  km depth. The existence of a possible third discontinuity at  $39 \pm 8$  km depth could not be excluded by current inversions, leading to an uncertainty in the estimate of the local size of the Martian crust. Teleseismic events recorded later in the mission were used to determine the crustal structure along the source-receiver path. Various studies seem to indicate that the existence of shallower interfaces in the first 50 km of the crust is location-dependent (see e.g., the review by Lognonné et al. [2023]).

The properties of the Martian upper mantle were determined by travel time inversions of various P and S phases. Such inversion methods can add constraints on the geochemical composition or thermodynamic evolution of Mars to converge to realistic  $v_p$  and  $v_s$  profiles [Khan et al., 2021; Drilleau et al., 2022]. Core-diffracted phases  $P_{\text{diff}}$  can also help constrain the deeper mantle properties [Durán et al., 2022]. The mantle shear velocity hence evolves from  $4.3 \text{ km}\cdot\text{s}^{-1}$  to  $4.5 \text{ km}\cdot\text{s}^{-1}$  in the upper mantle, decreases in the medium mantle, before reaching values of  $4.8 \text{ km}\cdot\text{s}^{-1}$  to  $5.0 \text{ km}\cdot\text{s}^{-1}$  at the mantle base with a possible mineral phase transition close to  $\sim 1000$  km depth (see e.g. Lognonné et al. [2023] for a more in-depth presentation of these models). In the same way, core-reflected phase (PcP, ScS, etc.) can be used to constrain the core radius. Stähler et al. [2021] estimate it with ScS phases at a  $1830 \pm 40$  km radius. More recent studies suggest that the core might be smaller [Irving et al., 2023], and enriched in light elements.

Some of the strongest seismic events of the InSight mission occurred by the end of the mission. Events S1000a and S1094b, with magnitudes of  $\sim 4.0$ , were detected on September 19, 2021 and December 24, 2021, respectively. Event S1000a marks the first detection of seismic surface waves during the InSight mission, suggesting a shallow source [Kim et al., 2022]. Subsequently, independent satellite imagery allowed to associate S1000a and S1094b to two large and freshly formed impact craters in the Amazonis Planitia and

Tempe Terra regions. At the same time, several peculiar VF events had been identified in SEIS records and could be associated to smaller, nearby impacts craters. Both sets of events provided scientists with an exact source-receiver distance, which in turn allowed to confirm the validity of the seismic models for P and S waves travel times [Garcia et al., 2022; Posiolova et al., 2022].

On both the Lunar and Martian missions, events of impact origin were detected and possibly localised. These events were of great importance for seismic investigation, as they were used as constrained sources in Lunar inversions, and provided measurements of teleseismic surface waves on Mars. In the following sections, such recordings of meteor and impact-generated seismic signals on Earth, the Moon and Mars will be described in more details.

### 1.3 Meteorite seismic signals

#### 1.3.1 Observations on Earth

As mentioned in section 1.1.2, energetic impacts, and therefore impact-generated seismic signals, are extremely rare on Earth. However, airbursts and meteor shock waves have been frequently detected by seismometers by way of seismo-acoustic coupling. In such cases, the shock wave acts as a pressure forcing on the ground, which induces ground motion and possibly generates long-range seismic waves.

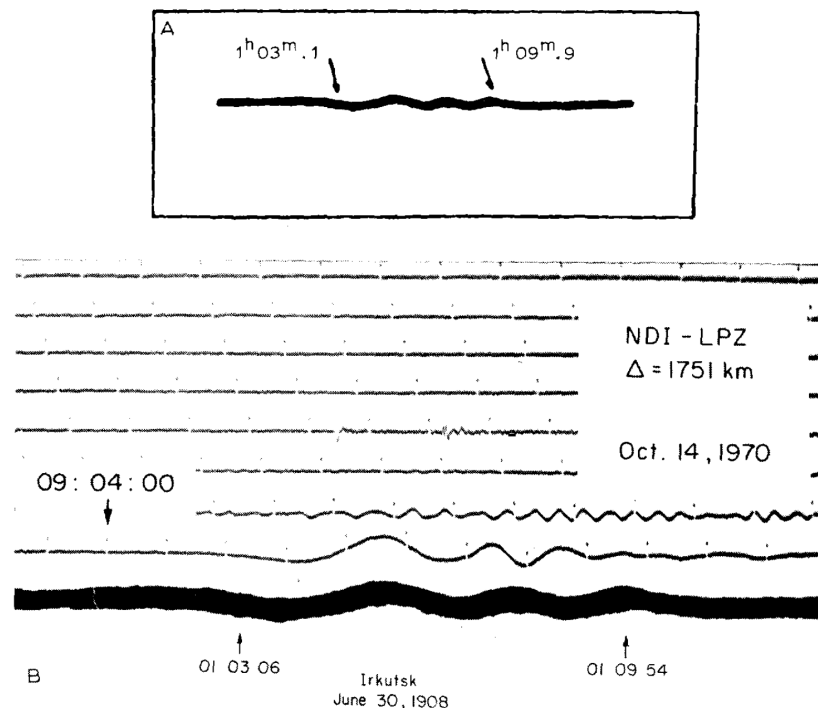


**Figure 1.9:** Comparison between the low frequency seismic signal recorded on a seismic station at Irkutsk (thick black lines, A and B, period of  $\sim 190$  s), Russia on June 30, 1908, and a signal recorded after an atmospheric explosion on October 14, 1970, in Lop-Nor, China (thin lines, B, period of 100s to 150s). The arrival times and fundamental periods of the Irkutsk signal are consistent with a source at Tunguska, similar to an explosion in the atmosphere. Figure reproduced from Ben-Menahem [1975].

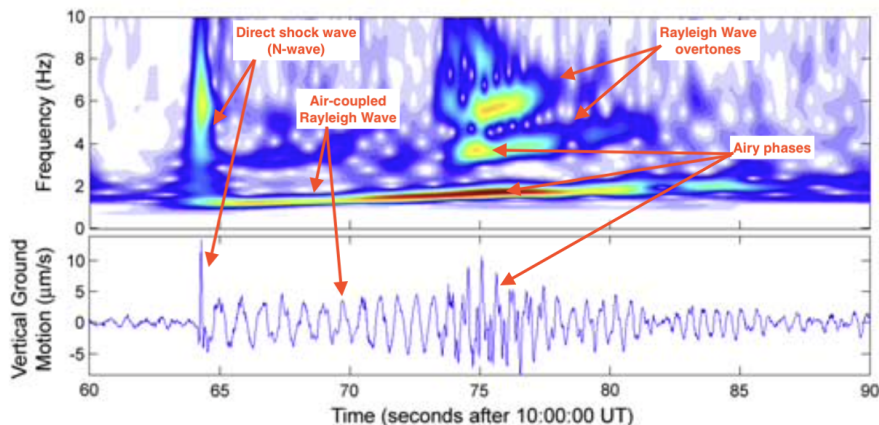


**Figure 1.10:** Spectrogram (top) and time series (bottom) of the vertical seismic ground velocity recorded during the Stardust capsule entry. The different arrivals are marked with arrows. Reproduced from [Edwards et al. \[2007\]](#), with added annotations.

Hence, following the Tunguska event, [Ben-Menahem \[1975\]](#) noted the similarities in shape and period between low-frequency ground motion recorded at Irkutsk, 973 km away from Tunguska’s airburst location, and the seismograms following an atmospheric explosion in China (see Fig. 1.9). This signal originates from the shock wave of the airburst, which excited normal modes of the atmosphere, and propagated from the source to the receiver at Irkutsk where its effect on the ground was recorded. During the Chelyabinsk airburst, W-shaped waveforms, characteristic of the conversion of a shock wave into a seismic velocity signal, were also recorded on the ARU station at 246 km from the event [[Tauzin et al., 2013](#)]. [Tauzin et al.](#) propose two possible origins for this signal: the Mach cone, i.e. the shock wave around the meteor trajectory, or the disruption of Chelyabinsk’ meteorite. Due to the lack of other nearby instruments, the directivity of the signal could not be determined with precision, and the two options remain possible. But directly below the meteor, the interaction of the powerful shock with the ground also generated air-coupled Rayleigh waves, which traveled from the shocked region to dozens of stations in Europe and Asia [[Tauzin et al., 2013](#)]. The moment magnitude of the atmospheric source associated to the meteor could be determined from an inversion of these air-coupled Rayleigh waves, and is equivalent to a  $M_w = 3.5 - 4.0$  explosion in the atmosphere [[Karakostas et al., 2018](#)]

The 2007 Carancas impact, mentioned in section 1.1.2, is the only case on Earth where acoustic and seismic waves were recorded following a crater-forming event [[Le Pichon et al., 2008](#); [Borovička & Spurný, 2008](#); [Brown et al., 2008](#)]. The signals produced by this impact were recorded on two infrasound stations of the IMS, I08BO at 80 km and I41PY at 1617 km from the crater, but also by several seismic stations of the Bolivian network, between 50 and 150 km distance (BBOD, BBOE, BBOK, LPAZ). [Tancredi et al. \[2009\]](#) analysed these seismic signals and reported the detection of crustal guided Pg and Sg waves, as well as seismic surface waves on station BBOD, associated to the impact. However, other authors conclude that the subsequent arrivals recorded on infrasound and seismic stations are likely coming from the meteor Mach cone, rather than from the impact itself. [[Gainville et al., 2017](#)] showed that most geometrical arrivals at seismic stations BBOD, BBOE and BBOK can be explained by rays coming from the trajectory and propagating through the troposphere or stratosphere. Therefore, there is currently no model explaining the recorded acoustic signal by a blast wave emitted at the crater location.

With the densification of seismic networks around the world and the improvement of detection methods at the beginning of the 21<sup>st</sup> century, the recording of coupled acoustic

waves from the flight of meteors has become increasingly common. Other notable examples are the detection of Rayleigh waves from a meteor falling over Canada in 1987 [Anglin & Haddon, 1987], or a bolide in 2003 over Arkansas [Langston, 2004].

To better understand this type of signals, ReVelle & Edwards [2007] and Edwards et al. [2007] analysed the re-entry of the Stardust spacecraft on January 15, 2006, returning with samples of cosmic dust and dust from comet Wild-2. An array of four microbarometers and two colocated seismometers was installed close to the end of the expected trajectory of the capsule. The first arrivals on acoustic sensors are "N-shaped" pressure signals, with a frequency of around 6 Hz: they are the direct arrival of the meteor Mach cones. Correspondingly, seismic velocity waveforms show a W-shape signal, which is the ground conversion of a N-wave in pressure. On seismometers, the shock-wave pulse is followed by a dispersed signal, typical of an air-coupled Rayleigh wave with frequency between 1.25 and 2 Hz, and by higher-frequency late arrivals, consistent with an Airy phase of several Rayleigh wave overtones (illustrated on Fig 1.10).

Following this work, similar multi-instrument experiments were conducted during the re-entry of the Hayabusa-1 and Hayabusa-2 capsules (JAXA) on June 13, 2010 and December 5, 2020 respectively, returning samples from the 25143 Itokawa and Ryugu asteroids [Yamamoto et al., 2011; Ishihara et al., 2012; Sansom et al., 2022]. Again, the shock wave signature was captured by seismometers.

Such controlled experiment, however, cannot fully reproduce the behaviour of real meteoroids. In many cases, such as Chelyabinsk or Carancas, questions on the nature and origin of observed signals remain. The densification of seismic and acoustic networks will surely help in the characterisation of future meteor entries on Earth.

### 1.3.2 Seismic detection of impacts on the Moon

In 1960, in an article entitled *A Lunar Seismic Experiment*, Press et al. [1960] presented the interest and feasibility of a seismic study of the Moon. They identify meteorite impacts as a potential source of signal, although a lot of uncertainty remains on the exact flux of meteoroids on the Moon, their efficiency at generating seismic signal, and whether propagation effects on the Moon would make these signals exploitable. Because of the similarities between impact and explosive craters, already noted by Eugene M. Shoemaker during its doctoral study of Meteor Crater, Arizona [Shoemaker, 1959], Press et al. [1960] chose to model potential meteoritic seismic signals on the Moon with scaling laws published in the literature for explosions. They stated the challenge of identifying such signals in the records of a potential Lunar seismometer:

*"The problem of separating meteoritic impacts from moonquakes arises, a task comparable to that of distinguishing earthquakes from nuclear explosions. The separation may be feasible if meteoritic impacts are comparable to surface explosions which excite seismic waves with signatures different from quake generated waves; If meteoritic impacts are similar to buried explosions, the problem is more difficult."*

A later study by Laster & Press [1968] attempted to improve estimates of the number of "audible" meteorite impacts by using updated meteorite statistics communicated by E. M. Shoemaker. They suggest that between 100 to 1000 events with recordable P waves could be captured on the Moon assuming a low seismic attenuation.

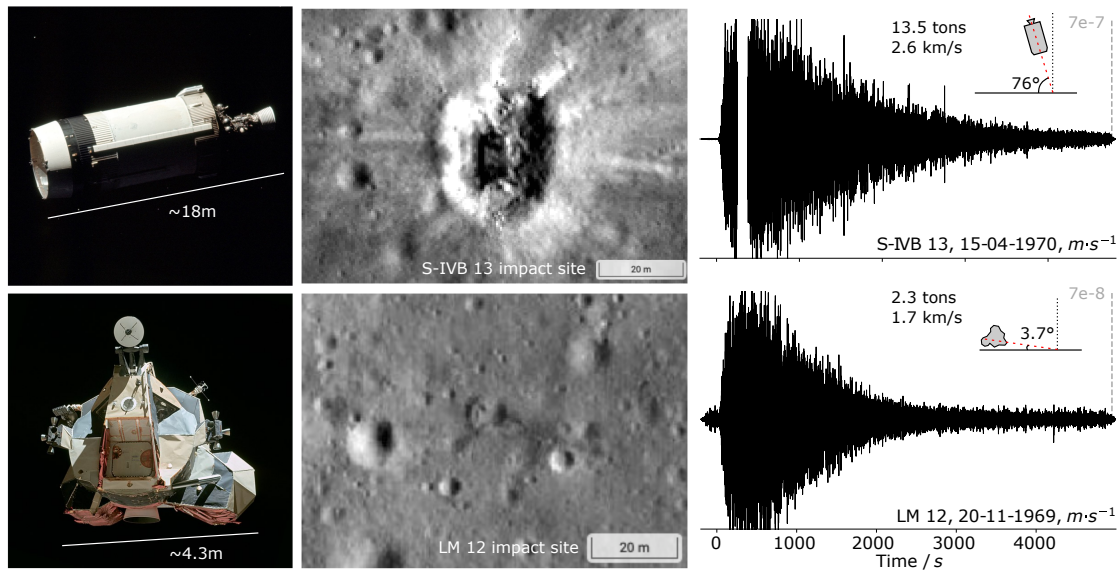


**Figure 1.11:** (Left) Pictures of the S-IVB booster and LM ascent module used as impactors for the Apollo artificial impact experiments. Lunar Reconnaissance Orbiter images of the crater left by S-IVB 13 [Plescia et al., 2016] and LM 12 [Stooke & Marcus, 2019] are shown in the centre. Their vertical component of the velocity signal recorded by Apollo 12 seismometer at  $4.4^\circ$  ( $135\text{ km}$ ) and  $2.4^\circ$  ( $73\text{ km}$ ) distance, respectively, are shown on the right. Note the order of magnitude difference in velocity amplitude of the signals. A graphic shows the geometry and parameters of each impact [Plescia et al., 2016; Toksöz et al., 1974].

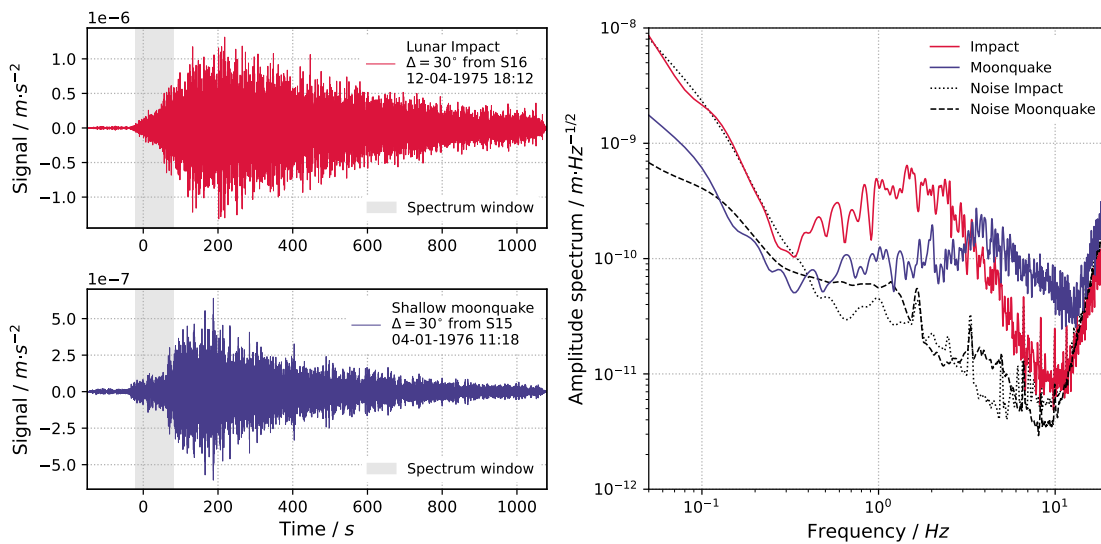


**Figure 1.12:** (Left) Vertical acceleration signal recorded by Apollo Short Period seismometers for a natural Lunar impact (top) and a shallow moonquake (bottom) both at an approximate epicentral distance of  $\sim 30^\circ$ . The signal has been filtered between 1 and 3 Hz. (Right) Amplitude spectrum of these events, combining the data of the Long Period and Short Period sensors following the method of Kawamura et al. [2017], using the 100 s time window shown on the left. The noise is computed by averaging the spectra of several same-length windows before the event. The impact spectrum shows a lower corner frequency and a stronger roll-off at high frequencies than the shallow moonquake.



To support the Apollo PSE and further understand the coupling between meteorites and seismic waves, McGarr et al. [1969] conducted a laboratory experiment at the Ames Research Center, in which projectiles were shot at high velocity in a target monitored by accelerometers. Their results highlight the high dependence of the produced seismic signal to the target properties, and suggest that between a dozen and a couple hundred meteorite impacts could be recorded within 1000 km of a seismic station for a Lunar surface similar to bonded or unconsolidated sand. More importantly, they also suggest that the impact of the empty S-IVB stage of the Saturn rocket, a couple hundreds kilometres away from the Apollo landing site, would carry a sufficient impulse to be detectable by a Lunar seismometer. Such experiment would be invaluable for the understanding of Lunar seismic signals, as it would provide a seismic event with a known origin time and location. This idea was strongly supported by [Latham et al., 1969] and the experiment was planned for Apollo 12.

Shortly after the landing of Apollo 11 and 12, Latham et al. [1970] reported on the first results of the PSE. The seismometers were active during the fall of the Apollo 12 Lunar Module (LM) ascent stage, 73 km away from station 12 and captured its signal. The authors noted the similarities in terms of temporal and spectral features between this signal and previously recorded events part of the "*L events*" family, which were recorded independently from any human activities on the Moon. Hence, it was strongly suspected that most of the L events recorded by Apollo 11 and in the first days of Apollo 12 were in fact meteorite impacts, akin in their physics to the artificial impact of the LM. Soon after this initial report, Latham et al. [1970] completed their analysis of artificial impacts following the impact of the Apollo 13 Saturn Booster (S-IVB) on April 15, 1970 at 135 km distance. The spacecrafts, their craters and their associated seismic signals are represented on Fig. 1.11. Again, the Apollo 13 impact signals resembled other L events, further consolidating the hypothesis that meteorite impacts compose a large part of the Apollo seismic records. Artificial impacts experiments were reproduced with the Apollo 14, 15, 16 and 17 missions.

Hence, on the Moon, the artificial impact experiments were instrumental in discriminating this type of source from other seismogenic processes. Contrary to Press et al. [1960] assumption, due to the specificities of Lunar seismic signals, discriminants used on Earth for earthquakes and explosions were not applicable to the Moon. In addition to helping with the discrimination of PSE signals, these impacts were also used as controlled sources in a wide region mostly around the Apollo 12 and 14 stations (Fig. 1.5), enabling a characterisation of impact seismic source [Onodera et al., 2021] and lunar scattering [Lognonné et al., 2009; Gudkova et al., 2011].

### 1.3.3 Seismic detection of impacts on Mars

In the years preceding the InSight mission, several studies inquired on the seismic detectability of meteorite impacts on Mars. Before the planned Mars 96 departure, Davis [1993] made an estimate of the expected seismic signal based of the Apollo PSE results. He compiled previous studies of the meteoroid flux on Mars and drew the following conclusions:

- Due to its closer proximity with the asteroid belt, the flux of meteoroid on Mars is higher than on the Earth and Moon.
- However, the entry velocity of meteoroids is reduced by about one quarter, with values of  $\sim 11 \text{ km}\cdot\text{s}^{-1}$  on Mars compared to  $\sim 16 \text{ km}\cdot\text{s}^{-1}$  on the Moon.

- Moreover, for identical entry velocities, the Martian atmospheric deceleration reduces the impact detectability compared to the Moon.

Upon estimating and multiplying these various factors, Davis concluded that the number of detectable impacts on Mars should still not be very different than on the Moon for a seismometer with Apollo sensitivity, with between 3 and 4 impacts detected every day. However, he emphasised the high degree of uncertainty present at each step of his approach.

One of the most critical data in estimating the number of detectable impacts is the estimate of the impact rate on Mars. Thank to the advances made in imaging the Martian surface at the beginning of the 21<sup>st</sup> century, it has become possible to update this estimate based on crater counting. [Teanyby & Wookey \[2011\]](#) used the cratering isochron calculated by [Hartmann \[2005\]](#) to evaluate the number of craters of a certain diameter formed over one year on Mars. By use of scaling laws, this number was related to the kinetic energy of the incoming impactor, and converted to a seismic energy using a *seismic efficiency* factor, as proposed by [McGarr et al. \[1969\]](#). Based on a representative Mars internal model including attenuation, their estimate of detectable impacts is considerably lower than [\[Davis, 1993\]](#), with only 1 impact detectable at teleseismic distances every 10 years. Later, [Teanyby \[2015\]](#) updated this prediction by including smaller impacts, which would be detectable at shorter distances from a Martian station. They predict between 0.1 to 30 detectable regional impacts per year. A study by [Schmerr et al. \[2019\]](#), making use of seismic waveform modelling, agrees with this prediction. Finally, [Lognonné & Johnson \[2015\]](#) took into account the non-uniformity of cratering on Mars surface according to the model of [Lefeuvre & Wieczorek \[2008\]](#). A Monte Carlo simulation is used to determine the number of detectable impacts within a certain momentum range, yielding about ten impact events with an amplitude larger than  $3 \times 10^9 \text{ m}\cdot\text{s}^{-2}$  every year.

Following these detectability studies, and as the InSight mission approached its landing, a global modeling and benchmarking study was conducted by [Daubar et al. \[2018\]](#) to further predict the characteristics of impact-generated seismic signals on Mars. A list of seismic discriminators for impacts was proposed:

- *First Motion*: The initial displacement carried by the P wave should be positive, corresponding to a compressive pulse.
- *S-wave energy*: By analogy with explosive events, impacts should produce more compressive (P) than shear (S) motion.
- *Magnitude ratio*: In a similar way, the magnitude computed from body waves and surface waves should have a different ratio for an impact compared to a tectonic event.
- *Frequency content*: By analogy with lunar seismograms, the spectrum of an impact seismic signal should present different features than a quake seismogram, including an increase in power at 1 Hz to 2 Hz and a smaller cut-off frequency.
- *Depth phases*: Due to the shallow location of the source, an impact seismic signal should contain depth phases corresponding to reflexions of P waves on crustal interfaces.

Based on these discriminators, mission scientists proposed a protocol in order to image every potential impact event identified in SEIS records. For each seismic detection, a request would be sent to orbital imagers with a target location, so that the exact crater size and epicentral distance could be measured.

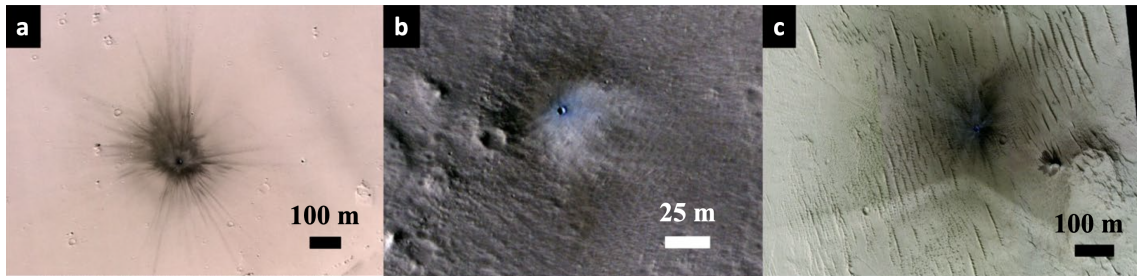


**Figure 1.13:** Examples of albedo disturbances found around fresh craters by the HiRISE color camera. (a) shows dark linear rays departing from the central crater, (b) displays a crater surrounded by a dark halo, and (c) shows a halo and some arcuate rays, also called *scimitars*, in the up-range direction from the impactor trajectory. Reproduced from Daubar et al. [2022].

Like on the Moon, the reality of Martian seismology challenged scientist expectations. As mentioned earlier, Martian seismograms display significant scattering and sometimes unclear P and S wave arrivals. This invalidates the *First Motion* criterion and makes measurements of the S wave energy or depth phases difficult. For the major part of the InSight mission, no surface waves were recorded, which voids the *Magnitude ratio* criterion. Finally, Mars seismic events exhibit a great range of frequency content, from LFs to VFs. As LF events are associated primarily with the tectonics of Cerberus Fossae, a discrimination based on cutoff frequency alone is ineffective. Once again, as on the Moon, pre-landing discriminators did not allow to identify impacts on Mars. Therefore, a different approach was chosen, which consisted in inspecting recent images from orbital imagers, in the hope of capturing a freshly formed crater.

At the time of the InSight mission, Mars was circled by several satellites. Among them, the Mars Reconnaissance Orbiter (MRO) [McEwen et al., 2007; Malin et al., 2007; Bell III et al., 2009], Mars Express [Neukum & Jaumann, 2004], the ExoMars Trace Gas Orbiter (TGO) [Thomas et al., 2017] are equipped with cameras of various resolutions in the visible spectrum, pointed at the ground. The northern hemisphere of Mars is to a great extent covered by dust, which can be displaced by surface events. This displacement results in an albedo change that can be captured by imagers. As an example, albedo disturbances caused by dust devils were observed by the HiRISE camera onboard MRO in the vicinity of the InSight landing site [Banerdt et al., 2020]. More importantly, Martian impacts also leave albedo disturbances, larger than the crater itself and detectable from space. Hence, fresh craters have been recorded over the years by cameras such as the Context camera (CTX) and HiRISE [Burleigh et al., 2012; Daubar et al., 2022], examples of which can be seen on Fig. 1.13. The date of formation of a crater can be constrained to within a few months to a few years in areas that have been imaged before and after the impact.

On April 6, 2019, the CTX camera detected an albedo feature consistent with a fresh impact dust disturbance, and not present on the latest image taken on February 21. The higher resolution HiRISE camera confirmed that a 1.5 m diameter crater had formed at  $\sim 40$  km from InSight. During the time-period constrained by CTX, only three events had been identified by MQS: S0085a, S0105a and S0116a. Unfortunately, none of these three events showed more than one feature (such as estimated distance, signal duration) in agreement with the location and size of the crater. It was concluded that this impact event might have generated a signal too low to be detectable, or that its signal was hidden within the noisy period of the Martian day [Daubar et al., 2020]. The impact discriminators were re-evaluated.

The year 2021 marked the arrival of several other spacecraft on Mars. The Perseverance rover landed on February 18, 2021 in Jezero Crater, at a distance of  $\approx 3500$  km from



InSight. The spacecraft Entry, Descent and Landing (EDL) system comprises two 77 kg tungsten devices called Cruise Mass Balance Devices (CMBD), which are jettisoned at high velocity in the upper atmosphere. These masses were predicted to impact the ground with a velocity close to  $4.0 \text{ km}\cdot\text{s}^{-1}$  and produce two craters. If detected, their impact would provide an information similar to the artificial impacts on the Moon, and a point of calibration for the discrimination of impact seismic signals on SEIS records. The signal amplitude of such impact was modelled using different techniques, including the stress glut method that will be discussed in Chapter 2 of this manuscript. The predicted signal amplitude spanned several order of magnitudes, with only a few of the models in favour of detectability by SEIS [Fernando et al., 2021]. Observations made on the day of landing showed no identifiable signal, thus providing an upper bound for the numerical value of the seismic efficiency of Martian impacts [Fernando et al., 2022].

The Zhurong rover, part of the Tianwen-1 mission of the Chinese National Space Administration (CNSA), landed on May 14, 2021,  $\approx 1900 \text{ km}$  from InSight, offering another opportunity to record signals from an artificial high-velocity object on Mars. Monitoring its EDL sequence with SEIS proved difficult due to the uncertainty of the landing time and target landing location. Moreover, because Zhurong's EDL sequence started from orbit, the velocity of any spacecraft hardware would be lower than for Perseverance. Eventually, the final landing time coincided with the high-noise level period of the Martian day at InSight location [Fernando et al., 2021]. As expected, again no identifiable signal was received by SEIS.

In the following months, SEIS recorded hundreds of new seismic events, but the existence of impact seismic signals in these records remained unclear. Then, in 2020 and 2021, on sols 533, 793, 981, and 986, 1034 and 1160 of the InSight mission [Garcia et al., 2022; Daubar et al., 2023], the SEIS instrument captured six peculiar events. These events exhibit the typical characteristics of the Very-high Frequency (VF) family of marsquakes, with seismic energy above 2.4 Hz and up to 10 Hz and higher. This VF energy shows a sharp onset in time, with the arrival of a crustal guided P-wave (Pg) and shortly after a guided S-wave (Sg), both followed by a decaying coda with a duration of several minutes, as can be seen on the spectrograms of Fig. 1.14. However, between 250 and 1200 s after the energy onset, these events also present one or several short low frequency (0.4 Hz to 4 Hz) wave trains. Most of them appear to be normally dispersed, i.e., with low frequency energy arriving before high frequency energy. These arrivals, also called "*Chirps*", are indicated with *C1*, *C2* and *C3* marks on Fig. 1.14.

These late dispersed arrivals are in agreements with simulation of infrasound propagating in a low-altitude atmospheric waveguide. Garcia et al. [2017] showed that such waveguide exist on Mars at nighttime, when the radiative cooling of the Martian surface generates a positive gradient of temperature with altitude. Waves trapped in a waveguide experience less geometric attenuation, and are therefore detectable over large distances from their source. In particular, meteor or meteorite infrasound generated within the waveguide, i.e. at less than a few kilometres altitude, could be recorded by InSight. This hypothesis prompted further analysis of the six VF events. The good quality and signal to noise ratio of the Martian chirp signals allowed to compute their polarisation in the horizontal plane, and to subsequently determine the azimuth of a possible crater, while the time delay between Pg-, Sg- and strongest acoustic arrivals was used to determine its distance. The CTX camera was then pointed toward these locations and confirmed the presence of fresh impact craters, with formation time window consistent with InSight recorded signals. High-resolution images and locations of these craters are shown on Fig. 1.15. Some of the dispersed signals, which we will discuss more in detail in Chapter 3, can be further analysed

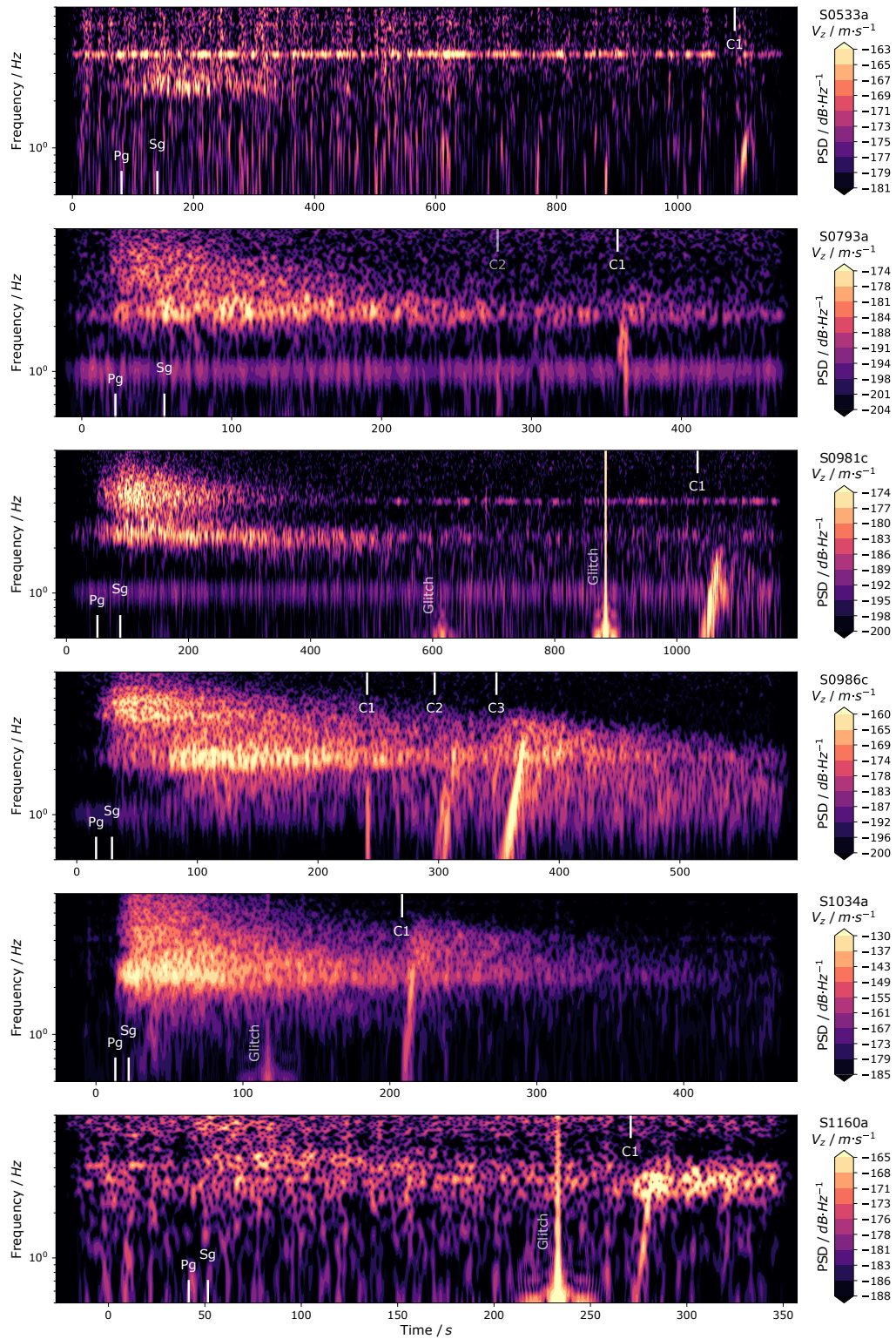


**Figure 1.14:** Spectrograms of impact-generated seismic events comprising "chirps" recorded during the InSight mission. Time is counted starting from the event origin time, in seconds. The arrivals of  $P_g$ -,  $S_g$ - waves and the dispersed seismo-acoustic arrivals are denoted by the letters  $P_g$ ,  $S_g$  (bottom) and  $CN$  (top), respectively, with timings from version 14 of the MQS catalog [InSight Marsquake Service, 2023]. For event S0793a, one additional arrival, marked  $C_2$ , is suggested to be the coupled air-wave of the meteor [Raphaël Garcia, *personal communication*]. Other low-frequency impulsive arrivals, such as at 600 and 900 s on S0981c, are glitches.



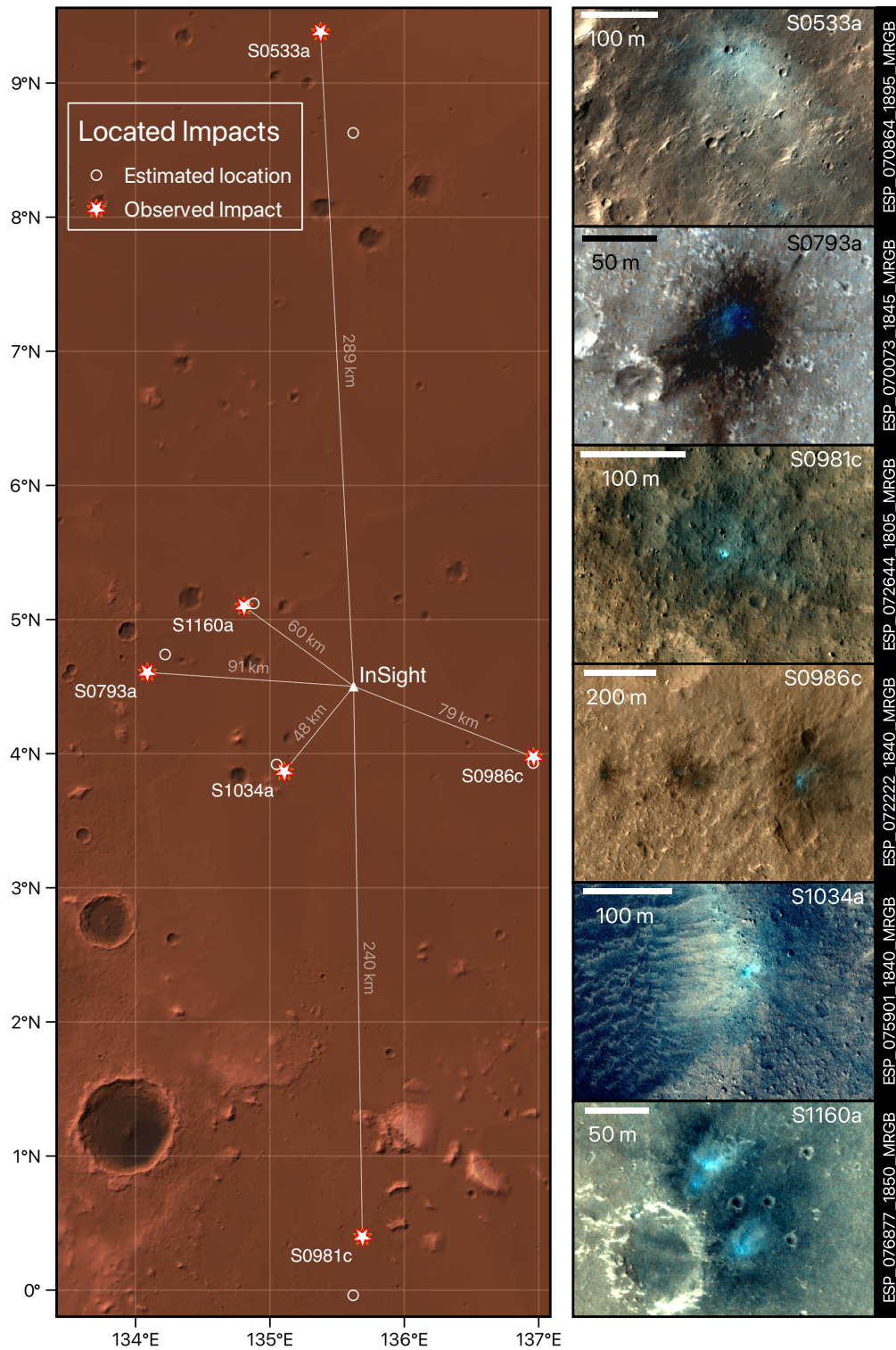


**Figure 1.15:** Map and images of all impacts detected seismically near InSight (300 km). The left plot shows the topography around InSight, extracted from MOLA/HRSC blended Digital Elevation Models [Ferguson et al., 2018]. The locations of impacts predicted from seismo-acoustic data are shown with circles, and the location of actual craters are shown with stars. Close-up views of these craters by the HiRISE imager [McEwen et al., 2007] (with enhanced colours) are shown on the right.

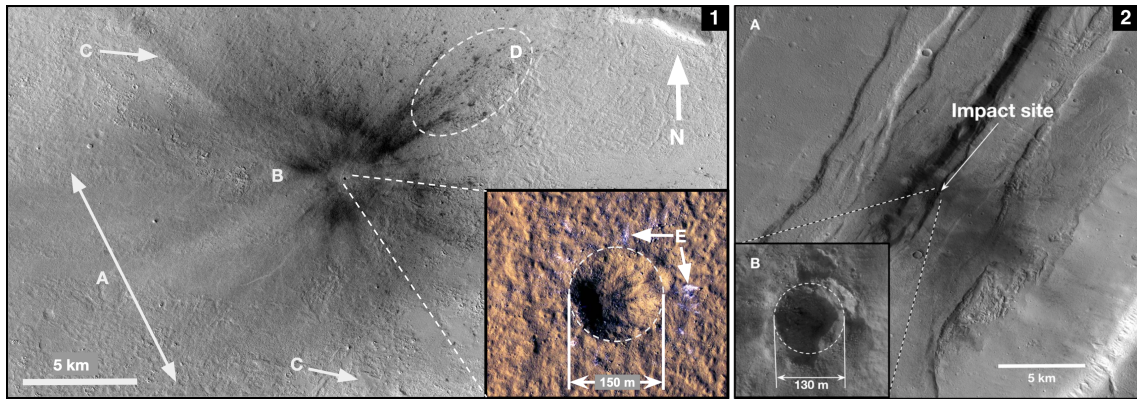


**Figure 1.16:** (1) CTX and HiRISE images of the impact crater associated to S1094b in Amazonis Planitia. The impactor came from the southwest with an azimuth of  $\sim 60^\circ$ . Regions A, B and C (arcuate rays) are thought to be albedo changes and dust lifting caused by the impactor shock wave. In region D and further downrange from the impact point, crater ejecta disturbed the surface. The close-up view of the crater shows water ice (E) excavated from the ground. (2) Impact crater associated to S1000a in Tempe Terra. The crater has formed on the side of a graben wall and surface features are less clear. Adapted from Posiolova et al. [2022], see main text and supplementary material for more details on these images.

to provide a detailed scenario of the associated meteoroid impact. Their observation was the first unambiguous detection of an impact seismic signal on Mars [Garcia et al., 2022].

In early 2022, the CTX camera, performing routine imaging of the Amazonis Planitia region, captured an albedo disturbance extending over more than 40 km, surrounding a  $\sim 150$  m diameter crater. The disturbed region was so large that they were visible on images of the MARCI camera, with has a low resolution but takes daily images of the planet. Hence, the formation time of this crater could be constrained to within a day on December 24, 2021. A second large crater was later discovered in the Tempe Terra region, and could also be constrained by MARCI to have formed on September 19, 2021. Images of both craters and their description can be found on Fig. 1.16. Due to the unprecedented size of these craters, MQS event detection catalog were immediately examined by Liliya Posiolova, a researcher at the Malin Space Science Systems and member of the InSight Science Team, who found that two of the largest events of the InSight mission, belonging to the BB family and with magnitude  $\sim 4.0$ , had occurred on the very same days. Events S1000a and S1094b mentioned earlier were therefore the second types of impact event and the very largest detected in SEIS records, this time thanks to orbital imaging [Posiolova et al., 2022]. The signal and spectrum of S1094b is compared to the largest non-impact marsquake, S1222a, on Fig. 1.17.

To this day, a total of 8 impacts events have been detected seismically and located on Mars [Daubar et al., 2023]. Their locations are represented on Fig. 1.8 alongside the quality A seismic events. The story of their discovery once again shows that early assumptions on their seismic signal did not suffice in identifying them: external information from orbital imaging and acoustics was needed to settle the question.

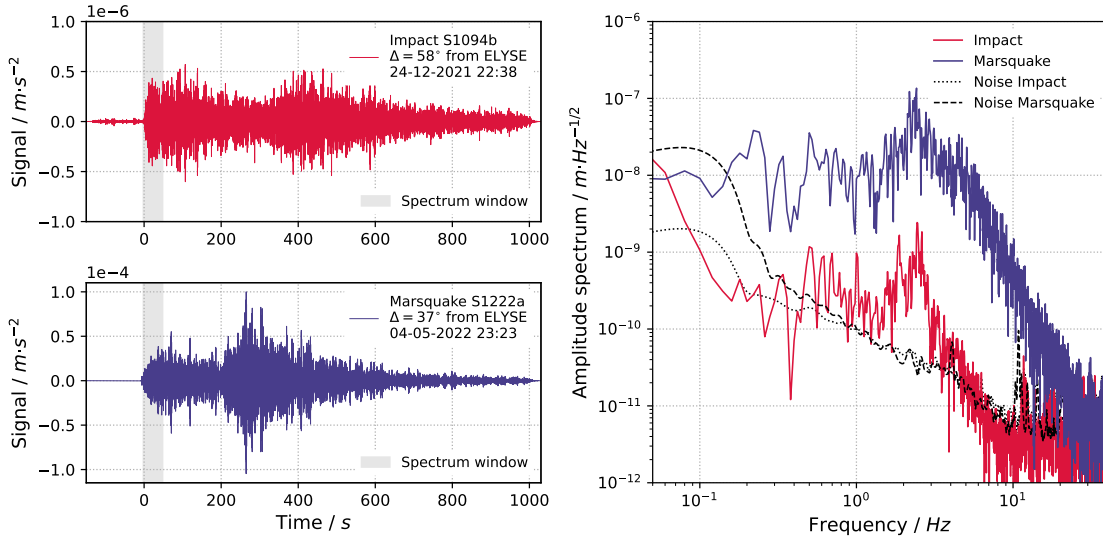


**Figure 1.17:** (Left) Vertical acceleration signal recorded by SEIS for impact S1094b (top) and marsquake 1222a (bottom) [Kawamura et al., 2023]. The signal has been filtered between 0.4 and 2 Hz. (Right) Amplitude spectrum of these events, computed with the 50 s time window shown on the left. The noise is computed by averaging the spectra of several same-length windows before the event. For Martian impact events, differences between frequency spectra are less marked than for Lunar ones (Fig. 1.12), the larger epicentral distance of these events making the interpretation of the high-frequency spectrum difficult due to attenuation effects.

## 1.4 Aim of this work

### 1.4.1 Identified questions of impact seismology

The observations of impact-generated seismic and seismo-acoustic signals on the Moon and Mars raise a number of questions. We have seen from the results of Martian and Lunar seismic experiments that impact events, both natural and artificial, are of tremendous importance to scientific investigations. They excite seismic waves at randomly distributed locations, over a wide distance range and, if crater coordinates are known, they provide a calibration for seismic models. However, we showed that impact signals challenge previous expectations and models.

For example, the discovery that Martian impact events can have a high-frequency or broad-band energy content, in particular extending above 2.4 Hz, challenges one of the observation made on the Moon, where the corner frequency measured for impact events is found between 1 and 2 Hz [Gudkova et al., 2015]. During the InSight mission, 70 VF events were recorded, including the six mentioned above. As I am writing, 59 have sufficiently clear P and S arrivals, allowing for a distance calculation. Following the discovery of InSight impact events, a study investigates the possibility that distant VF events, which do not present any chirp arrivals, could also originate from meteorite impacts [Zenhäusern et al., 2023] (*Preprint*). To test this hypothesis, an estimated crater size is associated to these VF events using scaling laws. The associated size-frequency distribution is checked against the current Martian crater isochrons. No contradiction between the crater-based curves and the VF-based curves is found. In other words, previous Martian crater statistics do not preclude the possibility that some, if not all of InSight VF events have an impact origin, and that additional impact events could be hiding in the current catalog of VF events. However, a definitive conclusion requires further inquiries into the way impacts



generate seismic signals. *Should Martian craters in the 3 m to 30 m diameter range really produce seismic signals of the VF family?*

In the same manner, moonquakes were shown to have a different frequency content than impact events. On Fig. 1.12, the spectrum and signal of a shallow Moonquake is compared to that of an event classified as impact. The spectrum of the impact event shows a lower frequency content compared to the shallow moonquake, with an increase in the spectrum amplitude around its corner frequency and a sharper roll-off beyond. This difference suggests that the generation of seismic waves by impacts and moonquakes is very distinct in nature. Hence, another questions of impact seismology could be: *Which factors influence the frequency content of impact-generated seismic signals?*

Another important observation was the absence of detectable signal during the impact of Perseverance EDL balance devices, or after the discovery of a 1.5 m diameter crater only 37 km away from InSight. As shown in above, one of the major factors in the detectability is the seismic efficiency of impact, i.e., the amplitude of the seismic signal produced by an impactor with certain parameters. The following question is raised: *How can we predict the magnitude of the seismic source for different impact sizes, taking into account the target material properties?*

Many authors have made the case that impacts-generated seismic signals are akin to those of explosions [Press et al., 1960; Lognonné et al., 1994]. Other authors preferred to model them as an impulse on a surface [McGarr et al., 1969]. Recordings of the Moon and Mars confirm that typical tectonic quakes and impacts present different features, but the nature of their mechanism has not yet been elucidated. Therefore, *what physical process, or source mechanism best models seismic waves generated by impacts?*

Finally, seismo-acoustic waves have proved to be an important component of short-distance impact signals recorded by InSight. Thus, the interaction of meteors and impactors with a planetary atmosphere is another process that requires a better understanding. The signals recorded on Mars represent a unique opportunity to study the complex interaction of a shock wave, the Martian atmospheric structure and the ground near the excited seismometer. *What do impact-generated seismo-acoustic signals tell us about meteorite shock wave generation? How do such shock waves interact with the atmosphere and ground in their path?*

Answers to these questions are needed to prepare future exploration of the solar system. Several missions involving planetary seismology have been planned in the future. The FSS mission mentioned above will certainly expand the Lunar impact catalog started during the Apollo era [Panning et al., 2022]. The DragonFly mission is planned to launch in 2027 and land on Saturn's moon Titan in 2034 and will carry a deployable seismometer and geophones [Lorenz et al., 2019; Barnes et al., 2021; Panning et al., 2020]. Although the dense atmosphere of Titan protects its from impact cratering [Korycansky & Zahnle, 2005], meteors shock waves could still constitute a source of seismic signal, as on Mars. Finally, impact experiments have been a key component of several asteroid exploration missions. In 2019, the Hayabusa-2 mission on asteroid 162173 Ryugu launched a 2 kg impactor on the surface in order to uncover some subsurface material [Arakawa et al., 2020]. In September 2022, the Double Asteroid Redirection Test (DART) mission, the first demonstration of such planetary defense method, successfully changed the orbit of asteroid Didymos around Dimorphos by crashing its 579 kg spacecraft at  $\sim 6.2 \text{ km}\cdot\text{s}^{-1}$  on its surface [Cheng et al., 2023]. Controlled impacts on asteroids have become technically feasible, and in the future could help investigate the interiors of asteroids. A better prediction of impact and meteor effects, and their seismic and acoustic detectability, is desired to support planned and proposed missions.

Finally, understanding meteor and meteorite processes is important for the Earth, where encounters with energetic meteoroids are rare but have significant effects. Improving our knowledge of meteor and impactor-generated seismic signals will help understand the characteristics of objects involved in the Carancas, Chelyabinsk or Tunguska events and their associated hazard, and any future events that will likely be recorded as the density of deployed infrasound and seismic networks increases. These questions are driving the following study.

### 1.4.2 Structure of this work

To answer the above questions, the present study aims at improving our understanding of the process of seismic wave generation by meteorites and meteors, our main motivation being the new observations of the InSight mission on Mars.

Explaining the frequency content and amplitude of Martian seismic signals calls for a new interpretation of their seismic source. In a first stage, this requires to model the process of seismic wave generation by impact cratering. This problem constitutes the first part of this study.

In Chapter 2, we present the notion of seismic source and the challenges of modelling complex physical processes like impacts. For the impact problem, a novel, exhaustive representation of the seismic source is made possible by combining the stress glut theory introduced by [Backus & Mulcahy \[1976\]](#) and numerical simulation of hypervelocity impacts. We present the development of a semi-analytical model of the impact seismic source using the seismic Representation Theorem. The non-linear phenomena occurring during the cratering process (mass advection, material plasticity, etc.) give rise to equivalent forces, which compose the source as viewed by seismologists. Concurrently, we develop and test a numerical model to measure these forces thanks to hydrocode impact simulations, and apply this method to several  $1000 \text{ m}\cdot\text{s}^{-1}$  impacts with various incidence angles. Through this method, an exhaustive interpretation of the impact seismic source mechanism and magnitude is made possible.

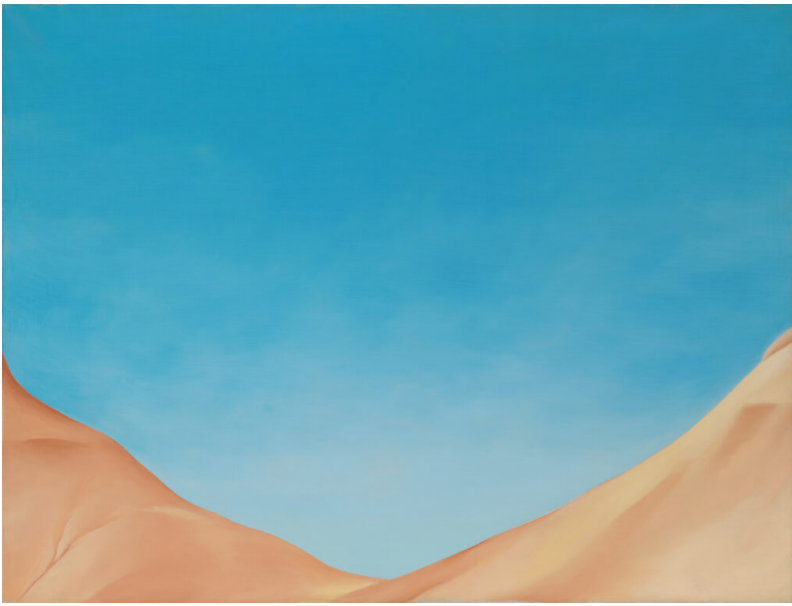
The observation of impact-generated seismo-acoustic signals is another important result of the InSight mission. [Garcia et al. \[2022\]](#) have showed that the properties of the atmosphere enabled the propagation of impact shock waves as guided infrasound. The ground properties at InSight location made their detection by seismic methods possible. Both the atmospheric propagation and the air-to-ground coupling are key processes which need to be understood to correctly interpret these seismic signals.

In Chapter 3, we represent InSight seismo-acoustic signals with a 1D analytical model of the propagation and coupling of guided infrasound. Thanks to this model, we show that information on the structure of the atmosphere and near-subsurface can be obtained from two measurable properties of the impact signals. Based on three of the InSight events, we perform a Bayesian inversion of the sound speed profile and the shear wave velocity below InSight. Our results are in agreement with other models of the Martian atmosphere, and support the use of impact seismo-acoustic data in combination with other InSight data to better discriminate between different models of the subsurface.

We conclude this manuscript with an inquiry into the other source processes at play during the meteor phenomena. We show that the numerical methods presented in Chapter 2 and the data and models of Chapter 3 enable a new way of studying impact blast waves and their seismic effects.







*Red Hills and Sky*, 1945, Georgia O'Keeffe

Georgia O'Keeffe Museum.

# The impact cratering seismic source

---

### Summary of the Chapter

This chapter presents the development of a new semi-analytical model of the impact cratering seismic source. The proposed model does not use any *a priori* assumptions on the mechanism of the source, such as the analogy between an impact and an impulse or an explosion. Instead, the source is defined directly from the equations of motion, and its terms can be calculated from a physics based numerical simulation of the impact process. We present the analytical development of the source model, and the construction and verification of a numerical method allowing to calculate the source terms from an impact simulation. The results shed light on the mechanism of the cratering source and its variations for oblique or vertical impacts.

We begin this chapter with an introduction of the notion of seismic source, and motivate this study by presenting the current knowledge of the impact cratering process, and the advantages brought by numerical modelling.

The main body of this chapter takes the form of an article, currently in review by *Geophysical Journal International*. The content of the article corresponds to the first submitted version. Note that substantial changes to the body and structure of the article were made after major revisions. After the conclusion of this article, we present one additional recent result, which quantifies the effects of impactor incidence angle on the impact seismic source mechanism. Two published articles, to which I contributed, are appended to this chapter. They present the development of a numerical model of impacts in Martian regolith, and the first analysis of the source of large impact events S1094b and S1000a on Mars.

### Related publications

- Froment, M., Lognonné, P., Larmat, C., Lei, Z., Rougier, E., Kawamura, T.. Numerical modeling of impact seismic sources using the stress glut theory. *In revision for GJI, 2023*.
- Froment, M., Rougier, E., Larmat, C., Lei, Z., Euser, B. et al. Lagrangian-based Simulations of Hypervelocity Impact Experiments on Mars Regolith Proxy. *Geophysical Research Letters*, 47(13), July 2020. doi: 10.1029/2020GL087393.
- Posiolova, L.V., Lognonné, P., Banerdt, W.B., Clinton, J., Collins, G.S. et al. Largest recent impact craters on Mars: Orbital imaging and surface seismic co-investigation. *Science*, pages 1–5, October 2022. doi: 10.1126/science.abq7704.

---

## Contents of the chapter

<b>2.1</b>	<b>General Introduction</b>	<b>33</b>
2.1.1	The notion of seismic source . . . . .	33
2.1.2	Numerical modelling of impacts . . . . .	37
2.1.3	The cratering process . . . . .	39
<b>2.2</b>	<b>Introduction</b>	<b>42</b>
<b>2.3</b>	<b>The Representation Theorem applied to impacts</b>	<b>45</b>
2.3.1	Representation of seismic sources . . . . .	45
2.3.2	Point-source of an impact . . . . .	47
2.3.3	Towards a more detailed source model . . . . .	52
<b>2.4</b>	<b>Numerical method and verification</b>	<b>53</b>
2.4.1	Numerical modeling of meteorite impacts . . . . .	53
2.4.2	Seismic source computation . . . . .	55
2.4.3	Verification - Software coupling . . . . .	58
<b>2.5</b>	<b>Results</b>	<b>61</b>
2.5.1	Source of a vertical and an oblique impact . . . . .	61
2.5.2	Verification of the point-source . . . . .	71
2.5.3	Simulating an extended source . . . . .	73
2.5.4	Towards Lunar and Martian data . . . . .	77
<b>2.6</b>	<b>Discussion</b>	<b>82</b>
<b>2.7</b>	<b>Conclusion</b>	<b>85</b>
<b>2.8</b>	<b>Additional Results</b>	<b>87</b>
	<b>Appendices</b>	<b>89</b>
A1	Equations of motion with surface mass losses . . . . .	89
A2	Representation of a seismic wavefield in a volume with constant mass . . . . .	90
A3	Representation Theorem for a variable-mass system . . . . .	91
A4	Stress Glut on a self-gravitating, rotating planet . . . . .	93
	<b>Supplementary Information</b>	<b>94</b>
SI-1	HOSS material models . . . . .	95
SI-2	Stress glut computation - single element test . . . . .	95
SI-3	Mesh test for seismic source computation . . . . .	100
SI-4	Fit of HOSS force and moment source time functions . . . . .	105
SI-5	Point source and coupled signals . . . . .	105

---

## 2.1 General Introduction

### 2.1.1 The notion of seismic source

#### History of seismic source representation

Theories on the origin of earthquakes have existed before seismology was made a quantitative science. The first phenomenological understanding of earthquake seismic sources appeared in the late 19<sup>th</sup> century, when it was accepted that earthquakes occur near faults and volcanoes. By the early 20<sup>th</sup> century, following some particularly large earthquakes in California and the work of H. F. Reid, the seismology community developed the idea that some earthquakes were caused by a build-up and sudden release of stress along faults. The main issue was then to relate the source mechanics to the seismic signals observed at a distance [Agnew, 2002].

Early propositions represented the source as system of forces, while alternative studies assumed the source to be a displacement discontinuity in an otherwise continuous elastic media. Burridge & Knopoff proved in 1964 that these representation are in fact equivalent, and that a displacement discontinuity along a fault surface has the same elastic effect as two couples of forces exerted parallel and perpendicular to it. Such *double couple* model is represented on Fig. 2.1. This is a fundamental concept of source seismology: any permanent displacement within the Earth can be associated to an equivalent system of forces applied to maintain this same permanent displacement in the elastic media.

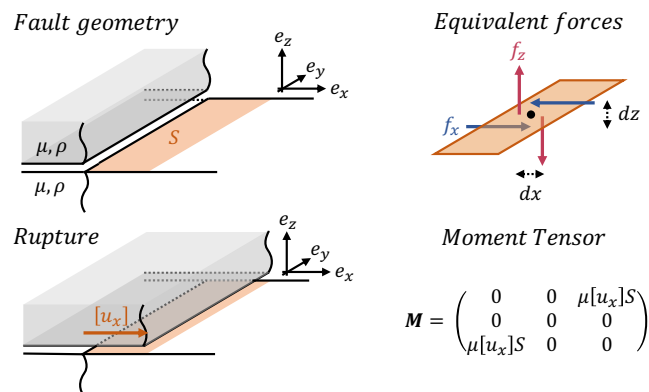


**Figure 2.1:** Simplified source mechanism, equivalent force system and moment tensor for a fault rupture. On the left, the ruptured fault is represented in orange.  $\mu$  and  $\rho$  are the shear modulus and density of the material surrounding the fault, and  $S$  the fault surface. The rupture results in a discontinuous displacement  $[u_x]$  along the fault. The point source model of the source in terms of equivalent forces (in N) and moments (in N·m) is shown on the right.

For earthquakes, the double-couple representation has proved to be a very strong model over the years. However, other seismogenic phenomena, such as volcanic or manmade explosions, require a different approach. Indeed, an explosion is a three-dimensional problem, where a small volume (and not a surface) is subject to a rapid expansion forming a cavity. In response, the material around this source volume is compressed. In such case, the source can be viewed as an isotropic displacement surrounding the point of energy release. The double-couple representation no longer holds, the source is instead viewed as three compressive couples of forces exerted in the three directions of space, and introducing a change in volume. This variation led to the introduction of a mathematical tool, the *moment tensor*, which acts as a library of all possible couples of forces in a three-

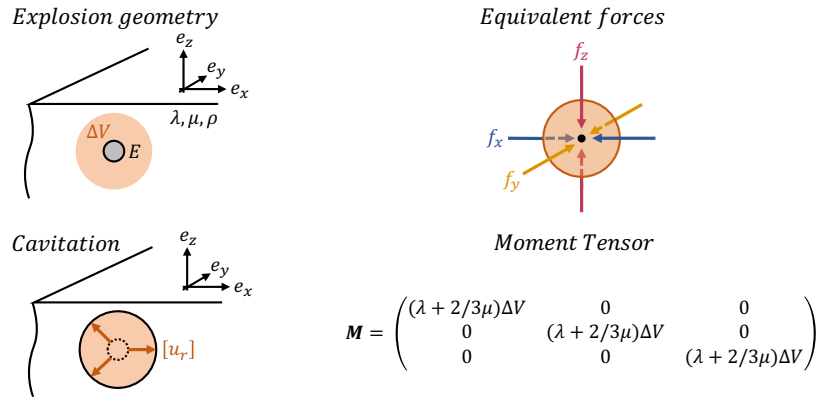


**Figure 2.2:** Simplified source mechanism, equivalent force system and moment tensor for an explosion. On the left, the volume where energy is released is represented in grey and the final cavity volume (source region) in orange.  $\mu$ ,  $\lambda$  and  $\rho$  are the Lamé constants and density of the material surrounding the source.  $E$  is the energy released at the explosion point and  $[u_r]$ ,  $\Delta V$  are the resulting displacement and volume change. The point source model of the source in terms of equivalent forces (in N) and moments (in N·m) is shown on the right.

dimensional cartesian space. Any *indigenous* seismic, i.e., a source present within the solid Earth and which does not change its momentum, can be represented in a first order approximation by a linear combination of the moment tensor components. The moment tensor and source mechanism of a fault rupture and explosion are represented on Fig. 2.1 and Fig. 2.2, respectively. Note however that not all seismic source on Earth are fully indigenous: volcanic eruption for example may cause a significant exchange of momentum between the solid Earth and the atmosphere by way of venting and mass loss. In such case, a moment tensor, i.e. a *dipole* of forces, can be an inappropriate source representation (see e.g. Kanamori & Given [1982]).

### The stress glut theory

The earthquake and explosion source share one common feature: the presence of a permanent deformation at the source region. This permanent deformation is proof that loads exerted on the source material exceeded its resistance, leading to irreversible damage. But how does such permanent deformation influence the surrounding intact material?

This question constitutes one of the fundamental problems of elasticity, which was discussed by Eshelby in 1957 and is known today as the *inclusion problem*. Eshelby considers an homogeneous elastic material, the *matrix*, containing a small inclusion of initial volume  $V^0$ . The inclusion is subject to a thermodynamic or plastic process which changes its shape, and subsequently apply stress on the surrounding material. To determine the final stress and strain of the inclusion and matrix, Eshelby performs a thought experiment in four operations, schematised on Fig. 2.3. First, the inclusion is taken out of the matrix, and let to deform without constraints until it reaches its final shape. The deformation of the inclusion is then called the *stress-free strain*, written  $\epsilon^T$ . In second time, imaginary forces are applied on the inclusion surface to bring it back to its original volume. In fact, this force field is simply the opposite of tractions required by Hooke's law to produce a strain equal to the stress-free strain;  $\mathbf{f}^T = -\mathbf{C}\epsilon^T\mathbf{n}$ , with  $\mathbf{C}$  the stiffness tensor and  $\mathbf{n}$  the normal to the inclusion surface. Finally, the inclusion is re-welded into the matrix, hence releasing forces  $-\mathbf{f}^T$  on its contact surface. Thus, thanks to this surface force field

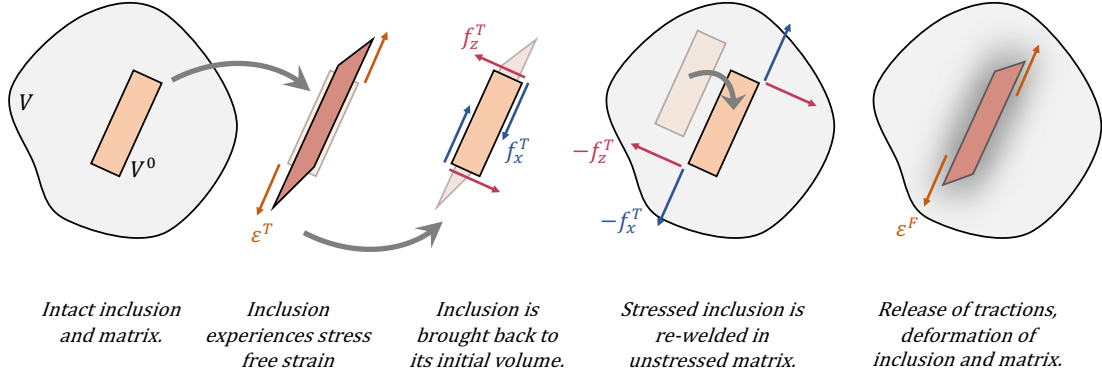


**Figure 2.3:** Graphic representation of Eshelby's inclusion problem and associated traction forces.

derived from the stress-free strain of the inclusion, the final deformation  $\epsilon^C$  of the matrix can be computed.

Via the inclusion problem, Eshelby showed that the amplitude of forces applied around a transformed volume depends on the amount of permanent plastic strain it experiences. However, Eshelby resolved a simplified static problem, as he considers the deformation of the inclusion and matrix to be instantaneous and only focus on their final state. In reality, the matrix responds dynamically to the evolution of strain in the inclusion. Hence, a more accurate representation of rupture during a seismic event requires to use the complete equations of motion.

The next step in the representation of complex seismic source was taken by [Backus & Mulcahy](#) with the introduction of the *stress glut*. [Backus & Mulcahy](#)'s interpretation replaces the notion of stress-free strain by a similar dual vision of stresses. The traditional equation of motion for seismology makes use of a model stress,  $\Psi$ , which is related to deformation  $\epsilon$  by a usually linear constitutive relation. Precisely, the relation between displacement  $\mathbf{u}$  and stress can be written in the simplest case as:

$$\rho \frac{\partial^2 \mathbf{u}}{\partial t^2} = \nabla \cdot \Psi, \quad (2.1)$$

with  $\nabla$  the gradient operator and  $\rho$  the material density. In the absence of pre-stress in the media, the constitutive relation is given by Hooke's law:

$$\Psi_{ij} = C_{ijkl} \epsilon_{kl}, \quad (2.2)$$

using tensor summation conventions. In the limit of infinitesimal strain,  $\epsilon$  can be related to  $\mathbf{u}$  by  $\epsilon_{kl} = \frac{1}{2} (\partial_k u_l + \partial_l u_k)$  with  $\partial_k$  the gradient in direction  $k$ .

In the source region, as in Eshelby's inclusion problem, this relation is no longer valid, as we have seen that the inclusion may experience a large strain  $\epsilon^T$  without being subject to any stress, only through thermoplastic and entropic processes. For example, phase transformations, dislocation, friction and plastic yield are phenomena which allow large deformation to occur with little change in stress. Therefore, as pointed out by [Backus & Mulcahy](#), the equations of motions need to be corrected in the source region to accommodate the true stress  $\mathbf{S}$  experienced by the ruptured material.

$$\begin{aligned} \rho \frac{\partial^2 \mathbf{u}}{\partial t^2} &= \nabla \cdot \Psi - \nabla \cdot \Pi, \\ \Pi &= \Psi - \mathbf{S}. \end{aligned} \quad (2.3)$$

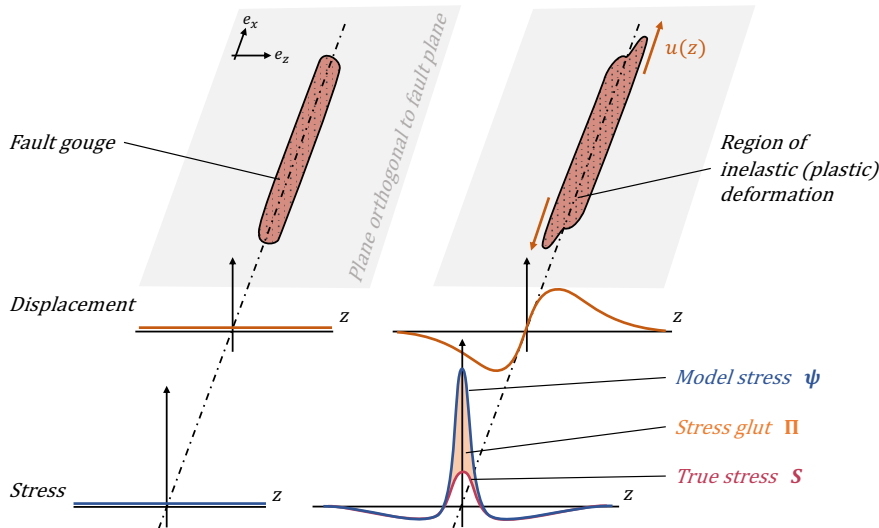


**Figure 2.4:** Stress glut formed during a fault rupture and relation with the region of inelastic displacement. The evolution of stresses and displacements in the direction perpendicular is depicted on graphs at the bottom. The region of the fault gouge is where the highest gradient of displacement, and therefore highest strain, is observed.

The correction term  $\Pi$  is called the stress glut, as it translates the fact that stress modelled from the deformation of the source region are usually much higher than true stress. Stress glut is a time-varying field, and is therefore adapted to a dynamical representation of earthquake rupture.

**Backus & Mulcahy** apply the stress glut theory to the fault rupture problem. During such event, the displacements and strains in the fault gouge, as represented in Fig. 2.4, are much larger than the surrounding medium. Due to these large strains, the gouge material weakens and its stress remains low. The elastic stress predicted from its total displacement, on the other hand, is significantly higher. Hence, a non zero stress-glut is present in the crack region, visible on Fig. 2.4.

An idealised earthquake rupture is often represented as a displacement discontinuity on both side of a surface. Following **Backus & Mulcahy [1976]** the stress glut in such case can be simplified to:

$$\begin{aligned} \Pi_{ij} &= C_{ijkl} n_k [u_l] && \text{on the fault,} \\ \Pi_{ij} &= 0 && \text{elsewhere.} \end{aligned} \quad (2.4)$$

Here  $[u_l]$  represents a displacement discontinuity in direction  $l$ , and  $n_k$  the component  $k$  of the normal to the fault. **Backus & Mulcahy** moreover showed that such stress glut field fills the requirements to be a *moment tensor density*: in the earthquake case, the integral of the stress glut gives the moment tensor of the seismic event. From the above result, the famous expression of the moment of a dislocation source from Fig. 2.1 is obtained:

$$M_{ij} = \mu S ([u_j] n_i + [u_i] n_j), \quad (2.5)$$

with  $\mu$  the shear modulus of the crack and  $S$  its surface, the displacement  $[\mathbf{u}]$  being parallel to the crack.

The stress glut and the stress-free strain fields are unique to each type of source. On the other hand, a single displacement field, moment tensors density or equivalent force system can be produced by multiple sources: exchanging axes  $x$  and  $z$  in Fig. 2.4 would indeed lead to the same moment tensor in Eq. 2.5. Therefore, if it can be obtained, the stress

glut field or the source strain field bring more information on the physics of the source than seismic measurements alone.

Authors have pointed out the limits of the stress glut in the version proposed by Backus & Mulcahy [1976]. For example, Takei & Kumazawa [1994], argued that Backus & Mulcahy [1976]'s theory fails to represent temporary changes of momentum or angular momentum made possible by mass advection. This is the case for volcanic venting, explosive spall, or landslides, during which significant momentum transport occurs. In such case, a moment tensor is not sufficient to represent the source, and a single force with a time-dependent amplitude can instead be derived from an "*inertial glut*" and a "*gravitational glut*". In a similar way, in a report by Archambeau & Scales [1989], the stress glut of Backus & Mulcahy [1976] is shown to overlook some effects, such as changes of mass in the source, and the non-linear transport terms of the equations of motion. Nowadays, the stress glut is present in seismic source studies mostly as a theoretical concept allowing the unification of seismic source representations [Dahlen & Tromp, 1998; Madariaga, 2015; Ichihara et al., 2016], although some studies have attempted to explicitly compute the stress glut generated by a fault rupture based on rock constitutive laws [Andrews, 1999; Hayek Valencia et al., 2022].

The stress glut representation of seismic sources is exhaustive and shares a close relationship to the physics of the source. Here, we propose to complement the representation of Backus & Mulcahy [1976] with the effects of mass and momentum transports. We will now show that progress in numerical modelling of shocked materials makes possible the explicit computation of stress glut and other terms of the seismic source.

### 2.1.2 Numerical modelling of impacts

The geometry of the earthquake seismic source shown on Fig. 2.1 is simple, and so is the associated motion during the fault rupture. At the first order, the double-couple representation of the earthquake seismic source succeeds in explaining most events. Impact cratering, on the other hand, is a complex 3D problem involving multiple timescales for the various stages of crater formation (see sec. 2.1.3), shock waves and high velocity flow of crater and ejecta material. This problem is not easily solved with a simple elastodynamic model, and experimental studies are limited in scale. Instead, the impact community relies on computational solid and fluid dynamics to study impact dynamics.

An accurate numerical simulation of the impact problem requires the resolution of shock waves and the evolution of velocity, stress and strain in space and time. Numerical Methods with these abilities are called *hydrocodes* or *shock-codes*. They solve the three equations of conservation for momentum, mass and energy, associated to a constitutive relation describing the response of simulated material to strain and temperature. The numerical implementation of conservation equations requires space to be discretised in 1D, 2D or 3D, which can be done in different ways. In *Eulerian* representations, physical variables are calculated on a fixed grid of points, through which the impacted material flows. This type of representation captures large deformation of material efficiently, but may lack precision in representing interfaces and sharp transitions in material properties or history-related state variables, because physical variables are averaged within each grid cells. In *Lagrangian* representations on the other hand, the grid flows with the material. In some cases, grid points represent a unique undeformable particle, and in other cases each cell of the grid models a deformable material element. Lagrangian codes precisely capture shocks and material transitions, but suffer from inaccuracies and stability issues when grid cells are too strongly distorted [Pierazzo & Collins, 2004; Pierazzo et al., 2008].



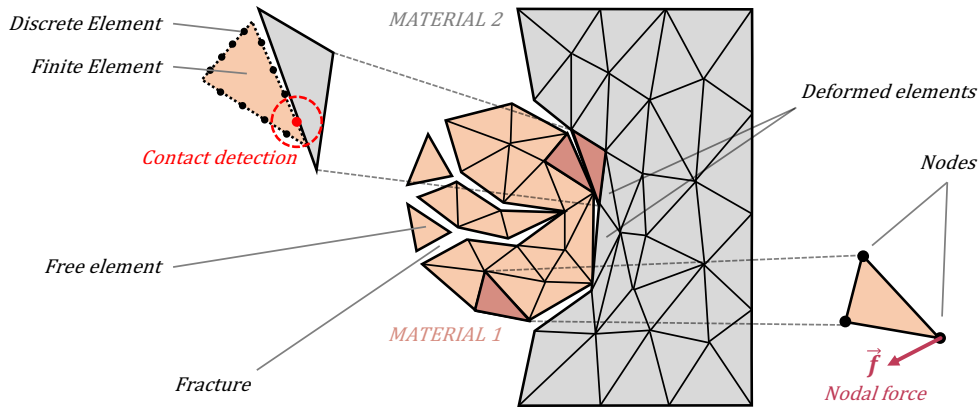


**Figure 2.5:** Representation of finite and discrete elements in a FDEM mesh as implemented by HOSS. Material 1 is put in contact with material 2, which generate deformation of elements in Material 2 and fractures in Material 1. Contact and fracture criterions are calculated using discrete elements shown on the top left.

Pierazzo et al. [2008] conducted a benchmarking study of several hydrocodes. Some of them, such as CTH [McGlaun et al., 1990] or ALE3D [Noble et al., 2017], are versatile multi-physics codes used worldwide for a variety of research and industrial applications. Others, like SOVA [Shuvalov et al., 1999] or iSALE (impact-SALE) [Wünnemann et al., 2006] are specialised in meteor and impact simulations. iSALE is based on the SALE hydrocode [Amsden et al., 1980], and alternates between Eulerian and Lagrangian representations for the efficient tracking of interfaces. It is equipped with several equations of state for shocked materials, such as the Tillotson [Tillotson, 1962] and ANEOS [Thompson & Lauson, 1974] equations of state, and includes parametric models for the compaction of porous materials [Collins et al., 2011]. iSALE can simulate impacts from the laboratory to the planetary scale, and its adaptability makes it one of the most prominent codes for impact studies today.

Meanwhile, in the past decades, development of pure Lagrangian simulation methods have brought new ways of simulating the behaviour of geologic materials, or geomaterials. Approaches of continuum mechanism often fail to model important discrete aspects of rocks and soils. Example of such discrete phenomena in geomaterials are brittle fracture, common in rocks such as granite, basalt and sandstone at low temperature, or friction effects present in granular materials under stress (sands, regolith, fault gouge...). To model such rheology, a numerical approach must resolve continuum, discontinuum, and particle dynamics. The combined Finite-Discrete Element Method (FDEM) was introduced to merge algorithms developed for the Finite Elements Method (FEM) and the Discrete Element Method (DEM) [Munjiza, 2004]. The FEM approach handles the deformation of materials under finite (and not only Infinitesimal) strains and rotation. On the other hand, the DEM provides solutions for crack formation and contact detection and interaction. By combining both approaches, the FDEM is able to resolve the dynamical onset of fractures and discontinuities within an initially continuous finite element mesh, and handles the interaction of individual entities by contact and friction. This novel framework yields excellent results for the simulation of laboratory fracture experiments [Lisjak et al., 2014; Euser et al., 2019], hydraulic and explosive fracturing [Zhao et al., 2014; Yan et al., 2016] and granular flow [Gao et al., 2018].

Figure 2.5 shows the discrete nature of a FDEM simulation mesh and the possible interactions between its elements. The FDEM solves an equation of the form:

$$\mathbf{M}\ddot{\mathbf{x}} + \mathbf{C}\dot{\mathbf{x}} = \mathbf{f}, \quad (2.6)$$

where  $\mathbf{x}$  is the displacement vector for the node of an element, and  $\dot{\cdot}$  and  $\ddot{\cdot}$  represent its first and second time derivative.  $\mathbf{M}$  is the mass matrix,  $\mathbf{C}$  the damping matrix and  $\mathbf{f}$  the vector of nodal forces. More precisely,  $\mathbf{f}$  includes forces resulting from the deformation of the element, which are calculated from its constitutive law, and forces resulting from contact and friction with other elements.

The Hybrid Optimization Software Suite (HOSS) [Knight et al., 2020] is an implementation FDEM developed at the Los Alamos National Laboratory. It is benchmarked against other codes for the simulation of hypervelocity impact [Caldwell et al., 2021]. Froment et al. [2020] further showed that the FDEM approach of HOSS succeeds in modelling laboratory-scale impacts in a granular and porous material similar to Martian regolith. In this study, a numerical model of regolith was proposed. This model combines an elasto-plastic representation of compression and pore collapse within volume elements, with the discrete approach, whereby each individual simulation elements is seen as a particle subject to compaction and friction. An impact experiment conducted at the NASA Ames Vertical Gun Range (AVGR) [Richardson & Kedar, 2013] and providing acceleration signals for impacts in a porous pumice sand was used for validation. The HOSS simulation results showed good agreement with the experimental waveforms. These benchmarking and validation exercises confirm that a FDEM-based approach is appropriate for simulating impacts in realistic surface materials. A complete description of this work can be found in the article "*Lagrangian-based Simulations of Hypervelocity Impact Experiments on Mars Regolith Proxy*" appended to this chapter. We will now introduce the modern view of impact cratering dynamics and how important parameters of the crater can be derived from simple scaling laws.

### 2.1.3 The cratering process

Impact cratering is in many way similar to the explosion cratering process. In both cases, a large amount of energy (in our case, the meteor kinetic energy) is released in a short amount of time on a planet's surface, producing a permanent deformation on a scale much larger than the object initially containing the energy, i.e., the meteor volume or the explosive charge. As a consequence, much of today's knowledge on impact cratering mechanics derived from military-driven studies on explosives and projectiles. The cratering process was initially studied though small

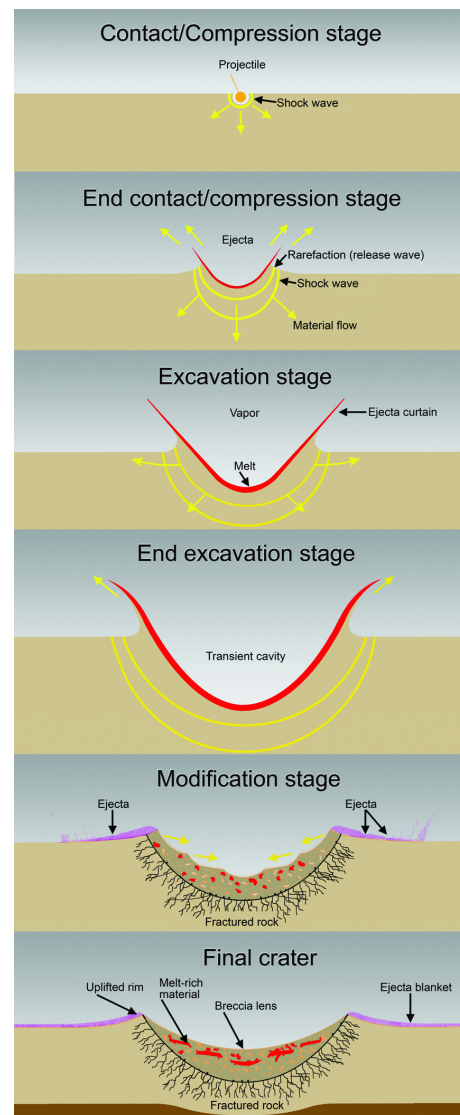


**Figure 2.6:** Graphic representation of the different stages of crater formation. Credit: Bevan M. French/David A. Kring/LPI/UA.

scale hypervelocity impact experiments (e.g., McGarr et al.'s experiments at the Ames Research Center during the Apollo era) and explosion tests. Today, the development of computational fluid dynamics, computational mechanics and high performance computing has considerably advanced these investigations, enabling studies of the cratering process over large time and space scales.

The current knowledge on crater formation and evolution is well summarised for example in Melosh's reference monograph on impact cratering [Melosh, 1989]. In nature, craters present different morphologies depending on their size and the properties of the impacted target. Simple craters present a bowl-shape form, more wide than deep, with a rim rising slightly above the undisturbed surface. Meteor Crater is an example of such simple crater on Earth (Fig. 1.3). Above a certain size, this morphology transitions to complex craters. On the Moon, this transition typically occurs for crater diameters larger than 10 km to 20 km, but this scale varies with a planet's gravity. Complex craters may present flat floors, with possible central peaks or terraces. Above a scale of a thousand kilometres, craters transition to multi-ringed basins, such as Mare Orientale on the Moon. We will focus here on simple craters, which are the most frequently formed in the solar system.

The formation of simple craters takes place in three stages, as illustrated in Fig. 2.6:

1. *The Contact and Compression stage.* This stage describes the first contact of the impactor with the target, and is the shortest in duration. The target material is put in motions with velocities close to the impactor velocities, and in many cases the local particle velocity exceeds the material wave velocity. In this case, a shock wave is formed, which subjects the target and impactor to pressures of MPa to GPa amplitude. Under such stress, a fraction of the impactor or target may change to liquid or vapour. Part of the material displaced and shocked by the impactor is ejected at high speed, forming the onset of the impact ejecta. The stage is considered complete when the approximately hemispherical shock wave has developed, which happens roughly when the impactor has penetrated the target by a distance corresponding to its diameter. Doing so, it loses most of its kinetic energy and momentum.
2. *The Excavation stage.* The shock wave generated during the Contact and Compression stage expands from the impact point. This shock initiates an excavation flow in the radial direction away from the impact point and gives rise to a transient crater. The excavation occurs on a time scale much longer than the shock itself. Material close to the surface continues to be ejected with decreasing speed: it is the ejecta curtain. Ejected material eventually starts to fall down in the presence of gravity.
3. *The Modification stage.* Under the effect of gravity, the steep slopes of the excavated crater collapse at its bottom. Their material covers the crater floor with a layer of debris called the breccia lens. Material within the ejecta curtain reaches the surface and forms an ejecta blanket.

Impact experiments and simulations led to the establishment of scaling laws relating crater dimensions (volume, radius, depth) to impactor and target properties. The  $\pi$ -group scaling proposed by Holsapple [1993] is now a reference relationship used in many areas of planetary science. The fundamental assumption of this scaling is that the impactor energy and momentum are instantaneously deposited at an ideal point in space: any parameters of the crater, ejecta or shock is then related to this *point source* through power laws.

The point source approximation was used to develop the first scaling laws for the effects of nuclear explosion in a perfect gas by Leonid Sedov in the Soviet Union, and at the same time by John von Neumann and G. I. Taylor in the United States. In the case of

an explosive blast, dimensional power laws depend only on the energy of the explosion. However, the impact phenomenon includes a substantial exchange of momentum with a solid half-space, hence the point source proposed by Holsapple is slightly more complex. The parameters describing the impactor are its radius  $a$ , its velocity  $U$  and density  $\delta$ . According to Holsapple, the dimension of a crater and impact shock depends not solely on the impactor kinetic energy,  $E_i = \frac{1}{2} \frac{4}{3} \pi (a^3 \delta U^2)$ , nor solely on its momentum,  $P_i = \frac{4}{3} \pi (a^3 \delta U)$ , but rather on a combination of both, materialised by the measure  $\pi = a \delta^\nu U^\mu$  and the variables  $\nu$  and  $\mu$ .

Holsapple propose that the only other parameters influencing crater dimensions are the strength of the target,  $Y$  in Pa, its surface gravity  $g$  and density  $\rho$ . He also ignore the effects of obliquity, atmospheres and long-time modification processes on the crater shape. By dimensional analysis, the following expression for the crater volume  $V$  can be obtained:

$$\pi_V = K_1 \left\{ \pi_2 \left( \frac{\rho}{\delta} \right)^{\frac{6\nu-2-\mu}{3\mu}} + \left[ K_2 \pi_3 \left( \frac{\rho}{\delta} \right)^{\frac{6\nu-2}{3\mu}} \right]^{\frac{2+\mu}{2}} \right\}^{\frac{-3\mu}{2+\mu}}, \quad (2.7)$$

with  $\pi_V = \frac{\rho V}{m}$ ,  $\pi_2 = \frac{ga}{U^2}$ ,  $\pi_3 = \frac{Y}{\rho U^2}$ .

For simple, bowl-shaped craters, the excavation radius  $R_e$  and crater depth  $D_e$  are scaled by:

$$R_e = K_r V^{\frac{1}{3}}, \quad D_e = K_d V^{\frac{1}{3}}, \quad (2.8)$$

and similarly for rim radius and height. The parameters  $K_1$ ,  $K_2$ ,  $K_r$ ,  $K_d$ ,  $\mu$ ,  $\nu$  can be computed from experimental data in different soils (see e.g. Holsapple [2022]).

Eq. 2.7 define two regimes for crater formation: for high values of target strength  $Y$  or small impactor sizes  $a$ , i.e. for  $\pi_3 \gg \pi_2$ , the crater is said to be in the *strength regime*, while for high values of  $g$  or large impactors, it is said to be in the *gravity regime*. In the strength regime, the mass excavated from the crater,  $\sim \rho V$ , is proportional to the impactor mass  $m$ .

This presentation of impact cratering mechanics concludes our general introduction. We hope to have provided the reader with an understanding of the main concepts of seismic source, numerical modelling and the physics of meteorite impacts. These concepts will be combined in the following pages, as we describe an analytical and numerical model of impact seismic sources.

# Numerical Modelling of Impact Seismic Sources Using the Stress Glut Theory

**Authors:** Marouchka Froment<sup>1,2</sup>, Philippe Lognonné<sup>1</sup>, Carène Larmat<sup>2</sup>, Zhou Lei<sup>2</sup>, Esteban Rougier<sup>2</sup> and Taichi Kawamura<sup>1</sup>

<sup>1</sup>*Université Paris-Cité, Institut de Physique du Globe de Paris, CNRS, Paris, France.*

<sup>2</sup>*Earth and Environmental Sciences Division, Los Alamos National Laboratory, Los Alamos, NM, USA.*

## 2.2 Introduction

As space exploration and instrumentation progress, seismic investigation of extra-terrestrial bodies has become possible and two space missions have been able to detect seismic waves generated by quakes and surface impacts. The first mission was the Apollo Lunar Surface Experiments (ALSEP), which deployed a network of four seismometers from 1969 to 1977 [Latham et al., 1969] on the Moon. The second was the InSight mission [Banerdt et al., 2020], which operated the Seismic Experiment for Interior Structure (SEIS), composed of a Short-Period (SP) and a Very Broad-Band (VBB) seismometer, from November 2018 to December 2022 on Mars [Lognonné et al., 2019, 2020; Giardini et al., 2020].

In agreement with pre-landing estimates [McGarr et al., 1969], ALSEP detected seismic signals from more than 1750 meteoroid impacts [Oberst & Nakamura, 1987, 1991; Latham et al., 1970; Nakamura et al., 1982]. Similarly on Mars, impacts were thought to be a potential source of detectable signals prior to the landing of InSight [Davis, 1993; Teanby & Wookey, 2011; Lognonné & Johnson, 2015; Teanby, 2015; Daubar et al., 2018]. Despite the lack of detections during the nominal mission from 2018 to 2020 [Daubar et al., 2020; Miljkovic et al., 2021; Fernando et al., 2022], several impacts were recorded during the extended mission. The first ones, located at close distances from InSight (e.g. less than 300 km), generated four very-high frequency (VF) seismic events identified by the Marsquake Service [Clinton et al., 2018; Ceylan et al., 2022] and were notably accompanied by late low-frequency, dispersed wave trains. These dispersed arrivals, predicted in pre-landing studies [Garcia et al., 2017], correspond to acoustic waves traveling through the Martian nighttime acoustic waveguide [Xu et al., 2022]. Using their seismic arrival times and back-azimuth [Garcia et al., 2022], the location of these events was determined and associated with fresh craters imaged around InSight by the Mars Reconnaissance Orbiter (MRO) cameras [Malin et al., 2007]. Two other very large craters,  $150 \pm 10$  m and  $130 \pm 12$  m in diameter, at 3460 km and 7455 km distance from InSight, were later detected by the MRO imager [Posiolova et al., 2022], and associated with seismic events recorded by SEIS on December 24 and on September 18, 2021. These two significant events produced a broadband energy with a moment larger than 4.

Impact seismic observations on both the Moon and Mars allow for the first time a comparative study, and as such raise a number of questions. For example, can a single approach relate the long period amplitude of the seismic signals to the crater size measured on both



celestial bodies? Can we predict seismic directivity effects for impacts with relatively oblique velocity such as the September 18, 2021 event [Posiolova et al., 2022]? In order to address these questions, we must integrate differences between the Martian or Lunar subsurface, and deconvolve the combined effects of wave propagation and wave generation on the observed signal in the time and frequency domain. Achieving this goal requires a model of the impact seismic source, accounting for the dynamical process during which the energy and momentum of the impactor is transferred into elastic energy within the target body. Such a model must quantify the magnitude of the impact seismic event, as well as the various time-scales of the source.

Existing models of the impact seismic source rely on small-scale laboratory experiments, scaling laws developed using far-field impact seismic signals on the Moon, or analytical models based on explosion seismology. In preparation for the Apollo mission, McGarr et al. [1969] proposed to describe the impact seismic source by measuring the ratio between the seismic energy  $E_s$  within the target and the kinetic energy  $E_k$  of the impactor. This energy ratio quantifies the amount of impactor energy that is converted into seismic waves and is called the *seismic efficiency*,  $k_s$ . It has been used in numerous impact related studies: the seismic efficiency of impacts can indeed be estimated using recordings of missiles, surface explosions and lunar impacts, or via hydrocode modelling [Latham et al., 1970; Shishkin, 2007; Güldemeister & Wünnemann, 2017; Rajšić et al., 2021].

More recently, in the frame of InSight pre-launch activities, scaling laws between the impact crater diameter and the *seismic moment* of the source,  $M_0$ , were proposed [Teanby & Wookey, 2011; Teanby, 2015; Wójcicka et al., 2020] (See the review of Daubar et al. [2018]). One advantage of the seismic moment over the seismic efficiency is that the former scales linearly with the peak displacement or the peak velocity of a seismogram, thus facilitating detectability analyses. It derives from a more complex mathematical object known as the *moment tensor*, which contains a representation of each force couples exerted on the target in every direction.

In the past, various models have been proposed to evaluate the seismic moment, either from modelling or data. Wójcicka et al. [2020] tested different methods to compute the seismic moment from hydrocode impact simulations. One method uses an analytical expression of the seismic moment of an explosion, obtained from the reduced displacement potential of compressional waves by Müller [1973]:

$$M_0 = \left(K + \frac{4G}{3}\right) S \langle D \rangle, \quad (2.9)$$

where  $K$  and  $G$  represent the bulk modulus and shear modulus of the target material, and  $\langle D \rangle$  represents the residual radial seismic displacement on a sphere of surface  $S$  surrounding the impact region. Another method by Walker [2003] uses the seismic impulse to derive a measure of the radial (in the cylindrical sense) component of the moment tensor:

$$M_{rr} = \frac{\int \rho v_r r \, dV}{t}, \quad (2.10)$$

with  $v_r$  the radial velocity at a radial distance  $r$  from the impact.

In both methods, the moment is computed directly from seismic amplitudes. Lognonné et al. [2009] on the other hand, estimated  $M_0$  from a scaling of artificial impact seismic data recorded by the Apollo seismometers. More precisely, in Lognonné et al. [2009] and Gudkova et al. [2011], the seismic amplitude of lunar impacts, and hence the seismic moment, is found to be proportional to the vertical component of the seismic impulse, which is amplified by ejecta. Lognonné et al. [1994] and Gudkova et al. [2015] were also the first studies to associate the seismic moment, or full seismic moment tensor of

the impact, to the notion of *stress-glut* field. This notion was introduced by [Backus & Mulcahy \[1976\]](#) to construct a general mathematical description of earthquake sources. The stress glut translates the plastic deformation happening at the source into a system of equivalent forces, and hence provides detailed information on the mechanisms driving the seismic signal.

All the aforementioned models show limits in describing the impact seismic source. The seismic efficiency proposed by [McGarr et al. \[1969\]](#) varies by several orders of magnitude across different studies: [Daubar et al. \[2018\]](#) report values of  $k_s$  ranging from  $10^{-6}$  to  $10^{-1}$  depending on the calculation method. The alternative approaches with the seismic moment reported above are not entirely satisfactory either. Many rely on the similitudes drawn between impacts and the formation of craters by shallow explosive sources, thus, the impact seismic source is considered isotropic. This characteristic is in contradiction with the apparent directivity of impacts, as evidenced by the ejecta and surface expression of recent impacts on Mars [[Posiolova et al., 2022](#)]. Such limitations could be avoided by using a full moment tensor description of the impact, as proposed by [Lognonné et al. \[1994\]](#) and [Gudkova et al. \[2015\]](#). However, as said above, seismic moment tensors aim at representing a system of force couples, and are by nature unable to convey any net momentum variation within the earth. Consequently, representing an impact only with a moment tensor leaves out the impulse of the impactor. Although authors have also dedicated efforts in measuring the seismic impulse of impacts [[McGarr et al., 1969](#); [Walker, 2003](#); [Gudkova et al., 2015](#)], no study to date was able to reconcile the respective contribution of momentum exchange and crater formation on the impact seismic source. Furthermore, finite source effects are not accounted for by the moment tensor, as it represents couples of forces exerted at a single point in space. These limitations justify a more physics-based approach to the development of impact seismic models.

Today, numerical simulations allows us to study in depth the dynamics and mechanical processes at play during a hypervelocity impact using validated and benchmarked hydrocodes [[Pierazzo et al., 2008](#); [Wünnemann et al., 2011](#); [Collins et al., 2012](#); [Güldenmeister & Wünnemann, 2017](#); [Wójcicka et al., 2020](#); [Rajšić et al., 2021](#); [Caldwell et al., 2021](#)]. Simulations can be performed at a variety of time and space scales, and with diverse impactor and target material properties. This helps in the identification of the impact parameters controlling the associated seismic signals, especially if a simple, meaningful image of impact-related deformation mechanisms can be extracted from the complex numerical results.

To this end, we propose here a new analytical representation of the impact seismic source based on the seismic Representation Theorem and the stress glut theory, in a similar way as [Burridge & Knopoff \[1964\]](#) and [Backus & Mulcahy \[1976\]](#). These theories allow us to develop a point source model composed of two terms adapted to the specificities of the impact source: a monopole, i.e. a 3-component vector force, and a dipole, or 6-component moment tensor. The stress glut field introduced by [Backus & Mulcahy \[1976\]](#) is a key factor in defining this point source. In this study, we introduce a new numerical method to compute the stress glut using hydrocode impact simulations, and derive the vector force and moment tensor from simulation results. Our computation is verified by comparing seismic signals generated from the numerical point-source with seismic signals prolonged directly from the non-linear impact simulation, via a software coupling approach. In addition to this signal-to-signal verification, some key parameters of the seismic signal, such as the seismic moment and cutoff frequency, can be extracted from simulation results and compared to results obtained on Mars and the Moon. Besides, the proposed full moment tensor description allows us to evaluate the common assumption of an explosive, isotropic source and to look for more complex source mechanisms.

The combination of a new analytical representation of the impact source with a physics-based numerical model allows for a detailed understanding of impact wave generation processes, with the ability to investigate their sensitivity to a wide range of parameters (impactor velocity, mass and angle, target strength and density, etc.). Moreover, this approach enables direct comparison of the impact source with other types of seismic sources, which may in the future allow better identification of impact-generated seismic signals on the solar system bodies.

## 2.3 The Representation Theorem applied to impacts

We first recall the equations representing the impact and its point-source. In what follows, vectors will be written as lower-case bold letters. Upper-case bold letters will be used to name tensors of order two or more. Operations on individual tensor and vector components will use Einstein summation conventions.

### 2.3.1 Representation of seismic sources

#### Equations of motion in an elastic solid.

Seismic wave equation (e.g. [Aki & Richards \[2002\]](#)), for a planetary body of volume  $V$  bounded by a surface  $\Sigma$ , is developed in the framework of continuum and linearised mechanics by the following equations:

$$\begin{aligned} \rho^0 \frac{\partial^2 u_i}{\partial t^2} &= \partial_j \Psi_{ij} + f_i^V && \text{in } V, \\ \Psi_{ij} n_j &= f_i^\Sigma && \text{on } \Sigma, \\ \Psi_{ij} &= C_{ijkl} \varepsilon_{kl}. \end{aligned} \tag{2.11}$$

In this system, the first line states the equation of elasto-dynamics, a linearised equation of motion for a material with constant density  $\rho^0$ , with  $\mathbf{u}(\mathbf{x}, t)$  the displacement field. The second line defines boundary conditions on  $\Sigma$ , and the system is closed by the constitutive equation of the material in  $V$ , stated in the last line: the stress field is written  $\Psi$  and is related in to the elastic strain  $\varepsilon_{kl} = \frac{1}{2}(\partial_k u_l + \partial_l u_k)$  by the stiffness tensor  $\mathbf{C}$ . Finally,  $f_i^\Sigma$  represents tractions applied on  $\Sigma$ , the boundary of  $V$ , and  $f_i^V$  is any linearised volume force acting within  $V$ . In particular,  $\mathbf{f}^V$  can incorporate linearised gravity, Coriolis and centrifugal forces, the latter described in details by [Dahlen & Tromp \[1998\]](#). We refer the reader to Appendix A4 for a discussion of this case.

#### Non-linear equations of motion

The system of equations 2.11 assumes a fully elastic material, which exhibits little changes in shape and no change in mass during its deformation. This representation of motion is limited and fails when dealing with large deformations and stresses caused by an extreme event such as an impact. In the following section, several assumptions made in section 2.3.1 are relaxed:

- The linearisation of the left side of the equation of motion is abandoned in order to account for the variations in the true local density  $\rho$  and the advection of momentum caused by the impact.



- The material of  $V$  is no longer considered ideally linear-elastic, i.e, stresses within it are no longer dictated by Hooke's law.
- Loss of mass and momentum through surface  $\Sigma$  is introduced to account for the reactive effect of impact ejecta.

The loss of mass through surface  $\Sigma$  is the major difference with respect to previous works, such as Lognonné et al. [1994], where the impact source (in this specific study, associated to the Shoemaker Levy 9 impact) was embedded in the volume. We develop the formalism in Appendix A1 by making use of the Reynolds Transport Theorem, following Irschik & Holl [2004]. The equation of motion in volume  $V$  remains the same as in fluid mechanism (e.g. Landau & Lifshitz [1987]) and can therefore be either written as:

$$\frac{\partial}{\partial t}(\rho v_i) = \partial_j S_{ij} + h_i^V - \partial_j(\rho v_i v_j), \quad (2.12)$$

or:

$$\rho \frac{d}{dt}(v_i) = \partial_j S_{ij} + h_i^V, \quad (2.13)$$

with  $\frac{d}{dt}$  the material derivative, and where  $\mathbf{v}$  is the velocity,  $\mathbf{h}^V$  is the volumetric density of forces and  $\mathbf{S}$  the non-linear stress tensor. The stress  $\mathbf{S}$  is different from the ideal elastic stress  $\Psi$  of Eq. 2.11 and does not *a priori* follow Hooke's law of elasticity.

In distinction to the equation of motion, the continuity of stress at the mass-less boundary of  $\Sigma$  must integrate the transfer of momentum through this surface by ejecta, which leads to:

$$S_{ij} n_j = f_i^\Sigma + \rho v_i (v_j - v_j^\Sigma) n_j, \quad (2.14)$$

with  $\mathbf{v}^\Sigma$  the velocity of the surface bounding the non-ejected material.

### Equivalent forces of the impact and seismic wavefield representation

An accurate representation of the seismic source of an impact requires non-linear phenomena described by Eqs. 2.12 and 2.14 to be accommodated into the elastic system of Eq. 2.11. To do so, following the method of Backus & Mulcahy [1976], non-linear effects are introduced in the form of equivalent volume and surface forces  $\gamma^V$  and  $\gamma^\Sigma$ . The updated system is the following:

$$\begin{aligned} \rho^0 \frac{\partial^2 u_i}{\partial t^2} &= \partial_j \Psi_{ij} + f_i^V + \gamma_i^V && \text{in } V, \\ \Psi_{ij} n_j &= f_i^\Sigma + \gamma_i^\Sigma && \text{on } \Sigma, \\ \Psi_{ij} &= C_{ijkl} \partial_k u_l. \end{aligned} \quad (2.15)$$

The equivalent forces are obtained by equating system 2.15 with the true boundary conditions in Eq. 2.14 and the true equation of motion in Eq. 2.12:

$$\begin{aligned} \Pi_{ij} &= \Psi_{ij} - S_{ij}, & \gamma_i^V &= \frac{\partial}{\partial t} [(\rho^0 - \rho) v_i] + h_i^V - f_i^V - \partial_j(\Pi_{ij} + \rho v_i v_j), \\ \gamma_i^\Sigma &= [\Pi_{ij} + \rho v_i (v_j - v_j^\Sigma)] n_j. \end{aligned} \quad (2.16)$$

Eq. 2.16 introduces the tensor  $\mathbf{\Pi}$ , which is the difference between ideal, elastic stresses and true, non-linear stresses associated to the current deformation state. It is named the *Stress Glut* and was first discussed in the work of Backus & Mulcahy [1976], who demonstrated its key role in explaining indigenous seismic sources such as earthquakes. The stress glut

measures the deviation of true stress from the stress predicted by Hooke's law, and is consequently related to the amount of plastic processes taking place in a seismic source region. The ability of a local thermo-plastic stress change to generate elastic motion was originally proven in Eshelby's famous inclusion problem [Eshelby, 1957]. As noted by several authors [Backus & Mulcahy, 1976; Madariaga, 2015], the stress glut is related, in a dynamic sense, to the *stress-free strain* proposed in Eshelby's static approach. We also note here the similarity of Eq. 2.16 with the expression proposed by Lognonné et al. [1994].

We will now definitively ignore gravity and will therefore assume that  $h_i^V$  and  $f_i^V$  are both null. Thanks to the seismic Representation Theorem, equivalent forces of Eq. 2.16 can now be used to build the response of the media to the seismic source, as further detailed in Appendix A2. When the surface  $\Sigma$  is a free surface, the expression of displacements anywhere in  $V$  is given by Eq. 2.17:

$$u_n(\mathbf{x}, t) = \int_{-\infty}^{+\infty} d\tau \iiint_V \gamma_i^V(\boldsymbol{\xi}, \tau) G_{in}(\boldsymbol{\xi}, t - \tau, \mathbf{x}, 0) dV(\boldsymbol{\xi}) + \int_{-\infty}^{+\infty} d\tau \iint_{\Sigma} G_{in}(\boldsymbol{\xi}, t - \tau, \mathbf{x}, 0) \gamma_i^{\Sigma}(\boldsymbol{\xi}, \tau) d\Sigma(\boldsymbol{\xi}). \quad (2.17)$$

Here,  $u_n$  is the  $n^{\text{th}}$  component of displacement recorded at time  $t$  and at coordinates  $\mathbf{x}$  in space. It is generated by a field of surface and volume forces  $\gamma^V$  and  $\gamma^{\Sigma}$  spread over coordinates  $\boldsymbol{\xi}$  in space and exerted at time  $\tau$ .  $G_{in}$  is the Green's function of the target medium. It is a mathematical tool which serves as a way to propagate information elastically from the sources at  $\boldsymbol{\xi}$  and  $\tau$  to the receiver at  $\mathbf{x}$  and  $t$ . The expression of the Green's function depends on the elastic equations of motion: if gravity and rotation of a planet are accounted for, the Green's function must be defined using the operators of gravito-elasticity and of Coriolis forces. We refer the reader to Appendix A4 or for example Dahlen & Tromp [1998] for more details on the linearised gravito-elastic equations of motion. Despite this change in equations, the Representation Theorem of Eq. 2.17 remains in essence the same [Dahlen & Tromp, 1998, section 5.3].

Note that most studies making use of the seismic Representation Theorem assume that the mass enclosed by surface  $\Sigma$  is constant. Again, the formation of ejecta during an impact constitutes a mass and momentum loss, which in turn adds equivalent terms in the Representation Theorem of Eq. 2.17. In this study, we do not account for the effects of variable mass and volume on the source, as we will find them to be negligible for the simulated impacts. However, the reader can find an exact version of Betti's relation for a variable-mass system in Appendix A3, as proposed by Minster [1974] and Archambeau & Scales [1989].

### 2.3.2 Point-source of an impact

#### The point-source approximation.

Given the equivalent forces and expression of displacements developed above, it is possible to further simplify the representation of the source, upon assuming that forces are applied to a point in space. To do so, a Taylor's expansion of the Green's function is conducted with respect to the coordinate  $\boldsymbol{\xi}$  - being the position of a source point in the volume - around the point-source located at  $\boldsymbol{\xi}^*$  (see e.g., Julian et al. [1998]). The spatial derivative

is defined on the inside of the free surface, for  $\xi_z < 0$ .

$$\begin{aligned} G_{in}(\boldsymbol{\xi}, t - \tau, \mathbf{x}, 0) &= G_{in}(\boldsymbol{\xi}^*, t - \tau, \mathbf{x}, 0) + (\xi_j - \xi_j^*) \frac{\partial G_{in}}{\partial \xi_j}(\boldsymbol{\xi}^*, t - \tau, \mathbf{x}, 0) \\ &+ \frac{(\xi_j - \xi_j^*)(\xi_k - \xi_k^*)}{2!} \frac{\partial^2 G_{in}}{\partial \xi_j \partial \xi_k}(\boldsymbol{\xi}^*, t - \tau, \mathbf{x}, 0) + o(|\boldsymbol{\xi}|^3). \end{aligned} \quad (2.18)$$

In the point-source approximation, the source is sufficiently small compared to the receiver's distance and other typical spatial variations ( $|\boldsymbol{\xi} - \boldsymbol{\xi}^*| \ll |\mathbf{x}|$ ). Therefore, we consider here that the first two terms of this Taylor series of  $G_{in}(\boldsymbol{\xi}^*)$  give a sufficiently good approximation of  $G_{in}(\boldsymbol{\xi})$ . The expression of  $G_{in}(\boldsymbol{\xi})$  is slipped into Eq. 2.17, and the quadrupole and higher-order terms are neglected.

$$\begin{aligned} u_n(\mathbf{x}, t) &\sim \int_{-\infty}^{+\infty} d\tau \iiint_V \gamma_i^V(\boldsymbol{\xi}, \tau) \left[ G_{in}(\boldsymbol{\xi}^*, t - \tau, \mathbf{x}, 0) + (\xi_j - \xi_j^*) \frac{\partial G_{in}}{\partial \xi_j}(\boldsymbol{\xi}^*, t - \tau, \mathbf{x}, 0) \right] dV(\boldsymbol{\xi}) \\ &+ \int_{-\infty}^{+\infty} d\tau \iint_{\Sigma} \left[ G_{in}(\boldsymbol{\xi}^*, t - \tau, \mathbf{x}, 0) + (\xi_j - \xi_j^*) \frac{\partial G_{in}}{\partial \xi_j}(\boldsymbol{\xi}^*, t - \tau, \mathbf{x}, 0) \right] \gamma_i^{\Sigma}(\boldsymbol{\xi}, \tau) d\Sigma(\boldsymbol{\xi}). \end{aligned} \quad (2.19)$$

$G_{in}$  is now only dependent on the point-source location,  $\boldsymbol{\xi}^*$ . Upon rearranging the integral terms, we obtain:

$$\begin{aligned} u_n(\mathbf{x}, t) &\sim \int_{-\infty}^{+\infty} d\tau \left\{ G_{in}(\boldsymbol{\xi}^*, t - \tau, \mathbf{x}, 0) \left[ \iiint_V \gamma_i^V(\boldsymbol{\xi}, \tau) dV(\boldsymbol{\xi}) \right. \right. \\ &\quad \left. \left. + \iint_{\Sigma} \gamma_i^{\Sigma}(\boldsymbol{\xi}, \tau) d\Sigma(\boldsymbol{\xi}) \right] \right. \\ &\quad \left. + \frac{\partial G_{in}}{\partial \xi_j}(\boldsymbol{\xi}^*, t - \tau, \mathbf{x}, 0) \left[ \iiint_V \gamma_i^V(\boldsymbol{\xi}, \tau) (\xi_j - \xi_j^*) dV(\boldsymbol{\xi}) \right. \right. \\ &\quad \left. \left. + \iint_{\Sigma} \gamma_i^{\Sigma}(\boldsymbol{\xi}, \tau) (\xi_j - \xi_j^*) d\Sigma(\boldsymbol{\xi}) \right] \right\}. \end{aligned} \quad (2.20)$$

From this expression of displacements, two key source parameters can be defined:

$$\begin{aligned} F_i(\tau) &= \iiint_V \gamma_i^V(\boldsymbol{\xi}, \tau) dV(\boldsymbol{\xi}) + \iint_{\Sigma} \gamma_i^{\Sigma}(\boldsymbol{\xi}, \tau) d\Sigma(\boldsymbol{\xi}), \\ M_{ij}(\boldsymbol{\xi}^*, \tau) &= \iiint_V \gamma_i^V(\boldsymbol{\xi}, \tau) (\xi_j - \xi_j^*) dV(\boldsymbol{\xi}) + \iint_{\Sigma} \gamma_i^{\Sigma}(\boldsymbol{\xi}, \tau) (\xi_j - \xi_j^*) d\Sigma(\boldsymbol{\xi}). \end{aligned} \quad (2.21)$$

All the operations above amount to expressing the equivalent forces  $\boldsymbol{\gamma}^V$  in a simplified way, as a development over  $\delta$ -Dirac distributions:

$$\hat{\gamma}_i(\boldsymbol{\xi}, \tau) = F_i(\tau) \delta(\boldsymbol{\xi} - \boldsymbol{\xi}^*) + M_{ij}(\boldsymbol{\xi}^*, \tau) \frac{\partial}{\partial \xi_j} \delta(\boldsymbol{\xi} - \boldsymbol{\xi}^*). \quad (2.22)$$

The final displacement signal is the convolution of a single force and a moment tensor with the Green's function of the propagating media:

$$u_n(\mathbf{x}, t) = F_i(\tau) * G_{in}(\boldsymbol{\xi}^*, t - \tau, \mathbf{x}, 0) + M_{ij}(\boldsymbol{\xi}^*, \tau) * \frac{\partial G_{in}}{\partial \xi_j}(\boldsymbol{\xi}^*, t - \tau, \mathbf{x}, 0). \quad (2.23)$$

The above developments mean that, once integrated over the volume  $V^t$  of the source region, the force field  $\boldsymbol{\gamma}^V$  and tractions  $\boldsymbol{\gamma}^{\Sigma}$  reduce to the following approximations:

- A vector force of the form  $\rightarrow$ , also called a *monopole*. It corresponds to the term  $F_i(\tau)$  in Eq. 2.21. This term encompasses all momentum changes caused by the seismic source.
- Force-less couples of the form  $\leftarrow \cdot \rightarrow$ , also called *dipoles*. They are contained in the moment tensor terms  $M_{ij}(\tau)$  in Eq. 2.21.

If a non-linear solution of the wavefield and stress field is modelled in the whole source volume, for example numerically, then the equivalent forces can be evaluated. We develop below the expression of the monopole and dipole in terms of these wavefields.

### Expression of the monopole of the impact source

The expressions of equivalent volume and surface forces from Eqs. 2.16 and 2.15 are inserted into the definition of  $F_i(\tau)$  (Eq. 2.21). The Gauss-Green-Ostrogradsky Theorem allows to simplify the expression of the net vector force exerted on Earth by the impact:

$$\begin{aligned} F_i(\tau) &= \iiint_V \gamma_i^V(\boldsymbol{\xi}, \tau) dV(\boldsymbol{\xi}) + \iint_{\Sigma} \gamma_i^{\Sigma}(\boldsymbol{\xi}, \tau) d\Sigma(\boldsymbol{\xi}) \\ &= \iiint_V \left( \rho^0 \frac{\partial v_i}{\partial t} - \partial_j \Psi_{ij} \right) (\boldsymbol{\xi}, \tau) dV(\boldsymbol{\xi}) + \iint_V \partial_j \Psi_{ij}(\boldsymbol{\xi}, \tau) dV(\boldsymbol{\xi}), \end{aligned} \quad (2.24)$$

or:

$$F_i(\tau) = \iiint_V \rho^0 \frac{\partial v_i}{\partial \tau}(\boldsymbol{\xi}, \tau) dV(\boldsymbol{\xi}). \quad (2.25)$$

This vector force is merely the change of momentum in the instantaneous target volume following the impact, in the approximation of constant density. Note here that the mass leaving volume  $V$  will lead, by momentum conservation, to a variation of the target momentum. Therefore, even though  $F_i(\tau)$  is an integral of momentum restricted to the target volume  $V$ , it includes by definition the impulse resulting from ejecta motion.

### Expression of the dipole of the impact source

An expression of moment tensor components is obtained by replacing equivalent volume and surfaces forces in Eq. 2.21 using their definition in Eqs. 2.16 and 2.15:

$$\begin{aligned} M_{ij}(\boldsymbol{\xi}^*, \tau) &= \iiint_V \frac{\partial}{\partial \tau} [(\rho^0 - \rho)v_i] (\boldsymbol{\xi}, \tau) (\xi_j - \xi_j^*) dV(\boldsymbol{\xi}) \\ &\quad - \iiint_V \frac{\partial}{\partial \xi_j} [\Pi_{ij} + \rho v_i v_j] (\boldsymbol{\xi}, \tau) (\xi_j - \xi_j^*) dV(\boldsymbol{\xi}) + \iint_{\Sigma} \Psi_{ij}(\boldsymbol{\xi}, \tau) n_j (\xi_j - \xi_j^*) d\Sigma(\boldsymbol{\xi}). \end{aligned} \quad (2.26)$$

Integration by part is used to further simplify the second and third integrals. Let  $(\xi_j - \xi_j^*)$  be our vector component, written  $e_j$ , and  $\Pi_{ij}$ ,  $\rho v_i v_j$  or  $\Psi_{ij}$  be our tensor components, written  $V_{ij}$ . We have:

$$\iiint_V e_j \partial_j V_{ij} dV = \iint_{\Sigma} e_j V_{ij} n_j dS - \iiint_V \partial_j e_j V_{ij} dV. \quad (2.27)$$

Applying equation 2.27 to the second term of equation 2.26, we get:

$$\begin{aligned}
M_{ij}(\boldsymbol{\xi}^*, \tau) = & \iiint_V \frac{\partial}{\partial \tau} [(\rho^0 - \rho)v_i](\boldsymbol{\xi}, \tau) (\xi_j - \xi_j^*) dV(\boldsymbol{\xi}) + \iint_{\Sigma} \Psi_{ij}(\boldsymbol{\xi}, \tau) n_j (\xi_j - \xi_j^*) d\Sigma(\boldsymbol{\xi}) \\
& - \iint_{\Sigma} [\Pi_{ij} + \rho v_i v_j](\boldsymbol{\xi}, \tau) n_j (\xi_j - \xi_j^*) d\Sigma(\boldsymbol{\xi}) + \iiint_V [\Pi_{ij} + \rho v_i v_j](\boldsymbol{\xi}, \tau) dV(\boldsymbol{\xi}),
\end{aligned} \tag{2.28}$$

which yield after rearranging the stress terms:

$$\begin{aligned}
M_{ij}(\boldsymbol{\xi}^*, \tau) = & \iiint_V \frac{\partial}{\partial \tau} [(\rho^0 - \rho)v_i](\boldsymbol{\xi}, \tau) (\xi_j - \xi_j^*) dV(\boldsymbol{\xi}) \\
& + \iint_{\Sigma} [S_{ij} - \rho v_i v_j](\boldsymbol{\xi}, \tau) n_j (\xi_j - \xi_j^*) d\Sigma(\boldsymbol{\xi}) \\
& + \iiint_V [\Pi_{ij} + \rho v_i v_j](\boldsymbol{\xi}, \tau) dV(\boldsymbol{\xi}).
\end{aligned} \tag{2.29}$$

Eq. 2.21 can also be rearranged differently if we recall from Eq. 2.15 that  $\gamma_i^V = \rho^0 \frac{\partial v_i}{\partial t} - \partial_j \Psi_{ij}$ . This time, using an integration by part on  $\partial_j \Psi_{ij}$ , surface integrals can be eliminated and we obtain:

$$\begin{aligned}
M_{ij}(\boldsymbol{\xi}^*, \tau) = & \iiint_V \frac{\partial(\rho^0 v_i)}{\partial \tau}(\boldsymbol{\xi}, \tau) (\xi_j - \xi_j^*) dV(\boldsymbol{\xi}) \\
& + \iiint_V \Psi_{ij}(\boldsymbol{\xi}, \tau) dV(\boldsymbol{\xi}).
\end{aligned} \tag{2.30}$$

This expression, which only requires volume integrals, is better suited for an evaluation with a numerical calculation. Like relation 2.25, it only requires the computation of velocity, elastic and non-linear stress fields within finite volume elements.

### Remarks on these results

This expression of the vector force and these two expressions of the moment tensor (Eqs. 2.29 and 2.30) conclude our derivation of the point-source. We can draw several conclusions from the above developments:

- We have shown that meteorite strikes, as well as any source, act on an idealised, elastic body by way of equivalent forces. These equivalent forces channel non-linear processes which are absent in the ideal, elastic model.
- We have recalled from the seismic Representation Theorem that the determination of these equivalent forces in a certain volume  $V$ , combined with the computation of the elastic medium Green's function, together provide a model of seismic displacements anywhere in  $V$ . Modelling these equivalent forces is thus key to modelling seismic displacements.
- The seismic source, as seen by the Representation Theorem, is distributed over the entire volume  $V$ . The point-source approximation allows to collapse it into a single point in space. Equivalent forces are then condensed into a monopole and a dipole approximation by integration over  $V$  and  $\Sigma$ . The monopole approximation takes the form of a three-component, time varying vector force conveying the change of momentum within  $V$ . The dipole approximation, also known as the moment-tensor, represents couples of forces exerted at the point-source, and accommodates

the inelastic deformation of  $V$ . It is a nine-component, time-varying tensor, with time-dependency possibly different for each of the components. In the absence of angular momentum change at the source, the moment tensor is symmetric and only has six unique components.

Equivalent forces derived above are dependent on physical fields such as density, velocity, true stresses and ideal stresses within the material. Numerical modelling of the impact will allow to evaluate the two point source terms. Meanwhile, the expression of  $\mathbf{F}$  and  $\mathbf{M}$  already provide insights into the mechanism at play at the impact seismic source:

- The vector force  $\mathbf{F}$  (Eq. 2.25) takes a rather elegant form, which is simply the integral of the linearised momentum within the instantaneous target volume. It hints at the fact that part of the impact seismic signal is due to momentum exchange between the impactor and ejecta. It also means that  $\mathbf{F}(t)$  should be an impulse-shaped function, which decays with time as the impacted volume slowly relaxes to a new equilibrium. As such, it is not able to describe the permanent deformation of the surface, i.e. the crater, as this would require the application of a constant equivalent force on the surface. Such permanent deformations are linked to the creation of plasticity, and will therefore be accommodated by the stress glut present in the dipole term of the point source.

The typical duration of the monopole impulse is strongly dependant on the dynamics of the impactor and ejecta. The deceleration of the impactor occurs mainly in the first stage of crater formation, called the contact and compression stage. Its duration is typically the time needed for the impactor to burry itself, i.e.  $r_i/(v_i \sin(\theta))$ , with  $r_i$ ,  $v_i$  the radius and velocity of the impactor, and  $\theta$  its incidence angle [Melosh, 1989; Melosh & Ivanov, 1999]. This contact and compression time should thus be one of the dominant time scales of the monopole source.

- The expression of  $M_{ij}(t)$  in Eq. 2.30 contains two integral terms. The first term is the first moment of momentum, which is similar in dimensions to the angular momentum ( $\mathbf{L} = \mathbf{r} \times \mathbf{p}$  for a point in space with momentum  $\mathbf{p}$ ). The second term is the ideal elastic stress, i.e. the stress computed from the non-linear strain field using an ideal elastic stiffness tensor. Therefore,  $M_{ij}(t)$  originates both from momentum exchange and from the non-linear elastic behaviour of material close to the source.

From Eq. 2.30, and recalling that  $\Psi_{ij} = \Pi_{ij} + S_{ij}$ , we see that the time-evolution of  $M_{ij}(t)$  depends on the time evolution of  $v_i(t)$ ,  $S_{ij}(t)$  and  $\Pi_{ij}(t)$ . We can infer some properties about the first integral of Eq. 2.30 from the behaviour of  $v_i(t)$  in the far field. As the impactor momentum dissipates into the target volume, regions of non-zero velocity will concentrate in the seismic P and S waves. In the far-field, these waves decay proportionally to  $1/|\boldsymbol{\xi}_{P,S} - \boldsymbol{\xi}^*|$ , where  $\boldsymbol{\xi}_{P,S}$  is the position of the P- or S- pulse with respect to the point-source [Aki & Richards, 2002]. Therefore, the first term of  $M_{ij}(t)$  should reach a constant value in the far field. Note also that this term is analogous to the expression of the radial seismic moment proposed by Walker [2003].

The second term of  $M_{ij}(t)$  should also converge to a constant value, illustrating the presence of a residual plastic deformation at the source location. Similarly to Backus & Mulcahy [1976], we can write that  $\lim_{t \rightarrow +\infty} \Psi_{ij}(\boldsymbol{\xi}, t) = \lim_{t \rightarrow +\infty} \Pi_{ij}(\boldsymbol{\xi}, t) = C_{ijkl} \varepsilon^P(\boldsymbol{\xi})$ , with  $\varepsilon^P(\boldsymbol{\xi})$  being the residual plastic strain field of the source. This non-zero value of  $M_{ij}$  after the seismic event mean that couples of forces are being permanently exerted within  $V$  in order to maintain its new permanently deformed shape.

We point out to the reader that there exists an interesting relationship between the integral of the stress glut and the expression of the seismic moment of an explosion due to Müller [1973] presented in section 2.2 (Eq. 2.9). In a discussion in 2005, Richards & Kim pointed out the debate surrounding two different expressions of the moment of an explosion. The expression of Müller [1973],  $M_{0,1} = (K + \frac{4G}{3}) \delta V$ , with  $\delta V = S \langle D \rangle$ , competed with another expression:  $M_{0,2} = K \Delta V$ . The difference between the volume changes  $\delta V$  and  $\Delta V$  involved in the two expressions was yet unclear. Richards & Kim [2005] resolved this debate by stating that these two moment definitions are in fact equivalent, but that the meaning of each volume is different. Precisely, the volume  $\Delta V$  in  $M_{0,2}$  corresponds to the permanent volume change experienced by the strongly loaded material of the source. Again, we find a parallel between the second integral of  $M_{ij}(t)$  (Eq. 2.30) and Müller's equivalent  $M_{0,2}$ . Indeed, if we consider a purely isotropic, compressive source and assume the plastic strain to be related to the volume change by  $\varepsilon_v^P = \frac{\Delta V}{V_{source}}$ , the second integral of  $M_{ij}(t)$  becomes:

$$\begin{aligned} \iiint_{V_{source}} \Psi_{ij} dV &= \iiint_{V_{source}} C_{ijkl} \varepsilon_v^P dV \\ &= K \frac{\Delta V}{V_{source}} V_{source} \\ &= K \Delta V = M_{0,2}. \end{aligned} \quad (2.31)$$

Thanks to Richards & Kim [2005], we can thus conclude that the last term of the definition of the seismic moment in Eq. 2.30 is equivalent to the expression  $M_{0,2}$  of Müller [1973] used in Wójcicka et al. [2020].

Finally, we indicate a possible further simplification of the Moment Tensor expression. We recall from an integration by part that  $\int_V S_{ij} dV = \int_\Sigma S_{ij} (\xi_j - \xi_j^*) d\Sigma - \int_V \partial_j S_{ij} (\xi_j - \xi_j^*) dV$ . In the far-field, where density changes and Reynolds inertial effects can be neglected, we have:  $\partial_j S_{ij}(t) (\xi_j - \xi_j^*) \sim \rho_0 \frac{\partial v_i}{\partial t} (\xi_j - \xi_j^*)$  from Eq. 2.12. This means that in the far field, the "angular momentum" integral and the "true stress" integral of Eq. 2.30 should amount to:

$$\iiint_V S_{ij}(\boldsymbol{\xi}, \tau) dV(\boldsymbol{\xi}) + \iiint_V \rho_0 \frac{\partial v_i}{\partial t}(\boldsymbol{\xi}, \tau) (\xi_j - \xi_j^*) dV(\boldsymbol{\xi}) = \iint_\Sigma S_{ij}(\boldsymbol{\xi}, \tau) (\xi_j - \xi_j^*) dS(\boldsymbol{\xi}), \quad (2.32)$$

and that the moment should be reduced to:

$$M_{ij}(\boldsymbol{\xi}^*, \tau) = \iint_\Sigma S_{ij}(\boldsymbol{\xi}, \tau) (\xi_j - \xi_j^*) d\Sigma(\boldsymbol{\xi}) + \iiint_V \Pi_{ij}(\boldsymbol{\xi}, \tau) dV(\boldsymbol{\xi}). \quad (2.33)$$

This approximation and the respective amplitudes of the two remaining source terms will be further discussed in section 2.5.1.

As a final note, we point out that, while this second integral of Eq. 2.30 yields a symmetric tensor by definition of the Cauchy stress tensor, this is not necessarily true for the first integral. In particular, if the impact problem is not cylindrically symmetric, such as during an oblique impact, the first integral conveys the change of angular momentum imparted to the celestial body by the bolide.

### 2.3.3 Towards a more detailed source model

All the above development aims at obtaining a simple model of the impact seismic source, in the form of a point of origin for a force and six couples of forces. While the point-source



approximation has proved to be successful in a large variety of seismic studies (inversion of sources, estimations of signal amplitude and magnitude, etc...), it does not provide a full description of the seismic source physics. One of its biggest limitations is that it overlooks the effects of the source *kinematics* and of its finite dimensions on the observed seismic signal.

In the previous section, we showed that the impact seismic source distinguished itself from a classical earthquake source by the addition of a vector force and an angular momentum. But another fundamental difference between these two sources is the geometry of the equivalent forces  $\gamma^V$  and  $\gamma^\Sigma$ . Indeed, an earthquake seismic sources is traditionally represented by a density of surface forces exerted on a single fault plane, and progressing with the fault rupture front at a rupture velocity  $v_r$  [Aki & Richards, 2002]. These surface forces are the body-force equivalent of the displacement discontinuity on both sides of the fault:  $\gamma_i(\boldsymbol{\xi}, \tau) = -\mu [u_i(\boldsymbol{\xi}, \tau)]_-^+ \frac{\partial}{\partial \xi_z} \delta(\xi_z)$ , where  $\mu$  is the shear modulus of the fault,  $[u_i(\boldsymbol{\xi}, \tau)]_-^+$  is the displacement discontinuity, and  $\xi_z = 0$  defines the fault plane. Hence, the source geometry is essentially 2D, and its kinematics are linked to the kinematics of the fault rupture front on a 2D plane. On the other hand, an impact seismic source is by essence three-dimensional, and only limited by the free-surface of the crater. The equivalent of the fault rupture front is the "*shock front*", i.e. the shock wave which extends radially from the impact point.

These distinctions between the earthquake and impact source are not included in the point-source model, even though they have an influence on the seismic signal. Indeed, when dropping the point-source approximation, the extended source acts like an antenna radiating from different points  $\boldsymbol{\xi}$  in space, each point exerting equivalent forces  $\gamma^V(\boldsymbol{\xi}, \tau)$  and  $\gamma^\Sigma(\boldsymbol{\xi}, \tau)$ . Hence, as the shock front progresses, the delayed radiation of two distinct points in space causes interferences in the generated seismic signal and alter its frequency content. This phenomenon has been at the focus of many studies: Savage [1966] investigated the radiation of an elliptical fault, Haskell [1969] chose to model a rectangular fault with unidirectional slip, and Madariaga [1976] improved the model of Savage [1966] by calculating the dynamics of stress in a circular nucleating rupture.

The development of these analytical "*extended source*" models requires a knowledge of the Green's function of the propagating media. An analytical expression of the Green's function can be obtained for a homogeneous, unbounded media and is appropriate to model deeply buried sources like earthquakes. However, impact happen on free surface. Several works addressed the so-called *Lamb's problem*, which aims at deriving the Green's function of a half-space analytically, but the solution remains complex and its application is not straightforward, even for simple source models as the one cited above. Therefore, this study will not address the problem of an analytically-derived extended source model. However, we will show in section 2.5.3 that we can reproduce an extended source numerically using the stress glut and velocity fields described above. The effects of the finite source dimension on the signal spectrum can then be measured.

## 2.4 Numerical method and verification

### 2.4.1 Numerical modeling of meteorite impacts

As seen above, analytical developments quickly reach a limit in their ability to describe the source. Further understanding of the impact seismic source requires us to compute several fields (velocity, stress, displacements) evolving in a strongly non-linear regime. Numerical

modelling is adequate to our development as it provides all the needed fields in a discretised space. In this section, a numerical method to simulate impacts and estimate the source terms developed in section 2.3 is presented. In particular, we develop a method to quantify the stress glut field. We also present the approach chosen to verify this computation.

### The HOSS software

We develop algorithms and numerical methods to compute the stress glut field using the Hybrid Optimization Software Suite (HOSS). HOSS is based on the Finite-Discrete Element Method (FDEM) [Munjiza, 2004; Knight et al., 2020], which combines the Finite Element method for the description of continuum, with the Discrete Element Method to simulate fractures, fragmentation and inter-particle interactions. HOSS supports large-scale parallelisation, making simulations of several million numerical elements in 3D possible [Lei et al., 2014]. It is equipped with a variety of tunable material models for an accurate description of metals and geomaterials. As such, HOSS has been applied to simulate various impact problems [Froment et al., 2020; Caldwell et al., 2021], and to model dynamic fracture processes at play during earthquake ruptures and their effects on the frequency content of near-field seismic radiation. [Okubo et al., 2019].

### Material models

HOSS' simulation domain is a user-defined mesh of tetrahedral elements, each of them constituting a Finite Element (FE). In the FDEM framework, the four bounding surfaces of each FE are discretised as well by a set of Discrete Elements (DE). These DEs describe the way in which two adjacent tetrahedrons interact: they can be elastically bounded and form one continuous volume, or they can behave as two distinct surfaces. This is the case for granular or fractured materials, where separated volumes interact via collision and friction. Consequently, HOSS material models are of two kinds, in order to define the response of both FEs and DEs to deformation.

The response of FEs is typically separated into a volumetric and a deviatoric material model. The volumetric model specifies the evolution of pressure as a function of the volumetric strain of an element, while the deviatoric model defines the six remaining deviatoric components of stress. In this work, two specific volumetric and deviatoric models were chosen as a base for a numerical definition of stress-glut. Froment et al. [2020] demonstrated their capability in modelling the response of a porous and granular material, such as the regolith present on the surface of Mars and the Moon, to impacts in laboratory conditions. Each of these models handles elasticity and plasticity in their own way, which leads to two separate methods of computation of the stress glut. FEs may also be subject to an additional damping stress, which is added in order to reproduce the visco-elastic behaviour of realistic geomaterials. This stress term is purely inelastic, and can be simply added to the measure of the stress glut. In this study, the contribution of damping on the stress glut was determined to be negligible, and it will hence be ignored in the following sections.

In contrast with FEs, the response of DEs depends on the current conformation of simulation elements. For two initially bounded, adjacent elements, it takes the form of a strain softening curve: elements with opposite motion gradually dissipate energy into a fracturing process, until their maximal fracture aperture is reached (see e.g. Rougier et al. [2014]). Beyond this point, the two elements become independent, and will interact together via a contact detection and friction algorithm associated to a penalty that prevents

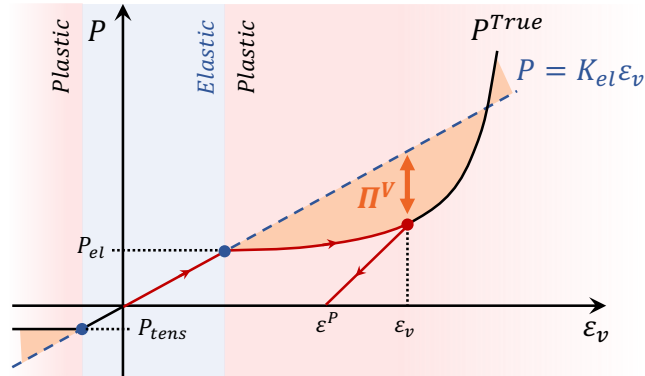


**Figure 2.7:** Graphic showing the computation method for the volumetric stress glut. The orange region denote regions where the difference between  $P^{True}$  (plain black and red curve) and the ideal pressure  $K_{el}\varepsilon_v$  (dashed blue line) is non zero.

interlocking. In the following approach, for simplicity, we do not consider the effect of fracturing on the impact seismic source. To ensure that the fracture phenomenon doesn't affect the estimate of the source, we define the material strain softening curve as having a small fracture energy compared to the energies of other dynamical processes. On the other hand, friction between particles is an important mechanism at play in the response of geo-materials and was an active force in our simulations. Although this inter-element friction has not been included in the equations of section 2.3.2 and in the following development, we discuss its possible effects on the seismic source in section 2.6.

## 2.4.2 Seismic source computation

### Computation of the stress glut

**The pressure glut** The volumetric deformation of the material is represented using the *SocCrush* model, based on an algorithm by Schatz [1974]. In this model, the deformation of an element is separated into three domains. At low pressure, the material follows Hooke's law: the pressure  $P$  and volumetric strain  $\varepsilon_v$  are related by  $P = K_{el}\varepsilon_v$ , with  $K_{el}$  being the bulk modulus of the elastic material. In this regime, the modelled pressure and the ideal, elastic pressure are equal: by definition, the volumetric term of the stress-glut (or "pressure glut") is thus zero (see Fig. 2.7). Above a certain limit stress, the pressure-strain relationship departs from this ideal linear behaviour and the material starts accumulating plasticity. Froment et al. [2020] as well as laboratory studies [Yamamuro et al., 1996; Luo et al., 2011; Housen et al., 2018] showed that an exponential curve provides a good description of the pore-crushing and compaction phenomenon that occur in a regolith-like material. In this regime, we have:

$$\Pi^V = K_{el}\varepsilon_v - P^{True} \neq 0. \quad (2.34)$$

Once pressure in the material starts decreasing, it follows a new linear-elastic unloading path back to  $P^{True} = 0$  (see Fig. 2.7). Each modelled element that has entered the pore-crush regime retains a final volumetric strain  $\varepsilon^P$ . Following Eq. 2.34, this means that in the last stages of deformation, its pressure-glut converges to  $\lim_{t \rightarrow \infty} \Pi^V(t) = K_{el}\varepsilon^P$ , as mentioned in the remarks of section 2.3.2.

**The deviatoric stress glut** We now consider deviatoric stresses using the algorithm described in Lei et al. [2020]. The deviatoric stresses of an element are related mathematically to seven different modes of deformation: one representing pure volumetric strain, which is handled by the method of section 2.4.2 above, and six modes of pure shear deformation. The six shear modes refer to six angles of deformation, written  $\varphi_{1-6}$ , which are measured within a reference material element. At each new simulation timestep  $t_{N+1}$ , the algorithm predicts the angles of the deformed material element,  $\varphi_{1-6}(t_{N+1})$ . It verifies whether the deformation associated to  $\varphi_{1-6}(t_{N+1})$  have brought the element beyond its yield surface. If it is the case, a correction is applied to  $\varphi_{1-6}(t_{N+1})$  using a return mapping method, so that corrected angles  $\varphi_{1-6}^E(t_{N+1})$  keep stresses within the yield surface. This correction is equivalent to a measure of plasticity: total angles  $\varphi_{1-6}(t_{N+1})$  are separated into "elastic angles"  $\varphi_{1-6}^E$ , and their plastic correction or "plastic angles"  $\varphi_{1-6}^P$ , as in:

$$\varphi_{1-6} = \varphi_{1-6}^E + \varphi_{1-6}^P. \quad (2.35)$$

After the correction step, a linear relationship transforms angles  $\varphi_{1-6}^E$  into the deviatoric Cauchy stress  $\mathbf{S}^D$  of the element. This action can be summarised by a linear operator  $F_{ij}$  (detailed steps can be found in Lei et al. [2020]):

$$S_{ij}^{D, True} = F_{ij}(\varphi_{1-6}^E). \quad (2.36)$$

By analogy with the volumetric stress glut, the deviatoric stress-glut  $\mathbf{\Pi}^D$  will thus be defined as the difference between ideal stresses "if all deformations associated to  $\varphi_{1-6}$  were elastic" and true stresses:

$$\begin{aligned} \Pi_{ij}^D &= \Psi_{ij}^{D, Ideal} - S_{ij}^{D, True} \\ &= F_{ij}(\varphi_{1-6}) - F_{ij}(\varphi_{1-6}^E). \end{aligned} \quad (2.37)$$

Because  $F_{ij}$  is linear, the deviatoric stress glut is simply obtained by computing the stresses associated to plastic angles:

$$\Pi_{ij}^D = F_{ij}(\varphi_{1-6}^P). \quad (2.38)$$

In the same way that a residual volumetric strain  $\varepsilon_P$  is created in the plastic regime of the volumetric model in section 2.4.2, the element might also accumulate a final plastic angle  $\varphi_{1-6}^P$  in each mode of shear deformation.

Note that this measure of plasticity requires us to compute the deformation of a reference element, with its own fixed reference axes. The computation steps hidden within the function  $F_{ij}$ , aim at mapping the deformation of this reference element onto the global simulation space, taking into account the position of each simulation element. Contrary to the volumetric stress-glut, which is a measure of the trace of the stress-glut tensor, and is consequently independent of any change of reference frame, the deviatoric stress-glut is sensitive to geometrical changes brought for instance by the rotation of a simulation element (see section SI-2 of the Supplementary Information for details). This sensitivity of deviatoric stress-glut to rotation can be problematic. Indeed, even if inelastic deformation has stopped and plastic angles  $\varphi_{1-6}^P$  are constant, the components of the stress-glut tensor will change over time as long as the position of the reference frame is changing with respect to the global simulation frame. Long-term variation of the stress-glut may appear, even though the exchange of forces with simulation elements may have ended.

In the next section, we propose a method to quantify the effect of rotation on the stress-glut tensor. The algorithms presented above for the computation of each component of the stress-glut field are tested for a single tetrahedral element in the Supplementary Information

### Post-Processing - Final numerical source representation

Computing the stress glut is one piece of the solution to the problem of representing the impact seismic source. Here, we state the protocol established for the full determination of the seismic point-source:

- A numerical simulation of an impact is run. The simulation domain must be large enough to encompass the entirety of the inelastic source region. The simulation is stopped when the displacement recorded on sensors outside the inelastic source region has stabilised.
- Images of the full simulation domain and its various fields ( $\mathbf{\Pi}^V$ ,  $\mathbf{\Pi}^D$ ,  $\mathbf{v}$ ...) are saved at regular time intervals of typically 0.1 ms for a meter-size crater. A shorter interval ( $\sim 1 \times 10^{-6}$  s) is used in the first few milliseconds of the impact to correctly capture the very fast exchange of momentum between the impactor and target.
- The volume integrals of Eqs. 2.25 and 2.30 are computed in a discrete way by summing variables over each simulation element. Because simulations are often run with a restricted domain due to computational costs (for example: a  $45^\circ$  or  $180^\circ$  cylindrical slice centred on the impact point), components of the physical fields or of the source have to be rotated or mirrored to recover the full  $360^\circ$  volume. In the source computation, a distinction between the ejecta (i.e., material not in contact anymore with the planet) and the target (i.e., the planet) is made, and the target volume is considered to be composed of every element whose centroid coordinate  $z_e$  is below the ground surface  $z = 0$ . For example, the force component of the source is given by:

$$F_i(\tau) = \frac{1}{t_{j+1} - t_j} \left[ \left( \sum_{e=0}^{N_{E,j+1}} \rho^0[e] v_i[e] V^0[e] \right)_{j+1} - \left( \sum_{e=0}^{N_{E,j}} \rho^0[e] v_i[e] V^0[e] \right)_j \right], \quad (2.39)$$

where  $j$  and  $j + 1$  designate two successive simulation images with time  $t_j$  and  $t_{j+1}$ , respectively,  $N_{E,j}$  is the number of element in the target domain at time  $t_j$ ,  $V^0[e]$  (resp.  $\rho^0[e]$ ) is the initial, undeformed volume (resp. density) of one of these elements, and  $v_i[e]$  the velocity of its centroid.

- To measure the influence of rotation on the integrated moment tensor, an alternative version is computed using the "corotated Cauchy stress"  $\bar{\Psi}$  as a measure of stress and stress glut. This alternative stress measure infers the finite rotation of an element from the polar decomposition of its deformation gradient  $\mathbf{F}[e]$  [Hoger & Carlson, 1984], such that:

$$\mathbf{F}[e] = \mathbf{R}[e] \mathbf{U}[e] = \mathbf{V}[e] \mathbf{R}[e], \quad (2.40)$$

where  $\mathbf{R}[e]$  is the rotation tensor. The corotated formulation of stresses is then:

$$\bar{\Psi}[e] = \mathbf{R}^T[e] \Psi[e] \mathbf{R}[e]. \quad (2.41)$$

These post-processing steps provide three measures of the point-source of the impact: one force component  $F_i(\tau)$ , and two time-varying moment tensors  $\bar{M}_{ij}(\boldsymbol{\xi}^*, \tau)$  and  $M_{ij}(\boldsymbol{\xi}^*, \tau)$ , with and without rotation correction.

### 2.4.3 Verification - Software coupling

#### SPECFEM3D coupling method

The point-source parameters retrieved with the above method constitute an approximated model of the impact dynamics. In order to test the ability of this model in describing the seismic wavefield away from the impact, we propose to compare two different wavefields: one is obtained by using the point-source terms as a seismic source, while the other is the prolongation of the complete non-linear wavefield provided by HOSS into the linear regime.

In opposition to the point-source, the wavefield simulated by HOSS represent a *"true"* solution to the impact problem, because it is obtained by solving the non-linear equations of motion, with realistic material models. The accuracy of HOSS results is only affected by the resolution of its simulation and the approximations made in the material models. At a sufficient distance away from the impact, strong shocks simulated by HOSS eventually reduce to linear elastic waves, enabling a comparison with the point-source signals. However, HOSS' approach is better applied at a high resolution near the source. Indeed, a small timestep and fine mesh are required to resolve rapid variations of physical fields in the impacted material, as well as contact interaction (typically, the timestep is close to  $dt = 10^{-8}$  s and the element size is  $dh = 10^{-3}$  m for a 10 cm wide impactor at 1000 m/s velocity). There is currently no way to coarsen the mesh efficiently passed the non-linear domain. This limits the simulation to relatively small domain sizes and durations, making it impossible to simulate a large linear propagation region. Consequently, we use another numerical code to model elastic waves at large distances.

Thus, we conduct the point-source verification at large distances from the crater by coupling the wavefield of HOSS with the SPECFEM3D code. While HOSS is a FDEM solver and provides a solution to the equations of motion in highly non-linear deformation regimes, SPECFEM3D is based on the spectral element method (SEM) and provides an efficient solution to the linear elasto-dynamic equation over large distances and in complex elastic media such as a layered Earth subsurface [Komatitsch & Vilotte, 1998] .

SPECFEM3D takes a variety of seismic sources as input, like a Centroid Moment Tensor or a vector force with arbitrary source time functions. Using the modelled point-source extracted from HOSS, the associated linear wavefield can thus be simulated up to distances 10s to 100s of times larger than HOSS' domain. In parallel, a method presented in Larmat et al. [2015] allows to couple HOSS' wavefield with SPECFEM3D, which is equivalent to prolongating the *"true"* solution farther into the elastic regime. The verification proposed here consists in comparing both solutions, i.e. the coupled and point-source generated seismic signals, at different receiver locations in the SPECFEM3D simulation domain, as schematised in Fig. 2.8.

In the Spectral Element Method, fields are spatially decomposed as a sum of base functions over each simulation element. The HOSS-SPECFEM3D coupling method relies on passing displacement time series extracted from HOSS to a corresponding spectral element node. The chosen element then acts as a source within the SPECFEM3D simulation. With a sufficiently dense network of source points, HOSS wavefront will be transferred to SPECFEM3D with a high accuracy. The main condition for a successful coupling is to ensure HOSS input time-series are linear, which means the coupling interface must be outside the inelastic source region.

The coupling points are generally chosen to match the grid points, also known as Gauss-Lobatto-Legendre (GLL) points, on the surface of a square box of SPECFEM3D elements.



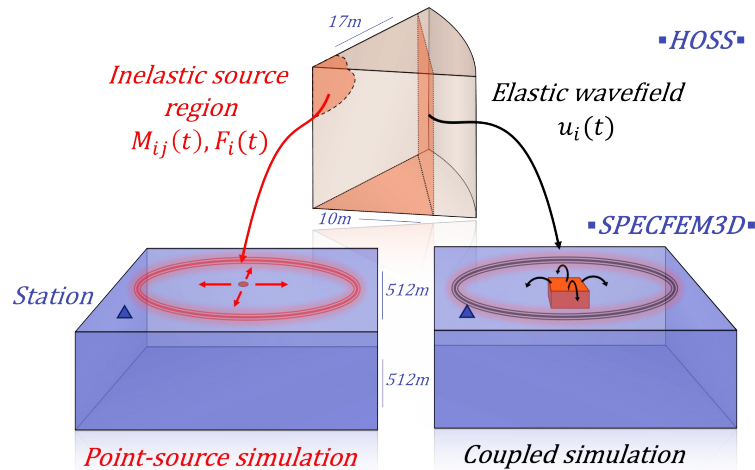


**Figure 2.8:** Graphic showing the principle of the verification method. On the top, the results of a HOSS simulation are shown. On the left side, the point-source components  $\mathbf{M}(\boldsymbol{\xi}^*, \tau)$  and  $\mathbf{F}(\tau)$  are extracted from the inelastic source region. They are used as inputs to a SPECFEM3D simulation, and provide an elastic "point-source" signal (red). On the left, the displacement wavefield of HOSS is recorded on a box away from the inelastic region. The wavefields are used as a source for a second SPECFEM3D simulation, which allows to prolongate HOSS' signal at larger distances (black). The two types of signals are recorded on common receiver to be compared.

The maximum signal frequency that can be transferred to SPECFEM3D corresponds to  $f_{max} \approx \frac{\beta}{\lambda}$ , with  $\beta$  the elastic S-wave velocity and  $\lambda$  the size of a spectral element. The coupled SPECFEM3D simulation will be able to run for as long as the provided HOSS displacement time series. A longer simulation duration requires us to extrapolate displacement waveforms and will introduce uncertainties, unless the extrapolation is straightforward, as in the case where the HOSS impact simulation has fully converged to a final static displacement field.

### Verification simulations

The source verification is performed with two different scenarios. The first scenario (A) consists in a spherical impactor hitting a target at 1000 m/s with a vertical incidence. The second scenario (B) replicates scenario (A), this time with a  $45^\circ$  incidence angle.

From the HOSS simulation, we extract the source parameters on one hand and record elastic displacement waveforms on a dense grid of GLL points on the other hand. The source parameters and displacement waveforms are used to generate two SPECFEM3D solutions, which are compared at various distances from the impact point. The inputs (geometry, material models) and outputs (sensors, raw and post-processed fields) of each of these simulations are described in the following sections.

**HOSS simulation geometry design** The construction of the mesh for the verification simulations was made according to the following protocol:

- (1) A rough mesh is built in order to estimate the size of the inelastic source region,  $R_s$  with a first run.
- (2) A more precise geometry is designed, in the form of a cylindrical sector, of  $45^\circ$  angle for the vertical impact and  $180^\circ$  for the oblique impact. Its radius and height must



be larger than  $\sqrt{2}R_s$  in order to ensure that all the points on the square coupling box will fit into the HOSS simulation domain while only recording signals in the elastic region, and prevents the box points from recording residual reflections on the absorbing boundary at the edge of the modelling volume.

- (3) The resulting mesh is about a hundred times larger than the impactor, which presents a computational challenge. To avoid prohibitive computational costs, the mesh element size gradually increases from the impact point to the outer limits. However, this must be done with caution, as a too big difference between the central and outer mesh elements would lead to unbalanced parallelisation domains and consequently slower simulation. In order to converge to a reasonable compromise between outer and central mesh, a mesh test is conducted by simulating a 1000 m/s impact on a smaller target region with varying mesh resolution.

The impactor is a basaltic sphere with radius  $r_i = 10$  cm hitting a cohesive soil. This target is a 17 m-wide cylindrical sector, extending a few meters beyond the expected non-linear source region. The mesh test and parameters of the final mesh for scenarios (A) and (B) are presented in the Supplementary Information (SI, section SI-3). The chosen meshes for scenarios (A) and (B) give a representation of the shock wave with amplitudes within 85% of the ones obtained with the finest mesh ( $l = 2$  cm). However, they provide a good compromise between accuracy, element number and load balance between parallelisation domains.

**HOSS material model design** For these verification tests, the impactor and target materials are simulated with a model adapted from [Wójcicka et al. \[2020\]](#). The target model was previously implemented in HOSS in order to simulate the impact of Perseverance’s entry balance masses on Mars [[Fernando et al., 2021](#)], and it aims at representing the response of the upper ten meters of the martian surface regolith. Other material models could have been used for this verification study, but this particular model is chosen due to its high elastic velocities ( $v_p = 1090$  m/s and  $v_s = 583$  m/s), which helps with simulation convergence.

The target deviatoric response is modelled using a Lundborg pressure-dependant strength model [[Lundborg, 1968](#)], with parameters from [Wójcicka et al. \[2020\]](#). The impactor is made of solid basalt and simulated with a Tillotson equation of state [[Tillotson, 1962](#)] and another Lundborg strength model. Parameter values for both materials can be found in Table 2.3 of the Supplementary Information (section 2.8).

**SPECFEM3D point-source and coupling simulation design** We present here the design of our SPECFEM coupling simulations. The domain is a cube 512 m in size with elements of 2 m, which amounts to  $\sim 16.8 \times 10^6$  elements. The timestep is equal to  $1.2 \times 10^{-4}$  s and the simulation duration is 1.8 s. The propagation material has the same density and elastic wave velocities as the HOSS materials in their elastic domain:  $\rho = 1589$  kg/m<sup>3</sup> (see Table 2.3 in the Supplementary Material),  $v_p = 1090$  m/s and  $v_s = 583$  m/s. It has no attenuation nor gravity. Receivers are placed every 50 m vertically below the source and on concentric circles every 50 m in radius from the source on the free surface.

For coupling simulations, the centre of the coupling box corresponds to the centre of the top surface of the cube ( $x = 0, y = 0, z = 0$ ). The coupling box occupies 7 elements in depth and 10 elements in width, for a total of 8081 GLL points.

For point-source simulations, the source is placed in the centre of the top surface of the cube ( $x = 0, y = 0, z = 0$ ). Here, we choose to compute an approximation of the Green's function of the material by simulating impulsive point-sources: impulsive forces are simulated using a Dirac delta source function and moment tensors using a Heaviside source function. The results of SPECFEM3D can then be safely convolved with the source time function derived from HOSS to obtain the correct point-source signal [Komatitsch & Tromp, 2002]. We generate one simulation for each separate component of the source. When using a point force, the Dirac impulse is represented by a triangle function with width  $2 \times dt$  and height  $1/dt$ . This ensures that the total momentum of the source is 1 Ns, and facilitates scaling with HOSS' source time function. Two simulations are run, with a force in the  $\vec{x}$  and  $\vec{z}$  directions respectively. When using a moment tensor source, the source is chosen to be SPECFEM3D internal Heaviside function, with a final value of 1 Nm. Four separate simulations are run for  $M_{xx}$ ,  $M_{yy}$ ,  $M_{zz}$  and  $M_{xz}$ .

As mentioned above, the duration of SPECFEM3D simulations being longer than the HOSS duration ( $\sim 120$  ms), HOSS source time function (for point-source simulations) and displacement waveforms (for coupling simulations) need to be extrapolated. In the case of coupling simulations, we perform the extrapolation by smoothly attenuating the velocity signal using a Hanning apodization window. In the case of point-source simulations, the extrapolation needed for HOSS source time functions is described in section 2.5.2.

## 2.5 Results

### 2.5.1 Source of a vertical and an oblique impact

Images of the simulated stress glut fields  $\Pi_{zz}^D$  and  $\Pi^V$  are shown on Fig. 2.9 for the vertical impact and on Fig. 2.10 for the oblique impact, at three different times. For both simulations, the stress glut field shows a transient stage until around 15 ms, during which the inelastic region is growing. After 15 ms, the field appears to have stabilised. The region of non-zero stress glut is larger for deviatoric processes (fourth line,  $\Pi_{zz}^D$ ) than for volumetric processes (third line,  $\Pi^V$ ). This is not surprising according to the definition of material response in section SI-1: the computation of the volumetric and deviatoric stress glut rely on two different material models. Volumetric stress glut appears when the pressure in the material exceeds its crushing strength  $P_{el}$ , while the presence of deviatoric stress glut is determined by the material's yield surface, i.e. its shear strength and internal friction, which lead to two different spatial dimensions. Note also that the deviatoric stress glut field grows at the same speed as the region of non-zero rotational velocity ( $\nabla \times \mathbf{v}$ ): this confirms that the deviatoric stress glut is inherently related to shear processes and thus to the shear (S) wave propagation. On the other hand, the volumetric stress glut follows the pressure (P) wave.

The craters formed in both simulations are shown 116 ms after the impact on Fig. 2.11. The vertical impactor results in a crater of about 70 cm depth, while the oblique impactor crater reaches only about 65 cm in depth. Moreover, while the vertical impactor remains at the bottom of the crater, the oblique one is subject to a rebound, and is shown to have escaped the crater at 116 ms (see Fig. 2.11b). This is an interesting behaviour, as the impactor rebound could enhance the impulse transferred to the target in the vertical direction. Although the 116 ms of simulation are not sufficient to capture the final crater dimension with zero gravity, we can estimate lower bounds for the final crater diameter of 1.9 m for the vertical scenario and 2 m for the oblique scenario.

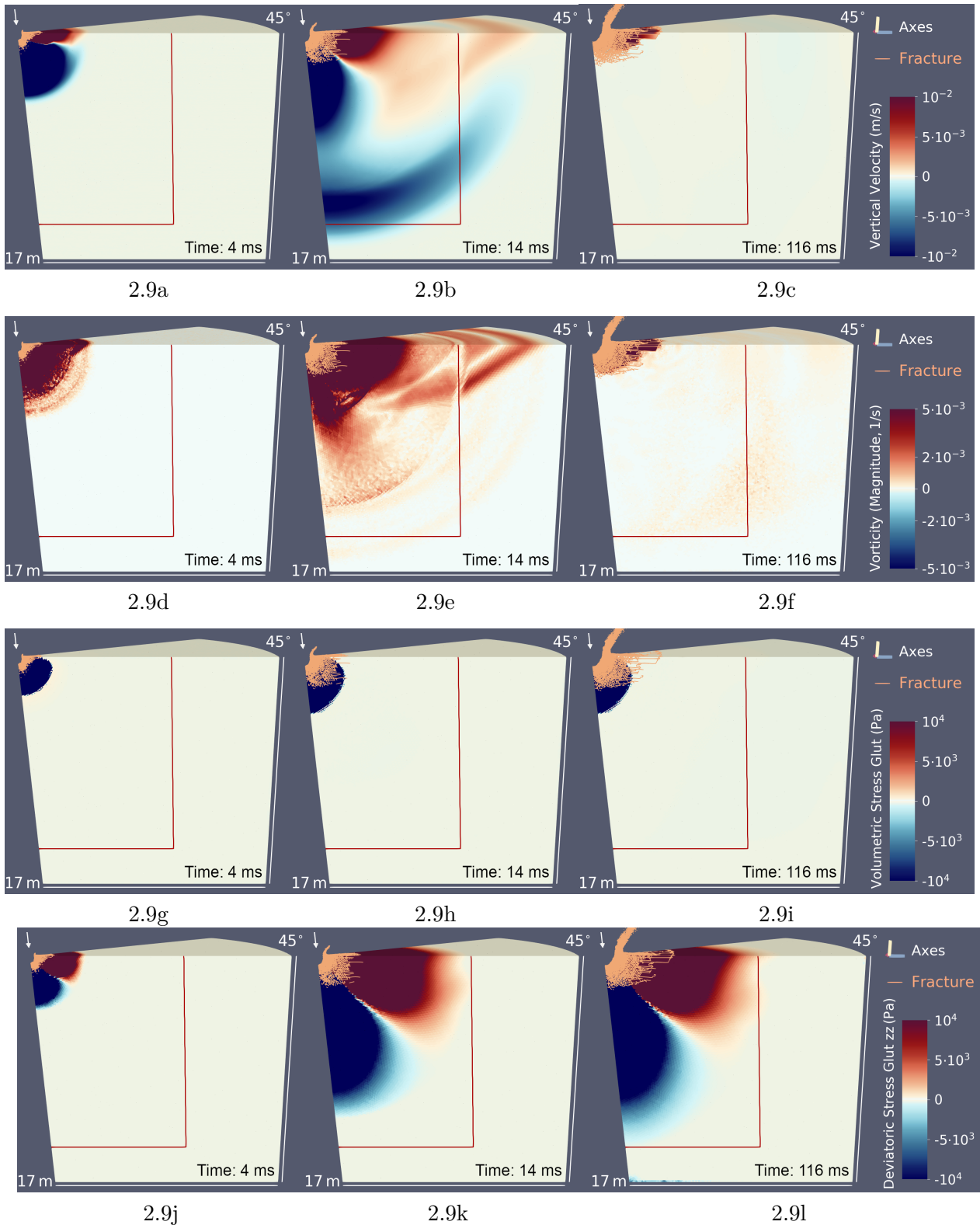


**Figure 2.9:** Stress glut and velocity fields of a vertical impact 4ms (left), 14ms (middle) and 116ms (right) after the impact on the top left of each cylindrical sector. The top line shows the vertical velocity field,  $V_z$  and the second the magnitude of  $\nabla \times \mathbf{v}$ , indicative of the presence of a shear wave and a conical surface P-S converted wave. The third line shows the volumetric stress glut field,  $\Pi^V$  and the bottom line the deviatoric stress glut component  $\Pi_{zz}^D$ . The orange lines close to the crater correspond to fractures opened in the target material. The dark red line represent the dimension on the coupling box used to record the seismic displacement wavefield. Note that it is chosen so as to be outside the non-linear source region, i.e. in a region where the stress glut is zero.

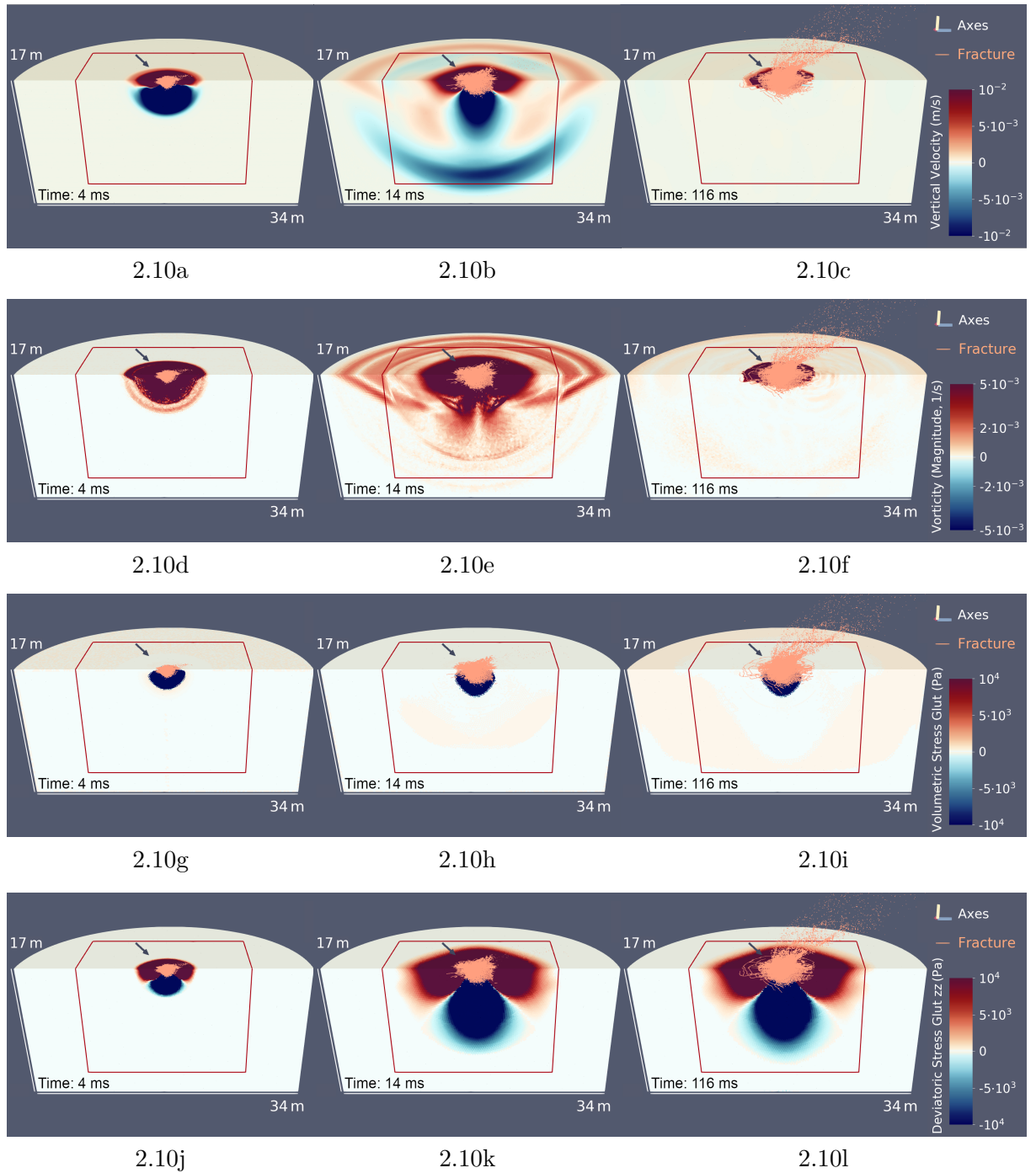


**Figure 2.10:** Same representation as Fig. 2.9 for the oblique impact.

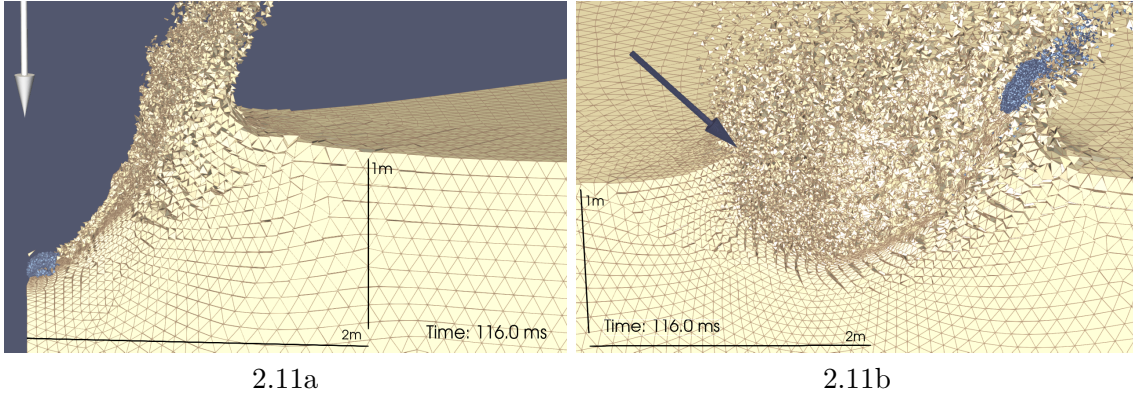


**Figure 2.11:** Crater of the vertical (left) and oblique (right) simulations after 116 ms. The light blue material represents the impactor. Simulation elements (tetrahedrons) are delimited by thin brown lines.

The stress, stress glut and velocity fields shown in Figs. 2.9 and 2.10 were integrated to obtain the point-source components, following the method of section 2.4.2. In order to generalise these results, we scale the obtained point source terms in time and in amplitude. The time is scaled to the duration of the contact and compression stage for the vertical impact:

$$\tau_N = \frac{r_i}{v_i}, \quad (2.42)$$

with  $r_i$  the impactor radius and  $v_i$  its total velocity. We find  $\tau_N = 1 \times 10^{-4}$  s. The point source force component is scaled to the measure:

$$F_N = \frac{P_i}{\tau_N}, \quad (2.43)$$

corresponding to the hypothesis that the total momentum  $P_i$  is delivered to the target within a time  $\tau_N$ . We have here  $F_N = 1.2 \times 10^8$  N. Finally, the point source moments are dimensionally scaled based on the equivalence between the seismic response to a point force and to a moment tensor (see e.g., [Aki & Richards \[2002\]](#)). This gives:

$$M_N = v_p P_i, \quad (2.44)$$

i.e., the scaling of the seismic moment proposed by [Daubar et al. \[2018\]](#) for a known impactor velocity and target P-wave velocity  $v_p$ . Here  $M_N = 1.3 \times 10^7$  Nm.

Fig. 2.12 shows the components of the force  $\mathbf{F}(\tau)$  representing the monopole of the seismic source, for both simulations. For the vertical impact, the vertical force amounts to  $0.28 F_N$  ( $\sim 3.3 \times 10^7$  N), compared to  $0.19 F_N$  ( $\sim 2.3 \times 10^7$  N) for the oblique impact. We remark that the maximum force is less than  $F_N$ , which suggests that the impactor momentum  $P_i$  is likely delivered at a deeper penetration depth, about 1.5 time the radius of the impactor. Since  $0.19 \approx \sin(45^\circ) \times 0.28$ , we can also say that the vertical force brought by the oblique impactor is well predicted by a simple projection of the force of the vertical impactor at  $45^\circ$ . However, the horizontal force reaches a maximum of only  $0.13 F_N$  ( $1.5 \times 10^7$  N), which seems to suggest that the transfer of momentum is less efficient in the  $\vec{x}$  direction. This observation might be explained by the lingering motion of the oblique impactor in the  $\vec{x}$  direction as observed in Fig. 2.11b, which reveals that the impactor keeps part of its horizontal momentum and does not transmit it to the target. It could also be due to a difference in the generation of ejecta between both cases.

Figs 2.13 and 2.14 display the components of the moment tensor extracted from HOSS, either with or without correcting for rotation. Individual components  $M_{ij}$  are shown, as



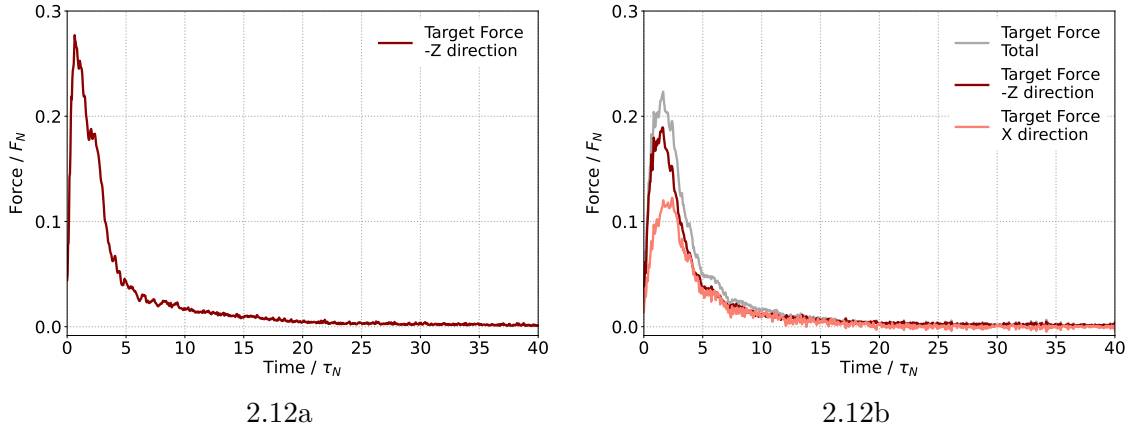


**Figure 2.12:** Force experienced by the target material for the vertical (left) and oblique (right) simulations. The sign of the force along the  $z$  axis has been inverted for clarity. The amplitudes and times are normalised to  $F_N = 1.2 \times 10^8$  N and  $\tau_N = 1 \times 10^{-4}$  s.

well as their volumetric and deviatoric decomposition, with  $M^V = \frac{1}{3}(M_{xx} + M_{yy} + M_{zz})$  the volumetric (or isotropic) term, and  $M_{ij}^D = M_{ij} - \delta_{ij}M^V$  the tensor of deviatoric terms. We adopt the traditional sign convention of seismology, where a positive moment signifies a compression of the material surrounding the source. These conventions are opposed to the ones of HOSS, where compressed material experiences a negative pressure. Note that, even after correcting for rotation in plots 2.13b and 2.14b, the moment source time function still shows residual variations instead of converging. When the target material reaches an equilibrium and a state of constant deformation, we would expect the moment to converge to a constant value. The observed residual variation is thought to be due to the ejecta elements still leaving the crater at large time scales, carrying with them part of the stress glut. Indeed, Figs. 2.9c and 2.10c indicate that some elements close to the crater still have strong positive vertical velocities after 116 ms. In the absence of gravity, they continue to escape the target domain, while they would eventually settle down if it was taken into account.

The oblique and vertical moment functions present similar amplitudes. However, some of the components differ strongly. In particular, the oblique simulation is characterised by the presence of a non-zero  $M_{xz}$  component. Without correcting for rotation (plots 2.13a and 2.14a), the  $M_{xx}$ ,  $M_{yy}$  and  $M_{zz}$  components have rather similar shapes in both the vertical and oblique simulation. However, the correction of rotation tends to considerably change these components: the amplitude of  $M_{zz}$  is increased in the vertical simulation (2.13b), while it is decreased in the oblique simulation (2.14b).

The decomposition of  $M_{ij}(\xi^*, \tau)$  into its volumetric and deviatoric components is a natural first step to understand the impact source mechanism: indeed this decomposition echoes the ways in which moments are integrated from a volumetric and a deviatoric stress glut. In a second step, a deeper understanding can be gained by further decomposing the deviatoric tensor  $M_{ij}^D(\xi^*, \tau)$ . When studying earthquake sources, it is common practice to diagonalise  $M_{ij}^D$ , and decompose it into a best-fitting Double-Couple (DC) source, based on its largest eigenvalues, and a minor Compensated-Linear Vector Dipole (CLVD) (see e.g. [Dahlen & Tromp, 1998; Shearer, 2019]). Alternatively,  $M_{ij}^D$  is sometimes decomposed in two best fitting DCs. In the case of a vertical impact with cylindrical symmetry,  $M_{ij}^D$  is already a CLVD with major axis in the  $z$  direction. Therefore, we choose to decompose the deviatoric moment tensor of the oblique impact on the same basis as the vertical impact, by first extracting a CLVD with diagonal  $(-M_{zz}^D/2, -M_{zz}^D/2, M_{zz}^D)$ . The remaining elements of  $M_{ij}^D$  form two DCs in the  $xx$ ,  $yy$  axes and  $xz$ ,  $zx$  axes. The advantage of this

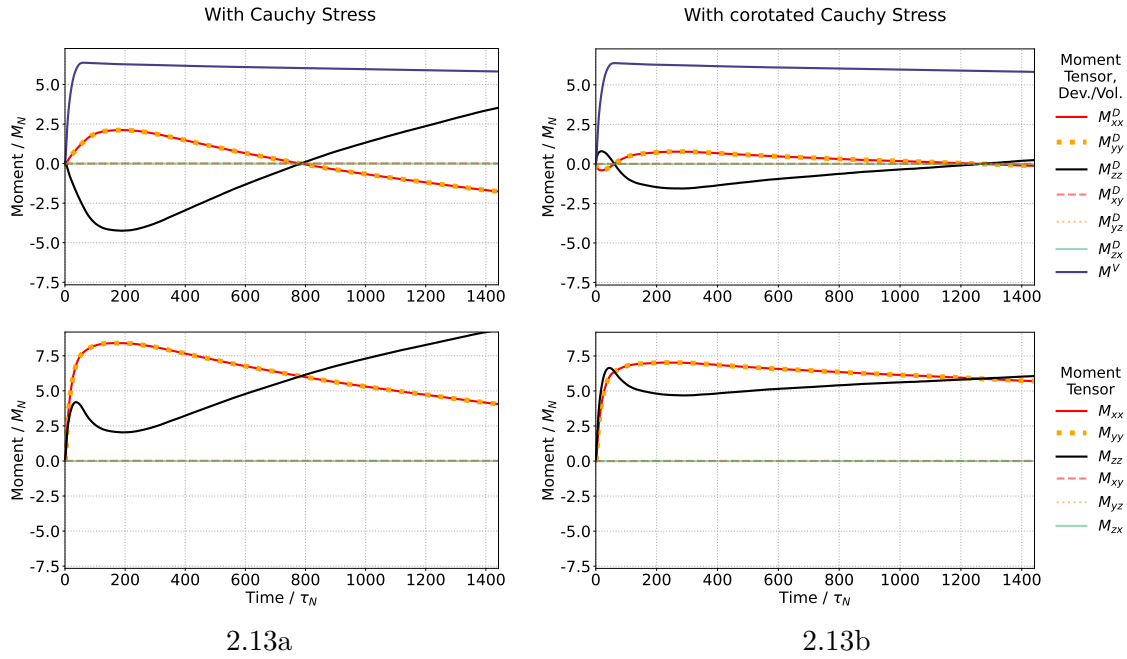


**Figure 2.13:** Components of moment tensor  $M(\xi^*, \tau)$  for the vertical impact. The amplitudes and times are normalised to  $M_N = 1.3 \times 10^7$  Nm and  $\tau_N = 1 \times 10^{-4}$  s. The components are separated into their deviatoric and volumetric components on the top line, then summed together on the bottom, such that  $M_{ij}(\xi^*, \tau) = M_{ij}^D(\xi^*, \tau) + \delta_{ij}M^V(\xi^*, \tau)$ . The left plots do not correct for rotation, while the plots on the right apply a rotation correction as described in section 2.4.2 using a polar decomposition of the deformation gradient of each simulation element before summing over the volume. Note that non-diagonal components of the moment tensor are all zero due to the symmetry of the problem, and  $M_{xx}(\xi^*, \tau) = M_{yy}(\xi^*, \tau)$ .

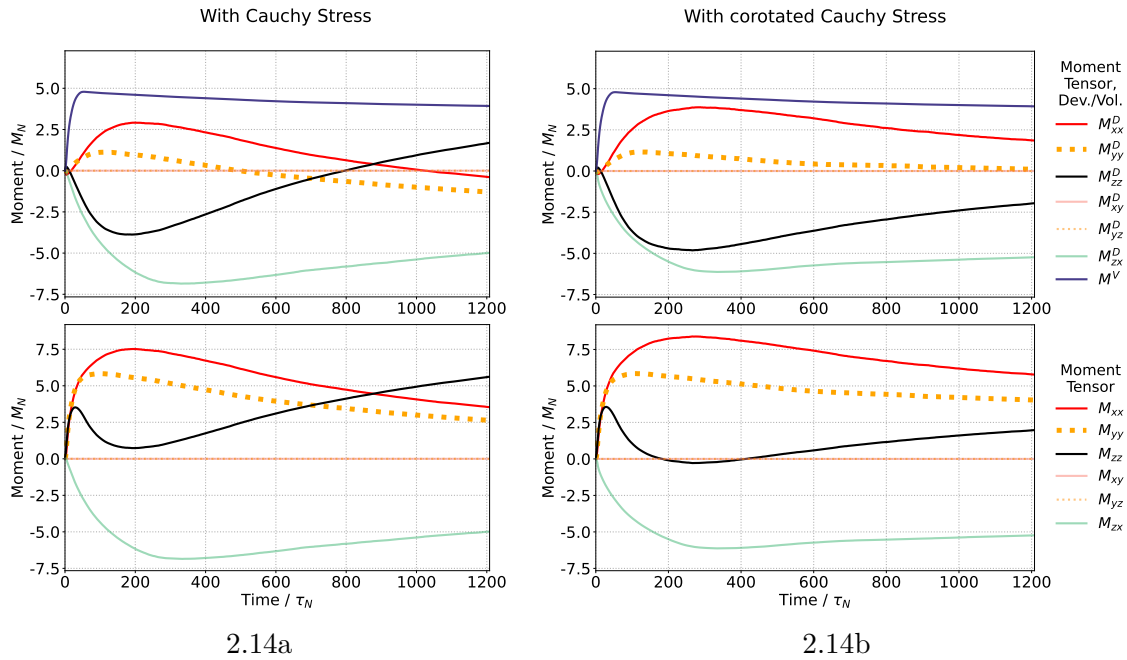


**Figure 2.14:** Same moment components as in Fig. 2.13 measured this time for an oblique impact. In the oblique case, the  $M_{xx}(\xi^*, \tau)$  and  $M_{yy}(\xi^*, \tau)$  components are no longer equal. Among the non-diagonal components of the moment tensor, only  $M_{xz}(\xi^*, \tau)$  (green curve) is non zero.



decomposition is that the principal axes of each sub-tensor are fixed in time, so that all the information on the time evolution of the moment tensor can be included in a separate factor. We can finally write the full moment tensor  $M_{ij}(\boldsymbol{\xi}^*, \tau)$  upon a sum of unit tensors:

$$\begin{aligned} \mathbf{M}(\boldsymbol{\xi}^*, \tau) = & M_0^{\text{ISO}} \hat{m}^{\text{ISO}}(t) \hat{\mathbf{M}}^{\text{ISO}} + M_0^{\text{CLVD}} \hat{m}^{\text{CLVD}}(t) \hat{\mathbf{M}}^{\text{CLVD}} \\ & + M_0^{\text{DC}_1} \hat{m}^{\text{DC}_1}(t) \hat{\mathbf{M}}^{\text{DC}_1} + M_0^{\text{DC}_2} \hat{m}^{\text{DC}_2}(t) \hat{\mathbf{M}}^{\text{DC}_2}. \end{aligned} \quad (2.45)$$

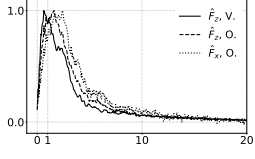
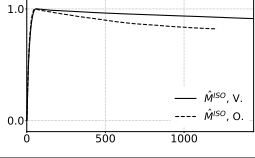
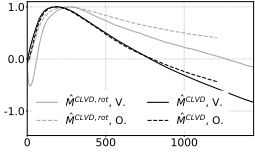
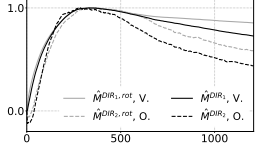
The definition of each base tensor  $\hat{\mathbf{M}}$ , their amplitude factor  $M_0$  and their normalised source time functions  $\hat{m}(\tau)$  can be found in Table 2.1, together with the vertical and horizontal force components. This decomposition sheds light on the two double-couple terms DC<sub>1</sub> and DC<sub>2</sub> conveying the effect of directivity in an oblique impact. We point out that the force and moment source time functions have quite distinct timescale. While the force pulse has a duration close to  $5 \times \tau_N$  ( $\sim 0.5$  ms) and is therefore dominated by the contact and compression stage, the moment components reach their peak between  $50 \tau_N$  and  $200 \tau_N$  (5 and 20 ms), which is in agreement with the formation time of the inelastic region in Figs. 2.9 and 2.10.

The contribution of each of these terms can be made clearer by placing the moment tensor  $M_{ij}(\boldsymbol{\xi}^*, \tau)$  on a Lune diagram. This type of diagram was proposed by [Tape & Tape \[2012\]](#) to facilitate discrimination of seismic sources on Earth: it maps every possible moment tensor onto a 2D space, giving them two coordinates  $(\delta, \gamma)$  calculated from their tensor eigenvalues. The proximity of the moment tensor to specific kind of sources (Isotropic, CLVD, DC) can this way be measured. On Fig. 2.15, we applied this representation to the vertical and oblique impact, using the original and co-rotated moment tensor.

For the vertical impact (left two plots of Fig. 2.15), both expressions of the moment tensor lie on the top part of the Lune diagram, in a region containing purely extensive sources. Because the source of a vertical impact has no DC component, it stays on the CLVD line and close to the pure explosion pole of the diagram. On the other hand, the source of the oblique impact possesses a DC component, and is not purely extensive (two plots on the right of Fig. 2.15). The effect of the directivity of the impact is visible from the white region of the beachball, where the source is compressed. The arc-length between two points in the Lune diagram measures the difference between two moment tensors in matrix space, if their orientation and norm are ignored [[Tape & Tape, 2019](#)]. The source of the oblique impact lies at equal distance from the Isotropic, CLVD and DC source in the Lune diagram, therefore, it is equally close to each of these physical source processes. We also note that the rotation correction diminishes the variability of the source in time: it describes a simpler source mechanism.

The moments represented in Figs 2.13 and 2.14 are computed by summing the two integrals of Eq. 2.30. In a final analysis of the seismic point source, we would like to test the hypothesis of section 2.3.2 on a possible simplification of the expression of  $M_{ij}(\boldsymbol{\xi}^*, \tau)$ . To this aim, we can plot integrals of Eq. 2.30 individually to determine their respective contribution. This was done in particular with the "angular momentum" term  $\int_V \frac{\partial \rho^0 v_i}{\partial \tau} (\xi_j - \xi_j^*) dV$  and the "true stress" term  $\int_V S_{ij} dV$ . As seen on Fig. 2.16, taken individually, the amplitude of these two terms is of about  $1 \times M_N$  ( $\sim 10^7$  Nm), thus comparable to the total moment components (Figs 2.13 and 2.14). However, the bottom plot of Fig. 2.16 shows that their sum is negligible after the first few milliseconds of the impact. We recall

**Table 2.1:** Normalisation and decomposition of the single force and moment tensor. The source time function of force and moment components are normalised and shown in the last column for the vertical and oblique scenario, with time scaled to  $\tau_N = r_i/v_i$ , the contact and compression length scale for the vertical impact. The amplitude of each component is given in units of  $F_N = P_i/\tau_N$  for the single force and in units of  $M_N = v_P P_i$  for the moments. For the deviatoric terms of the moment (bottom two plots), the source time function obtained using the corotated Cauchy Stress is also shown in grey, and its amplitude is given between parenthesis. The seismic moment  $M_0$  of each impact is computed using the formula:  $M_0 = \max_t \left\{ \frac{1}{\sqrt{2}} \left[ \sum_{ij} M_{ij}^2(t) \right]^{1/2} \right\}$ , with  $M_{ij}$  the total moment tensor in Nm. The moment magnitude is defined as  $M_w = \frac{2}{3} (\log_{10} M_0 - 9.1)$ , with  $M_0$  in Nm.

Monopole Term		Expression	Amplitude ( $F_0$ in units of $F_N$ )		Normalised Source Time Function $\hat{f}(t)$ (Time in units of $\tau_N$ )
			Vertical	Oblique	
Vertical Force	$\hat{F}_z = \begin{bmatrix} 0 \\ 0 \\ 1 \end{bmatrix}$	-0.28	-0.19		
Horizontal Force	$\hat{F}_x = \begin{bmatrix} 1 \\ 0 \\ 0 \end{bmatrix}$	-	0.12		
Dipole Term		Expression	Amplitude ( $M_0^X$ in units of $M_N$ )		Normalised Source Time Function $\hat{m}(t)$ (Time in units of $\tau_N$ )
			Vertical	Oblique	
Isotropic	$\hat{M}^{\text{ISO}} = \begin{bmatrix} 1 & 0 & 0 \\ 0 & 1 & 0 \\ 0 & 0 & 1 \end{bmatrix}$	6.36	4.77		
Compensed Linear Vector Dipole	$\hat{M}^{\text{CLVD}} = \begin{bmatrix} -\frac{1}{2} & 0 & 0 \\ 0 & -\frac{1}{2} & 0 \\ 0 & 0 & 1 \end{bmatrix}$	-4.23 (-1.55)	-3.86 (-4.80)		
Directivity terms (for an oblique impact)	$\hat{M}^{\text{DC}_1} = \begin{bmatrix} 0 & 0 & 1 \\ 0 & 0 & 0 \\ 1 & 0 & 0 \end{bmatrix}$ $\hat{M}^{\text{DC}_2} = \begin{bmatrix} 1 & 0 & 0 \\ 0 & -1 & 0 \\ 0 & 0 & 0 \end{bmatrix}$	-	-6.83 (-6.10)		
Seismic moment $M_0$ (Nm)		$1.11 \times 10^8$ ( $1.02 \times 10^8$ )	$1.22 \times 10^8$ ( $1.22 \times 10^8$ )		
Moment Magnitude $M_w$		-0.70 (-0.73)	-0.68 (-0.68)		

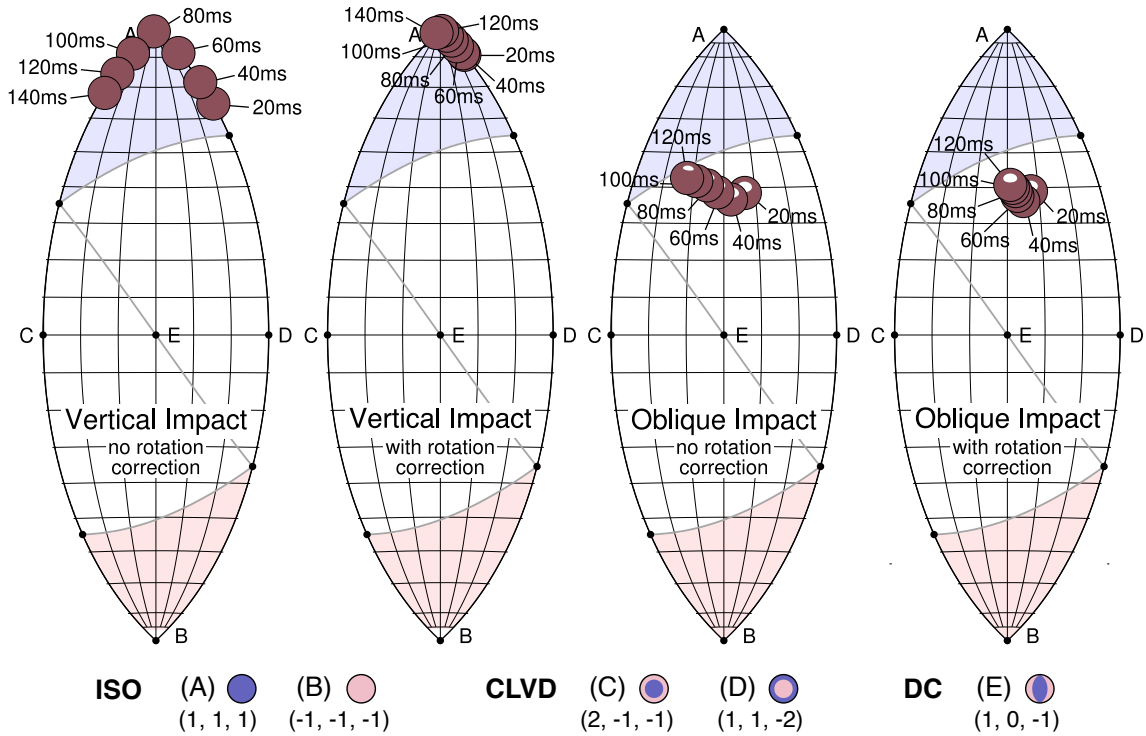


**Figure 2.15:** Lune diagram of the vertical (left two plots) and oblique (right two plots) impact moment focal mechanisms. For different times  $t_n$ , the moment tensor  $M_{ij}(t_n)$  is plotted as a beachball at its coordinates  $(\gamma, \delta)$  on the Lune diagram [Tape & Tape, 2012, 2015]. Values of  $M_{ij}(t_n)$  can be read from Fig. 2.13 and 2.14. The blue-shaded region at the top of the diagram contain moment tensors for which the beachball representation is completely black, i.e., the source region is purely in tension. The pink-shaded region contains all pure-white beachball, where the source region is purely in compression. Typical ideal seismic sources (Isotropic, CLVD, Double-Couple) are marked by points (A, B, C, D and E) on the Lune plot and identified at the bottom of the plot by their coordinates  $(\lambda_1, \lambda_2, \lambda_3)$ , where  $\lambda_i$  are the tensor eigenvalues such that  $\lambda_1 \geq \lambda_2 \geq \lambda_3$ . A small blue-pink beachball associated to these mechanism is also plotted. Plots are produced using routines from the `mtuq` python package [Modrak et al., 2018].

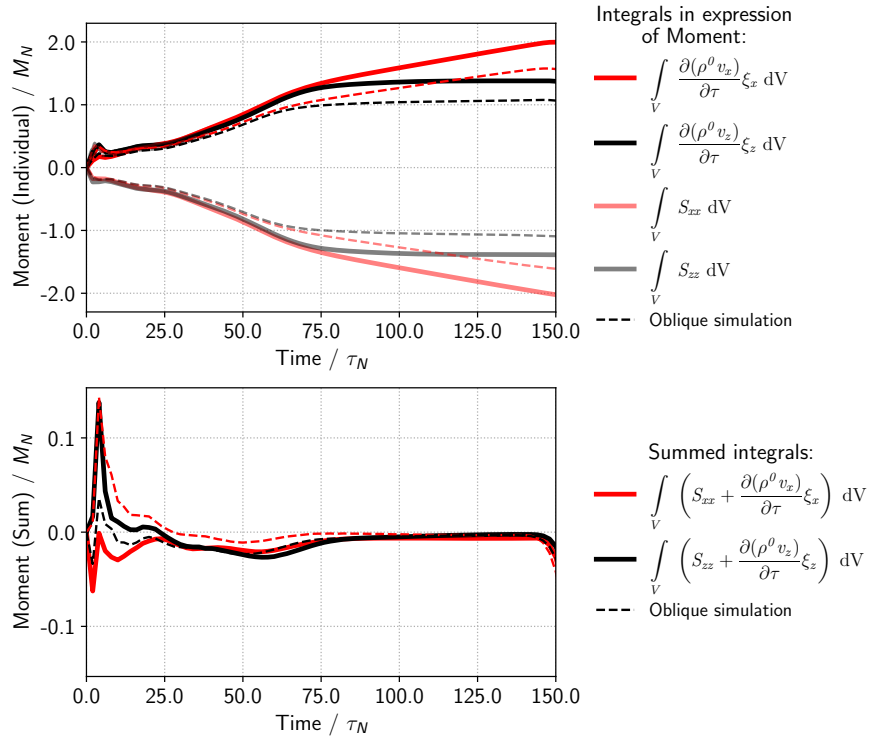


**Figure 2.16:** Plot of two of the Cauchy stress components  $\int_V S_{ij} dV$  and of the "angular momentum" components  $\int_V \frac{\partial(\rho^0 v_i)}{\partial \tau} (\xi_j - \xi_j^*) dV$  for the vertical (plain line) and oblique (dashed line) scenarios. Each components has individually a large amplitude ( $\sim 1 \times M_N$  or  $\sim 10^7$  Nm, top plot), but has a negligible amplitude when summed ( $\sim 0.1 \times M_N$  or  $\sim 10^6$  Nm, bottom plot). This plot uses the classical measure of Cauchy Stress, although a similar trend can be observed when using the corotated Cauchy stress. The amplitudes and times are normalised to  $M_N = 1.3 \times 10^7$  Nm and  $\tau_N = 1 \times 10^{-4}$  s.

the exact expression of their sum:

$$\begin{aligned}
 \iiint_V \left[ S_{ij} + \frac{\partial(\rho^0 v_i)}{\partial \tau} (\xi_j - \xi_j^*) \right] (\boldsymbol{\xi}, \tau) dV(\boldsymbol{\xi}) &= \iiint_V \frac{\partial}{\partial \tau} [(\rho^0 - \rho) v_i] (\boldsymbol{\xi}, \tau) (\xi_j - \xi_j^*) dV(\boldsymbol{\xi}) \\
 &+ \iint_{\Sigma} [S_{ij} - \rho v_i v_j] (\boldsymbol{\xi}, \tau) (\xi_j - \xi_j^*) n_j d\Sigma(\boldsymbol{\xi}) \\
 &+ \iiint_V [\rho v_i v_j] (\boldsymbol{\xi}, \tau) dV(\boldsymbol{\xi}).
 \end{aligned} \tag{2.46}$$

The fact that the term on the left of Eq. 2.46 is negligible might be associated to different explanations based on the term of the right: either the three terms compensate each other, or they are individually negligible. For example, as mentioned in section 2.3.2, it is likely that the terms  $[(\rho^0 - \rho) v_i] (\xi_j - \xi_j^*)$  and  $(\rho v_i v_j)$  are negligible except in the very first milliseconds of the impact, when the velocity of target particles are comparable to those of the impactor, leaving only the stress term  $S_{ij}$ . As mentioned in Section 2.2, the "angular momentum" term is analogous to the definition of the radial moment  $M_{rr}$  proposed by Walker [2003] and used in Wójcicka et al. [2020] (Eq. 2.10). We observed that it is compensated by the Cauchy stress, making a total seismic moment contribution of zero. Whether Eq. 2.10 is really representative of the source moment thus deserves to be debated.

## 2.5.2 Verification of the point-source

### Extrapolation of the source time function

In the previous section, the matrix components of the point source and their time-series were obtained. As presented in section 2.4.3, this source model can be convolved with an elastic Green's function, here obtained with SPECFEM3D, to simulate seismic signals at any given distance. To do so, we need to ensure that HOSS source time series and SPECFEM3D Green's functions have the same duration. In other words, the curves of Fig. 2.13 and 2.14 must be extrapolated to 1.8 s. We propose to represent our source time functions by an integrable pulse function shown to successfully fit impulses recorded in laboratory impact experiments [Daubar et al., 2018], with name "*Jeffreys pulse*" [Jeffreys, 1931]. Another advantage of the Jeffreys pulse is that its integral is a converging function at  $\lim t \rightarrow +\infty$ , which is required for our moment source time function, to represent the end of ejecta formation and crater equilibration. Its expression is:

$$j(t, \tau, c) = ct e^{-t/\tau}, \quad (2.47)$$

where  $c$  and  $\tau$  are parameters. Its integral is given by:

$$J(t, \tau, c) = (-c\tau t - c\tau^2)e^{-t/\tau} + C. \quad (2.48)$$

with  $C = c\tau^2$  chosen to ensure the source is zero at  $t = 0$ . The force source time functions are fit with a sum of two pulses using a least-square method. The moment source time function, which contains more complexity at early times, is fit with a sum of two integrated pulses  $J(t)$  and one pulse  $j(t)$  when required. The deviatoric components  $M_{xx}^D$  and  $M_{zz}^D$  are fit independently from the volumetric component  $M^V$ . We then have  $M_{xx} = M^V + M_{xx}^D$ ,  $M_{zz} = M^V + M_{zz}^D$ , and  $M_{yy}$  is deduced from  $M^V - M_{xx}^D - M_{zz}^D$  to ensure that the fit of the deviatoric components does not add any amplitude to the volumetric component. The parameters of the fit can be found in Table SI-2.4 of the Supplementary Material (section SI-4). The results of the fit in the time domain, as well as the spectrum of the force  $\mathbf{F}(\tau)$  and moment rate  $\frac{\partial \mathbf{M}}{\partial \tau}(\boldsymbol{\xi}^*, \tau)$  are shown in Fig. SI-2.33.

The fit of these source time functions highlights three distinct time-scales  $\tau$  within the source. First, as noted in section 2.5.1, a time scale of the order of  $1 \times 10^{-4}$  s, corresponding to the duration of the contact and compression stage, governs the source time function of the single force component, or in other words the transfer of momentum between the impactor and the target. The moment source time functions are composed of two time-scales of  $1 \times 10^{-3}$  s and  $1 \times 10^{-2}$  s ( $10 \tau_N$  and  $100 \tau_N$ ). The former has a stronger amplitude, and is likely associated to the formation of the strongly damaged region of the crater. The later could be linked to the continued escape of the ejecta and the late stage of the crater formation process, before the equilibrium is reached. However, the length of the time series, which is only a few times larger than the observed time-scale, might not be long enough to fully capture these slow phenomena. Additionally, it is likely that the late stage crater formation and equilibration process will be strongly modified by the presence of gravity, which adds a timescale of its own and limits the escape of ejecta, but was ignored in this study.

### Coupled and point-source signals

We run the verification simulations using SPECFEM3D. Verification simulations are purely elastic modelling using the extrapolated point source components on one side, and the

coupled HOSS-SPECFEM3D waveforms on the other side. Multiple SPECFEM3D simulations are performed to retrieve a separate Green's function for  $F_x$ ,  $F_z$ ,  $\mathbf{M}^{ISO}$  and the non-zero elements of  $\mathbf{M}^D$ . The total point-source signal is then the sum of displacements obtained for each simulated Green's function convolved with each corresponding source time function. For both impactor scenarios, a comparison of point-source and coupled models is shown on Fig. 2.17. The receiver is placed at coordinates (283, 283, 0) m on the surface, at a distance of 400 m from the impact point. We use the non-rotated source series (see section 2.4.2) to compute these point-source signals. We also show the spectra of the P- and the S-waves, which are calculated from two separate windows of the displacement time series using a Fast Fourier Transform.

At 400 m distance, we observe a good match at low frequency between the point-source and coupled signals. The horizontal displacements are better matched than the vertical displacement series. The arrival times of the P- and S-waves are also matched by the point-source signal in the time domain. However, the overall ratio between the point-source amplitude and the coupled waveform amplitude is  $\sim 5$  and  $\sim 15$  for the P- and S- waves, respectively. This discrepancy is confirmed in the frequency domain: while the point-source spectrum of the P wave displays a trend similar to the coupled spectrum, it appears shifted by a constant positive factor. On the other hand, the point-source spectrum of the S-wave presents a significant excess of energy, of more than an order of magnitude, with respect to the coupled waveform above 2 Hz. A similar tendency is observed at smaller distances from the impact. Signals recorded at 100, 200 and 300 m can be found in the Supplementary Material (Figs. 2.34, 2.35, 2.36).

Fig. 2.18 shows the respective amplitude of different components of the point-source source in the total P-wave signal: the vertical and horizontal force terms, the isotropic (or explosive) term, the CLVD and DCs. For both the vertical and oblique impact, the P and S wave point-source signals appear to be dominated by the isotropic and CLVD components (plain dark blue and green curves). It is interesting to note that the single force components,  $F_x$  and  $F_z$ , produce a lower amplitude signal than the moment source. In the low-frequency limit, their amplitude is more than one order of magnitude lower than the summed point-source signal, for both the vertical and oblique impact simulations. Whether this partition of energy between force and moments is maintained for impacts of higher velocity remains to be investigated. Indeed, we have shown that the moment is determined by the amount of inelastic damage, while the force is related to the amount of momentum transfer. Both processes might depend differently on the impactor velocity. The  $DC_2$  component has a low contribution to the overall point source signal. This is expected, as it has the lowest amplitude of all moment components in Table 2.1. We also remark the even lower amplitude of the  $DC_1$  ( $M_{zx}$ ) component of the oblique impact source. While the amplitude of its source time function is comparable to the other tensor components (about  $\sim 7 M_N$  or  $\sim 9 \times 10^7$  Nm, see Table 2.1 and Fig. 2.14), the resulting displacement amplitude is several orders of magnitude lower than the combined point-source. This can be explained by the radiation pattern of a double-couple source on the surface: here, the receiver is placed in the same alignment as the  $M_{zx}$  couples. According to Equation 4.33 in Aki & Richards [2002], we find that the amplitude of the near, intermediate and far-field displacement should be zero with  $\theta = \pi/2$  and  $\phi = 0$ .

In the time domain (Fig. 2.17a and 2.17b), the vertical coupled and point-source displacement signals ( $u_z$ ) present a discrepancy at long time scales. Indeed, the coupled displacement signal appears to be converging to a negative, static value of vertical displacement of about  $-3 \times 10^{-7}$  m at 400 m distance. This behaviour is not observed in any of the point-source  $u_z$  components produced with HOSS source time functions. A static displacement does also exist in the  $u_x$  and  $u_y$  coupled displacement signal and is correctly

reproduced by the point-source, but its amplitude is about four times smaller than in the vertical direction. The reason for this discrepancy is not clear. It might indicate a missing analytical term in the definition of the force or moment tensor, which, in their current form, do not account for the permanent deformation of the free surface due to the crater. Using a simple convolution with a step function, we find that a constant vertical force of about  $-5 \times 10^5$  N, i.e. two orders of magnitudes smaller than the main force pulse, would be needed to fit the residual  $u_z$  displacement.

### 2.5.3 Simulating an extended source

Spectral and time-domain differences observed between the coupled and point-source signals in section 2.5.2 could be due to the limits of the point-source description. Indeed, although the source model presented in section 2.5.2 seems to produce satisfying results at low frequency for the  $u_x$  and  $u_y$  displacements, the discrepancies in the high-frequency part of the spectrum are significant. As presented in section 2.3.3, a point-source is limited in its ability to model the interferences, or antenna effect, occurring within the finite source volume itself. This finite-source effect determines the cutoff frequency and pulse shape of earthquakes [Aki & Richards, 2002].

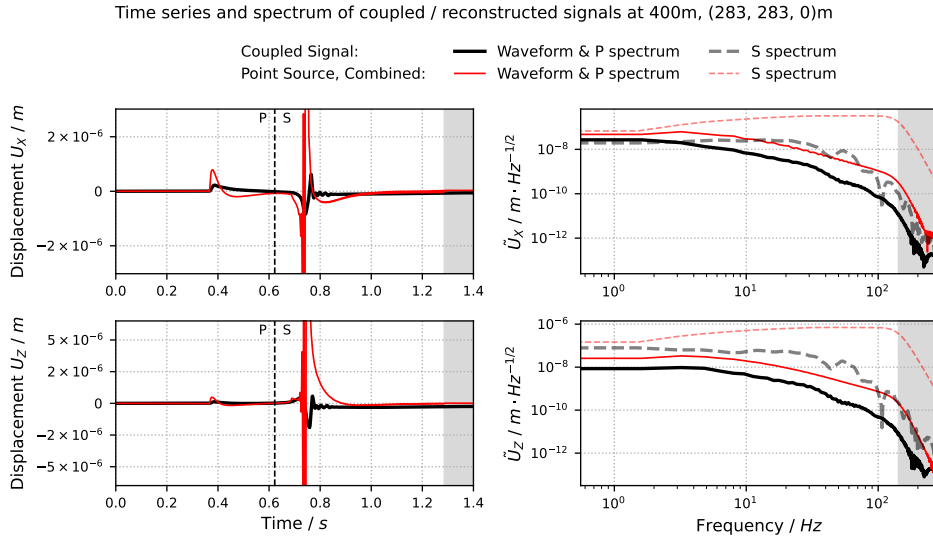
Their displacement spectra usually presents an omega-square ( $\omega^{-2}$ ) roll-off at high frequencies. This property has been explained by the presence of a "stopping phase", i.e. the abrupt end to the fault rupture associated to a slope discontinuity in the source time function (see e.g. Aki & Richards [2002]; Madariaga [2015]). Similarly for explosive sources, the roll-off was linked to the number of poles and zeros in the Laplace transform of the radial stress radiated from the source, in the approximation of spherical symmetry [Denny & Johnson, 1991]. However, slow earthquakes [Supino et al., 2020], as well as explosions in weak materials [Ford et al., 2011], are sometimes better explained using an omega-cubed model (with  $\omega^{-3}$  roll-off). 3D seismic sources could also be more efficient at damping high frequency energy than fault source, due to interferences happening in one supplementary dimension. Therefore, we propose to compare the spectral characteristic of our impact signal to the  $\omega$ -squared ( $\Omega_2$ ) and  $\omega$ -cubed ( $\Omega_3$ ) model of Aki [1967] and Brune [1970]:

$$\Omega_2(\omega) = \frac{\Omega_0}{\left[1 + \left(\frac{\omega}{\omega_c}\right)^2\right]} \quad \text{and} \quad \Omega_3(\omega) = \frac{\Omega_0}{\left[1 + \left(\frac{\omega}{\omega_c}\right)^2\right]^{3/2}}. \quad (2.49)$$

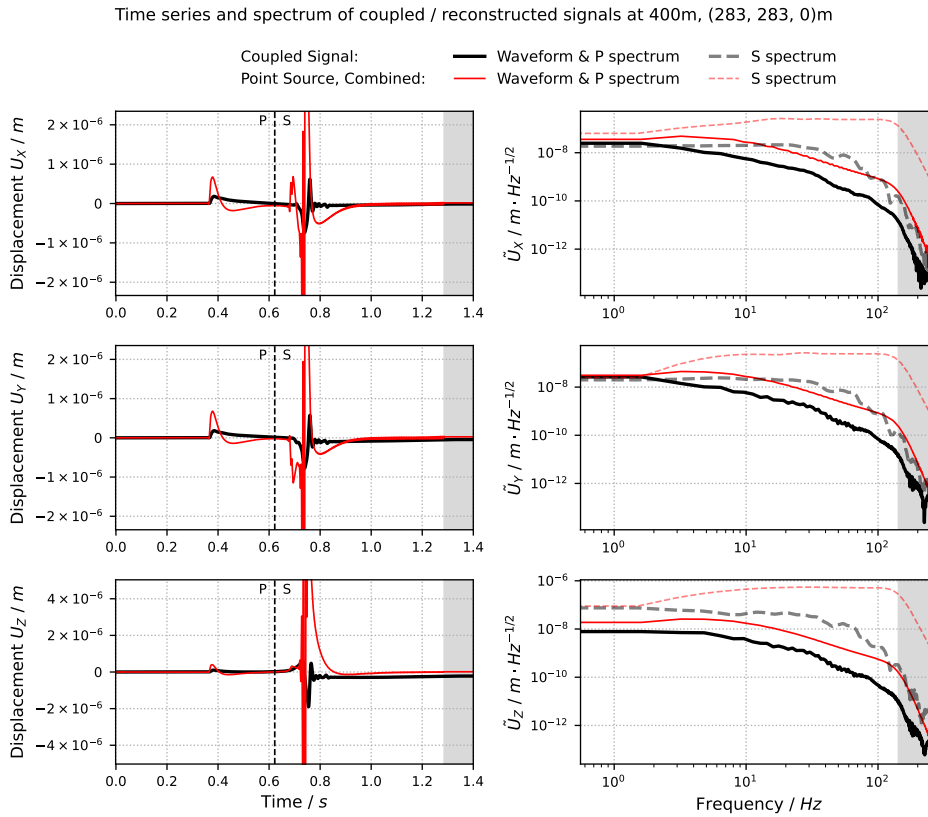
To do so, models  $\Omega_2$  and  $\Omega_3$  are fit to the P- and S-wave coupled spectrum in order to determine variables  $\Omega_0$ ,  $\omega_c$  (or  $f_c = \omega_c/2\pi$ ) and the misfit. Results and a further description of the fitting method can be found in section SI-5 of the supplementary material. We find that the  $\Omega_3$  model accomplishes overall a better fit to the coupled spectra than the  $\Omega_2$  model. However, the signal being contaminated by numerical noise above the cutoff frequency, it is difficult to discriminate with confidence between the two models. Using the  $\Omega_3$  model the cutoff frequencies of the P- and S-wave are  $f_{c,P} = 18.8 \pm 6.0$  and  $f_{c,S} = 23.8 \pm 8.8$  Hz. Considering that the cutoff frequency is limited by interferences between the two furthest points of the source, we can estimate the source size necessary to generate  $f_{c,P}$  and  $f_{c,S}$  by  $D_s = c/f_c$ . Taking the minimal velocity and maximal cutoff frequency of our system, we find that the seismic source must be at least  $v_s/f_{c,S} = 24$  m in size. This is in agreement with the typical size of the stress glut source in Fig. 2.9 and 2.10.

In order to further investigate the effects of the point-source hypothesis, we propose to simulate an extended source using SPECFEM3D and the point source model extracted



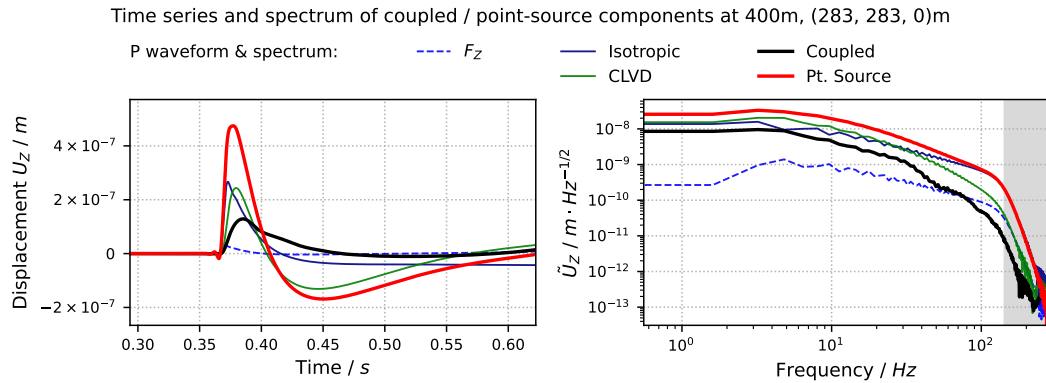


2.17a

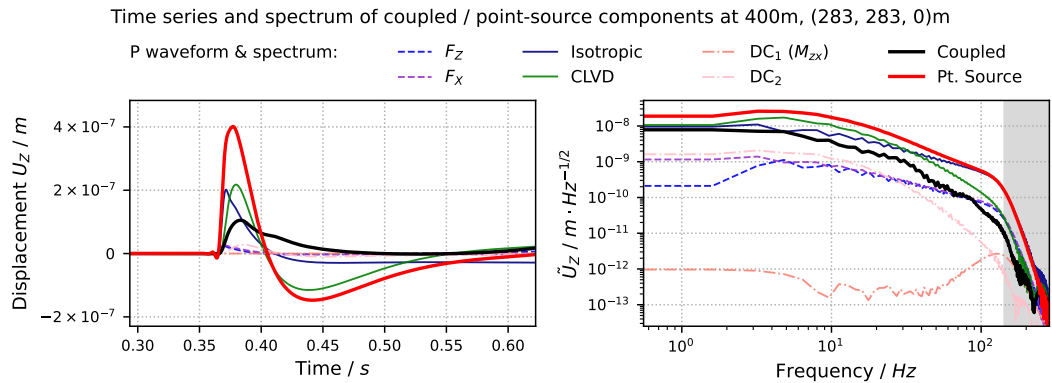


2.17b

**Figure 2.17:** Results of the comparison between coupled (black) and combined point-source (red) waveforms. The combined point-source signal (red) sums the displacements obtained for each individual modelled point-source components ( $M_{xx}$ ,  $M_{yy}$ ,  $F_z$ , etc...), while the coupled signal (black) is purely prolonged from HOSS simulations. Results are shown for a vertical impact (2.17a) and an oblique impact (2.17b). The left column represents displacement signals  $U_x$ ,  $U_y$ ,  $U_z$  in three directions for a sensor at 400 m from the source/origin. For the vertical impact,  $U_y$  is omitted as it is equal to  $U_x$  in this azimuth. All signals have been low-pass-filtered using a order 5 Butterworth filter with cutoff period of 7 ms ( $\sim 140$  Hz). The right column represent the associated spectrum, normalised by  $\sqrt{2dt/N}$ ,  $N$  being the number of samples in the waveform. These spectrum have been computed by separating the P- and the S- wave in the displacement time series: the P wave spectrum is shown with plain lines and the S wave with dashed lines. The grey shaded region on the left plots indicates the time at which residual reflections on the simulation boundaries start contaminating the signal, and on the right the low-pass-filtered region.



2.18a



2.18b

**Figure 2.18:** Vertical displacement signal (left) and spectra (right) of the P-wave in Fig. 2.17, decomposed to show the contribution of the single-forces  $F_z$  and  $F_x$ , the isotropic term, the CLVD and the directivity terms  $DC_1$  and  $DC_2$  to the total point-source signal (red curve). The coupled signal is also shown for reference. To obtain each of these point source components, SPEC3D Green's functions were convolved with the source time functions defined in Table 2.1, without rotation correction. Panel (2.18a) shows the signals associated to the vertical impact source, and panel (2.18b) the signals associated to the oblique impact source. Note the absence of the term  $F_x$  and the directivity terms  $DC_1$  and  $DC_2$  in the vertical impact case (2.18a) due to cylindrical symmetry.

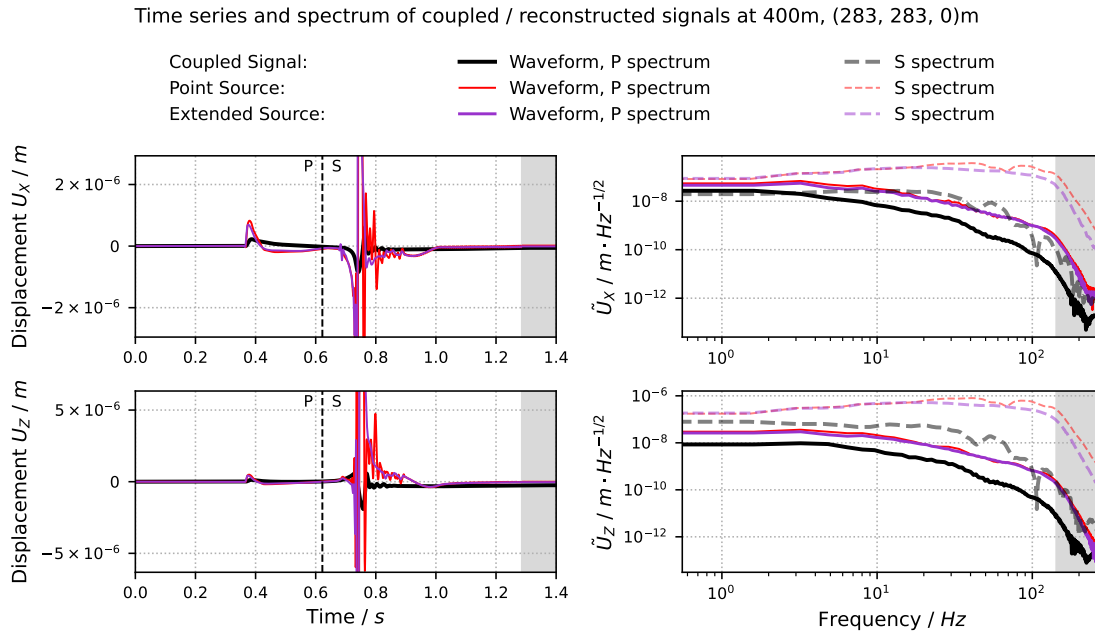


**Figure 2.19:** Comparison between the coupled signal (black), the point-source signal (red), and two models of an extended source, at 400 m distance. The purple signal is the result of a SPEC-FEM3D simulation with 19652 sources placed on a grid around the impact point. Signals are filtered as in Fig. 2.17 and 2.18.

from HOSS. This approach revisits the computation method of section 2.4.2 for the vertical impact scenario. Instead of integrating the momentum and stress glut fields over the entirety of the HOSS volume, we start by cutting the simulation space into 19652 cubes, 1 m in size, and bin HOSS elements depending on which cube they belong to. Next, the source time function terms of Eqs. 2.30 and 2.25 are computed within each cube, providing 19652 new point-sources positioned at the centre of the cubes. Each source time function is then extrapolated to 1.8 s using a Hanning apodization method, and stored in SPEC-FEM3D data files. For the nine components of the source (i.e.,  $F_x$ ,  $F_y$ ,  $F_z$ ,  $M_{xx}$ ,  $M_{yy}$ ,  $M_{zz}$ ,  $M_{xy}$ ,  $M_{yz}$  and  $M_{zx}$ ), we run a separate simulation containing 19652 sources and source time functions. The resulting signal is shown on Fig. 2.19 in purple, compared to the coupled signal in black and the point-source signal in red.

The spectra show clearly that the extended source simulated with method (1) is unable to sufficiently damp the high-frequency energy of the P and S-wave. In fact, the point-source and extended source signals appears almost identical. Using the same method as above, the typical cutoff frequency found for the P- and S- extended signal are  $f_{ce,P} = 37 \pm 12$  Hz and  $f_{ce,S} = 130 \pm 21$  Hz. This very high frequency of the S-wave means that most of the signal interfere within a radius smaller than 4.5 m in diameter.

To better understand the effect of source extension, Fig. 2.20 displays S-wave spectra obtained from the pure isotropic moment tensor component on one side, and from the  $M_{xx}^D$  deviatoric component on the other side. This allows to visualise the effect of source extension on each component. We recall that the isotropic part of the moment tensor is mostly an integral of the volumetric stress glut,  $\Pi^V$ , while the deviatoric terms of the moment depend mostly of  $\Pi^D$ . When considering only the isotropic source (left on Fig. 2.20), the effect of source extension is barely visible: the plain and dashed dark blue curves for the point and extended source respectively are almost superimposed. On the other hand, for the deviatoric source component  $M_{xx}^D$  (right on Fig. 2.20), the results show that the extended source significantly reduces the high-frequency content of the signal in the

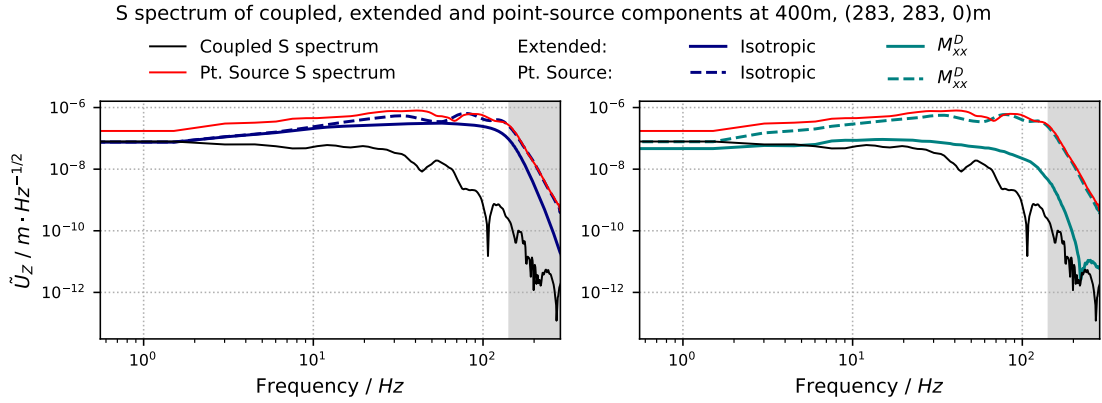


**Figure 2.20:** Effect of source extension on the seismic signal at 400 m distance. The S-wave spectra obtained using the point-source Isotropic and Deviatoric  $M_{xx}^D$  components (dashed blue and green lines) are compared to those obtained with the extended source (plain green and blue lines). The coupled and total point-source spectrum are also plotted for comparison. When considering only the isotropic source (left), the effect of source extension is barely visible on the spectrum, as seen on the plain and dashed dark blue curves. On the other hand, for the Deviatoric  $M_{xx}^D$  source (right), including source extension in the modelling result significantly reduces the high-frequency content of the signal in the S-wave window.

S-wave window. This discrepancy is easily explained by the stress glut field dimensions displayed in Fig. 2.9: while the deviatoric stress glut occupies more than 10 m radius, it represents only a portion of the total source according to Table 2.1. On the other hand, the volumetric stress glut dominates the source in amplitude, but occupies less than a 2 m in radius. In other words, the small dimensions of the volumetric stress glut prevent the sufficient damping of the S-wave energy within the extended source simulation.

It is clear that, in order to model a signal with the proper frequency content, a larger volumetric source is required. But Fig. 2.20 also shows that, despite the larger dimensions of the deviatoric stress glut, even signals simulated with the extended deviatoric source still remain at least one order of magnitude above the coupled signal at 100 Hz. All these observation lead to the conclusion that either the amplitude of the stress glut is overestimated, or its spatial dimensions are underestimated. The explanation for both is likely a missing term in the numerical definition of the stress glut, which we discuss in section 2.6.

## 2.5.4 Towards Lunar and Martian data

### Signal at regional distances

Here, we investigate the evolution of seismic waveforms at regional distances ( $> 100$  km). Variations in seismic velocities and the effects of seismic attenuation will start to affect the signal after a few kilometres of propagation. These propagation effects can be modelled on Mars in a simple way taking into account the current knowledge on the Martian subsurface, and using parameters estimated from the analysis of the recent impacts [Garcia et al., 2022]. We propose to place the receiver at  $r = 100$  km distance from the 1000 m/s vertical impact. For the simplicity of the discussion, we consider the propagation media homogeneous and similar to the Martian crust. Thus, the wave experiences a geometric attenuation in  $1/r$ . We use 4000 m/s for the velocity of P-waves and 2310 m/s for S-waves, as in Garcia et al. [2022]. Similarly, a quality factor  $Q_\kappa = 3500$  is used for the attenuation

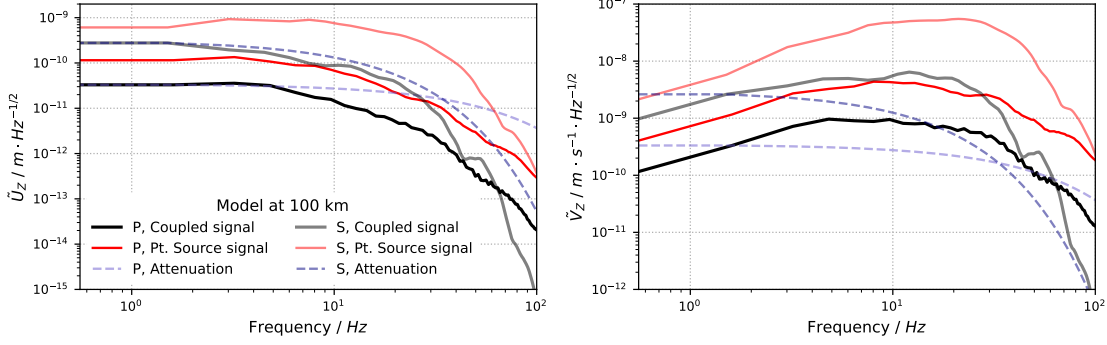


**Figure 2.21:** Spectra of the coupled and point-source signals extrapolated from 400 m distance up to 100 km distance, using an attenuation and crust model from [Garcia et al., 2022]. The right plot represents vertical displacement and the left plot vertical velocities of the S and P waves. The attenuation spectra is represented with dashed blue lines.

of P-waves, following the interpretation of the P-wave spectrum of events S0981c and S0986c, and  $Q_\mu = \frac{4}{9}Q_\kappa$ . Scattering is neglected in these attenuation values. With these parameters, the P- and S-wave spectra at  $r = 100$  km distance can be estimated from the signal at 400 m in the following way:

$$\begin{aligned} \tilde{u}_{z,P}(r = 100 \text{ km}, \omega) &= \tilde{u}_{z,P}(r = 400 \text{ m}, \omega) \frac{400}{100 \times 10^3} \exp \left[ -\omega \frac{100 \times 10^3 - 400}{2v_p Q_\kappa} \right] \\ \tilde{u}_{z,S}(r = 100 \text{ km}, \omega) &= \tilde{u}_{z,S}(r = 400 \text{ m}, \omega) \frac{400}{100 \times 10^3} \exp \left[ -\omega \frac{100 \times 10^3 - 400}{2v_s Q_\mu} \right]. \end{aligned} \quad (2.50)$$

The resulting spectrums of the displacements  $\tilde{u}_z$  and the velocities  $\tilde{v}_z$  associated to the P and S waves are shown on Fig. 2.21. The simulated P-wave low-frequency amplitudes are about one to two orders of magnitude smaller than for event S0793a ( $3 \times 10^{-9} \text{ m} \cdot \text{Hz}^{-1/2}$  at 2 Hz) and S0986c ( $2 \times 10^{-9} \text{ m} \cdot \text{Hz}^{-1/2}$  at 2 Hz), with only  $3 \times 10^{-11} \text{ m} \cdot \text{Hz}^{-1/2}$  for the coupled signal at 2 Hz. This is consistent with a smaller impact crater of about 2 m diameter for this simulation, compared to 3.9 m and 5.7 m observed on Mars for S0793a and S0986c. The P-wave cutoff frequency measured in the attenuated spectra using the  $\Omega_3$  model is  $f_c = 11 \pm 6$  Hz (See SI-SI-5 and Fig. SI-2.38). Although smaller than the value obtained in section 2.5.3 without attenuation ( $f_{c,P} = 18.8$  Hz), it is also higher than observed for InSight's detected events, i.e. 9.4 Hz for S0793a and 8.0 Hz for S0986c. We also note that the S-wave spectra represented in Fig. 2.21 are strongly contaminated by attenuation above 10 Hz, thus the apparent cutoff frequency (also about 10 Hz) at this distance is less than the true source cutoff,  $f_{c,S} = 23.8$  Hz and the high-frequency roll-off appears stronger than for the P wave.

### Comparison of the model with recorded Lunar and Martian Impacts

We compare the seismic moment computed by HOSS for a 1000 m/s impact to estimates obtained for large Lunar impacts [Gudkova et al., 2011; Daubar et al., 2018] and for Martian events S0793a, S0981c, S0986c and S1094b [Garcia et al., 2022; Posiolova et al., 2022]. The amplitude of the seismic motion generated by an event depends on the value of the source seismic moment,  $M_0$ , but also on the mechanical properties of the source region (see e.g. Aki & Richards [2002]). Therefore, in order to properly compare seismic moments from impact sources on different bodies with varying surface materials, as on the

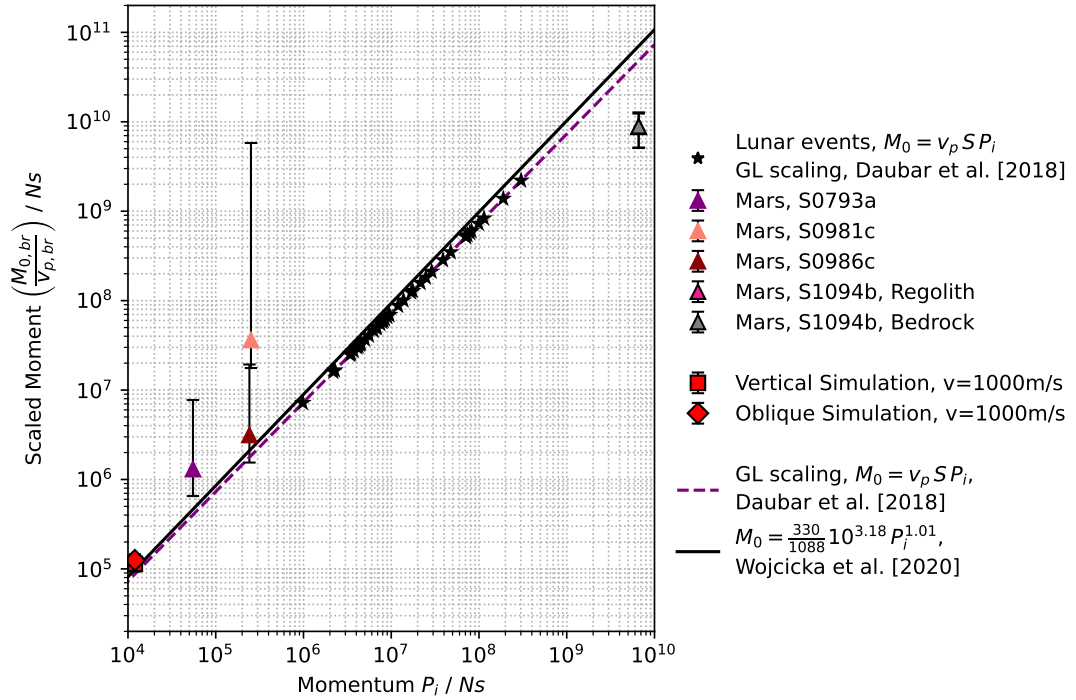


**Figure 2.22:** Scaling of different impact seismic moments estimates with their impactor momentum,  $(P_i)$ . To reduce biases due to the difference in surface material on the Moon and Mars, the moments  $M_0$  from each study are converted to a reference moment  $M_{0,br}$  in an underlying bedrock material, using Eq. 2.51 and values in Table 2.2, and divided by  $v_{p,br}$  for consistency in units. The momentum of Lunar impact events is given by Gudkova et al. [2015]. Their unscaled seismic moment  $M_0$  is calculated from  $M_0 = v_p S (P_i)$ , with  $S = 1.5$  the ejecta amplification factor and  $v_p = 330$  m/s. The associated Gudkova-Lognonné (GL) scaling relationship is shown by the dashed purple line. The scaling relationship found by Wójcicka et al. [2020] in a material with  $v_p = 1088$  m/s is shown with a black line, converted to the Lunar seismic velocities using a multiplication by a factor  $330/1088$ . The momentum of Martian impact events S0793a, S0981c and S0986c were estimated by Garcia et al. [2022] using a statistical model of meteoroid entry [Collins et al., 2022]. Their unscaled seismic moment was estimated from a numerical waveform fitting, in a reference model with a surface sedimentary layer given by Table 2.2. The seismic moment of the large event S1094b was estimated by Posiolova et al. [2022] in two different materials using a scaling relationship between seismic moment and crater diameter from Wójcicka et al. [2020]. Uncertainties shown for Martian impact seismic moments are taken from the literature, and might not represent the uncertainty in the impacted material properties. Finally, the scaled moments of our 1000 m/s oblique and vertical impacts simulations are shown in the lower end of the graph.



Moon, on Mars, and in a numerical simulation, one must first establish a common reference source material. Daubar et al. [2018] supposed that the impact-generated seismic wave was measured in a strong bedrock layer beneath the impact region, with density  $\rho_{br}$  and P-wave velocity  $v_{p,br}$ . Let the amplitude of P-waves in the bedrock layer be fixed, then an impact with seismic moment  $M_0$  happening in an overlaying layer with density  $\rho$  and P-wave velocity  $v_p$  corresponds to a moment  $M_{0,br}$  in bedrock given by [Daubar et al., 2018]:

$$M_{0,br} = M_0 \frac{\rho_{br} v_{p,br}^3}{\rho v_p^3} \frac{2\rho v_p}{\rho_{br} v_{p,br} + \rho v_p}. \quad (2.51)$$

Here, the first fraction corresponds to an amplitude scaling term, and the second fraction to the transmission factor for seismic waves going from the unconsolidated source material to the solid bedrock. A similar approach was followed by Posiolova et al. [2022] when comparing the seismic moment estimated from P-wave amplitudes using a seismic model at 50 km depth on Mars, with the seismic moments computed in a regolith or fractured basaltic material analogous to the Martian surface. Here, we choose to compare Lunar, Martian and simulated seismic moments by first converting them into a moment  $M_{0,br}$  in a bedrock with  $\rho_{br} = 2700 \text{ kg/m}^3$  and  $v_{p,br} = 1000 \text{ m/s}$ , as in Daubar et al. [2018], using Eq. 2.51. The material properties  $\rho$  and  $v_p$  of the source layer are chosen so as to match the seismic models used in each study when computing  $M_0$ . For example, the Lunar impacts are assumed to have occurred in a material with  $v_p = 330 \text{ m/s}$  and  $\rho = 2000 \text{ kg/m}^3$ , as in Daubar et al. [2018]. Other values of  $v_p$  and  $\rho$  for Martian impacts and our simulations are reported in the third and fourth columns of Table 2.2, with associated references. The obtained moments  $M_{0,br}$  are divided by  $v_{br}$  to obtain results in Ns, and plotted against the impactor momentum  $P_i$  in Fig. 2.22. Despite the significant discrepancies in the calculation methods for  $M_0$  between these studies, the graph indicates that our results are in trend with the seismic moments calculated for small Martian Impacts and with the scaling determined for Lunar impacts.

Previous studies have also proposed a comparison of impact source duration estimates,  $\tau = 1/f_c$ , on the Moon and Mars [Gudkova et al., 2015; Garcia et al., 2022; Posiolova et al., 2022]. However, again, Gudkova et al. [2015] have shown that this seismic parameter is sensitive to surface material properties, such as regolith porosity. Garcia et al. [2022] also observed that Lunar impact events are characterised by a longer source duration than similar Martian events. The authors relate the longer Lunar impact source duration to the lower seismic velocities of the Lunar regolith, which result in slower source dynamics. To be able to better compare sources properties on Mars, the Moon and in our simulations, we propose to base our comparison on another useful scaling variable for seismic sources: the estimate of the *source size*, ( $\tau v_s$ ), obtained by multiplying the source duration and the S-wave velocity at the source location. Just like the scaling of Fig. 2.22, this multiplication by  $v_s$  aims at reducing the bias associated to the difference in surface properties between each impact type. However, some hypotheses must still be made for the choice of  $v_s$  and  $\tau$  on the Moon and Mars.

For Lunar and Martian impacts, we adopt values of  $v_s$  found in the literature for a source depth of approximately 10 m, and 20 m for the largest Martian impact S1094b (see Table 2.2). This is a first order estimate, which does not account for variation of  $v_s$  with depth, or the variation of source depth with the size of the crater. In addition, when using real seismic data, the estimation of the source duration or cutoff frequency is not straightforward. Indeed, its value depends on the time window chosen to compute the source spectra: long time windows will contain a mixture of P- and S-waves with potentially different source time scales. The determination of  $\tau$  is also affected by scattering and attenuation phenomena at regional distances. In Gudkova et al. [2015], source durations of



**Table 2.2:** Parameters used for the scaling of seismic moments and source size estimates (Figs. 2.22 and 2.23). Seismic moments of Fig. 2.22 are all scaled to a reference bedrock material with density  $\rho_{br}$  and velocity  $v_{p,br}$ , following a method similar to Daubar et al. [2018] (see also Posiolova et al. [2022]). The value of  $\rho$  and  $v_p$  in Eq. 2.51 are chosen so as to best match the seismic models used in the determination of  $M_0$  in the corresponding literature. For the scaling of the source size  $\tau v_s$  in Fig. 2.23, we use estimates of  $v_s$  at source depth, i.e. about  $\sim 10$  m for small impacts and  $\sim 20$  m for the large impact of S1094b on Mars. The last column gives  $v_i$ , the typical impactor velocity on each surface types used to compute the kinetic energy.

Impact type	References	$v_p$	$\rho$	$v_s$	$v_i$
		m/s	kg/m <sup>3</sup>	(at source depth) m/s	km/s
Lunar impacts	Daubar et al. [2018] ( $v_p, \rho$ ) Gudkova et al. [2011] ( $v_i$ ) Tanimoto et al. [2008] ( $v_s$ )	330	2000	100 (10 m)	2 (artificial) 20 (natural)
Mars, small impacts	Garcia et al. [2022] ( $v_p, \rho, v_i$ ) Larmat et al. [2020] ( $v_s$ )	744	1800	300 (10 m)	6
Mars, S1094b (bedrock)	Posiolova et al. [2022] ( $v_i$ ) Wójcicka et al. [2020]; Rajšić et al. [2021b] ( $v_p, \rho$ ) Larmat et al. [2020] ( $v_s$ )	2045	2150	400 (20 m)	10
Mars, S1094b (regolith)	Posiolova et al. [2022] ( $v_i$ ) Wójcicka et al. [2020]; Rajšić et al. [2021b] ( $v_p, \rho$ ) Larmat et al. [2020] ( $v_s$ )	1088	1589	400 (20 m)	10
Simulation	This work	1090	1589	583	1
Bedrock (Reference)	Daubar et al. [2018]	1000	2700	-	-

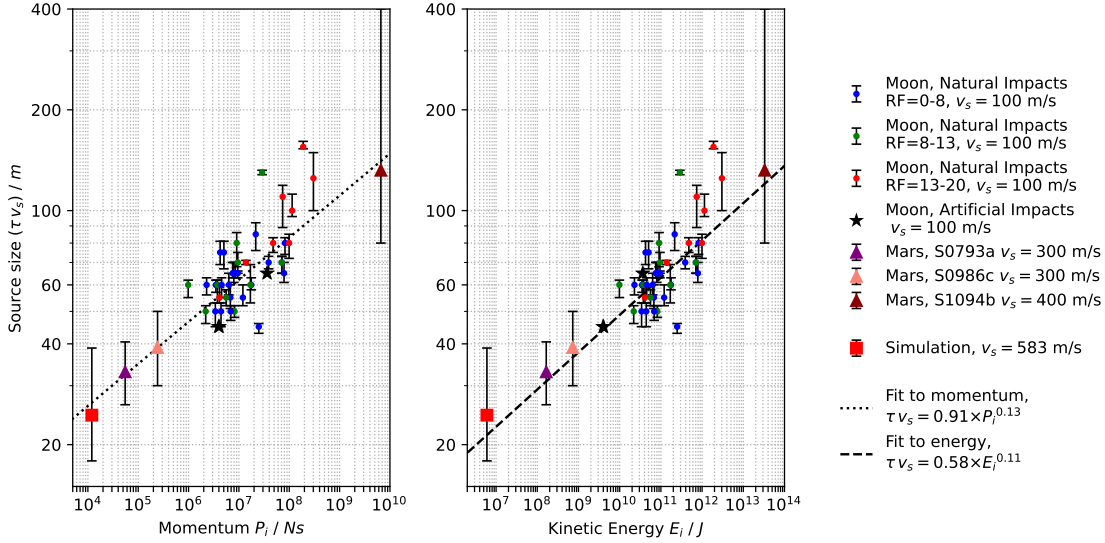


**Figure 2.23:** Scaling of the "Source size" estimate,  $(\tau v_s)$ , with the impactor momentum  $P_i$  on the right and the impactor kinetic energy  $E_i$  on the left. The kinetic energy is computed from the impactor momentum by  $E_i = P_i \times v_i/2$ . Different values of  $v_s$  and  $v_i$  are used depending on the impact type, which are given in Table 2.2. For Lunar events,  $v_s = 100$  m/s corresponds to the S-wave velocity of Lunar regolith at 10 m depth [Tanimoto et al., 2008]. Lunar impacts are separated in three groups depending on the regolith thickness function (RF) at their location following Gudkova et al. [2015]. We use  $v_s = 300$  m/s for the small Martian events and  $v_s = 400$  m/s for event S1034a, which are the S-wave velocities at 10 m and 20 m depth respectively in a lava-flow subsurface model modified for Martian conditions [Lesage et al., 2018; Larmat et al., 2020; Daubar et al., 2020; Posiolova et al., 2022]. For our simulation results,  $v_s = 583$  m/s, as given by our material model. A power-law fit to the data is represented by dotted and dashed lines, respectively for the momentum and the energy scaling.

large Lunar events were computed on long time windows using a fit to a function  $\hat{s}(\omega, \tau)$  which included an attenuation model and an  $\omega^{-3}$  roll-off at high frequency. To better match these results, we use the fit of the  $\Omega_3$  model to the coupled S-wave as our estimate of the source duration  $\tau_S = 1/f_{c,S}$ . For small Martian events [Garcia et al., 2022], the source duration was estimated from a fit of a  $\Omega_3$  model to the first  $\sim 5$  s of signal arrival, in order to isolate the P-wave information and limit contamination from seismic scattering. We suppose that these Martian results have a  $\pm 2$  Hz uncertainty.

With these limitations in mind, we plot the source size  $\tau v_s$  as a function of the impactor momentum  $P_i$  and impactor kinetic energy  $E_i$  on Fig. 2.23. On both scalings, we find that Martian and Lunar events follow a similar trend, with an overall increase of the source size with impactor energy or momentum. Source size estimates align with impactor momentum and energy with a slope of 0.13 and 0.11, respectively. The numerical simulation estimate is again consistent with Lunar and Martian data.

## 2.6 Discussion

The model developed in section 2.3 provides an exhaustive description of the impact seismic source. Contrary to previous studies, which proposed models based on the seismic moment of explosions, or on the seismic impulse, we introduce an expression of impact-generated displacements which combines a 9-component moment tensor and a vector force, both varying in time. In support of this model, we develop a new numerical method

to compute the stress glut, an essential parameter in the seismic source. This mixed analytical/numerical approach is able to better represent the temporal and mechanical complexity of the impact phenomenon. It also offers different levels of approximations, from the point source to the extended source representation.

A key finding of this study is that the impact seismic source cannot be rigorously described with only an impulse, nor with only its seismic moment: in fact, its point source expression is a combination of both. By decomposing the moment tensor into its isotropic and deviatoric component, we find that a CLVD mechanism is present in both a vertical and oblique impact source, and that an additional significant DC mechanism must be accounted for in an oblique impact. Hence, impacts are not similar to pure isotropic explosions. Different source-time functions, with different time scale, are associated to each of these mechanisms, as listed on Table. 2.1. We note that, although the vector force must appear in the description of the impact source to convey the transfer of momentum, its contribution to the seismic amplitudes in the far field is limited, and the signal appears dominated by the dipole of the source.

The method proposed in this study relies on non-linear impact simulations to compute the seismic source terms. As such, the definition of the stress glut in the numerical model is key to properly retrieve the source. At low frequency, the seismic signal obtained using this stress glut model agrees with the prolonged non-linear signal to within an order of magnitude. However, at high frequency, we note strong discrepancies between the spectra obtained from the stress glut and from the coupling. We pinpoint below several current limitations of the stress glut model.

First, in section 2.4, we note that element finite rotation in space affects stress glut measurements significantly. The problem of rotation effects ties in to a fundamental question in material mechanics, which is the definition of stress and strain for finite deformation. The classical stress measure in seismology is the Cauchy Stress Tensor, which describes the forces applied to a volume element in its deformed configuration. Other stress measures, like the Second Piola-Kirchhoff stress tensor, can also be used to better describe pre-stressed media (see e.g. [Dahlen & Tromp \[1998\]](#)). However, these stress measures are only valid in cases where deformation can be considered infinitesimal, with the infinitesimal strain tensor defined as  $\varepsilon_{ij} = \frac{1}{2}(\frac{\partial u_i}{\partial x_j} + \frac{\partial u_j}{\partial x_i})$  [[Dahlen & Tromp, 1998](#); [Aki & Richards, 2002](#)]. In impact simulations, deformations can have a scale comparable to the typical size of the volume element, and infinitesimal strain theory is no longer applicable. Instead, finite strain theory describes deformations using the deformation gradient tensor introduced in section 2.4.2, which relate the current configuration of a volume element to its initial configuration. It is unclear at this time whether the difference in stress and strain definition in classical seismology and in the finite-strain theory used by HOSS could introduce some errors in the definition of equivalent forces, and how the finite rotation of the elastic material at the source might influence the seismic signal.

Secondly and more importantly, a limit of this study lies in the fundamentally different mathematical frameworks used in classical seismology, with respect to the Finite-Discrete element method used in HOSS. Indeed, while equivalent forces derived in Eq. 2.16 are valid in a purely continuous world, the reality of material deformation and the approach followed by HOSS includes discontinuities. In section SI-1, we explained that we purposely left out the effect of inter-element fracture and friction in our description of the source. This is a strong approximation, as we know that friction mimics a plastic process at play within granular geomaterials. Moreover, friction is a damping mechanism, or energy sink, that might contribute to the reduction of high-frequency energy within the source region. Its absence in the point-source model could explain the excess of high-frequency energy in

the signals of Figs. 2.17, 2.18 and 2.19. To measure its effect on the source, inter-element friction should be accounted for in the expression of equivalent forces. However, given that this process is considered to be a surface action in HOSS' numerical framework, it cannot be simply represented in the form of an additional stress glut tensor. In fact, the action of friction forces would be better understood by rewriting the equations of section 2.3.1 in the form of a mass-spring system rather than with the equations of continuum mechanics. Due to the extensive reformulation required to include this additional frictional and discrete processes in our description of the source, we leave it for a future study.

We also want to emphasise the discrepancy in vertical displacement between the coupled and point-source signals. Such difference hints at the fact that our analytical model might need to be refined in order to accommodate a permanent vertical force. Further testing of the point-source representation could involve including higher-order moments, such as quadrupoles, in the Green's function expansion of Eq. 2.18. Higher-order moments have indeed a strong potential to investigate finite-source effects and mechanism complexity [Stump & Johnson, 1982; Jordan & Juarez, 2019]. To insist on analytical developments, we recall that in section 2.5.3, an  $\omega^{-3}$  seismic source spectrum was used to model the high-frequency content of the displacement spectra. Although this model is intuitively appealing for a 3D seismic source, it does not directly relate to impact dynamics or to their equations of motion. Another possible improvement of the source model would be to analytically derive the effect of the source extension on the spectrum, in a similar way as Savage [1966] or Haskell [1966]. As was mentioned in section 2.3.3, an explicit modelling of the source radiation require an analytical expression of the Green's function. In a half-space, this is referred to as Lamb's problem, and closed-form solutions for the Green's functions are not available for every component of motion. However, it might be possible to simplify the problem by focusing on the spectrum of P- and S- pulses in the far-field.

Another example of possible limitations is the omission of gravity in the analytical expressions of moments (section 2.3) and in simulations (section 2.4). Gravity is known to have an influence on the dynamics of crater and ejecta formation [Holsapple, 1993; Froment et al., 2020], and therefore might influence the long-term decay of the source time functions in Figs 2.13 and 2.14. Gravity also cause the target to be pre-stressed, and ejecta and other transport of mater are susceptible to change this pre-stressed state after impact. In Appendix A4, we propose a modification of equivalent forces  $\gamma^V$  and  $\gamma^S$  to include the non-linear effects of gravity in the stress glut theory. It is also possible to include gravity in HOSS simulations, although at an increased computational cost. Indeed, adding a constant vertical acceleration requires to give the simulated material enough time to relax to its lithostatic, or pre-stressed equilibrium, and we leave this study for future investigations. However, even without gravity, simulation initial and boundary conditions influence long-term dynamics, as evidenced by the slow drift in our modelled source time function.

Despite the frequency content differences between modelled and prolonged signals, we show that some key parameters of the modelled impact seismic source match global trends observed on Mars and the Moon. We emphasise that comparisons between Lunar, Martian and simulation data is challenging, due to the absence of direct measurements of impactor or material properties. For example, in the data presented above, impactor momentum was inferred from crater measurements [Collins et al., 2022] or from signal amplitudes [Gudkova et al., 2011] using different models. Seismic velocities are estimated from a variety of Martian and Lunar seismic models, which at this time cannot account for local variations on different parts on the planetary surface. Still, we note that the scaled seismic moments and source size estimates obtained with HOSS are in trend with Lunar and Martian results.

This is to our knowledge the first time that a trend is evidenced between the impactor energy and momentum and the estimated source size. Fig. 2.23 indicates that the source size estimate for Lunar and Martian impacts scales as the impactor momentum and kinetic energy to the power 0.13 and 0.11 respectively. This result can be connected to existing scaling laws for impact cratering. It is known that impact crater size or depth does not scale directly with energy ( $E_i = r_i^3 \rho_i v_i^2 / 2$ ) or momentum ( $p_i = r_i^3 \rho_i v_i$ ): instead, the pi-scaling introduced by Holsapple [1993] proposes that crater dimensions scale with a mixed point-source measure  $\mathcal{C} = r_i v_i^\mu \rho_i^\nu$ , with  $1/3 < \mu < 2/3$  and  $\nu \approx 1/3$ . For an impact in the strength regime in Lunar regolith or a dry soil, crater size scales with energy to the power  $3\mu/6 = 0.2$ . This is a power greater than the one observed in Fig. 2.23, which suggests that our source size estimate is not directly proportional to crater size. This observation, although preliminary, shows that further investigations of the impact seismic source on planetary bodies is needed to be able to relate it to classical scaling laws for impacts, or for seismic sources on Earth.

In particular, this study focused on only two impact scenarios with a common impactor velocity of 1000 m/s. This impact velocity is in the lower than the mean Martian impact velocity by a factor of  $\sim 10$ , and than the mean lunar impact velocity by a factor of  $\sim 20$  [Le Feuvre & Wieczorek, 2011]. To be applicable to real impact scenarios, our model will need to be tested for a range of target materials, impactor velocities and angles closer to the observed range.

## 2.7 Conclusion

We introduce an analytical model relating the mechanical fields of the meteorite impact phenomena (i.e., velocity field, plastic and elastic stress fields in the shocked material) to the seismic displacements recorded at any distance from the formed crater using the seismic Representation Theorem and the stress glut theory. A point-source model of the impact is obtained, which associates a time-varying vector force and a time-varying moment tensor exerted at the impact point. We subsequently develop a numerical method to estimate the different terms involved in the seismic source, in particular the stress glut field. The point source terms are obtained by volume integration of the source fields produced by a 3D non-linear numerical simulation of the impact using the HOSS software. Our numerical calculation of the stress glut relies on a measure of plasticity in the non-linear shocked material.

We propose a verification method for this numerical model, which allows us to compare the signal modelled from the point-source to the signal directly extracted from a non-linear impact simulations using a software coupling method between HOSS and SPECFEM3D. The comparison reveals that at low frequency, the modelled P- and S-wave signals agree with the coupled signal to within an order of magnitude. The modelled point source signal presents significantly higher amplitudes at high frequency.

This coupling method allows us to study the respective contribution of various source terms on the impact seismic signal. We show that the source is mostly dominated by the moment tensor components, which can be decomposed into the sum of an isotropic, a CLVD and a DC mechanism. For an oblique impact, each of these terms significantly influences the source radiation. We also study the effect of source spatial extension on the signal spectra. We show that, for a vertical, 1000 m/s impact simulation generating a 2 m crater, finite source effects are not sufficient to explain the lack of high-frequency energy in the coupled spectrum compared to the modelled point-source spectrum. We hypothesise the absence of some stress glut terms in our numerical description, in particular terms

associated to inter-element frictional processes inherent to the combined Finite-Discrete Element Method implemented in the HOSS software. Investigation of the "frictional stress glut" might lead to an improvement of this point source model in the future.

Despite these discrepancies, we have shown with a simple propagation model that the properties of the impact generated P-wave 100 km away from the source scales with spectral properties of small impact recorded seismically during the InSight mission. We also showed that, once scaled with the material seismic properties, the measured seismic moment and source duration agree well with measurements made on Lunar and Martian data. The comparison also reveals a possible scaling relationship between seismic source size and impactor energy and momentum. In the future, we hope to conduct a more complete validation study of the seismic source parameters, and to further investigate the scaling of these key source parameters.

The proposed model is here applied to impact phenomena, which are a rather exotic source from the point of view of Earth seismology, but the developments remain true for any other type of source, such as explosions, volcanoes or of course the earthquake sources, for which the stress glut was initially invented by [Backus & Mulcahy \[1976\]](#). In fact, the stress glut field can be computed for any mechanical disruption in a solid medium, as long as the right initial and boundary conditions are provided.



## 2.8 Additional Results

Following the submission of the above work for publication, the author has explored the effect of obliquity on the moment tensor mechanism of the impact source. In addition to the vertical and  $45^\circ$  incidence impact simulations presented above, two simulations with a  $22.5^\circ$  and  $67.5^\circ$  incidence angle were designed. These simulations use the same geometry and material models as scenario (B), and the same post-processing was applied.

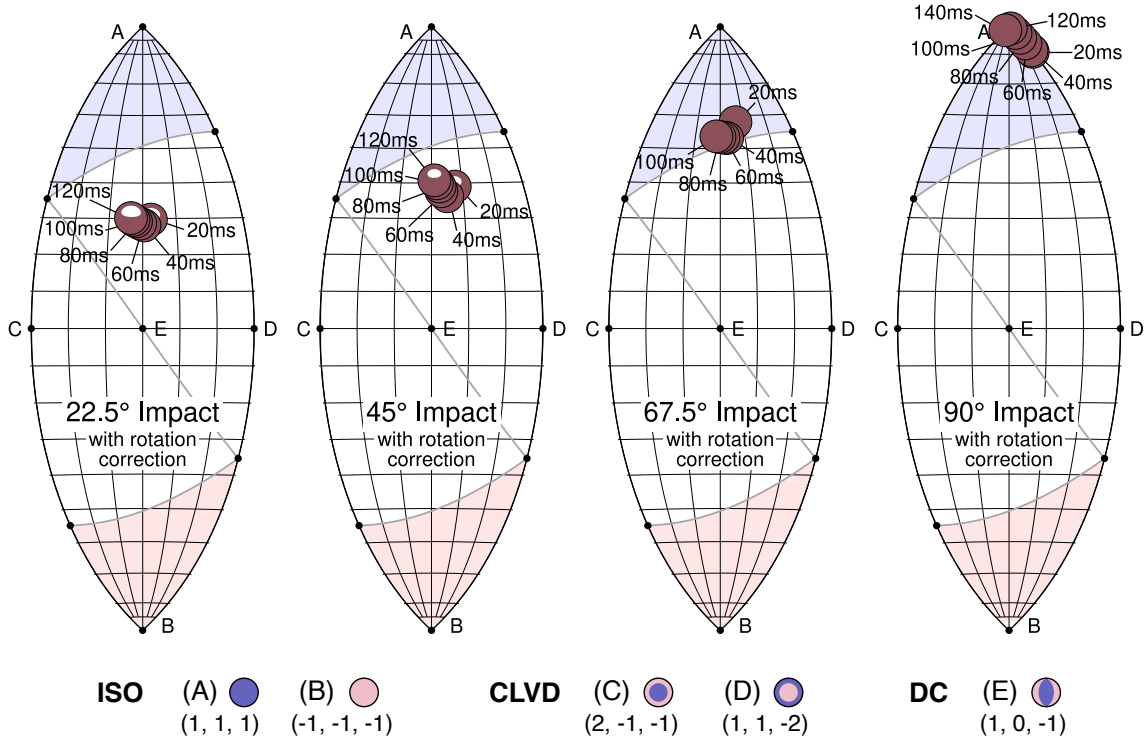


**Figure 2.24:** Lune diagram for the moment tensor of an impact with a  $22.5^\circ$ ,  $45^\circ$ ,  $67.5^\circ$  and  $90^\circ$  incidence angle from the horizontal. The conventions used are the same as in Fig. 2.15.

Lune diagrams for these four impact scenarios are shown on Fig. 2.24. The  $67.5^\circ$  angle simulation generates a source with a DC component, which brings it in the region between scenario (A) and scenario (B) in the Lune diagram. In the same way, the moment tensor of the  $22.5^\circ$  lies beneath the oblique impact of scenario (B) in the diagram, and is closer to a pure DC by approximately  $10^\circ$  of latitude.

To analyse the evolution of the source more precisely, we plotted the evolution of source parameters of Table 2.1 with incidence angle, for all four simulations, as well as the evolution of parameters  $(\gamma, \delta)$  of the Lune diagram at time  $t = 20$  ms. The results are shown on Fig. 2.25.

The vertical component of the vector force presents a smooth increasing trend with incidence angle  $i$ , which is fit well with a function proportional to  $\sin(i)$ . On the other end, the horizontal component of the force peaks around  $i = 45^\circ$  and is well fit by  $\sin(2i)$ , suggesting that this incidence angle is the most efficient at transferring horizontal force. This could be due to the fact that strongly oblique impactors tend to slide out of the crater, thus keeping most of their horizontal momentum in their escape. Such behavior was observed for the  $22.5^\circ$  impact.

The total seismic moment  $M_0$  of these impacts shows a less smooth trend, with a relatively constant seismic moment above  $45^\circ$  of incidence, and an apparent decrease for  $22.5^\circ$ .



This decrease could once again be due to the loss of momentum caused by the impactor escape. Individual components of the decomposed moment tensor show various trends. The isotropic (or explosive) moment tends to decrease smoothly with incidence angle, in a trend similar to the vertical force  $F_z$ .  $\hat{M}^{DC_2}$ , on the other hand, shows an increase for low incidence angles, but this trend depends on the correction of rotation effects. Component  $\hat{M}^{DC_1}$  peaks at  $45^\circ$  angle, just like force component  $F_x$ . The evolution of the CLVD component is the most complex, with a possible peak at  $45^\circ$  depending on the rotation correction.

Finally, we look at the lune coordinates of the four moment tensors at time  $t = 20$  ms, roughly at the end of the formation of the stress glut field. Both coordinates are seemingly increasing with incidence angle, and show a possible convergence towards  $\delta \leq 30^\circ$  and  $\gamma = 0^\circ$  for an incidence angle of zero.

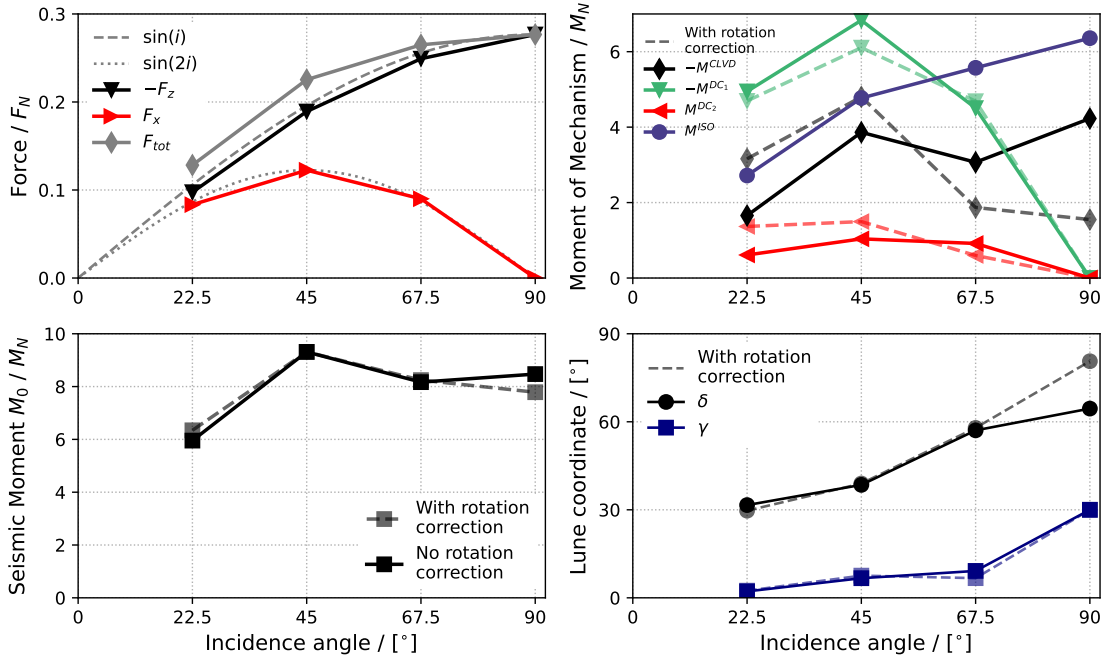


**Figure 2.25:** Evolution of the source mechanism with impact incidence angle. The evolution of the vertical and horizontal force, normalised by  $F_N$ , is shown on the top left. The evolution of the amplitude of  $\vec{M}^{ISO}$ ,  $\vec{M}^{CLVD}$ ,  $\vec{M}^{DC_1}$  and  $\vec{M}^{DC_2}$ , normalised by  $M_N$ , are shown on the top right. The total seismic moment of each simulation, calculated from the moment tensor as in Table 2.1, is shown on the bottom left. The coordinates  $(\gamma, \delta)$  of the beachball calculated at  $t = 20$  ms, are shown on the bottom right.

Thanks to the semi-analytical model presented in the above article, such parametric study of the impact seismic source has become possible. Understanding the evolution of the source mechanism with incidence angle has important implications for predicting the P-/S- wave amplitude ratio and magnitude of impact signals. Indeed, these preliminary results tend to indicate that the moment tensor mechanism evolves continuously with incidence angle, while the seismic moment and signal amplitude are roughly constant above  $45^\circ$ . Therefore, the assumption that the impact seismic signal is proportional to the vertical component of the impact momentum might be true only over a limited range of incidence angles. In the future, a more thorough parametric study could bring insights into the effects of impact velocity on the seismic source amplitudes.

# Appendices

## A1 Equations of motion with surface mass losses

The equation of motion of a variable-mass system is given by the generalised form of the Reynolds Transport Theorem. This theorem was introduced by Osborne Reynolds [Reynolds, 1903], and is commonly known in a restricted form applicable to material volumes, i.e. volumes surrounding a constant set of particles in motion, whose surface moves together with the outermost particles. The generalised form accounts for cases where mass (and thus particles) is allowed to flow through the surface: the surface thus moves at a velocity  $\mathbf{v}^\Sigma$ , distinct from the particle velocity  $\mathbf{v}$ . Using the formalism of Irschik & Holl [2004] (Equation 4.6), the generalised Reynolds Transport Theorem writes:

$$\frac{d_\Sigma}{dt} \left[ \iiint_{V^t} \rho \mathbf{v} \, dV \right] = \frac{d}{dt} \left[ \iiint_V \rho \mathbf{v} \, dV \right] + \iint_{\Sigma^t} \rho \mathbf{v} (\mathbf{v}^\Sigma - \mathbf{v}) \cdot \mathbf{d}\Sigma. \quad (52)$$

In Eq. 52,  $V^t$  and  $\Sigma^t$  refer to the variable volume and surface at time  $t$  and  $V$  designates the instantaneous material volume composed of the particles of  $V^t$ . Following Irschik & Holl [2004], the derivative  $\frac{d_\Sigma}{dt}$  means that the measure of the total momentum within  $V^t$  takes into account the inflow and outflow of mass through  $\Sigma^t$ , while the derivative  $\frac{d}{dt}$  simply considers variation of momentum of the set of particles instantaneously present in  $V$ . Using Cauchy's momentum equation on this material volume, the following expression of the conservation of momentum is obtained:

$$\frac{d_\Sigma}{dt} \left[ \iiint_{V^t} \rho \mathbf{v} \, dV \right] = \iint_{\Sigma^t} \mathbf{S} \cdot \mathbf{n} \cdot \mathbf{d}\Sigma + \iiint_{V^t} \mathbf{h}^V \, dV + \iint_{\Sigma^t} \rho \mathbf{v} (\mathbf{v}^\Sigma - \mathbf{v}) \cdot \mathbf{d}\Sigma. \quad (53)$$

Here,  $\mathbf{S}$  represents the true, non-linear stress exerted in the strongly shocked medium. It is different from the ideal elastic stress  $\Psi$  of Eq. 2.11 and does not follow Hooke's law of elasticity. Similarly,  $\mathbf{h}^V$  stands for the non-linear volume forces applied to  $V^t$ . This global expression of the conservation of momentum can be completed by a local form on an mesoscopic volume element. To this aim, we make use of equations (2.3d) of Irschik & Holl [2004]:

$$\frac{d_\Sigma}{dt} \left[ \iiint_{V^t} \rho \mathbf{v} \, dV \right] = \iiint_{V^t} \frac{\partial}{\partial t} (\rho \mathbf{v}) \, dV + \iint_{\Sigma^t} \rho \mathbf{v} \mathbf{v}^\Sigma \cdot \mathbf{d}\Sigma, \quad (54)$$

and write:

$$\begin{aligned} \iiint_{V^t} \frac{\partial}{\partial t} (\rho \mathbf{v}) \, dV + \iint_{\Sigma^t} \rho \mathbf{v} \mathbf{v}^\Sigma \cdot \mathbf{d}\Sigma &= \iint_{\Sigma^t} \mathbf{S} \cdot \mathbf{n} \cdot \mathbf{d}\Sigma + \iiint_{V^t} \mathbf{h}^V \, dV + \iint_{\Sigma^t} \rho \mathbf{v} (\mathbf{v}^\Sigma - \mathbf{v}) \cdot \mathbf{d}\Sigma \\ \iiint_{V^t} \frac{\partial}{\partial t} (\rho \mathbf{v}) \, dV &= \iint_{\Sigma^t} \mathbf{S} \cdot \mathbf{n} \cdot \mathbf{d}\Sigma + \iiint_{V^t} \mathbf{h}^V \, dV - \iint_{\Sigma^t} (\rho \mathbf{v}) \mathbf{v} \cdot \mathbf{d}\Sigma. \end{aligned} \quad (55)$$

Upon using the Gauss-Green-Ostrogradsky divergence theorem on the surface integrals of Eq. 55 and projecting in direction  $i$ , this yields:

$$\frac{\partial}{\partial t} (\rho v_i) = \partial_j S_{ij} + h_i^V - \partial_j (\rho v_i v_j). \quad (56)$$

Finally, true non-linear tractions on the surface  $\Sigma^t$  now write:

$$S_{ij}n_j = f_i^\Sigma + \rho v_i(v_j - v_j^\Sigma)n_j, \quad (57)$$

where  $f_i^\Sigma$  denote external forces applied to surface  $\Sigma$  in direction  $i$  and  $n_j$  is the normal to surface  $\Sigma$  projected in direction  $j$ .

## A2 Representation of a seismic wavefield in a volume with constant mass

Let  $V$  be a volume with surface  $\Sigma$ . Let  $\mathbf{u}(\boldsymbol{\xi}, \tau)$  be an elastic displacement field generated by surface tractions  $\boldsymbol{\Psi}(\mathbf{u}, \tau) \cdot \mathbf{n} = \mathbf{f}^\Sigma$  on surface  $\Sigma$  with normal  $\mathbf{n}$ , and volume forces  $\mathbf{f}^V$  within  $V$ . Let  $\mathbf{v}(\boldsymbol{\xi}, \tau)$  be a second displacement field, produced by different tractions  $\boldsymbol{\Psi}(\mathbf{v}, \tau) \cdot \mathbf{n} = \mathbf{g}^\Sigma$  on  $\Sigma$  and volume forces  $\mathbf{g}^V$  in  $V$ . The equations of motion for  $\mathbf{u}$  and  $\mathbf{v}$  are:

$$\begin{aligned} \rho^0 \frac{\partial^2 \mathbf{u}}{\partial \tau^2} &= \nabla \cdot \boldsymbol{\Psi}(\mathbf{u}, \tau) + \mathbf{f}^V \\ \rho^0 \frac{\partial^2 \mathbf{v}}{\partial \tau^2} &= \nabla \cdot \boldsymbol{\Psi}(\mathbf{v}, \tau) + \mathbf{g}^V. \end{aligned} \quad (58)$$

Betti's Reciprocal Relation, which is valid everywhere within  $V$ , rearranges the elastic equations of motion for  $\mathbf{u}$  and  $\mathbf{v}$  as:

$$\begin{aligned} &\iiint_V (\mathbf{f}^V - \rho \frac{\partial^2 \mathbf{u}}{\partial \tau^2}) \cdot \mathbf{v} \, dV(\boldsymbol{\xi}) + \iint_\Sigma \boldsymbol{\Psi}(\mathbf{u}, \tau) \cdot \mathbf{n} \cdot \mathbf{v} \, d\Sigma(\boldsymbol{\xi}) \\ &= \iiint_V (\mathbf{g}^V - \rho \frac{\partial^2 \mathbf{v}}{\partial \tau^2}) \cdot \mathbf{u} \, dV(\boldsymbol{\xi}) + \iint_\Sigma \boldsymbol{\Psi}(\mathbf{v}, \tau) \cdot \mathbf{n} \cdot \mathbf{u} \, d\Sigma(\boldsymbol{\xi}). \end{aligned} \quad (59)$$

Note that this relationship is also true when both  $V$  and  $\Sigma$  vary in time. Classically, the next step consists in integrating both part of the equation from time  $\tau = -\infty$  to time  $\tau = +\infty$ . We can further add the condition that  $\mathbf{u}$ ,  $\frac{\partial \mathbf{u}}{\partial \tau}$ ,  $\mathbf{v}$  and  $\frac{\partial \mathbf{v}}{\partial \tau}$  are all everywhere zero before a certain time  $\tau_0$  in the past, and evaluate the field  $\mathbf{v}$  at a time  $t - \tau$ , where  $t$  is a fixed time. In the case where  $V$  and  $\Sigma$  are fixed volumes and surfaces, the time integrals over the acceleration terms  $\rho \frac{\partial^2 \mathbf{u}}{\partial \tau^2} \cdot \mathbf{v}$  and  $\rho \frac{\partial^2 \mathbf{v}}{\partial \tau^2} \cdot \mathbf{u}$  cancel each other, and the following expression of Betti's theorem is obtained:

$$\begin{aligned} &\int_{-\infty}^{\infty} d\tau \iiint_V [\mathbf{u}(\boldsymbol{\xi}, \tau) \cdot \mathbf{g}^V(\boldsymbol{\xi}, t - \tau) - \mathbf{v}(\boldsymbol{\xi}, t - \tau) \cdot \mathbf{f}^V(\boldsymbol{\xi}, \tau)] \, dV(\boldsymbol{\xi}) \\ &= \int_{-\infty}^{\infty} d\tau \iint_\Sigma [\mathbf{v}(\boldsymbol{\xi}, t - \tau) \cdot \boldsymbol{\Psi}(\mathbf{u}, \tau) \cdot \mathbf{n} - \mathbf{u}(\boldsymbol{\xi}, \tau) \cdot \boldsymbol{\Psi}(\mathbf{v}, t - \tau) \cdot \mathbf{n}] \, d\Sigma(\boldsymbol{\xi}). \end{aligned} \quad (60)$$

Note however, that if volume  $V$  and surface  $\Sigma$  are considered to be varying in time, the simplification of the acceleration terms must be carried more carefully. For this special case, additional analytical terms appear, which were derived by [Minster \[1974\]](#) and [Archambeau & Scales \[1989\]](#). In this study, we do not account for the effects of variable mass and volume, as we will find them to be negligible for the studied impact. However, the reader can find an exact version of Betti's relation for variable volumes and surfaces in the Appendix A3 below.

In a last step,  $\mathbf{v}$  is chosen to be the Green's function of the propagation medium,  $v_i(\mathbf{x}, t) = G_{in}(\mathbf{x}, t - \tau, \boldsymbol{\xi}, 0)$ . It represents the  $i^{\text{th}}$  component of displacement produced at time  $t - \tau$

and position  $\mathbf{x}$  within  $V$  by an impulse volume force located at position  $\boldsymbol{\xi}$  and time 0 and directed towards the  $n^{\text{th}}$  direction of space. The volume force and boundary conditions associated to  $\mathbf{v}$  are:

$$\begin{aligned} g_i^V(\boldsymbol{\xi}, t - \tau) &= \delta_{in} \delta(\mathbf{x} - \boldsymbol{\xi}) \delta(t - \tau) && \text{in } V \\ g_i^\Sigma(\boldsymbol{\xi}, t - \tau) &= C_{ijkl} \frac{\partial G_{kn}}{\partial \xi_l} && \text{on } \Sigma. \end{aligned} \quad (61)$$

Reintroducing this new expression of  $\mathbf{v}$  in Eq. 59 gives rise to the Representation Theorem, here written in the  $n^{\text{th}}$  direction of motion and for a constant volume  $V$ :

$$\begin{aligned} u_n(\mathbf{x}, t) &= \int_{-\infty}^{+\infty} d\tau \iiint_V f_i^V(\boldsymbol{\xi}, \tau) G_{in}(\boldsymbol{\xi}, t - \tau, \mathbf{x}, 0) dV(\boldsymbol{\xi}) \\ &+ \int_{-\infty}^{+\infty} d\tau \iint_\Sigma G_{in}(\boldsymbol{\xi}, t - \tau, \mathbf{x}, 0) f_i^\Sigma(\boldsymbol{\xi}, \tau) d\Sigma(\boldsymbol{\xi}) \\ &- \int_{-\infty}^{+\infty} d\tau \iint_\Sigma u_i(\boldsymbol{\xi}, \tau) n_j C_{ijkl} \frac{\partial G_{kn}}{\partial \xi_l}(\boldsymbol{\xi}, t - \tau, \mathbf{x}, 0) d\Sigma(\boldsymbol{\xi}). \end{aligned} \quad (62)$$

A list of several special-case depending on various boundary conditions can be found in [Aki & Richards \[2002\]](#). In the case considered here,  $\Sigma$  is chosen to be a free surface, which leads to  $C_{ijkl} n_j \frac{\partial G_{kn}}{\partial \xi_l} = 0$  everywhere on  $\Sigma$  and cancels the first part of the last term of Eq. 62. We replace the generic forces  $\mathbf{f}^V$  and  $\mathbf{f}^\Sigma$  by equivalent surface and volume forces  $\boldsymbol{\gamma}^V$  and  $\boldsymbol{\gamma}^\Sigma$  which are the non-linear sources of motion (see Eq. 2.15 of section 2.3.1). The expression of displacements anywhere in  $V$  is then given by Eq. 63:

$$\begin{aligned} u_n(\mathbf{x}, t) &= \int_{-\infty}^{+\infty} d\tau \iiint_V \gamma_i^V(\boldsymbol{\xi}, \tau) G_{in}(\boldsymbol{\xi}, t - \tau, \mathbf{x}, 0) dV(\boldsymbol{\xi}) \\ &+ \int_{-\infty}^{+\infty} d\tau \iint_\Sigma G_{in}(\boldsymbol{\xi}, t - \tau, \mathbf{x}, 0) \gamma_i^\Sigma(\boldsymbol{\xi}, \tau) d\Sigma(\boldsymbol{\xi}). \end{aligned} \quad (63)$$

### A3 Representation Theorem for a variable-mass system

As mentioned in the previous section (appendix A2), Betti's Representation Theorem as found in [\[Aki & Richards, 2002\]](#) does not account for changes in volume and surfaces. We report here on the form obtained by [Minster \[1974\]](#) and [Archambeau & Scales \[1989\]](#). The starting point is Betti's Reciprocal Relation (Eq. 59), which we copy here:

$$\begin{aligned} &\iiint_V (\mathbf{f} - \rho \frac{\partial^2 \mathbf{u}}{\partial \tau^2}) \cdot \mathbf{v} dV(\boldsymbol{\xi}) + \iint_\Sigma \boldsymbol{\Psi}(\mathbf{u}) \cdot \mathbf{n} \cdot \mathbf{v} d\Sigma(\boldsymbol{\xi}) \\ &= \iiint_V (\mathbf{g} - \rho \frac{\partial^2 \mathbf{v}}{\partial \tau^2}) \cdot \mathbf{u} dV(\boldsymbol{\xi}) + \iint_\Sigma \boldsymbol{\Psi}(\mathbf{v}) \cdot \mathbf{n} \cdot \mathbf{u} d\Sigma(\boldsymbol{\xi}). \end{aligned} \quad (64)$$

In the following step, both parts of the equation are integrated between time  $\tau = -\infty$  and time  $\tau = +\infty$ . We add the condition that  $\mathbf{u}$ ,  $\frac{\partial \mathbf{u}}{\partial \tau}$ ,  $\mathbf{v}$  and  $\frac{\partial \mathbf{v}}{\partial \tau}$  are all everywhere zero before a certain time  $\tau_0$  in the past, and evaluate field  $\mathbf{v}$  at a time  $t - \tau$ , where  $t$  is a fixed time.

This time, instead of adopting the simplification of Eq. 60, we must further develop the time integral of momentum over a time-varying volume,  $V^\tau$ :

$$\int_{-\infty}^{\infty} d\tau \iiint_{V^\tau} \left( \rho \frac{\partial^2 \mathbf{v}}{\partial \tau^2} \cdot \mathbf{u} - \rho \frac{\partial^2 \mathbf{u}}{\partial \tau^2} \cdot \mathbf{v} \right) dV^\tau(\boldsymbol{\xi}). \quad (65)$$

We modify the double derivatives on the right and write:

$$\begin{aligned} \int_{-\infty}^{\infty} d\tau \iiint_{V^\tau} \left( \rho \frac{\partial^2 \mathbf{v}}{\partial \tau^2} \cdot \mathbf{u} - \rho \frac{\partial^2 \mathbf{u}}{\partial \tau^2} \cdot \mathbf{v} \right) dV^\tau(\boldsymbol{\xi}) &= \int_{-\infty}^{\infty} d\tau \iiint_{V^\tau} \left[ \frac{\partial}{\partial \tau} \left( \rho \frac{\partial \mathbf{v}}{\partial \tau} \cdot \mathbf{u} \right) - \rho \frac{\partial \mathbf{v}}{\partial \tau} \cdot \frac{\partial \mathbf{u}}{\partial \tau} \right. \\ &\quad \left. - \frac{\partial}{\partial \tau} \left( \rho \frac{\partial \mathbf{u}}{\partial \tau} \cdot \mathbf{v} \right) + \rho \frac{\partial \mathbf{v}}{\partial \tau} \cdot \frac{\partial \mathbf{u}}{\partial \tau} \right] dV^\tau(\boldsymbol{\xi}). \end{aligned} \quad (66)$$

Only two terms are left on the right side of Eq. 66. As was proposed by several authors [Minster, 1974; Archambeau & Scales, 1989], Eq. 65 can be developed using the Reynolds Transport Theorem of Appendix A1. Following equation (2.3d) of Irschik & Holl [2004], this gives:

$$\begin{aligned} \int_{-\infty}^{\infty} d\tau \iiint_{V^\tau} \frac{\partial}{\partial \tau} \left( \rho \frac{\partial \mathbf{v}}{\partial \tau} \cdot \mathbf{u} - \rho \frac{\partial \mathbf{u}}{\partial \tau} \cdot \mathbf{v} \right) dV^\tau(\boldsymbol{\xi}) &= \int_{-\infty}^{\infty} d\tau \left[ \frac{d_s}{d\tau} \iiint_{V^\tau} \left( \rho \frac{\partial \mathbf{v}}{\partial \tau} \cdot \mathbf{u} - \rho \frac{\partial \mathbf{u}}{\partial \tau} \cdot \mathbf{v} \right) dV^\tau(\boldsymbol{\xi}) \right. \\ &\quad \left. - \iint_{\Sigma^\tau} \left( \rho \frac{\partial \mathbf{v}}{\partial \tau} \cdot \mathbf{u} - \rho \frac{\partial \mathbf{u}}{\partial \tau} \cdot \mathbf{v} \right) \cdot \mathbf{v}^\Sigma \cdot \mathbf{n} d\Sigma^\tau(\boldsymbol{\xi}) \right]. \end{aligned} \quad (67)$$

In Eq. 67,  $\mathbf{v}^\Sigma$  represents the velocity of the moving surface  $\Sigma^\tau$ . Similarly to the case of fixed volume and surfaces (see Appendix A2), the first integral on the right cancels upon applying the right initial conditions on  $\mathbf{u}$  and  $\mathbf{v}$  and their derivatives, and evaluating  $\mathbf{v}$  at time  $t - \tau$ . We are left with a supplementary term to Betti's theorem, which now writes:

$$\begin{aligned} &\int_{-\infty}^{\infty} d\tau \iiint_{V^\tau} \left[ \mathbf{u}(\boldsymbol{\xi}, \tau) \cdot \mathbf{g}^V(\boldsymbol{\xi}, t - \tau) - \mathbf{v}(\boldsymbol{\xi}, t - \tau) \cdot \mathbf{f}^V(\boldsymbol{\xi}, \tau) \right] dV^\tau(\boldsymbol{\xi}) \\ &= \int_{-\infty}^{\infty} d\tau \iint_{\Sigma^\tau} \left[ \mathbf{v}(\boldsymbol{\xi}, t - \tau) \cdot \boldsymbol{\Psi}(\mathbf{u}, \tau) \cdot \mathbf{n} - \mathbf{u}(\boldsymbol{\xi}, \tau) \cdot \boldsymbol{\Psi}(\mathbf{v}, t - \tau) \cdot \mathbf{n} \right] d\Sigma^\tau(\boldsymbol{\xi}) \\ &\quad - \iint_{\Sigma^\tau} \left[ \rho \frac{\partial \mathbf{v}}{\partial \tau}(\boldsymbol{\xi}, t - \tau) \cdot \mathbf{u}(\boldsymbol{\xi}, \tau) - \rho \frac{\partial \mathbf{u}}{\partial \tau}(\boldsymbol{\xi}, \tau) \cdot \mathbf{v}(\boldsymbol{\xi}, t - \tau) \right] \cdot \mathbf{v}^\Sigma(\tau) \cdot \mathbf{n} d\Sigma^\tau(\boldsymbol{\xi}). \end{aligned} \quad (68)$$

Introducing the Green's function in Eq. 68, as in Eq. 62 of Appendix A2, we obtain the exact version of the Representation Theorem, here written in the  $n^{\text{th}}$  direction of motion and for a varying volume  $V^\tau$ :

$$\begin{aligned} u_n(\mathbf{x}, t) &= \int_{-\infty}^{+\infty} d\tau \iiint_{V^\tau} f_i^V(\boldsymbol{\xi}, \tau) G_{in}(\boldsymbol{\xi}, t - \tau, \mathbf{x}, 0) dV^\tau(\boldsymbol{\xi}) \\ &\quad + \int_{-\infty}^{+\infty} d\tau \iint_{\Sigma^\tau} G_{in}(\boldsymbol{\xi}, t - \tau, \mathbf{x}, 0) \left[ f_i^\Sigma(\boldsymbol{\xi}, \tau) + \rho v_i v_j^\Sigma(\boldsymbol{\xi}, \tau) n_j \right] d\Sigma^\tau(\boldsymbol{\xi}) \\ &\quad - \int_{-\infty}^{+\infty} d\tau \iint_{\Sigma^\tau} u_i(\boldsymbol{\xi}, \tau) n_j \left[ C_{ijkl} \frac{\partial G_{kn}}{\partial \xi_l}(\boldsymbol{\xi}, t - \tau, \mathbf{x}, 0) + \rho \frac{\partial G_{in}}{\partial \tau}(\boldsymbol{\xi}, t - \tau, \mathbf{x}, 0) v_j^\Sigma(\boldsymbol{\xi}, \tau) \right] d\Sigma^\tau(\boldsymbol{\xi}). \end{aligned} \quad (69)$$

We note that an additional artificial surface force  $\tilde{f}_i^\Sigma(\boldsymbol{\xi}, \tau) = \rho v_i v_j^\Sigma(\boldsymbol{\xi}, \tau) n_j$  and an artificial surface stress  $\tilde{\Psi}_{ij}(\boldsymbol{\xi}, \tau) = \rho \frac{\partial G_{in}}{\partial \tau}(\boldsymbol{\xi}, t - \tau, \mathbf{x}, 0) v_j^\Sigma(\boldsymbol{\xi}, \tau)$  appear in the Representation Theorem.

## A4 Stress Glut on a self-gravitating, rotating planet

Modelling wave propagation in a planet subject to its own gravity and rotation requires to adapt the equations of motion of sections 2.3.1 and 2.3.1. Under the effect of gravity and rotation, the planet is initially in a state of hydrostatic equilibrium, which implies the existence of a pre-stress. Elastic deformations represent perturbations of this pre-stress, which the traditional Cauchy stress tensor cannot appropriately describe. Moreover, material put in motion by a seismic wave can itself redistribute mass and perturb the gravitational field, which in return acts on the wave dynamics. The equations of motions of a self-gravitating and rotating body were presented in a number of works. [Lognonné & Clévéché \[2002\]](#) presented a review of the theory of normal modes, starting from the gravito-elastic equations of motion. [Dahlen & Tromp \[1998\]](#) exhaustively address the issue of the definition of stress in continuum mechanics, as well as the derivation of appropriate linearised equations of motion and boundary conditions.

In most applications, the studied planet is considered to be hydrostatic, or quasi-hydrostatic. This implies a distribution of density which is roughly laterally homogeneous. Within such approximation, a relationship exists between the equilibrium stress, gravitational and centrifugal potentials, and the equations of motion can be made independent from the previous history of stresses.

Let us consider a planet of volume  $V$  and surface  $\Sigma$ . In its initial hydrostatic equilibrium, the planet has a density field  $\rho^0$ , an initial static Cauchy stress tensor  $\mathbf{T}^0$  and rotation vector  $\boldsymbol{\Omega}$ . In the following section, for the sake of concision, we adopt vector notations. At equilibrium, the equilibrium gravitational field is:

$$\mathbf{g}^0 = -\nabla\phi^0, \quad (70)$$

with  $\phi^0$  the gravitational potential defined by Poisson's equation using the gravitational constant  $G$ :

$$\nabla^2\phi^0 = 4\pi G\rho^0 \quad \text{and} \quad \phi^0(\mathbf{x}) = -G \iiint_V \frac{\rho^{0'}}{\|\mathbf{x} - \mathbf{x}'\|} dV(\mathbf{x}'). \quad (71)$$

The centrifugal potential  $\psi$  of the rotating planet is defined by:

$$\psi(\mathbf{r}) = -\frac{1}{2} \left[ \Omega^2 r^2 - (\boldsymbol{\Omega} \cdot \mathbf{r})^2 \right]. \quad (72)$$

Finally, the equations of the hydrostatic equilibrium is:

$$\nabla \cdot \mathbf{T}^0 = \rho^0 \nabla (\phi^0 + \psi). \quad (73)$$

The onset of a seismic wave perturbs the initial position of particles. Using a Lagrangian description of the motion, this perturbation can be written:

$$\mathbf{r}(\mathbf{x}, t) = \mathbf{x} + \mathbf{u}(\mathbf{x}, t), \quad (74)$$

with  $\mathbf{x}$  the initial position of particles and  $\mathbf{u}$  the Lagrangian displacement vector. In reaction to the motion, we consider that other physical fields experience first order perturbations, such that  $q^L(\mathbf{x}, t) = q^0(\mathbf{x}, t) + q^{L1}(\mathbf{x}, t)$  in the Lagrangian description and

$q^E(\mathbf{r}, t) = q^0(\mathbf{r}, t) + q^{E1}(\mathbf{r}, t)$  in the Eulerian description.  $q^{L1}$  is the first order Lagrangian perturbation of quantity  $q^L$ , and is related to the first order Eulerian perturbation by  $q^{L1} = q^{E1} + \mathbf{u} \cdot \nabla q^0$ , which is a form of linearised and integrated material derivative. With these notations, the conservation of mass in  $V$  is written:

$$\rho^{E1} = -\nabla \cdot (\rho^0 \mathbf{u}). \quad (75)$$

The first order Eulerian perturbation of the gravitational potential is:

$$\phi(\mathbf{x}) = -G \iiint_V \frac{\rho^{0'} \mathbf{u}' \cdot (\mathbf{x} - \mathbf{x}')}{\|\mathbf{x} - \mathbf{x}'\|^3} dV(\mathbf{x}'), \quad (76)$$

associated to a first order perturbation of the gravitational field  $\mathbf{g}^{E1} = -\nabla \phi^{E1}$ . The full, non-linearised equation of motion is more easily written in the Eulerian form:

$$\rho^E \left( D_t \mathbf{v}^E + 2\mathbf{\Omega} \times \mathbf{v}^E \right) = \nabla^E \cdot \mathbf{T}^E - \rho^E \nabla^E (\phi^E + \psi). \quad (77)$$

Upon linearising each field as above, and neglecting second and higher-order terms, it becomes:

$$\rho^0 \left( \partial_t^2 \mathbf{u} + 2\mathbf{\Omega} \times \partial_t \mathbf{u} \right) = \nabla \cdot \mathbf{T}^{E1} - \rho^0 \nabla \phi^{E1} - \rho^{E1} \nabla (\phi^0 + \psi). \quad (78)$$

The Lagrangian perturbation in stress,  $\mathbf{T}^{L1}$ , is more useful than  $\mathbf{T}^{E1}$  in continuum mechanics as it is directly related to the gradient of deformation  $\nabla \mathbf{u}$ . Precisely,  $\mathbf{T}^{L1}$  is the incremental Lagrangian Cauchy stress, which in linearised form writes  $\mathbf{T}^{L1} = \mathbf{C} : \frac{1}{2} [\nabla \mathbf{u} + (\nabla \mathbf{u})^T]$  with  $\mathbf{C}$  is the stiffness tensor.  $T_{ij}^{L1}$  is thus equivalent to the ideal stress  $\Psi_{ij}$  defined in the main text. Upon applying the relationship between Lagrangian and Eulerian perturbations and using the hydrostatic equilibrium, we can finally rewrite Eq. 78 as:

$$\rho^0 \left( \partial_t^2 \mathbf{u} + 2\mathbf{\Omega} \times \partial_t \mathbf{u} \right) = \nabla \cdot \mathbf{T}^{L1} - \nabla \left[ \rho^0 \mathbf{u} \cdot \nabla (\phi^0 + \psi) \right] - \rho^0 \nabla \phi^{E1} - \rho^{E1} \nabla (\phi^0 + \psi). \quad (79)$$

In tensor notation, Eq. 79 becomes:

$$\rho^0 \left( \frac{\partial^2 u_i}{\partial t^2} + 2\epsilon_{ijk} \Omega_j \frac{\partial u_k}{\partial t} \right) = \partial_j T_{ij}^{L1} - \partial_i \left( \rho^0 u_j \partial_j (\phi + \psi) \right) + \rho^0 g_i^{E1} - \rho^{E1} \partial_i (\phi + \psi). \quad (80)$$

The previous developments bring a few additional terms to the version of the equation of motion proposed in Eq. 2.11 of section 2.3.1. In fact, the simple volume force  $f_i^V$  of Eq. 2.11 is now expressed as a function of displacements  $\mathbf{u}$ :  $f_i^V = \rho^0 g_i^{E1} - 2\rho^0 \epsilon_{ijk} \Omega_j \frac{\partial u_k}{\partial t} - \partial_i (\rho^0 u_j \partial_j (\phi + \psi)) - \rho^{E1} \partial_i (\phi + \psi)$ . This dependance of  $f_i^V$  on  $\mathbf{u}_i$  means that the definition of the Green's function changes with respect to Appendix A2, as  $G_{in}$  is no longer solution to the same equation of motion. The newly defined Green's function depends on a symmetric operator of gravito-elasticity and an antisymmetric operator for Coriolis forces (see e.g. Lognonné & Clévéde [2002]). A demonstration of the Representation Theorem using this form of the linearised equations of motion can be found in Dahlen & Tromp [1998, section 5.3].

Changes in the equations of motion also require changes in the definition of the equivalent forces. As in section 2.3.1, using  $\rho^E = \rho$ , we rewrite  $\gamma^V$  as:

$$\begin{aligned} \gamma^V = & \partial_t \left[ (\rho^0 - \rho) \mathbf{v} \right] - \nabla \cdot (\mathbf{T}^{L1} - \mathbf{S} + \rho \mathbf{v} \otimes \mathbf{v}) + 2\mathbf{\Omega} \times (\rho^0 - \rho) \mathbf{v} \\ & + \nabla \left[ \rho^0 \mathbf{u} \cdot \nabla (\phi^0 + \psi) \right] + \rho^0 \nabla \phi^{E1} - (\rho^0 - \rho) \nabla \phi^0 - \rho \nabla \phi - \rho^0 \nabla \psi. \end{aligned} \quad (81)$$

We identify in this expression the stress glut  $\mathbf{\Pi} = \mathbf{T}^{L1} - \mathbf{S}$ .



# Supplementary Information

## SI-1 HOSS material models

In the verification tests presented in the main text, the impactor and target materials are simulated with a model adapted from [Wójcicka et al. \[2020\]](#).

To obtain the target volumetric model (SocCrush), we start by taking the same elastic regime as in [Wójcicka et al. \[2020\]](#), defined by its bulk modulus and elastic compaction threshold. Then, an experimental scaling law for the compaction of sand materials [[Luo et al., 2011](#)] is used to obtain the compaction curve of a 44% porosity sand. The pore crush regime is then obtained by fitting this curve using the model developed by [Froment et al. \[2020\]](#). Finally, the elastic regime is connected to the the first point of the fit, resulting in a linear transition between both regimes. The target deviatoric response is modelled using a Lundborg pressure-dependant strength model [[Lundborg, 1968](#)], with the parameters of [Wójcicka et al. \[2020\]](#). The impactor is made of solid basalt and simulated with a Tillotson equation of state [[Tillotson, 1962](#)] and another Lundborg strength model. Parameter values for both materials can be found in Table 2.3 below.

## SI-2 Stress glut computation - single element test

The implementation of the method described in sections 2.4.2 and 2.4.2 of the main text is tested by deforming a single tetrahedral element in different controlled modes. The stress glut computed by HOSS is measured and compared to the value expected from a separate numerical algorithm written in Python.

### Isotropic compression and extension

The first test consists in a successive compression and extension of a tetrahedral element, represented in Fig. 2.26a. Fig. 2.26b represents the path in  $\{Pressure, Volumetric\ strain\}$  space followed by the tetrahedral element during a deformation at medium pressure. Initially, the element follows an elastic loading path, represented by the dashed line in Fig. 2.26b, before entering a plastic regime corresponding to the collapse and compaction of pores. It is then unloaded and brought back to its original state. As shown by Fig. 2.26c, during the compression stage, the volumetric stress glut is equal to zero for a short time of 0.01 s, which corresponds to the elastic loading. The volumetric stress glut then increases steadily, as the computed pressure in the pore-crush regime keeps growing further away from the ideal elastic curve. Once the element is unloaded, Fig. 2.26b shows that it follows a linear path of decreasing pressure. The unloading path being almost parallel to the elastic model, the volumetric stress glut varies only modestly between 0.05 and 0.06 s of unloading. Then, the tension in the elements reaches its tensile strength  $P_{tens}$  and cannot decrease anymore, therefore the element follows a path at constant pressure  $P = P_{tens}$  until it is brought back to its initial volume. The associated volumetric strain decreases in Fig. 2.26c, as the loading path bring the element closer to its original shape with  $\varepsilon_V = 0$ .

When subject to a larger loading, the behaviour of the element has some similarity. In Fig. 2.26d, two loading histories are presented in red and dark red. The equation of state of the material imposes an exponential increase of pressure with strain for large loads. Thus, above a strain  $\varepsilon_V = 0.38$ , the Pressure/volumetric strain curve in Fig. 2.26d crosses the ideal-elastic curve. In this specific case, illustrated by the purple dot in Figs 2.26d,

**Table 2.3:** Parameters of the impactor and target material models, adapted for HOSS from the basalt and regolith properties of Wójcicka et al. [2020].

Parameter		Impactor	Target
		Basalt	44% Porosity Regolith
<b>Equation of state</b>		Tillotson	SocCrush
Density ( $\text{kg}\cdot\text{m}^{-3}$ )	$\rho_0$	2860	1589
Compressional wave velocity ( $\text{m}\cdot\text{s}^{-1}$ )	$\alpha$	3301	1090
Bulk modulus (GPa)	$K_{el}$	19.3	1.17
<b>Tillotson model</b>			
Tillotson Parameter	$a$	0.5	-
Tillotson Parameter	$b$	0.8	-
Bulk Modulus (GPa)	$A$	19.3	-
Tillotson Parameter (GPa)	$B$	29.3	-
<b>Pore-crush model</b>			
Porosity	$\phi_0$	0	0.44
Max. strain of the elastic regime	$\varepsilon_{el}$	-	$-8 \times 10^{-5}$
Max. pressure of the elastic regime (MPa)	$P_{el}$	-	0.1
Min. strain of pore-crush regime	$\varepsilon_c$	-	$-1 \times 10^{-2}$
Min. pressure of pore-crush regime (MPa)	$P_c$	-	4.0
Compaction exponent	$m$	-	4.8
Transition Bulk Modulus (MPa)	$K_{trans}$	-	80
Full-Crush Bulk Modulus (GPa)	$K_{fc}$	-	44.0
<b>Strength Model</b>		Lundborg	Lundborg
Shear wave velocity ( $\text{m}\cdot\text{s}^{-1}$ )	$\beta$	1764	583
Shear modulus (GPa)	$G$	8.9	0.54
Poisson ratio	$\nu$	0.3	0.3
Internal friction coefficient	$\mu$	0.7	0.6
Limiting strength (GPa)	$Y_m$	1.0	0.25
Cohesion (kPa)	$Y_0$	5	5

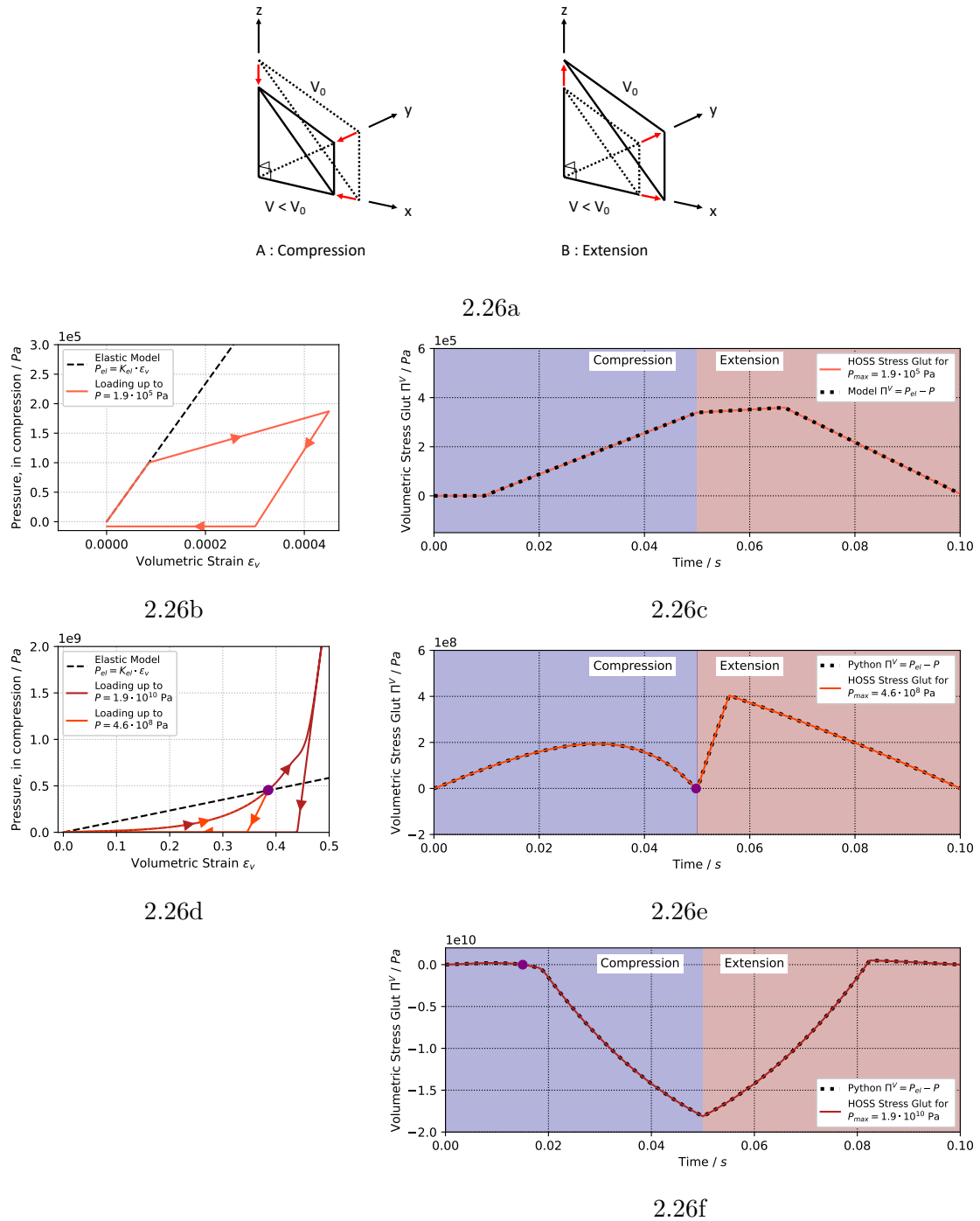


**Figure 2.26:** Computation of the volumetric stress glut for a single regular tetrahedral element subject to isotropic compression followed by extension (2.26a). (2.26b) (resp. (2.26d)) shows the loading path of the element at low (resp. high) pressure, in Pressure/Volumetric strain space. The dashed black line represents the Hooke's law with  $P_{el} = K_{el} \cdot \varepsilon_v$ . The right plots, (2.26c), (2.26e) and (2.26f), show the evolution in time of the volumetric stress glut corresponding to these loading paths, where the colored lines represent HOSS results and the dotted black lines the values obtained with Python for  $\Pi^V = P_{el}(t) - P(t)$ . Note the purple dot on plots (2.26d), (2.26e) and (2.26f): they indicate the time at which the plastic regime of the equation of state brings pressure above the ideal elastic model. The material becomes stiffer than it initially was, which leads to a negative stress glut in (2.26f).

2.26e and 2.26f, the volumetric stress glut is equal to zero. For very large loads illustrated

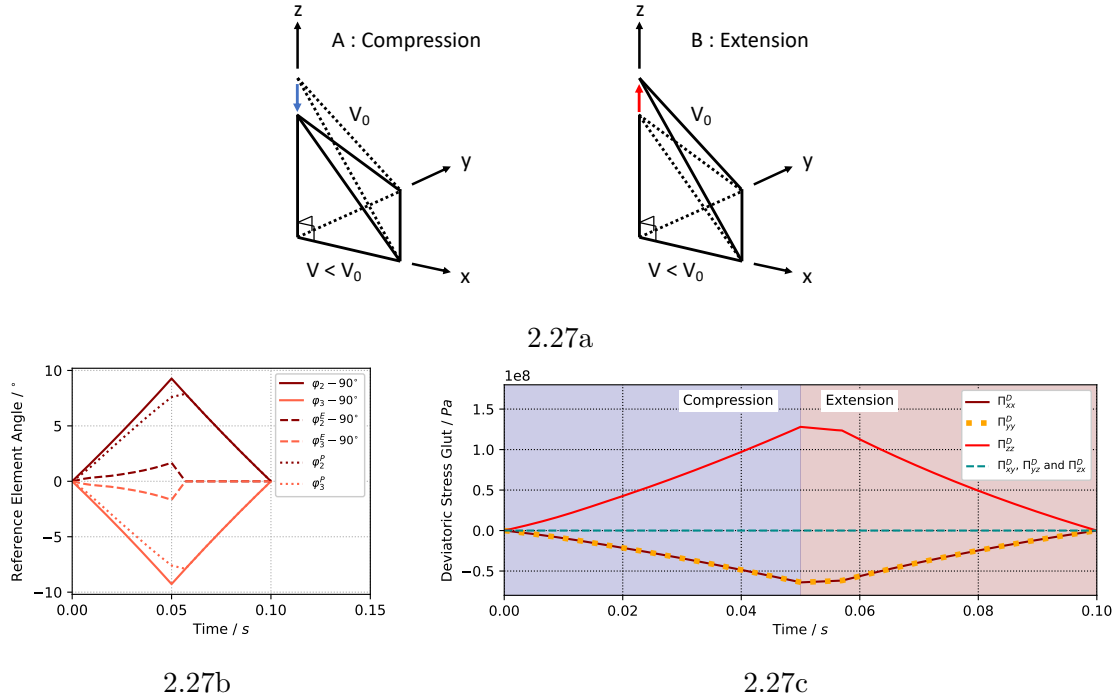


**Figure 2.27:** Computation of the deviatoric stress glut for a single tetrahedral element subject to compression followed by extension in the vertical direction (2.27a). (2.27b) shows the angles measured in the reference element at different steps of the loading. Note that all angles but  $\varphi_2$  and  $\varphi_3$  are zero in this particular scenario. The angles are decomposed through the sum  $\varphi_{2,3} = \varphi_{2,3}^E + \varphi_{2,3}^P$ . The right plot, (2.27c), shows the evolution in time of the deviatoric stress glut corresponding to this loading. Note that, because the algorithm is calculating the deviatoric stress glut, we have  $\Pi_{xx}^D + \Pi_{yy}^D + \Pi_{zz}^D = 0$  at all time. Moreover, in this situation, non-diagonal terms of the stress glut are zero.

by the dark red curve of Fig. 2.26f, the Volumetric stress glut even switches sign, as the damaged material becomes stiffer than the initial elastic regime.

In both loading cases, the volumetric stress glut computed by HOSS is compared to the solution of a Python algorithm in black, as a verification of the implementation.

### Unidirectional shear with volume change

In a second test, the element is deformed unidirectionally upon pulling on one of its node, as shown on Fig. 2.27a. Fig. 2.27b shows the decomposition of each inner angle  $\varphi_{1-6}$  into its elastic and plastic part. We refer the reader to [Lei et al. \[2020\]](#) for a detailed definition of these angles in a tetrahedral element. To ease comparison between the angles, the total and elastic angles are corrected by their initial value  $\varphi^0 = \pi/2$ , which corresponds to a zero stress. Due to the large deformations involved, the yield limit of the material is reached very quickly and angles are mostly plastic: the evolution of  $\varphi_{2,3}^P$  is very close to the evolution of  $\varphi_{2,3} - \varphi^0$ . During the extension of the element, the plasticity dominates deformation to the point that elastic angles  $\varphi_{2,3}^E$  return to their non-stressed value of  $\varphi^0 = \pi/2$ , indicating that all deformation is contained within  $\varphi_{2,3}^P$ . The associated deviatoric stress glut components  $\Pi_{xx}^D$ ,  $\Pi_{yy}^D$  and  $\Pi_{zz}^D$  increase in absolute value until the extension stage, and return to zero when the element regains its initial shape. Note that we have  $\Pi_{xx}^D = \Pi_{yy}^D$  due to the symmetry of the problem, and  $\Pi_{xx}^D + \Pi_{yy}^D + \Pi_{zz}^D = 0$ , as expected for deviatoric stresses.

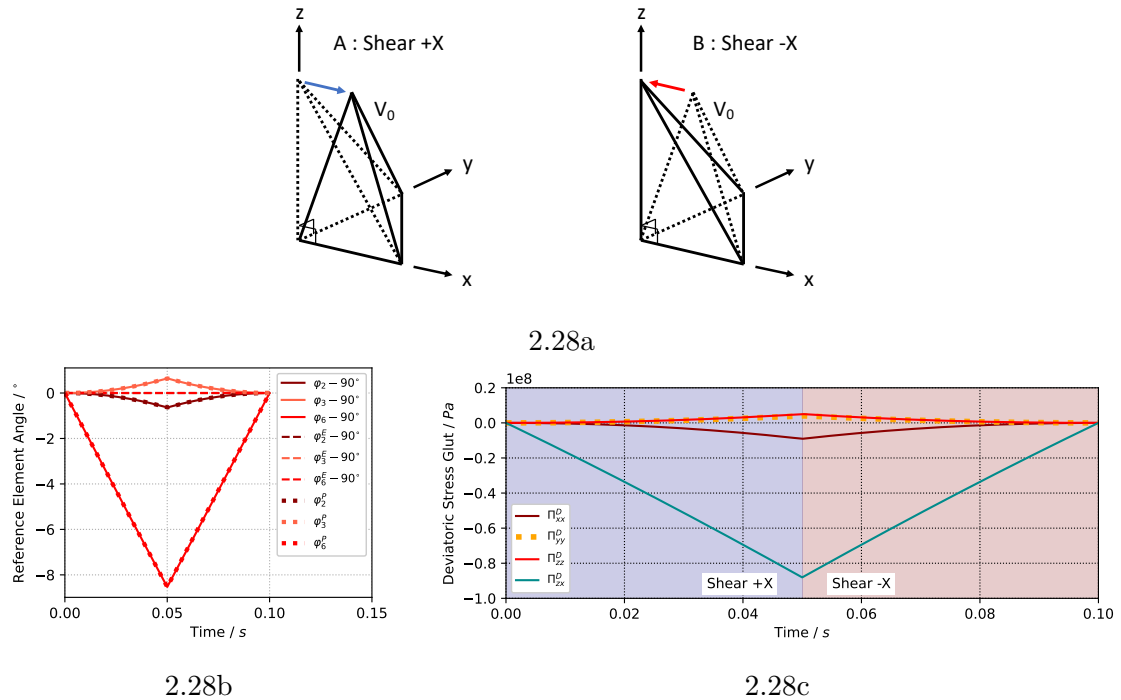


**Figure 2.28:** Computation of the deviatoric stress glut for a single tetrahedral element subject to shear in the horizontal direction (2.28a). This mode of deformation doesn't change the element's volume, and as such does not generate volumetric stress glut  $\Pi^V$ . (2.28b) shows the angles measured in the reference element at different steps of the shearing. This time,  $\varphi_2$ ,  $\varphi_3$  and  $\varphi_6$  are non-zero and almost 100% of the deformation is plastic. Indeed, the plot shows  $\varphi_{2,3,6}^E \approx 0$  and  $\varphi_{2,3,6}^P \approx \varphi_{2,3,6}^D$ . The right plot, (2.28c), shows the evolution in time of the deviatoric stress glut corresponding to this loading. For this mode of deformation,  $\Pi_{xz}^D$  appears to be the dominant term of the deviatoric stress glut tensor.

### Purely deviatoric shear

Another test is conducted for a shear deformation without any volume change. In this case, the upper node of the tetrahedral element is sheared in the  $\vec{x}$  direction, as described by Fig. 2.28a. Fig. 2.28b shows that angle  $\varphi_6$  is the one dominating the deformation, with up to  $8^\circ$  of deformation, and that almost all of it is plastic. Similarly, Fig. 2.28c shows that  $\Pi_{zx}^D$  is the strongest component of the deviatoric stress glut tensor.

### Plastic deformation followed by rigid-body rotation

The last test aims at showing the effect of element finite rotation on the deviatoric stress glut components. In this example, as seen on Fig. 2.29a, the element is sheared similarly to the second test until a time of 0.02 s (stage (A)), at which all deformation is stopped. After stage (A), the element is no longer accumulating any plasticity, as rigid body rotation does not induce any change in the reference element. In Fig. 2.29b, it is clearly seen from the history of the reference angles that  $\varphi_{1-6}$ ,  $\varphi_{1-6}^E$  and  $\varphi_{1-6}^P$  are constant after  $t = 0.02$  s. At 0.03s (stage (C)), a  $90^\circ$  rotation of the element is conducted. This drastically changes the components of the computed stress glut. In fact, according to Fig. 2.29c, components  $\Pi_{xx}^D$  and  $\Pi_{zz}^D$  exchange their values, and  $\Pi_{xz}^D$  become temporarily non-zero. This evolution of stresses within the element is expected for the Cauchy-Stress representation that is applied in HOSS. Indeed, stresses are constant within the reference frame of the element, but not in the observation frame: rotation corresponds to a change of projection from the

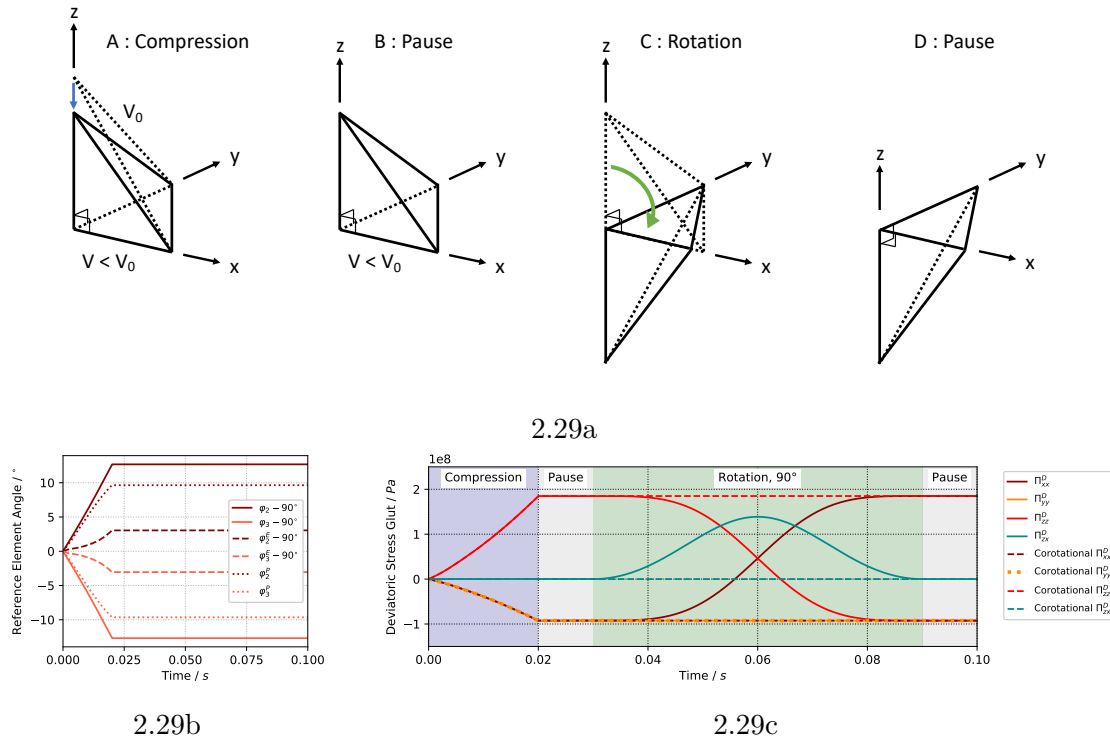


**Figure 2.29:** Computation of the deviatoric stress glut for a single tetrahedral element subject to: (A) shear in the vertical direction and (C) a 90-degree rigid-body rotation about the  $y$  axis (2.29a). (2.29b) shows the angles measured in the reference element at different steps of the experiment.

reference element to the real element. The observed variation of stress wrongly suggests that substantial plasticity is still being generated within the tetrahedral element.

To counter this effect, a polar decomposition of the deformation gradient tensor associated to the reference element can be performed. We use  $F = RU$ , with  $F$  the deformation gradient,  $R$  the rotation tensor and  $U$  the right Cauchy-Green deformation tensor. The "corotational deviatoric stress glut tensor" is computed by  $\hat{\Pi}^D = R^T \Pi^D R$ . The associated stress glut components show no evolution during rigid-body rotation (see dashed lines in Fig. 2.29c). This decomposition method provides a way to remove rigid-body rotation effects in a large-scale simulation. However, one must keep in mind that the principal axes of rotation of tensor  $R$  will be different for each element of the simulation. Therefore, integrating the corotated stress glut over the target volume as in Equation 2.30 amounts to summing entities measured in different reference frames

Whether rotation effects must be taken into account in the representation of a seismic source is an open question. On one hand, this is problematic, as it may appear that the stress glut is evolving in time, even though no further plastic processing are occurring within the element. On the other hand, one can also consider finite rotation to be part of the inelastic processes generated by the source in a more general way, in which case they should be taken into account in the final seismic source representation.

### SI-3 Mesh test for seismic source computation

The design of the verification simulations meshes presented in section 2.4.3 of the main text was done in the following three steps, using the software CUBIT from Coreform:

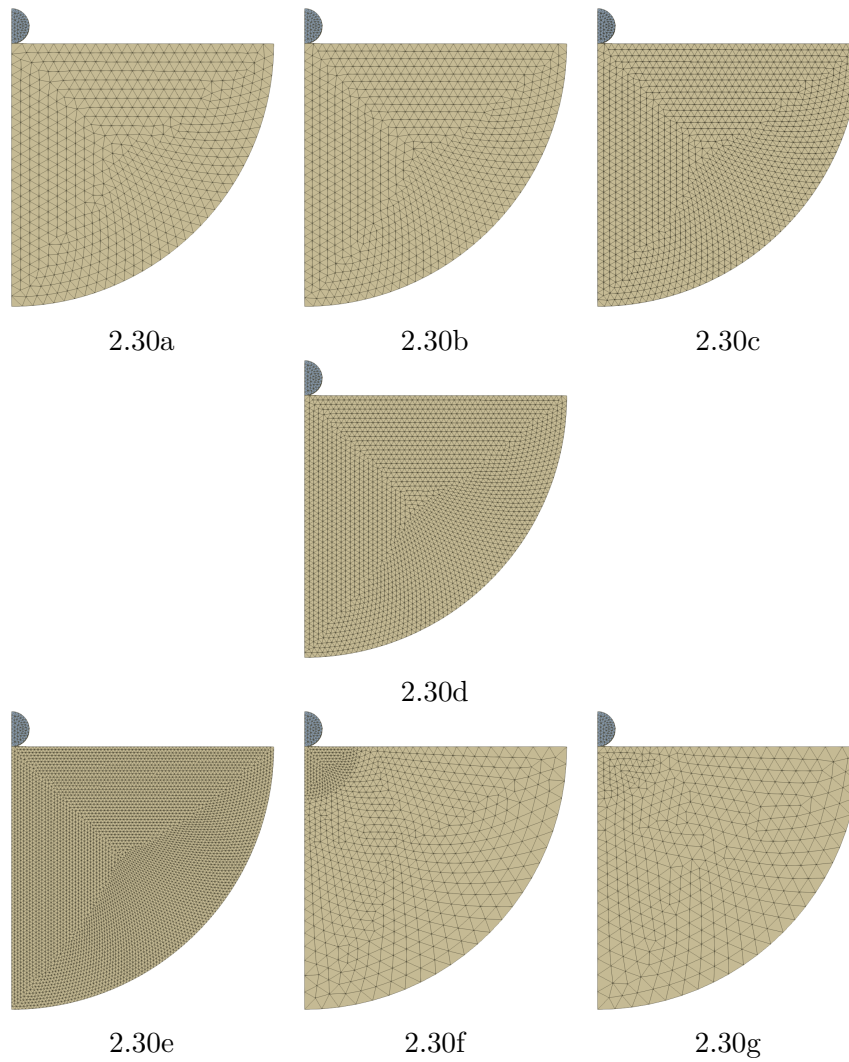


**Figure 2.30:** 3D Tetrahedral meshes tested in this work. In each case, the impactor (in blue) is meshed with tetrahedrons of size  $l = 2$  cm. From mesh (2.30a) to mesh (2.30e), the target (light brown) is meshed with a uniform tetrahedron size corresponding to  $l = [6, 5, 4, 3, 2]$  cm, in decreasing order. The last two meshes, (2.30f) and (2.30g), are composed of a central spherical region with radius  $3 \times r_i$ , followed by a gradient mesh increasing to  $l = 10$  cm. The central region of mesh (2.30f) has  $l = 2$  cm, and is used to simulate vertical impacts (scenario (A)) in the following study. The central region of mesh (2.30g) has  $l = 4$  cm, for the simulation of oblique impacts (scenario (B)).



- (1) A rough mesh is built in order to estimate the size of the inelastic source region,  $R_s$  with a first run.
- (2) A more precise geometry is designed, in the form of a 45 or 180° cylindrical sector, whose radius must be larger than  $\sqrt{2}R_s$ . This ensures all the points on the square coupling box will fit into the HOSS simulation domain while only recording signals in the elastic region. The HOSS simulation domain is equipped with non-reflecting boundaries. The radius and depth of the cylinder can be made a little larger than  $\sqrt{2}R_s$  to prevent the box points from recording residual reflections on the absorbing boundary conditions.
- (3) The resulting mesh is about a hundred times larger than the impactor, which presents a computational challenge. To avoid prohibitive computational costs, the mesh element size is made to gradually increase from the impact point to the outer limits. However, this must be done with caution, as a too big difference between the central and outer mesh elements would lead to unbalanced parallelisation domains and consequently slower simulation. In order to converge to a reasonable compromise between outer and central mesh, a mesh test is conducted by simulating a 1000 m/s impact on a smaller target region with varying mesh resolution.

The results of each of the three steps are described below:

**Step (1):** The impactor is a basaltic sphere with radius  $r_i = 10$  cm radius hitting a cohesive soil. The obtained source has a size  $R_s \approx 10$  m in radius and  $D_s \approx 12$  m in depth.

**Step (2):** A 17 m-wide cylinder is designed for scenari (A) and (B) to extend a little over the 14 m required size.

**Step (3):** The outer mesh has an element size of 22 cm for scenario (A) and 28 cm for scenario (B). To determine the performances of different mesh sizes in the crater region, the mesh test is conducted with a 1.5 m ( $15 \times r_i$ ) hemispherical target, cut over a 45° sector. The effect of various target resolutions below the impactor are investigated with 5 meshes of element size  $l$  varying between  $3/5$  and  $1/5$  of the impactor radius ( $l = [2, 3, 4, 5, 6]$ cm). These mesh are shown on Fig. 2.30. Although several studies have shown that a resolution of 10 to 20 elements (Cells) Per Projectile Radius (CPPR) are necessary to obtain accurate pressure profiles in impact simulation [Pierazzo et al., 2008; Caldwell et al., 2021], here computational costs limits the resolution of the target elements to  $l = 2$  cm ( $1/5 \times r_i$ ), which corresponds to 5 CPPR for the impactor. To improve the balance of parallelisation domains within the final 17 m wide mesh, two additional "gradient" meshes are tested. For scenario (A), the gradient presents a central region, at a distance inferior to  $3r_i$  from the impactor, with  $l = 2$  cm (see Fig. 2.30f). Then, the mesh size increases regularly to  $l = 10$  cm at  $r = 1.5$  m. For scenario (B), the central region has an element size of  $l = 4$  cm (see Fig. 2.30g).

Each hemispherical target domain is equipped with 42 sensors placed every 10 cm on three lines inclined with an angle of 0, 45 and 90° from the horizontal. For each mesh, the pressure and velocity recorded on these points are compared, as well as the crater shape 3 ms after the impact. The results of this mesh test are presented on Fig. 2.31 and Fig. 2.32. Fig. 2.31 shows relatively consistent crater depths 3 ms after the impact, expect for mesh 2.30a. The lifted material on the crater rim has a higher definition for the smallest element sizes (2.30d, 2.30e, 2.30f). On Fig. 2.32a, the pressure amplitude decay with

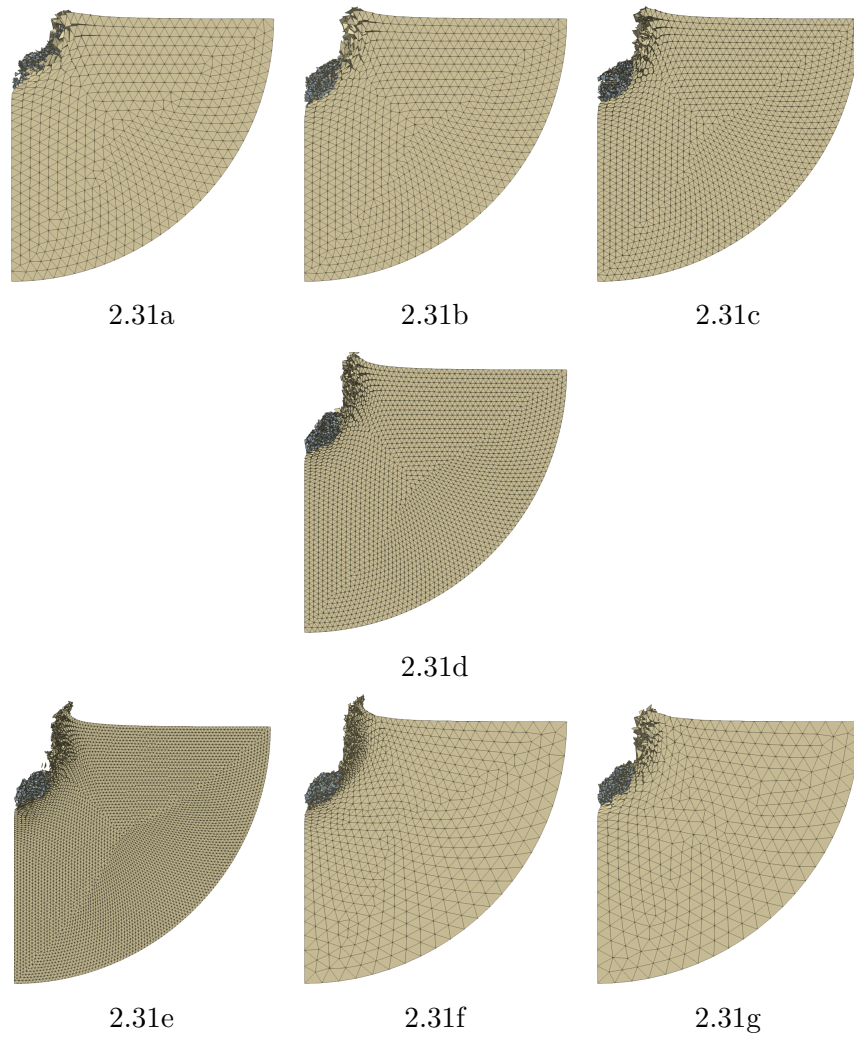


**Figure 2.31:** Image of the distribution of elements for each distinct mesh 2.98 ms after the 1000 m/s impact. The crater of mesh (2.31a) shows a shallower depth than the others.

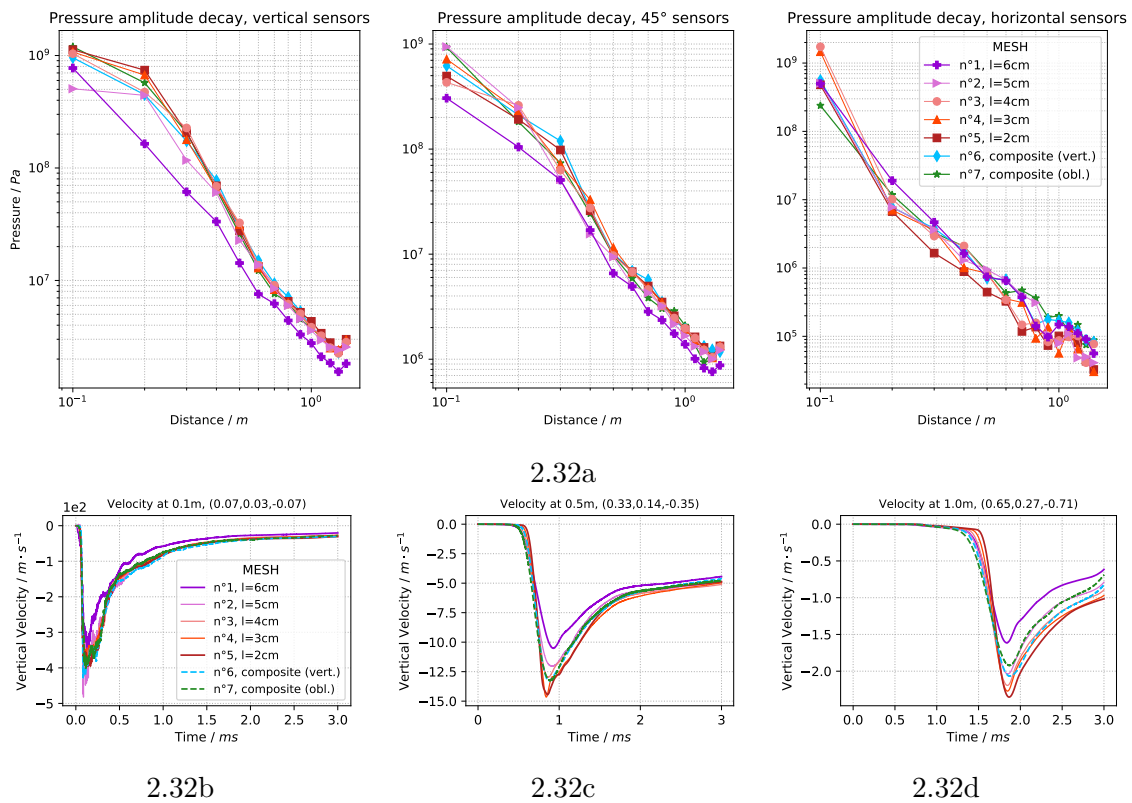


**Figure 2.32:** (2.32a) Pressure amplitude decay in three different directions for each distinct mesh. Fig. (2.32b) (resp (2.32c) and (2.32d)) shows the vertical velocity wave recorded at 0.1 m (resp 0.5 and 1.0 m) in a 45° direction below the surface. The finest mesh (n°5, dark red line) acts as a reference.

distance is plotted for each of the three lines of sensors. The finest mesh ( $l = 2$  cm) yields higher pressure values overall directly below the impactor, while meshes 2.30a and 2.30b have pressures up to four times smaller. On the contrary, meshes 2.30a and 2.30b appears to provide pressure values 2.5 times higher on average horizontally from the impact. This means that the pressure wave produced by finer mesh is more directional, with more energy released in the direction of the impactor. Fig. 2.32b to Fig. 2.32d show recorded vertical velocity waves at 0.1, 0.5 and 1 m away from the impact, at a  $45^\circ$  angle. Coarser meshes show a smoother onset of the wave, which can be explained by the fact that larger finite elements will filtrate more high frequencies. The amplitude of the wave is strongly underestimated with  $l = 6$  cm, with  $-1.6$ m/s maximal velocities for mesh 2.30a, compared to  $-2.4$ m/s for mesh 2.30e. From these tests, we can deduce that the performances of the gradient meshes 2.30f and 2.30g lie between the ones of homogeneous meshes with  $l = 5$  cm and  $l = 4$  cm. This means that they do not simulate impact shock waves with the highest possible accuracy, but their results rather lie within 15% of the ones obtained with the finest mesh ( $l = 2$  cm). However, these gradient mesh provide a good compromise between accuracy, element number and load balance between parallelisation domains.

#### SI-4 Fit of HOSS force and moment source time functions

We report here the results of the fit of the force ( $F_i(\tau)$ ) and moment ( $M_{ij}(\xi^*, \tau)$ ) source time functions computed in section 2.5.2 of the main text. The pulse and integrated pulse functions used to extrapolate the source time functions is the following :

$$j(t, \tau, c) = ct e^{-t/\tau} \quad (2.82)$$

where  $c$  and  $\tau$  are parameters. Its integral is given by :

$$J(t, \tau, c) = (-c\tau t - c\tau^2)e^{-t/\tau} + C. \quad (2.83)$$

with  $C = c\tau^2$  chosen to ensure the source is zero at  $t = 0$ . The force source time functions are fit with a sum of two pulses. The moment source time function, which contains more complexity at early times, is fit with a sum of two integrated pulses  $J(t)$  and one pulse  $j(t)$  when required. The deviatoric components  $M_{xx}^D$  and  $M_{zz}^D$  are fit independently from the volumetric component  $M^V$ . We then have  $M_{xx} = M^V + M_{xx}^D$  and  $M_{zz} = M^V + M_{zz}^D$ .  $M_{yy}$  is deduced from  $M^V - M_{xx}^D - M_{zz}^D$  to ensure that the fit of the deviatoric components does not add any amplitude to the volumetric component. The parameters of the fit can be found in Table 2.4. The results of the fit in the time domain, as well as the spectrum of the force  $\mathbf{F}(\tau)$  and moment rate  $\frac{\partial M}{\partial \tau}(\xi^*, \tau)$  are shown in Fig. 2.33.

#### SI-5 Point source and coupled signals

##### Signals at various distances

We present on Figs. 2.34, 2.35 and 2.36 the comparison between point-source and coupled signals for a receiver placed at 100, 200 and 300 m from the impact respectively. These results can be compared to the 400 m distance case shown in the main text. They show that, at various distances, the low-frequency spectral amplitude of coupled and point-source signals agree to within a factor 3 for the P wave and 5 for the S wave. The peak point-source S amplitude in the waveform plot is larger than the coupled peak S amplitude by a factor  $\sim 15$  to  $\sim 20$  at these three distances.

**Table 2.4:** Parameters of the fit of the oblique and vertical point source components by Jeffrey's pulses. Time  $t$  is expressed in seconds, and functions  $j(t, \tau, c)$  and  $J(t, \tau, c)$  are defined in equations 2.82 and 2.83, respectively. The parameters  $\tau$  have been coloured according to their order of magnitude : **red** for a timescale of the order of  $1 \times 10^{-4}$ , **orange** for  $1 \times 10^{-3}$  and **blue** for  $1 \times 10^{-2}$ .

	Vertical	Oblique
$F_z$ [Nm]	$j(t, \underline{9.7910^{-5}}, -8.5910^{11}) + j(t, \underline{5.8610^{-4}}, -1.0810^{10})$	$j(t, \underline{1.2110^{-4}}, -4.7910^{11}) + j(t, \underline{6.4810^{-4}}, -5.56 \times 10^9)$
$F_x$ [Nm]	-	$j(t, \underline{1.3410^{-4}}, 2.4410^{11}) + j(t, \underline{3.7810^{-4}}, 1.5210^{10})$
$M^V$ [Nm]	$J(t, \underline{7.1510^{-4}}, -1.6110^{14}) + J(t, \underline{5.1410^{-2}}, 2.9910^9)$	$J(t, \underline{6.5110^{-4}}, -1.4610^{14}) + J(t, \underline{2.9910^{-2}}, 1.2810^{10})$

#### Using Cauchy stress

$M_{xx}^D$ [Nm]	$M^V - M_{zz}^D/2$	$J(t, \underline{4.8210^{-3}}, -2.1010^{12}) + J(t, \underline{3.7710^{-2}}, 4.5410^{10})$
$M_{yy}^D$ [Nm]	$M^V - M_{zz}^D/2$	$M^V - M_{xx}^D - M_{zz}^D$
$M_{zz}^D$ [Nm]	$J(t, \underline{3.2010^{-3}}, 6.2910^{12}) + J(t, \underline{5.0910^{-2}}, -5.4410^{10})$	$J(t, \underline{3.9210^{-3}}, 4.1410^{12}) + J(t, \underline{3.7710^{-2}}, -7.2110^{10})$
$M_{zx}^D$ [Nm]	-	$J(t, \underline{6.9310^{-3}}, 2.1210^{12}) + J(t, \underline{4.4010^{-2}}, -2.4710^{10}) + j(t, \underline{5.5610^{-3}}, 8.8610^9)$

#### Using corrotated Cauchy stress

$M_{xx}^D$ [Nm]	$M^V - M_{zz}^D/2$	$J(t, \underline{5.0910^{-3}}, -2.1910^{12}) + J(t, \underline{5.3610^{-2}}, 1.7610^{10}) + j(t, \underline{9.0510^{-4}}, 7.7210^9)$
$M_{yy}^D$ [Nm]	$M^V - M_{zz}^D/2$	$M^V - M_{xx}^D - M_{zz}^D$
$M_{zz}^D$ [Nm]	$J(t, \underline{5.1210^{-3}}, 9.0710^{11}) + J(t, \underline{5.2710^{-2}}, -1.2410^{10}) + j(t, \underline{2.4510^{-3}}, -1.4410^{10})$	$J(t, \underline{4.2110^{-3}}, 3.9810^{12}) + J(t, \underline{4.5610^{-2}}, -2.9310^{10}) + j(t, \underline{7.4610^{-4}}, -1.2410^{10})$
$M_{zx}^D$ [Nm]	-	$J(t, \underline{6.8910^{-3}}, 2.0310^{12}) + J(t, \underline{2.2510^{-2}}, -5.5310^{10}) + j(t, \underline{4.5110^{-3}}, 1.2410^{10})$

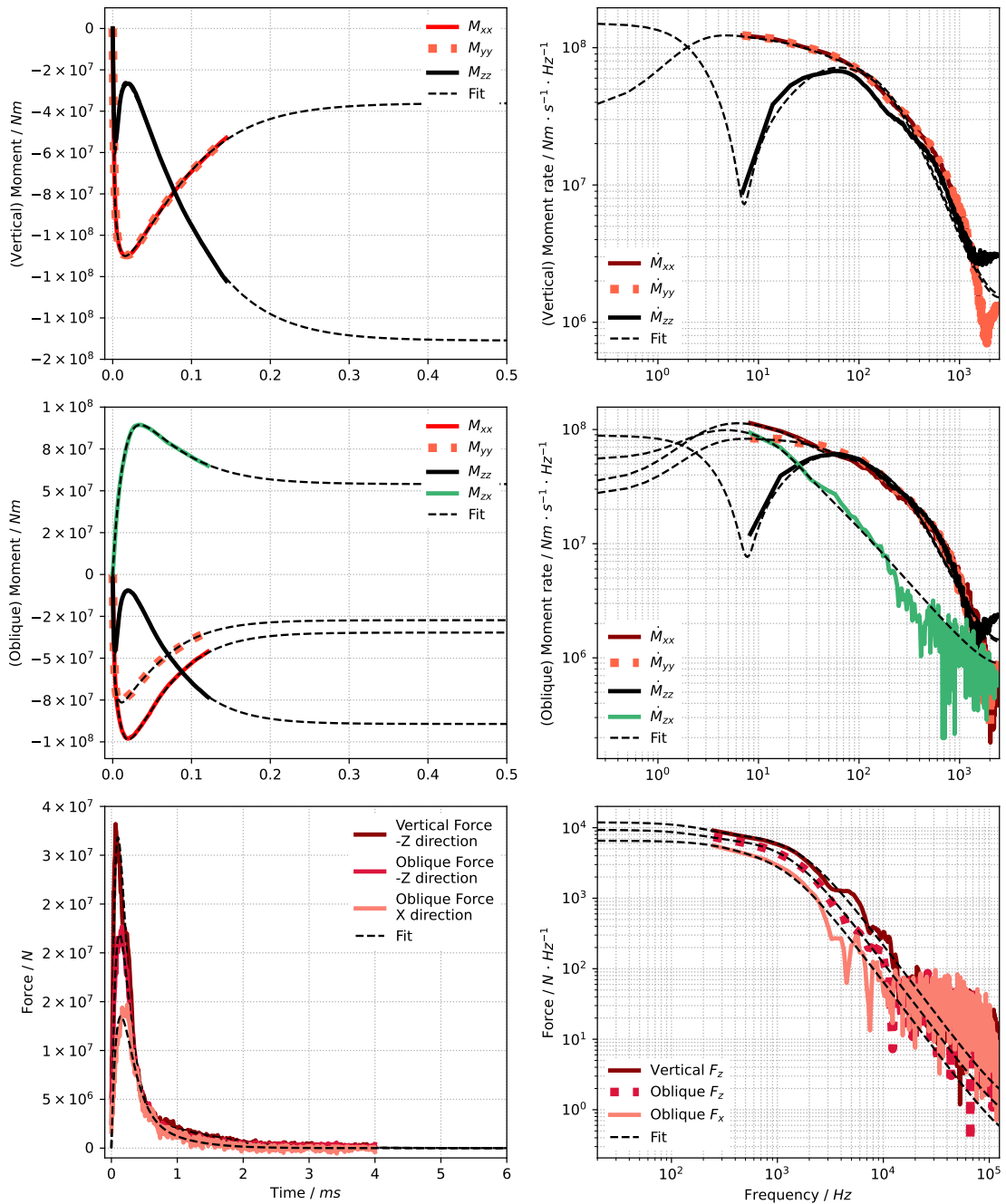


**Figure 2.33:** Result of the fit and prolongation of the moment components for a vertical impact simulation simulation (top), an oblique impact simulation (middle), and the fit of the force of both scenarios (bottom). The moment shown here are not corrected for rotation. The spectrum of the force and of the moment rate  $\frac{\partial M}{\partial \tau} = \dot{M}$  are shown on the right, normalised by the sampling rate of each curve,  $dt$ .

**Table 2.5:** Misfit between the P- and S- wave spectra at 400 m and the result of the  $\Omega_3$  and  $\Omega_2$  model fits. The misfit to the coupled signal is lower with the  $\Omega_3$  model for both the P- and S-wave.

$f_c$ , [Hz]	P- wave		S- wave	
	Coupled signal	Point source signal	Coupled signal	Point source signal
$\Omega_3$	2.0	6.5	46.5	6.2
$\Omega_2$	11.6	1.1	71.0	6.2

### Estimate of the cutoff frequency

The cutoff frequency of the P- and S- signal are estimated from three different fit to their amplitude spectrum up to 130 Hz. A first method fits two asymptotes to the low-frequency ( $0 < f < 5$  Hz) and high-frequency ( $30 < f < 130$  Hz) part of the spectrum. The two other methods fit an  $\omega$ -squared ( $\Omega_2$ ) and an  $\omega$ -cubed ( $\Omega_3$ ) model to the signal [Aki, 1967; Brune, 1970], inverting for parameters  $f_c = \omega_c/2\pi$  and  $\Omega_0$  as defined below:

$$\Omega_2(\omega) = \frac{\Omega_0}{\left[1 + \left(\frac{\omega}{\omega_c}\right)^2\right]} \quad \text{and} \quad \Omega_3(\omega) = \frac{\Omega_0}{\left[1 + \left(\frac{\omega}{\omega_c}\right)^2\right]^{3/2}}, \quad (2.84)$$

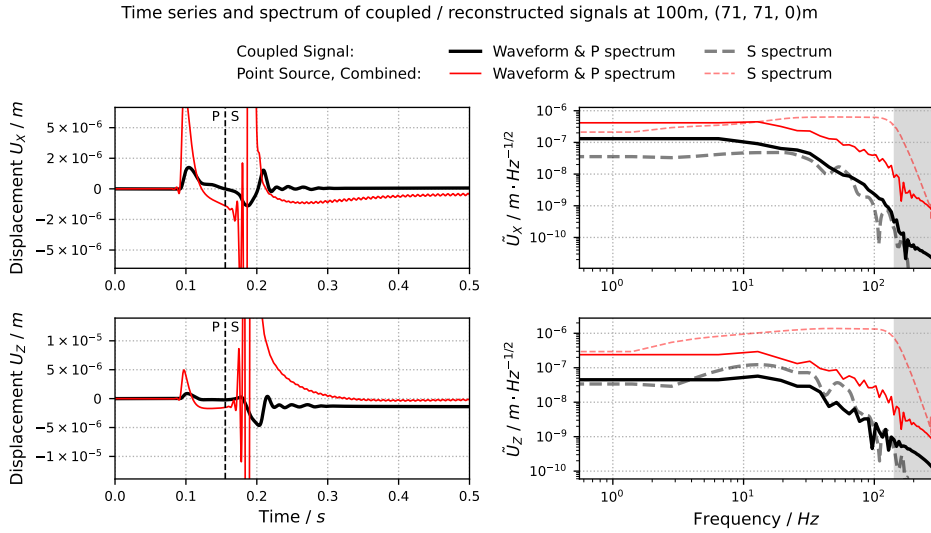
The result for each fit is shown on Fig. 2.37. The respective fit of the  $\Omega_2$  and  $\Omega_3$  models are shown in Table 2.5, computed as follows:

$$\chi^2 = \sum_{i=0}^N \{\log [\tilde{u}_z(f_i)] - \log [\Omega_3(f_i)]\}^2, \quad (2.85)$$

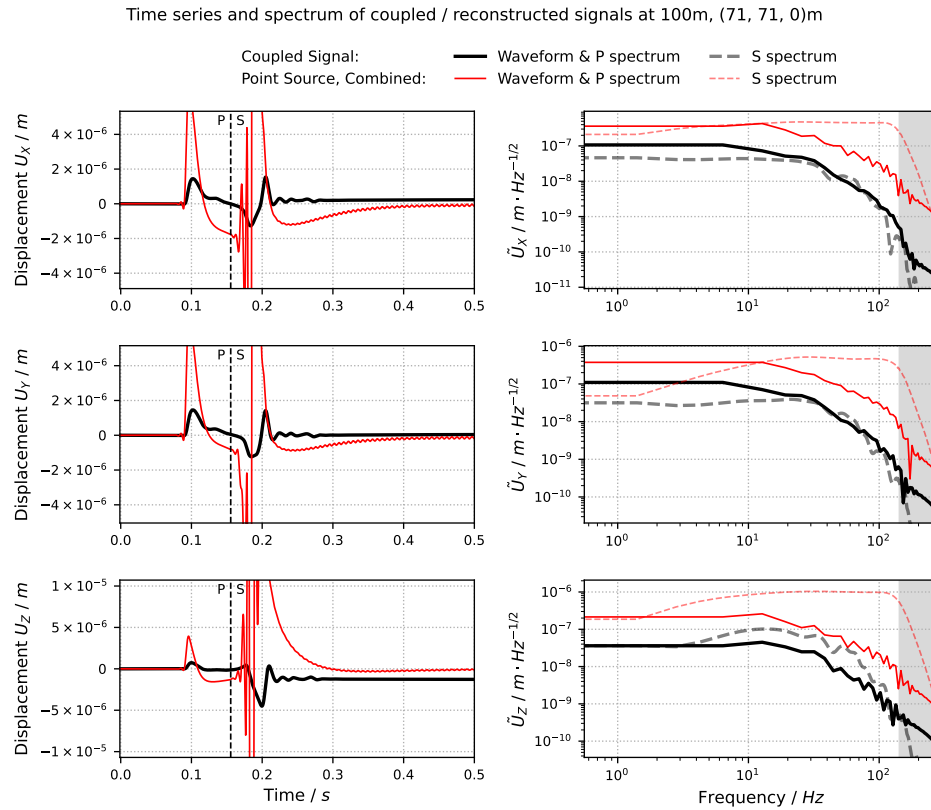
and respectively for  $\Omega_2$ , with  $N$  the total number of frequency samples.

A fit can also be performed on the waveforms prolonged to 100 km, as in section 2.5.4. However, estimates of  $f_c$  are then biased by the attenuation effect present at high frequency in the spectrum. Results in this case are shown on Fig. 2.38.



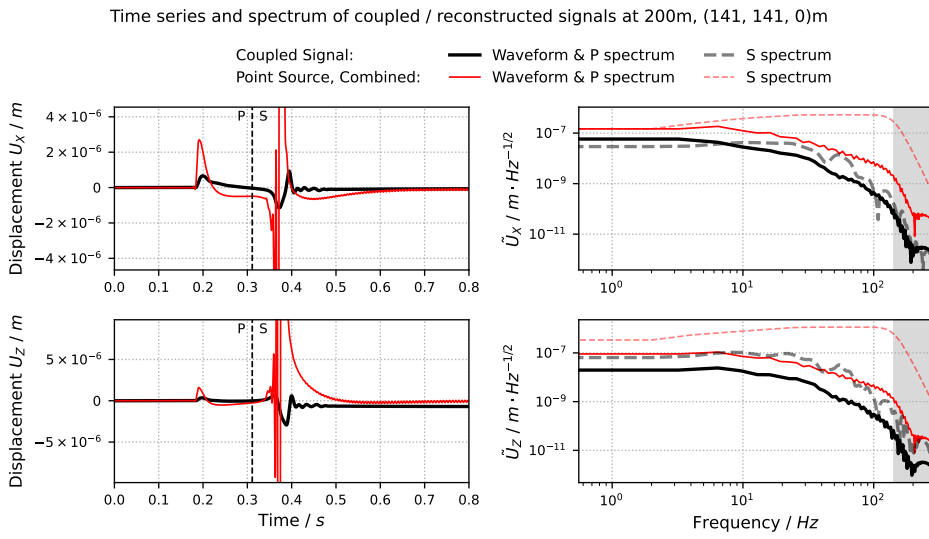


2.34a

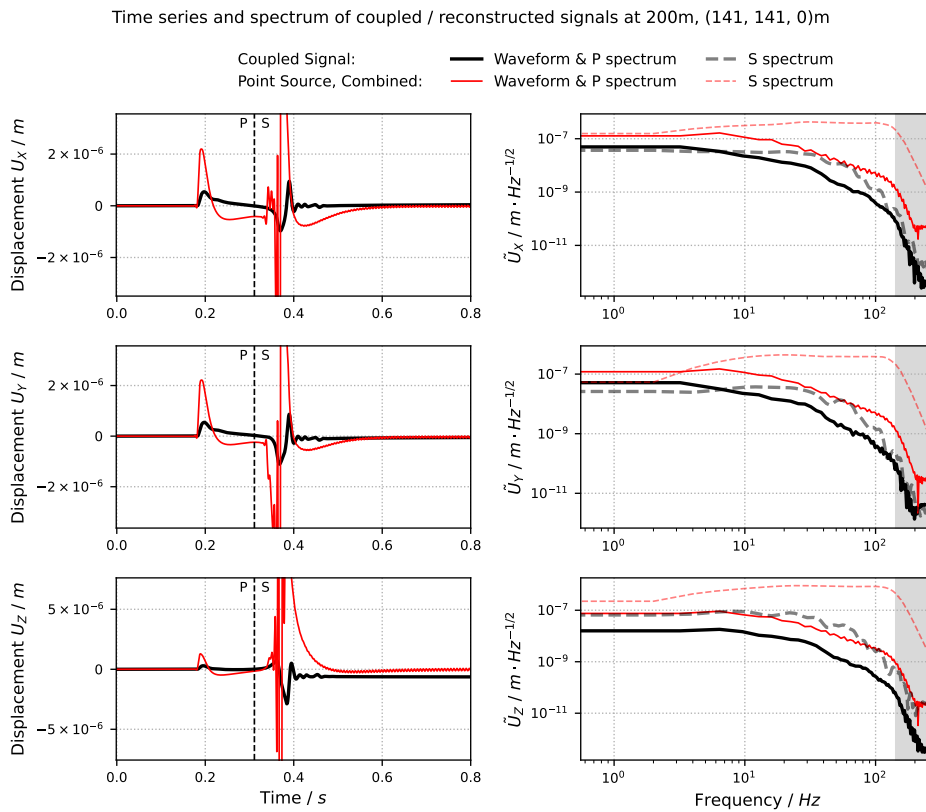


2.34b

**Figure 2.34:** Comparison between coupled (black) and combined point-source (red) waveforms at 100 m source-receiver distance, for a vertical impact (2.34a) and an oblique impact (2.34b). The left column depicts displacement signals  $U_x$ ,  $U_y$ ,  $U_z$ . For the vertical impact,  $U_y$  is omitted as it is equal to  $U_x$  in this azimuth. The combined point-source signal (red) sums the displacements obtained for each individual components of the source ( $M_{xx}$ ,  $M_{yy}$ ,  $F_z$ , etc...). All signals have been low-pass-filtered using an order 5 Butterworth filter with cutoff frequency of 7 ms. The right column represent the associated spectrum, normalised by  $\sqrt{2dt/N}$ ,  $N$  being the number of samples in the waveform. These spectrum have been computed by separating the P- and the S-wave in the displacement time series : the P-wave spectrum is shown with plain lines and the S-wave with dashed lines. The grey shaded region on the left plots indicates the time at which residual reflections on the simulation boundaries start contaminating the signal, and on the right the low-pass-filtered region.

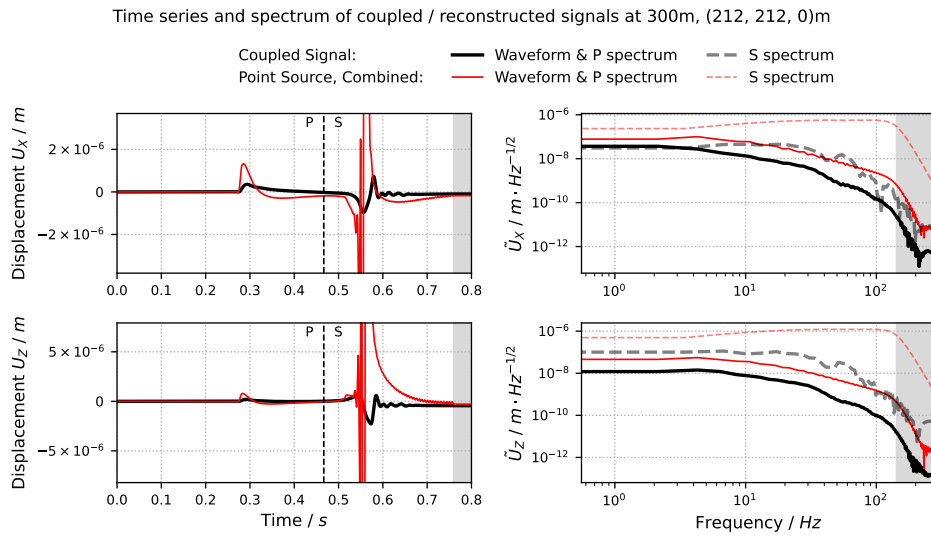


2.35a

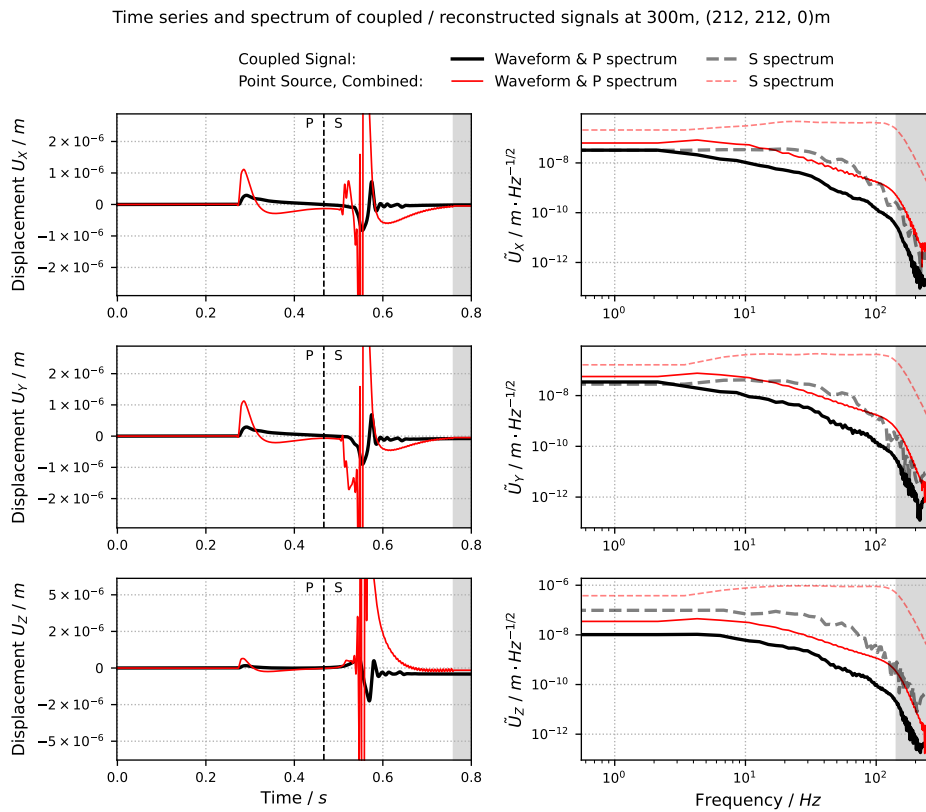


2.35b

**Figure 2.35:** Results of the comparison between coupled (black) and combined point-source (red) waveforms at 200 m source-receiver distance. Signal processing is the same as in Fig. 2.34.



2.36a



2.36b

**Figure 2.36:** Results of the comparison between coupled (black) and combined point-source (red) waveforms at 300 m source-receiver distance. Signal processing is the same as in Fig. 2.34.

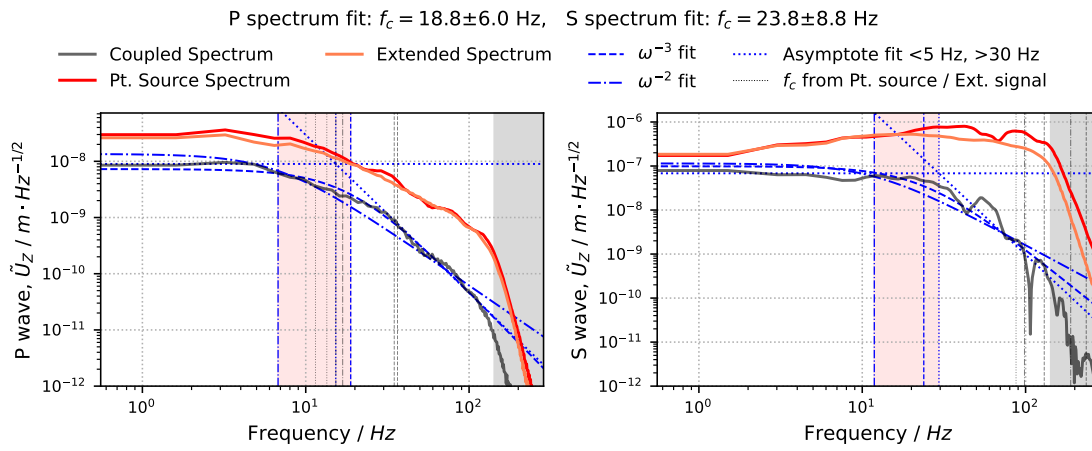


**Figure 2.37:** Results of the fit of the coupled P-wave (left) and S-wave (right). The three values of  $f_c$  obtained with the  $\Omega_3$ ,  $\Omega_2$  and asymptote model are marked with vertical blue lines. The result obtained with the  $\Omega_3$  model is indicated at the top, with uncertainties estimated from the total range of models. Results obtained from the fit of the point-source signal are indicated by thin vertical black lines.

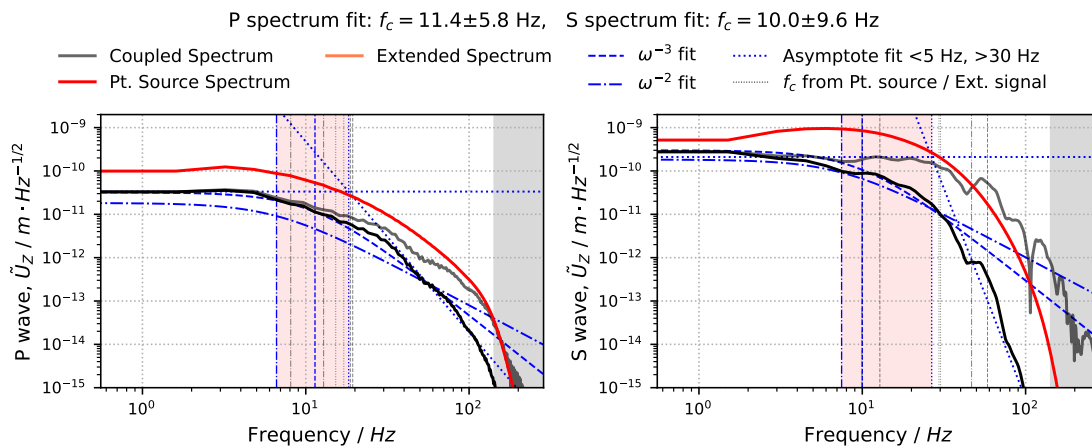


**Figure 2.38:** Results of the fit of the coupled P-wave (left) and S-wave (right) at 100 km distance, calculated by scaling and attenuating the signals recorded at 400 m distance. Legend and labels follow Fig. 2.37. The original coupled signal at 400 m, scaled to the amplitude of  $3 \times 10^{-10} \text{ m} \cdot \text{Hz}^{-1/2}$  and without any attenuation effect, is shown in dark grey to better illustrate the effect of attenuation on the spectrum at these distances.



**Copyrighted Material 1**

Not authorized for online diffusion.

Froment, M., Rougier, E., Larmat, C., Lei, Z., Euser, B. et al.  
Lagrangian-based Simulations of Hypervelocity Impact Experiments  
on Mars Regolith Proxy. *Geophysical Research Letters*, 47(13), July  
2020. <https://doi.org/10.1029/2020GL087393>.

**Copyrighted Material 1**

Not authorized for online diffusion.

Froment, M., Rougier, E., Larmat, C., Lei, Z., Euser, B. et al.  
Lagrangian-based Simulations of Hypervelocity Impact Experiments  
on Mars Regolith Proxy. *Geophysical Research Letters*, 47(13), July  
2020. <https://doi.org/10.1029/2020GL087393>.



**Copyrighted Material 1**

Not authorized for online diffusion.

Froment, M., Rougier, E., Larmat, C., Lei, Z., Euser, B. et al.  
Lagrangian-based Simulations of Hypervelocity Impact Experiments  
on Mars Regolith Proxy. *Geophysical Research Letters*, 47(13), July  
2020. <https://doi.org/10.1029/2020GL087393>.

**Copyrighted Material 1**

Not authorized for online diffusion.

Froment, M., Rougier, E., Larmat, C., Lei, Z., Euser, B. et al.  
Lagrangian-based Simulations of Hypervelocity Impact Experiments  
on Mars Regolith Proxy. *Geophysical Research Letters*, 47(13), July  
2020. <https://doi.org/10.1029/2020GL087393>.

**Copyrighted Material 1**

Not authorized for online diffusion.

Froment, M., Rougier, E., Larmat, C., Lei, Z., Euser, B. et al.  
Lagrangian-based Simulations of Hypervelocity Impact Experiments  
on Mars Regolith Proxy. *Geophysical Research Letters*, 47(13), July  
2020. <https://doi.org/10.1029/2020GL087393>.

**Copyrighted Material 1**

Not authorized for online diffusion.

Froment, M., Rougier, E., Larmat, C., Lei, Z., Euser, B. et al.  
Lagrangian-based Simulations of Hypervelocity Impact Experiments  
on Mars Regolith Proxy. *Geophysical Research Letters*, 47(13), July  
2020. <https://doi.org/10.1029/2020GL087393>.

**Copyrighted Material 1**

Not authorized for online diffusion.

Froment, M., Rougier, E., Larmat, C., Lei, Z., Euser, B. et al.  
Lagrangian-based Simulations of Hypervelocity Impact Experiments  
on Mars Regolith Proxy. *Geophysical Research Letters*, 47(13), July  
2020. <https://doi.org/10.1029/2020GL087393>.

**Copyrighted Material 1**

Not authorized for online diffusion.

Froment, M., Rougier, E., Larmat, C., Lei, Z., Euser, B. et al.  
Lagrangian-based Simulations of Hypervelocity Impact Experiments  
on Mars Regolith Proxy. *Geophysical Research Letters*, 47(13), July  
2020. <https://doi.org/10.1029/2020GL087393>.

## Copyrighted Material 2

Not authorized for online diffusion.

Posiolova, L.V., Lognonné, P., Banerdt, W.B., Clinton, J., Collins, G.S. et al. Largest recent impact craters on Mars: Orbital imaging and surface seismic co-investigation. *Science*, pages 1–5, October 2022. <https://doi.org/10.1126/science.abq7704>.



## Copyrighted Material 2

Not authorized for online diffusion.

Posiolova, L.V., Lognonné, P., Banerdt, W.B., Clinton, J., Collins, G.S. et al. Largest recent impact craters on Mars: Orbital imaging and surface seismic co-investigation. *Science*, pages 1–5, October 2022. <https://doi.org/10.1126/science.abq7704>.

## Copyrighted Material 2

Not authorized for online diffusion.

Posiolova, L.V., Lognonné, P., Banerdt, W.B., Clinton, J., Collins, G.S. et al. Largest recent impact craters on Mars: Orbital imaging and surface seismic co-investigation. *Science*, pages 1–5, October 2022. <https://doi.org/10.1126/science.abq7704>.

## Copyrighted Material 2

Not authorized for online diffusion.

Posiolova, L.V., Lognonné, P., Banerdt, W.B., Clinton, J., Collins, G.S. et al. Largest recent impact craters on Mars: Orbital imaging and surface seismic co-investigation. *Science*, pages 1–5, October 2022. <https://doi.org/10.1126/science.abq7704>.

## Copyrighted Material 2

Not authorized for online diffusion.

Posiolova, L.V., Lognonné, P., Banerdt, W.B., Clinton, J., Collins, G.S. et al. Largest recent impact craters on Mars: Orbital imaging and surface seismic co-investigation. *Science*, pages 1–5, October 2022. <https://doi.org/10.1126/science.abq7704>.





*Red Hills, Lake George, 1927, Georgia O'Keeffe*  
The Phillips Collection.

# Impact-generated seismo-acoustic signals on Mars

---

### Summary of the Chapter

The previous chapter focused on the seismic source related to the impact cratering process. Using the representation theorem and numerical simulation of the impact dynamics and associated seismic signals, we proposed a model of this seismic source in terms of equivalent forces. This study reveals the complexity of the impact source mechanisms, and brings new perspectives for the definition of *impact discriminators* mentioned in section 1.4.1.

On Mars, six small impact craters, with distance of less than 300 km from InSight, could be associated to seismic signals in SEIS records. Their characterisation would not have been possible without the simultaneous detection of short seismo-acoustic signals produced by the impact atmospheric shock wave. These signals represent a unique opportunity to better understand the production of acoustic waves by impacts, the propagation of infrasound in the Martian atmosphere, and the problem of air-to-ground coupling.

The following chapter begins with an introduction of shock wave generation by meteors and meteorites, their transition to acoustic waves and the phenomenon of seismic coupling. We then present the impact-generated seismo-acoustic signals recorded by InSight. We detail the creation of a 1D-model of infrasound propagation in a layered atmosphere and their coupling into seismic signal via ground compliance published by Xu et al. [2022]. We conduct a parametric study of this model and show that some properties of the atmosphere and subsurface of Mars can be inverted from these unusual seismic signals. Finally, we present the results of an inversion of events S0986c, S1034a and S0981c.

### Related publications

- Xu, Z., Froment, M., Garcia, R.F., Beucler, É., Onodera, K. et al. Modeling Seismic Recordings of High-Frequency Guided Infrasound on Mars. *Journal of Geophysical Research: Planets*, 127(11), 2022. doi: 10.1029/2022JE007483.



---

## Contents of the chapter

<b>3.1</b>	<b>Introduction</b>	131
3.1.1	Atmospheric shock waves from meteors and meteorites . . . . .	131
3.1.2	Phenomenology of air-to-ground coupling . . . . .	137
3.1.3	Martian chirp signals . . . . .	139
<b>3.2</b>	<b>Seismo-acoustic model of a guided meteorite infrasound</b>	144
3.2.1	Modelling of dispersed infrasound . . . . .	144
3.2.2	Modelling of seismic signals coupled from infrasound . . . . .	145
3.2.3	Characteristics of the model . . . . .	146
<b>3.3</b>	<b>Inversion method</b>	147
3.3.1	Model parametrisation and sensitivity . . . . .	147
3.3.2	The Markov chain Monte Carlo inversion method . . . . .	153
3.3.3	Data selection . . . . .	158
<b>3.4</b>	<b>Inversion of the atmospheric structure</b>	159
3.4.1	Test of the inversion method . . . . .	159
3.4.2	Atmospheric structure inverted for three individual events . . . . .	162
<b>3.5</b>	<b>Inversion of InSight near-surface structure</b>	162
3.5.1	Test of the subsurface inversion . . . . .	162
3.5.2	Subsurface model inverted from event H/V ratio . . . . .	166
<b>3.6</b>	<b>Discussion</b>	168
3.6.1	Interpretation of the atmospheric inversion . . . . .	168
3.6.2	Interpretation of the subsurface inversion . . . . .	169
<b>3.7</b>	<b>Conclusion</b>	171
	<b>Appendices</b>	173
A1	The propagator matrix method for compliance . . . . .	173
A2	The propagator matrix method for guided infrasound . . . . .	175
A3	Test of different MCMC implementations . . . . .	177

---

## 3.1 Introduction

### 3.1.1 Atmospheric shock waves from meteors and meteorites

#### Shock wave generation

On planets with atmospheres, such as Mars and the Earth, the interaction of a high-speed meteor with the surrounding gas induce shock waves. As in the impact cratering process, the shock wave is created by the significant compression and heating of fluid close to the meteor in a short amount of time. Depending on the various fates of a meteor described in section 1.1.1, the produced shock waves can be of three kinds:

- *A ballistic shock wave:* This type of shock forms around objects falling with a speed exceeding the speed of sound in the atmosphere, and is represented on part (a) of Fig. 3.1.
- *An airburst shock wave:* The burst of a meteor results in a sudden enhancement of its ablation and heating, and a strong deceleration. These combined effects form shock discontinuities in pressure and temperature around the disrupted meteor. The airburst phenomenon, represented on part (b) of Fig 3.1, is akin to an airborne explosion.
- *A surface blast:* In a similar fashion, the high-velocity collision of a meteorite with the surface causes significant heating and a pressure increase at the point of impact. The generated shock is thought to be similar to that of a surface or very shallow explosion.

On Earth, the first two types of shock wave generation processes dominate. On Mars however, all three are present.

In the following sections, the characteristics of these shock waves and relevant associated scaling relations are detailed.

**Meteor ballistic shock properties** Shocks produced by supersonic objects have been studied extensively since the forties, for military applications and due to the growing needs of the aeronautical industry. As a common example, supersonic aircrafts travelling faster than the speed of sound are known to generate shock waves, experienced at the surface as a *sonic boom*. Drawing on a study of line source shock waves proposed by Tsikulin [1969], ReVelle [1976] proposed the first theory of shock generation by meteors. His results were summarised in a review by Edwards [2009].

The dominant process at play in the generation of a shock wave by a meteor is not ablation, but rather the action of *drag forces* of the ambient air. At supersonic speeds, a detached conical shock, called *Mach cone*, forms around the blunt meteor body. The aperture angle  $\beta$  of the cone is related to its Mach number, defined as the ratio of the meteor velocity to the speed of sound in the air:  $M = v_i/c_s$ . We have for a spheroid body:

$$\sin \beta = \frac{1}{M} \quad (3.1)$$

The speed of a fireball being typically between 10 and 20 km·s<sup>-1</sup>, and the average speed of sound on Earth being close to 300 m·s<sup>-1</sup>,  $M$  is considerably higher than 1 and the Mach cone can be approximated by a cylinder with  $\beta \approx 0$ . Moreover, the motion of the meteor

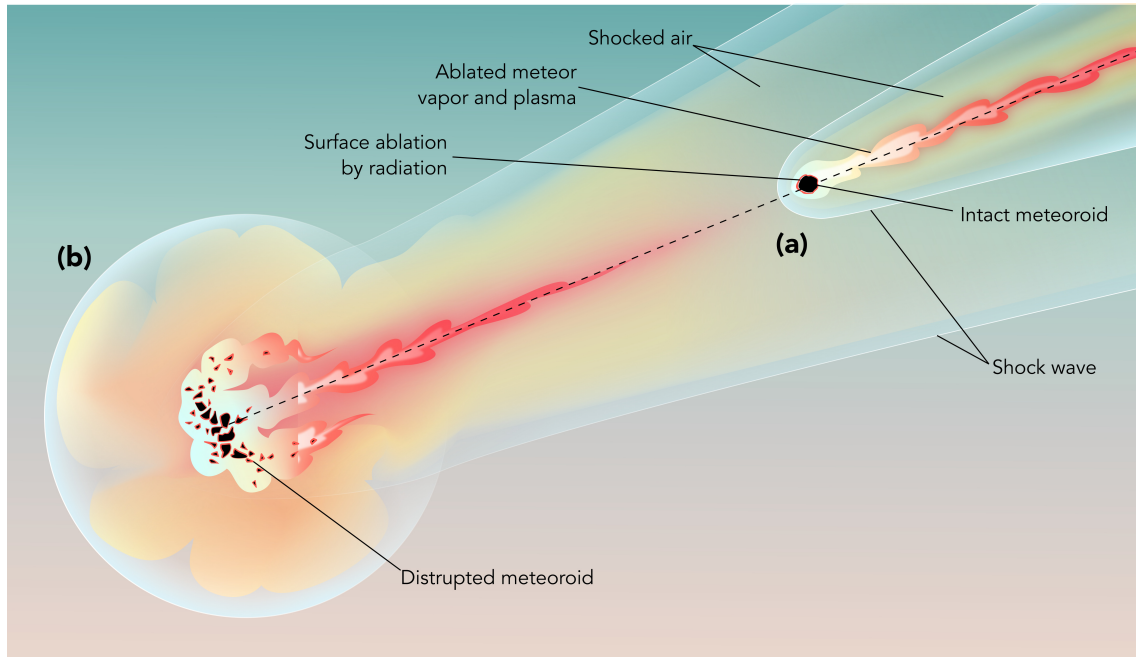


**Figure 3.1:** Graphic representation of the fireball (a) and airburst (b) phenomena. The high velocity of the bolide generates a shock wave, surrounding a region containing shocked air mixed with vapour ablated from the meteoroid.

being  $M$  times faster than its associated acoustic wave, the deposition of energy along its trajectory can be considered instantaneous over a line, which justifies the choice of the line-source theory by ReVelle [1976] and Tsikulin [1969]. Within a small radius  $R_0$  from the trajectory of the meteor, the overpressure  $\Delta P$  generated by drag forces is comparable to the background atmospheric pressure  $P_0$ : the air is therefore in a regime of strong shock. ReVelle [1976] obtained a measure of  $R_0$  from the equations of aerodynamics:

$$R_0 = \left( \frac{E_0}{P_0} \right)^{1/2}. \quad (3.2)$$

Using an expression of drag forces on the meteor, this expression can be simplified into:

$$R_0 \approx M d_i, \quad (3.3)$$

with  $d_i$  the diameter of the meteoroid.

The radius  $R_0$  is a key parameter to model the evolution of the shock wave as it propagates away from its line source, and transitions into an acoustic wave.

**Shock wave from airbursts** The aerodynamic load applied to a falling meteoroid may lead to its fragmentation or even full disintegration. Fragmentation occurs when the *ram pressure*, i.e. the pressure exerted against the front of the bolide, exceeds its internal strength. It is usually initiated by the presence of internal defects in the meteoroid. If the meteoroid presents a sufficiently porous or permeable surface, drag forces can begin to deform it, offering even more surface to aerodynamic forces [Svetsov et al., 1995; Tabetah & Melosh, 2018]. Thus, a catastrophic breakup may occur, during which each meteor fragments experiences an enhanced deceleration and heating. The kinetic energy of the bolide is suddenly transferred to its environment, causing the airburst [Tabetah & Melosh, 2018].

Due to the random nature of the fragmentation process, which can occur at multiple point over a meteor trajectory and with variable intensity, airburst-generated shock waves are complex [Edwards et al., 2008; Edwards, 2009], and most existing studies rely on numerical modelling to calculate shock variables on a case-by-case basis [Shuvalov & Artemieva, 2002; Shuvalov et al., 2013; Robertson & Mathias, 2017].

**Surface blast** Owing to the lack of observation of such phenomenon on Earth, few studies have attacked the problem of hypervelocity meteorite impact blasts. The impact process is merely assumed to be similar to a surface explosion.

Models for explosive blast waves have been developed for conventional and nuclear explosives. Similarly to ballistic shock cones, detonations have a strongly non-linear shock signature in the vicinity of the source, and scaling can relate the energy of an explosion to the pressure amplitude in the shock and its duration (see e.g., a review by Garces [2019]).

### Shock wave evolution

In the early stage of shock wave generation, the shock takes the form of a sharp discontinuity in fluid pressure, velocity and density. But quickly, non-linear effects of these strong discontinuities lead to a distortion of the shock front. The action of viscosity and heat transfer, as well as molecular relaxation phenomena, also contribute to its attenuation. Eventually, discontinuities are smoothed out enough so that the shock becomes a weakly non-linear acoustic wave. We describe here some characteristics of the evolution of meteor and explosion shock waves.

In the meteor scenario, the strongly non-linear shock wave propagates cylindrically away from the trajectory. The distance travelled by the wave is usually represented by a variable  $x = r/R_0$ , equal to the radial distance scaled to the shock radius  $R_0$  (Eq. 3.3). The evolution of strong ballistic shock waves in the near-field of the Mach cone can be solved numerically. One of the earliest result is due to Plooster [1970], who solved the 1D Lagrangian equations of motion away from a line source where energy is released. More recently, Henneton et al. [2015] and Nemeč et al. [2017] use computational fluid dynamics simulations solving the Euler equations for a compressible, inviscid flow. Fig. 3.2 represent typical results for the spatial pressure field in the vicinity of the source obtained by Henneton et al. [2015]. At distances  $x \ll 1$ , the sharp discontinuity of the pressure field is visible, followed by a region of constant pressure in space. This wavefield is analogous to the self-similar pressure field of an explosive blast developed independently by Sedov [Sedov, 1946], Taylor [Taylor, 1997] and von Neumann [Bethe et al., 1947]. At  $x \gtrsim 1$ , or similarly for  $\Delta P/P_0 \lesssim 1$ , the pressure field decays into a sharp discontinuity, followed by a region of negative pressure.

After propagating a distance of about  $10R_0$ , the shock wave overpressure is sufficiently low compared to  $P_0$  and becomes a weakly non-linear *N-wave*. This type of wave is well known in aeronautics and is typical of the sonic boom heard after supersonic aircrafts. The term was coined by DuMond et al. [1946] due to the typical shape of the pressure time series. He showed that the evolution of a N-wave depends on two competing effects. On one hand, strong over- and under-pressure pulses have different propagation velocity: the high-pressure regions propagate faster than the speed of sound of the air at rest, while low-pressure regions propagate slower. Due to this effect, the peaks at the head and tail of the N-wave have increasingly steeper slopes, eventually becoming quasi-vertical discontinuities. Another effect is that the width, and therefore the period of the wave increases with time, while the pressure gradient in the middle decreases. On the other hand, viscosity

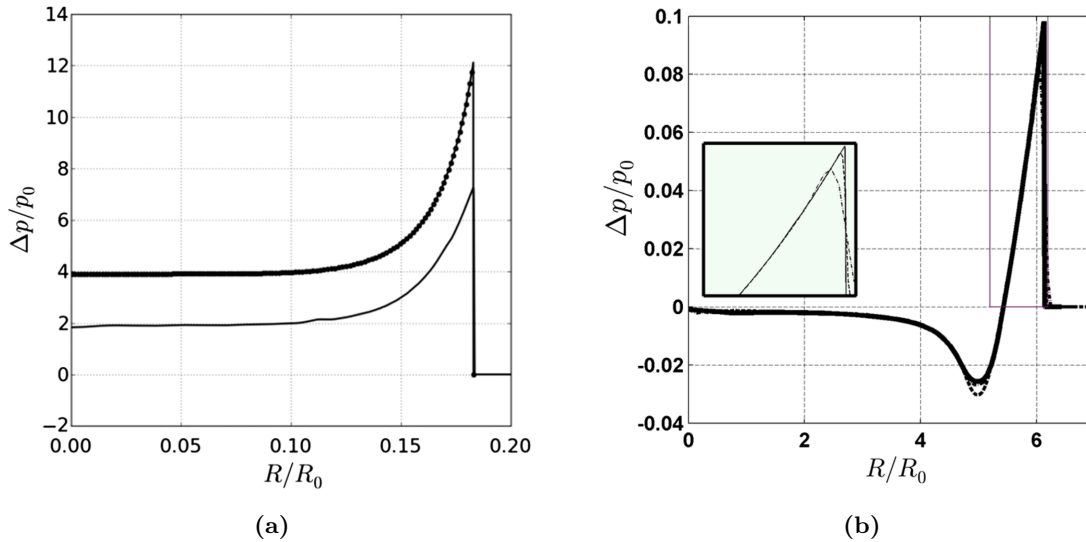


**Figure 3.2:** Near field decay of the pressure wavefield of a Mach cone with distance  $x = R/R_0$  from the trajectory. Here, a typical pressure field from the simulation results of [Henneton et al. \[2015\]](#) is reproduced at  $x \approx 0.1$  (a) and  $x \approx 6$  (b) away from the meteor trajectory. At  $x \approx 6$ , the wavefield starts to decay into a N-wave. This transition occurs when the overpressure  $\Delta P = P - P_0$  of the shock becomes comparable to the atmospheric pressure  $P_0$ .

and thermal conductivity act to reduce sharp discontinuities in pressure and temperature and smooth out the edges of the N-wave. Over time, the second phenomenon takes over the first, and progressively transforms the N-wave into a linear acoustic oscillation. This stage is represented schematically on Fig. 3.3.

What is important for the study of such infrasound sources is the frequency content of the wave when it passes into the linear regime. [ReVelle \[1976\]](#) found that, at a distance  $x = 10$  from the cylindrical source, the period of the ballistic shock wave could be approximated by:

$$\tau_0 = \frac{2.81 R_0}{c_s}. \quad (3.4)$$

Hence, meteoroids larger than 20 cm and with speeds close to  $10 \text{ km}\cdot\text{s}^{-1}$  produce signals with frequency below 20 Hz, which justifies their being referred to as infrasound. [DuMond et al. \[1946\]](#) showed that the weakly-nonlinear propagation of N-wave signals leads to an increase in its period as the fourth-root of the propagation distance. In this weakly non linear regime, a relation for meteor infrasound period  $\tau$  was obtained by [ReVelle \[1976\]](#):

$$\tau = 0.562 \tau_0 x^{1/4} \quad \text{for } x \geq 10. \quad (3.5)$$

The evolution of shocks from meteorite impacts or airburst is less well known, but can once again be assumed to be analogous to that of a surface explosion. Models for the pressure source of explosive blast waves have been developed for conventional and nuclear explosives. Similarly to ballistic shock cones, detonations have a strongly non-linear pressure signature in the vicinity of the source. A detonation pulse is typically characterised by a quasi-instantaneous pressure increase, followed by an exponential decay with a possible negative pulse [[Kinney & Graham, 1985](#)]. [Garces \[2019\]](#) proposed a review of simple existing models for these types of sources, example of which are shown on Fig. 3.4. Note the close resemblance of these pulses to the decayed meteor shock wave at  $x \approx 6$  in Fig. 3.2.

Distances and pressure away from an explosion are traditionally scaled to the explosive yield  $W$  in kg of TNT to the power  $1/3$ , with a additional factor for the geometry of the

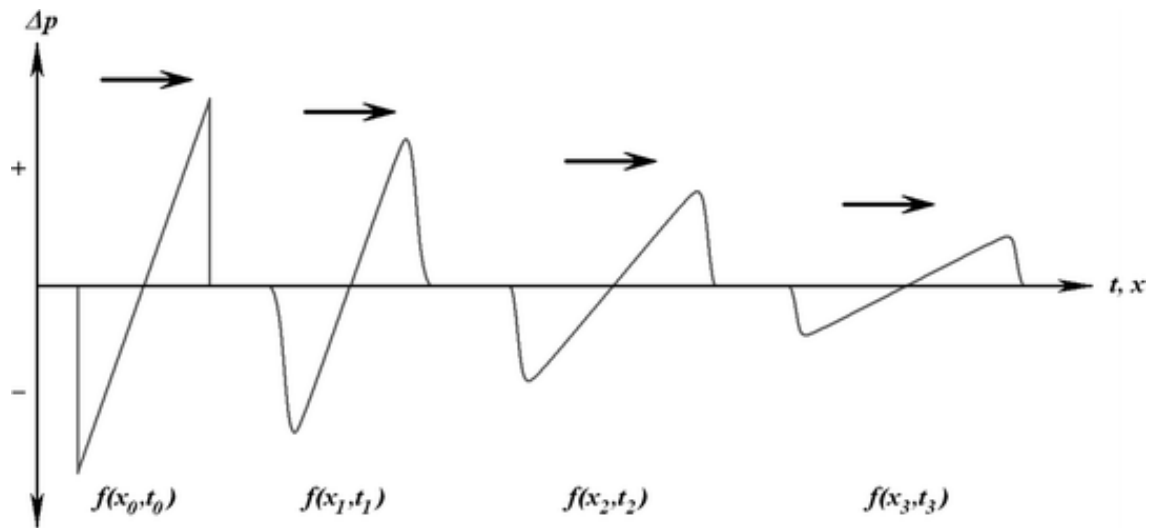


**Figure 3.3:** Evolution of a weakly non-linear N-wave under the effect of atmospheric attenuation processes. The duration and fundamental period of the wave increase as its amplitude decrease, and sharp discontinuities are progressively smoothed out. Reproduced from [Edwards \[2009\]](#).

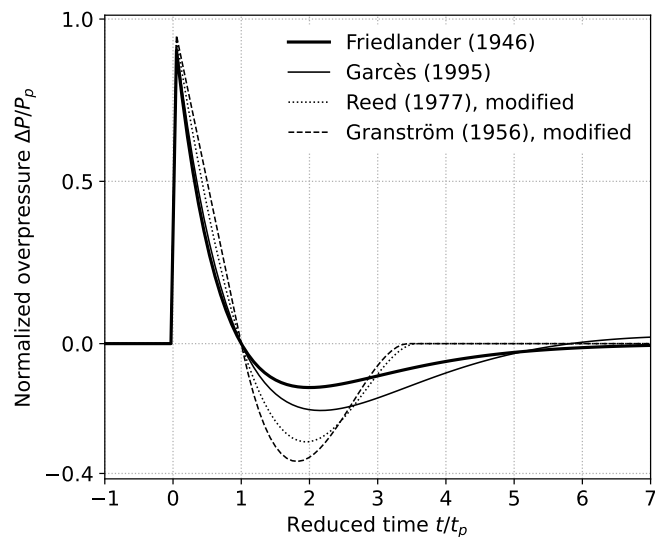


**Figure 3.4:** Different models for the blast wave associated to the detonation of a high explosive, following the review of [Garcès \[2019\]](#). The pulses are adapted from [Friedlander & Taylor \[1997\]](#), [Garcès \[1995\]](#), [Reed \[1977\]](#) and [Granström \[1956\]](#), and represent the blast wave as it reaches the weakly non-linear regime ("*far-field*"). Pressure and time are normalised to the typical duration  $t_p$  and amplitude  $P_p$  of the positive pulse tabulated by [Kinney & Graham \[1985\]](#).

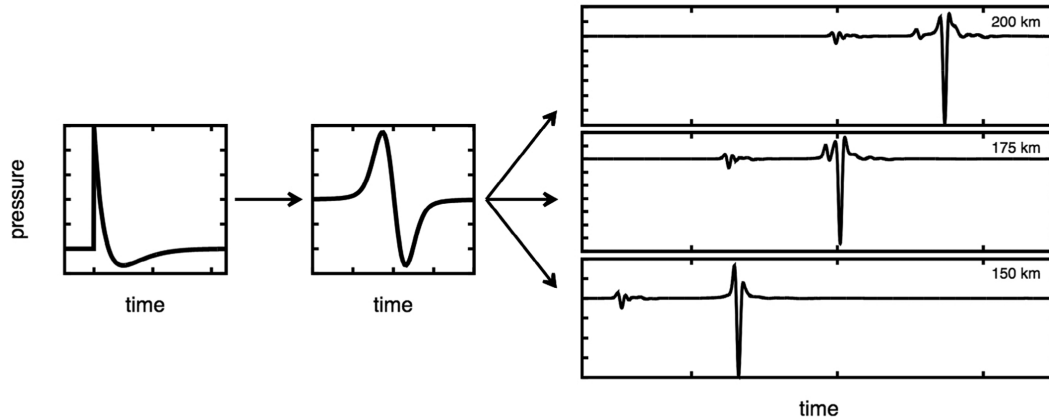


**Figure 3.5:** Schematic representation of the evolution of an explosion blast wave with distance, reproduced from Blom et al. [2018]. The blast initially evolves as a non-linear shock-wave (left), then decays into a linear acoustic wave (middle), before being subject to dispersive effects as it propagates and refracts in the Earth atmosphere (right).

explosion (1 kg of TNT being equivalent to  $4.184 \times 10^6$  J). Kim & Rodgers [2016] and Kim & Rodgers [2017] have shown that the blast wave can be considered linear acoustic starting at a distance of  $20 \text{ m} \cdot \text{kg}^{-1/3}$  from the source. For a 1 kiloton source, this would correspond to a distance of 2 km. Around  $100 \text{ m} \cdot \text{kg}^{-1/3}$ , the decayed blast wave resembles the N-wave of a sonic boom [Kim & Rodgers, 2016]. However, atmospheric refraction effects already affect the wave amplitude over  $100 \text{ m} \cdot \text{kg}^{-1/3}$ .

The evolution of the blast wave from the non-linear regime, to the linear regime and down to regional distances is illustrated on Fig. 3.5. Again, the transition from the blast wave to an acoustic wave affects its period. For a high explosive (HE) blast wave, the yield can be expressed as a function of the pulse dominant period in the far-field,  $T_0$  [Garces, 2019]:

$$\frac{W}{1 \text{ kg HE}} = \left( \frac{T_0}{0.0416} \right)^{3.34}. \quad (3.6)$$

It is still unknown today whether such relationships and blast pulse models can be applied to the meteorite impact case. However, impact and explosions are similar in the way that both the kinetic energy of the impactor and the chemical yield of the explosive are released within a very small volume, which is the reason why they can be considered as "point sources" for scaling purposes [Holsapple, 1993]. If we replace yield by kinetic energy in Eq. 3.6, we get:

$$\frac{T_0}{0.0416} = \left( \frac{E_i}{4.184 \times 10^6 \text{ J}} \right)^{0.3} \quad (3.7)$$

Taking an impact energy of  $1 \times 10^8$  J, similar to the ones estimated for small martian impacts [Garcia et al., 2022], the expected dominant blast period in the far-field would thus be  $T_0 \approx 0.1$  s, or a frequency of  $f_0 = 10$  Hz.

### Propagation of acoustic waves

As strong shocks are attenuated and their period increased, they eventually become linear infrasound. Still, even a strictly linear infrasound wave is subject to distortion as it travels through the atmosphere. This corresponds to the rightmost phenomenon illustrated on Fig. 3.5: atmospheric propagation effects, such as refractions in the upper atmosphere,



scattering of the wave against atmospheric heterogeneities, and combination of multiple ray paths, generate several additional arrivals in signals recorded by pressure sensors at long distance from the source. Therefore, the evolution of the waveform from the weakly non-linear regime to the linear regime, where its period becomes constant, is a difficult problem. An estimation of meteor acoustic signals at regional distances is best performed using numerical methods. In the present chapter, we will see that in certain cases, the propagation of an acoustic wave in a refracting atmosphere can be successfully described by an analytical model.

### 3.1.2 Phenomenology of air-to-ground coupling

Upon reaching the solid ground, a shock wave or attenuated infrasound can be viewed as an incoming acoustic P wave or as a force field on the surface: this is the problem of air-to-ground coupling. We will detail in this section the different ways in which an incident pressure perturbation transmits to a solid medium.

Seismo-acoustic coupling phenomena are most of the time ignored by both acousticians and seismologists: the former like to consider the surface of the Earth as ideally rigid and undeformable, while the later view it as a free-surface where normal and tangential stresses vanish. In reality, ground motion during significant seismic events can trigger acoustic waves [Afraimovich et al., 2001; Artru et al., 2004]. We have seen in section 1.3.1 that seismic recording of meteors and airburst on Earth are also common, and the focus of this section is the problem of transmission of acoustic waves to the ground.

In the case of meteors, Edwards et al. [2008] lists three main coupling processes:

- The direct coupling of the shock wave with the surface: a seismometer then records the overpressure in the form of a N-wave in displacement and a W-pulse in velocity. This type of observations have been illustrated in section 1.3.1.
- An air-coupled Rayleigh wave, usually preceding or following the direct air wave. This Rayleigh wave can be quasi-monochromatic in frequency [Press & Ewing, 1951; Ewing, 1957] or dispersive as during Chelyabinsk (section 1.3.1) [Tauzin et al., 2013].
- A rare precursory arrival, which is a special case of Rayleigh wave generation observed notably for near-surface explosions. These waves can be produced close to the source in the presence of an elastic layer with fast wave velocities at the surface. They propagate faster than the speed of sound, and are therefore recorded before the coupled shock wave [Anglin & Haddon, 1987].

In the more general case, the problem of air-to-ground coupling is analogous to the problem of the transmission of an incident pressure wave from a fluid halfspace to a solid halfspace. Depending on the distance of the source to the point of ground contact, the nature of the incident wavefield differs. We detail below different cases of coupling in complement to the list of Edwards et al. [2008].

**Close to the source: a spherical wavefield** At close distances from an atmospheric source, which can be elevated for an airburst or shock wave, or on the ground for an impact, the wavefront cannot be approximated by a plane wave. For a given dominant frequency of the signal, this is typically the case when the receiver is located  $\approx 0$  to 10 units of wavelengths away from the source. The wavefront, usually spherical or cylindrical, intersects the surface with a range of angles of incidence  $i$ . This is a special case of Lamb's

problem [Lamb, 1997], where an impulsive force is imposed on the surface of an elastic solid. The resolution of the reflection and transmission problem requires relatively involved analytical technique, such as the Cagniard-deHoop method and integrations around poles in the complex plane [Aki & Richards, 2002]. Today, a numerical resolution using finite difference or spectral element methods is favoured [Komatitsch & Vilotte, 1998; Martire et al., 2022]. For very large source exciting fundamental modes of vibration, normal mode theory can also be used [Karakostas et al., 2018]. Overall, the incident wavefront will result in the generation of P- and S- waves, Rayleigh waves, and some more peculiar waves such as a conical "head wave" (also named "lateral wave" or "von Schmidt" wave) joining the P- and the S- wavefront [Schröder & Scott, 2001]. This case is represented on part (a) and (b) of Fig. 3.6.

**At intermediate distances: an incident plane wavefield** At distances large enough so that most of the wavefield can be approximated by a plane wave, the types of waves that are transmitted to the ground are highly dependent on the incidence of the wavefield and on the velocities of the subsurface. According to Snell-Descartes law, the existence and incidence of a transmitted wavefield are related to the velocity ratio between the atmosphere and the first subsurface layer. We have:

$$\frac{\sin i}{c_s} = \frac{\sin i_p}{v_p} = \frac{\sin i_s}{v_s} \quad (3.8)$$

For P-wave, a transmitted wave exists if  $i < \arcsin(c_s/v_p)$ . For S-wave, if  $i < \arcsin(c_s/v_s)$ . Martire et al. [2020] named this case the *wave-wave* mode. When  $i > \arcsin(c_s/v_s)$ , the incident pressure wave is called *post-critical*. P- and S- waves can no longer be transmitted, however, different types of evanescent waves can still exist in the subsurface [Woods et al., 2015]. Among them are Rayleigh waves, which are a combination of evanescent P- and SV- waves. In a homogeneous elastic media, the speed  $v_R$ , and therefore the transmission angle of Rayleigh waves are fixed, with  $v_R < v_s$ . In a layered elastic media, Rayleigh waves are dispersive and possess a phase velocity  $v_R(\omega)$ , their critical angle is therefore

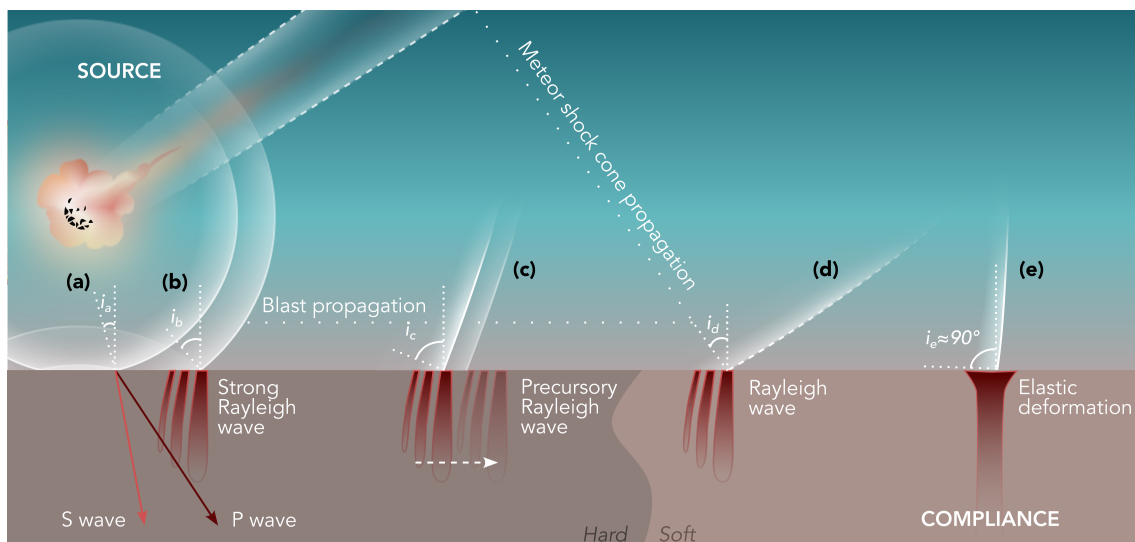


**Figure 3.6:** Schematic representation of various types of air-to-ground coupled motion. The infrasound coming from the meteor shock cone are represented with dashed white lines, while the airburst (or possibly the impact blast wave) is represented with plane white lines. The incidence angles for cases (a), (b), (c), (d) and (e) are also shown. Associated seismic waves and ground motion is represented are listed on the bottom part of the figure.

$i_R = \arcsin(c_s / \min[v_R(\omega)])$ . Cases of Rayleigh wave generation by plane wavefield are represented on case (d) of Fig. 3.6. When the incidence of the plane acoustic wave is low, it can trigger Rayleigh wave even in surfaces whose velocity is much larger than the speed of sound. This may happen at intermediate distances from the source. The geometric expansion of the wave then brings the apparent velocity of the infrasound closer to  $c_s$  and lower than  $v_R$ : this is the precursory Rayleigh wave case, illustrated in case (c) of Fig. 3.6. Other types of post-critical waves, which we will not describe further here, are detailed in the literature [Dunkin & Corbin, 1970; Schröder & Scott, 2001; Langston, 2004].

**At large distances: a pressure forcing** At large distance from the source, most low incidence rays are refracted upwards and escape in the stratosphere [Edwards et al., 2008]. This effect is even more pronounced on Mars compared to the Earth, due to the absence of a stratospheric or thermospheric channel [Lognonné et al., 2016]. Only rays with high incidence angle (i.e., close to horizontal) manage to propagate close to the surface, possibly trapped within a low-altitude atmospheric waveguide. The wavefront can therefore be considered plane, with wavenumber  $\mathbf{k} = k_x \mathbf{e}_x$  and  $\mathbf{e}_x$  parallel to the surface. The apparent horizontal velocity of the wave is the phase velocity of the acoustic wave,  $c_s(\omega)$ . Seismic waves can therefore be transmitted only if the critical angle of P-, S- and Rayleigh waves is higher than  $90^\circ$ . This requires  $v_R$ ,  $v_p$  or  $v_s$  to be inferior to  $c_s$ , which is characteristic of a very unconsolidated surface layer and relatively common for soils [Edwards et al., 2008].

However, if the velocity of shear and Rayleigh wave in the subsurface is higher than the velocity of the horizontally propagating acoustic wave, no seismic wave is generated. Instead, the ground reacts to the pressure perturbation carried by the wave in an elastic way, equilibrating vertical stress above and below the surface. In that case, horizontal displacement suffers from a  $90^\circ$  phase shift compared to the pressure pulse [Stein & Wysession, 1991]. This is also the case when the pressure perturbation is not carried by an acoustic wave, but for example by wind, at slower speed. This scenario was studied by Sorrells et al. [1971], who showed that ground displacements recorded by seismometers in a noisy atmosphere could be explained by the *compliance* of the ground to the slowly propagating pressure perturbations. Sorrells [1971] and Sorrells & Goforth [1973] developed a quasi-static theory to relate the amplitude of pressure perturbations to the amplitude of ground motion in a homogeneous elastic media, neglecting second order inertial terms in the equilibration of stress. An exact solution for a layered subsurface can be derived using a propagator matrix method, as presented in Aki & Richards [2002] (Chapters 5 and 7). This analytical method has been used in various works on the Earth oceans and atmosphere, and on Mars [Crawford et al., 1991; Tanimoto & Wang, 2019; Kenda et al., 2020]. It is further applied in the present study and detailed in Appendix A1.

With this phenomenological and theoretical introduction now complete, we move on to the description of seismo-acoustic signals detected by InSight and their modelling.

### 3.1.3 Martian chirp signals

In Chapter 2, we presented a numerical model of the impact cratering seismic source and compared the results of our model to parameters of Martian impact seismic events recorded by SEIS. As mentioned in the introduction of this work, some of these events could be identified as impacts due to the presence of peculiar short low-frequency arrivals, several minutes after the main VF arrival. These signals will constitute the core of the current chapter. We will show that an analytical model of these signals can be proposed,

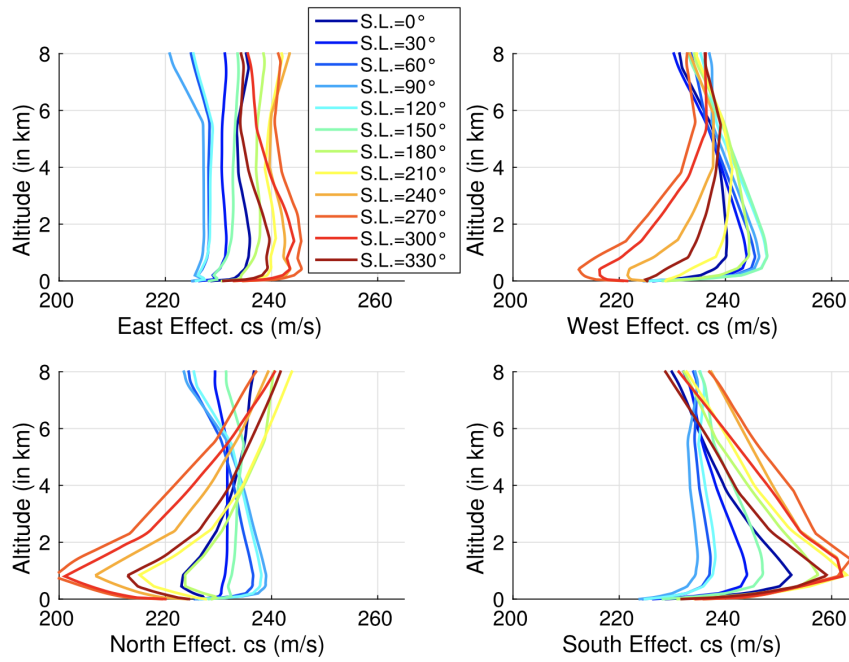


**Figure 3.7:** Average effective sound-speed profile from 0 km to 10 km altitude on Mars in four different propagation directions. Different colours represent different seasons measured by the solar longitude ( $L_s$ , or S.L.), with  $90^\circ$  being the northern summer solstice and  $270^\circ$  the northern winter solstice. Reproduced from Garcia et al. [2017]

and that this model can be used to infer the properties of the Martian atmosphere and subsurface

Events S0533a, S0793a, S0981c, S0986c, S1034a and S1160a, presented in Fig. 1.14 of the introduction, are six VF events detected by the SEIS instrument on Mars. In distinction to other VF events recorded during the InSight mission, their main seismic arrivals (marked as Pg and Sg on Fig. 1.14) are followed by one or multiple late low-frequency wave trains. Some of these arrivals show a normal dispersion, which means that their low frequency content arrives before their high-frequency content.

Such dispersed signals, here referred to as "*Chirps*", have also been recorded on Earth by pressure and seismic sensors. Herrin et al. [2006] report the detection of eight normally dispersed infrasound signals offshore from the Republic of Korea in 2005. They explain such dispersion by the existence of an ephemeral low velocity waveguide in the Earth's atmosphere, which might have been caused by a channel of warm air over the ocean surface. Later, Negraru & Herrin [2009] reported similar observations following test surface explosions in Texas and New Mexico. Meteorological sensors present in the area of these tests show a clear inversion of temperature above the surface, responsible again for a low altitude waveguide. The authors modelled the refraction and reflexion of acoustic waves in a simplified, 1-layer model of the atmospheric waveguide and showed that the observed dispersion could be reproduced. More recently, Xu et al. [2022] observed dispersion in the seismo-acoustic signals recorded during the Baumgarten explosion at an Austrian gas facility in 2017 Schneider et al. [2018].

Garcia et al. [2017] shows that a similar waveguide may exist on Mars at nighttime, when the radiative cooling of the Martian surface generates a positive gradient of temperature with altitude. In particular, in the summer of the northern hemisphere (solar longitude of approximately  $L_s \approx 90^\circ$ ), this positive gradient exists in the first kilometre above the

surface. Consequently, the speed of sound also increases with altitude, causing a refraction of acoustic waves towards the ground. The presence of strong surface winds during certain seasons can amplify this effect in certain azimuths. Indeed, an acoustic wave travels at the effective speed of a media, given by:

$$c_{s,eff} = c_{s,T} + \mathbf{w} \cdot \frac{\mathbf{k}}{\|\mathbf{k}\|}, \quad (3.9)$$

with  $\mathbf{w}$  the wind vector and  $c_{s,T}$  the *static* or *thermodynamic* sound speed computed from temperature and density. : This wind effect is strongest towards the south-east during northern winter, and towards the south-west during northern summer on Mars [Garcia et al., 2017]. The associated effective sound speed profiles are shown on Fig. 3.7. The authors simulate the propagation of Martian infrasound in such waveguide and show that they are subject to a reduced geometrical attenuation. A later study by Martire et al. [2020] shows that some of the signals recorded by SEIS can be explained by the air-to-ground coupling of guided infrasound. However, the study is not able to associate these signals to a known source.

Nevertheless, both work strongly support the possibility of recording guided infrasound on Mars. Fig. 3.8 shows each individual chirps and low-frequency signals recorded after the aforementioned VF events. The strong similarity of SEIS chirps with signals reported by Negraru & Herrin [2009] and Herrin et al. [2006] and synthetic waveforms modelled by Martire et al. [2020], which are all generated by a low-altitude source, prompted their interpretation as impact-generated guided infrasounds by Garcia et al. [2022]. The high signal-to-noise ratio of these arrivals makes the analysis of their polarisation possible and provides a back-azimuth. Furthermore, the analysis of time delays between seismic and acoustic arrivals allows to estimate a distance and origin time. As mentioned in the introduction, orbital imagery of the proposed location revealed the presence of fresh craters, whose formation time was in agreement with SEIS records. Thus, the combination of imaging and seismic analysis allowed to confirm the impact nature of four of these VF events. Two additional craters were identified by a subsequent imaging campaign, which bring the number of confirmed infrasound-producing impact events to six for the entire InSight mission [Daubar et al., 2023]. The date, location and arrival times of these events are reported in Table 3.1.

The analysis of Garcia et al. [2022] sheds some light on the source of the recorded infrasound arrivals. One of the most interesting events among those of Fig. 1.14 and Table 3.1 is S0986c. This events presents a succession of three low-frequency arrivals (C1, C2 and C3), of which only the later two are dispersed. The absence of dispersion in the fist one means that the source of the infrasound signals was outside of the Martian waveguide, i.e. at high altitude. Moreover, the time serie of the C1 arrival in Fig. 3.8 shows a characteristic impulsive W-shape in velocity, consistent with the ground coupling of a shock N-wave (see sec. 3.1.2). Therefore, Garcia et al. [2022] interpret it as the signature of the shock cone of a meteor falling near InSight. The crater associated to S096c is clustered, which means that its meteor experienced a disruption. Such energetic event, if occurring at low altitude, could explain the second signal (C2), more complex and dispersed. The last and strongest signals, C3 for S0986c, can be chronologically attributed to the impact itself. In the case of S0986c, such chronology of events is in agreement with the azimuth measured for each signal and with the inferred trajectory of the meteor [Garcia et al., 2022]. Among the events listed in Table 3.1, those presenting a single crater also show a single chirp, which further supports that the impact is the main infrasound-generating event. Note that another non-dispersed, W-shaped arrival, shown on Fig. 3.8 (C2), has been identified for event S0793a and can be associated either to the shock cone or disruption of its meteor outside above the waveguide (Raphaël Garcia, personal communication).



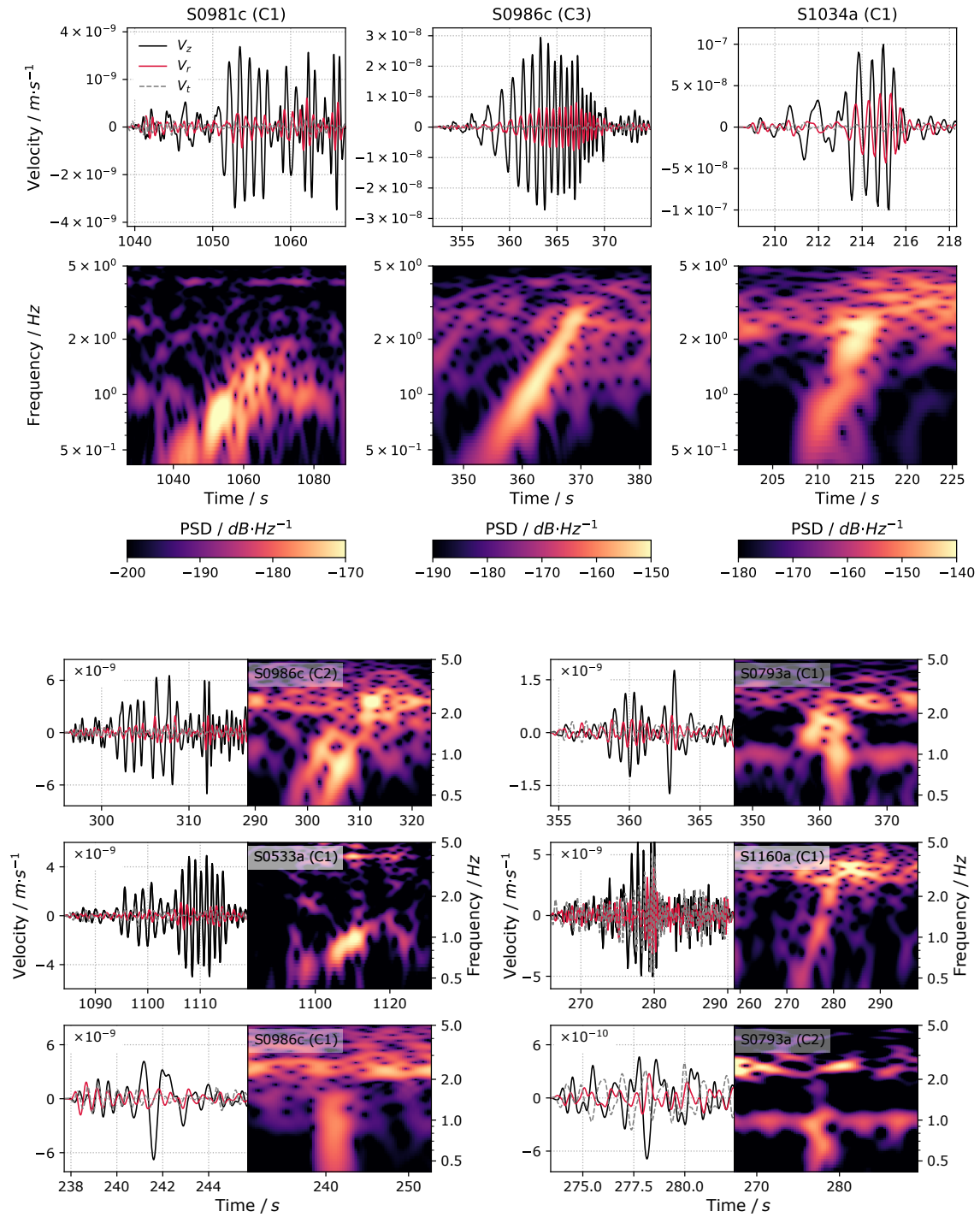


**Figure 3.8:** Individual time series and spectrograms of recorded seismo-acoustic signals showing vertical velocity. Time series have been filtered in the  $[0.5, 2]$  Hz range, except for S0533a (C1) in the  $[0.5, 1]$  Hz range. Signals with good signal to noise ratio and clear dispersion, S0981c, S0986c (C3) and S1034a, are shown on the top. S0986c (C2) and S0793a (C1) are more complex signals, while S0533a and S1160a have a poor signal to noise ratio. Finally, S0986c (C1) and the possible S0793a (C2) signals do not show any dispersion, and instead display the typical W-shaped pulse of coupled sonic booms.

**Table 3.1:** Location, date and parameters of each impact event of the InSight mission associated to a chirp signal. Distances were computed with a Martian flattening factor of 0.00589 and an equatorial radius of 3396.2 km, using the reference InSight coordinates [Golombek et al., 2020].

Event name	S0533a	S0793a	S0981c	S0986c	S1034a	S1160a
<b>Seismic data</b>						
UTC date	2020-05-27	2021-02-18	2021-08-31	2021-09-05	2021-10-23	2022-03-02
UTC start time	13:48:26	19:36:23	04:04:01	05:23:58	18:26:43	06:56:40
UTC origin time	13:46:52	19:36:06	04:03:13	05:23:44	18:26:30	06:56:26
UTC Pg- time	13:48:13	19:36:28	04:04:03	05:24:00	18:26:43	06:56:42
UTC Sg- time	13:49:12	19:37:01	04:04:41	05:24:13	18:26:52	06:56:52
UTC Chirp(s)	C1	14:05:06	19:42:03	04:20:27	05:27:44	18:29:58
time	C2	-	19:40:43	-	05:28:40	-
	C3	-	-	-	05:29:31	-
<b>Orbital observations</b>						
Latitude [°N]	9.382	4.606	0.397	3.974	3.866	5.099
Longitude [°E]	135.377	134.087	135.689	136.963	135.107	134.807
Distance [km]	286.3	91.0	240.5	85.0	48.2	59.6
Back-azimuth [°]	357.1	273.9	179.1	111.3	219.3	306.0
Crater type	cluster	single	single	cluster	single	cluster
Effective crater diameter [m]	11.9	3.9	7.24	6.1	9.2	3.2

Following [Negraru & Herrin \[2009\]](#), we know that the dispersion of Martian chirps depends on the nature of the atmospheric waveguide. The dispersion analyzed by the authors can be well explained by the effective atmospheric sound speed profiles measured in the proximity of the source and receivers. However, in the case of InSight, dispersed infrasound were not recorded by pressure sensors, which do not have a sufficient sensitivity in this frequency range, but rather by a seismometer. Consequently, air-to-ground coupling has affected the recorded seismo-acoustic waves. This means that InSight chirp signals contain information on both the local atmospheric structure and the subsurface structure near InSight.

On Mars, measurements of atmospheric sound speed are sparse. Consequently, the recording of dispersed infrasound could provide precious informations for the validation of Mars climate models, such as the Mars Climate Database (MCD) [[Millour et al., 2015, 2018](#)]. Additionally, several authors have proved that seismo-acoustic signals could be used to invert subsurface seismic properties, with ocean bottom seismometers (e.g., [Crawford et al. \[1991\]](#)) or with near-surface seismometers (e.g., [Tanimoto & Wang \[2019\]](#)). On Mars, seismic signals generated by pressure vortices around the lander have been used to infer the near-surface structure below InSight [[Kenda et al., 2020](#); [Lognonné et al., 2020](#)]. The seismic recording of meteor infrasound provides a new opportunity to investigate InSight's subsurface, with a completely different source type.

To further analyse these impact-generated seismo-acoustic signals, and improve our knowledge of the Martian atmospheric and subsurface structure, a model of the infrasound dispersion and ground coupling is needed. We present in the following sections the development of such model by [Xu et al. \[2022\]](#), and the inversion of effective sound speed profiles and shear wave velocity structure below InSight from three meteorite chirp signals.



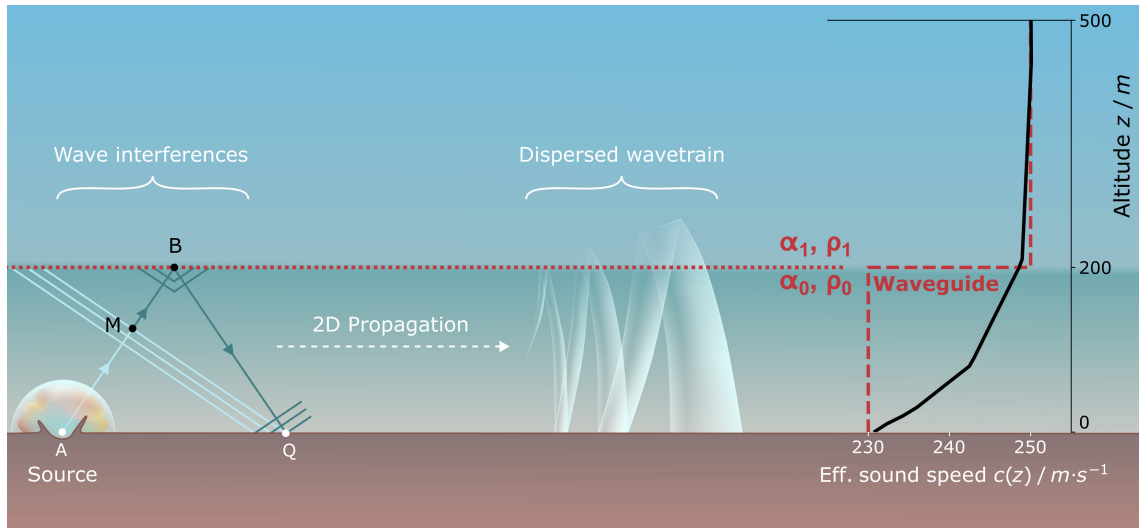


**Figure 3.9:** Schematic representation of the Martian atmospheric waveguide and the dispersion phenomenon. The effective sound speed profile predicted at InSight location during event S0986c by the Mars Climate Database is represented in black on the right, and a simplified, 2-layer model of the waveguide is represented in red. Interferences between incident and reflected plane waves in the waveguide are represented on the right. The resulting normally dispersed wavefield (long periods arriving before the short) is depicted in the middle.

## 3.2 Seismo-acoustic model of a guided meteorite infrasound

### 3.2.1 Modelling of dispersed infrasound

As shown by [Negraru & Herrin \[2009\]](#), infrasound dispersion occurs when acoustic waves are refracted downward in a layered atmosphere. The process is illustrated, with a simple two-layer model on Fig. 3.9. This two-layer model is a simplified version of the effective sound-speed profile predicted by MCD at InSight location, during event S0986c. Over 200 m,  $c_z$  increases from 230 to 250  $\text{m}\cdot\text{s}^{-1}$ , thus direct waves coming from the source interfere with waves reflected at the top of the waveguide. Only waves with adequate frequencies survive and become trapped in the waveguide. As a result, *modes* of propagation appear, whose phase velocity depends on frequency. The result is a horizontally propagating dispersed waveform (Fig 3.9, middle), defined by the horizontal wave number  $k$  such that:

$$\mathbf{k} = k \mathbf{e}_x \quad \text{and} \quad k = \frac{\omega}{c(\omega)}, \quad (3.10)$$

with  $\omega$  the pulsation of the wave in a mode and  $c(\omega)$  its variable phase velocity.

For a 1D propagation in a 1-layer waveguide with height  $H$ , such as on Fig. 3.9, the dispersion relation relating  $k$  and  $\omega$  has an analytical expression, given by [Negraru & Herrin \[2009\]](#). In their study, the ground surface is considered as an ideally rigid surface. With the notations of Fig. 3.9,  $k$  and  $\omega$  are related by:

$$kH \sqrt{\frac{c^2}{\alpha_0^2} - 1} - \tan^{-1} \left[ \frac{\rho_1}{\rho_0} \sqrt{\frac{\frac{\alpha_0^2}{c^2} - \alpha_1^2}{1 - \frac{\alpha_0^2}{c^2}}} \right] = n\pi. \quad (3.11)$$

$n \in \mathbb{N}$  identifies different modes of dispersion. For a fixed value of  $\omega$ , this equation only has a discrete number of solutions for the phase velocity  $c$ , which depend on  $n$ . The fundamental mode is solution to Eq. 3.11 for  $n = 0$ , with  $c \in [\alpha_0, \alpha_1]$ .

Relationship 3.11 is analogous to the dispersion relationship of Love waves in seismology [Aki & Richards, 2002]. Just like Love waves, acoustic waves propagate in a layered media, requiring the continuity of one stress component at each layer boundary: the pressure  $P$  for acoustic waves and the shear stress  $\sigma_{yz}$  for Love waves. Due to these similarity, as in section 1.3.1 and Appendix A1, the propagator matrix method developed to compute the dispersion relation of Love waves can be applied to dispersed infrasound [Aki & Richards, 2002]. This method was adapted for martian chirps by Xu et al. [2022] and is described in details in Appendix A2.

For a certain value of  $\omega$ , and mode number  $n$ , the wave number  $k_n(\omega)$  and its characteristic phase velocity  $c_n(\omega)$  are obtained with the propagator matrix method. The plane wave propagating within the waveguide is composed of a mixture of these modes, and the total pressure perturbation is a sum of *pressure eigenfunctions*:

$$p(k, z, \omega) = \sum_{n=0}^{n_{max}} p_n(k_n, z, \omega). \quad (3.12)$$

The amplitude of each pressure eigenfunction determines which modes is dominant in the waveguide. Due to the source-receiver reciprocity [Aki & Richards, 2002], the altitude at which the pressure eigenfunction reaches its maximum is also the altitude at which a source is the most efficient at exciting the waveguide.

Following Xu et al. [2022], the infrasound wave recorded at a distance  $x$  from the source can be expressed as:

$$P(x, \omega) = S(\omega) \frac{e^{-i\pi/4}}{\sqrt{\frac{\pi}{2} kx}} \frac{P^2(\omega, 0)}{\int P^2(\omega, z) dz} e^{-a(\omega)x} e^{i(kx - \omega t)}. \quad (3.13)$$

In this expression,  $\exp[-i\pi/4]/\sqrt{kx\pi/2}$  is a geometrical attenuation factor for cylindrical waves [Landau & Lifshitz, 1987] and  $P^2(\omega, 0)/\int P^2(\omega, z) dz$  normalises the pressure eigenfunction amplitude. The exponential factor  $\exp[-a(\omega)x]$  models the effect of the Martian atmospheric attenuation on the propagating acoustic wave, which can be modelled following Bass & Chambers [2001]. Finally,  $S(\omega)$  is the source time function in the frequency domain.

Note that similar solutions to the problem of a trapped acoustic wave have been proposed in the past. For example, Waxler [2002] developed the pressure wavefield over a sum of complex vertical and horizontal eigenfunctions accounting for amplitude loss (attenuation) at the ground surface. This method does not, however, account for complex subsurface structures.

### 3.2.2 Modelling of seismic signals coupled from infrasound

In the previous section, we modelled a plane acoustic wave trapped in an atmospheric waveguide. This pressure perturbation has a variable phase velocity  $c(\omega)$  and propagates along the  $\vec{x}$  direction. Consequently, if the velocity of the surface is higher than  $c(\omega)$ , the acoustic waves couples to the ground via compliance and can be modelled according to the propagation matrix method of Appendix A1. In the frequency domain, the conversion from pressure to ground velocity is a pure amplitude effect, apart from a  $\pi/2$  phase shift

for vertical ground velocities. The compliance depends on the perturbation velocity (here  $c(\omega)$ ), the subsurface structure, and the frequency.

We write the compliance function as  $C_{v_x/p}(c(\omega), \omega)$  and  $C_{v_z/p}(c(\omega), \omega)$  in the horizontal and vertical directions of motion, respectively. After traveling to InSight location, a meteorite generated dispersed infrasound generated the following ground motions:

$$\begin{aligned} V_x(\omega) &= S(\omega) \frac{e^{-i\pi/4}}{\sqrt{\frac{\pi}{2}kx}} \frac{P^2(\omega, 0)}{\int P^2(\omega, z) dz} e^{-a(\omega)d} e^{i(kx-\omega t)} C_{v_x/p}(c(\omega), \omega), \\ V_z(\omega) &= S(\omega) \frac{e^{-i\pi/4}}{\sqrt{\frac{\pi}{2}kx}} \frac{P^2(\omega, 0)}{\int P^2(\omega, z) dz} e^{-a(\omega)d} e^{i(kx-\omega t)} C_{v_z/p}(c(\omega), \omega), \end{aligned} \quad (3.14)$$

with  $x$  the distance between InSight and the source crater. From these expressions, we can obtain the model horizontal-to-vertical amplitude ratio (H/V ratio) of the signal:

$$HV = V_x(\omega)/V_z(\omega) = \frac{C_{v_x/p}(c(\omega), \omega)}{C_{v_z/p}(c(\omega), \omega)}. \quad (3.15)$$

### 3.2.3 Characteristics of the model

The model of coupled dispersed infrasound proposed in Eq. 3.14 presents two particularities. Firstly, the phase of the waveforms is defined as:

$$\varphi(\omega) = \tan^{-1} \left( \frac{\text{Im}\{V(\omega)\}}{\text{Re}\{V(\omega)\}} \right) = \tan^{-1} \left( \frac{\text{Im}\{\mathcal{V}(\omega)\}}{\text{Re}\{\mathcal{V}(\omega)\}} \right), \quad (3.16)$$

with

$$\mathcal{V} = \frac{V(\omega)}{\|V(\omega)\|} = e^{i(kx-\omega t-\pi/4)} \frac{S(\omega)}{\|S(\omega)\|}. \quad (3.17)$$

Consequently, the phase of the signal only depends on (1) the phase of the source and (2) the properties on the dispersion relation  $k = \omega/c(\omega)$ , which, as seen in section 3.2.1, is directly related to the atmospheric structure.

Secondly, the  $HV$  ratio defined in Eq. 3.15 is only dependent on the compliance functions. We have seen that  $C_{v_x/p}$  and  $C_{v_z/p}$  both depend on the perturbation velocity, in our case the dispersed infrasound phase velocity  $c(\omega)$ , and on the subsurface structure.

The dependance of the signal phase and  $HV$  ratio on the atmospheric and subsurface structure, respectively, means that information on the Martian atmosphere and near surface could be inverted from two independent sets of data. Knowing the azimuth of the source for meteorite impact, the computation of the  $HV$  ratio is straightforward. The phase velocity cannot be measured directly from the seismo-acoustic waveforms recorded by InSight, however, we know that their *group velocity* is also dependent on the atmospheric structure. The group velocity measures the propagation velocity of a wave packet containing multiple frequencies, such as the dispersed infrasound considered here. It is defined and related to the phase velocity by:

$$v_g(\omega) = \frac{\partial \omega}{\partial k} = \frac{c(\omega)}{1 - \frac{\omega}{c(\omega)} \frac{\partial c}{\partial \omega}}. \quad (3.18)$$

It can be calculated from InSight waveforms, knowing the distance and time of origin of the signals, by:

$$v_g(f) = \frac{d}{t_f - t_0}, \quad (3.19)$$

with  $t_f$  the arrival time of a wave packet with dominant frequency  $f$  and  $t_0$  the origin time. In the case of InSight detected signals, the source distance is known, but the origin time was inferred from the travel times of P-, S- and acoustic waves. No hypothesis was made on the mean sound speed velocity, which was inverted together with  $t_0$ . Therefore, group velocity measurement do not depend on prior hypotheses on the atmospheric structure, but depend on seismic wave velocities and picks.

### 3.3 Inversion method

#### 3.3.1 Model parametrisation and sensitivity

To further study the possibility of an inversion of group velocities and  $HV$  ratios, we study different parameterisation of the atmosphere and subsurface, and investigate their effect on the phase and group velocities, and on the compliance function. We base our study on chirp C3 of event S0986c and on the subsurface model proposed in Xu et al. [2022].

**Parameterisation of the atmosphere** The MCD effective sound speed and density profiles at InSight location during event S0986c are shown in black on Fig. 3.10. These profiles are piecewise linear and have a resolution of approximately 50 m. The effective sound speed increases from 230 to 250 m·s<sup>-1</sup> up to 500 m altitude.

We first study the effect of different discretisation of the effective sound speed and density profiles on the phase and group velocity. Fig. 3.10 shows a comparison of group and phase velocities computed with 250-, 150- and 4-layer discretisations of MCD profiles. The height chosen to position the halfspace is different for each model. Model (1) and (2) are fine discretisations of the MCD profile, with a halfspace at 2500 m and 1500 m, respectively. Fig. 3.10 show that they both result in identical group velocities at high frequencies. However, properties at the top of the atmospheric profile (position and speed in the halfspace) influence phase velocities at low frequency. Indeed, MCD sound speed profiles show an inversion above 500 m altitude. Waves with large wavelengths "see" this large-scale sound speed inversion which cancels the effect of the low-altitude waveguide and prevents them from being trapped. On the other hand, high frequency waves are more sensitive to small scale variations in the atmospheric profiles and are efficiently trapped in both model (1) and model (2). With model (3), which presents a strictly monotonic increase of sound speed with altitude, all wavelengths are effectively trapped. Although this model has less resolution than models (1) and (2), it reproduces the main features of MCD profiles. Fig. 3.10 confirms that such a simple model yields group velocities in agreement with model (1) and (2) between 0.5 and 10 Hz.

To go further, we also show on Fig. 3.11 the pressure eigenfunction and integral term of Eq. 3.14,  $P^2(\omega, 0) / \int P^2(\omega, z) dz$ , obtained with each model. Although the integral term does not influence the group velocity of the dispersed signal, it plays a role in its amplitude spectra. Fig. 3.11 shows that pressure eigenfunctions are similar for each model, except at low frequency (0.5 Hz) due to the different choices of halfspace. The integral term of models (1) and (2) are similar from 1 Hz to 20 Hz. However, the lower resolution of (3) results in a more approximative computation of the integral  $\int P(\omega, z) dz$ , and a poorer agreement with model (1) and (2).

A layered representation can seem artificial for an atmospheric profile, because planetary atmosphere do not present strong discontinuities in temperature or density. However, these two studies allow to confirm that such **low-resolution approximations of MCD**

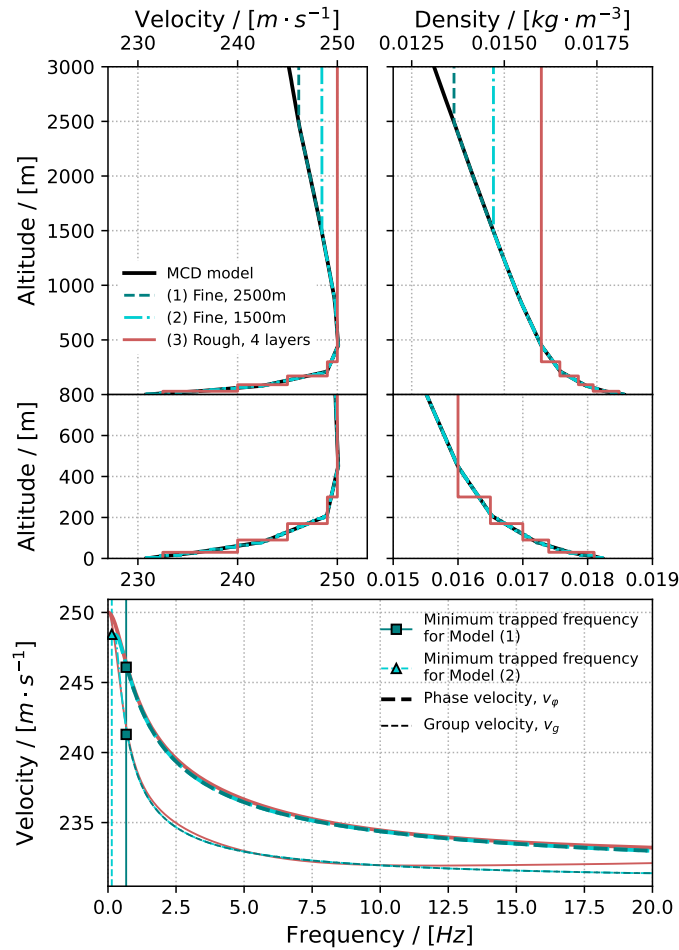


**Figure 3.10:** Sensitivity of the group velocity calculated with the propagator matrix method to the discretisation of atmospheric profiles. Top plots depict the tested atmospheric profiles, zoomed in on the middle plots. The black curves represent MCD profiles at InSight location during event S0986c. Models (1) and (2) are very fine discretisation of these profiles, with different altitudes of 1500 m and 2500 m for the waveguide’s top half space. Model (1) is a less precise representation of the waveguide, with 4 layers and a halfspace. Bottom plots represent the obtained group and phase velocity for each of the three models. The decreasing sound speed velocity above 500 m limits trapping of low frequencies in the waveguide: With a halfspace sound speed of  $c = 246 \text{ m}\cdot\text{s}^{-1}$ , model (1) only traps waves above 0.7 Hz, while model (2) traps waves above 0.1 Hz. All waves are trapped with model (3).

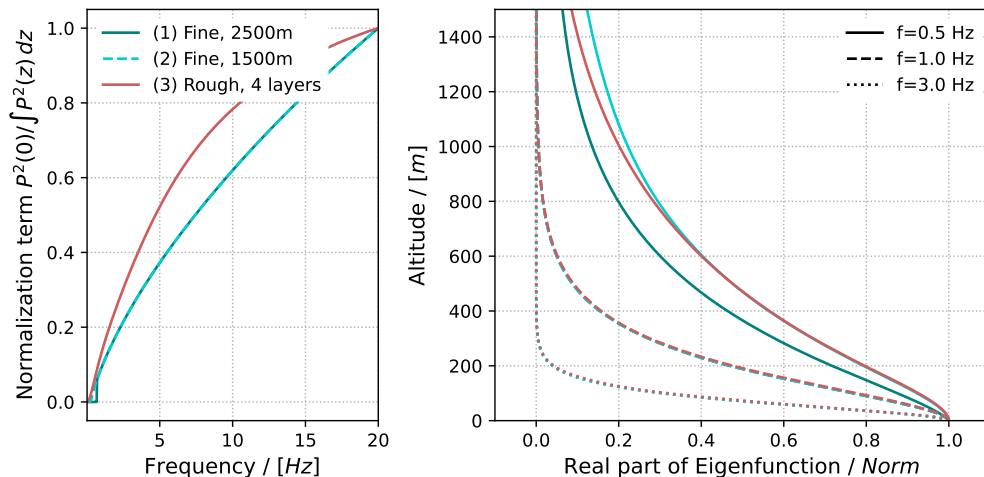


**Figure 3.11:** (Left) Normalized pressure term of Eq. 3.14,  $P^2(\omega, 0) / \int P^2(\omega, z) dz$ , and (Right) Pressure eigenfunctions at different frequencies for each discretised model of Fig. 3.10. The real part of the pressure eigenfunction is shown, normalised to its maximum value. All three eigenfunctions appear identical at high frequencies (1 and 3 Hz, but differences exist at 0.5 Hz due to the differences in halfspace sound speed between models. Despite presenting identical pressure eigenfunctions above 1 Hz model (3) displays a different normalisation term than model (1) and (2) (left), due to the higher imprecision of the integration.

**models can be sufficient to reproduce group velocities of dispersed infrasound,** with as few as four layers. Other properties, such as the signal spectrum, might require a finer resolution to be faithful to MCD’s piecewise linear characteristics.

Another important test consists in assessing the sensitivity of group velocity to different parameters of the model. We have shown in Eq. 3.11 and Box. A2 that the dispersion relation depends on the sound speed and density profiles in the atmosphere. To determine how each of these parameters influences the group velocity result, we conducted a parametric analysis on Fig. 3.12. Model (3) is chosen as a baseline, and density or sound speed are perturbed in turn at surface, medium or halfspace altitude while keeping all other parameters fixed. Results of Fig. 3.12 show that group velocity are sensitive to the surface sound speed at high frequency, and to the halfspace sound speed at low frequency. Density has considerably less influence on the group velocity than sound speed. Hence, **sound speed profiles can be inverted from group velocity measurements but not density profiles, which need to be fixed.**

Finally, we investigate the effect of the source time function ( $S(\omega)$  in Eq. 3.14) on the dispersed infrasound waveform. Although the source will not influence the group velocity, it has an effect on the amplitude and phase of the recorded signal. As explained in section 3.1.1, little is currently known on the pressure source generated by a meteorite impact. However, several hypotheses can be made. The first consists in considering the source timescale to be much smaller than the propagation and dispersion timescales. The source time function can then be modelled by a Dirac impulse,  $\delta(t)$ . On the other end, we showed in section 3.1.1 that surface explosions typically generate finite-duration pulses, which decay in the form of N-shape waveforms during their weakly non-linear propagation phase. Such signals can for example be modelled by a gaussian, or by the first derivative of a gaussian function. The dominant period of these signals is related to the explosive yield, and for S0986c, we can assume a period of 0.1 s as explained in section 3.1.1.

The amplitude and phase spectra of these three source time functions are shown on Fig. 3.13. The ideal Dirac source naturally has no effect on the phase and amplitude spectra of

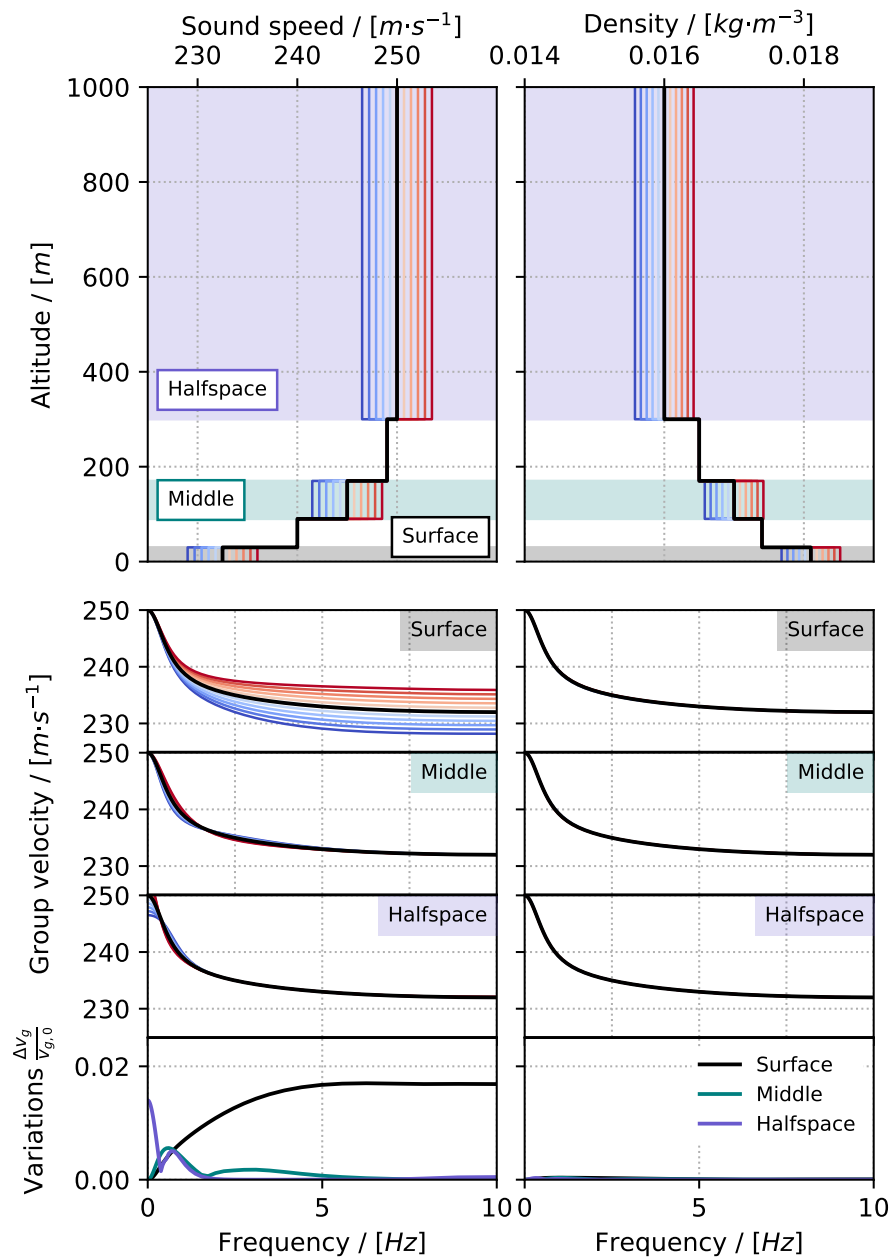


**Figure 3.12:** Sensitivity of the group velocity to changes in sound speed and density. For each group velocity curve shown in the middle plots, the value of either density or sound speed in one of the layers has been changed while all other layers remained identical to model (3) of Fig. 3.10. The bottom plot shows variations of  $v_g$  with respect to the unperturbed model, for changes made in the halfspace (blue), the middle of the profile (green), and the surface (black). At low frequency, group velocity appears sensitive to changes in the halfspace, while most high-frequency variations are related to changes at surface level. Group velocities are strongly more sensitive to variations in sound speed than in density.



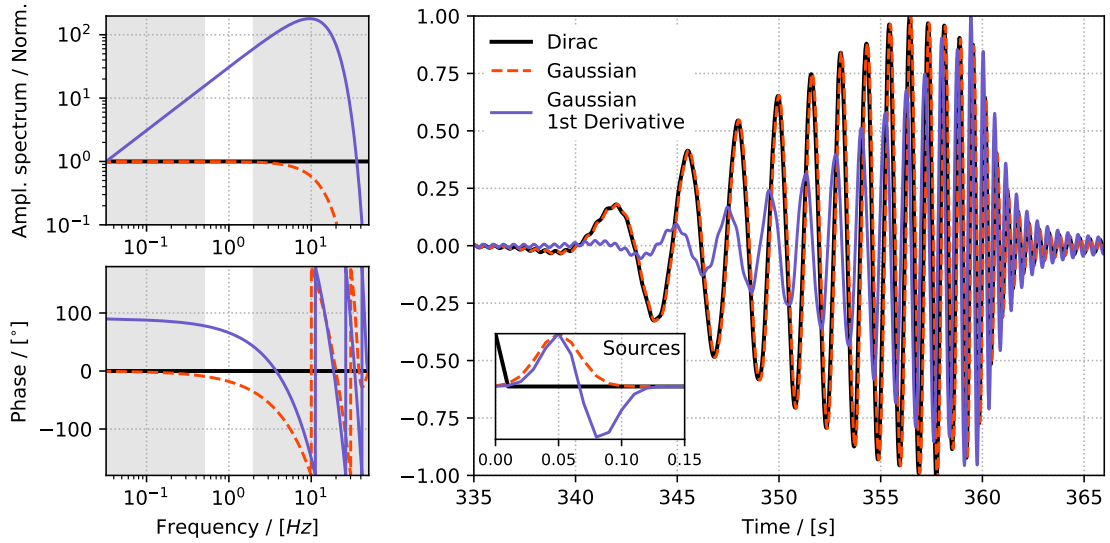


**Figure 3.13:** Sensitivity of the pressure waveform to different types of acoustic source time functions, shown as an insert on the right plot. The amplitude spectrum and phase spectrum of a Dirac source, a Gaussian source, and the first derivative of a Gaussian are shown on the left. Pressure waveforms computed with each of these sources and with model (3) of Fig. 3.10 are shown on the right, filtered between 0.5 and 2 Hz and including atmospheric attenuation. A Dirac source has no effect on the amplitude spectra or phase of a dispersed pressure wave. Between 0.5 and 2 Hz, a gaussian source with a 10 Hz corner frequency does not result in significant phase changes or amplitude effects. However, a gaussian derivative function similar to a N-wave presents a  $90^\circ$  phase shift with respect to a Dirac source, and its amplitude spectra is increasing until its corner frequency of 10 Hz, resulting in a waveform peaking around 2 Hz.

the dispersed infrasound. In the frequency range of S0986c chirps, between 0.5 and 2 Hz, a gaussian function with period of 0.1 s also has negligible effects on the pressure waveform. However, the spectrum of a N-shaped gaussian first derivative presents a significant overshoot at 10 Hz, which results in a pressure waveform peaked around the high frequency arrivals. It also presents a  $\approx 90^\circ$  phase variation at low frequencies. Both the gaussian and gaussian derivative pulses undergo changes in phase at the dominant frequency of the signal and its overtones.

Unfortunately, phase and amplitude properties of the source cannot be easily extracted from the recorded signal, except with a priori assumptions. Indeed, spectral amplitudes are driven by several other effects, such as the compliance, pressure eigenfunctions and atmospheric attenuation. Similarly, the signal phase may be affected by propagation effects that are not modelled here, such as reflection on the topography. For these reasons, inverting the phase (Eq. 3.17) of the signal or its amplitude spectrum is not possible without emitting strong hypotheses, and **an inversion of group velocities is preferred to retrieve the atmospheric structure.**

**Parameterisation of the subsurface** In a similar way as the atmosphere, we study the influence of various parameters of the subsurface on the H/V ratio of a ground-coupled infrasound. To do so, we use the 3-layer model derived by Xu et al. [2022], referred to as the ZX model. The parameters of this model are summarised in Table 3.2.

We test the sensitivity of the H/V ratio to changes in the layer thickness, the Poisson's ratio and the S-wave velocity. The results are displayed on Fig. 3.14. This parametric analysis shows that the parameters of the central layer, between 1 and 40 m depth, has

**Table 3.2:** Parameters of a 3-layers model of the subsurface below InSight derived by Xu et al. [2022] (ZX model). The Poisson’s ratio is  $\nu = 0.22$  and the density is related to P-wave velocity by Gardner’s relationship [Gardner et al., 1974].

Layer Number	$v_p$ [m · s <sup>-1</sup> ]	$v_s$ [m · s <sup>-1</sup> ]	Density [kg · m <sup>-3</sup> ]	Thickness [m]
1	117	70	1019	0.6
2	384	230	1372	40
3	3000	1700	2760	+∞

the most influence on the H/V ratio below 2 Hz. In particular, variations in shear wave velocity has a strong effect on  $HV$ , with very small variation in the middle layer leading to up to 5% variations around 5 Hz. On the other hand, variations in the lower halfspace have negligible effects on the H/V ratio. We note that changes in layer thickness have a similar, but less strong effect on  $HV$  as changes of the upper shear wave velocity: this means that some trade-offs exist between both parameters. On the other hand, varying the Poisson’s ratio and  $v_p/v_s$  ratio in layer 2 has a global effect, with higher values of  $\nu$  leading to lower and even negative values of  $HV$ .

We note that for some models of Fig. 3.14, the  $HV$  function diverges above 4 Hz. This feature is directly related to the phenomenon of seismo-acoustic coupling and is due to the generation of Rayleigh waves in the subsurface. This is further illustrated on Fig. 3.15 when varying the thickness of layer 2. For a typical event such as S0986c, the infrasound phase velocity modelled with MCD profiles is close to the shear wave velocity in the first 2 layers. The phase velocity of Rayleigh waves in the fundamental and 1st higher mode can be computed for each perturbed model. Due to the low seismic velocities of the subsurface models, these curves intersect the infrasound phase velocity at a certain frequency, where the infrasound converts into a Rayleigh wave.

As explained further in Appendix. A1, Rayleigh waves are solution to the same sets of equations as the ones defining compliance, except that they do not require a pressure forcing on the ground to exist, as they are free surface solutions. In other words, they exist even for  $P = 0$  (see Eq. 39 of Appendix. A1). To ensure the existence of finite displacement despite a zero pressure, the compliance function  $C_{x/p} = u_x/P$  must diverge to infinity, which is observed on Fig. 3.15 at the intersection frequency. Between two modes of the Rayleigh wave, the vertical compliance function is cancelled, as identified by diamonds in the centre-right of Fig. 3.15. This leads to a divergence of the H/V ratio as per Eq. 3.15. Therefore, the diverging nature of  $HV$  at frequency  $f_h$  is related to the existence of a Rayleigh wave at  $f < f_h$ .

Infrasound produced during the re-entry of the Stardust capsule generated air-coupled Rayleigh waves [Edwards et al., 2007]. As shown on Fig. 1.10 of the introduction, such signals appear as quasi-monochromatic horizontal stripes in spectrograms, with a duration much longer than the coupled shock wave itself. We can expect that air-coupled Rayleigh wave produced by impact infrasound on Mars would produce similar features in SEIS recordings. In the spectrograms of Fig. 1.14, the only resembling signal is the excitation of the 2.4 Hz mode following some of the dispersed infrasound (see e.g., the chirps of events S1160a and S0986c in Fig. 1.14 of section 1). This means that an inversion of  $HV$  from impact chirps must exclude any subsurface models producing Rayleigh waves below 2 Hz.

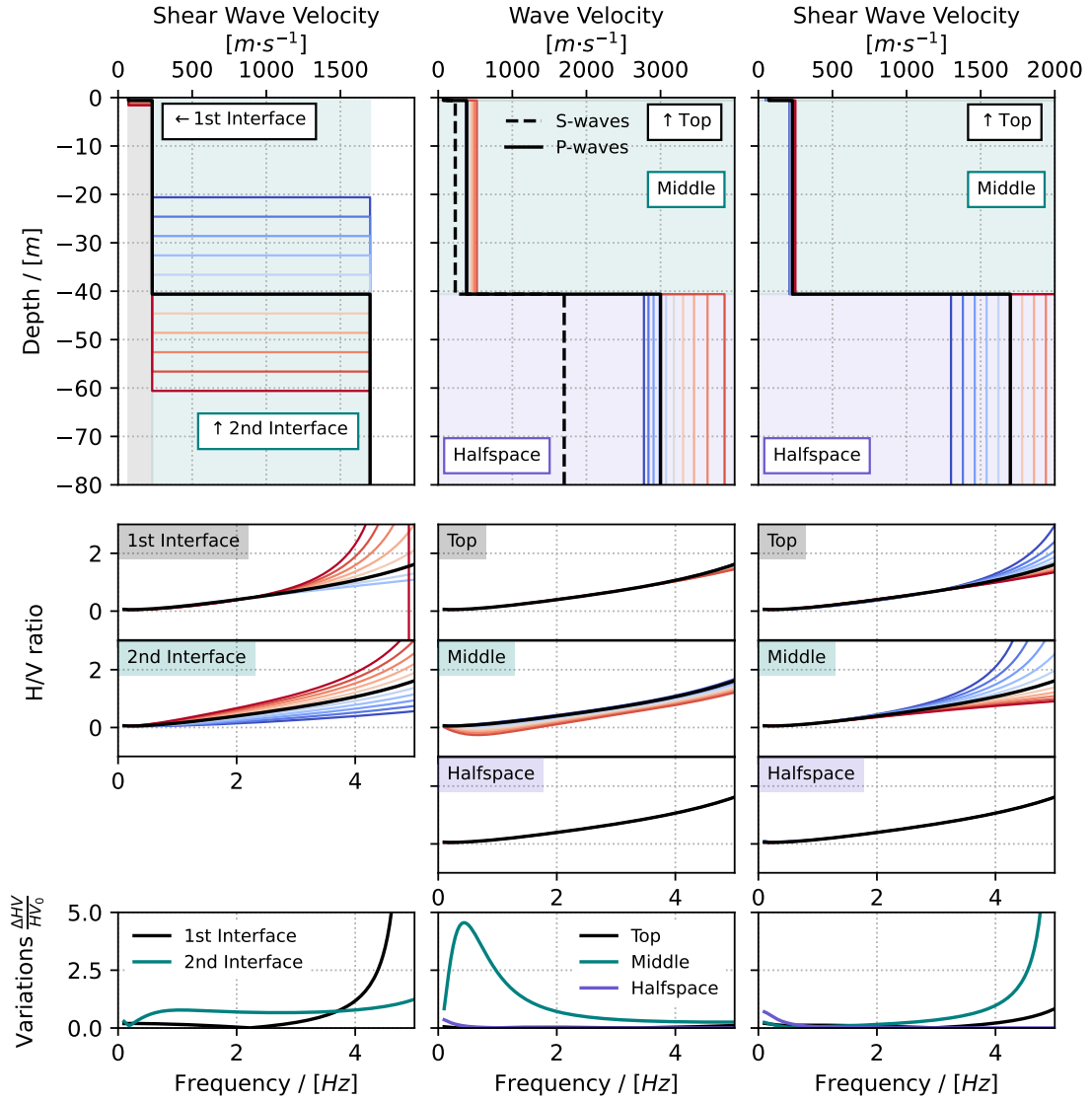


**Figure 3.14:** Sensitivity of the HV ratio to changes in the layer thickness, the Poisson's ratio and the S-wave velocity, based on the ZX model. In the left column, the thickness of the first and second layer are varied. In the center column, the Poisson's ratio is varied successively in each layer from  $\nu = 0.2$  to  $0.4$ ,  $v_s$  is kept constant and  $v_p$  is computed from  $v_p = v_s \sqrt{\frac{2-2\nu}{1-2\nu}}$ . All other parameters are constant. Finally, in the third column, the shear wave velocity is varied successively in each layer, all other parameters being constant. The H/V ratio for each layer are compared to the original ZX model in the three central lines, and the percentage of variation of HV is plotted for each layer on the bottom line.

### 3.3.2 The Markov chain Monte Carlo inversion method

The previous parametric studies showed that chirp group velocities and H/V ratio are sensitive to different parameters of the atmosphere and the subsurface. However, in the absence of an exact knowledge of the impact pressure source time function, the full phase of the signal cannot be used in an inversion.

Group velocities can be modelled with a limited number of layers, typically less than 10. A layered model provide an equivalent representation of the atmosphere to a smoother, piecewise-linear model averaging the maximum and minimum value of two successive layers (Fig. 3.10). Each of these layers is parametrised by its effective sound speed, while

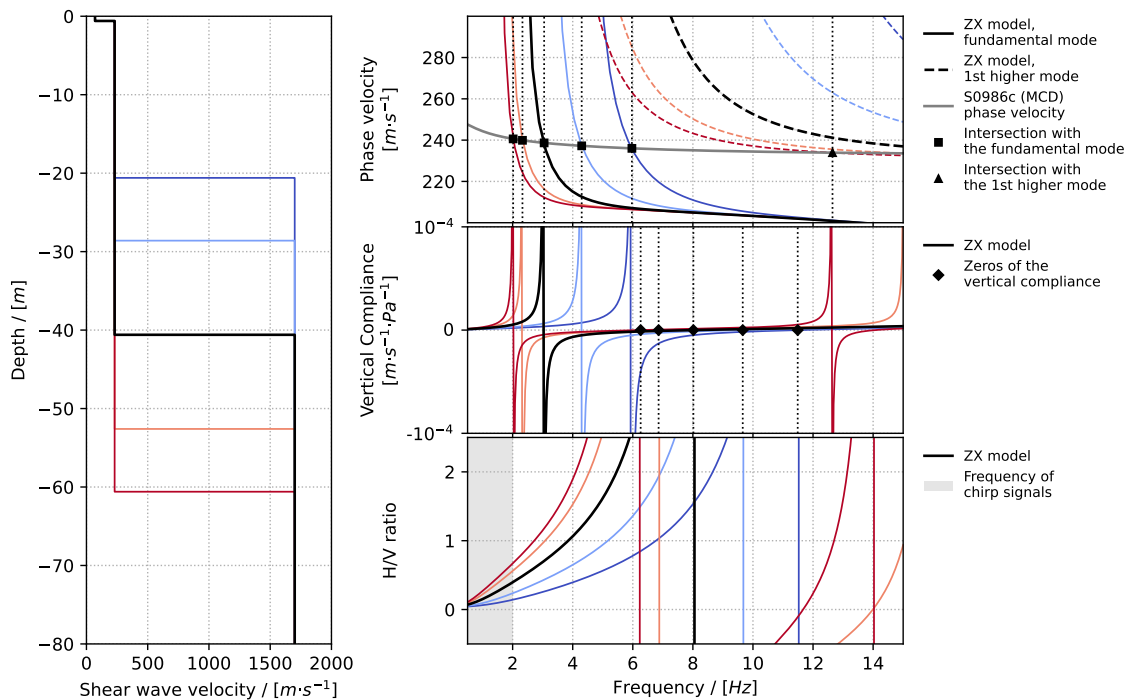


**Figure 3.15:** Generation of Rayleigh waves by the coupling of a dispersed infrasound with different subsurface models (left). The phase velocity of the infrasound is based on the MCD atmospheric profile for S0986c. For each model, the Rayleigh wave dispersion curves of the fundamental and 1st higher mode are computed using the Hermann `surf96` fortran code [Herrmann, 2013] wrapped to Python (top right). When the acoustic wave phase velocity curve intersects the Rayleigh ones, a Rayleigh wave is generated in the solid media, and the compliance term diverges (middle right). Between two Rayleigh modes, the vertical compliance function is cancelled, which leads to a divergence of the H/V ratio (bottom right).

the atmospheric density can be fixed based on MCD profiles as it does not significantly influence group velocities.

The H/V ratio of the coupled infrasound can be modelled from the compliance of a layered subsurface. It is mostly dependent on shear wave velocities and layer thicknesses, but presents particular features due to the presence of Rayleigh waves. Below 2 Hz,  $HV$  is also sensitive to the Poisson's ratio at medium depths (1 m to 40 m). All of these parameters can be inverted from the data, but trade offs between them need to be assessed. This supports the use of a Bayesian inversion such as the Markov chain Monte Carlo method.

### The Bayesian approach

An inverse problem consists in inferring a mathematical model for a physical system from an ensemble of information, or data, measured on the system. Due to the uncertainty in the measurements of the data, caused by instrumental or external noise, and to the existence of trade-offs between parameters, most of the time the inversion does not have a single solution, and the inverse problem is said to be *ill-posed*. A significant challenge in inverse problems resides in explicitly attributing some uncertainty to the model parameters extracted from the data, and to restrict the solution space using some a priori knowledge on the model parameters.

The Bayesian approach addresses this issue by considering each sought model parameters as a random variable [Tarantola, 2005]. Let  $\mathbf{m}$  be the model parameters and  $\mathbf{d}$  a vector containing the data. The Bayesian inversion problem answers the question: "Given the available measurements  $\mathbf{d}$ , what is the probability that the model parameters are equal to  $\mathbf{m}$ ?". In other words, it computes the conditional probability of  $\mathbf{m}$  given  $\mathbf{d}$ , the probability density function (PDF)  $P(\mathbf{m}|\mathbf{d})$ . As per the fundamental theorem of probabilities, the PDF can be rewritten as follow :

$$P(\mathbf{m}|\mathbf{d}) = \frac{P(\mathbf{d}|\mathbf{m})P(\mathbf{m})}{P(\mathbf{d})}. \quad (3.20)$$

$P(\mathbf{m}|\mathbf{d})$  is called the *posterior* distribution. It depends on  $P(\mathbf{d}|\mathbf{m})$ , the *likelihood*, and  $P(\mathbf{m})$ , the *prior* distribution of parameters.  $P(\mathbf{d})$  is the data probability and acts as a normalisation factor.

If the assumption that measurements of  $\mathbf{d}$  have a Gaussian error distribution, the likelihood can be expressed as the product of the Gaussian residuals between each data point  $d_i$  with measurement error  $\sigma_i$ , and associated synthetic value  $d_i(\mathbf{m})$ . For a set of  $N$  measurements, this yields:

$$P(\mathbf{d}|\mathbf{m}) = \prod_{i=1}^N \frac{1}{\sqrt{2\pi\sigma_i^2}} \exp \left[ -\frac{|d_i - d_i(\mathbf{m})|^2}{2\sigma_i^2} \right]. \quad (3.21)$$

### The Metropolis-Hastings sampling method

As the data probability  $P(\mathbf{d})$  is in general treated as a normalisation factor, the main aspects of a Bayesian inversion is to derive the likelihood and prior PDFs. The prior is designed to restrict the parameter ranges to values measured in experiments or predicted by other studies. It usually takes the form of a normal or uniform distribution which encompasses the physically possible values of  $\mathbf{m}$ .

On the other hand, determining the likelihood requires to explore the parameter space and measure the distance of  $\mathbf{d}(\mathbf{m})$  to  $\mathbf{d}$ . A trivial approach consists in a simple grid search, but such method can be time consuming as it also explores areas of very low likelihood. The Markov chain Monte Carlo (MCMC) method, on the other hand, allows to explore the posterior space more efficiently. With this method, a correlated chain of samples of the model space is generated, whose PDF converges towards the desired posterior distribution [Mosegaard & Tarantola, 1995]. This means that areas of high posterior probability will be explored more often. Although the MCMC method succeeds in uncovering the trade-offs and uncertainty of model parameters, it is not the most efficient at determining the minimum misfit between data and models.

The Metropolis-Hastings algorithm is a popular sampler for MCMC methods, which generates new samples based on an acceptance criterion [Metropolis et al., 1953; Hastings, 1970]. The algorithm departs from a random initial model and goes through a large number of iterations. At each iteration, a *candidate* model, written  $\tilde{\mathbf{m}}$ , is generated randomly from a perturbation of a *current* model  $\hat{\mathbf{m}}$  stored in the memory. The *acceptance ratio*  $\alpha(\tilde{\mathbf{m}}, \hat{\mathbf{m}})$  is used to compare the likelihood and prior probability of the current and candidate models, such that:

$$\alpha(\tilde{\mathbf{m}}, \hat{\mathbf{m}}) = \min \left( 1, \frac{P(\mathbf{d}|\tilde{\mathbf{m}})P(\tilde{\mathbf{m}})}{P(\mathbf{d}|\hat{\mathbf{m}})P(\hat{\mathbf{m}})} \right). \quad (3.22)$$

The current model is replaced by the candidate with probability  $\alpha(\tilde{\mathbf{m}}, \hat{\mathbf{m}})$ , allowing the Markov chain to move through the parameter space. The acceptance probability is proportional to the candidate and current likelihood ratio, therefore, samples of the model

space which produce a low misfit to the data are accepted with a higher probability, and thus high-likelihood regions of the parameter space are sampled more extensively.

### Advanced McMC techniques

A key problem of McMC methods resides in the proposal stage, when a candidate model is generated from a current sample. Two model samples taken very close to each other have similar likelihood values, and the candidate model will therefore be accepted with a probability close to 1. On the other hand, to efficiently explore the posterior space, the McMC sampler must generate samples sufficiently distant from each other. When a posterior distribution is dimensionally complex or multimodal, a small proposal distance will not succeed in exploring different modes, as samples generated in the region of low likelihood between two modes will be systematically rejected. On the other hand, a large proposal distance will be able to sample several modes but fine regions of the posterior distribution will be badly explored.

The Metropolis-Hastings algorithm is successful in sampling smooth, uni-modal posterior distributions but is limited when dealing with such highly non-linear multi-modal distributions, or when two parameters of the model space are strongly correlated [Sambridge, 2014]. For such class of inverse problems, several types of advanced sampling techniques exist.

**Parallel Tempering** The *Parallel Tempering* (PT) technique was initially proposed by Geyer [1991] and Falcioni & Deem [1999]. PT is shown to significantly improve the exploration of the posterior distribution and the computation time in several applications of McMC to geophysical inversion problems [Dosso et al., 2012; Sambridge, 2014].

The PT algorithm consists in running several "tempered" Markov chains in parallel, in addition to the original chain. A *tempered* chain is a Markov chain whose posterior distribution has been artificially smoothed by introducing a temperature parameter  $T$  in the expression of the likelihood :

$$P(\mathbf{m}|\mathbf{d}, T) = P(\mathbf{d}|\mathbf{m})^{1/T} P(\mathbf{m}). \quad (3.23)$$

The original chain has a temperature  $T = 1$  and is also called the *cold* chain. It represents the true posterior PDF. Note that, for  $T \rightarrow +\infty$ , the posterior PDF converges toward the prior distribution  $P(\mathbf{m})$ , meaning that the PDF is no longer constrained by the data, and solely by the *a priori* distribution. Because they present a smoother PDF, high-temperature chains have a high acceptance rate of candidate models. Indeed, considering a uniform prior ( $P(\tilde{\mathbf{m}}) = P(\hat{\mathbf{m}}) = 1$ ), the acceptance ratio  $\alpha(\tilde{\mathbf{m}}, \hat{\mathbf{m}})$  of a cold chain transforms into  $\alpha(\tilde{\mathbf{m}}, \hat{\mathbf{m}}, T) = \alpha(\tilde{\mathbf{m}}, \hat{\mathbf{m}})^{1/T}$  for a hot chains, which takes values closer to 1 as  $T$  increases. Hot chains are thus able to explore the parameter space more efficiently than cold chain, and a chain with  $T \rightarrow +\infty$  simply samples uniformly from the prior.

Each tempered chain evolved following a classical Metropolis-Hastings algorithm. Then, every few steps, the PT scheme lets random pairs of chains with different values of  $T$  exchange their current model. This is done according to an "acceptance ratio of swap". Let  $i$  be the index of a chain at temperature  $T_i$  and  $j$  the index of a chain at temperature  $T_j$ . The acceptance ratio for a swap between two temperatures is given by:

$$\alpha_s(\hat{\mathbf{m}}_i, \hat{\mathbf{m}}_j) = \min \left( 1, \left[ \frac{P(\hat{\mathbf{m}}_j|\mathbf{d})}{P(\hat{\mathbf{m}}_i|\mathbf{d})} \right]^{1/T_i} \left[ \frac{P(\hat{\mathbf{m}}_i|\mathbf{d})}{P(\hat{\mathbf{m}}_j|\mathbf{d})} \right]^{1/T_j} \right), \quad (3.24)$$



where  $P(\hat{\mathbf{m}}_i|\mathbf{d})$  represents the probability of current model  $\hat{\mathbf{m}}_i$  for a temperature of 1. This swapping step allows hotter chains to eventually exchange information with the cold chain. The hotter chain might explore areas of the posterior distribution that are out of reach of the cold chain, but which present similar or better likelihood values. This technique improves convergence, as it prevents the cold chain to become stuck in a local maximum of the posterior distribution, and increases mixing between regions of similar probability.

The PT method is easy to implement following the algorithms of Sambridge [2014]. Open source parallel version are also implemented in Python, such as the `ptmcmc` sampler [Ellis & van Haasteren, 2017]. In the following study, an in-house code following Sambridge [2014] was constructed.

**Ensemble Sampling** The affine invariant *ensemble sampling* (ES) method was proposed by Goodman & Weare [2010]. It aims at improving the efficiency of sampling highly skewed posterior distribution, where one of the model parameters is strongly constrained by the data and others are not, or when strong trade-offs exist. Similarly to the PT, the ES technique takes advantage of multiple chains, or samplers, running in parallel. Each sampler departs from a different origin model. At each step, a proposal is made based on the position of all samplers of the ensemble. One type of proposal is called the *stretch move*, whereby a sampler moves via an affine transformation in the direction of another sampler.

The ES method is implemented in a popular open-source Python module called `emcee` [Foreman-Mackey et al., 2013].

For the two inversion problems at hand, both the parallel tempering and ensemble sampling method are appropriate. In Appendix A3, the performances of three implementations of the above methods are evaluated.

### Convergence of a McMC inversion

By definition of a Markov chain, models  $\mathbf{m}$  sampled from the posterior distribution with the McMC method are inherently correlated with each other. An important assessment of the quality of the inversion consist in measuring the amount of statistically significant samples within a chain. A chain requires a certain number of steps  $\tau_c$  before it "forgets" its origin sample, i.e., before multiple portions of  $\tau_c$  samples become similar to each other.  $\tau_c$  is equivalent to the auto-correlation time of a chain, which writes based on Foreman-Mackey et al. [2013]:

$$\tau_c(N) = 1 + 2 \sum_{\tau=1}^N \frac{\hat{C}_f(\tau)}{\hat{C}_f(0)}, \quad (3.25)$$

with  $\hat{C}_f(\tau)$  the autocorrelation function with lag  $\tau$ , given by:

$$\hat{C}_f(\tau) = \frac{1}{N-\tau} \sum_{n=1}^{N-\tau} (f_n - \mu_f)(f_{n+\tau} - \mu_f). \quad (3.26)$$

$f_n$  is the content of a chain of length  $n$  and  $\mu_f = \frac{1}{N} \sum_{n=1}^N f_n$  is the mean value of the total chain. In practice,  $\tau_c$  can be calculated progressively during a McMC run. Its value initially varies with increasing number of samples  $N$ , as the Markov chain explores the parameter space and converges towards the minimum-likelihood region: this is the *burn-in* stage. With a sufficient number of samples,  $\tau_c$  eventually converges. The posterior



distribution can be considered sufficiently sampled for  $N \approx 50\tau_c$  for an ensemble sampler, or  $N \approx 1000\tau_c$  for a single sampler method.

### 3.3.3 Data selection

Among the events shown in Fig. 3.8, only S0981c, S0986c and S1034a provide chirps with unambiguous group velocities and sufficiently high signal-to-noise ratio (S.N.R). Their group velocity measurement, obtained with the same method as Garcia et al. [2022], are shown on Fig. 3.16. The MCD effective sound speed profile at InSight location and at the date of these events is also provided, as well as the model group velocity for these profiles. In all three cases, it appears that the main sound speed increase occurs below 250 m altitude, with a maximum increase of  $20 \text{ m}\cdot\text{s}^{-1}$  for S0986c. For this event, the thermodynamic sound speed,  $c_T$ , differs strongly from the effective sound speed,  $c_{eff}$ , which means that the main cause for the waveguide are winds travelling from the crater to the receiver.

Another particularity of these events is that the group velocity predicted from the MCD models is different from the measured one. For S0981c and S0986c, the measured group velocity curves appear shifted to lower values compared to group velocities modelled using MCD effective sound speed profiles. A model with no wind (the MCD thermodynamic sound speed profile) is also unable to perfectly fit the data. The MCD effective sound speed profile for S1034a presents an inversion above 250 m altitude, which prevents low-frequency waves to be trapped in the waveguide. Moreover, the group velocities modelled with MCD differ strongly from the measurement below 1 Hz. These discrepancies can be explained in two different ways: (1) The MCD model is calculated at InSight location, but weather conditions may be variable along the trajectory of the waves from the crater to the receiver, causing variations in wave speed, or (2) the winds might be overestimated in these MCD models. The case of S0981c, for which a model with no wind is not sufficient to fit the data, seems to indicate that (1) is more likely. An inversion of the group velocity will provides insights into the range of profiles that can explain these measurements.

Fig. 3.17 represents the amplitude spectra and H/V ratio of the three chosen events, obtained from fast Fourier transforms of 15 s to 20 s time-windows centred around the dispersed signal. The noise of each spectra is computed by averaging amplitude spectra of same-size time-windows taken before and after the chirp, and the noise of  $HV$  is simply:

$$\sigma_{HV} = \left| \frac{V_x}{V_z} \right| \sqrt{\left( \frac{\sigma_{V_x}}{V_x} \right)^2 + \left( \frac{\sigma_{V_z}}{V_z} \right)^2}. \quad (3.27)$$

The effect of atmospheric attenuation is apparent on the high-frequency part of the spectra, with the furthest event, S0981c, showing the least energy above 2 Hz. The 2.4 Hz resonance [Dahmen et al., 2021] is also noticeable for events S0986c and S1034a. The strong noise during S0981c prevents a proper measurement of the  $HV$  ratio, but the S.N.R of S0986c and S1034a is high between 0.5 and 2 Hz. The noise level  $\sigma_{HV}$  is provided to the McMC inversion as in Eq. 3.21, so that regions with low S.N.R naturally weigh less in the total likelihood of a model.

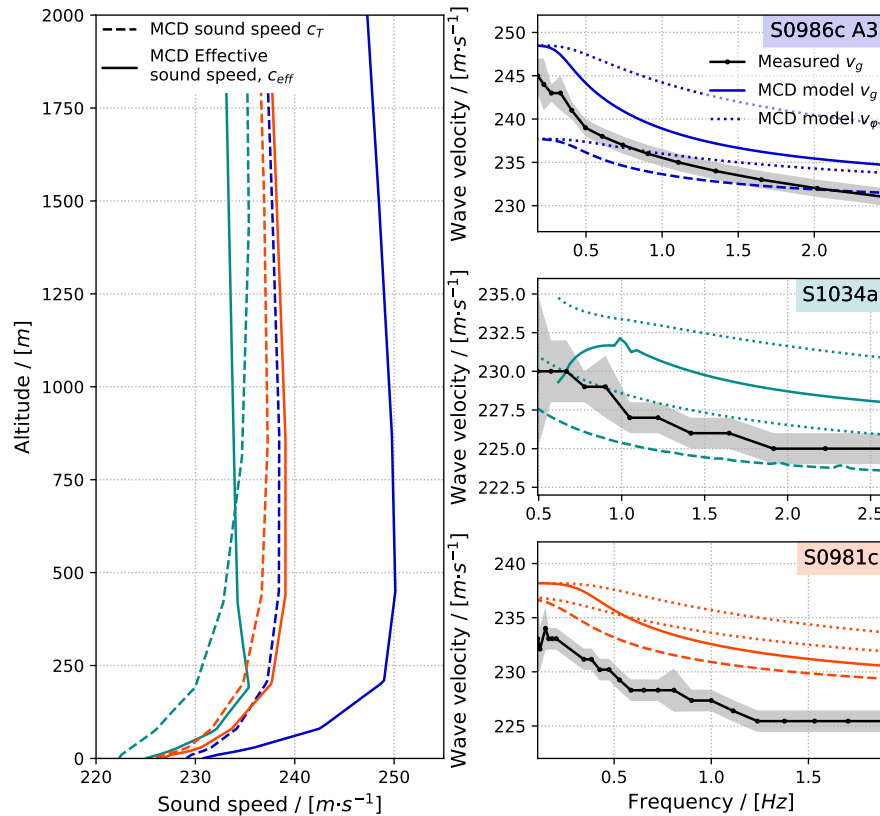


**Figure 3.16:** (left) MCD effective ( $c_{eff}$ ) and thermodynamic ( $c_T$ ) sound speed profiles for the three events S0986c, S0981c and S1034a. (right) Group velocities measured for each chirp event, and modelled with the corresponding MCD effective sound speed profiles. The model in plain line uses MCD effective sound speed profile, including the effects of winds, while the model in dashed lines use the purely thermodynamic sound speed profiles.

### 3.4 Inversion of the atmospheric structure

A detailed test of different parallelised MCMC implementations and their performance can be found in Appendix A3. For both the atmospheric and subsurface inversion problems, we found that a in-house implementation of the MCMC method provided a quick convergence and a higher number of independent samples per simulation time. Therefore, this is the method chosen in this present section and the following one.

First, we conduct a synthetic test of the proposed atmospheric inversion. We then present sound speed profiles inverted for events S0986c, S1034a and S0981c.

#### 3.4.1 Test of the inversion method

To avoid overfitting the group velocity curves, the influence of the number of layers on the model misfit was measured. Inversion simulations were performed based on the group velocity curves of S0986c, with a single layer, as in the model of Negraru & Herrin [2009] and up to six layers below a halfspace. Prior bounds for the layer thickness were chosen

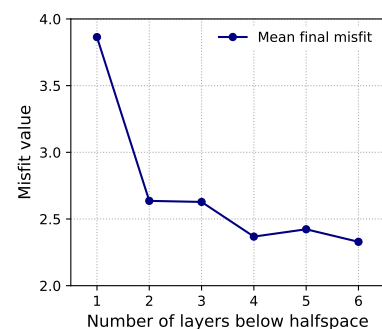


**Figure 3.18:** Mean misfit measured in the last portion of Markov chains as a function of the number of atmospheric layers below the halfspace.

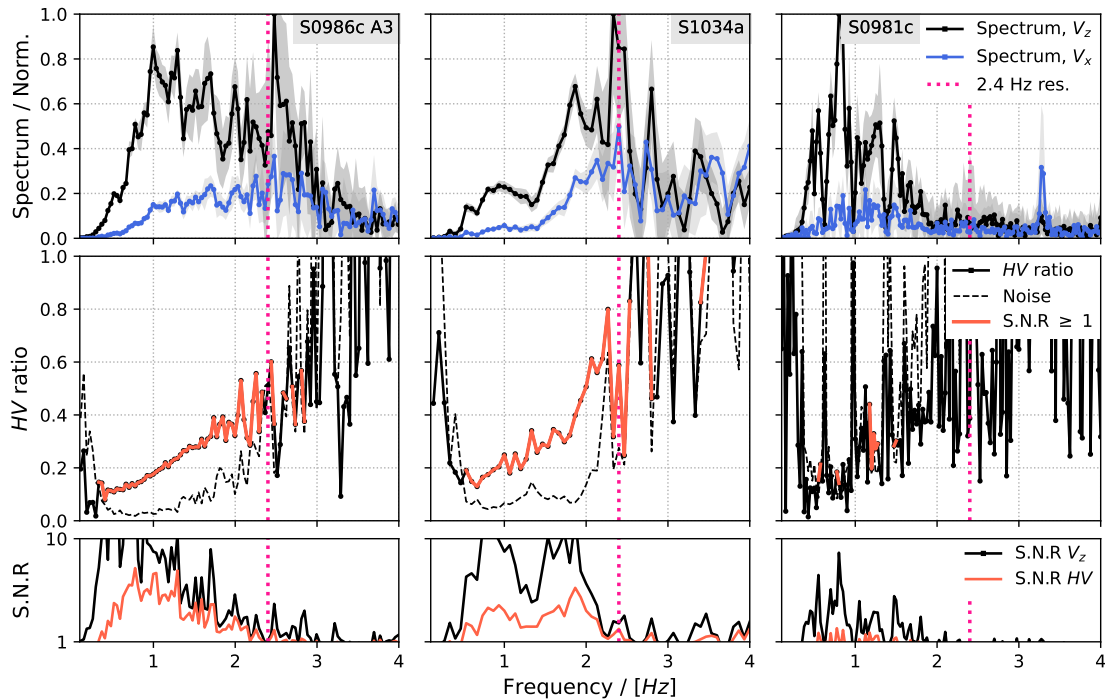


**Figure 3.17:** (top) Amplitude spectra of the vertical velocity  $V_z$  and horizontal velocity  $V_x$  signals for each selected chirp event. The 2.4 Hz resonance is marked with a pink dashed line. (middle) Corresponding H/V ratio and its noise level. (bottom) Signal-to-noise ratio (S.N.R.) of the vertical velocity spectrum and the HV ratio. Regions where the signal to noise ratio of  $HV$  is higher than 1 are marked in orange in the middle plots.

identical for each layer, with upper bounds such that the maximum interface altitude would be 1600 m. Hence, for a two-layer model, each layer thickness may be picked within [5, 800] m, whereas it is selected within [5, 400] m for a four-layer model. The priors for the effective sound speed are a uniform distribution within [220, 240] m·s<sup>-1</sup> in the first layer. Starting from the third layer, variations of effective sound speed are allowed within [-5, 15] m·s<sup>-1</sup>. Negative variations of sound speeds are not allowed in the second layer, or in the halfspace of the 1-layer model.

The mean misfit achieved in the last portion of these Markov chains is displayed on Fig. 3.18. The measurements show that no significant improvement of the misfit is obtained above four layers. Therefore, all the following simulations are designed with a four-layer atmosphere with a top halfspace. To test the performance of the inversion itself, a synthetic group velocity curve was generated using the simplified MCD model (3) for S0986c (see Fig. 3.10). The uncertainty of the actual S0986c data was used as the weight  $\sigma$  of the inversion.

Fig. 3.19 shows the posterior probability density distribution (PDF) of the atmospheric models retrieved by the McMC inversion, compared to the initial synthetic model. The model with the smallest misfit (or *maximum likelihood*, hereafter referred to as ML) appears close to the initial model and the MCD profile on which it was based. The high-density regions of the posterior PDF appear to be centred around the ML and synthetic model, with a spread of approximately 10 m·s<sup>-1</sup>. The PDF values are higher below  $\sim 750$  m altitude, above which posterior models have a more diffuse distribution. Fig. 3.19 compares the group velocity curves computed with 100 models randomly picked from the posterior with the data, showing that the posterior fits the group velocity measurements

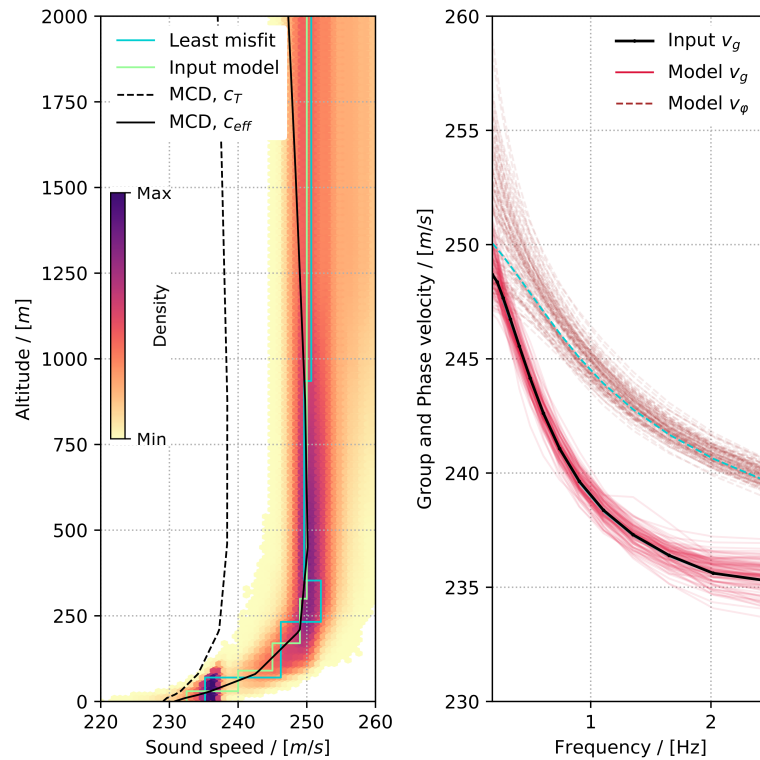


**Figure 3.19:** (Left) PDF of models extracted from the posterior distribution of the synthetic atmosphere inversion. The MCD models for S0986c are represented in black, the original synthetic model is displayed in yellow and the best fit model in turquoise. The colorbar indicates the minimum and maximum PDF values. (Right) Synthetic group velocity curve in black, compared to 100 group velocity randomly picked from the posterior distribution. The associated phase velocity curves are also shown with dashed brown curves, and the best fit in turquoise.

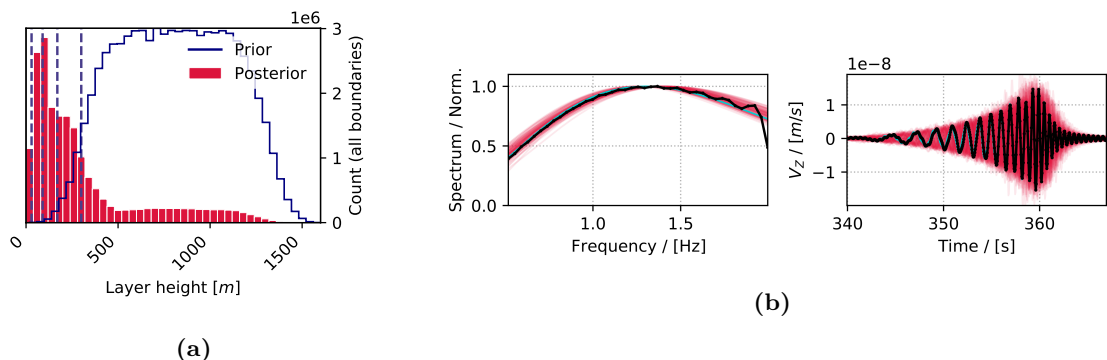


**Figure 3.20:** (a) Histogram of the altitude of layers in all models produced by the synthetic atmosphere inversion. The blue curve represents the histogram of layer altitude for 10,000 models picked from the prior. (b) Normalised spectrum and vertical velocity signal. The black curve represents the inverted synthetic data, while the red curves are a superposition of 100 posterior models. The turquoise curve represents the best fit to the data.

within their uncertainty. All associated phase velocity curves lay within  $\pm 1 \text{ m}\cdot\text{s}^{-1}$  of each other at 1 Hz.

Fig. 3.20a displays the histogram of layer height found in the posterior distribution. This plot shows that the inversion is more likely to find changes in sound speed below  $\sim 500 \text{ m}\cdot\text{s}^{-1}$ , in agreement with the MCD profiles. Using the ZX subsurface model and a Dirac source, we calculate the waveforms and spectra associated to the synthetic model and to 100 models from the posterior distribution, shown on Fig. 3.20b. As expected from an inversion of group velocities only, the retrieved models are able to fit the envelope of the signal, i.e., the travel time of an energy packet, but cannot reproduce its phase.

### 3.4.2 Atmospheric structure inverted for three individual events

Following these synthetic tests, an inversion of the group velocity measured for S0986c, S1034a and S0981c is performed. We invert the sound speed profile with a four-layer model and priors similar to the synthetic tests.

The inverted posterior PDF of models is shown for each event on Fig. 3.21, and the histogram of layer heights on Fig. 3.22. For all three events, the density of posterior models is highest below  $\sim 100 \text{ m}$  altitude, which confirms that the inversion is highly sensitive to the surface effective sound speed. For event S0986c, the ML model and the region of high model density show lower effective sound speed values than the MCD model, but a similar shape with varying altitude. For event S1034a, models are more diffuse above  $\sim 250 \text{ m}$  altitude, but both the PDF and the ML model show the possibility of an inversion in sound speed around  $\sim 200 \text{ m}$ , in agreement with the MCD effective sound speed profiles. In contrast with the two other events, the PDF of S0981c shows a well defined, narrow PDF with a high density of models for the whole range of altitudes up to  $2000 \text{ m}$ . The results are once again in trend with MCD profiles, despite a shift of about  $5 \text{ m}\cdot\text{s}^{-1}$  towards lower values for the PDF.

All three histograms shown on Fig. 3.22 indicate that the main variations in effective sound speed occur at less than  $500 \text{ m}$  altitude. This trend that cannot be solely explained by the prior bounds for layer thickness (blue curves in Fig. 3.22), which means that it is an information retrieved from the data.

## 3.5 Inversion of InSight near-surface structure

### 3.5.1 Test of the subsurface inversion

#### Inversion with large priors

As in section 3.4.1, we design a synthetic test of the subsurface inversion. In a similar manner as model (3) designed for S0986c, we simplified the MCD models for S0981c and S1034a to obtain synthetic phase velocity curves for three events. We used the ZX subsurface model (Table 3.2 [Xu et al., 2022]) and these phase velocities to construct three synthetic  $HV$  ratio curves. The ZX model is a least-misfit model found by a simple grid search using events S0986c and S0981c, and thus represents a good target solutions for the McMC inversions.

For all the following inversions, we model the subsurface using four layers on top of a halfspace. Indeed, previous inversion studies performed with SEIS data have found sev-

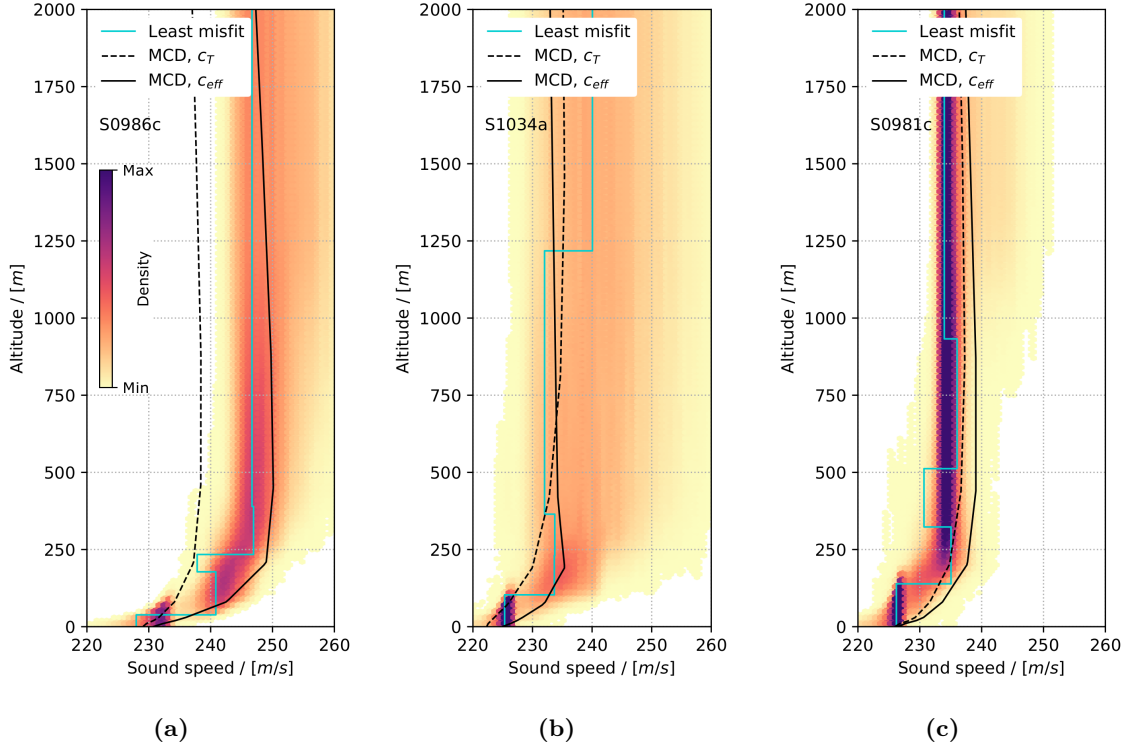


**Figure 3.21:** Posterior probability density of atmospheric models inverted from the group velocity measurements of S0986c (a), S1034a (b) and S0981c (c). The colorbar indicate the minimum and maximum PDF values across all three inversions. The MCD thermodynamic and effective sound speed profiles of Fig. 3.16 are shown for each events.

eral structures in the first hundreds of meters below the surface using four-layer models [Hobiger et al., 2021; Carrasco et al., 2023].

A key aspect of MCMC inversions is the choice of prior bounds. Like Hobiger et al. [2021], in order to avoid placing subjective limits to the subsurface parameters, we perform initial inversions with large, identical uniform prior bounds in each layer. The shear wave velocity is picked within  $[100, 3000] \text{ m}\cdot\text{s}^{-1}$ , and the four layer thickness within  $[0.1, 75] \text{ m}$ . Hence, the maximum depth allowed for an interface is 300 m. The P- wave velocity is calculated from a Poisson ratio of  $\nu = 0.22$  and the density using Gardner’s relationship [Gardner et al., 1974], as in Xu et al. [2022]. The upper velocity value of  $v_s = 3000 \text{ m}\cdot\text{s}^{-1}$  is high for near-surface material, but possible for materials such as intact basalt found in the InSight region [Knapmeyer-Endrun et al., 2017].

Results of the inversions of the synthetic  $HV$  curves with loose priors are found on Fig. 3.23a. We can see that posterior models fit the synthetic  $HV$  curve well at low frequency, but less at high frequency, where the signal-to-noise ratio is lower (Fig. 3.23c). On Fig. 3.23b, the histogram of layer depth shows a high probability of layer transition a little above 40 m depth, close to the input model. However, the first transition of the ZX model, at 0.6 m depth, is not recovered. This can be explained by the low sensitivity of the H/V ratio to very shallow variations in shear wave velocity. In addition, due to the large prior layer thickness chosen here, the MCMC has a higher probability of proposing models with deeper interfaces.

The synthetic PDF shows that the ML model agrees well with the low shear wave velocities of the ZX model above 40 m depth. However, the shear wave velocity in the halfspace is not well matched by the posterior models, which favour values of  $v_s$  higher than the synthetic



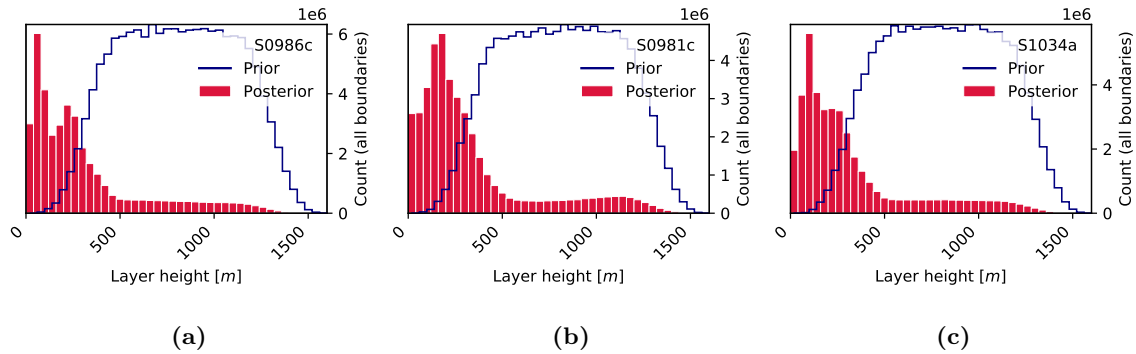


**Figure 3.22:** Posterior distribution of layer altitude for each atmospheric model inversion (red). The prior distribution, which is a sum of uniform distributions, is indicated in blue. The histogram shows that the main changes in effective sound speed occur within  $\sim 500$  m altitude.

model. As shown in Fig. 3.14, the  $H/V$  ratio is not sensitive to the shear wave velocity in the halfspace between 0.1 and 2 Hz, which means that any high-velocity model is equally probable from the perspective of the prior and the likelihood.

### Inversion with reduced priors

To further test the inversion method, and due to the low observed sensitivity to deep structures, we reduce the prior bounds for layer thickness to allow for more variations in the upper 100 m of the subsurface. Hence, the new prior for the first layer allows a thickness within  $[0.1, 10]$  m, for the second layer within  $[1, 20]$  m and the last within  $[0.1, 70]$  m. The prior bounds for shear wave velocity are left the same.

With such values, the posterior model distribution differs strongly from Fig. 3.23. Fig. 3.24 shows 400 models randomly picked from the posterior distribution of Fig. 3.23, and from the new inversion with reduced priors. The new inversion produces two family of models: one similar to the input model, with an interface at 40 m depth, and a second one presenting a thin high-velocity layer around 15 m depth. This second family differs strongly from the input ZX model.

An important conclusion can be drawn from these synthetic tests: the posterior distribution of the  $HV$  inversion is multimodal. Which of the modes is preferably selected by the inversion depends on the definition of prior bounds. Hence, caution must be used when interpreting inverted models.

### Influence of Rayleigh waves

First results show that a great number of models selected by the McMC algorithm provide a good fit to the  $HV$  curves, but present a divergence of compliance values between 0.5 and 2 Hz. This divergence, which was already mentioned in section 3.3.1, means that the conversion of the guided infrasound generates a Rayleigh wave. This type of conversion results in a quasi-monochromatic signal which is not found in any of the recorded chirp waveforms. Consequently, such models should be rejected by the McMC simulation.

To do so, we implement a verification step which checks for divergence of the compliance function between 0.5 and 2 Hz, or for intersections between the infrasound phase velocity and the Rayleigh wave phase velocity for the proposed subsurface model. Models which one of these criterions are given a likelihood of  $-\infty$  which leads to their rejection. The



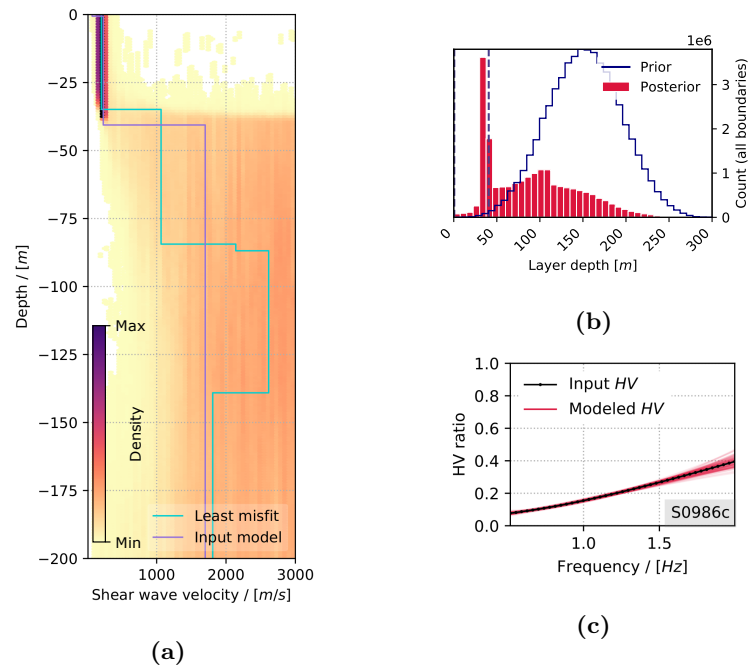


**Figure 3.23:** (a) PDF of models extracted from the posterior distribution of the synthetic subsurface inversion. The original synthetic model is displayed in purple and the ML model in turquoise. (b) Histogram of the depth of layers in the posterior distribution. The blue curve represent the histogram of layer depth for 10,000 models picked from the prior distribution. Interfaces of the ZX model are represented with dashed vertical lines (c) HV curve for 100 models picked from the posterior, compared to the synthetic curve for S0986c.

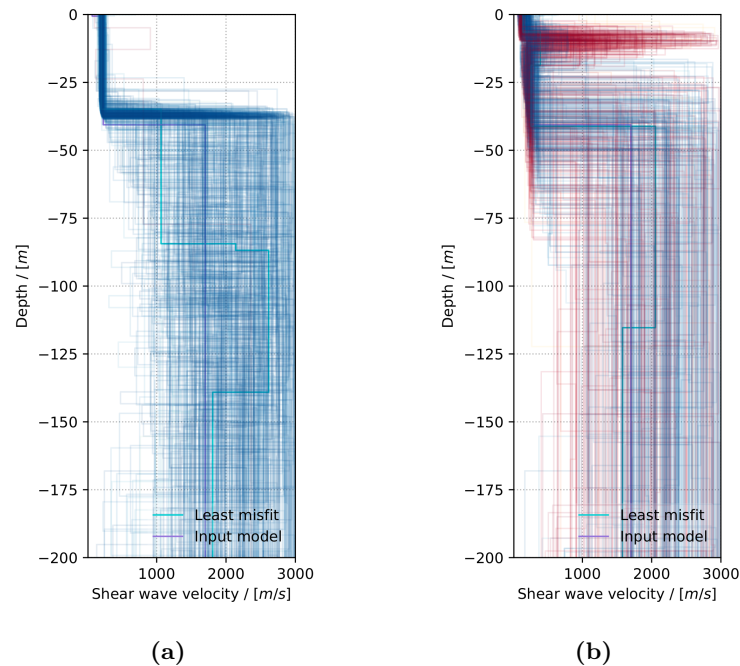


**Figure 3.24:** (a) 400 models extracted from the large-prior inversion. (b) 400 models extracted from the reduced-prior inversion, colored in red when presenting a high-velocity layer around 15 m depth.

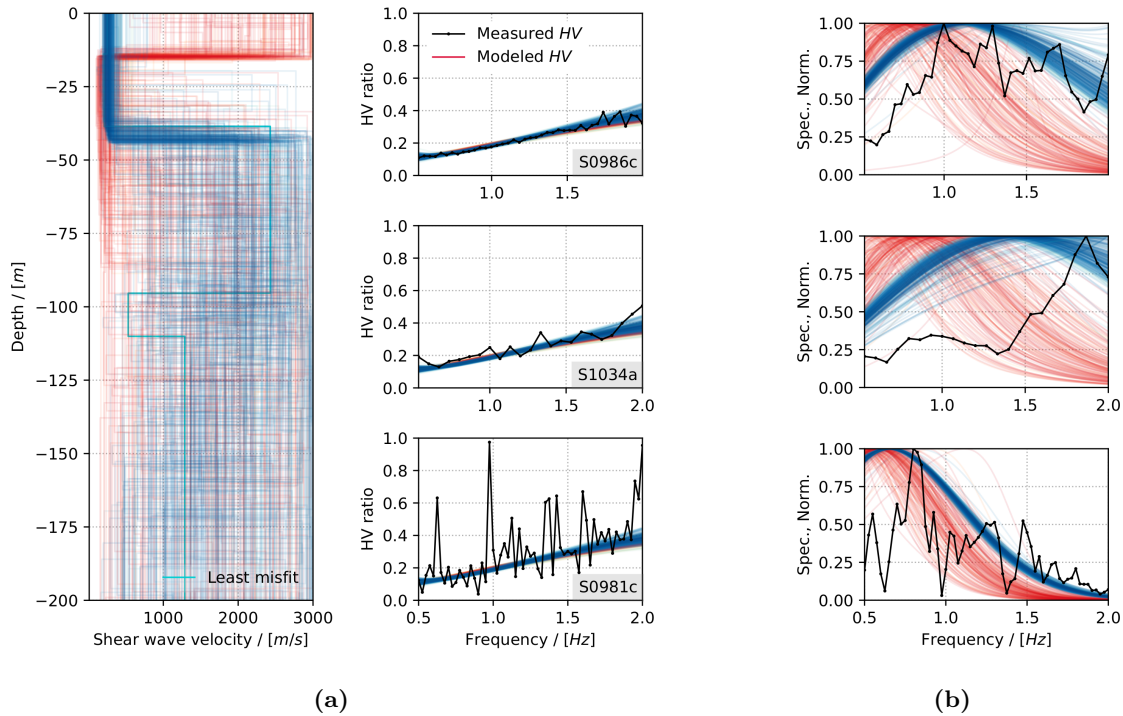


**Figure 3.26:** (a) Family of models showing an interface and high shear wave velocity values around 15 m depth are represented in orange, and other models in blue, among 400 total models. Within each family, a darker color means a lower misfit. The  $HV$  curves for each family of models are compared to the data on the right of the figure. (b) Spectra measured for each event in black, compared to the spectra modelled for each family of models, assuming a Dirac source.

posterior PDFs obtained with and without this rejection step were found to be identical, hence it was implemented in all subsequent inversions.

### 3.5.2 Subsurface model inverted from event H/V ratio

#### Main features of the inverted models

A first inversion of the chirp  $HV$  data is performed using the large prior bounds. The histogram of posterior interface depth is shown on Fig. 3.25 and shows a high concentration of interfaces at 15 and 40 m depth. However, as in the synthetic tests, these two interfaces belong to two different families of models, shown on Fig. 3.26. Both families present an equally good fit to the  $HV$  curves for each event, but their associated spectra, obtained using an ideal Dirac source, differ. The spectra of the 15 m family present a stronger decay above 1 Hz, while the 40 m family aligns better with the low frequency and high frequency portions of the spectra. Nevertheless, the information from event spectra was not used in the inversion. Hence, modeled spectra can illustrate the different features of both families of models, but cannot be used to advocate for one or the other subsurface structure.

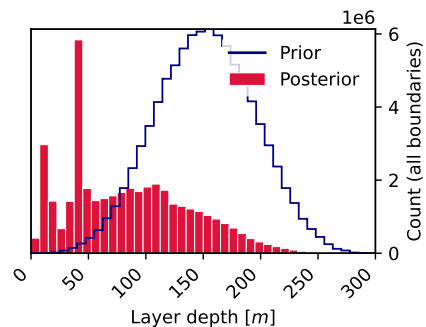


**Figure 3.25:** Histogram of interface depths inverted from the chirp data using large prior bounds.

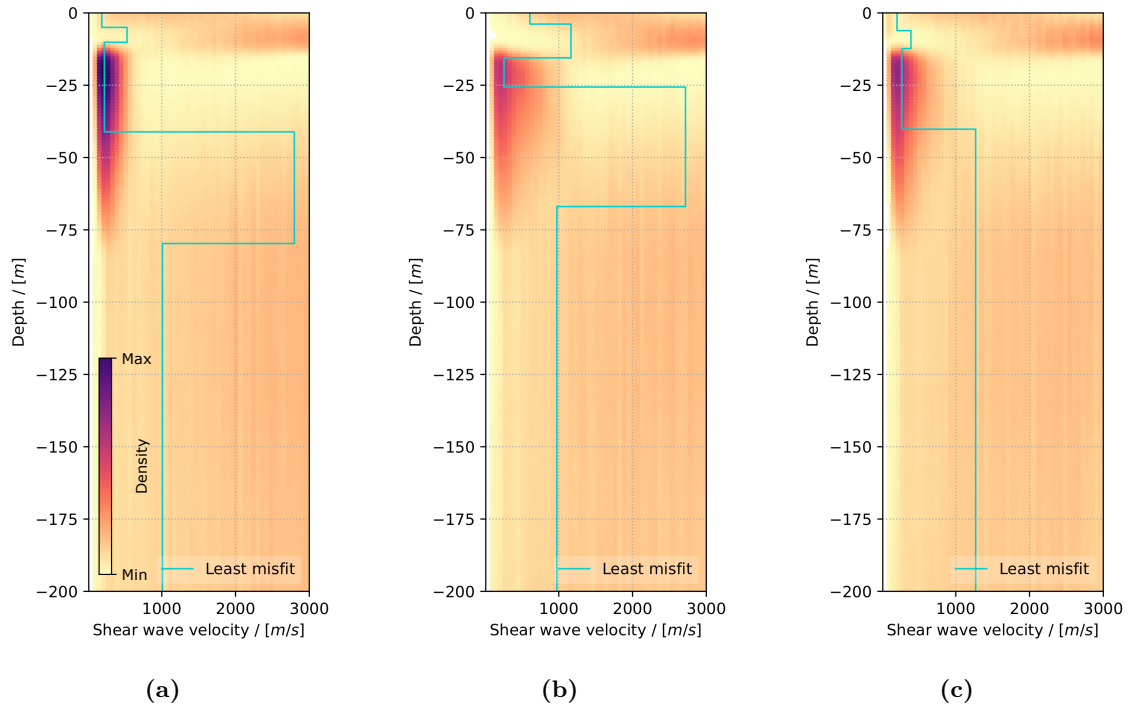


**Figure 3.28:** Compared density of probability inverted with narrow prior bounds and with a fixed Poisson ratio of 0.22 (a) and 0.3 (b). In (c), the Poisson ratio is treated as a model parameter picked uniformly between 0.2 and 0.4. The least-misfit model corresponds to the turquoise line.

### Effects of prior bounds and Poisson ratio

As in the synthetic tests, we perform a second inversion using reduced prior bounds for the layer thickness. The resulting histogram of interface depth is shown on Fig. 3.27. With these new prior bounds, the peak at 40 m is muted and the one at 15 m is enhanced from Fig. 3.25. Effectively, models of the first family have been replaced by models of the 15 m family.

The effect of the choice of Poisson's ratio on these results was also tested. In this work and previous studies of the InSight subsurface,  $\nu$  is selected within the range of values expected for rocky material, i.e. between 0.2 and 0.4 [Hobiger et al., 2021]. Here, we compare the PDF obtained previously with reduced prior bounds and with a Poisson ratio of 0.22, to a PDF calculated with a Poisson ratio of 0.3. In a third inversion, we treat  $\nu$  as a model parameter with a uniform prior between 0.2 and 0.4.

As shown by Fig. 3.28, a higher value of  $\nu$  or a parametric  $\nu$  does not narrow down the PDF. On the contrary, a value of 0.3 results in a smoother density of probability. No significant differences are observed in other statistical products of the MCMC simulation. As confirmed by our sensitivity analysis, the inversion is weakly sensitive to the Poisson ratio, hence its inversion only provide loose constraints. The histogram of posterior values of  $\nu$  shows a slightly higher probability around  $\nu = 0.3$  and a minimum misfit for  $\nu = 0.23$  (see Fig. 3.29).

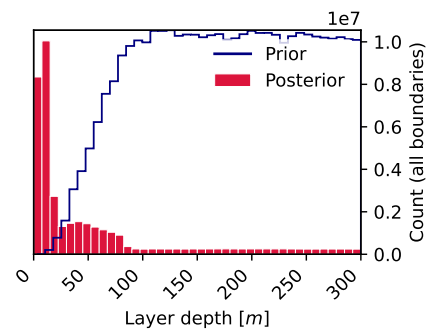


**Figure 3.27:** Histogram of interface depths inverted from the chirp data using reduced prior bounds.

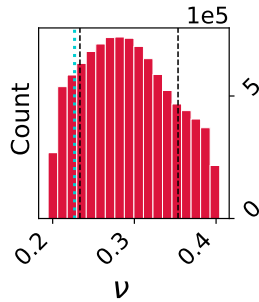


**Figure 3.29:** Histogram of inverted Poisson ratio values. The least misfit is shown in turquoise. 68% of inverted parameters are comprised between the two dashed black lines.

## 3.6 Discussion

### 3.6.1 Interpretation of the atmospheric inversion

The inversion of the atmosphere confirms some of the observations made in the parametric study of our 1D model. First, the discretisation of the atmospheric structure does not produce an unphysical, layered solution for the atmosphere. On the contrary, the histograms of Fig. 3.22 show that layer heights are loosely defined between 0 and 500 m, all providing an equally good fit to the group velocity. The posterior PDF of Fig. 3.21 supports a smooth variation of effective sound speed with altitude, except between 100 m to 150 m where a sharp increase in sound speed must be accommodated by the four-layer profile.

The PDFs also show that the definition of the atmospheric profile (or sharpness of the PDF) is improved with increasing impact distance. Indeed, event S1034a, with a crater at 48 km distance, presents a wide distribution of posterior model, in particular at high altitude. On the other hand, event S0981c, with a crater at 241 km, presents a narrow distribution of sound speed values up to 2000 m altitude. This difference can be explained by the phenomenon of dispersion: the longer a dispersed infrasound travels, the longer high-frequency energy will be delayed with respect to low frequency. This results in a chirp of longer duration, and facilitates measurements of the group velocity in the data. Although the increased distance of the event limits the measurements of high frequencies, which are dissipated through atmospheric absorption, it allows for a better measurement of the group velocity at low frequency, where the dispersion curve is subject to larger variations. Hence, the lower measurement uncertainty for S0981c in Fig. 3.16 is the reason for its narrower PDF.

We noted that for S0981c and S0986c, the inverted PDF lags about  $2 \text{ m}\cdot\text{s}^{-1}$  to  $5 \text{ m}\cdot\text{s}^{-1}$  below the effective sound speed profile  $c_{eff}$  predicted by MCD. For S0981c, although the high-density region of the PDF follows the same trend as the MCD profiles, it is also below the thermodynamic sound speed profile  $c_T$ , not accounting for wind effects. Several hypotheses can be made to explain these differences:

- A variability in weather conditions along the infrasound propagation path is the most likely explanation for these differences. Indeed, the MCD profiles used in this study were measured at InSight location, 48 km to 286 km from each of the detected chirp source. On Mars, as on Earth, temperature, insolation and wind conditions may vary substantially over such a distance. Hence, the MCD profile calculated at InSight is not representative of the conditions experienced by the infrasound waves during their propagation. Instead, a model averaging the MCD wind and temperature profiles

at different points of the trajectory could provide a better idea of the true Martian atmospheric structure and its uncertainty.

- The group velocity data itself possess several sources of uncertainty. Key to the measurement of group velocity is the knowledge of the origin time  $t_0$  of an event, in our case the time of impact. The origin times presented in Table 3.1 and section 3.2.3 were calculated from the arrival times of P and S waves, with an hypothesis on the relationship between  $v_p$  and  $v_s$ . For events in the close vicinity of InSight, such as S1034a, a 1 s uncertainty in the estimation of  $t_0$  can lead to a  $1 \text{ m}\cdot\text{s}^{-1}$  difference in group velocity. However, this is less likely to impact the group velocity measurements of further events such as S0981c.
- Another possibility is the uncertainty in wind prediction by MCD climate models. MCD profiles have a resolution of a few tens of meters close to the surface. In addition, measurements of Martian wind speeds close to the surface are rare: InSight provided the longest records of wind measurements to date. Therefore, MCD models have not been validated against a wide range of observations.

Finally, we have seen that the inversion of group velocities is unable to reproduce the signal phase. To include the phase information to the inversion, some hypothesis on the phase of the source, i.e. the impact blast wave, must be made. This source can be complex, as seen from the multiple trough and nodes in the chirp spectra (Fig. 3.17). In addition, inversions of the phase of a signal are inherently complex due to the phenomenon of *cycle-skipping*: multiple models may lead to similar signals, shifted by approximately one cycle in the time domain and presenting an equally good fit to the data. Due to this phenomenon, the posterior distribution of atmospheric models inverted using the phase would likely be multimodal.

### 3.6.2 Interpretation of the subsurface inversion

Results of the subsurface inversion must be interpreted carefully. Indeed, we have shown that the posterior distribution of models fitting the chirp events H/V ratios is bimodal. The two posterior modes form two families of models:

- Family 1 (F1), is found in an inversion with large prior bounds. It presents two main features: low shear waves velocities of around  $200\text{-}300 \text{ m}\cdot\text{s}^{-1}$  down to about  $\sim 40$  m depth, followed by an increase of  $v_s$ . The values of  $v_s$  below 40 m depth are not strongly constrained.
- Family 2 (F2), is retrieved both with large and small prior bounds. Models of F2 present a layer of high shear wave velocity ( $>2000 \text{ m}\cdot\text{s}^{-1}$ ) in the uppermost part of the subsurface. The onset depth of this layer is unclear, but the posterior distribution indicates a likely lower limit of 15 m depth. This high-velocity layer transitions to a low-velocity media with  $v_s = 150 - 300 \text{ m}\cdot\text{s}^{-1}$ .

The choice of prior model bounds strongly influences the posterior probability of each mode. The existence of two possible families of solutions to the inverse problem means that either our dataset, or our prior knowledge of the subsurface bring insufficient constraints.

The dataset used in this work, i.e., the H/V ratios of coupled infrasound waves, is limited in its bandwidth. Indeed, the chirp S.N.R is greater than one only between 0.5 Hz to 2 Hz, thus bringing information on only a limited portion of the infrasound coupling process.

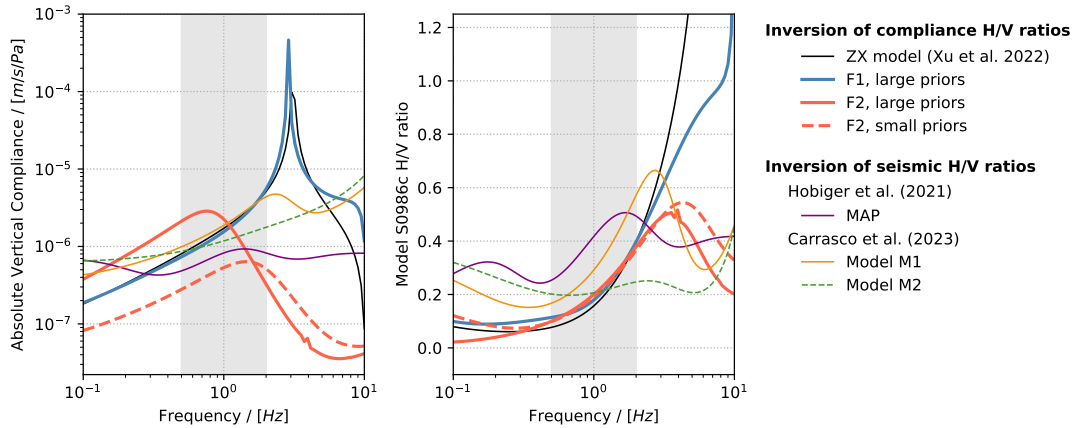


**Figure 3.30:** (left) Comparison of vertical compliance amplitude for different subsurface models. (right) Comparison of H/V ratio predicted for event S0986c with different subsurface models. Labels F1 and F2 designate compliance and  $HV$  curves calculated with typical subsurface models from families F1 and F2, depicted on Fig. 3.31. Models from the present chirp inversion are compared to models proposed by previous studies, which inverted the H/V ratio of ambient seismic noise and of Martian seismic events [Hobiger et al., 2021; Carrasco et al., 2023]. The frequency band where the chirp inversion is performed is shown in gray.

Additionally, the  $HV$  dataset is limited by its nature, as we have seen that trade-offs exist between the subsurface layer thickness and shear wave velocities. Hence, families F1 and F2 show that two distinct subsurface models can lead to similar  $HV$  curves.

Reducing these uncertainties can be done in two ways. One is to increase the bandwidth, or reduce the noise of the data. As can be seen on Fig. 3.30, although families F1 and F2 present similar  $HV$  curves between 0.5 and 2 Hz, they diverge significantly above 4 Hz. Models of type F1 tend to produce diverging  $HV$  curves at high frequency due to the presence of a Rayleigh wave, while models of type F2 peak around 4 Hz. Therefore, an increased bandwidth for the  $HV$  ratio could provide additional information on the subsurface models. Unfortunately, InSight chirp events are limited in number and the effects of atmospheric attenuation prevent the recording of high frequency coupled signal.

The second possibility is to complete the  $HV$  data with another type of data, which do not suffer from the same trade-offs. As an example, we have seen that despite their similar  $HV$  curves, model families F1 and F2 produce distinct model amplitude spectra (Fig. 3.26b). As illustrated by Fig. 3.30, this comes from the fact that F1 and F2 also produce different compliance functions  $|C_{v_z/p}(\omega)|$ . While models of family F1 present a divergence around 3 Hz, the compliance of the F2 family peaks smoothly around 1 Hz. In addition, the compliance is also variable amongst models of the F2 family, which indicates that further discrimination could be made possible by employing other datasets.

In the absence of pressure measurements for the impact infrasound, combining the event amplitude spectrum to the H/V ratio measurements could help discriminate between the shapes of different compliance functions. However, the amplitude spectrum  $|V_z(\omega)|$  of Eq. 3.14 is also a function of the source spectrum  $S(\omega)$ . Spectra displayed in the previous sections have been computed with an ideal, Dirac impulse source, but as shown in section 3.3.1 and Fig. 3.13, the spectrum of more complex gaussian or N-wave sources is not flat. Reflections on the topography along the infrasound trajectory can also lead to more spectral complexity. Hence, an inversion for the compliance function could be considered to further discriminate these models, but requires several additional hypotheses.



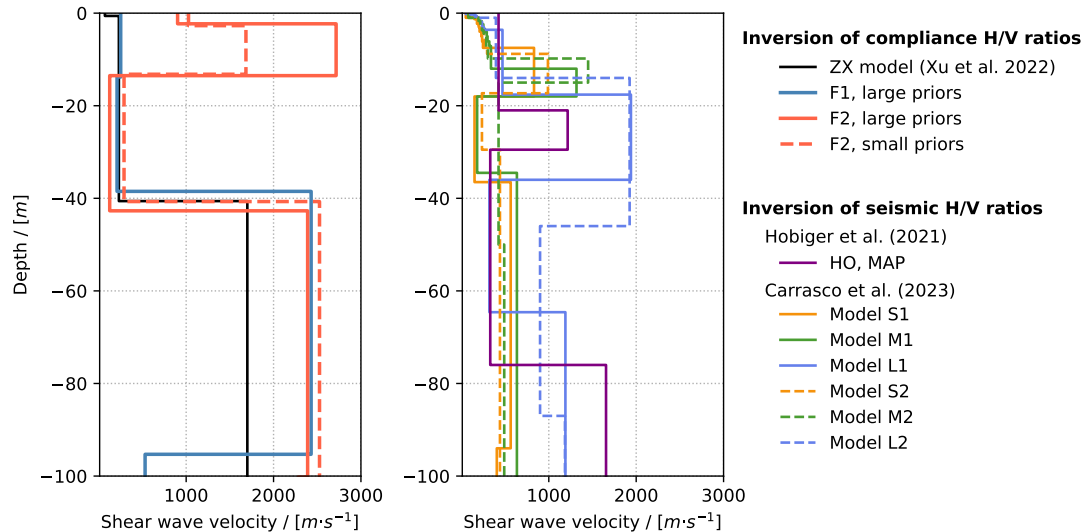


**Figure 3.31:** Comparison of various models of the shear wave velocity in the first 100 m below InSight. Models on the left have been computed using compliance H/V ratios or chirp events [Xu et al., 2022], while models on the right have been inverted from the H/V ratio of ambient seismic noise [Hobiger et al., 2021] and of seismic events [Carrasco et al., 2023].

Discriminating between the F1 and F2 family is an important challenge, which can help harmonise the results from the various inversions of the subsurface of InSight. Indeed, the studies of Hobiger et al. [2021] and Carrasco et al. [2023] mentioned in this chapter have both proposed subsurface models presenting a high-velocity layer in the first 40 m beneath InSight. This layer is associated to a possible low-velocity sedimentary layer inserted between basaltic lava flows of two distinct eras. The upper high-velocity layer would correspond to the youngest of these lava flows [Warner et al., 2017; Hobiger et al., 2021].

These subsurface profiles are shown on Fig. 3.31 for a comparison with typical models extracted from families F1 and F2. The shallow high-velocity layer in models S1, S2, M1 and M2 of Carrasco et al. [2023], and the Maximum A Posteriori model (MAP) of Hobiger et al. [2021] is analogous to the upper layer found in family F2. However, the subsurface models of Carrasco et al. [2023] and Hobiger et al. [2021] were inverted from the H/V ratio of ambient InSight events or from the ambient seismic noise, and not from seismo-acoustic data. Consequently the compliance and H/V ratio modelled for S0986c using these models differ from those of modelled with F1 and F2. More analysis is needed to reconcile these various views of InSight near-subsurface.

### 3.7 Conclusion

Impact chirp events represent a unique dataset for the InSight mission, as well as for the field of planetary seismology. This is indeed the first recording of impact-generated infrasound on another planet. In addition, the signal dispersion confirms the existence of a low-altitude Martian waveguide predicted by MCD models.

Using a 1D model of acoustic wave propagation in a layered atmosphere, we explain the dispersion of impact-generated guided infrasound. We show that this dispersion is sensitive to the evolution of effective sound velocity with altitude. Therefore, we perform an inversion of the group velocities of events S0981c, S0986c and S1034a and retrieved



atmospheric sound speed profiles in agreement with MCD predictions. This atmospheric inversion could be improved by using the information contained in the phase of each signal, provided that the phase of the source, i.e., the impact blast, is known.

The impact chirp events also form a new class of signals detected by SEIS via air-to-ground coupling, adding to dust devils and pressure vortices. The coupling of pressure perturbations into seismic ground motion can, in both case, be modelled with the compliance theory. The  $H/V$  ratio is thus simply the ration of horizontal to vertical compliance, and depends mainly on the shear wave velocity and layering in the subsurface. Based on the  $HV$  curves measured for three impact chirp events, we perform a bayesian inversion of the subsurface structure, and show that the posterior solution is multimodal and sensitive to the choice of prior model. One of the two families of models obtained presents a shallow high-velocity layer, in agreement with previous studies. However, the information contained in the chirp  $H/V$  ratio is not sufficient to further select amongst the possible subsurface structures. Combining the  $HV$  curves with additional chirp data, such as the chirp spectrum, could help narrow down the posterior model space, but requires a knowledge of the impact blast spectra at the source.

## A1 The propagator matrix method for compliance

Here, we present the analytical developments leading to a numerical method for the computation of compliance. We adopt a cartesian coordinate system, with  $\mathbf{e}_x$  the direction of propagation,  $\mathbf{e}_y$  the transverse direction, and  $\mathbf{e}_z$  pointing downwards from the ground surface. In the absence of strong topographic features, acoustic waves are not able to generate shear stress on the ground surface. SH waves are therefore prohibited. Therefore, following [Aki & Richards \[2002\]](#), we look for displacements under the surface in the form:

$$\begin{aligned} u_x &= r_1(k, z, \omega)e^{i(kx-\omega t)}, \\ u_y &= 0, \\ u_z &= ir_2(k, z, \omega)e^{i(kx-\omega t)}. \end{aligned} \quad (28)$$

$\mathbf{u} = (u_x, u_y, u_z)$  takes the form of a plane wave with propagation along  $\mathbf{e}_x$  and amplitude given by  $r_1$  and  $r_2$  depending on  $z$ .  $u_z$  is multiplied by  $i$  to convey the phase shift between horizontal and vertical motion. In the same manner, stresses  $\sigma_{zx}$  and  $\sigma_{zz}$  must be continuous with depth across interfaces, and can be expressed by:

$$\begin{aligned} \sigma_{zx} &= r_3(k, z, \omega)e^{i(kx-\omega t)}, \\ \sigma_{zz} &= ir_4(k, z, \omega)e^{i(kx-\omega t)}. \end{aligned} \quad (29)$$

Other stresses are either null or discontinuous across interfaces. Using Hooke's law, their expression can be further developed as a differential equation relating them to displacements. In matrix form, the relationship between  $r_1$ ,  $r_2$ ,  $r_3$  and  $r_4$  and their derivatives with respect to depth is:

$$\frac{d}{dz} \begin{bmatrix} r_1 \\ r_2 \\ r_3 \\ r_4 \end{bmatrix} = \begin{bmatrix} 0 & k & 1/\mu(z) & 0 \\ -k\lambda(z)/[\lambda(z) + 2\mu(z)] & 0 & 0 & 1/[\lambda(z) + 2\mu(z)] \\ k^2\zeta(z) - \omega^2\rho(z) & 0 & 0 & k\lambda(z)/[\lambda(z) + 2\mu(z)] \\ 0 & -\omega^2\rho(z) & -k & 0 \end{bmatrix} \begin{bmatrix} r_1 \\ r_2 \\ r_3 \\ r_4 \end{bmatrix}, \quad (30)$$

with  $\zeta(z) = 4\mu(z)[\lambda(z) + \mu(z)]/[\lambda(z) + 2\mu(z)]$ . In other words:

$$\frac{d\mathbf{f}(z)}{dz} = \mathbf{A}(z)\mathbf{f}(z) \quad (31)$$

with  $\mathbf{f}(z)$  a  $4 \times 1$  column vector called the *motion-stress vector*. Such equation possesses some typical solutions which are combinations of eigenvectors of  $\mathbf{A}$ . In this particular case,  $\mathbf{f}$  can be expressed as a superposition of upgoing and downgoing P- and S- waves (which can be evanescent in the case of compliance) [[Aki & Richards, 2002](#)]. This yields:

$$\mathbf{f} = \mathbf{F}\mathbf{w} = \mathbf{F} \begin{bmatrix} \dot{P} \\ \dot{S} \\ \dot{P} \\ \dot{S} \end{bmatrix} \quad (32)$$

with  $\dot{P}$ ,  $\dot{S}$  and  $\dot{P}$ ,  $\dot{S}$  the amplitude of downgoing and upgoing P- and S- waves, respectively and  $\mathbf{F}$  matrix whose columns are the base solutions of Eq. 31. The elements of  $\mathbf{F}$  are given in Eq. 7.55 of [Aki & Richards \[2002\]](#). The *propagator matrix*  $\mathbf{P}$  is a mathematical operator, function of depth  $z$  and  $z_0$ , such that :

$$\mathbf{f}(z) = \mathbf{F}(z)\mathbf{w}(z) = \mathbf{P}(z, z_0)\mathbf{f}(z_0). \quad (33)$$

This is a recursive relationship. In particular, the propagation matrix is solution to:

$$\frac{d}{dz}\mathbf{P}(z, z_0) = \mathbf{A}(z)\mathbf{P}(z, z_0), \quad (34)$$

and

$$\mathbf{P}(z, z_0)^{-1} = \mathbf{P}(z_0, z) \quad \text{and} \quad \mathbf{P}(z_0, z_0) = \mathbf{I}. \quad (35)$$

Within a single layer, between depths  $z_k$  and  $z_{k+1}$ ,  $\mathbf{A}$  is independent of  $z$  and from Eq. 34, the propagator matrix takes a simple expression:

$$\mathbf{P}(z_{k+1}, z_k) = \exp[(z_{k+1} - z_k)\mathbf{A}]. \quad (36)$$

The coefficients of  $\mathbf{P}$  are thus simply obtained by diagonalizing  $\mathbf{A}$ . In our case,  $\mathbf{A}$  has four eigenvalues,  $\pm\gamma = \pm\sqrt{k^2 - \omega^2/v_p^2}$  and  $\pm\nu = \pm\sqrt{k^2 - \omega^2/v_s^2}$ , and the sixteen coefficients of  $\mathbf{P}$  are given in Eq. 7.45 of Aki & Richards [2002]. Using this propagation matrix, the wavefield in the deepest layer of our model can be obtained from the product of propagator matrices of all superior layers, and the wavefield at the surface:

$$\mathbf{f}(z_N) = \mathbf{F}(z_N)\mathbf{w}(z_N) = \mathbf{P}(z_N, z_{N-1}) \dots \mathbf{P}(z_2, z_1)\mathbf{P}(z_1, z_0)\mathbf{f}(z_0) \quad (37)$$

We reverse this expression, taking advantage of Eq. 35:

$$\mathbf{f}(z_0) = \mathbf{P}(z_0, z_1)\mathbf{P}(z_1, z_2) \dots \mathbf{P}(z_{N-1}, z_N)\mathbf{F}(z_N)\mathbf{w}(z_N) = \mathbf{B}\mathbf{F}(z_N)\mathbf{w}(z_N). \quad (38)$$

In the case of compliance of the ground to a pressure perturbation, we know that no source of wavefield or reflections can exist in the bottom layer. In fact, it is considered a halfspace, with amplitudes  $\dot{P} = 0$  and  $\dot{S} = 0$ . Therefore, Eq. 38 can be simplified and written only as a function of downgoing P- and S- waves in the bottom halfspace:

$$\mathbf{f}(z_0) = \mathbf{B} \left[ \mathbf{F}^P(z_N)\dot{P}(z_N) + \mathbf{F}^S(z_N)\dot{S}(z_N) \right], \quad (39)$$

with  $\mathbf{F}^P(z_N)$  and  $\mathbf{F}^S(z_N)$  the first and second column of matrix  $\mathbf{F}$  in the halfspace. In the same way, we can write according to boundary conditions:

$$\mathbf{f}(z_0) = \mathbf{f}(z=0) = \begin{bmatrix} u_x(z=0, t) \\ u_z(z=0, t) \\ 0 \\ P \end{bmatrix}. \quad (40)$$

We can see that the shear stresses  $\sigma_{zx}$  must always be zero in the top layer. This brings a condition on the amplitude of P- and S- waves in the bottom halfspace. We get:

$$\dot{S}(z_N) = -\frac{BF_3^P}{BF_3^S}\dot{P}(z_N) = q\dot{P}(z_N), \quad (41)$$

where 3 denotes the third element of the  $4 \times 1$  matrix product of  $\mathbf{B}$  and  $\mathbf{F}^{P/S}$ . The new expression of  $\mathbf{w}$  is  $\mathbf{w} = [1, q, 0, 0]$ . Finally, the vertical and horizontal compliance are expressed by:

$$C_{x/p} = i \frac{[B(\mathbf{F}^P + q\mathbf{F}^S)]_1}{[B(\mathbf{F}^P + q\mathbf{F}^S)]_4}, \quad (42)$$

$$C_{z/p} = -\frac{[B(\mathbf{F}^P + q\mathbf{F}^S)]_2}{[B(\mathbf{F}^P + q\mathbf{F}^S)]_4},$$

in terms of displacements and

$$\begin{aligned} C_{v_x/p} &= -\omega \frac{[B(F^P + qF^S)]_1}{[B(F^P + qF^S)]_4}, \\ C_{v_z/p} &= -i\omega \frac{[B(F^P + qF^S)]_2}{[B(F^P + qF^S)]_4}, \end{aligned} \quad (43)$$

in terms of velocities. In the theory of Sorrells [1971], the material is considered to be composed of only a halfspace, such that  $\mathbf{f}(z_0) = \mathbf{F}(z_N)\mathbf{w}(z_N)$ . Further approximations are made, considering that the pressure perturbation propagates at  $c_s \ll v_s$  and its frequency is also low:  $\omega z \ll 2v_s^2/c_s$ . These quasi-static approximations lead to a simple expression for displacement compliance, in terms of Lamé constants  $\lambda$  and  $\mu$  and seismic velocities:

$$\begin{aligned} C_{x/p} &= \frac{i}{k_x} \frac{1}{2(\lambda + \mu)} = \frac{i}{2\rho k_x} \frac{1}{v_p^2 - v_s^2} \\ C_{z/p} &= \frac{-1}{2k_x} \frac{\lambda + 2\mu}{\mu(\lambda + \mu)} = \frac{-1}{2\rho k_x} \frac{v_p^2}{v_s^2(v_p^2 - v_s^2)}. \end{aligned} \quad (44)$$

## A2 The propagator matrix method for guided infrasound

We present the adaptation of the propagator matrix method to a guided plane pressure wave in the atmosphere. Contrary to the solid media considered in Appendix A1, the atmosphere is not able to sustain shear waves. Stresses are therefore purely described by a pressure perturbation:

$$P = p(k, z, \omega)e^{i(kx - \omega t)}, \quad (45)$$

with  $x$  the direction of propagation of a plane wave in the waveguide and  $k$  its horizontal wave number. Velocity perturbations  $\mathbf{V} = (v_x, v_y, v_z)$  generated by the pressure wave are expressed by:

$$\begin{aligned} V_x &= v_x(k, z, \omega)e^{i(kx - \omega t)}, \\ V_y &= 0, \\ V_z &= v_z(k, z, \omega)e^{i(kx - \omega t)}. \end{aligned} \quad (46)$$

At low frequency, thermal gradients and heat transfer created by the acoustic wave are small, therefore the propagation of sound can be considered adiabatic and modelled using the Euler equations for compressible fluids :

$$\begin{aligned} D_t \rho &= -\rho(\nabla \cdot \mathbf{v}), \\ D_t \mathbf{v} &= -\frac{\nabla p}{\rho} + \mathbf{g}, \\ D_t e &= -\frac{p}{\rho}(\nabla \cdot \mathbf{u}), \end{aligned} \quad (47)$$

where  $\rho$  is the density of the air,  $e$  its internal energy per unit mass, and  $D_t$  the material derivative, taking into account the transport due to pre-existing winds and currents. Here, following the analysis of Xu et al. [2022], we ignore wind inertial effects. Considering the Bulk modulus of the fluid,  $K = \rho \frac{dp}{d\rho} = \rho \alpha^2$ , and using cartesian coordinates in 2D, we obtain the following relationship between  $p$ ,  $v_x$  and  $v_y$ :

$$\begin{aligned} \partial_t p &= -K(\partial_x v_x + \partial_z v_z), \\ \partial_x p &= -\rho \partial_t v_x, \\ \partial_z p &= -\rho \partial_t v_z. \end{aligned} \quad (48)$$

with  $\partial_t$ ,  $\partial_x$  and  $\partial_z$  representing the first derivatives over time and cartesian spatial coordinates. We recall that both  $\rho$  and  $\alpha$  define the structure of the atmosphere and are varying with altitude. We finally add to equation 48 a set of boundary conditions - the rigid surface condition, such that:

$$v_z(z = 0) = 0. \quad (49)$$

In the frequency domain, the system of Equation 48 can be put into matrix form. We note that  $v_x = \frac{kp}{\rho\omega}$ , which simplifies system 48 into :

$$\partial_z \begin{bmatrix} p \\ v_z \end{bmatrix} = \begin{bmatrix} 0 & -i\omega\rho \\ \frac{i}{\rho\omega} \left( k^2 - \frac{\omega^2}{\alpha^2} \right) & 0 \end{bmatrix} \begin{bmatrix} p \\ v_z \end{bmatrix}. \quad (50)$$

As in Appendix A1, we recognise the vector  $\mathbf{f} = [p, v_z]$  as the *motion-stress vector*, leading to the first-order partial differential relation  $\partial_z \mathbf{f} = \mathbf{A}\mathbf{f}$ . At  $z \rightarrow +\infty$ , both  $p$  and  $v_z$  must vanish in the absence of an active source. Considering a constant sound speed  $\alpha_\infty$  above the waveguide at  $z > z_{top}$ , the converging solutions of Eq. 50 are:

$$\begin{aligned} p(\omega, z) &= e^{-\sqrt{k^2 - \frac{\omega^2}{\alpha_\infty^2}} z}, \\ v_z(\omega, z) &= -\frac{i}{\omega\rho_\infty} \sqrt{k^2 - \frac{\omega^2}{\alpha_\infty^2}} e^{-\sqrt{k^2 - \frac{\omega^2}{\alpha_\infty^2}} z} \quad \text{for } z > z_{top}. \end{aligned} \quad (51)$$

For a certain value of  $c$ , iterative methods can be used to solve the Eq. 50 downward from  $z = z_{top}$  to  $z = 0$ . The true solution for guided wave must ensure that  $\mathbf{f}[2](z = 0) = v_z(z = 0) = 0$ , in accordance with the boundary conditions Eq. 49, which is possible only for certain values of  $c$ . Finding the solutions for vectors  $\mathbf{f}$  is therefore essentially both an integration problem and a root-finding problem. The integration problem is  $\partial_z \mathbf{f}(z) = \mathbf{A}(z)\mathbf{f}(z)$ , which can be solved by a classic Runge-Kutta method for any continuous sound speed profile  $\alpha(z)$  and density profile  $\rho(z)$ , or with the propagator matrix method for simplified "staircase" profiles. The root-finding problem is  $\mathbf{f}[2](c, z = 0) = 0$ , which can be solved by a Newton-Raphson method.

As in Appendix A1, the propagator matrix  $P(z, z_0)$  in a layer with constant sound speed and density can be obtained from a diagonalization of matrix  $\mathbf{A}$ . Eigenvalues of  $\mathbf{A}$  are:

$$\pm \gamma = \pm \sqrt{k^2 - \frac{\omega^2}{\alpha_n^2}}, \quad (52)$$

and matrix  $\mathbf{V}$  containing its two eigenvectors is:

$$\mathbf{V} = \begin{bmatrix} 1 & 1 \\ -\frac{\gamma}{i\omega\rho_n} & \frac{\gamma}{i\omega\rho_n} \end{bmatrix}, \quad (53)$$

which leads to the following expression of  $P(z, z_0)$ :

$$\begin{aligned} P(z, z_0) &= e^{\mathbf{A}(z-z_0)} = \mathbf{V} e^{\mathbf{S}(z-z_0)} \mathbf{V}^{-1} \\ &= \begin{bmatrix} \cosh[\gamma(z-z_0)] & \frac{\omega\rho_n}{i\gamma} \sinh[\gamma(z-z_0)] \\ \frac{i\gamma}{\omega\rho_n} \sinh[\gamma(z-z_0)] & \cosh[\gamma(z-z_0)] \end{bmatrix}. \end{aligned} \quad (54)$$

The expression of  $\mathbf{f}(z = 0) = \mathbf{f}(z_0)$  is therefore:

$$\mathbf{f}(z_0, c) = \mathbf{P}(z_0, z_1) \mathbf{P}(z_1, z_2) \dots \mathbf{P}(z_{top-1}, z_{top}) \mathbf{f}(z_{top}, c). \quad (55)$$

The expression of the derivative of  $\mathbf{f}$  with respect to phase velocity,  $\frac{d\mathbf{f}}{dc}$ , is also needed by the Newton-Raphson method. Its recursive expression is:

$$\frac{d\mathbf{f}}{dc}(z_{n+1}, c) = \frac{d\mathbf{P}}{dc}(z_{n+1}, z_n, c)\mathbf{f}(z_n, c) + \mathbf{P}(z_{n+1}, z_n, c)\frac{d\mathbf{f}}{dc}(z_n, c). \quad (56)$$

Multiple roots  $c_n$  may be found with the Newton-Raphson methods: these roots define modes of propagation with increasing phase velocity.

### A3 Test of different McMC implementations

We implemented an inversion of chirp group velocity and H/V ratio using three different methods: the `emcee` sampler [Foreman-Mackey et al., 2013], the `ptmcmc` sampler [Ellis & van Haasteren, 2017] and an in-house implementation of parallel tempering following the algorithm of Sambridge [2014]. Both `emcee` and `ptmcmc` require to run multiple chains in parallel, which is done with Python `multiprocessing` module for `emcee` and the `open MPI` library for `ptmcmc`. We parallelised our in-house implementation of McMC referred to as `mymcmc`, using `multiprocessing` by running the tempering step in series and several independent chains in parallel.

A comparison of these methods was performed using the same synthetic models as presented in sections 3.4.1 and 3.5.1. The posterior distributions of atmospheric and subsurface models were inverted with the `emcee`, `ptmcmc` and `mymcmc` to measure their computational efficiency and convergence time.

Curves representing the convergence of the autocorrelation time with increasing iterations are shown on Fig. 32a for the atmospheric inversion and on Fig 33a for the subsurface inversion. The `ptmcmc` and `mymcmc` method both converge to an autocorrelation time of around 200 for the atmosphere and 1000 for the subsurface, while `emcee` shows higher number for 20 parallel samplers. The total run time of both simulations were measured and reported on Table 3. When accounting for the total number of iterations run over 10 CPUs, the `mymcmc` method seems to provide a higher number of uncorrelated samples faster, with around 2.3 h for 1000 independent samples.

All three methods provide consistent posterior probability distribution of models and layer positions. Fig. 32b (resp. 33b) shows the histogram of interface height (resp. depth) retrieved by the atmospheric (resp. subsurface) inversion. The results for the three inversion methods are almost undistinguishable. In the same way, Fig. 34 and 35 show the posterior probability density distribution (PDF) of models for both inversions. Again, these distributions are similar and align well with the input model.

**Table 3:** Computational cost and convergence of a synthetic inversion using the Ensemble Sampler emcee, the Parallel Tempering implementation ptmcmc and an in-house implementation (mymcmc).

Method	emcee	ptmcmc	mymcmc
Number of CPUs used	10	10	10
Total number of iterations performed (all chains)	$10 \times 10^6$	$1 \times 10^6$	$5 \times 10^6$
<b>Atmospheric inversion</b>			
Run time in hours	17	10.7	18.5
Autocorrelation time $\tau_c$	3000	200	200
Estimated time for 1000 independent samples (hrs)	5	2	1
<b>Subsurface inversion</b>			
Run time in hours	9	3.6	11.5
Autocorrelation time $\tau_c$	4000	1000	1000
Estimated time for 1000 independent samples (hrs)	3.6	3.6	2.3

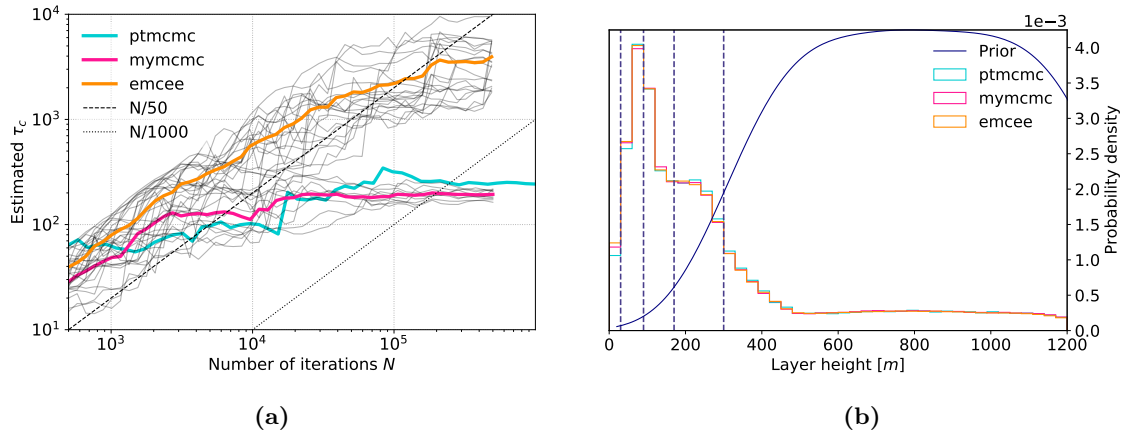


**Figure 32:** (left) Autocorrelation time estimated during the MCMC inversion of a synthetic group velocity curve for S0986c, run with three different methods. (right) Histogram of the layer heights inverted for the atmospheric structure.

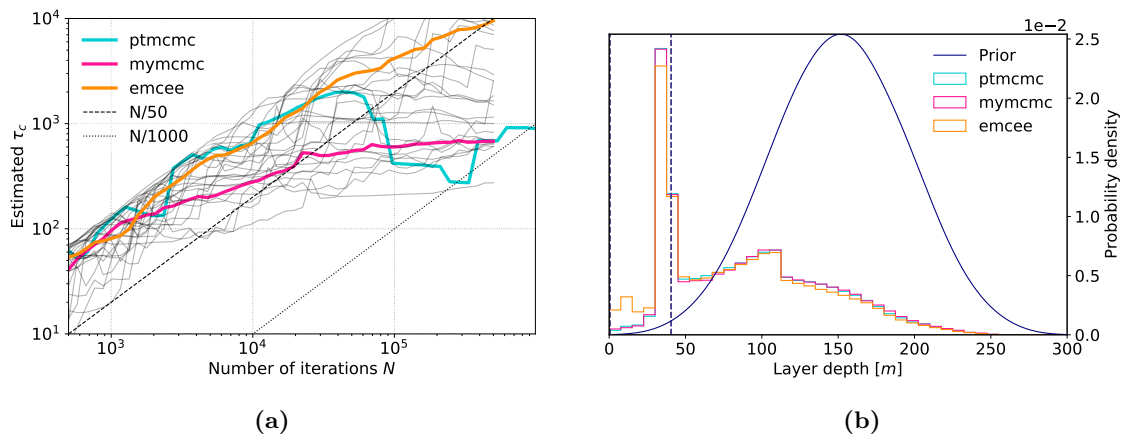


**Figure 33:** (left) Autocorrelation time estimated during the MCMC inversion of three synthetic H/V ratio curves, run with three different methods. (right) Histogram of the layer depths inverted for the subsurface structure.



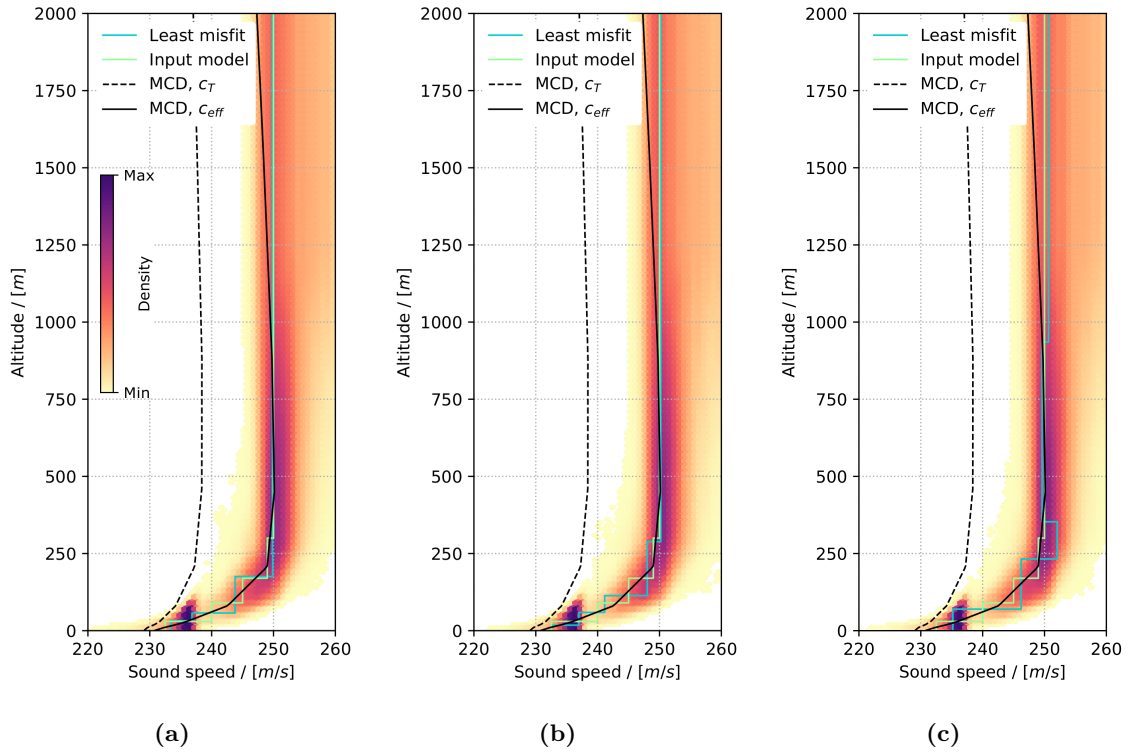


**Figure 34:** Posterior probability density of atmospheric models inverted from a synthetic group velocity curve obtained from MCD profile for S0986c, with the `emcee` (a), `ptmcmc` (b) and `mymcmc` (c) methods. The color scale is indicative.

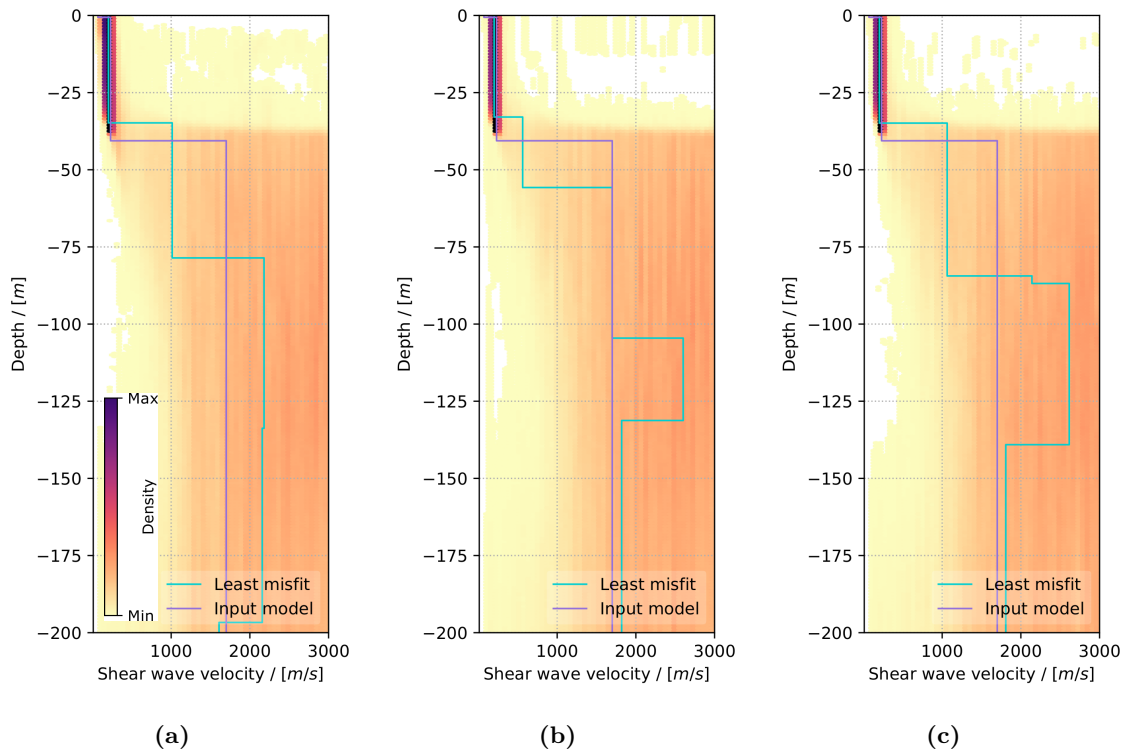


**Figure 35:** Posterior probability density of subsurface models inverted from synthetic H/V ratio curves with the `emcee` (a), `ptmcmc` (b) and `mymcmc` (c) methods. The color scale is indicative, as in Fig. 34.



## Modeling Seismic Recordings of High-Frequency Guided Infrasond on Mars



### Key Points:

- We analytically compute the dispersion relationship of guided infrasond in 1D atmospheric models from Mars and Earth
- We model the ground response to guided infrasond to fit the corresponding seismic observation due to meteorite impacts on Mars
- We utilize the seismic recording due to guided infrasond to constrain the subsurface structures

### Supporting Information:

Supporting Information may be found in the online version of this article.

### Correspondence to:

Z. Xu,  
zongboxu@ipgp.fr

### Citation:

Xu, Z., Froment, M., Garcia, R. F., Beucler, É., Onodera, K., Kawamura, T., et al. (2022). Modeling seismic recordings of high-frequency guided infrasond on Mars. *Journal of Geophysical Research: Planets*, 127, e2022JE007483. <https://doi.org/10.1029/2022JE007483>

Received 14 JUL 2022  
Accepted 1 NOV 2022

Zongbo Xu<sup>1</sup> , Marouchka Froment<sup>1,2</sup>, Raphaël F. Garcia<sup>3</sup> , Éric Beucler<sup>4,5</sup> , Keisuke Onodera<sup>6</sup>, Taichi Kawamura<sup>1</sup>, Philippe Lognonné<sup>1</sup> , and William Bruce Banerdt<sup>7</sup> 

<sup>1</sup>Université Paris Cité, Institut de physique du globe de Paris, CNRS, Paris, France, <sup>2</sup>Earth and Environmental Sciences Division, Los Alamos National Laboratory, Los Alamos, NM, USA, <sup>3</sup>Institut Supérieur de l'Aéronautique et de l'Espace (ISAE-SUPAERO), Université de Toulouse, Toulouse, France, <sup>4</sup>Nantes Université, Université Angers, Le Mans Université, CNRS, UMR 6112, Laboratoire de Planétologie et Géosciences, Nantes, France, <sup>5</sup>Nantes Université, UGE, Univ Angers, CNAM, CNRS, UAR 3281, Observatoire des sciences de l'univers Nantes Atlantique, Nantes, France, <sup>6</sup>Earthquake Research Institute, The University of Tokyo, Tokyo, Japan, <sup>7</sup>Jet Propulsion Laboratory, California Institute of Technology, Pasadena, CA, USA

**Abstract** NASA's Interior Exploration using Seismic Investigations, Geodesy and Heat Transport (InSight) mission records several high-frequency (>0.5 Hz) dispersive seismic signals on Mars. These signals are due to the acoustic-to-seismic coupling of infrasond generated by the entry and impact of meteorites. This dispersion property is due to infrasond propagating in a structured atmosphere, and we refer to this dispersive infrasond as guided infrasond. We propose to model the propagation of guided infrasond and the seismic coupling to the ground analytically; we use a 1D layered atmosphere on a three-layer solid subsurface medium. The synthetic ground movements fit the observed dispersive seismic signals well and the fitting indicates that the regolith beneath InSight is about 40-m in thickness. We also examine and validate the previously-published subsurface models derived from InSight ambient seismic vibration data.

**Plain Language Summary** Under particular weather conditions, the Martian atmosphere displays a special sound-wave velocity profile, where the wave velocity becomes larger with increasing altitude within a few hundred meters. When an infrasond signal—a low-frequency (<20 Hz) sound wave inaudible to humans—propagates through such a structure, the infrasond exhibits dispersion: its propagation velocity depends on its frequency. We refer to such infrasond as guided infrasond. Guided infrasond can deform the ground, and have been recorded by the seismometer of NASA's Interior Exploration using Seismic Investigations, Geodesy and Heat Transport (InSight) mission on the Martian surface. We propose to model these recordings using the physics of sound waves traveling above a compliant solid ground. We show that our modeling results can fit well the seismic recordings of guided infrasond on Mars. We apply our modeling to the subsurface models from a different InSight seismic observation to check if these models can explain our seismic recordings. This modeling constitutes a new tool to investigate the subsurface structure of Mars, and is also useful for the investigation of Titan and Venus.

## 1. Introduction

NASA's InSight (Interior Exploration using Seismic Investigations, Geodesy and Heat Transport) mission landed on the Martian surface in November 2018 and has since been conducting geophysical and meteorological observation (Banerdt et al., 2020). To achieve its objectives, InSight is equipped with a Very Broad Band (VBB) and a Short Period (SP) seismometer, which together constitute the SEIS (Seismic Experiment for Internal Structure) instrument (Lognonné et al., 2019). SEIS is operated in combination with a weather station, Auxiliary Payload Sensor Suite (APSS) including an atmospheric pressure sensor and wind and temperature sensors, to perform meteorological observation (Banfield et al., 2019). Due to power issues appearing in the second Martian year of the mission, SP and APSS have become temporarily unavailable, and VBB has been kept on most of the time. Thus only the VBB seismic data is available for analyzing the seismic events in this study.

The ground motion recorded by InSight originates from different types of sources, most of which are marsquakes (e.g., Giardini et al., 2020) or atmospheric seismic events like pressure drops (e.g., Lognonné et al., 2020). The recent seismic recordings provides a new type of seismic events, a dispersive wave train following a typical very-high-frequency marsquake (Clinton et al., 2021), where a dispersive wave train means that the wave velocity,

© 2022. The Authors.

This is an open access article under the terms of the [Creative Commons Attribution-NonCommercial-NoDerivs License](https://creativecommons.org/licenses/by-nc-nd/4.0/), which permits use and distribution in any medium, provided the original work is properly cited, the use is non-commercial and no modifications or adaptations are made.

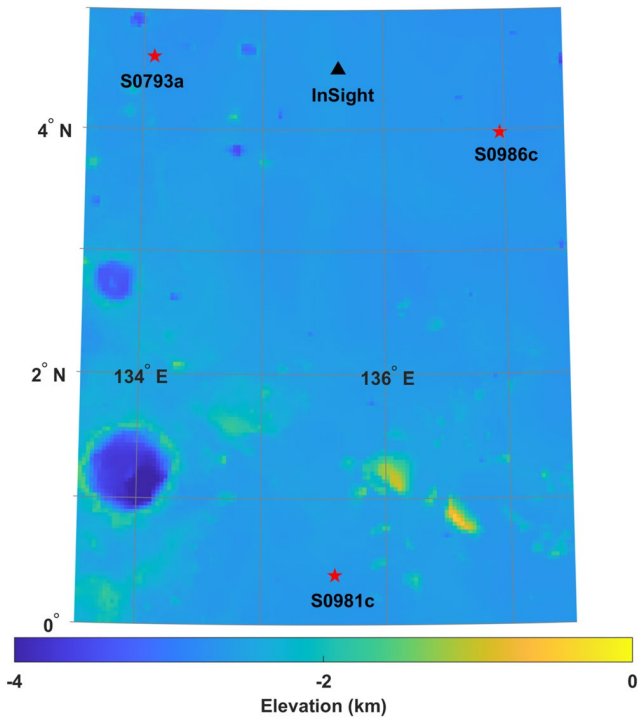


**Figure 1.** Topography map (Smith et al., 2001) of the Martian surface around InSight and three impact locations (S0793a, S0981c, and S0986c). The impact locations are constrained by CTX images (Garcia et al., 2022).

also arrival time, depends on frequency. This wave train appears about a few hundred of seconds after the P arrivals, such as in events S0793a, S0981c, and S0986c. Based on analysis of seismic arrival times and satellite imagery, Garcia et al. (2022) demonstrate that these events are generated by meteorite impacts on the Martian surface (Figure 1). Thus, the high-frequency seismic energy arriving before the dispersive waves is due to the meteorite cratering process (Figure 2a).

The meteors not only generate the craters but also interact with the Martian atmosphere during entry and impacting, which generates infrasound, that is, acoustic waves with a frequency lower than 20 Hz (Figure 2). The infrasound propagation medium—the atmosphere—can exhibit a particular structure, where the infrasound propagation velocity is smaller near the ground surface than at higher altitudes (about a few hundred meters). In such structures, multiple infrasound propagation paths interfere with each other, and the interference generates dispersion (Herrin et al., 2006; Negraru & Herrin, 2009), similar to the mechanism of Love waves in seismology (e.g., Aki & Richards, 2002). This infrasound velocity model in Earth is referred to as nocturnal boundary layer in acoustic-wave literature (e.g., Waxler, 2004), since such a model is usually generated when the temperature on the ground surface decreases at night, leading to a cooling of the lower atmosphere. This phenomenon is common on Mars due to the quick cooling down of the Martian surface at night and/or high-altitude winds (e.g., Garcia et al., 2017). In this study, we refer to this atmospheric structure as a waveguide, and we refer to the interfered infrasound waves as guided infrasound. Guided infrasound can be simulated numerically by solving the acoustic wave equations (e.g., Garcia et al., 2017; Martire et al., 2020). This numerical simulation approach can address complicated atmospheric models like a laterally heterogeneous atmosphere with winds, but is computationally expensive. One can

also model the guided infrasound waveform analytically by calculating the phase/group velocity (i.e., dispersion) within a laterally-homogeneous two-layer atmospheric model (Negraru & Herrin, 2009). This analytical approach is much faster and less computationally expensive than the numerical simulation, and is therefore well suited to explore different atmospheric parameters and their associated guided infrasound. However, former studies remain limited to two-layer atmospheric models. In this study, we extend this analytical approach to a multiple-layer model using the propagation matrix method described in seismic surface-wave studies (e.g., Aki & Richards, 2002). Note that in this study we focus on the high-frequency guided infrasound, while on Earth, the low-frequency ( $<0.02$  Hz) guided infrasound also exists (e.g., Harkrider, 1964; Pekeris, 1948; Press & Harkrider, 1962).

We use the VBB seismic data (InSight Mars SEIS Data Service, 2019a, 2019b) to study guided infrasound observed on Mars, because infrasound propagates with atmospheric perturbations and the perturbations deform the ground (e.g., Sorrells, 1971; Tanimoto & Wang, 2019). One has observed this type of coupling due to atmospheric pressure drops through seismic recordings on both Earth and Mars (e.g., Kenda et al., 2020; Lognonné et al., 2020; Lorenz et al., 2015). Furthermore one also observes infrasound deforming Earth's ground surface due to acoustic sources such as volcanic activities (e.g., Ichihara et al., 2012), meteors (e.g., Edwards et al., 2008), and ground surface explosions (e.g., Gibbons et al., 2007; Schneider et al., 2018). Conversion of an atmospheric pressure perturbation into ground deformation is called compliance, and the intensity of compliance is determined by the subsurface structure and the propagation velocity of the perturbation (e.g., Ben-Menahem & Singh, 2012; Ewing et al., 1957; Sorrells et al., 1971). We detail computation of compliance in Section 3.

We propose to analytically model the seismic recordings due to guided infrasound, and we refer to the recordings as chirps. We demonstrate computation of the guided infrasound phase and group velocities in multiple-layer atmospheric models (Section 2). We then introduce the compliance and our subsurface velocity model (Section 3). We combine the guided infrasound and the compliance to generate a synthetic chirp; we use the synthetic chirp to fit the observed ones (Section 4). We finally discuss the implication of our modeling to the previously-published subsurface models and the infrasound propagation in the Martian atmosphere (Section 5). Our research can aid

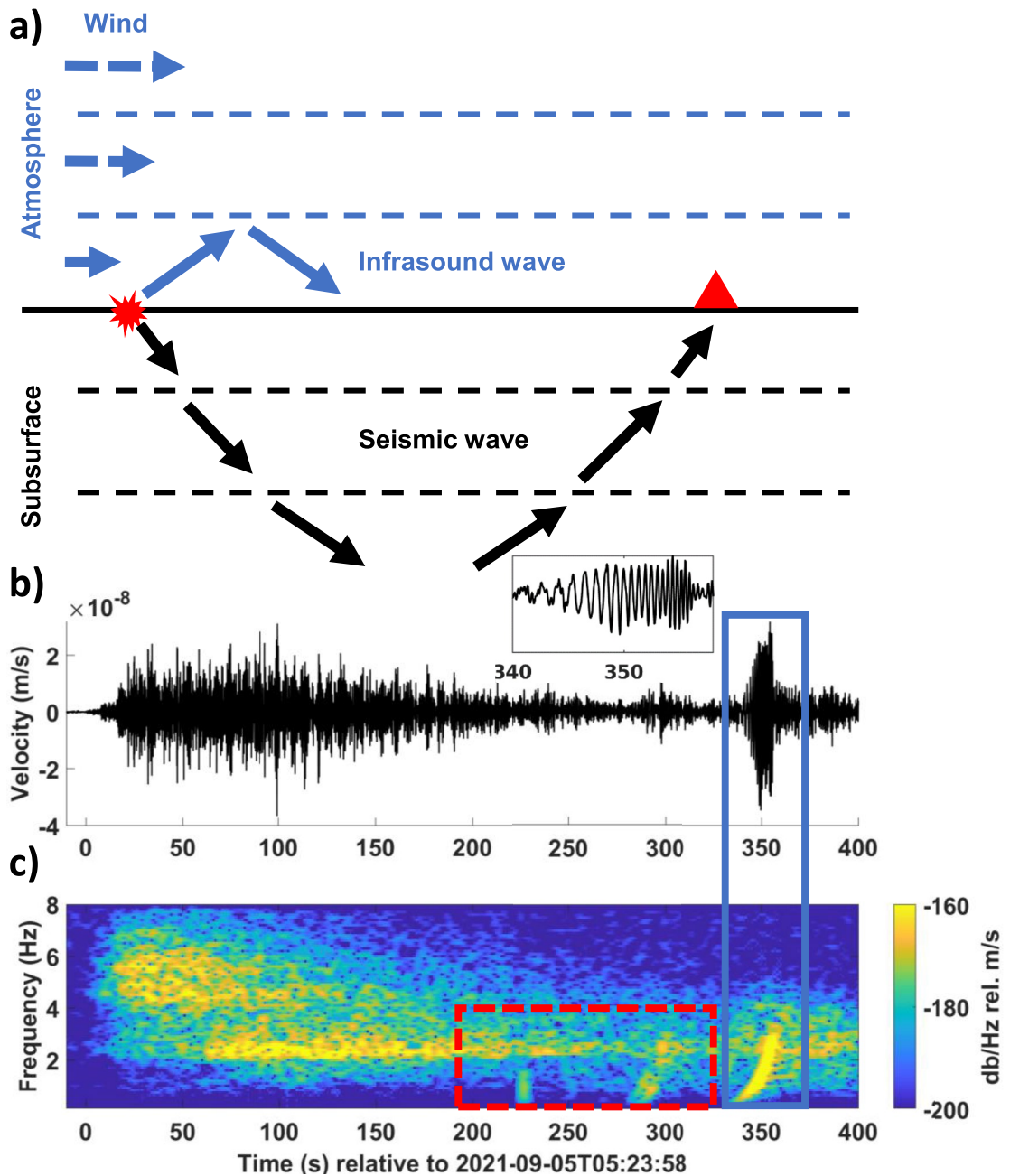


**Figure 2.** Illustration of the S0986c event (a) and data (b and c). (a) The meteor of the S0986c impact interacts with the Martian subsurface and atmosphere, generating seismic waves (from 0 to about 200 s in panel (b)) and infrasound (after 200 s in panel (b)), respectively. The vertical scales of the atmosphere and the subsurface are in hundred meter and kilometer, respectively. (b) The S0986c VBB vertical-component data. The data is bandpass filtered between 0.1 and 8 Hz. The insert shows a zoom of the chirp in the blue box. (c) Spectrogram of the data in panel (b). The blue box indicates the chirp spectrogram. The red box indicates other arrivals of infrasound energy. The time axis is in Coordinated Universal Time.

the investigation of atmospheric and subsurface properties, not only on Mars and Earth but also on other bodies with atmosphere such as Titan and Venus.

## 2. Modeling Guided Infrasond

### 2.1. Theory

We solve the dispersion of the guided infrasond in a multiple-layer atmospheric model theoretically. We present an example of the Martian guided infrasond in this section and an Earth example in Appendix A. We assume the atmosphere to be adiabatic, which leads to the following 2D governing equations:

$$-\partial_z p = \rho D_t v_z, \quad (1)$$

$$-\partial_x p = \rho D_t v_x, \quad (2)$$

$$-D_t p = K (\partial_z v_z + \partial_x v_x), \quad (3)$$

where  $\partial_z$  denotes the partial derivative with respect to altitude ( $z$ ),  $p$  is the atmospheric pressure perturbation conveyed by the infrasond wave,  $\rho$  is the air density, and  $K$  is the incompressibility;  $v_z$  and  $v_x$  are the particle velocities in the vertical and horizontal directions, respectively.  $D_t$  denotes the material derivative with respect to time. Indeed, the advection of momentum cannot be ignored here, as the horizontal wind velocity ( $w_x$ , Tables S1–S3 in Supporting Information S1) can reach up to about 15 m/s on the Martian surface. The effect of  $w_x$  is made explicit by rewriting the above equations as:

$$-\partial_z p = \rho (\partial_t + w_x \partial_x) v_z, \quad (4)$$

$$-\partial_x p = \rho (\partial_t + w_x \partial_x) v_x, \quad (5)$$

$$-(\partial_t + w_x \partial_x) p = K (\partial_z v_z + \partial_x v_x). \quad (6)$$

Since in the three impact events, the cross winds deviate the infrasond propagation direction by less than 5° (Garcia et al., 2022), we neglect the cross wind effect and project the total wind speed to the guided infrasond propagation direction to achieve  $w_x$ . Besides the above equations, a set of boundary conditions is also needed. We adopt a rigid ground surface, such as:

$$v_z(z = 0) = 0. \quad (7)$$

Note that one may choose an elastic ground-surface boundary condition and then the right hand side of the above equation would not be zero anymore (e.g., Waxler, 2002). We justify our rigid boundary condition in Section 5.3. We use the radiation boundary condition for the top boundary. The 2D geometry assumed here is a good approximation for a real 3D geometry only if the cross-wind can be neglected (e.g., Nijs & Wapenaar, 1992). Other second-order factors are not considered here, such as the effect of static pressure or gravity (e.g., Pierce, 1990).

We compute the guided infrasond phase velocities by solving the above equations (Equations 4–6) and the boundary conditions (e.g., Equation 7). One can adopt normal mode expansion to solve the equations, and Assink (2012) presents a complete review of this approach mathematically. However, this approach is not designed specifically for guided infrasond and is built on an elastic boundary condition, instead of our rigid one (Equation 7). Thus, we propose a simpler method. We assume that guided infrasond propagates horizontally as a plane wave:

$$p = P(\omega, z) \exp(i(\omega t - kx)), \quad (8)$$

$$v_z = V_z(\omega, z) \exp(i(\omega t - kx)), \quad (9)$$

$$v_x = V_x(\omega, z) \exp(i(\omega t - kx)), \quad (10)$$

where  $\omega$  is the angular frequency,  $z$  is altitude,  $t$  is the propagation time,  $k$  is the horizontal wavenumber, and  $x$  is the propagation distance. Note that  $\omega/k$  gives the phase velocity. Based on Equations 5, 8 and 10, we notice that

$$V_x = \frac{kP}{\rho(\omega - w_x k)}. \quad (11)$$



We then rewrite the governing equations in a matrix form as

$$\partial_z \begin{bmatrix} P \\ V_z \end{bmatrix} = \begin{bmatrix} 0 & -i(\omega - w_x k) \rho \\ -i\omega/\alpha^2/\rho + iw_x k/\rho/\alpha^2 + ik^2/(\omega - w_x k)/\rho & 0 \end{bmatrix} \begin{bmatrix} P \\ V_z \end{bmatrix}, \quad (12)$$

where  $\alpha$  is the infrasound velocity, and  $\alpha^2 = K/\rho$ . Note that Press and Harkrider (1962) and Nijs and Wapenaar (1990) have achieved similar equations as Equation 12. Press and Harkrider (1962) study the low-frequency (<0.02 Hz) guided infrasound considering gravity, and Nijs and Wapenaar (1990) study acoustic wave propagation and do not consider the guided infrasound.

We use the propagation matrix method (e.g., Aki & Richards, 2002) to solve Equation 12. This equation is in the form of  $\partial_z \vec{f} = \mathbf{A} \vec{f}$ , where  $\vec{f}$  is normally referred to as eigenfunctions and  $\vec{f}$  here contains  $P$  and  $V_z$ . The propagation matrix is defined as  $\mathbf{M}(z, z') = \exp[(z - z')\mathbf{A}]$  between two altitudes,  $z$  and  $z'$ . We use  $\mathbf{M}$  to calculate the eigenfunctions at  $z$  from  $z'$  as

$$\vec{f}(z) = \mathbf{M}(z, z') \vec{f}(z'). \quad (13)$$

We observe that Equation 13 intuitively satisfies Equation 12. For a 1D atmospheric model, with a right phase velocity (i.e.,  $\omega/k$ ) at frequency  $\omega$ , we can calculate the eigenfunctions at all altitudes, and the eigenfunction values on the ground surface would satisfy the boundary condition (Equation 7). The computation is detailed in Section S1 in Supporting Information S1. Based on the phase velocity, we can also compute the group velocity as the variation of  $\omega$  over the variation of  $k$  (e.g., Aki & Richards, 2002).

## 2.2. S0986c Guided Infrasound

We use an atmospheric model of Mars to illustrate the eigenfunctions and the group velocities of the S0986c guided infrasound (Figure 3). We adopt the atmospheric model parameters (acoustic-wave velocity, wind speed, air density, and altitude) from the Mars Climate Database (MCD; Millour et al., 2018). We project the wind speed along the backazimuth of SEIS with regards to the S0986c impact location (Figure 1 and Table S3 in Supporting Information S1); the cross wind of this event atmospheric model does not obviously affect the infrasound propagating from the impact location to InSight (Garcia et al., 2022). Note that MCD models the Martian climate at a global scale and could be biased at local scale like our cases. Thus, we modify the acoustic-wave velocity by fitting the synthetic group velocity to the measurement from the chirp (Garcia et al., 2022). We add (subtract) a constant value to (from) acoustic-wave velocities at all altitudes, which moves the whole synthetic group-velocity curve up (down) but does not change the synthetic group-velocity shape (Figure 3c). The sum of the projected wind speed and the modified acoustic-wave velocity is called the effective velocity (Figure 3a). The effective velocity of this event increases gradually with altitude until about 500 m and then decreases slightly. We discretize the wind speed and the acoustic-wave velocity to form a 1D layered model, and then compute the phase velocity (Figure 3c) and the atmospheric pressure eigenfunctions ( $P$ , Figure 3b). The pressure eigenfunctions are real valued and maximal on the ground surface. We also observe that a high-frequency (3 Hz) eigenfunction decays faster than a low frequency one (1 Hz) with increasing altitude. The pressure eigenfunction represents the amplitudes ( $P$  in Equation 8) of the guided infrasound at different altitudes. For example, in this case, we would receive a lower-amplitude guided infrasound with an atmospheric-pressure sensor at 500 m altitude (like a balloon) compared to a sensor on the ground surface. The eigenfunctions also represent the excitation amplitude of the guided infrasound due to the source-receiver reciprocity (e.g., Aki & Richards, 2002; Landau & Lifshitz, 2013). Therefore an infrasound source at 500 m would generate weaker guided infrasound compared to a source on the ground surface. We use the phase velocity later in our computation of compliance (Section 3) and our chirp modeling (Section 4).

## 2.3. Higher-Mode Guided Infrasound

We present the fundamental-mode guided infrasound in the above. The fundamental-mode represents the lowest-phase-velocity root in solving Equation 12 at each frequency, while the higher-velocity roots may also exist (Figure S1 in Supporting Information S1) and are referred to as the higher modes. The fundamental mode usually dominates guided infrasound in observations (e.g., Negraru & Herrin, 2009). Thus in the group-velocity



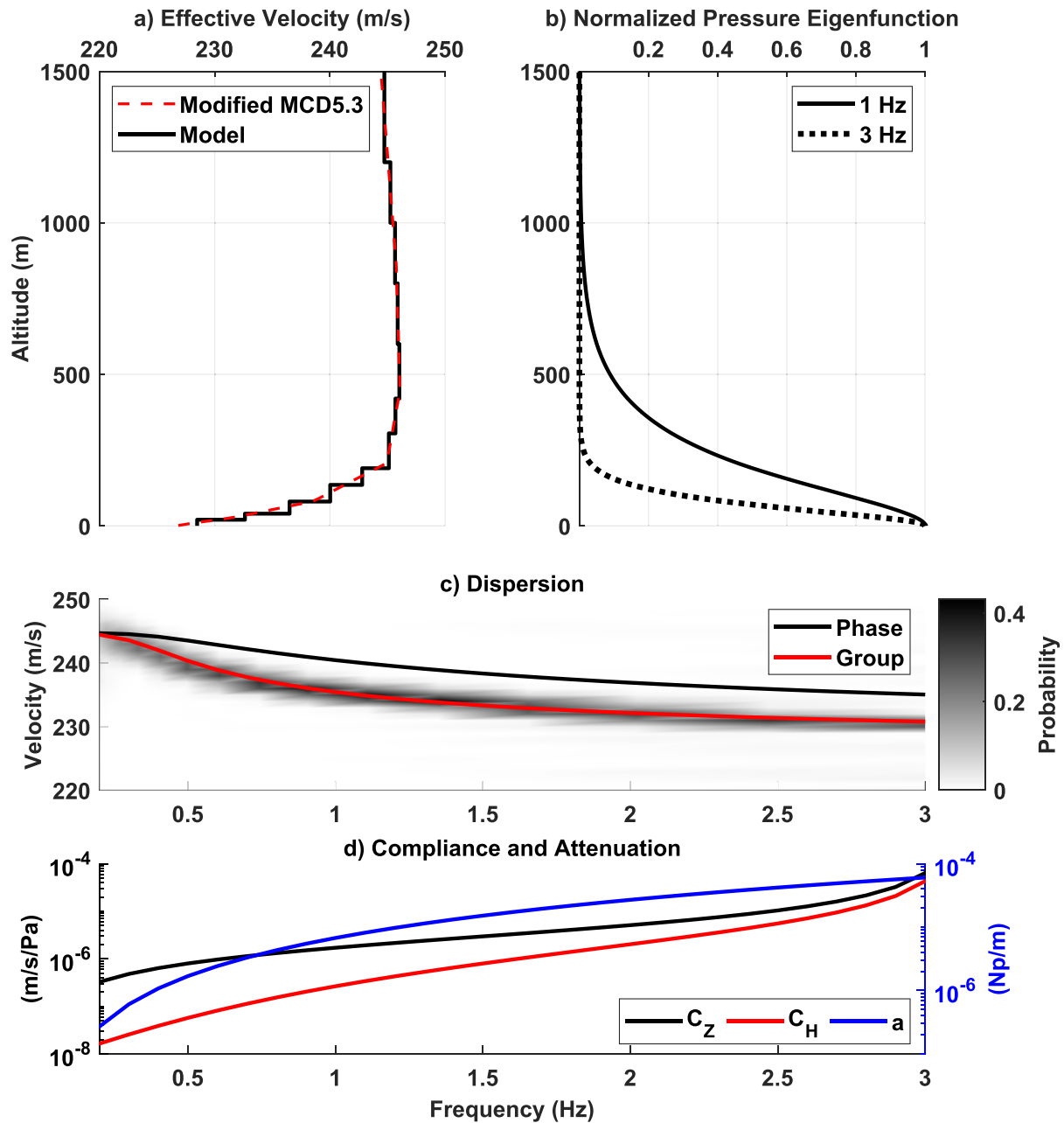


**Figure 3.** The infrasound velocity model (a), eigenfunctions (b), dispersion (c), and compliance (d) for S0986c. (a) We compute the infrasound velocity and the wind speeds from Mars Climate Database for S0986c (Millour et al., 2018) and subtract 4 m/s from the velocity at all altitudes (red dashed line). The black line represents our 1D layered model. (b) Two different-frequency pressure eigenfunctions are normalized by each maximum value for visualization. (c) The gray background is the group-velocity measurement of the S0986c chirp (Garcia et al., 2022). (d) The vertical (black) and horizontal (blue) compliance is based on the phase velocity (c) and a subsurface velocity model (Table 1). The infrasound attenuation (blue) is from Bass and Chambers (2001) for 200 K temperature.

measurement of S0981c and S0986c, we only observe the trends corresponding to the fundamental modes (Figures S1b and S1c in Supporting Information S1).

We also demonstrate the domination of the fundamental-mode by computing the contribution of both the fundamental and higher modes to the pressure on the ground surface as  $P^2(z=0)/\int P^2(z)dz$ . The pressure eigenfunction ( $P$ ) is real valued if the corresponding mode is a trapped mode (e.g., Chakravarthy, 2008; Lognonné et al., 1998). However, at some frequencies, the eigenfunctions become complex valued, and the imaginary parts represent the energy leakage of the guided infrasound to the top halfspace (e.g., Press & Harkrider, 1962; Radovich &

De Bremaecker, 1974). Thus, we only use the real part of the eigenfunctions on the ground surface in computing the contributions (Figure S1 in Supporting Information S1). We observe that for S0981c and S0986c, the contribution of the fundamental modes are at least one magnitude (a factor of 10) larger than the higher modes at each frequency. However, for S0793a, the 1st-higher mode contributes more than the fundamental mode. We investigate this phenomenon in detail in Section 5.2.

### 3. Compliance: Acoustic-to-Seismic Conversion

Atmospheric pressure perturbations, for example, caused by wind or infrasound, can deform the ground at shallow depths on planets with atmosphere (e.g., Ben-Menahem & Singh, 2012; Sorrells, 1971), like the atmospheric noise recorded by SEIS on Mars (Garcia et al., 2020; Lognonné et al., 2020; Stutzmann et al., 2021). Furthermore, when the infrasound horizontal apparent velocity is equal to the seismic-wave velocities of the subsurface, the infrasound would convert into seismic waves (e.g., Ewing et al., 1957; Langston, 2004). To summarize these different types of acoustic-to-seismic coupling, Edwards et al. (2008) list the possible conversion scenarios for homogeneous and isotropic elastic subsurface media. Note that in this study, we mainly focus on the so-called normal coupling, that is, atmospheric pressure perturbations deforming the ground surface without generating seismic waves, but the following theory remains applicable to all the scenarios mentioned above. Due to the frequency band we use (here from 0.5 to about 2 Hz), we only consider the compliance in this study and ignore other effects like tilt (Garcia et al., 2020).

Compliance is the amplitude relationship between the pressure perturbation and the ground deformation. Compliance is determined by the subsurface structure and the propagation velocity of the pressure perturbation in the atmosphere overlaying the subsurface (e.g., Ben-Menahem & Singh, 2012; Ewing et al., 1957; Sorrells, 1971), based on the assumption that the perturbation propagates like a plane wave. Note that the plane-wave assumption even holds for a complex pressure wavefield, since the complex wavefield can be decomposed into plane waves (e.g., Kenda et al., 2017). In the subsurface media, the ground motion and normal stress ( $\tau_{zz}$ ) are defined as:

$$u_z(z) = U_z(\omega, z)\exp(i(\omega t - kx)), \quad (14)$$

$$u_x(z) = iU_x(\omega, z)\exp(i(\omega t - kx)), \quad (15)$$

$$\tau_{zz}(z) = T_{zz}(\omega, z)\exp(i(\omega t - kx)), \quad (16)$$

where  $u_z$  and  $u_x$  are the vertical and horizontal ground velocities, respectively;  $\omega$ ,  $k$ ,  $t$ , and  $x$  are the same as in guided infrasound (Equation 8) while  $z$  here is the depth below the surface. The  $i$  in front of  $U_x$  in Equation 15 represents the  $\pi/2$  phase shift between the horizontal and vertical components of the ground motion (e.g., Sorrells, 1971). We then write compliance as the amplitude ratio of the vertical (horizontal) ground velocities over the atmospheric pressure perturbation:

$$C_z = \frac{u_z(z=0)}{p(z=0)} = \frac{U_z(\omega, z=0)}{P(\omega, z=0)} = -\frac{U_z(\omega, z=0)}{T_{zz}(\omega, z=0)}, \quad (17)$$

$$C_x = \frac{u_x(z=0)}{p(z=0)} = \frac{iU_x(\omega, z=0)}{P(\omega, z=0)} = -\frac{iU_x(\omega, z=0)}{T_{zz}(\omega, z=0)}, \quad (18)$$

where  $T_{zz}(z=0) = -P(z=0)$  (Equations 8 and 16) implies the continuity of normal stress on the ground surface. The minus sign is due to the different sign conventions between atmospheric studies and seismology. In acoustics wave studies (Section 2), the atmospheric pressure compressing the ground surface is defined as being positive, that is, exerting a force in the vertically downward direction on the ground surface. However, in seismology, a positive normal stress acting on a surface corresponds to a traction in the outward normal direction, that is, the vertically upward direction on the flat ground surface. Note that here we refer to the vertical ground velocity as  $u_z$ , not to be mistaken with the vertical particle velocity in the atmosphere, that is,  $v_z$  in Section 2.

To calculate the compliance values, we use the equation of motion and Hooke's law in 1D media (e.g., Aki & Richards, 2002, Chap. 7.2) and the zero-shear-stress boundary condition on the ground surface:

$$\tau_{zx} = 0. \quad (19)$$

**Table 1**  
*Parameters for a Three-Layer Subsurface*

Layer number	$V_p$ (m/s)	$V_s$ (m/s)	Density (kg/m <sup>3</sup> )	Thickness (m)
1	117	70	1,019	0.6
2	384	230	1,372	40
3	3,000	1,700	2,760	$\infty$

*Note.* The first two layers are regolith. In the first two layers, we calculate  $V_p$  from  $V_s$  based on the 0.22 Poisson's ratio (e.g., Morgan et al., 2018); we compute the density applying Gardner's empirical relationship (Gardner et al., 1974) to  $V_p$ .

Our computation is similar to Tanimoto and Wang (2019) where one does not assume the propagation velocity of pressure perturbation much slower than the shear-wave velocity of the subsurface medium. In this study, we use a three-layer velocity model simplified from the shallow (<100 m) geological structure under InSight (e.g., Warner et al., 2022). The first layer is made of thin soft regolith, as suggested by the analyses of the Martian atmospheric pressure drops (Kenda et al., 2020; Onodera, 2022) and of the hammerings of InSight's Heat Flow and Physical Properties (HP<sup>3</sup>) instrument (Lognonné et al., 2020). This surface layer is interpreted as fine-sand-dominated regolith. The second layer possesses a higher wave velocity than the first layer and represents coarse regolith (e.g., Warner et al., 2017). The third layer (i.e., halfspace) corresponds to the bedrock, composed of fractured basalt (e.g., Morgan et al., 2018). We use this three-layer model to compute compliance in the waveform modeling (Section 4). We achieve the parameters of the

second layer through a waveform fitting in Section 4. Note that this model is simple and may not reflect the complexity of the real subsurface under InSight. We discuss possible improvement to this model in Section 5.4.

We notice that the difference of vertical velocities on the ground surface between the atmosphere and the subsurface give rise to a contradiction. In Section 2, we assume the vertical atmosphere velocity on the ground surface to be zero (Equation 7). The particle velocity should be continuous at the fluid-solid (i.e., atmosphere-ground) interface, and thus  $u_z(z = 0) = 0$ . However, a nontrivial compliance requires the vertical movements of the ground surface to be non-zero, that is,  $u_z(z = 0) \neq 0$ . We address this contradiction in Section 5.3. Note that such contradiction does not exist for the horizontal velocities, since the horizontal velocity of the ground surface is not necessarily continuous with the horizontal atmospheric particle velocity.

#### 4. Waveform Forward Modeling

We model synthetic chirp, the seismic recording due to guided infrasound, by combining the theories of guided infrasound (Section 2) and compliance (Section 3). The far-field synthetic ground velocity recordings of chirps ( $u$ ) in the time domain are written as:

$$u_z = \mathcal{F}^{-1} \left[ S(\omega) \exp(-ikx - ax) \frac{\exp(-i\pi/4)}{\sqrt{kx\pi/2}} \frac{P^2(\omega, 0)}{\int P^2(\omega, z) dz} C_z(\omega) \right], \quad (20)$$

$$u_x = \mathcal{F}^{-1} \left[ S(\omega) \exp(-ikx - ax) \frac{\exp(-i\pi/4)}{\sqrt{kx\pi/2}} \frac{P^2(\omega, 0)}{\int P^2(\omega, z) dz} C_x(\omega) \right], \quad (21)$$

where  $\mathcal{F}^{-1}$  denotes the inverse Fourier transform, and  $S$  is the source time function of guided infrasound.  $k$  is guided infrasound horizontal wavenumber and is from our calculation of the guided infrasound phase velocity (Section 2).  $x$  is infrasound traveling distance from the infrasound source to InSight (Table 2).  $a$  is the intrinsic attenuation coefficient for infrasound (Figure 2d and Bass & Chambers, 2001).  $\exp(-i\pi/4)/\sqrt{kx\pi/2}$  is from the far-field approximation of a 3D cylindrical wave (e.g., Landau & Lifshitz, 2013).  $P^2(\omega, 0)/\int P^2(\omega, z) dz$  is the normalized pressure eigenfunction, representing the source excitation and sensor receiving on the ground surface.  $C_z$  ( $C_x$ ) is the vertical (horizontal) compliance (Section 3). We use the three-layer subsurface velocity model (Table 1) in computing the compliance, where the model is from simplification of the shallow geological structure under InSight (e.g., Warner et al., 2022). We benchmark our modeling approach against a numerical simulation software, SPECFEM2D-DG (Martire et al., 2020), in Appendix B.

We use the synthetic chirp to fit the one due to an impact. We assume that the infrasound source generated by the meteor impacting is impulsive and thus the source time function ( $S$  in Equations 20 and 21) is a delta function in the time domain and a constant in the frequency domain. The source location is at the same location as the impact crater. Note that the source time function generated by a meteorite interacting with the Martian atmosphere in the impact is worth further investigation, but is beyond the scope of this study. Since the infrasound source is on the ground surface, we mainly observe the guided infrasound on InSight (Garcia et al., 2022).

**Table 2**  
*The Origin Time Estimates and the Geometry Information of the Three Impact Events Relative to InSight (Garcia et al., 2022)*

Event	Estimated origin time (UTC)	Distance (km)	Backazimuth (°)
S0793a	2021-2-18T19:36:06	91.1	274.2
S0981c	2021-8-31T04:3:13	243.6	179.2
S0986c	2021-9-5T05:23:44	85.1	111.6

We use the observed chirps from two events (S0981c and S0986c) in the fitting. For each event, we use the origin time estimate from the seismic arrival time (Table 2, Garcia et al., 2022). The infrasound source is at the crater associated to the events. The satellite images of these craters provide the exact distances and backazimuth (Table 2). Note that these distances and backazimuth are matched closely by analysis of the two seismic recordings, for example, body-wave arrival times and chirp polarization (Garcia et al., 2022). We focus on the vertical and radial components, where the radial direction is parallel to a great path from the seismic source to InSight. For the seismic recordings of the two events, we rotate the north and east components to the radial direction based on the backazimuth (Table 2). We apply a band-

pass filter to the components of each chirp. For each chirp, we choose the filter band to have high signal-to-noise ratios and to avoid spectral anomaly like the sharp amplitude drop at 2.3 Hz in the S0986c vertical component (Figure 4). In the following waveform fitting, we refer to the filtered data as real data. A chirp also exists in the S0793a recording. However, that chirp displays complex properties (e.g., higher-mode), which deserve to be discussed independently (Section 5.2).

We compute the misfit between the synthetic and real chirps like

$$\chi = \sum_j \frac{1}{T} \int_T \left| \frac{u_z(s_j)}{\max(|u_z(s_j)|)} - \frac{u_z^o(s_j)}{\max(|u_z^o(s_j)|)} \right| + \left| \frac{u_x(s_j)}{\max(|u_x(s_j)|)} - \frac{u_x^o(s_j)}{\max(|u_x^o(s_j)|)} \right| dt \quad (22)$$

where  $s_j$  represents each event; the integral is done in the time window of each chirp (Figure 4) and  $T$  is the time window length for each chirp. We fix the first and third layers of the model, and only vary the  $V_s$  and the layer thickness of the second layer to find the misfit minimum (Figure 5). The S0981c misfit mainly varies with the layer thickness but does not change obviously with  $V_s$  when the thickness is less than 40 m (Figure 5a). The S0986c misfit presents a sloping area (Figure 5b) where the different combinations of the two parameters give similar misfits, which is known as trade-off in the geophysical inverse theory. In the total misfit of the two events (Figure 5c), the  $V_s$  and the layer thickness from the minimum provide good waveform fitting between the synthetic and real chirps (Figure 4). We discuss this model in the geological context in Section 5.1.

## 5. Discussion

Our analytical waveform modeling aid us validating the Martian subsurface models from other observations (Section 5.1). By combining our modeling and the Martian atmospheric model, we provide an explanation for the S0793a seismic observation (Section 5.2). We also discuss how to improve our modeling in the future (Section 5.3 and 5.4).

### 5.1. Implication for the Subsurface Structure

Our waveform fitting provides a velocity model where the  $V_s$  increases with depth (Table 1). In this model, the first layer is interpreted as fine-sand-dominated regolith (e.g., Grott et al., 2021). Compared to the  $V_s$  of the first layer, the second-layer  $V_s$  is larger and thus corresponds well to a coarse regolith where pebbles exist. The second layer is of 40-m thickness, close to the estimate of the maximum surficial regolith thickness around InSight; however, the geological model beneath the InSight indicates that this coarse regolith layer is interrupted by a basalt layer (e.g., Warner et al., 2022). Note that the geological model is built by considering the velocity models from the horizontal-to-vertical (H/V) ratio measurement of the InSight ambient seismic vibration (Hobiger et al., 2021); we refer to the velocity models as the H/V models. To further investigate this layer thickness contradiction, we check how the synthetic waveforms from the H/V models fit the chirps.

We choose one of the H/V models (Figure 6a), which is close to the geological model, and then generate the synthetic waveforms (Figures 6b–6e) following our computation in Section 4. We notice that for S0981c, the radial-component waveform of the H/V model possesses larger amplitudes than the observed chirp; for S0986c, the radial component from the H/V model does not fit the observed waveform around 5:29:50. The total misfit

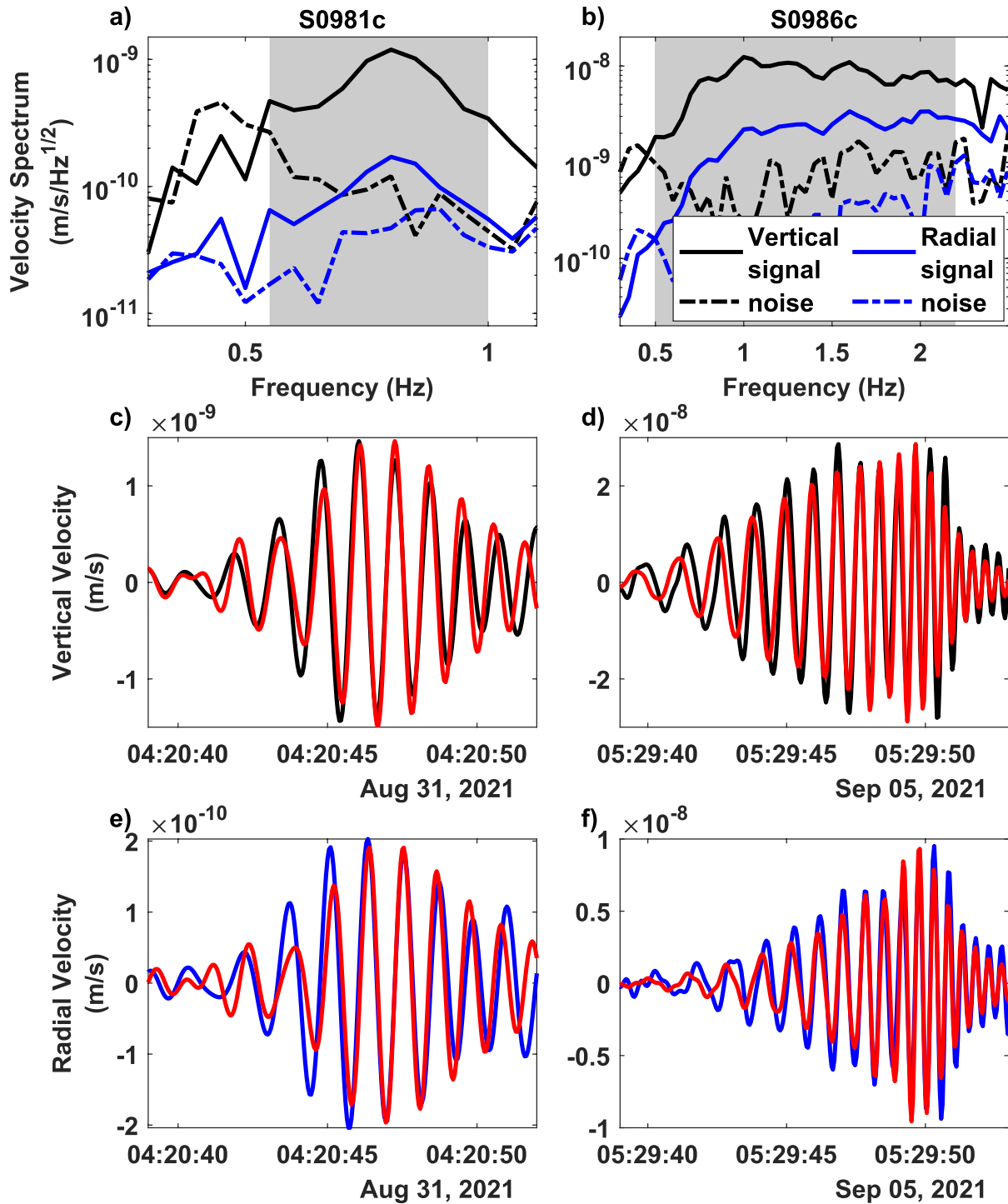


**Figure 4.** The vertical- and radial-component amplitude spectra of the chirps and noise (a and b) and the waveform fitting of the chirps in the time domain (c–f). The black and blue waveforms are the observed data and the red waveforms are the synthetic data. For each event, the signal spectra are from the time window used in the second and third rows, and the noise spectra are from the same-window-length recordings before the chirp. The gray areas indicate the frequency bands used in filtering the chirps, from 0.55 to 0.9 Hz for S0981c and from 0.5 to 2.2 Hz for S0986c.

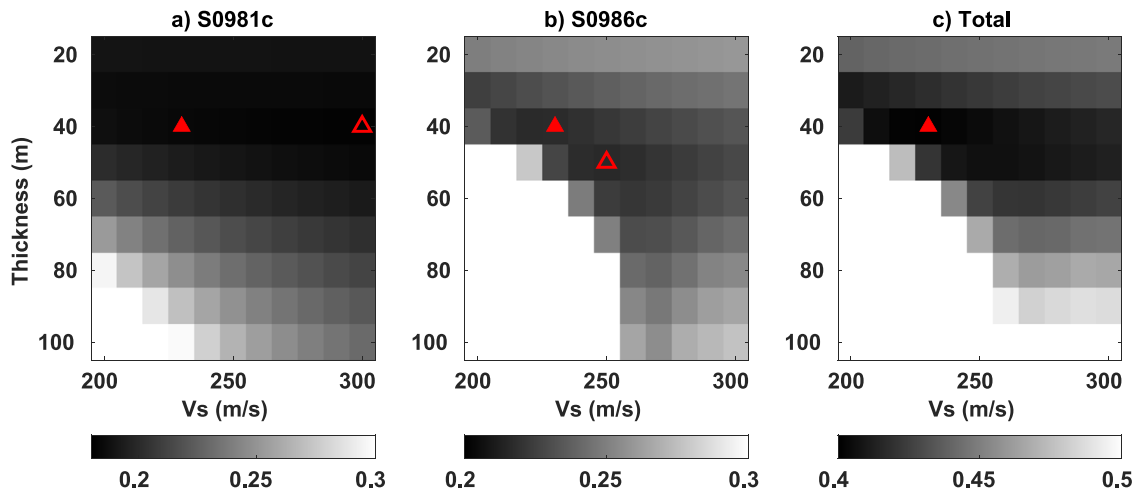


**Figure 5.** The misfit between the synthetic and observed chirp signals varies with the  $V_s$  and the thickness of the second subsurface layer (Table 1). The gray color indicates the misfit value. The red triangles correspond to the least misfit of the two events, while the empty triangle (a and b) corresponds to the least misfit of each event. The empty areas are the parameter combinations where the misfit values are larger than the color bar maximum or an air-coupled Rayleigh wave is excited.

of the H/V model (Equation 22) is 0.44, 15% larger than the total misfit of our three-layer model, 0.40. Thus, our model provides a better waveform fitting to the chirps than the H/V model. We repeat the above process with the other three H/V models (Figures S2–S4 in Supporting Information S1). We notice that all the three models provides smaller radial-component amplitudes compared to the real chirps.

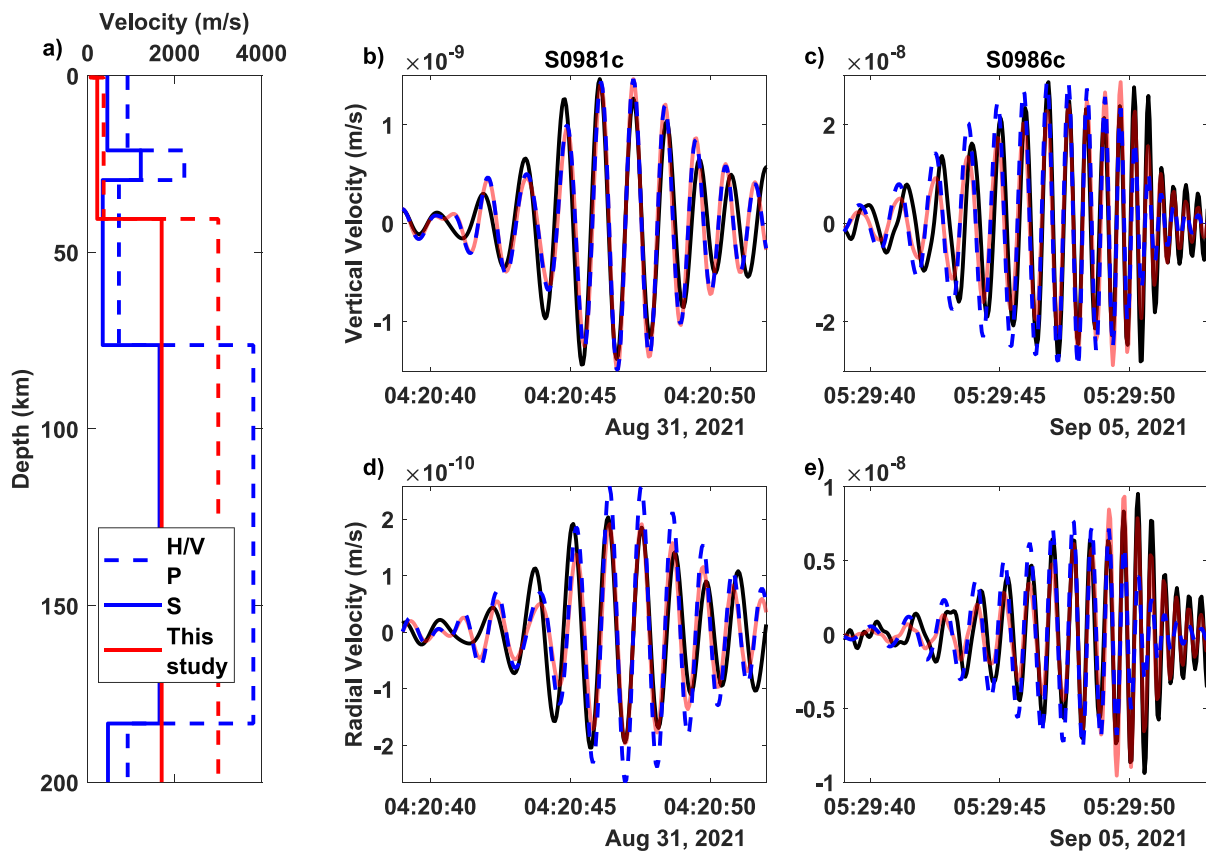


**Figure 6.** Comparison of the chirp waveform fitting between the H/V and the three-layer models. The dashed and solid lines (a) represent the P- and S-wave velocities, respectively. The H/V model (blue) is the weakly-constrained maximum a posteriori estimation from Hobiger et al. (2021) and provides the blue dashed waveforms (b–e). The black and red waveforms (b–e) are the same observed and synthetic chirps from Figure 4, respectively.



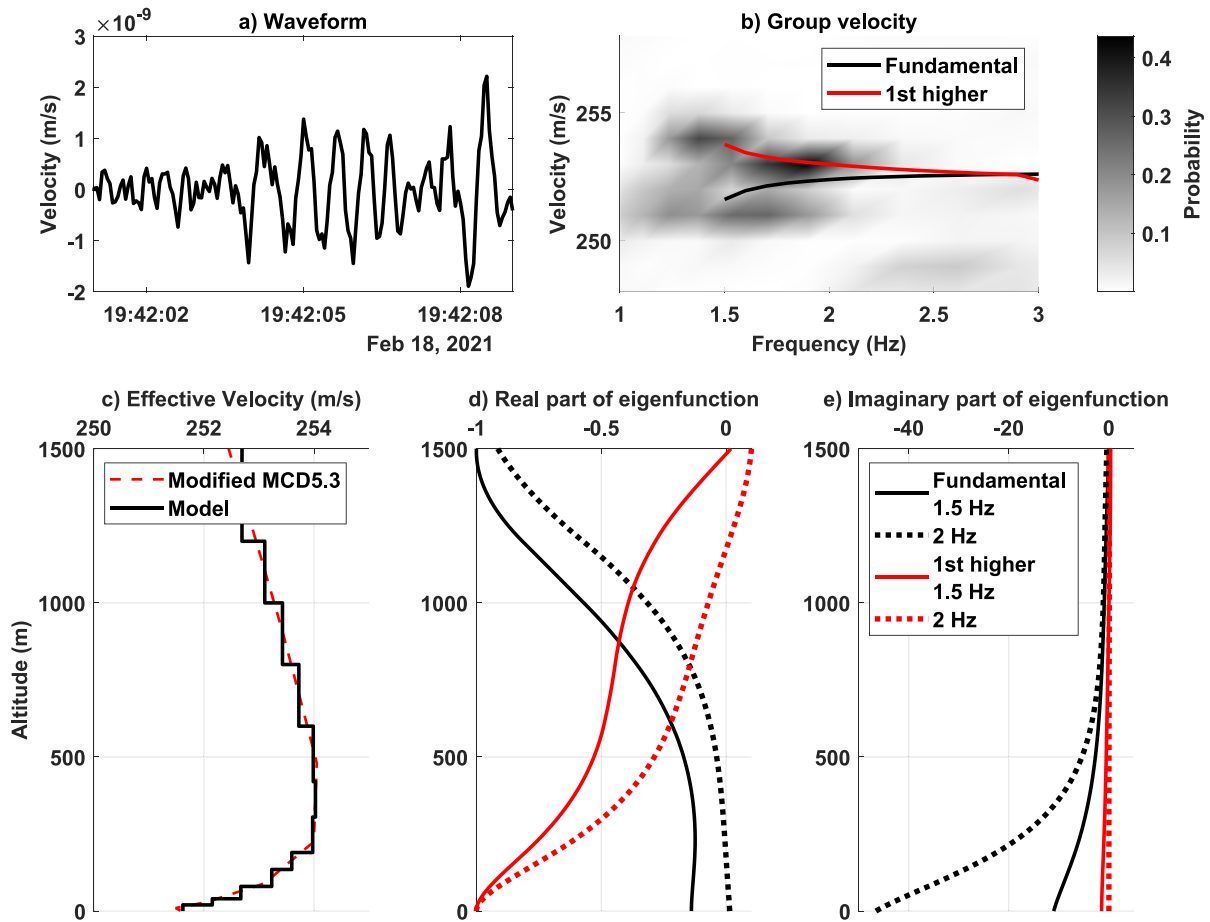


**Figure 7.** (a) The S0793a chimp bandpass filtered between 0.5 and 8 Hz. (b) Comparison of the group-velocity measurement from the chimp (gray) to the synthetic group velocity of the fundamental- and first-higher mode. These modes are from a 1D layered model modified from the Mars Climate Database model (c) (Table S1 in Supporting Information S1). We also compute the eigenfunctions corresponding to these modes and normalize each eigenfunction by its maximum real value (d and e).

The synthetic waveforms from the H/V models fit the vertical component of the recordings (Figure 6 and Figures S2–S4 in Supporting Information S1). Thus, the H/V models does not contradict with the chimp observation. Meanwhile, this waveform fitting difference between the H/V and our models could be due to the different sensitivities of the H/V ratio and the compliance to a same elastic property (e.g., Kenda et al., 2020; Maupin, 2017). Therefore, even through our model explain the chirps better than the H/V models, we cannot determine if our model is closer to the real subsurface than the H/V models. In order to achieve an accurate subsurface model, we need to incorporate the chimp observation, the H/V ratio measures, and other available data like the normalized compliance measures from the Martian pressure drops (e.g., Kenda et al., 2020; Onodera, 2022).

## 5.2. Higher-Mode Guided Infrasound From the Atmospheric Model

The S0793a seismic recording includes a chimp signal in the time domain (Figure 7a). However, in opposition to the S0986c and S0981c group velocity measurement, which yields a single monotonous trend (Figure 3c and Figure S1b in Supporting Information S1), the measurement of the S0793a chimp provides two trends (Figure 7b): a horizontal one from 1 to 2 Hz at around 251 m/s, and a sloping one with decreasing velocity, from about 1.2 to 2.3 Hz. The horizontal trend may correspond to an infrasound propagating directly from the impact and requires further investigation. It is ambiguous to attribute the sloping trend to a guided infrasound, since the bandwidth of the trend is short and the trend is not as continuous as the ones of S0981c and S0986c (Figures S1b and S1c in Supporting Information S1). In the rest of this subsection, we present that the sloping trend can be explained by the higher-mode guided infrasound, while we also recognize that there could be other interpretations for the trend like the scattered infrasound (i.e., echoes, Garcia et al., 2022).



We compute the fundamental- and 1st-higher-mode group velocities and the eigenfunctions of this guided infrasound by applying our computation (Section 2) to the corresponding infrasound velocity model (Figure 7c). The synthetic fundamental-mode group velocity increases with increasing frequency, opposite of the measured group velocity (black curve in Figure 7b). The fundamental-mode eigenfunctions are complex valued, instead of real valued as in S0986c (Section 3b). The real parts of the eigenfunctions are close to zero on the ground surface and increase from the surface to the 1500-m altitude (Figure 7d). This means that this fundamental-mode guided infrasound possesses smaller amplitude on the ground surface than at 1,500 m altitude. The imaginary parts of the eigenfunctions are large near the ground surface (Figure 7e) and represent energy leakage of the guided infrasound to the top halfspace (e.g., Press & Harkrider, 1962; Radovich & De Bremaecker, 1974). Thus this fundamental mode possesses weak pressure on the ground surface.

The 1st-higher-mode guided infrasound of the S0793a atmosphere model possesses a stronger pressure than the fundamental-mode on the ground surface (Figure S1d in Supporting Information S1). We notice that the 1st-higher-mode group velocity agrees with the ground-velocity measurement (the sloping trend in Figure 7b). Furthermore, the real part of the 1st-higher-mode eigenfunctions presents a maximum absolute value on the ground surface, while the imaginary part is close to zero on the ground surface compared to the fundamental-mode. Therefore, the 1st-higher-mode guided infrasound could generate the recorded S0793a chirp.

### 5.3. The Free Surface Boundary Condition

On the ground surface, the vertical particle velocity ( $v_z$ ) in the atmosphere is equal to the vertical ground velocity ( $u_z$ ). This yields:

$$v_z(z = 0) = -u_z(z = 0), \quad (23)$$

where the minus sign is due to different conversion of the positive  $z$ -axis direction in atmosphere (altitude) and the subsurface (depth). The formula above and Equation 4 lead to

$$\partial_z P(z = 0) = \rho(\partial_t + w_x \partial_x) u_z(z = 0), \quad (24)$$

where  $\rho$  is the air density. We rewrite this equation as

$$\partial_z P(z = 0) = -i\rho(\omega - w_x k) \frac{U_z(z = 0)}{T_{zz}(z = 0)} P(z = 0), \quad (25a)$$

$$= i\rho(\omega - w_x k) C_z P(z = 0). \quad (25b)$$

The expected value for  $C_z$  on Mars is around  $10^{-5}$  m/s/Pa and  $\rho$  is about  $0.02$  kg/m<sup>3</sup>. Thus, between 0.5 and 3 Hz,  $\partial_z P(z = 0)$  is on the order of  $10^{-5}$  of  $P(z = 0)$ . We can conclude that the guided-infrasound atmospheric pressure is almost constant near the ground surface and thus  $v_z \approx 0$  (Equation 4). This justifies the rigid ground-surface boundary condition used in our derivation of guided infrasound (Equation 7). Our benchmark (Appendix B) also validates that our modeling result agrees well with the numerical simulation where  $v_z$  is continuous on the ground surface, the atmosphere-solid-earth boundary.

We notice that the continuous- $v_z$  boundary condition is necessary for modeling the coupled normal mode between a planet atmosphere and the solid planet (e.g., Lognonné et al., 1998; Tanimoto, 2001; Watada, 1995). Thus in order to be able to model the coupled mode, we will incorporate this boundary condition into our modeling in future.

### 5.4. Potential Improvement and Future Work

In our forward modeling, we assume the boundary between the atmosphere and the ground to be flat. However, the ground surface topography affects the compliance (e.g., Bishop et al., 2021) by altering the guided infrasound horizontal wavenumber relative to the ground surface. To incorporate the topography into the compliance computation, we can compute the spatial wavenumber of the topography and combine the wavenumber with the one of guided infrasound, similar to the microseism studies which consider ocean waves coupling with topographic seafloors (e.g., Ardhuin et al., 2015).

Since our forward modeling is fast in computation, one can adopt this modeling to perform a Markov-chain Monte Carlo inversion of the atmospheric and subsurface parameters from the chirp signals. A Markov-chain Monte Carlo inversion explores different parameter combinations (e.g., Tarantola, 2005). As we demonstrate the trade-off between the shear-wave velocity and layer thickness in our three-layer subsurface model (Section 4), we expect more parameter trade-offs if the subsurface model possesses more than three layers. We also expect a trade-off between the atmospheric and subsurface parameters, since the compliance computation depends on the guided-infrasound phase velocity from the atmospheric model. Thus the inversion could aid us to assess these trade-offs between both the atmospheric (like infrasound velocity) and the subsurface (e.g.,  $V_s$  and layer thickness) parameters.

## 6. Conclusion

We analytically model chirp, the seismic waveform due to the coupling between guided infrasound and the ground. We theoretically demonstrate the guided-infrasound propagation in a 1D atmospheric model and compute the guided-infrasound phase and group velocities. Our group velocities match well with the measures from the S0981c and S098c chirp observation on Mars. We convert the guided infrasound into a chirp through compliance of a three-layer subsurface velocity model. We validate our modeling through a benchmark.

By applying our modeling to the Martian atmospheric model, we model synthetic chirps to fit the real chirp recordings of S0981c and S0986c. Through the waveform fitting, we achieve a three-layer Martian subsurface velocity model, where the coarse regolith is 40-m thick. We also apply our modeling to examine the velocity models from the InSight ambient-seismic-vibration H/V ratio observation and present that these models explain a part of the chirp recordings but do not provide a good fitting as our three-layer model. Therefore, we need to incorporate all the available observations to constrain the Martian subsurface structure estimation.

## Appendix A: Guided Infrasound on Earth

We present a terrestrial example of chirp, where the infrasound source is the 2017-12-12 Baumgarten gas hub explosion in Austria. This event generates both seismic waves and infrasound. These infrasound couples to the ground and are recorded by local seismic stations (Schneider et al., 2018). From these stations, we choose one from AlpArray (Hetényi et al., 2018), A333A (Figure A1), at the northeast of the explosion. The A333A vertical-component recording presents a chirp (Figure A1b), from which we measure the group velocity (Figure A1d). Our group-velocity measurement method is detailed in Panning et al. (2015) and Drilleau et al. (2020). We choose an atmospheric profile used in Schneider et al. (2018) and follow the computation in Section 2 to compute the synthetic group velocity. The difference between the measured and synthetic group velocity indicates that we can improve the Earth low-altitude (<3,000 m) atmospheric model using the guided infrasound.

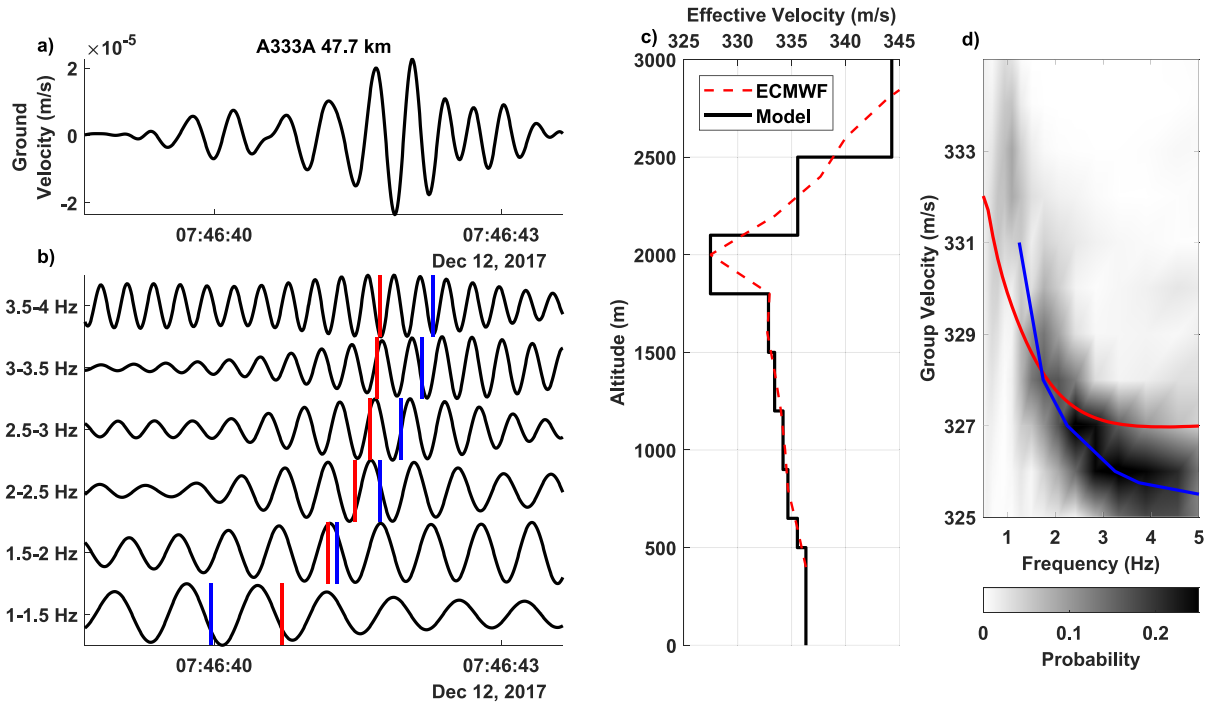


**Figure A1.** Illustration of the A333A chirp (a and b) and computation of the group velocity (c and d). We bandpass filter the A333A vertical-component velocity recording between 0.5 and 5 Hz (a) and in multiple narrow bands (b). We measure group velocity from the recording (a) and pick the probability maximum at each frequency as the group velocity (blue line in panel (d)). Based on the ECMWF profile used in Schneider et al. (2018), we plot the effective acoustic-wave velocity profile (red dashed line in panel (c)) and the 1D layered model (black line in panel (c)). From the 1D model, we compute the synthetic group velocity (red line in panel (d)). We convert the synthetic and measured group velocities at the narrow bands to the corresponding arrival times (red and blue bars in panel (b)).

## Appendix B: Benchmark

We benchmark our modeling against a numerical simulation software, SPECIFEM2D-DG (Martire et al., 2020). SPECIFEM2D-DG can model acoustic and seismic waves in a coupled solid-fluid system. Garcia et al. (2022) utilize this software to simulate the seismic recording at InSight location due to the S0793a, S0981c, and S0986c impacts. We choose the S0981c simulation result in this benchmark. Garcia et al. (2022) use the S0981c atmospheric model from MCD (Millour et al., 2018) and a four-layer subsurface model (Table B1). Garcia et al. (2022) set the pressure and seismic receivers 246 km away from the source and the seismic receiver at 5 m under the ground surface. We use the same models and the same receiver setting. We compare our modeling result to the one from Garcia et al. (2022): the group velocity (Figure B1a), the compliance (Figure B1b), and the pressure and seismic waveforms (Figure B2). Those match well in the frequency domain or the time domain. Note that in the seismic waveform comparison, since SPECIFEM2D-DG is for the 2D space, instead of the 3D, we have to modify Equations 20 and 20 by removing the 3D cylindrical wave term:

$$u_z = \mathcal{F}^{-1} \left[ S(\omega) \exp(-ikx - ax) \frac{P^2(\omega, 0)}{\int P^2(\omega, z) dz} C_z(\omega) \right], \quad (\text{B1})$$

$$u_x = \mathcal{F}^{-1} \left[ S(\omega) \exp(-ikx - ax) \frac{P^2(\omega, 0)}{\int P^2(\omega, z) dz} C_x(\omega) \right]. \quad (\text{B2})$$

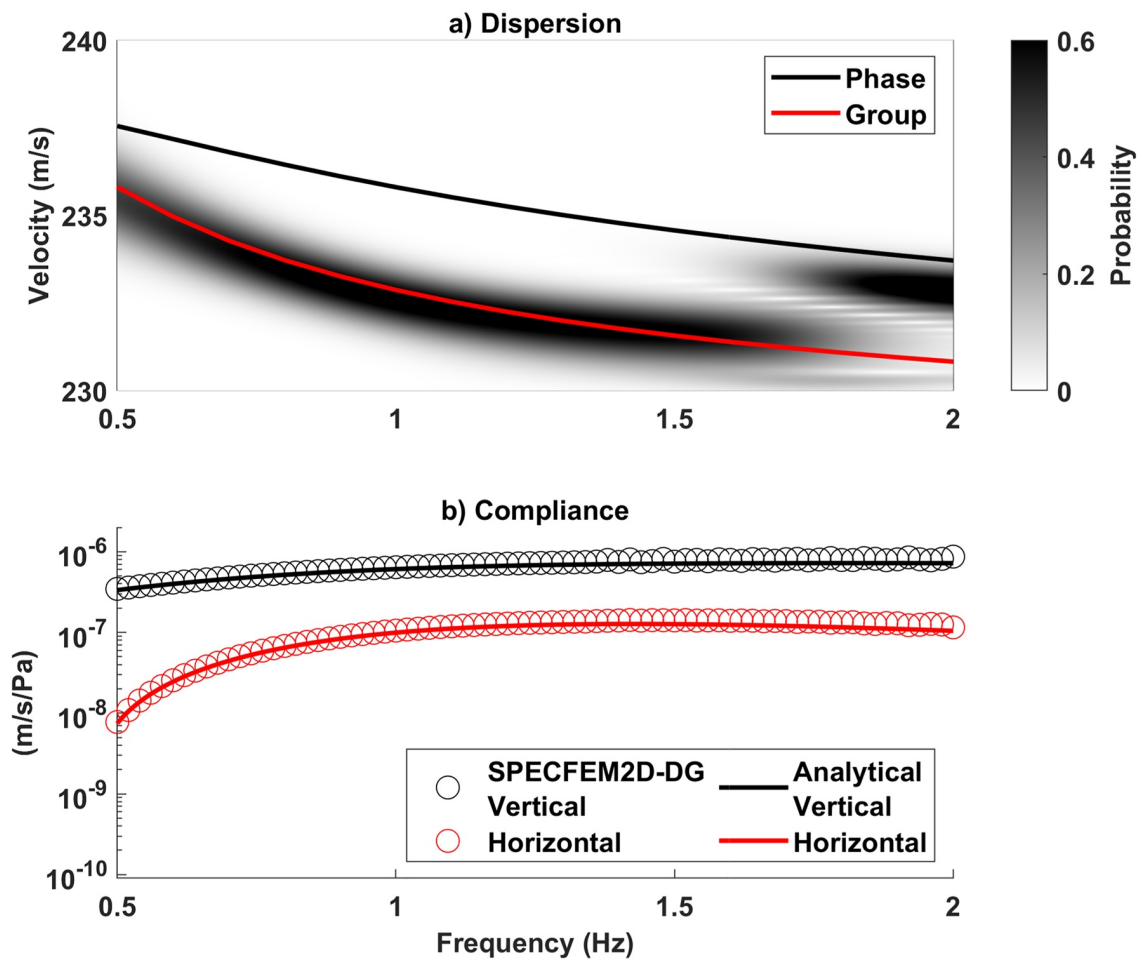


**Figure B1.** The comparison of the group velocity and compliance from our analytical approach to SPECFEM2D-DG. The group velocity measurement and compliance values from SPECFEM2D-DG are the gray background (a) and the empty circles (b), respectively. The estimates from our analytical approach are in the curves (a and b).

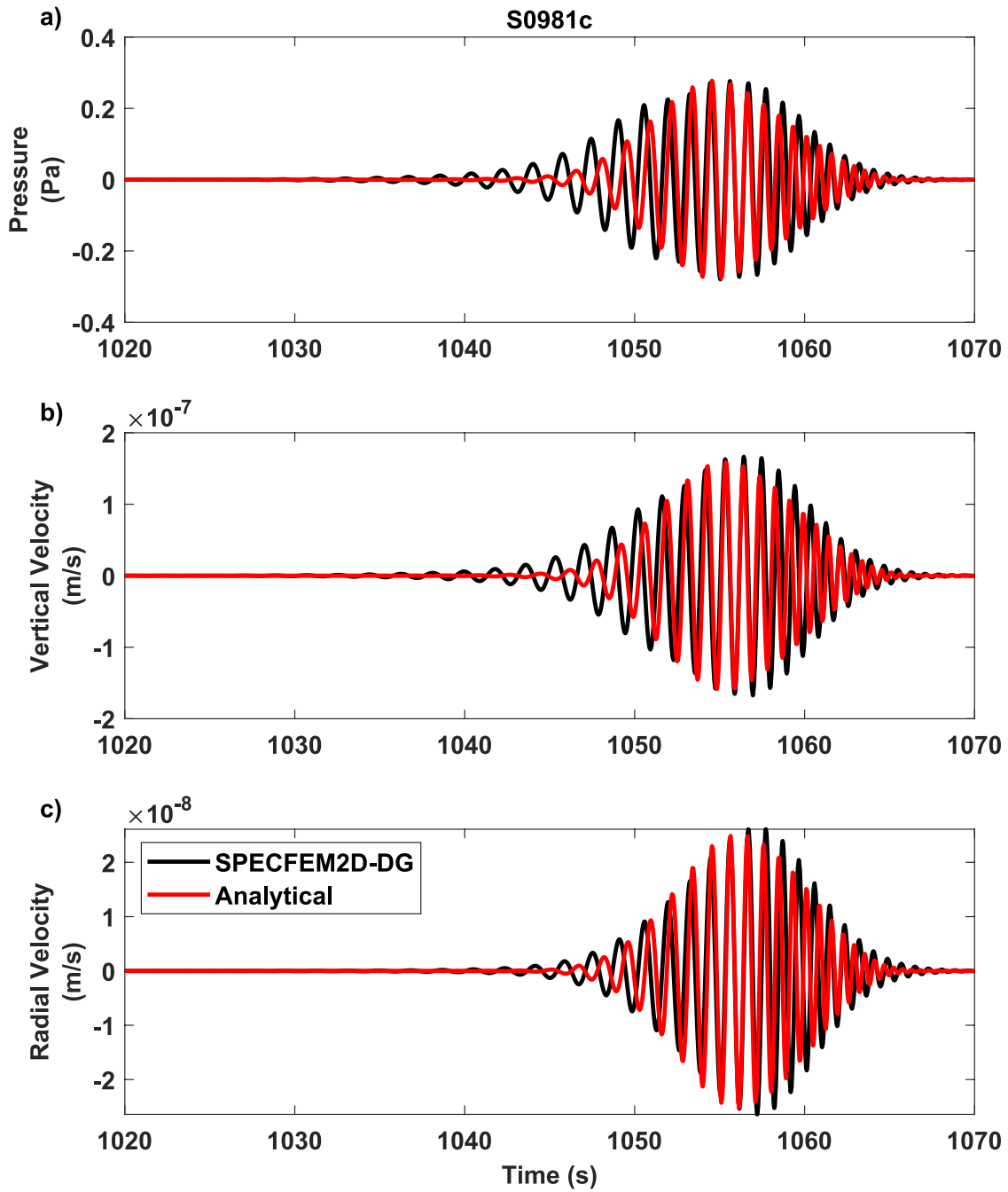


**Figure B2.** The waveform comparison of the atmospheric pressure, vertical velocity, and horizontal velocity from our analytical approach to SPECFEM2D-DG. The waveforms are all bandpass filtered between 0.5 and 2 Hz. We normalize our waveforms by the maximum value of the pressure from SPECFEM2D-DG.

**Table B1**

*The Subsurface Velocity Model Used in Garcia et al. (2022)*

Layer number	$V_P$ (m/s)	$V_S$ (m/s)	Density (kg/m <sup>3</sup> )	Thickness (m)
1	744	398	1,800	100
2	3,800	1,850	2,304	9,900
3	4,500	2,800	2,570	14,000
4	6,224	3,753	2,863	∞

*Note.* We only use this model in the benchmark section.

## Data Availability Statement

The Martian topography data are from the NASA PDS Geosciences Node (Neumann et al., 2003). The InSight seismic waveform data are available from the IPGP Datacenter, IRIS-DMC and the NASA PDS (InSight Mars SEIS Data Service, 2019a, 2019b). The Martian atmospheric parameters are from MCD (Millour et al., 2018). The codes for computation of the guided infrasound are available in Xu (2022).

## Acknowledgments

The authors acknowledge the NASA, the CNES, their partner agencies and institutions (UKSA, SSO, DLR, JPL, IPGP-CNRS, ETHZ, IC, and MPS-MPG) and the flight operations team at JPL, SISMOC, MSDS, IRIS-DMC, and PDS for providing the SEED SEIS data. This study is InSight contribution number 242 and LA-UR-22-25146. ZX thanks Eléonore Stutzmann, Ludovic Margerin, and Dylan Mikesell for fruitful discussion. ZX also thanks Aymeric Spiga's help in accessing the Earth atmospheric model and discussion about the Mars atmosphere. The authors thank the AlpArray Seismic Network Team; the authors thank Wayne Crawford, Stefan Heimers, and John Clinton for their help in accessing the AlpArray data. The authors also thank Felix M. Schneider for providing the conversion from the atmospheric temperature to acoustic-wave velocity. The authors thank editor Laurent Montési, reviewer Toshiro Tanimoto, and an anonymous reviewer for their constructive feedback that helped improve this manuscript. This research is supported by the ANR MAGIS (ANR-19-CE31-0008-08) and the Initiative d'Excellence (IdEx) Université Paris Cité (ANR-18-IDEX-0001). MF is funded by the Center for Space and Earth Science of LANL.

## References

- Aki, K., & Richards, P. G. (2002). *Quantitative seismology*. Science Books.
- Ardhuin, F., Gualtieri, L., & Stutzmann, E. (2015). How ocean waves rock the Earth: Two mechanisms explain microseisms with periods 3 to 300 s. *Geophysical Research Letters*, *42*(3), 765–772. <https://doi.org/10.1002/2014gl062782>
- Assink, J. D. (2012). *Infrasound as upper atmospheric monitor* (PhD thesis).
- Banerdt, W. B., Smrekar, S. E., Banfield, D., Giardini, D., Golombek, M., Johnson, C. L., et al. (2020). Initial results from the InSight mission on Mars. *Nature Geoscience*, *13*(3), 183–189. <https://doi.org/10.1038/s41561-020-0544-y>
- Banfield, D., Rodriguez-Manfredi, J., Russell, C., Rowe, K., Leneman, D., Lai, H., et al. (2019). InSight Auxiliary Payload Sensor Suite (APSS). *Space Science Reviews*, *215*(1), 1–33. <https://doi.org/10.1007/s11214-018-0570-x>
- Bass, H. E., & Chambers, J. P. (2001). Absorption of sound in the Martian atmosphere. *Journal of the Acoustical Society of America*, *109*(6), 3069–3071. <https://doi.org/10.1121/1.4744345>
- Ben-Menahem, A., & Singh, S. J. (2012). *Seismic waves and sources*. Springer Science & Business Media.
- Bishop, J. W., Fee, D., Modrak, R., Tape, C., & Kim, K. (2021). Spectral element modeling of acoustic to seismic coupling over topography. *Journal of Geophysical Research: Solid Earth*, *127*(1), e2021JB023142. <https://doi.org/10.1029/2021jb023142>
- Chakravarthy, G. V. R. (2008). *Love wave propagation in Viscoelastic media* (Theses and dissertations). Boise State University.
- Clinton, J. F., Ceylan, S., van Driel, M., Giardini, D., Stähler, S. C., Böse, M., et al. (2021). The Marsquake catalogue from InSight, sols 0–478. *Physics of the Earth and Planetary Interiors*, *310*, 106595. <https://doi.org/10.1016/j.pepi.2020.106595>
- Drilleau, M., Beucler, E., Lognonné, P., Panning, M. P., Knapmeyer-Endrun, B., Banerdt, W. B., et al. (2020). MSS/1: Single-station and single-event marsquake inversion. *Earth and Space Science*, *7*(12), e2020EA001118. <https://doi.org/10.1029/2020ea001118>
- Edwards, W. N., Eaton, D. W., & Brown, P. G. (2008). Seismic observations of meteors: Coupling theory and observations. *Reviews of Geophysics*, *46*(4), RG4007. <https://doi.org/10.1029/2007rg000253>
- Ewing, W. M., Jardetzky, W. S., Press, F., & Beiser, A. (1957). *Elastic waves in layered media*. McGRAW-HILL Book.
- Garcia, R. F., Brissaud, Q., Rolland, L., Martin, R., Komatitsch, D., Spiga, A., et al. (2017). Finite-difference modeling of acoustic and gravity wave propagation in Mars atmosphere: Application to infrasounds emitted by meteor impacts. *Space Science Reviews*, *211*(1), 547–570. <https://doi.org/10.1007/s11214-016-0324-6>
- Garcia, R. F., Daubar, I. J., Beucler, É., Posiolova, L., Collins, G. S., Lognonné, P., et al. (2022). Seismological location and orbital imaging of newly formed craters on Mars. *Nature Geoscience*, *15*(10), 774–780. <https://doi.org/10.1038/s41561-022-01014-0>
- Garcia, R. F., Kenda, B., Kawamura, T., Spiga, A., Murdoch, N., Lognonné, P. H., et al. (2020). Pressure effects on the SEIS-InSight instrument, improvement of seismic records, and characterization of long period atmospheric waves from ground displacements. *Journal of Geophysical Research: Planets*, *125*(7), e2019JE006278. <https://doi.org/10.1029/2019je006278>
- Gardner, G., Gardner, L., & Gregory, A. (1974). Formation velocity and density—The diagnostic basics for stratigraphic traps. *Geophysics*, *39*(6), 770–780. <https://doi.org/10.1190/1.1440465>
- Giardini, D., Lognonné, P., Banerdt, W. B., Pike, W. T., Christensen, U., Ceylan, S., et al. (2020). The seismicity of Mars. *Nature Geoscience*, *13*(3), 205–212.
- Gibbons, S. J., Ringdal, F., & Kværna, T. (2007). Joint seismic-infrasound processing of recordings from a repeating source of atmospheric explosions. *Journal of the Acoustical Society of America*, *122*(5), EL158–EL164. <https://doi.org/10.1121/1.2784533>
- Grott, M., Spohn, T., Knollenberg, J., Krause, C., Hudson, T. L., Piqueux, S., et al. (2021). Thermal conductivity of the Martian soil at the InSight landing site from HP3 active heating experiments. *Journal of Geophysical Research: Planets*, *126*(7), e2021JE006861. <https://doi.org/10.1029/2021je006861>
- Harkrider, D. G. (1964). Theoretical and observed acoustic-gravity waves from explosive sources in the atmosphere. *Journal of Geophysical Research*, *69*(24), 5295–5321. <https://doi.org/10.1029/jz069i024p05295>
- Herrin, E. T., Kim, T. S., & Stump, B. W. (2006). Evidence for an infrasound waveguide. *Geophysical Research Letters*, *33*(7), L07815. <https://doi.org/10.1029/2005gl025491>
- Hetényi, G., Molinari, I., Clinton, J., Bokelmann, G., Bondár, I., Crawford, W. C., et al. (2018). The AlpArray seismic network: A large-scale European experiment to image the Alpine orogen. *Surveys in Geophysics*, *39*(5), 1009–1033. <https://doi.org/10.1007/s10712-018-9472-4>



- Hobiger, M., Hallo, M., Schmelzbach, C., Stähler, S., Fäh, D., Giardini, D., et al. (2021). The shallow structure of Mars at the InSight landing site from inversion of ambient vibrations. *Nature Communications*, 12(1), 1–13. <https://doi.org/10.1038/s41467-021-26957-7>
- Ichihara, M., Takeo, M., Yokoo, A., Oikawa, J., & Ohminato, T. (2012). Monitoring volcanic activity using correlation patterns between infrasound and ground motion. *Geophysical Research Letters*, 39(4), L04304. <https://doi.org/10.1029/2011gl050542>
- InSight Mars SEIS Data Service. (2019a). *Data Service, InSight SEIS data bundle*. PDS Geosciences (GEO) Node. <https://doi.org/10.17189/1517570>
- InSight Mars SEIS Data Service. (2019b). *SEIS raw data, InSight mission*. IPGP, JPL, CNES, ETHZ, ICL, MPS, ISAE-Supaero, LPG, MFSC. <https://doi.org/10.18715/SEIS.INSIGHT.XB>
- Kenda, B., Drilleau, M., Garcia, R. F., Kawamura, T., Murdoch, N., Compaire, N., et al. (2020). Subsurface structure at the InSight landing site from compliance measurements by seismic and meteorological experiments. *Journal of Geophysical Research: Planets*, 125(6), e2020JE006387. <https://doi.org/10.1029/2020je006387>
- Kenda, B., Lognonné, P., Spiga, A., Kawamura, T., Kedar, S., Banerdt, W. B., et al. (2017). Modeling of ground deformation and shallow surface waves generated by Martian dust devils and perspectives for near-surface structure inversion. *Space Science Reviews*, 211(1), 501–524. <https://doi.org/10.1007/s11214-017-0378-0>
- Landau, L. D., & Lifshitz, E. M. (2013). *Fluid mechanics: Landau and Lifshitz: Course of theoretical physics, volume 6* (Vol. 6). Elsevier.
- Langston, C. A. (2004). Seismic ground motions from a bolide shock wave. *Journal of Geophysical Research*, 109(B12), B12309. <https://doi.org/10.1029/2004jb003167>
- Lognonné, P., Banerdt, W., Pike, W., Giardini, D., Christensen, U., Garcia, R. F., et al. (2020). Constraints on the shallow elastic and anelastic structure of Mars from InSight seismic data. *Nature Geoscience*, 13(3), 213–220. <https://doi.org/10.1038/s41561-020-0536-y>
- Lognonné, P., Banerdt, W. B., Giardini, D., Pike, W. T., Christensen, U., Laudet, P., et al. (2019). SEIS: InSight's seismic experiment for internal structure of Mars. *Space Science Reviews*, 215(1), 1–170. <https://doi.org/10.1007/s11214-018-0574-6>
- Lognonné, P., Clévédy, E., & Kanamori, H. (1998). Computation of seismograms and atmospheric oscillations by normal-mode summation for a spherical Earth model with realistic atmosphere. *Geophysical Journal International*, 135(2), 388–406. <https://doi.org/10.1046/j.1365-246x.1998.00665.x>
- Lorenz, R. D., Kedar, S., Murdoch, N., Lognonné, P., Kawamura, T., Mimoun, D., & Bruce Banerdt, W. (2015). Seismometer detection of dust devil vortices by ground tilt. *Bulletin of the Seismological Society of America*, 105(6), 3015–3023. <https://doi.org/10.1785/0120150133>
- Martire, L., Garcia, R. F., Rolland, L., Spiga, A., Lognonné, P. H., Banfield, D., et al. (2020). Martian infrasound: Numerical modeling and analysis of InSight's data. *Journal of Geophysical Research: Planets*, 125(6), e2020JE006376. <https://doi.org/10.1029/2020je006376>
- Maupin, V. (2017). 3-D sensitivity kernels of the Rayleigh wave ellipticity. *Geophysical Journal International*, 211(1), 107–119. <https://doi.org/10.1093/gji/ggx294>
- Millour, E., Forget, F., Spiga, A., Vals, M., Zakharov, V., & Montabone, L. (2018). *Mars climate database*. In *From Mars Express to ExoMars, 27–28 February 2018, Madrid, Spain*.
- Morgan, P., Grott, M., Knappmeyer-Endrun, B., Golombek, M., Delage, P., Lognonné, P., et al. (2018). A pre-landing assessment of regolith properties at the InSight landing site. *Space Science Reviews*, 214(6), 1–47. <https://doi.org/10.1007/s11214-018-0537-y>
- Negraru, P. T., & Herrin, E. T. (2009). On infrasound waveguides and dispersion. *Seismological Research Letters*, 80(4), 565–571. <https://doi.org/10.1785/gssrl.80.4.565>
- Neumann, G. A., Abshire, J. B., Aharonson, O., Garvin, J. B., Sun, X., & Zuber, M. T. (2003). Mars Orbiter Laser Altimeter pulse width measurements and footprint-scale roughness. *Geophysical Research Letters*, 30(11), 1561. <https://doi.org/10.1029/2003gl017048>
- Nijs, L., & Wapenaar, C. (1990). The influence of wind and temperature gradients on sound propagation, calculated with the two-way wave equation. *Journal of the Acoustical Society of America*, 87(5), 1987–1998. <https://doi.org/10.1121/1.399326>
- Nijs, L., & Wapenaar, C. (1992). Reply to: "Comments on the influence of wind and temperature gradients on sound propagation calculated with the two-way wave equation" [J. Acoust. Soc. Am. 91, 498–500 (1992)]. *Journal of the Acoustical Society of America*, 91(1), 501–504. <https://doi.org/10.1121/1.402737>
- Onodera, K. (2022). *Subsurface structure of the Moon and Mars deduced from 3D seismic wave propagation simulation and analysis of Apollo and InSight seismic data* (Doctoral dissertation). The Graduate University for Advanced Studies, SOKENDAI and Université de Paris Cité.
- Panning, M. P., Beucler, É., Drilleau, M., Mocquet, A., Lognonné, P., & Banerdt, W. B. (2015). Verifying single-station seismic approaches using Earth-based data: Preparation for data return from the InSight mission to Mars. *Icarus*, 248, 230–242. <https://doi.org/10.1016/j.icarus.2014.10.035>
- Pekeris, C. (1948). The propagation of a pulse in the atmosphere. Part II. *Physical Review*, 73(2), 145–154. <https://doi.org/10.1103/physrev.73.145>
- Pierce, A. D. (1990). Wave equation for sound in fluids with unsteady inhomogeneous flow. *Journal of the Acoustical Society of America*, 87(6), 2292–2299. <https://doi.org/10.1121/1.399073>
- Press, F., & Harkrider, D. (1962). Propagation of acoustic-gravity waves in the atmosphere. *Journal of Geophysical Research*, 67(10), 3889–3908. <https://doi.org/10.1029/jz067i010p03889>
- Radovich, B., & De Bremaecker, J. C. (1974). Body waves as normal and leaking modes—Leaking modes of Love waves. *Bulletin of the Seismological Society of America*, 64(2), 301–306. <https://doi.org/10.1785/bssa0640020301>
- Schneider, F. M., Fuchs, F., Kolínský, P., Caffagni, E., Serafin, S., Dorminger, M., & Bokelmann, G. (2018). Seismo-acoustic signals of the Baumgarten (Austria) gas explosion detected by the AlpArray seismic network. *Earth and Planetary Science Letters*, 502, 104–114. <https://doi.org/10.1016/j.epsl.2018.08.034>
- Smith, D. E., Zuber, M. T., Frey, H. V., Garvin, J. B., Head, J. W., Muhleman, D. O., et al. (2001). Mars Orbiter Laser Altimeter: Experiment summary after the first year of global mapping of Mars. *Journal of Geophysical Research*, 106(E10), 23689–23722. <https://doi.org/10.1029/2000je001364>
- Sorrells, G. G. (1971). A preliminary investigation into the relationship between long-period seismic noise and local fluctuations in the atmospheric pressure field. *Geophysical Journal International*, 26(1–4), 71–82. <https://doi.org/10.1111/j.1365-246x.1971.tb03383.x>
- Sorrells, G. G., McDonald, J. A., Der, Z., & Herrin, E. (1971). Earth motion caused by local atmospheric pressure changes. *Geophysical Journal International*, 26(1–4), 83–98. <https://doi.org/10.1111/j.1365-246x.1971.tb03384.x>
- Stutzmann, É., Schimmel, M., Lognonné, P., Horleston, A., Ceylan, S., van Driel, M., et al. (2021). The polarization of ambient noise on Mars. *Journal of Geophysical Research: Planets*, 126(1), e2020JE006545. <https://doi.org/10.1029/2020je006545>
- Tanimoto, T. (2001). Continuous free oscillations: Atmosphere-solid Earth coupling. *Annual Review of Earth and Planetary Sciences*, 29(1), 563–584. <https://doi.org/10.1146/annurev.earth.29.1.563>
- Tanimoto, T., & Wang, J. (2019). Theory for deriving shallow elasticity structure from colocated seismic and pressure data. *Journal of Geophysical Research: Solid Earth*, 124(6), 5811–5835. <https://doi.org/10.1029/2018jb017132>
- Tarantola, A. (2005). *Inverse problem theory and methods for model parameter estimation* (Vol. 89). SIAM.



- Warner, N., Golombek, M., Ansan, V., Marteau, E., Williams, N., Grant, J., et al. (2022). In situ and orbital stratigraphic characterization of the InSight landing site—A type example of a regolith-covered lava plain on Mars. *Journal of Geophysical Research: Planets*, 127(4), e2022JE007232. <https://doi.org/10.1029/2022je007232>
- Warner, N., Golombek, M., Sweeney, J., Fergason, R., Kirk, R., & Schwartz, C. (2017). Near surface stratigraphy and regolith production in southwestern Elysium Planitia, Mars: Implications for Hesperian-Amazonian terrains and the InSight lander mission. *Space Science Reviews*, 211(1), 147–190. <https://doi.org/10.1007/s11214-017-0352-x>
- Watada, S. (1995). *Part I. Near-source acoustic coupling between the atmosphere and the solid earth during volcanic eruptions. Part II. Near-field normal mode amplitude anomalies of the Landers earthquake* (Doctoral dissertation). California Institute of Technology. <https://doi.org/10.7907/IJSE5-G397>
- Waxler, R. (2002). A vertical eigenfunction expansion for the propagation of sound in a downward-refracting atmosphere over a complex impedance plane. *Journal of the Acoustical Society of America*, 112(6), 2540–2552. <https://doi.org/10.1121/1.1514930>
- Waxler, R. (2004). Modal expansions for sound propagation in the nocturnal boundary layer. *Journal of the Acoustical Society of America*, 115(4), 1437–1448. <https://doi.org/10.1121/1.1646137>
- Xu, Z. (2022). ZongboXu/HFGI: v1.0.0 (version v1.0.0) [Software]. Zenodo. <https://doi.org/10.5281/zenodo.7079346>





*Abstraction Blue*, 1927, Georgia O'Keeffe  
Museum Of Modern Arts.

---

# Conclusion and Perspectives

---

In Chapter 2 and 3, we brought some answers to the questions of impact seismology raised in the Introduction. We summarise here the main conclusions that can be drawn from our work. We also recall the limitations and challenges encountered, and present new horizons of research that we believe could be helpful in overcoming them.

## 4.1 Exploring the impact seismic source - and other sources

### 4.1.1 An exhaustive source model

In Chapter 2, we developed a new semi-analytical model of an impact seismic source. The source is represented by an ensemble of equivalent forces, which convey the non-linear and plastic processes at play during crater formation, as well as the exchange of momentum between the impactor and target. We showed that a key component of these equivalent forces, the stress glut field of [Backus & Mulcahy \[1976\]](#), can be computed numerically from elasto-plastic models of the target material response, yielding a numerical measure of the impact seismic source terms.

Among the questions raised in section 1.4.1 was: *"What physical process, or source mechanism best models seismic waves generated by impacts?"* From the equivalent force representation developed in Chapter 2, the impact can be viewed both as an extended source, or as a point source. We present a point source representation which, for the first time, combines a single force with a seismic moment tensor. Hence, an impact acts both as an impulse, as was already proposed by [McGarr et al. \[1969\]](#) or [Lognonné et al. \[2009\]](#), and as a shear or explosive mechanism via couples of forces, as was noted by several other authors [[Lognonné et al., 1994](#); [Walker, 2003](#); [Wójcicka et al., 2020](#)]. This combined source stems from the physics of the impact process itself, during which both momentum exchange and explosive kinetic energy release act together to form an impact crater. Hence, our work answers this first question by proposing the first exhaustive description of the impact seismic source physics.

Additionally, we showed in Chapter 2 that these source terms are not equally important in modelling the impact seismic signal at large distances. In particular, in the far field, the point force term contributes only marginally to the seismic signal amplitude. In conclusion, a moment tensor suffices in representing an impact source. This moment tensor is not purely explosive, and we showed that it contains a significant non-diagonal

component for oblique impacts, which can be well described by a double couple with respect to the vertical axis. We showed that the source time function, or moment rate of each mechanism remains mostly unchanged with the impactor incidence angle, however the respective amplitude of each moment component evolves as a function of obliquity. Ultimately, our proposed moment tensor source can be reconstituted from four amplitude terms and four normalised source time functions, each associated to unit isotropic, CLVD and double-couple moment tensors mechanisms. Our study of impact obliquity at the end of Chapter 2 provides an estimate of the respective amplitude of each term.

In Chapter 2, the frequency content of impact seismic signals was also investigated. This property of the seismic signal connects with two of the questions raised in section 1.4.1: "*Which factors influence the frequency content of impact-generated seismic signals?*" and "*Should Martian craters in the 3 m to 30 m diameter range really produce seismic signals of the VF family?*" We showed in Chapter 2 that seismic signals associated to a point-source model have an excess of energy at high-frequency compared to signals simulated by a hydrocode. However, the spatial extension of the source is another of its important characteristics, which affects the seismic signal in the far field. In our case, the impact source extension is determined by the region where non-linear and plastic processes are significant. We have shown that seismic signals generated from an extended deviatoric stress glut field present a lower corner frequency than those generated with a deviatoric point-source. Hence, the frequency content of impact-induced seismic waves are related to the spatial extension of damage and non-linearities, and not to the dynamics of the shock itself.

As we conclude this work, the damaged and non-linear region of an impact simulation is considered to be bounded by the stress glut field. However, we have seen that the stress glut extension alone cannot explain the cutoff frequency of the signal produced by numerical simulations. Other dissipative processes at play in numerical simulations, such as friction across discontinuities, might have been overlooked in the definition of equivalent forces. Thus, the task of harmonising the equations of motions of the seismic representation theorem and of numerical frameworks such as HOSS FDEM approach must be undertaken in the future.

Nevertheless, the coupling between HOSS and SPEC3D, and the comparison of simulation results and Lunar and Martian recordings reveals an interesting trend: the source size and signal cutoff frequency are seemingly related to the medium shear wave velocities and the impactor energy and momentum. In particular, according to this observation, a similar impactor will generate a signal of shorter duration in a stronger medium. This brings some insights into the different frequency content of Martian and Lunar impact waveforms, presented in section 1.4.1. The model developed here provides a new opportunity to study the effect of the source finite dimensions and its relation to signal spectral characteristics, and could bring new elements to the debate on the impact origin of InSight VF events (section 1.4.1).

Finally, we inquired in section 1.4.1 of the Introduction on the possibility to "*predict the magnitude of the seismic source for different impact sizes, taking into account the target material properties*". We showed in Chapter 2 that our stress glut-based source representation successfully reproduces the long-period seismic wave amplitudes from a hydrocode simulation. Additionally, Figs. 2.22 and 2.23 showed that Martian and Lunar impact signals produced by craters of various sizes are better understood when accounting for the differences in target properties on the Lunar and Martian surface. Indeed, the amplitude of a seismic wave depends both on the seismic moment of the source and on the seismic velocities of the propagation media. This means that estimating the seismic

velocities and mechanical properties of an impacted surface is key to correctly interpret impact-generated seismic signals.

To conclude this summary of Chapter 2, we recall that the semi-analytical model proposed in this study is not limited to impact seismic sources, nor is it tied to a single numerical method. A measure of stress glut can be achieved with any numerical model supporting plastic behaviours, i.e. most shock codes. Care must however be taken in defining the ideal elastic stress  $\Psi$ , which conveys the seismologist's view of stress and strains. Provided that a numerical model can be designed, this semi-analytical model is valid for many other types of sources. In particular the stress-glut based source representation could bring insights into the complexity of volcanic or explosive source mechanisms, for which both force and moment tensor representation also exist. Transient momentum variations are possible on earth during volcanic venting, explosive spall, landslides, or cavity collapse [Kanamori & Given, 1982; Stump, 1985; Day & McLaughlin, 1991; Takei & Kumazawa, 1994] but their importance relative to dipolar forces is not always clear.

#### 4.1.2 Towards scaling relationships and validation

Physics aims at proposing simplified, but objective models of natural phenomena. The quality and usefulness of a model depends on its ability to be informative, accurate and predictive. A model is informative when it successfully relates observables (e.g., crater size, seismic wave amplitude, frequency... ) to the concepts developed in the framework of a theory (elastodynamics, material plasticity, thermodynamics) using mathematical relationships. It is accurate when the available observables are closely reproduced by these mathematical relationships. Finally, it is predictive when its accuracy extends to a wide range of possible observables produced by a single phenomenon.

We have shown in this work that the stress glut model of the impact seismic source is informative, as it relates different source mechanisms to the mechanics of crater formation. We have shown that the cutoff frequency or seismic moment produced by the numerical model where in trend with Martian and Lunar observations, however our model still lacks a proper validation of its accuracy. To test it, real impact seismic signals with well estimated impactor parameter, such as the Apollo artificial impacts, or the small and large martian impacts could be used as a benchmark. Their impact craters can be reproduced numerically as was done by Rajšić et al. [2021b], and their source parameters can be calculated and used to produce a model of regional seismic signal. Such approach presents a number of limitations, mainly due to the difficulty in simulating seismic wave propagation in the highly scattering Martian and Lunar crust. Nevertheless, some aspects of the signals, such as its P/S amplitude ratio, cutoff frequency and magnitude could be compared to the model prediction to evaluate its accuracy. Thanks to the wide range of impact crater size provided by the artificial Lunar impacts, and the small and large Martian crater, such source validation would cover a large range of real-life scenarios.

As for prediction purpose, it is important to develop scaling laws involving physical observables of the seismic source and its associated signal. For the cratering process, the  $\pi$ -scaling employs a measure combining momentum and energy of the impactor [Holsapple, 1993]. The amplitude and magnitude of earthquakes scales with the dimension and rupture length of the source [Aki & Richards, 2002], while the magnitude of an explosion scales mainly with its yield [Denny & Johnson, 1991]. Recent works have proposed scaling of the P-wave amplitude, corner frequency or seismic moment of an impact based on the observed crater size or the impact momentum [Gudkova et al., 2015; Teanby, 2015; Wójcicka et al., 2020]. In this work, we have shown for the first time a scaling relation between

the impact momentum and the cutoff frequency, valid for 2 set of seismic data ( Moon and Mars) and one set of synthetics (our work). We have shown that possible scaling relationships between the impact source size and kinetic energy, between the seismic moment and impact momentum and finally between the impact angle and source components could be further investigated. The development and validation of such scaling laws would be of great values for future missions of planetary seismology.

## 4.2 Impact-generated Infrasond

### 4.2.1 Dispersed infrasonds: a unique dataset for InSight

Impact-generated "chirps" are unique signals, the only of their kind recorded during the InSight mission. Conversion of atmospheric pressure perturbations to ground displacement have been observed for pressure vortices, dust devils, and wind-driven fluctuations [Kenda et al., 2020; Garcia et al., 2020], but these perturbations are not waves and are instead transported by winds at velocities much lower than the speed of sound. Other candidate coupled infrasond signals were proposed by Garcia et al. [2021] but could not be associated to any known source or distance to a source. The impact-generated chirps are the first coupled infrasonic signals whose source type and source location are known.

In addition, these signals are only the second clear example of infrasond trapped in the nighttime Martian waveguide, following the events described by Martire et al. [2020]. In section 1.4.1, we asked *"how impact shock waves interact with the atmosphere and ground in their path"*. In the case of Martian nearby impact, the origin of the chirps is known and their propagation can be modelled. In Chapter 3, we showed that the group velocity of dispersed signals act as a probe of the low-altitude Martian atmospheric sound speed. Three high-quality events were used to invert a model of the atmosphere, which agrees with MCD profiles on the same date and at InSight location.

Chapter 3 also answers the second part of this introductory question by analytically modelling the coupling of dispersed infrasond with the ground near InSight using compliance. In fact, we showed that InSight chirp signals are unique for they provide the first clear example of compliance effects for a high-velocity pressure perturbation on Mars. The velocity of the perturbation is comparable to the sound speed  $c_s$  on Mars of  $220 \text{ m}\cdot\text{s}^{-1}$  to  $260 \text{ m}\cdot\text{s}^{-1}$ , hence, at  $f = 1\text{Hz}$ , the perturbation probes the subsurface over scales comparable to  $c_s/f \approx 220 - 260\text{m}$ . This scale is much larger than what could be achieved using dust devils, with a typical propagation velocity of  $5 \text{ m}\cdot\text{s}^{-1}$  and a depth sensitivity of  $\sim 5\text{m}$  at  $1 \text{ Hz}$  [Kenda et al., 2020]. Here, our study allowed to constrain subsurface properties to within  $\sim 50\text{m}$  beneath InSight.

### 4.2.2 Possible improvements of the model

Despite the unprecedented richness of this data, the study of Chapter 3 presents several limitations.

The first limitation, which was mentioned in Chapter 3, is the sparsity of data points for the subsurface inversion. Indeed, only three events, S0981c, S0986c and S1034a, present a sufficient signal-to-noise ratio for the inversion of both their group velocity and their H/V ratio. More importantly, the signal to noise ratio of the chirp is high only in a limited frequency range of  $0.5\text{Hz}$  to  $2\text{Hz}$ . We have shown in our synthetic test that, with this limited data and bandwidth, the subsurface inversion is not able to fully discriminate



between several solutions for the shear wave velocity profile and interface depths. With the information contained in this data and our prior knowledge on the position of possible interface, two families of models are possible. The first, with an interface at 40 m, is similar to the model proposed by [Xu et al. \[2022\]](#). The second, with a high velocity layer in the upper 20 m beneath InSight, resembles subsurface models inverted using different datasets [[Hobiger et al., 2021](#); [Carrasco et al., 2023](#)].

As discussed in Chapter 3, inversions of compliance H/V ratios, similarly to inversions of Rayleigh waves ellipticity [[Hobiger et al., 2021](#); [Carrasco et al., 2023](#)], suffer from trade-offs between parameters  $v_s$  and  $H_g$ . One way to limit these trade-offs could be to conduct a joint inversion of multiple datasets, having varying depth sensitivities and covariance between model parameters. A future work could for example combine measurements from ambient vibrations and from chirp compliance.

Another important limitation is our lack of information on the pressure source, or source time function, of impact events. In section 1.4.1, we asked "*what impact-generated seismic-acoustic signals tell us about meteorite shock wave generation*". The conclusions of Chapter 3 are that the modelled chirp signal is a combination of the atmospheric structure, the subsurface structure and the source spectral characteristics. In the absence of knowledge on the source phase, the phase of the chirp signals cannot be retrieved, and the model signals do not fully align with the observed waveforms. In the same way, we highlighted that the chirps spectra could be used as discriminants between the two families of subsurface models. However, this spectrum is also a function of the impact blast source, and would especially not be flat at high frequencies for a source of the  $N - wave$  type. Therefore, modelling the impact blast source is necessary to exploit this data in its entirety and further refine atmospheric and subsurface models.

## 4.3 Towards a multi-physics view of the source

### 4.3.1 The problem of impact blast waves

The impact problem is multi-physics in nature. We have seen in Chapter 2 that the physics of friction, in addition to the physics of plasticity, might need to be included in the Representation Theorem for a complete description of the impact seismic source. In the same way, we showed in Chapter 3 that a physical model of the impact blast, i.e. the interaction of the impactor with the Martian atmosphere during crater formation is needed to fully explain InSight chirp signals.

The impact blast wave forms at the same time as the crater. It is likely that its timescale is similar to that of the contact and compression stage of impact cratering (see section 2.1.3), where ground shock waves are created by high-velocity displacements. Therefore, the target and impactor material both flow through the atmosphere, and the physics of impact blasts cannot be dissociated from the physics of cratering and ejecta formation. Thus, modelling this shock wave requires a dual consideration of the high-stress and high-strain rate deformation of a solid, the high-velocity flow of a fluid, and their interaction.

Such a complex problem calls for advanced numerical techniques and is not extensively addressed in the field of planetary sciences. Most studies of meteoroid-generated shock waves focus on the meteor and airburst phenomena. As an example, [Henneton et al. \[2015\]](#); [Nemec et al. \[2017\]](#) simulated the shock produced by a meteor on Earth using CFD simulations and an idealised undeformable meteor. Earlier studies have provided models of airburst for a strengthless bolide, i.e., a bolide behaving as a compressible

liquid in its fall. The SOVA code presented by Shuvalov et al. [1999] enabled simulations of a Tunguska-like event, including ablation and radiation effects and modelling the high-altitude disruption of a meteor [Shuvalov & Artemieva, 2002]. The SOVA code also provided one of the rare simulations of shock waves produced during impact cratering.

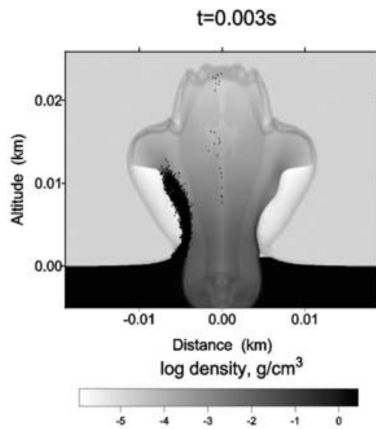


**Figure 4.1:** Shock wave produced by the impact of a 1 m radius stone meteor with a velocity of  $20 \text{ km}\cdot\text{s}^{-1}$ . The shock is represented in terms of density. The dust and ejecta lifted by the impact are shown on the left part of the image. Reproduced from Nemtchinov et al. [2002].

Notably, it was used in a study of impact-mobilised dust in the Martian atmosphere by Nemtchinov et al. [2002] and Kosarev et al. [2002]. In this work, the formation of the crater, the shock wave and the advection of dust particles are modelled concurrently, as shown on Fig. 4.1. Several studies have proposed a more realistic model of the meteor body, such as Shuvalov & Trubetskaya [2010], who included internal friction. More recently, Robertson & Mathias [2017] studied the Chelyabinsk airburst and meteor fragmentation and provided the solid bolide with a strength and porosity model. Other studies have effectively produced coupled shock and tsunami waves for an asteroid impact in the Earth oceans [Gisler et al., 2003; Robertson & Gisler, 2019]. However, most of these studies focus on very large meteoroids, 20 m to 300 m in size, and do not concern themselves with classical acoustic or seismic shock waveforms. Therefore, their approach of the subject is relatively distant from that of a seismologist or acoustician.

Codes such as HOSS and iSALE possess a fluid/solid coupling capability and are powerful tools for the simulation of impact cratering. We have moreover shown that they were successfully employed for the study of shock [Pierazzo et al., 2008; Caldwell et al., 2021] and seismic waves produced by impacts [Güldemeister & Wünnemann, 2017; Froment et al., 2020; Wójcicka et al., 2020; Rajšić et al., 2021]. It is therefore possible, with today's numerical tools, to further investigate impact blast waves.

### 4.3.2 Numerical modelling of impact shock waves

#### Coupled Fluid/Solid simulations with HOSS/FSIS

The HOSS software is equipped with a Fluid Solid Interaction Solver (FSIS) tailored for the Finite-Discrete Element Method [Munjiza et al., 2020]. FSIS solves the 2D or 3D Navier Stokes equations for compressible fluids. The fluid domain consists of an Eulerian grid superimposed with the solid Lagrangian grid described in Chapter 2. Both domains share the same integration time step. In the centre of each Eulerian cell, the Equation of State (EOS) of the fluid material is calculated from internal energy and density variables. The velocity variables are used to compute viscous nodal forces. Energy, momentum and mass are transported through the Eulerian grid.

The contact between solid and fluid materials is handled via the immersed boundary method. The FSIS algorithm detects fluid nodes which are in contact, or engulfed, in a solid element. Then, the fluid and solid velocities are corrected by a factor depending on an interaction force  $\mathbf{f}$ , which is prescribed by the relative velocity of fluid and solid nodes and by a *penalty* factor. Hence, the fluid and solid domain interact by exchanging momentum.

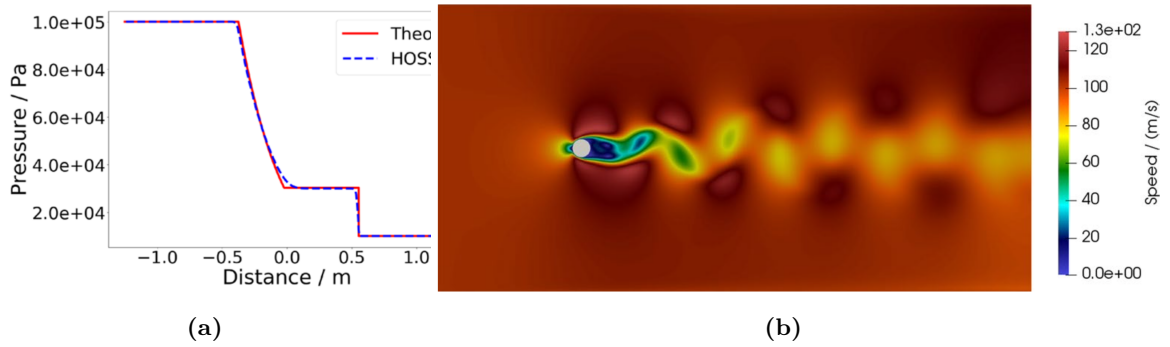


**Figure 4.2:** Results of verification tests conducted with HOSS/FSIS. (a) shows the results of a Sod shock tube problem. The pressure field calculated by HOSS matches the theoretical solution 1 ms after the tube domains are released. (b) displays the 2D velocity field of a fluid flowing at  $100 \text{ m}\cdot\text{s}^{-1}$  from the left around a spherical obstacle. A von Karman vortex street forms in the wake of the sphere. Reproduced from Fig. 15 and Fig. 22 of [Munjiza et al. \[2020\]](#).

The HOSS/FSIS implementation is able to resolve shocks: [Munjiza et al. \[2020\]](#) describe a verification performed with the well-known 1D *Sod problem*. In this test, an imaginary tube is separated into two domains containing gas with two different pressures and densities. At an initial time  $t = 0$ , the separation between both domains is removed, and a pressure and density discontinuity propagates in the tube in the form of a shock wave. As shown on Fig. 4.2a, the HOSS/FSIS results for pressure, density and temperature fields agree with the known analytical solution. Another important verification problem is the Von Karman vortex street, also described in [Munjiza et al. \[2020\]](#). In this problem, a solid circular object is fixed in place inside a viscous fluid flowing against it at a constant velocity. This results in the formation of alternating vortices in the wake of the object, creating an oscillatory flow. [Munjiza et al. \[2020\]](#) tested this problem with a  $100 \text{ m}\cdot\text{s}^{-1}$  fluid velocity and obtained oscillations consistent with von Karman’s theory (see Fig. 4.2b). Despite being conducted with flow velocities much smaller than a typical meteor velocity, the two problems are similar in nature. The success of these two tests supports the use of HOSS/FSIS for simulating meteorite impact blast waves.

### Preliminary tests of a meteor shock wave simulation

To further test the possibility of modelling this phenomenon, we perform a test simulation of a meteor shock wave in conditions similar to the S1094b impact on Mars. Hydrocode impact simulations performed by [Posiolova et al. \[2022\]](#) modelled this impact with a 5 m diameter impactor with an impact velocity of  $12 \text{ km}\cdot\text{s}^{-1}$ . We designed a 2D plane-strain simulation of the shock cone produced by the fall of this meteor with HOSS/FSIS.

The Martian atmosphere is composed of 94.9% of carbon dioxide  $\text{CO}_2$ , 2.79% of Nitrogen  $\text{N}_2$ , 2.08% of Argon, and traces of oxygen and other molecular gases. At first order, the Martian atmosphere can thus be modelled by a pure  $\text{CO}_2$  gas.  $\text{CO}_2$  is heavily used in industrial application, and its thermodynamical properties are relatively well known between 100 and 1000 K. A reference equation of state for carbon dioxide is due to [Span & Wagner \[1996\]](#), who fit  $\text{CO}_2$  thermodynamical properties to an ensemble of experimental results. The Span & Wagner EOS (SWEOS) is valid in the fluid and supercritical region such that  $216 \leq T \leq 1100 \text{ K}$  and  $0 \leq P \leq 800 \text{ MPa}$ . Several authors have conducted numerical studies of shocks in  $\text{CO}_2$  using this EOS, such as [Giljarhus et al. \[2012\]](#), [Hammer et al. \[2013\]](#) and [Fang et al. \[2019\]](#), who developed two-phase and three-phase solvers for flows in compressible  $\text{CO}_2$ . However, due to its semi-analytical nature, the SWEOS cannot

be extrapolated to high-temperature regions. This can be a problem for the modelling of impact blasts or meteor shocks, in which the temperature could reach values in the tens of thousands of K. Instead, purely analytical EOS are preferred.

Collins et al. [2023] used the iSALE shock code to evaluate the pressure close to the point of impact of the S1094b crater. In this preliminary study, they find that the overpressure is in the order of 0.1 MPa in the vicinity of the crater. In the conditions of pressure and temperature of Mars and for this impact problem, CO<sub>2</sub> is thus purely in the vapour and gas phase. Böttcher et al. [2012] showed that in the vapour state, CO<sub>2</sub> can be well represented numerically using the Peng-Robinson EOS (PREOS), instead of the more exact but more complex SWEOS. PREOS is an adaptation of the Van der Waals equation of state. It aims at better predicting the thermodynamics of a species when the attraction and repulsion between molecules becomes strong.

The PREOS was coded in HOSS/FSIS with the parameters of CO<sub>2</sub>. A 150 by 300 m 2D fluid domain is designed, in which a 5 m diameter 2D spherical impactor is fixed. The fluid properties are described by PREOS, without viscosity or heat conduction, and flows with a velocity of 12 km·s<sup>-1</sup> against the fixed impactor. The steady-state velocity, temperature and overpressure ( $\Delta P = P - P_0$ ) fields around the meteor are presented on Fig. 4.3. The overpressure field shows that the air in the bow shock around the meteor is strongly compressed, with pressure of the order of 0.1 MPa consistent with the modelling of Collins et al. [2023]. The shock gas expands and decompresses in the meteor wake, except directly behind the meteor where a conical recompression region is visible. This wake geometry is in agreement with current theory, as presented for instance by Silber et al. [2018].

In the first panel of Fig. 4.3, the relative velocity between the meteor and initial incoming fluid is shown. In this new reference frame, the fluid flows in the same general direction as the meteor. Directly behind the meteor, a thin region of fluid flows at close to 12 km·s<sup>-1</sup>. This effect would be attenuated with the addition of viscosity. The last panel shows the temperature of the wake. Its values are extremely high, reaching more than 50 000 K in front and behind the meteor. However, this simple simulation does not account for plasma formation or radiation processes. In reality, part of the internal energy of the wake is dissipated by light emission and by the excitation and dissociation of CO<sub>2</sub> molecules. Hence, Henneton et al. [2015] noted that the temperature meteor shock simulated with an ideal gas could be overestimated by a factor five compared to a simulation accounting for real gas ionisation.

The overpressure field in the direction perpendicular to the trajectory, and at increasing distances behind the meteor, is represented on Fig. 4.4, normalized by the radius  $R_0 \approx 130$  of the cylindrical shock wave (see section 3.1.1). At close distance from the impactor, the shock overpressure presents two strong peaks corresponding to the bow shock and the recompression region of Fig. 4.4. The recompression shock merges with the bow shock 300 m behind the impactor. Such pressure field geometry is one again in agreement with the very near-field shocks modelled by Henneton et al. [2015].

### Perspectives for coupled shock wave simulations

The results of these meteor shock wave tests are promising and strongly support the development of a fully coupled impact simulation with HOSS/FSIS. The first step of a future study should be the investigation of meteor shock waves with a 2D axi-symmetric or a 3D mesh domain. Additionally, the material model of CO<sub>2</sub> could be improved by providing it with viscosity, as in Fenghour et al. [1998], or thermal conductivity, available from Scalabrin et al. [2006]. Real gas effects such as the molecular dissociation and plasma

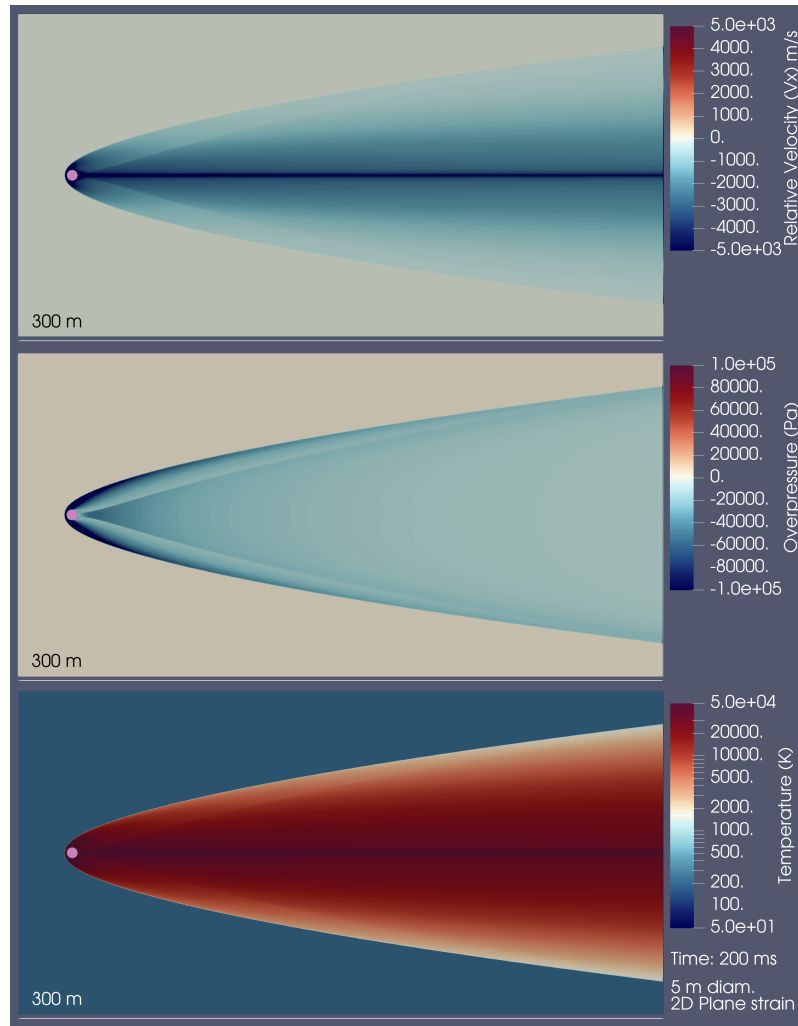


**Figure 4.3:** HOSS/FSIS simulation of a 5 m diameter bolide (pink) fixed in a  $12 \text{ km}\cdot\text{s}^{-1}$  flow of  $\text{CO}_2$  in Martian conditions of pressure and temperature. The simulation uses a 2D plane-strain representation, which means that the bolide is supposed to have infinite dimensions in the direction perpendicular to the image. The top panel represents fluid velocities along the  $x$  direction, shifted by  $12 \text{ km}\cdot\text{s}^{-1}$ . The middle panel depicts the overpressure  $P - P_0$  around the bolide, and the last panel shows the temperature field using a logarithmic scale.

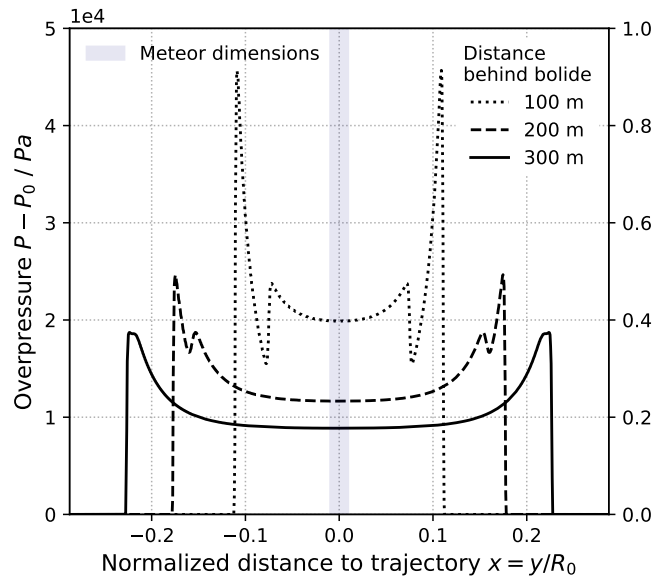


**Figure 4.4:** Overpressure recorded in the direction perpendicular to the trajectory in the simulation of Fig. 4.3, on three lines positioned 100 m, 200 m and 300 m behind the meteor. The distance away from the trajectory has been normalised by the radius  $R_0 \approx 130$  of the meteor shock wave, here calculated with  $M \approx 52$  and  $d_i = 2.5$  m (see section 3.1.1).

formation could also be included in the future, in an approach similar to [Henneton et al. \[2015\]](#). The properties of the shock, such as its detachment distance or aperture angle can be verified against results from the literature [[Henneton et al., 2015](#); [Nemec et al., 2017](#); [Silber et al., 2018](#)]. A cratering simulation can then be designed, where a deformable impactor and its shock cone impact a solid surface.

Consequently, it is possible in the near-future to conduct a quantitative investigation of a meteorite impact blast wave for small craters. Simulation results for the pressure amplitude and time series can be compared to literature results for explosions mentioned in the introduction (section 3.1.1). A coupled simulation allows to measure not only the properties of the blast, but also the effect of atmospheric interaction on the cratering seismic source described in Chapter 2. The effects of the blast loading on the surroundings of the crater can be quantified from the results of the simulation, and can help shed light on the dust features observed on some Martian impacts, such as scimitars and asymmetric halos (see Fig. 1.16 and 1.16 of the introduction). Models have been proposed by [Ivanov et al. \[2020\]](#) and [Ivanov \[2021\]](#) to explain these features by shock wave interaction.

### 4.3.3 A new view of the source

In the previous chapters, different aspects of the impact-generated seismic signals were investigated. First, we proposed an equivalent force representation of the impact cratering seismic source. Numerical modelling of these source terms provided promising results for the future development of scaling relations for the impact source. This approach is also applicable to other problems of seismology requiring a quantitative source description. In a second time, we showed that seismo-acoustic signals produced by impact shock waves on Mars contains precious information on its atmosphere and subsurface. Thanks to a 1D model of infrasound propagation and coupling, this information can be retrieved.

Both this source and seismo-acoustic wave models would benefit from the inclusion of additional physics. We highlighted an important next step, which is the investigation of impact blast waves and their interaction with the surface. Together, seismic source modelling, seismo-acoustic coupling theory and shock wave theory pave the way towards a complete understanding of impact seismic signals on Mars.





---

# Bibliography

---

- [1] Afraimovich, E.L., Perevalova, N.P., Plotnikov, A.V. and Uralov, A.M. The shock-acoustic waves generated by earthquakes. *Annales Geophysicae*, 19(4):395–409, April 2001. ISSN 1432-0576. doi: 10.5194/angeo-19-395-2001.
- [2] Agnew, D.C. 1 History of seismology. In *International Geophysics*, volume 81, pages 3–11. Elsevier, 2002. ISBN 978-0-12-440652-0. doi: 10.1016/S0074-6142(02)80203-0.
- [3] Agnor, C. On the Character and Consequences of Large Impacts in the Late Stage of Terrestrial Planet Formation. *Icarus*, 142(1):219–237, November 1999. ISSN 00191035. doi: 10.1006/icar.1999.6201.
- [4] Aki, K. Scaling law of seismic spectrum. *Journal of Geophysical Research (1896-1977)*, 72(4):1217–1231, 1967. ISSN 2156-2202. doi: 10.1029/JZ072i004p01217.
- [5] Aki, K. and Richards, P.G. Quantitative Seismology, 2nd Ed. *Quantitative Seismology, 2nd Ed., by Keiiti Aki and Paul G. Richards. Published by University Science Books, ISBN 0-935702-96-2, 704pp, 2002., 2002.*
- [6] Albarède, F. Volatile accretion history of the terrestrial planets and dynamic implications. *Nature*, 461(7268):1227–1233, October 2009. ISSN 1476-4687. doi: 10.1038/nature08477.
- [7] Amsden, A.A., Ruppel, H.M. and Hirt, C.W. SALE: A simplified ALE computer program for fluid flow at all speeds. Technical Report LA-8095, Los Alamos National Lab. (LANL), Los Alamos, NM (United States), June 1980.
- [8] Anderson, D.L., Miller, W.F., Latham, G.V., Nakamura, Y., Toksöz, M.N. et al. Seismology on Mars. *Journal of Geophysical Research (1896-1977)*, 82(28):4524–4546, 1977. ISSN 2156-2202. doi: 10.1029/JS082i028p04524.
- [9] Andrews, D.J. Test of two methods for faulting in finite-difference calculations. *Bulletin of the Seismological Society of America*, 89(4):931–937, August 1999. ISSN 1943-3573, 0037-1106. doi: 10.1785/BSSA0890040931.
- [10] Anglin, F.M. and Haddon, R.a.W. Meteoroid sonic shock-wave-generated seismic signals observed at a seismic array. *Nature*, 328(6131):607–609, August 1987. ISSN 1476-4687. doi: 10.1038/328607a0.
- [11] Antier, K. and FRIPON/Vigie-ciel. Une météorite normande issue de 2023 CX1 retrouvée! – FRIPON/Vigie-ciel, February 2023.
- [12] Arakawa, M., Saiki, T., Wada, K., Ogawa, K., Kadono, T. et al. An artificial impact on the asteroid (162173) Ryugu formed a crater in the gravity-dominated regime. *Science*, 368(6486):67–71, April 2020. doi: 10.1126/science.aaz1701.

- [13] Archambeau, C.B. and Scales, J. Theoretical Models of Earthquake Phenomena and the Physical Significance of Seismic Moment Tensor Expansions. Technical report, Cooperative Institute for Research in Environmental Sciences, Boulder, CO, June 1989.
- [14] Artru, J., Farges, T. and Lognonné, P. Acoustic waves generated from seismic surface waves: Propagation properties determined from Doppler sounding observations and normal-mode modelling. *Geophysical Journal International*, 158(3):1067–1077, September 2004. ISSN 0956-540X. doi: 10.1111/j.1365-246X.2004.02377.x.
- [15] Astapowitsch, I.S. Air waves caused by the fall of the meteorite on 30th June, 1908, in Central Siberia. *Quarterly Journal of the Royal Meteorological Society*, 60(257):493–504, 1934. ISSN 1477-870X. doi: 10.1002/qj.49706025708.
- [16] Backus, G. and Mulcahy, M. Moment tensors and other phenomenological descriptions of seismic sources – I. Continuous displacements. *Geophysical Journal International*, 46(2):341–361, 08 1976. ISSN 0956-540X. doi: 10.1111/j.1365-246X.1976.tb04162.x.
- [17] Backus, G. and Mulcahy, M. Moment tensors and other phenomenological descriptions of seismic sources – II. Discontinuous displacements. *Geophysical Journal International*, 47(2):301–329, 1976.
- [18] Banerdt, W.B., Smrekar, S.E., Banfield, D., Giardini, D., Golombek, M. et al. Initial results from the InSight mission on Mars. *Nature Geoscience*, 2020. doi: <https://doi.org/10.1038/s41561-020-0544-y>.
- [19] Banfield, D., Rodriguez-Manfredi, J.A., Russell, C.T., Rowe, K.M., Leneman, D. et al. InSight Auxiliary Payload Sensor Suite (APSS). *Space Science Reviews*, 215 (1):4, 2019.
- [20] Banfield, D., Spiga, A., Newman, C., Forget, F., Lemmon, M. et al. The atmosphere of Mars as observed by InSight. *Nature Geoscience*, 13(3):190–198, March 2020. ISSN 1752-0908. doi: 10.1038/s41561-020-0534-0.
- [21] Barker, M.K., Mazarico, E., Neumann, G.A., Zuber, M.T., Haruyama, J. et al. A new lunar digital elevation model from the Lunar Orbiter Laser Altimeter and SELENE Terrain Camera. *Icarus*, 273:346–355, July 2016. ISSN 0019-1035. doi: 10.1016/j.icarus.2015.07.039.
- [22] Barnes, J.W., Turtle, E.P., Trainer, M.G., Lorenz, R.D., MacKenzie, S.M. et al. Science Goals and Objectives for the Dragonfly Titan Rotorcraft Relocatable Lander. *The Planetary Science Journal*, 2(4):130, July 2021. ISSN 2632-3338. doi: 10.3847/PSJ/abfdcf.
- [23] Barringer, D.M. Coon Mountain and Its Crater. *Proceedings of the Academy of Natural Sciences of Philadelphia*, 57:861–886, 1905. ISSN 0097-3157.
- [24] Bass, H.E. and Chambers, J.P. Absorption of sound in the Martian atmosphere. *The Journal of the Acoustical Society of America*, 109(6):3069–3071, June 2001. ISSN 0001-4966. doi: 10.1121/1.1365424. Publisher: Acoustical Society of America.
- [25] Bell III, J.F., Wolff, M.J., Malin, M.C., Calvin, W.M., Cantor, B.A. et al. Mars Reconnaissance Orbiter Mars Color Imager (MARCI): Instrument description, calibration, and performance. *Journal of Geophysical Research: Planets*, 114(E8), 2009. ISSN 2156-2202. doi: 10.1029/2008JE003315.

- [26] Ben-Menahem, A. Source parameters of the siberian explosion of June 30, 1908, from analysis and synthesis of seismic signals at four stations. *Physics of the Earth and Planetary Interiors*, 11(1):1–35, September 1975. ISSN 0031-9201. doi: 10.1016/0031-9201(75)90072-2.
- [27] Bethe, H.A., Fuchs, K., Hirschfelder, J.O., Magee, J.L., Peieris, R.E. et al. BLAST WAVE. Technical Report LA-2000, Los Alamos National Lab. (LANL), Los Alamos, NM (United States), August 1947.
- [28] Blom, P.S., Dannemann, F.K. and Marcillo, O.E. Bayesian characterization of explosive sources using infrasonic signals. *Geophysical Journal International*, 215(1): 240–251, October 2018. ISSN 0956-540X. doi: 10.1093/gji/ggy258.
- [29] Borovička, J. and Spurný, P. The Carancas meteorite impact – Encounter with a monolithic meteoroid. *Astronomy & Astrophysics*, 485(2):L1–L4, July 2008. ISSN 0004-6361, 1432-0746. doi: 10.1051/0004-6361:200809905.
- [30] Böttcher, N., Taron, J., Kolditz, O., Park, C.H. and Liedl, R. Evaluation of thermal equations of state for CO<sub>2</sub> in numerical simulations. *Environmental Earth Sciences*, 67(2):481–495, September 2012. ISSN 1866-6299. doi: 10.1007/s12665-012-1704-1.
- [31] Briaud, A., Ganino, C., Fienga, A., Mémin, A. and Rambaux, N. The lunar solid inner core and the mantle overturn. *Nature*, 617(7962):743–746, May 2023. ISSN 1476-4687. doi: 10.1038/s41586-023-05935-7.
- [32] Brown, P., ReVelle, D.O., Silber, E.A., Edwards, W.N., Arrowsmith, S. et al. Analysis of a crater-forming meteorite impact in Peru. *Journal of Geophysical Research: Planets*, 113(E9), 2008. ISSN 2156-2202. doi: 10.1029/2008JE003105.
- [33] Brown, P.G., Assink, J.D., Astiz, L., Blaauw, R., Boslough, M.B. et al. A 500-kiloton airburst over Chelyabinsk and an enhanced hazard from small impactors. *Nature*, 503(7475):238–241, November 2013. ISSN 1476-4687. doi: 10.1038/nature12741.
- [34] Brune, J.N. Tectonic stress and the spectra of seismic shear waves from earthquakes. *Journal of Geophysical Research*, 75(26):4997–5009, September 1970. ISSN 01480227. doi: 10.1029/JB075i026p04997.
- [35] Burleigh, K.J., Melosh, H.J., Tornabene, L.L., Ivanov, B., McEwen, A.S. et al. Impact airblast triggers dust avalanches on Mars. *Icarus*, 217(1):194–201, January 2012. ISSN 00191035. doi: 10.1016/j.icarus.2011.10.026.
- [36] Burridge, R. and Knopoff, L. Body force equivalents for seismic dislocations. *Bulletin of the Seismological Society of America*, 54(6A):1875–1888, December 1964. ISSN 0037-1106. doi: 10.1785/BSSA05406A1875.
- [37] Caldwell, W.K., Euser, B., Plesko, C.S., Larmat, C., Lei, Z. et al. Benchmarking Numerical Methods for Impact and Cratering Applications. *Applied Sciences*, 11(6): 2504, January 2021. doi: 10.3390/app11062504. Number: 6 Publisher: Multidisciplinary Digital Publishing Institute.
- [38] Cameron, A.G.W. and Ward, W.R. The Origin of the Moon. In *Lunar and Planetary Science Conference*, volume 7, page 120, March 1976.
- [39] Campus, P. and Christie, D.R. Worldwide Observations of Infrasonic Waves. In Le Pichon, A., Blanc, E. and Hauchecorne, A., editors, *Infrasound Monitoring for Atmospheric Studies*, pages 185–234. Springer Netherlands, Dordrecht, 2009. ISBN 978-1-4020-9508-5. doi: 10.1007/978-1-4020-9508-5\_6.

- [40] Carrasco, S., Knapmeyer-Endrun, B., Margerin, L., Schmelzbach, C., Onodera, K. et al. Empirical H/V spectral ratios at the InSight landing site and implications for the martian subsurface structure. *Geophysical Journal International*, 232(2): 1293–1310, February 2023. ISSN 0956-540X. doi: 10.1093/gji/ggac391.
- [41] Ceplecha, Z., Borovička, J., Elford, W.G., ReVelle, D.O., Hawkes, R.L. et al. Meteor Phenomena and Bodies. *Space Science Reviews*, 84(3):327–471, September 1998. ISSN 1572-9672. doi: 10.1023/A:1005069928850.
- [42] Ceylan, S., Clinton, J.F., Giardini, D., Stähler, S.C., Horleston, A. et al. The marsquake catalogue from InSight, sols 0–1011. *Physics of the Earth and Planetary Interiors*, 333:106943, December 2022. ISSN 0031-9201. doi: 10.1016/j.pepi.2022.106943.
- [43] Cheng, A.F., Agrusa, H.F., Barbee, B.W., Meyer, A.J., Farnham, T.L. et al. Momentum transfer from the DART mission kinetic impact on asteroid Dimorphos. *Nature*, 616(7957):457–460, April 2023. ISSN 1476-4687. doi: 10.1038/s41586-023-05878-z.
- [44] Christie, D.R. and Campus, P. The IMS Infrasound Network: Design and Establishment of Infrasound Stations. In Le Pichon, A., Blanc, E. and Hauchecorne, A., editors, *Infrasound Monitoring for Atmospheric Studies*, pages 29–75. Springer Netherlands, Dordrecht, 2009. ISBN 978-1-4020-9508-5. doi: 10.1007/978-1-4020-9508-5\_2.
- [45] Chyba, C.F. The cometary contribution to the oceans of primitive Earth. *Nature*, 330(6149):632–635, December 1987. ISSN 1476-4687. doi: 10.1038/330632a0.
- [46] Chyba, C.F., Thomas, P.J. and Zahnle, K.J. The 1908 Tunguska explosion: Atmospheric disruption of a stony asteroid. *Nature*, 361(6407):40–44, January 1993. ISSN 1476-4687. doi: 10.1038/361040a0.
- [47] Clinton, J., Giardini, D., Böse, M., Ceylan, S., van Driel, M. et al. The Marsquake Service: Securing Daily Analysis of SEIS Data and Building the Martian Seismicity Catalogue for InSight. *Space Science Reviews*, 214(8):133, December 2018. ISSN 1572-9672. doi: 10.1007/s11214-018-0567-5.
- [48] Collins, G.S., Melosh, H.J. and Wünnemann, K. Improvements to the  $\varepsilon$ - $\alpha$  porous compaction model for simulating impacts into high-porosity solar system objects. *International Journal of Impact Engineering*, 38(6):434–439, June 2011. ISSN 0734-743X. doi: 10.1016/j.ijimpeng.2010.10.013.
- [49] Collins, G.S., Melosh, H.J. and Osinski, G.R. The Impact-Cratering Process. *Elements*, 8(1):25–30, February 2012. ISSN 1811-5209, 1811-5217. doi: 10.2113/gselements.8.1.25.
- [50] Collins, G.S., Newland, E.L., Schwarz, D., Coleman, M., McMullan, S. et al. Meteoroid Fragmentation in the Martian Atmosphere and the Formation of Crater Clusters. *Journal of Geophysical Research: Planets*, 127(7):e2021JE007149, 2022. ISSN 2169-9100. doi: 10.1029/2021JE007149.
- [51] Collins, G.S., Miljković, K., Wojcicka, N., Rajšić, A., Lognonné, P. et al. Modeling the 150-m diameter “Christmas Eve” impact crater on Mars. In *54th Lunar and Planetary Science Conference 2023*, volume 2297, Houston, TX, 2023.
- [52] Crawford, W.C., Webb, S.C. and Hildebrand, J.A. Seafloor compliance observed by long-period pressure and displacement measurements. *Journal of Geophysical*

- Research: Solid Earth*, 96(B10):16151–16160, 1991. ISSN 2156-2202. doi: 10.1029/91JB01577.
- [53] Dahlen, F. and Tromp, J. *Theoretical global seismology*. Princeton university press, 1998. ISBN 9780691001241. doi: <https://doi.org/10.2307/j.ctv131bvfd>.
- [54] Dahmen, N.L., Zenhäusern, G., Clinton, J.F., Giardini, D., Stähler, S.C. et al. Resonances and Lander Modes Observed by InSight on Mars (1–9 Hz). *Bulletin of the Seismological Society of America*, 111(6):2924–2950, October 2021. ISSN 0037-1106. doi: 10.1785/0120210056.
- [55] Daly, R.T. and Schultz, P.H. The delivery of water by impacts from planetary accretion to present. *Science Advances*, 4(4):eaar2632, April 2018. doi: 10.1126/sciadv.aar2632.
- [56] Daubar, I.J., Lognonné, P., Teanby, N.A., Collins, G.S., Clinton, J. et al. A new crater near insight: Implications for seismic impact detectability on mars. *Journal of Geophysical Research: Planets*, 125(8):e2020JE006382, 2020. doi: <https://doi.org/10.1029/2020JE006382>.
- [57] Daubar, I.J., Dundas, C.M., McEwen, A.S., Gao, A., Wexler, D. et al. New Craters on Mars: An Updated Catalog. *Journal of Geophysical Research: Planets*, 127(7):e2021JE007145, 2022. ISSN 2169-9100. doi: 10.1029/2021JE007145.
- [58] Daubar, I.J., Lognonné, P., Teanby, N.A., Miljkovic, K., Stevanović, J. et al. Impact-seismic investigations of the InSight mission. *Space Science Reviews*, 214(8):132, 2018. doi: <https://doi.org/10.1007/s11214-018-0562-x>.
- [59] Daubar, I.J., Fernando, B.A., Garcia, R.F., Grindrod, P.M., Zenhäusern, G. et al. Two Seismic Events from InSight Confirmed as New Impacts on Mars. *The Planetary Science Journal*, 4(9):175, September 2023. ISSN 2632-3338. doi: 10.3847/PSJ/ace9b4.
- [60] Davis, P.M. Meteoroid Impacts as Seismic Sources on Mars. *Icarus*, 105(2):469–478, October 1993. ISSN 0019-1035. doi: 10.1006/icar.1993.1142.
- [61] Day, S.M. and McLaughlin, K.L. Seismic source representations for spall. *Bulletin of the Seismological Society of America*, 81(1):191–201, February 1991. ISSN 0037-1106. doi: 10.1785/BSSA0810010191.
- [62] de Vries, J., Nimmo, F., Melosh, H.J., Jacobson, S.A., Morbidelli, A. et al. Impact-induced melting during accretion of the Earth. *Progress in Earth and Planetary Science*, 3(1):7, March 2016. ISSN 2197-4284. doi: 10.1186/s40645-016-0083-8.
- [63] Denny, M.D. and Johnson, L.R. The Explosion Seismic Source Function: Models and Scaling Laws Reviewed. In *Explosion Source Phenomenology*, pages 1–24. American Geophysical Union (AGU), 1991. ISBN 978-1-118-66382-0. doi: 10.1029/GM065p0001.
- [64] Dewey, J. and Byerly, P. The early history of seismometry (to 1900). *Bulletin of the Seismological Society of America*, 59(1):183–227, February 1969. ISSN 0037-1106. doi: 10.1785/BSSA0590010183.
- [65] Dones, L. and Tremaine, S. Why Does the Earth Spin Forward? *Science*, 259(5093):350–354, January 1993. doi: 10.1126/science.259.5093.350.

- [66] Dosso, S.E., Holland, C.W. and Sambridge, M. Parallel tempering for strongly non-linear geoacoustic inversion. *The Journal of the Acoustical Society of America*, 132(5):3030–3040, November 2012. ISSN 0001-4966. doi: 10.1121/1.4757639. Publisher: Acoustical Society of America.
- [67] Drilleau, M., Samuel, H., Garcia, R.F., Rivoldini, A., Perrin, C. et al. Marsquake Locations and 1-D Seismic Models for Mars From InSight Data. *Journal of Geophysical Research: Planets*, 127(9):e2021JE007067, 2022. ISSN 2169-9100. doi: 10.1029/2021JE007067.
- [68] DuMond, J.W.M., Cohen, E.R., Panofsky, W.K.H. and Deeds, E. A Determination of the Wave Forms and Laws of Propagation and Dissipation of Ballistic Shock Waves. *The Journal of the Acoustical Society of America*, 18(1):97–118, July 1946. ISSN 0001-4966. doi: 10.1121/1.1916347.
- [69] Dunkin, J.W. and Corbin, D.G. Deformation of a layered, elastic, half-space by uniformly moving line loads. *Bulletin of the Seismological Society of America*, 60(1):167–191, February 1970. ISSN 0037-1106. doi: 10.1785/BSSA0600010167.
- [70] Durán, C., Khan, A., Ceylan, S., Charalambous, C., Kim, D. et al. Observation of a Core-Diffracted P-Wave From a Farside Impact With Implications for the Lower-Mantle Structure of Mars. *Geophysical Research Letters*, 49(21):e2022GL100887, 2022. ISSN 1944-8007. doi: 10.1029/2022GL100887.
- [71] Dziewonski, A.M. and Anderson, D.L. Preliminary reference Earth model. *Physics of the Earth and Planetary Interiors*, 25(4):297–356, June 1981. ISSN 0031-9201. doi: 10.1016/0031-9201(81)90046-7.
- [72] Edwards, W.N. Meteor Generated Infrasound: Theory and Observation. In Le Pichon, A., Blanc, E. and Hauchecorne, A., editors, *Infrasound Monitoring for Atmospheric Studies*, pages 361–414. Springer Netherlands, Dordrecht, 2009. ISBN 978-1-4020-9508-5. doi: 10.1007/978-1-4020-9508-5\_12.
- [73] Edwards, W.N., Eaton, D.W., McCausland, P.J., ReVelle, D.O. and Brown, P.G. Calibrating infrasonic to seismic coupling using the Stardust sample return capsule shockwave: Implications for seismic observations of meteors. *Journal of Geophysical Research*, 112(B10):B10306, October 2007. ISSN 0148-0227. doi: 10.1029/2006JB004621.
- [74] Edwards, W.N., Eaton, D.W. and Brown, P.G. Seismic observations of meteors: Coupling theory and observations. *Reviews of Geophysics*, 46(4):RG4007, December 2008. ISSN 8755-1209. doi: 10.1029/2007RG000253.
- [75] Ellis, J. and van Haasteren, R. jellis18/ptmcmcsampler: Official release, October 2017. URL <https://doi.org/10.5281/zenodo.1037579>.
- [76] Eshelby, J.D. The determination of the elastic field of an ellipsoidal inclusion, and related problems. *Proceedings of the royal society of London. Series A. Mathematical and physical sciences*, 241(1226):376–396, aug 1957. doi: 10.1098/rspa.1957.0133.
- [77] European Space Agency. Seventh shooting star ever spotted before it struck, February 2023. URL [https://www.esa.int/ESA\\_Multimedia/Images/2023/02/Seventh\\_shooting\\_star\\_ever\\_spotted\\_before\\_it\\_struck](https://www.esa.int/ESA_Multimedia/Images/2023/02/Seventh_shooting_star_ever_spotted_before_it_struck).
- [78] Euser, B., Rougier, E., Lei, Z., Knight, E.E., Frash, L.P. et al. Simulation of Fracture Coalescence in Granite via the Combined Finite–Discrete Element Method. *Rock*



- Mechanics and Rock Engineering*, 52(9):3213–3227, September 2019. ISSN 1434-453X. doi: 10.1007/s00603-019-01773-0.
- [79] Ewing, W.M. *Elastic Waves in Layered Media*. New York,: McGraw-Hill, 1957.
- [80] Falcioni, M. and Deem, M.W. A biased Monte Carlo scheme for zeolite structure solution. *The Journal of Chemical Physics*, 110(3):1754–1766, January 1999. ISSN 0021-9606. doi: 10.1063/1.477812. Publisher: American Institute of Physics.
- [81] Fang, Y., Poncet, S., Nesreddine, H. and Bartosiewicz, Y. An open-source density-based solver for two-phase CO<sub>2</sub> compressible flows: Verification and validation. *International Journal of Refrigeration*, 106:526–538, October 2019. ISSN 0140-7007. doi: 10.1016/j.ijrefrig.2019.05.016.
- [82] Fenghour, A., Wakeham, W.A. and Vesovic, V. The Viscosity of Carbon Dioxide. *Journal of Physical and Chemical Reference Data*, 27(1):31–44, January 1998. ISSN 0047-2689. doi: 10.1063/1.556013.
- [83] Fergason, R., Hare, T. and Laura, J. HRSC and MOLA blended digital elevation model at 200m v2, 2018.
- [84] Fernando, B., Wójcicka, N., Froment, M., Maguire, R., Stähler, S.C. et al. Listening for the Landing: Seismic Detections of Perseverance’s Arrival at Mars With InSight. *Earth and Space Science*, 8(4):e2020EA001585, 2021. ISSN 2333-5084. doi: 10.1029/2020EA001585.
- [85] Fernando, B., Wójcicka, N., Han, Z., Stott, A., Ceylan, S. et al. Questions to Heaven. *Astronomy & Geophysics*, 62(6):6.22–6.25, December 2021. ISSN 1366-8781. doi: 10.1093/astrogeo/atab103.
- [86] Fernando, B., Wójcicka, N., Maguire, R., Stähler, S.C., Stott, A.E. et al. Seismic constraints from a Mars impact experiment using InSight and Perseverance. *Nature Astronomy*, 6(1):59–64, January 2022. ISSN 2397-3366. doi: 10.1038/s41550-021-01502-0.
- [87] Folkner, W.M., Dehant, V., Le Maistre, S., Yseboodt, M., Rivoldini, A. et al. The Rotation and Interior Structure Experiment on the InSight Mission to Mars. *Space Science Reviews*, 214(5):100, August 2018. ISSN 0038-6308, 1572-9672. doi: 10.1007/s11214-018-0530-5.
- [88] Ford, S.R., Walter, W.R., Ruppert, S.D., Matzel, E.M., Hauk, T.F. et al. Toward an Empirically-Based Parametric Explosion Spectral Model. Technical Report ADA568895, Lawrence Livermore National Laboratory, CA, USA, Tucson, AZ, September 2011.
- [89] Foreman-Mackey, D., Hogg, D.W., Lang, D. and Goodman, J. emcee: The MCMC Hammer. *Publications of the Astronomical Society of the Pacific*, 125(925):306–312, March 2013. ISSN 00046280, 15383873. doi: 10.1086/670067. arXiv: 1202.3665.
- [90] Franck, L., Guillaume, R., Claire, B., Leonard, K. and Philipp, B. Comparison on seismometer sensitivity following ISO 16063-11 standard. In Gazal, S., editor, *19th International Congress of Metrology (CIM2019)*, page 27003, Paris, France, 2019. EDP Sciences. ISBN 978-2-7598-9069-9. doi: 10.1051/metrology/201927003.
- [91] Friedlander, F.G. and Taylor, G.I. The diffraction of sound pulses I. Diffraction by a semi-infinite plane. *Proceedings of the Royal Society of London. Series A. Mathematical and Physical Sciences*, 186(1006):322–344, January 1997. doi: 10.1098/rspa.1946.0046.

- [92] Froment, M., Rougier, E., Larmat, C., Lei, Z., Euser, B. et al. Lagrangian-based Simulations of Hypervelocity Impact Experiments on Mars Regolith Proxy. *Geophysical Research Letters*, 47(13), July 2020. ISSN 0094-8276, 1944-8007. doi: 10.1029/2020GL087393.
- [93] Fukao, Y., Widiyantoro, S. and Obayashi, M. Stagnant slabs in the upper and lower mantle transition region. *Reviews of Geophysics*, 39(3):291–323, 2001. ISSN 1944-9208. doi: 10.1029/1999RG000068.
- [94] Gagnepain-Beyneix, J., Lognonné, P., Chenet, H., Lombardi, D. and Spohn, T. A seismic model of the lunar mantle and constraints on temperature and mineralogy. *Physics of the Earth and Planetary Interiors*, 159(3):140–166, December 2006. ISSN 0031-9201. doi: 10.1016/j.pepi.2006.05.009.
- [95] Gainville, O., Henneon, M. and Coulouvrat, F. A re-analysis of Carancas meteorite seismic and infrasound data based on sonic boom hypothesis. *Geophysical Journal International*, 209(3):1913–1923, June 2017. ISSN 0956-540X. doi: 10.1093/gji/ggx122.
- [96] Gao, K., Euser, B.J., Rougier, E., Guyer, R.A., Lei, Z. et al. Modeling of Stick-Slip Behavior in Sheared Granular Fault Gouge Using the Combined Finite-Discrete Element Method. *Journal of Geophysical Research: Solid Earth*, 123(7):5774–5792, 2018. ISSN 2169-9356. doi: 10.1029/2018JB015668.
- [97] Garces, M. Explosion Source Models. In Le Pichon, A., Blanc, E. and Hauchecorne, A., editors, *Infrasound Monitoring for Atmospheric Studies: Challenges in Middle Atmosphere Dynamics and Societal Benefits*, pages 273–345. Springer International Publishing, Cham, 2019. ISBN 978-3-319-75140-5. doi: 10.1007/978-3-319-75140-5\_8.
- [98] Garces, M.A. *The Acoustics of Volcanic Explosions*. PhD thesis, University of California, San Diego, January 1995.
- [99] Garcia, R.F., Gagnepain-Beyneix, J., Chevrot, S. and Lognonné, P. Very preliminary reference Moon model. *Physics of the Earth and Planetary Interiors*, 188(1-2):96–113, September 2011. ISSN 00319201. doi: 10.1016/j.pepi.2011.06.015.
- [100] Garcia, R.F., Brissaud, Q., Rolland, L., Martin, R., Komatitsch, D. et al. Finite-Difference Modeling of Acoustic and Gravity Wave Propagation in Mars Atmosphere: Application to Infrasounds Emitted by Meteor Impacts. *Space Science Reviews*, 211(1):547–570, October 2017. ISSN 1572-9672. doi: 10.1007/s11214-016-0324-6.
- [101] Garcia, R.F., Khan, A., Drilleau, M., Margerin, L., Kawamura, T. et al. Lunar Seismology: An Update on Interior Structure Models. *Space Science Reviews*, 215(8):50, November 2019. ISSN 1572-9672. doi: 10.1007/s11214-019-0613-y.
- [102] Garcia, R.F., Kenda, B., Kawamura, T., Spiga, A., Murdoch, N. et al. Pressure Effects on the SEIS-InSight Instrument, Improvement of Seismic Records, and Characterization of Long Period Atmospheric Waves From Ground Displacements. *Journal of Geophysical Research: Planets*, 125(7):e2019JE006278, 2020. ISSN 2169-9100. doi: 10.1029/2019JE006278.
- [103] Garcia, R.F., Murdoch, N., Lorenz, R., Spiga, A., Bowman, D.C. et al. Search for Infrasound Signals in InSight Data Using Coupled Pressure/Ground Deformation Methods. *Bulletin of the Seismological Society of America*, 111(6):3055–3064, October 2021. ISSN 0037-1106. doi: 10.1785/0120210079.

- [104] Garcia, R.F., Daubar, I.J., Beucler, É., Posiolova, L.V., Collins, G.S. et al. Newly formed craters on Mars located using seismic and acoustic wave data from InSight. *Nature Geoscience*, pages 1–7, September 2022. ISSN 1752-0908. doi: 10.1038/s41561-022-01014-0.
- [105] Gardner, G.H.F., Gardner, L.W. and Gregory, A.R. Formation velocity and density—the diagnostic basics for stratigraphic traps. *GEOPHYSICS*, 39(6):770–780, December 1974. ISSN 0016-8033. doi: 10.1190/1.1440465.
- [106] Geyer, C.J. Markov Chain Monte Carlo Maximum Likelihood. In *Computing Science and Statistics: Proceedings of the 23rd Symposium on the Interface*, pages 156–163, New York, 1991. American Statistical Association.
- [107] Giardini, D., Lognonné, P., Banerdt, W.B., Pike, W.T., Christensen, U. et al. The seismicity of Mars. *Nature Geoscience*, 2020. doi: <https://doi.org/10.1038/s41561-020-0539-8>.
- [108] Giardini, D., Ceylan, S., Clinton, J., Lognonné, P. and Stähler, S. The Seismicity of Mars Observed by the NASA InSight Mission. *European Review*, 30(5):639–656, October 2022. ISSN 1062-7987, 1474-0575. doi: 10.1017/S1062798722000254.
- [109] Gilbert, G.K. *The Moon's Face: A Study of the Origin of Its Features*. Philosophical Society of Washington, 1893.
- [110] Giljarhus, K.E.T., Munkejord, S.T. and Skaugen, G. Solution of the Span–Wagner Equation of State Using a Density–Energy State Function for Fluid-Dynamic Simulation of Carbon Dioxide. *Industrial & Engineering Chemistry Research*, 51(2): 1006–1014, January 2012. ISSN 0888-5885. doi: 10.1021/ie201748a.
- [111] Gillet, K., Margerin, L., Calvet, M. and Monnereau, M. Scattering attenuation profile of the Moon: Implications for shallow moonquakes and the structure of the megaregolith. *Physics of the Earth and Planetary Interiors*, 262:28–40, January 2017. ISSN 00319201. doi: 10.1016/j.pepi.2016.11.001.
- [112] Gisler, G., Weaver, R., Gittings, M. and Mader, C. Two- and three-dimensional asteroid ocean impact simulations. *International Journal of Impact Engineering*, 29 (1):283–291, December 2003. ISSN 0734-743X. doi: 10.1016/j.ijimpeng.2003.09.023.
- [113] Golombek, M., Warner, N.H., Grant, J.A., Hauber, E., Ansan, V. et al. Geology of the InSight landing site on Mars. *Nature Communications*, 11(1):1014, February 2020. ISSN 2041-1723. doi: 10.1038/s41467-020-14679-1.
- [114] Golombek, M., Williams, N., Warner, N.H., Parker, T., Williams, M.G. et al. Location and Setting of the Mars InSight Lander, Instruments, and Landing Site. *Earth and Space Science*, 7(10):e2020EA001248, 2020. ISSN 2333-5084. doi: 10.1029/2020EA001248.
- [115] Golombek, M., Hudson, T., Bailey, P., Balabanska, N., Marteau, E. et al. Results from InSight Robotic Arm Activities. *Space Science Reviews*, 219(3):20, March 2023. ISSN 1572-9672. doi: 10.1007/s11214-023-00964-0.
- [116] Goodman, J. and Weare, J. Ensemble samplers with affine invariance. *Communications in Applied Mathematics and Computational Science*, 5(1):65–80, January 2010. ISSN 2157-5452, 1559-3940. doi: 10.2140/camcos.2010.5.65.
- [117] Granström, S.A. *Loading Characteristics of Air Blasts from Detonating Charges*. Lindståhl, 1956.

- [118] Gudkova, T.V., Lognonné, P. and Gagnepain-Beyneix, J. Large impacts detected by the Apollo seismometers: Impactor mass and source cutoff frequency estimations. *Icarus*, 211(2):1049–1065, February 2011. ISSN 0019-1035. doi: 10.1016/j.icarus.2010.10.028.
- [119] Gudkova, T., Lognonné, P., Miljković, K. and Gagnepain-Beyneix, J. Impact cutoff frequency – momentum scaling law inverted from Apollo seismic data. *Earth and Planetary Science Letters*, 427:57–65, October 2015. ISSN 0012821X. doi: 10.1016/j.epsl.2015.06.037.
- [120] Güldemeister, N. and Wünnemann, K. Quantitative analysis of impact-induced seismic signals by numerical modeling. *Icarus*, 296:15–27, November 2017. ISSN 0019-1035. doi: 10.1016/j.icarus.2017.05.010.
- [121] Halliday, I., Blackwell, A.T. and Griffin, A.A. The Frequency of Meteorite Falls on the Earth. *Science*, 223(4643):1405–1407, 1984. ISSN 0036-8075.
- [122] Hammer, M., Ervik, Å. and Munkejord, S.T. Method Using a Density–Energy State Function with a Reference Equation of State for Fluid–Dynamics Simulation of Vapor–Liquid–Solid Carbon Dioxide. *Industrial & Engineering Chemistry Research*, 52(29):9965–9978, July 2013. ISSN 0888-5885, 1520-5045. doi: 10.1021/ie303516m.
- [123] Hartmann, W.K. Terrestrial and lunar flux of large meteorites in the last two billion years. *Icarus*, 4(2):157–165, May 1965. ISSN 00191035. doi: 10.1016/0019-1035(65)90057-6.
- [124] Hartmann, W.K. Ancient lunar mega-regolith and subsurface structure. *Icarus*, 18(4):634–636, April 1973. ISSN 0019-1035. doi: 10.1016/0019-1035(73)90066-3.
- [125] Hartmann, W.K. Martian cratering 8: Isochron refinement and the chronology of Mars. *Icarus*, 174(2):294–320, April 2005. ISSN 0019-1035. doi: 10.1016/j.icarus.2004.11.023.
- [126] Hartmann, W.K. and Davis, D.R. Satellite-sized planetesimals and lunar origin. *Icarus*, 24(4):504–515, April 1975. ISSN 0019-1035. doi: 10.1016/0019-1035(75)90070-6.
- [127] Hartmann, W.K. and Neukum, G. Cratering Chronology and the Evolution of Mars. In Kallenbach, R., Geiss, J. and Hartmann, W.K., editors, *Chronology and Evolution of Mars*, Space Sciences Series of ISSI, pages 165–194, Dordrecht, 2001. Springer Netherlands. ISBN 978-94-017-1035-0. doi: 10.1007/978-94-017-1035-0\_6.
- [128] Haskell, N.A. Total energy and energy spectral density of elastic wave radiation from propagating faults. Part II. A statistical source model. *Bulletin of the Seismological Society of America*, 56(1):125–140, February 1966. ISSN 0037-1106. doi: 10.1785/BSSA0560010125.
- [129] Haskell, N.A. Elastic displacements in the near-field of a propagating fault. *Bulletin of the Seismological Society of America*, 59(2):865, 04 1969. ISSN 0037-1106. doi: 10.1785/BSSA0590020865.
- [130] Hastings, W.K. Monte Carlo Sampling Methods Using Markov Chains and Their Applications. *Biometrika*, 57(1):97–109, 1970. ISSN 0006-3444. doi: 10.2307/2334940. Publisher: [Oxford University Press, Biometrika Trust].

- [131] Hayek Valencia, J.N., May, D., Pranger, C. and Gabriel, A.A. Diffuse thick fault representation in 2D SEM for earthquake dynamic rupture simulations. In *EGU22*, volume EGU22-12539, EGU General Assembly 2022, Vienna, Austria, March 2022. Copernicus Meetings. doi: 10.5194/egusphere-egu22-12539.
- [132] Henneton, M., Gainville, O. and Coulouvrat, F. Numerical Simulation of Sonic Boom from Hypersonic Meteoroids. *AIAA Journal*, 53(9):2560–2570, September 2015. ISSN 0001-1452, 1533-385X. doi: 10.2514/1.J053421.
- [133] Herrin, E.T., Kim, T.S. and Stump, B.W. Evidence for an infrasound waveguide. *Geophysical Research Letters*, 33(7), 2006. ISSN 1944-8007. doi: 10.1029/2005GL025491.
- [134] Herrmann, R.B., Benz, H. and Ammon, C.J. Monitoring the Earthquake Source Process in North America. *Bulletin of the Seismological Society of America*, 101(6): 2609–2625, December 2011. ISSN 0037-1106. doi: 10.1785/0120110095.
- [135] Herrmann, R.B. Computer Programs in Seismology: An Evolving Tool for Instruction and Research. *Seismological Research Letters*, 84(6):1081–1088, November 2013. ISSN 0895-0695. doi: 10.1785/0220110096.
- [136] Hobiger, M., Hallo, M., Schmelzbach, C., Stähler, S.C., Fäh, D. et al. The shallow structure of Mars at the InSight landing site from inversion of ambient vibrations. *Nature Communications*, 12(1):6756, November 2021. ISSN 2041-1723. doi: 10.1038/s41467-021-26957-7.
- [137] Hoger, A. and Carlson, D.E. Determination of the stretch and rotation in the polar decomposition of the deformation gradient. *Quarterly of Applied Mathematics*, 42 (1):113–117, 1984. ISSN 0033569X, 15524485.
- [138] Holsapple, K.A. The scaling of impact processes in planetary sciences. *Ann. Rev. Earth Planet. Sci.*, 21:333–373, 1993.
- [139] Holsapple, K.A. The scaling of impact processes in planetary sciences. *Ann. Rev. Earth Planet. Sci.*, 21:333–373, 1993. doi: 10.1146/annurev.earth.21.050193.002001.
- [140] Holsapple, K.A. IMPACTS – A program to calculate the effects of a hypervelocity impact into a Solar System body, March 2022.
- [141] Housen, K.R., Sweet, W.J. and Holsapple, K.A. Impacts into porous asteroids. *Icarus*, 300:72–96, January 2018. ISSN 00191035. doi: 10.1016/j.icarus.2017.08.019.
- [142] Ichihara, M., Kusakabe, T., Kame, N. and Kumagai, H. On volume-source representations based on the representation theorem. *Earth, Planets and Space*, 68(1): 14, January 2016. ISSN 1880-5981. doi: 10.1186/s40623-016-0387-3.
- [143] Ida, S., Canup, R.M. and Stewart, G.R. Lunar accretion from an impact-generated disk. *Nature*, 389(6649):353–357, September 1997. ISSN 1476-4687. doi: 10.1038/38669.
- [144] InSight Marsquake Service. Mars seismic catalogue, insight mission; v8 2021-10-01, 2021. URL <https://www.insight.ethz.ch/seismicity/catalog/v8>.
- [145] InSight Marsquake Service. Mars Seismic Catalogue, InSight Mission; V14 2023-04-01, 2023.

- [146] Irschik, H. and Holl, H.J. Mechanics of variable-mass systems—Part 1: Balance of mass and linear momentum. *Applied Mechanics Reviews*, 57(2):145–160, April 2004. ISSN 0003-6900. doi: 10.1115/1.1687409.
- [147] Irving, J.C.E., Lekić, V., Durán, C., Drilleau, M., Kim, D. et al. First observations of core-transiting seismic phases on Mars. *Proceedings of the National Academy of Sciences*, 120(18):e2217090120, May 2023. doi: 10.1073/pnas.2217090120.
- [148] Ishihara, Y., Hiramatsu, Y., Yamamoto, M.y., Furumoto, M. and Fujita, K. Infra-sound/seismic observation of the Hayabusa reentry: Observations and preliminary results. *Earth, Planets and Space*, 64(7):655–660, July 2012. ISSN 1880-5981. doi: 10.5047/eps.2012.01.003.
- [149] Ivanov, B. Mars surface dust activation at small meteoroid’s impacts. Technical Report EGU21-10018, Copernicus Meetings, March 2021.
- [150] Ivanov, B., Barnes, G., Daubar, I., Dundas, C., McEwen, A. et al. New craters on Mars: Air shock wave traces. Technical Report EGU2020-4212, Copernicus Meetings, March 2020.
- [151] Ivanov, B.A. Mars/Moon Cratering Rate Ratio Estimates. *Space Science Reviews*, 96(1):87–104, April 2001. ISSN 1572-9672. doi: 10.1023/A:1011941121102.
- [152] Jeffreys, H. On the Cause of Oscillatory Movement in Seismograms. *Geophysical Supplements to the Monthly Notices of the Royal Astronomical Society*, 2(8):407–416, June 1931. ISSN 2051-1965. doi: 10.1111/j.1365-246X.1931.tb04462.x.
- [153] Jordan, T.H. and Juarez, A. Representation of complex seismic sources by orthogonal moment-tensor fields. *Geophysical Journal International*, 216(3):1867–1889, March 2019. ISSN 0956-540X, 1365-246X. doi: 10.1093/gji/ggy492.
- [154] Julian, B.R., Miller, A.D. and Foulger, G.R. Non-double-couple earthquakes 1. Theory. *Reviews of Geophysics*, 36(4):525–549, November 1998. ISSN 87551209. doi: 10.1029/98RG00716.
- [155] Kamigaichi, O., Saito, M., Doi, K., Matsumori, T., Tsukada, S. et al. Earthquake Early Warning in Japan: Warning the General Public and Future Prospects. *Seismological Research Letters*, 80(5):717–726, September 2009. ISSN 0895-0695. doi: 10.1785/gssrl.80.5.717.
- [156] Kanamori, H. and Given, J.W. Analysis of long-period seismic waves excited by the May 18, 1980, eruption of Mount St. Helens—A terrestrial monopole? *Journal of Geophysical Research: Solid Earth*, 87(B7):5422–5432, 1982. ISSN 2156-2202. doi: 10.1029/JB087iB07p05422.
- [157] Karakostas, F., Rakoto, V., Lognonné, P., Larmat, C., Daubar, I. et al. Inversion of Meteor Rayleigh Waves on Earth and Modeling of Air Coupled Rayleigh Waves on Mars. *Space Science Reviews*, 214(8):127, December 2018. ISSN 0038-6308, 1572-9672. doi: 10.1007/s11214-018-0566-6.
- [158] Kawakatsu, H. and Yamamoto, M. 4.15 - Volcano Seismology. In Schubert, G., editor, *Treatise on Geophysics (Second Edition)*, pages 389–419. Elsevier, Oxford, January 2015. ISBN 978-0-444-53803-1. doi: 10.1016/B978-0-444-53802-4.00081-6.
- [159] Kawamura, T., Kobayashi, N., Tanaka, S., Lognonné, P. and Gagnepain-Beyneix, J. Search for Farside Deep Moonquakes: Source Determination of Unlocated Deep

- Moonquakes with Apollo 17 Lunar Surface Gravimeter. In *41st Lunar and Planetary Science Conference*, volume LPI Contribution No. 1533, page 1766, The Woodlands, Texas, March 2010.
- [160] Kawamura, T., Lognonné, P., Nishikawa, Y. and Tanaka, S. Evaluation of deep moonquake source parameters: Implication for fault characteristics and thermal state. *Journal of Geophysical Research: Planets*, 122(7):1487–1504, 2017. ISSN 2169-9100. doi: 10.1002/2016JE005147.
- [161] Kawamura, T., Clinton, J.F., Zenhäusern, G., Ceylan, S., Horleston, A.C. et al. S1222a—The Largest Marsquake Detected by InSight. *Geophysical Research Letters*, 50(5):e2022GL101543, 2023. ISSN 1944-8007. doi: 10.1029/2022GL101543.
- [162] Kelley, M.S., Vilas, F., Gaffey, M.J. and Abell, P.A. Quantified mineralogical evidence for a common origin of 1929 Kollaa with 4 Vesta and the HED meteorites. *Icarus*, 165(1):215–218, September 2003. ISSN 0019-1035. doi: 10.1016/S0019-1035(03)00149-0.
- [163] Kenda, B., Drilleau, M., Garcia, R.F., Kawamura, T., Murdoch, N. et al. Subsurface Structure at the InSight Landing Site From Compliance Measurements by Seismic and Meteorological Experiments. *Journal of Geophysical Research: Planets*, 125(6):e2020JE006387, 2020. ISSN 2169-9100. doi: 10.1029/2020JE006387. [\\_eprint: https://onlinelibrary.wiley.com/doi/pdf/10.1029/2020JE006387](https://onlinelibrary.wiley.com/doi/pdf/10.1029/2020JE006387).
- [164] Khan, A. and Mosegaard, K. An inquiry into the lunar interior: A nonlinear inversion of the Apollo lunar seismic data. *Journal of Geophysical Research: Planets*, 107(E6): 3–1–3–23, 2002. ISSN 2156-2202. doi: 10.1029/2001JE001658.
- [165] Khan, A., Ceylan, S., Van Driel, M., Giardini, D., Lognonné, P. et al. Upper mantle structure of Mars from InSight seismic data. *Science*, 373(6553):434–438, July 2021. ISSN 0036-8075, 1095-9203. doi: 10.1126/science.abf2966.
- [166] Kim, D., Banerdt, W.B., Ceylan, S., Giardini, D., Lekić, V. et al. Surface waves and crustal structure on Mars. *Science*, 378(6618):417–421, October 2022. doi: 10.1126/science.abq7157.
- [167] Kim, K. and Rodgers, A. Waveform inversion of acoustic waves for explosion yield estimation. *Geophysical Research Letters*, 43(13):6883–6890, 2016. ISSN 1944-8007. doi: 10.1002/2016GL069624.
- [168] Kim, K. and Rodgers, A. Influence of low-altitude meteorological conditions on local infrasound propagation investigated by 3-D full-waveform modeling. *Geophysical Journal International*, 210(2):1252–1263, August 2017. ISSN 0956-540X. doi: 10.1093/gji/ggx218.
- [169] Kinney, G.F. and Graham, K.J. *Explosive Shocks in Air*. Springer Berlin Heidelberg, Berlin, Heidelberg, 1985. ISBN 978-3-642-86684-5 978-3-642-86682-1. doi: 10.1007/978-3-642-86682-1.
- [170] Knapmeyer-Endrun, B., Golombek, M.P. and Ohrnberger, M. Rayleigh Wave Ellipticity Modeling and Inversion for Shallow Structure at the Proposed InSight Landing Site in Elysium Planitia, Mars. *Space Science Reviews*, 211(1):339–382, October 2017. ISSN 1572-9672. doi: 10.1007/s11214-016-0300-1.
- [171] Knapmeyer-Endrun, B., Panning, M.P., Bissig, F., Joshi, R., Khan, A. et al. Thickness and structure of the martian crust from InSight seismic data. *Science*, 373



- (6553):438–443, July 2021. ISSN 0036-8075, 1095-9203. doi: 10.1126/science.abf8966.
- [172] Knight, E.E., Rougier, E., Lei, Z., Euser, B., Chau, V. et al. HOSS: an implementation of the combined finite-discrete element method. *Computational Particle Mechanics*, 7(5):765–787, October 2020. ISSN 2196-4378, 2196-4386. doi: 10.1007/s40571-020-00349-y.
- [173] Komatitsch, D. and Tromp, J. Spectral-element simulations of global seismic wave propagation—I. Validation. *Geophysical Journal International*, 149(2):390–412, May 2002. ISSN 0956-540X. doi: 10.1046/j.1365-246X.2002.01653.x.
- [174] Komatitsch, D. and Vilotte, J.P. The spectral element method: an efficient tool to simulate the seismic response of 2D and 3D geological structures. *Bulletin of the seismological society of America*, 88(2):368–392, 04 1998. ISSN 0037-1106. doi: 10.1785/BSSA0880020368.
- [175] Korycansky, D. and Zahnle, K. Modeling crater populations on Venus and Titan. *Planetary and Space Science*, 53(7):695–710, June 2005. ISSN 00320633. doi: 10.1016/j.pss.2005.03.002.
- [176] Kosarev, I.B., Losseva, T.V., Nemtchinov, I.V., Shuvalov, V.V. and Greeley, R. Atmospheric Disturbances and Radiation Impulses Caused by Large-Meteoroid Impacts on the Surface of Mars. I. Formation and Evolution of Dust Cloud. *Solar System Research*, 36(3):175–192, May 2002. ISSN 1608-3423. doi: 10.1023/A:1015894213795.
- [177] Lamb, H. I. On the propagation of tremors over the surface of an elastic solid. *Philosophical Transactions of the Royal Society of London. Series A, Containing Papers of a Mathematical or Physical Character*, 203(359-371):1–42, January 1997. doi: 10.1098/rsta.1904.0013.
- [178] Landau, L.D. and Lifshitz, E.M. *Fluid Mechanics: Landau and Lifshitz: Course of Theoretical Physics, Volume 6*. Elsevier, 1987. ISBN 978-1-4831-6104-4.
- [179] Langston, C.A. Seismic ground motions from a bolide shock wave. *Journal of Geophysical Research: Solid Earth*, 109(B12), 2004. ISSN 2156-2202. doi: 10.1029/2004JB003167.
- [180] Larmat, C.S., Steedman, D.W., Rougier, E., Delorey, A. and Bradley, C.R. Coupling hydrodynamic and wave propagation modeling for waveform modeling of SPE. In *AGU Fall Meeting Abstracts*, volume 2015, pages S53B–2799, December 2015.
- [181] Larmat, C., Onodera, K., Maguire, R. and Lognonné, P. Modelling to resolve whether SEIS, the seismometer of the NASA Insight lander, has detected the formation of a 1.5m diameter crater which occurred about 40km away., 2020.
- [182] Laster, S.J. and Press, F. A new estimate of lunar seismicity due to meteorite impact. *Physics of the Earth and Planetary Interiors*, 1(3):151–154, April 1968. ISSN 00319201. doi: 10.1016/0031-9201(68)90003-4.
- [183] Latham, G., Ewing, M., Press, F. and Sutton, G. The Apollo Passive Seismic Experiment. *Science*, 165(3890):241–250, July 1969. ISSN 0036-8075, 1095-9203. doi: 10.1126/science.165.3890.241.

- [184] Latham, G., Ewing, M., Dorman, J., Press, F., Toksoz, N. et al. Seismic Data from Man-Made Impacts on the Moon. *Science*, 170(3958):620–626, November 1970. ISSN 0036-8075, 1095-9203. doi: 10.1126/science.170.3958.620. Publisher: American Association for the Advancement of Science Section: Reports.
- [185] Latham, G.V., Ewing, M., Press, F., Sutton, G., Dorman, J. et al. Passive Seismic Experiment. *Science*, 167(3918):455–457, January 1970. ISSN 0036-8075, 1095-9203. doi: 10.1126/science.167.3918.455.
- [186] Lazarewicz, A.R. Viking Marsquakes 1976—Seismic Archaeology. *Journal of Geophysical Research: Planets*, 128(7):e2022JE007660, July 2023. ISSN 2169-9097, 2169-9100. doi: 10.1029/2022JE007660.
- [187] Le Feuvre, M. and Wieczorek, M.A. Nonuniform cratering of the Moon and a revised crater chronology of the inner Solar System. *Icarus*, 214(1):1–20, July 2011. ISSN 0019-1035. doi: 10.1016/j.icarus.2011.03.010.
- [188] Le Pichon, A., Antier, K., Cansi, Y., Hernandez, B., Minaya, E. et al. Evidence for a meteoritic origin of the September 15, 2007, Carancas crater. *Meteoritics & Planetary Science*, 43(11):1797–1809, 2008. ISSN 1945-5100. doi: 10.1111/j.1945-5100.2008.tb00644.x.
- [189] Le Pichon, A., Blanc, E. and Hauchecorne, A., editors. *Infrasound Monitoring for Atmospheric Studies: Challenges in Middle Atmosphere Dynamics and Societal Benefits*. Springer International Publishing, Cham, 2019. ISBN 978-3-319-75138-2 978-3-319-75140-5. doi: 10.1007/978-3-319-75140-5.
- [190] Lefeuvre, M. and Wieczorek, M. Nonuniform cratering of the terrestrial planets. *Icarus*, 197(1):291–306, September 2008. ISSN 00191035. doi: 10.1016/j.icarus.2008.04.011.
- [191] Lei, Z., Rougier, E., Knight, E.E. and Munjiza, A. A framework for grand scale parallelization of the combined finite discrete element method in 2d. *Computational Particle Mechanics*, 1(3):307–319, September 2014. ISSN 2196-4378, 2196-4386. doi: 10.1007/s40571-014-0026-3.
- [192] Lei, Z., Bradley, C.R., Munjiza, A., Rougier, E. and Euser, B. A novel framework for elastoplastic behaviour of anisotropic solids. *Computational Particle Mechanics*, 7(5):823–838, October 2020. ISSN 2196-4378, 2196-4386. doi: 10.1007/s40571-020-00345-2.
- [193] Lesage, P., Heap, M.J. and Kushnir, A. A generic model for the shallow velocity structure of volcanoes. *Journal of Volcanology and Geothermal Research*, 356:114–126, May 2018. ISSN 0377-0273. doi: 10.1016/j.jvolgeores.2018.03.003.
- [194] Linkin, V., Harri, A.M., Lipatov, A., Belostotskaja, K., Derbunovich, B. et al. A sophisticated lander for scientific exploration of Mars: Scientific objectives and implementation of the Mars-96 Small Station. *Planetary and Space Science*, 46(6): 717–737, June 1998. ISSN 0032-0633. doi: 10.1016/S0032-0633(98)00008-7.
- [195] Lisjak, A., Tatone, B.S.A., Grasselli, G. and Vietor, T. Numerical Modelling of the Anisotropic Mechanical Behaviour of Opalinus Clay at the Laboratory-Scale Using FEM/DEM. *Rock Mechanics and Rock Engineering*, 47(1):187–206, January 2014. ISSN 1434-453X. doi: 10.1007/s00603-012-0354-7.

- [196] Lognonné, P. and Johnson, C.L. 10.03 - Planetary Seismology. In Schubert, G., editor, *Treatise on Geophysics (Second Edition)*, pages 65–120. Elsevier, Oxford, January 2015. doi: 10.1016/B978-0-444-53802-4.00167-6.
- [197] Lognonné, P., Zharkov, V.N., Karczewski, J.F., Romanowicz, B., Menvielle, M. et al. The seismic OPTIMISM experiment. *Planetary and Space Science*, 46(6):739–747, June 1998. ISSN 0032-0633. doi: 10.1016/S0032-0633(98)00009-9.
- [198] Lognonné, P., Banerdt, W.B., Giardini, D., Pike, W.T., Christensen, U. et al. SEIS: Insight’s Seismic Experiment for Internal Structure of Mars. *Space Science Reviews*, 215(1):12, 2019.
- [199] Lognonné, P., Banerdt, W., Pike, W., Giardini, D., Christensen, U. et al. Constraints on the shallow elastic and anelastic structure of Mars from InSight seismic data. *Nature geoscience*, 2020. doi: <http://doi.org/10.1038/s41561-020-0536-y>.
- [200] Lognonné, P., Banerdt, W., Clinton, J., Garcia, R., Giardini, D. et al. Mars Seismology. *Annual Review of Earth and Planetary Sciences*, 51(1):643–670, May 2023. ISSN 0084-6597. doi: 10.1146/annurev-earth-031621-073318.
- [201] Lognonné, P., Mosser, B. and Dahlen, F. Excitation of jovian seismic waves by the Shoemaker-Levy 9 cometary impact. *Icarus*, 110(2):180–195, 1994.
- [202] Lognonné, P. and Clévéde, E. 10 - Normal Modes of the Earth and Planets. In Lee, W.H.K., Kanamori, H., Jennings, P.C. and Kisslinger, C., editors, *International Geophysics*, volume 81 of *International Handbook of Earthquake and Engineering Seismology, Part A*, pages 125–cp1. Academic Press, January 2002. doi: 10.1016/S0074-6142(02)80213-3.
- [203] Lognonné, P., Gagnepain-Beyneix, J. and Chenet, H. A new seismic model of the Moon: Implications for structure, thermal evolution and formation of the Moon. *Earth and Planetary Science Letters*, 211(1):27–44, June 2003. ISSN 0012-821X. doi: 10.1016/S0012-821X(03)00172-9.
- [204] Lognonné, P., Karakostas, F., Rolland, L. and Nishikawa, Y. Modeling of atmospheric-coupled Rayleigh waves on planets with atmosphere: From Earth observation to Mars and Venus perspectives. *The Journal of the Acoustical Society of America*, 140(2):1447–1468, August 2016. ISSN 0001-4966. doi: 10.1121/1.4960788.
- [205] Lognonné, P., Le Feuvre, M., Johnson, C.L. and Weber, R.C. Moon meteoritic seismic hum: Steady state prediction. *Journal of Geophysical Research*, 114(E12):E12003, December 2009. ISSN 0148-0227. doi: 10.1029/2008JE003294.
- [206] Lorenz, R.D., Panning, M., Stahler, S., Shiraiishi, H., Yamada, R. et al. Titan Seismology with Dragonfly: Probing the Internal Structure of the Most Accessible Ocean World. In *50th Lunar and Planetary Science Conference*, volume LPI Contribution No. 2132, page 2173, The Woodlands, Texas, March 2019.
- [207] Lundborg, N. Strength of rock-like materials. *International Journal of Rock Mechanics and Mining Sciences & Geomechanics Abstracts*, 5(5):427–454, September 1968. ISSN 0148-9062. doi: 10.1016/0148-9062(68)90046-6.
- [208] Luo, H., Lu, H., Cooper, W.L. and Komanduri, R. Effect of Mass Density on the Compressive Behavior of Dry Sand Under Confinement at High Strain Rates. *Experimental Mechanics*, 51(9):1499–1510, November 2011. ISSN 0014-4851, 1741-2765. doi: 10.1007/s11340-011-9475-2.

- [209] Madariaga, R. Seismic Source Theory. In *Treatise on Geophysics*, pages 51–71. Elsevier, 2015. ISBN 978-0-444-53803-1. doi: 10.1016/B978-0-444-53802-4.00070-1.
- [210] Madariaga, R. Dynamics of an expanding circular fault. *Bulletin of the Seismological Society of America*, 66(3):639–666, June 1976. ISSN 0037-1106. doi: 10.1785/BSSA0660030639.
- [211] Malin, M.C., Bell III, J.F., Cantor, B.A., Caplinger, M.A., Calvin, W.M. et al. Context Camera Investigation on board the Mars Reconnaissance Orbiter. *Journal of Geophysical Research: Planets*, 112(E5), 2007. ISSN 2156-2202. doi: 10.1029/2006JE002808.
- [212] Mallet, R. On the Dynamics of Earthquakes; Being an Attempt to Reduce Their Observed Phenomena to the Known Laws of Wave Motion in Solids and Fluids. *The Transactions of the Royal Irish Academy*, 21:51–105, 1846. ISSN 0790-8113.
- [213] Martire, L., Martin, R., Brissaud, Q. and Garcia, R.F. SPECFEM2D-DG, an open-source software modelling mechanical waves in coupled solid–fluid systems: The linearized Navier–Stokes approach. *Geophysical Journal International*, 228(1):664–697, January 2022. ISSN 0956-540X. doi: 10.1093/gji/ggab308.
- [214] Martire, L., Garcia, R.F., Rolland, L., Spiga, A., Lognonné, P.H. et al. Martian Infrasonic: Numerical Modeling and Analysis of InSight’s Data. *Journal of Geophysical Research: Planets*, 125(6):e2020JE006376, 2020. ISSN 2169-9100. doi: 10.1029/2020JE006376.
- [215] Maruyama, S., Santosh, M. and Zhao, D. Superplume, supercontinent, and post-perovskite: Mantle dynamics and anti-plate tectonics on the Core–Mantle Boundary. *Gondwana Research*, 11(1):7–37, January 2007. ISSN 1342-937X. doi: 10.1016/j.gr.2006.06.003.
- [216] Matoza, R.S., Fee, D., Assink, J.D., Iezzi, A.M., Green, D.N. et al. Atmospheric waves and global seismoacoustic observations of the January 2022 Hunga eruption, Tonga. *Science*, 377(6601):95–100, July 2022. doi: 10.1126/science.abo7063.
- [217] McEwen, A.S., Eliason, E.M., Bergstrom, J.W., Bridges, N.T., Hansen, C.J. et al. Mars Reconnaissance Orbiter’s High Resolution Imaging Science Experiment (HiRISE). *Journal of Geophysical Research: Planets*, 112(E5), 2007. ISSN 2156-2202. doi: 10.1029/2005JE002605.
- [218] McGarr, A., Latham, G.V. and Gault, D.E. Meteoroid impacts as sources of seismicity on the Moon. *Journal of Geophysical Research*, 74(25):5981–5994, November 1969. ISSN 01480227. doi: 10.1029/JB074i025p05981.
- [219] McGlaun, J.M., Thompson, S.L. and Elrick, M.G. CTH: A three-dimensional shock wave physics code. *International Journal of Impact Engineering*, 10(1):351–360, January 1990. ISSN 0734-743X. doi: 10.1016/0734-743X(90)90071-3.
- [220] Melosh, H.J. *Impact Cratering : A Geologic Process*. Series: Oxford Monographs on Geology and Geophysics ; No. 11. Oxford University Press ; Oxford : Clarendon Press, New York, January 1989.
- [221] Melosh, H.J. and Ivanov, B.A. Impact crater collapse. *Annual Review of Earth and Planetary Sciences*, 27(1):385–415, May 1999. ISSN 0084-6597, 1545-4495. doi: 10.1146/annurev.earth.27.1.385.

- [222] Metropolis, N., Rosenbluth, A.W., Rosenbluth, M.N., Teller, A.H. and Teller, E. Equation of State Calculations by Fast Computing Machines. *The Journal of Chemical Physics*, 21(6):1087–1092, June 1953. ISSN 0021-9606. doi: 10.1063/1.1699114. Publisher: American Institute of Physics.
- [223] Miljkovic, K., Daubar, I.J., Rajsic, A., Neidhart, T., Sansom, E.K. et al. New Impact Craters on Mars Since the Landing of the InSight Mission. *Lunar and Planetary Science Conference*, LPI Contribution No. 2548(2548):1758, March 2021.
- [224] Millour, E., Forget, F., Spiga, A., Navarro, T., Madeleine, J.B. et al. The Mars Climate Database (MCD version 5.2). In *European Planetary Science Congress 2015*, volume EPSC2015, page 438, Nantes, France, October 2015.
- [225] Millour, E., Forget, F., Spiga, A., Vals, M., Zakharov, V. et al. Mars Climate Database. *From Mars Express to ExoMars*, page 68, 2018.
- [226] Minster, J.B. *Elastodynamics of Failure in a Continuum*. PhD thesis, California Institute of Technology, 1974.
- [227] Modrak, R., Silwal, V., Alvizuri, C.R. and Tape, C. Moment tensor estimation and uncertainty quantification using mtuq, instaseis, obspy and pymc. In *American Geophysical Union, Fall Meeting 2018*, volume 2018, pages S53E–0458, December 2018.
- [228] Mosegaard, K. and Tarantola, A. Monte Carlo sampling of solutions to inverse problems. *Journal of Geophysical Research: Solid Earth*, 100(B7):12431–12447, 1995. ISSN 2156-2202. doi: 10.1029/94JB03097.
- [229] Munjiza, A., Rougier, E., Lei, Z. and Knight, E.E. FSIS: A novel fluid–solid interaction solver for fracturing and fragmenting solids. *Computational Particle Mechanics*, 7(5):789–805, October 2020. ISSN 2196-4378, 2196-4386. doi: 10.1007/s40571-020-00314-9.
- [230] Munjiza, A.A. *The Combined Finite-Discrete Element Method*. John Wiley & Sons, April 2004. ISBN 978-0-470-02017-3. doi: 10.1002/0470020180.
- [231] Murdoch, N., Spiga, A., Lorenz, R., Garcia, R.F., Perrin, C. et al. Constraining Martian Regolith and Vortex Parameters From Combined Seismic and Meteorological Measurements. *Journal of Geophysical Research: Planets*, 126(2):e2020JE006410, 2021. ISSN 2169-9100. doi: 10.1029/2020JE006410.
- [232] Müller, G. Seismic moment and long-period radiation of underground nuclear explosions. *Bulletin of the Seismological Society of America*, 63(3):847–857, June 1973. ISSN 0037-1106.
- [233] Nagihara, S., Nakamura, Y., Lewis, L.R., Williams, D.R., Taylor, P.T. et al. Search and Recovery Efforts for the ALSEP Data Tapes. In *42nd Lunar and Planetary Conference*, The Woodlands, TX, March 2011.
- [234] Nakamura, Y., Latham, G.V. and Dorman, H.J. Apollo Lunar Seismic Experiment—Final summary. *Journal of Geophysical Research: Solid Earth*, 87(S01):A117–A123, 1982. ISSN 2156-2202. doi: <https://doi.org/10.1029/JB087iS01p0A117>.
- [235] Nakamura, Y., Latham, G.V., Dorman, H.J. and Harris, J.E. (revised 2008 from 1981 version) passive Seismic Experiment, Long Period Event Catalog, Final Version (1969 Day 202 - 1977 Day 273, ALSEP Stations 11, 12, 13, 14, 15, and 16). Technical Report, Univ. Texas, Austin, Institute for Geophysics [updated 2018], 2008.

- [236] Negraru, P.T. and Herrin, E.T. On Infrasound Waveguides and Dispersion. *Seismological Research Letters*, 80(4):565–571, July 2009. ISSN 0895-0695. doi: 10.1785/gssrl.80.4.565.
- [237] Nemec, M., Aftosmis, M.J. and Brown, P.G. Numerical prediction of meteoric infrasound signatures. *Planetary and Space Science*, 140:11–20, June 2017. ISSN 0032-0633. doi: 10.1016/j.pss.2017.03.003.
- [238] Nemtchinov, I.V., Shuvalov, V.V. and Greeley, R. Impact-mobilized dust in the Martian atmosphere: IMPACT-MOBILIZED DUST IN MARS' ATMOSPHERE. *Journal of Geophysical Research: Planets*, 107(E12):17–1–17–8, December 2002. ISSN 01480227. doi: 10.1029/2001JE001834.
- [239] Neukum, G. and Jaumann, R. HRSC: The High Resolution Stereo Camera of Mars Express. In *Mars Express: The Scientific Payload*, volume 1240, pages 17–35, August 2004.
- [240] Neumann, G.A., Lemoine, F.G., Smith, D.E. and Zuber, M.T. The Mars Orbiter Laser Altimeter Archive: Final Precision Experiment Data Record Release and Status of Radiometry. In *34th Annual Lunar and Planetary Science Conference*, volume 2003, page 1978, League City, TX, March 2003.
- [241] Noble, C.R., Anderson, A.T., Barton, N.R., Bramwell, J.A., Capps, A. et al. ALE3D: An Arbitrary Lagrangian-Eulerian Multi-Physics Code. Technical Report LLNL-TR-732040, Lawrence Livermore National Lab. (LLNL), Livermore, CA (United States), May 2017.
- [242] Nunn, C., Nakamura, Y., Kedar, S. and Panning, M.P. A New Archive of Apollo's Lunar Seismic Data. *The Planetary Science Journal*, 3(9):219, September 2022. ISSN 2632-3338. doi: 10.3847/PSJ/ac87af.
- [243] Oberst, J. and Nakamura, Y. Distinct meteoroid families identified on the lunar seismograms. *Journal of Geophysical Research: Solid Earth*, 92(B4):E769–E773, 1987.
- [244] Oberst, J. and Nakamura, Y. A search for clustering among the meteoroid impacts detected by the Apollo lunar seismic network. *Icarus*, 91(2):315–325, June 1991. ISSN 0019-1035. doi: 10.1016/0019-1035(91)90027-Q.
- [245] O'Brien, D., Morbidelli, A. and Levison, H. Terrestrial planet formation with strong dynamical friction. *Icarus*, 184(1):39–58, September 2006. ISSN 00191035. doi: 10.1016/j.icarus.2006.04.005.
- [246] Okubo, K., Bhat, H.S., Rougier, E., Marty, S., Schubnel, A. et al. Dynamics, Radiation, and Overall Energy Budget of Earthquake Rupture With Coseismic Off-Fault Damage. *Journal of Geophysical Research: Solid Earth*, 124(11):11771–11801, 2019. ISSN 2169-9356. doi: 10.1029/2019JB017304.
- [247] Onodera, K., Kawamura, T., Tanaka, S., Ishihara, Y. and Maeda, T. Numerical Simulation of Lunar Seismic Wave Propagation: Investigation of Subsurface Scattering Properties Near Apollo 12 Landing Site. *Journal of Geophysical Research: Planets*, 126(3):e2020JE006406, 2021. ISSN 2169-9100. doi: 10.1029/2020JE006406.
- [248] Onodera, K., Kawamura, T., Tanaka, S., Ishihara, Y. and Maeda, T. Quantitative Evaluation of the Lunar Seismic Scattering and Comparison Between the Earth, Mars, and the Moon. *Journal of Geophysical Research: Planets*, 127(12), December 2022. ISSN 2169-9097, 2169-9100. doi: 10.1029/2022JE007558.

- [249] Panning, M.P., Kedar, S., Bowles, N., Bugby, D., Calcutt, S. et al. Farside Seismic Suite (FSS): Surviving the Lunar Night and Delivering the First Seismic Data from the Farside of the Moon. In *53rd Lunar and Planetary Science Conference*, volume 2678, page 1576, The Woodlands, TX, March 2022.
- [250] Panning, M.P., Lorenz, R., Shiraishi, H., Yamada, R., Stähler, S. et al. Seismology on Titan: A seismic signal and noise budget in preparation for Dragonfly. In *SEG International Exposition and Annual Meeting*. OnePetro, October 2020. doi: 10.1190/segam2020-3426937.1.
- [251] Perrin, C., Rodriguez, S., Jacob, A., Lucas, A., Spiga, A. et al. Monitoring of Dust Devil Tracks Around the InSight Landing Site, Mars, and Comparison With In Situ Atmospheric Data. *Geophysical Research Letters*, 47(10):e2020GL087234, 2020. ISSN 1944-8007. doi: 10.1029/2020GL087234.
- [252] Pierazzo, E., Artemieva, N., Asphaug, E., Baldwin, E.C., Cazamias, J. et al. Validation of numerical codes for impact and explosion cratering: Impacts on strengthless and metal targets. *Meteoritics & Planetary Science*, 43(12):1917–1938, 2008. ISSN 1945-5100. doi: 10.1111/j.1945-5100.2008.tb00653.x.
- [253] Pierazzo, E. and Collins, G. A Brief Introduction to Hydrocode Modeling of Impact Cratering. In Dypvik, H., Burchell, M.J. and Claeys, P., editors, *Cratering in Marine Environments and on Ice*, Impact Studies, pages 323–340. Springer, Berlin, Heidelberg, 2004. ISBN 978-3-662-06423-8. doi: 10.1007/978-3-662-06423-8\_16.
- [254] Plescia, J., Robinson, M., Wagner, R. and Baldrige, R. Ranger and Apollo S-IVB spacecraft impact craters. *Planetary and Space Science*, 124:15–35, May 2016. ISSN 00320633. doi: 10.1016/j.pss.2016.01.002.
- [255] Plooster, M.N. Shock Waves from Line Sources. Numerical Solutions and Experimental Measurements. *The Physics of Fluids*, 13(11):2665–2675, November 1970. ISSN 0031-9171. doi: 10.1063/1.1692848.
- [256] Popova, O.P., Jenniskens, P., Emel’yanenko, V., Kartashova, A., Biryukov, E. et al. Chelyabinsk Airburst, Damage Assessment, Meteorite Recovery, and Characterization. *Science*, 342(6162):1069–1073, November 2013. doi: 10.1126/science.1242642.
- [257] Posiolova, L.V., Lognonné, P., Banerdt, W.B., Clinton, J., Collins, G.S. et al. Largest recent impact craters on Mars: Orbital imaging and surface seismic co-investigation. *Science*, pages 1–5, October 2022. doi: 10.1126/science.abq7704.
- [258] Press, F. and Ewing, M. Ground roll coupling to atmospheric compressional waves. *Geophysics*, 16(3):416–430, July 1951. ISSN 0016-8033. doi: 10.1190/1.1437684.
- [259] Press, F., Buwalda, P. and Neugebauer, M. A lunar seismic experiment. *Journal of Geophysical Research (1896-1977)*, 65(10):3097–3105, 1960. ISSN 2156-2202. doi: 10.1029/JZ065i010p03097.
- [260] Rajšić, A., Miljković, K., Collins, G.S., Wünnemann, K., Daubar, I.J. et al. Seismic Efficiency for Simple Crater Formation in the Martian Top Crust Analog. *Journal of Geophysical Research: Planets*, 126(2):e2020JE006662, 2021. ISSN 2169-9100. doi: 10.1029/2020JE006662.
- [261] Rajšić, A., Miljković, K., Wójcicka, N., Collins, G.S., Onodera, K. et al. Numerical Simulations of the Apollo S-IVB Artificial Impacts on the Moon. *Earth and Space Science*, 8(12), December 2021b. ISSN 2333-5084, 2333-5084. doi: 10.1029/2021EA001887.



- [262] Rayleigh, L. On Waves Propagated along the Plane Surface of an Elastic Solid. *Proceedings of the London Mathematical Society*, s1-17(1):4–11, 1885. ISSN 1460-244X. doi: 10.1112/plms/s1-17.1.4.
- [263] Reed, J.W. Atmospheric attenuation of explosion waves. *The Journal of the Acoustical Society of America*, 61(1):39–47, January 1977. ISSN 0001-4966. doi: 10.1121/1.381266.
- [264] ReVelle, D.O. On meteor-generated infrasound. *Journal of Geophysical Research (1896-1977)*, 81(7):1217–1230, 1976. ISSN 2156-2202. doi: 10.1029/JA081i007p01217.
- [265] ReVelle, D.O. and Edwards, W.N. Stardust-An artificial, low-velocity “meteor” fall and recovery: 15 January 2006. *Meteoritics & Planetary Science*, 42(2):271–299, February 2007. ISSN 10869379, 19455100. doi: 10.1111/j.1945-5100.2007.tb00232.x.
- [266] Revelle, D.O. A quasi-simple ablation model for large meteorite entry: Theory vs observations. *Journal of Atmospheric and Terrestrial Physics*, 41(5):453–473, May 1979. ISSN 0021-9169. doi: 10.1016/0021-9169(79)90071-0.
- [267] Reynolds, O. *Papers on mechanical and physical subjects*, volume III. The sub-mechanics of the universe. Cambridge [Eng.] : The University Press, 1903.
- [268] Richards, P.G. and Kim, W.Y. Equivalent Volume Sources for Explosions at Depth: Theory and Observations. *Bulletin of the Seismological Society of America*, 95(2): 401–407, April 2005. ISSN 0037-1106. doi: 10.1785/0120040034.
- [269] Richards, P.G., Wu, Z., Kim, W.Y. and Schaff, D.P. Seismic Monitoring of Nuclear Explosions. In Gupta, H.K., editor, *Encyclopedia of Solid Earth Geophysics*, Encyclopedia of Earth Sciences Series, pages 1429–1442. Springer International Publishing, Cham, 2021. ISBN 978-3-030-58631-7. doi: 10.1007/978-3-030-58631-7\_8.
- [270] Richardson, J.E., Steckloff, J.K. and Minton, D.A. Impact-produced seismic shaking and regolith growth on asteroids 433 Eros, 2867 Šteins, and 25143 Itokawa. *Icarus*, 347:113811, September 2020. ISSN 00191035. doi: 10.1016/j.icarus.2020.113811.
- [271] Richardson, J. and Kedar, S. An experimental investigation of the seismic signal produced by hypervelocity impacts. In *Lunar and Planetary Science Conference*, volume 44, page 2863, 2013.
- [272] Robertson, D.K. and Mathias, D.L. Effect of yield curves and porous crush on hydrocode simulations of asteroid airburst. *Journal of Geophysical Research: Planets*, 122(3):599–613, 2017. ISSN 2169-9100. doi: 10.1002/2016JE005194.
- [273] Robertson, D.K. and Gisler, G.R. Near and far-field hazards of asteroid impacts in oceans. *Acta Astronautica*, 156:262–277, March 2019. ISSN 0094-5765. doi: 10.1016/j.actaastro.2018.09.018.
- [274] Romanowicz, B. and Gung, Y. Superplumes from the Core-Mantle Boundary to the Lithosphere: Implications for Heat Flux. *Science*, 296(5567):513–516, April 2002. ISSN 0036-8075, 1095-9203. doi: 10.1126/science.1069404.
- [275] Rougier, E., Knight, E.E., Broome, S.T., Sussman, A.J. and Munjiza, A. Validation of a three-dimensional Finite-Discrete Element Method using experimental results of the Split Hopkinson Pressure Bar test. *International Journal of Rock Mechanics and Mining Sciences*, 70:101–108, September 2014. ISSN 1365-1609. doi: 10.1016/j.ijrmms.2014.03.011.

- [276] Sambridge, M. A Parallel Tempering algorithm for probabilistic sampling and multimodal optimization. *Geophysical Journal International*, 196(1):357–374, January 2014. ISSN 0956-540X. doi: 10.1093/gji/ggt342.
- [277] Sansom, E.K., Devillepoix, H.A.R., Yamamoto, M.y., Abe, S., Nozawa, S. et al. The scientific observation campaign of the Hayabusa-2 capsule re-entry. *Publications of the Astronomical Society of Japan*, 74(1):50–63, February 2022. ISSN 0004-6264. doi: 10.1093/pasj/psab109.
- [278] Savage, J.C. Radiation from a realistic model of faulting. *Bulletin of the Seismological Society of America*, 56(2):577–592, April 1966. ISSN 0037-1106. doi: 10.1785/BSSA0560020577.
- [279] Scalabrin, G., Marchi, P., Finezzo, F. and Span, R. A Reference Multiparameter Thermal Conductivity Equation for Carbon Dioxide with an Optimized Functional Form. *Journal of Physical and Chemical Reference Data*, 35(4):1549–1575, December 2006. ISSN 0047-2689. doi: 10.1063/1.2213631.
- [280] Schatz, J.F. SOC73, a one-dimensional wave propagation code for rock media. Technical report, California Univ., Lawrence Livermore Lab., Livermore, CA (USA)., 11 1974.
- [281] Schmerr, N.C., Banks, M.E. and Daubar, I.J. The Seismic Signatures of Recently Formed Impact Craters on Mars. *Journal of Geophysical Research: Planets*, 124(11):3063–3081, 2019. ISSN 2169-9100. doi: 10.1029/2019JE006044.
- [282] Schneider, F.M., Fuchs, F., Kolínský, P., Caffagni, E., Serafin, S. et al. Seismo-acoustic signals of the Baumgarten (Austria) gas explosion detected by the AlpArray seismic network. *Earth and Planetary Science Letters*, 502:104–114, November 2018. ISSN 0012-821X. doi: 10.1016/j.epsl.2018.08.034.
- [283] Schröder, C.T. and Scott, W.R. On the complex conjugate roots of the Rayleigh equation: The leaky surface wave. *The Journal of the Acoustical Society of America*, 110(6):2867–2877, December 2001. ISSN 0001-4966. doi: 10.1121/1.1419085.
- [284] Schulte, P., Alegret, L., Arenillas, I., Arz, J.A., Barton, P.J. et al. The Chicxulub Asteroid Impact and Mass Extinction at the Cretaceous-Paleogene Boundary. *Science*, 327(5970):1214–1218, March 2010. doi: 10.1126/science.1177265.
- [285] Scott, R.H. I. Note on a series of barometrical disturbances which passed over Europe between the 27th and the 31st of August, 1883. *Proceedings of the Royal Society of London*, 36(228-231):139–143, 1883. doi: 10.1098/rspl.1883.0087.
- [286] Sedov, L.I. Propagation of strong shock waves. *Journal of Applied Mathematics and Mechanics*, 10:241–250, January 1946. ISSN 0021-8928.
- [287] Shearer, P.M. Introduction to Seismology, May 2019.
- [288] Sheriff, R.E. and Geldart, L.P. *Exploration Seismology*. Cambridge University Press, Cambridge, second edition, 1995. ISBN 978-0-521-46826-8. doi: 10.1017/CBO9781139168359.
- [289] Shishkin, N.I. Seismic efficiency of a contact explosion and a high-velocity impact. *Journal of Applied Mechanics and Technical Physics*, 48(2):145–152, March 2007. ISSN 0021-8944, 1573-8620. doi: 10.1007/s10808-007-0019-6.

- [290] Shoemaker, E.M. *Impact Mechanics at Meteor Crater, Arizona*. PhD thesis, Princeton University, October 1959.
- [291] Shoemaker, E.M. Interpretation of Lunar Craters. *Physics and Astronomy of the Moon*, pages 283–359, 1962.
- [292] Shoemaker, E.M. *Impact Mechanics at Meteor Crater, Arizona*. The Moon Meteorites and Comets. The University of Chicago Press, Chicago, January 1963.
- [293] Shuvalov, V.V. and Artemieva, N.A. Numerical modeling of Tunguska-like impacts. *Planetary and Space Science*, 50(2):181–192, February 2002. ISSN 0032-0633. doi: 10.1016/S0032-0633(01)00079-4.
- [294] Shuvalov, V.V. and Trubetskaya, I.A. The influence of internal friction on the deformation of a damaged meteoroid. *Solar System Research*, 44(2):104–109, April 2010. ISSN 1608-3423. doi: 10.1134/S0038094610020036.
- [295] Shuvalov, V.V., Artem'eva, N.A. and Kosarev, I.B. 3D hydrodynamic code sova for multimaterial flows, application to Shoemakerlevy 9 comet impact problem. *International Journal of Impact Engineering*, 23(1, Part 2):847–858, December 1999. ISSN 0734-743X. doi: 10.1016/S0734-743X(99)00129-3.
- [296] Shuvalov, V.V., Svetsov, V.V. and Trubetskaya, I.A. An estimate for the size of the area of damage on the Earth's surface after impacts of 10–300-m asteroids. *Solar System Research*, 47(4):260–267, July 2013. ISSN 1608-3423. doi: 10.1134/S0038094613040217.
- [297] Silber, E.A., Boslough, M., Hocking, W.K., Gritsevich, M. and Whitaker, R.W. Physics of meteor generated shock waves in the Earth's atmosphere – A review. *Advances in Space Research*, 62(3):489–532, August 2018. ISSN 0273-1177. doi: 10.1016/j.asr.2018.05.010.
- [298] Sorrells, G.G. and Goforth, T.T. Low-frequency earth motion generated by slowly propagating partially organized pressure fields. *Bulletin of the Seismological Society of America*, 63(5):1583–1601, October 1973. ISSN 0037-1106. doi: 10.1785/BSSA0630051583.
- [299] Sorrells, G.G., McDonald, J.A., Der, Z.A. and Herrin, E. Earth Motion Caused by Local Atmospheric Pressure Changes. *Geophysical Journal International*, 26(1-4): 83–98, December 1971. ISSN 0956-540X. doi: 10.1111/j.1365-246X.1971.tb03384.x.
- [300] Sorrells, G.G. A preliminary investigation into the relationship between long-period seismic noise and local fluctuations in the atmospheric pressure field. *Geophysical Journal International*, 26(1-4):71–82, 1971.
- [301] Span, R. and Wagner, W. A New Equation of State for Carbon Dioxide Covering the Fluid Region from the Triple-Point Temperature to 1100 K at Pressures up to 800 MPa. *Journal of Physical and Chemical Reference Data*, 25(6):1509–1596, November 1996. ISSN 0047-2689. doi: 10.1063/1.555991.
- [302] Spohn, T., Grott, M., Smrekar, S.E., Knollenberg, J., Hudson, T.L. et al. The Heat Flow and Physical Properties Package (HP3) for the InSight Mission. *Space Science Reviews*, 214(5):96, August 2018. ISSN 0038-6308, 1572-9672. doi: 10.1007/s11214-018-0531-4.

- [303] Stähler, S.C., Khan, A., Banerdt, W.B., Lognonné, P., Giardini, D. et al. Seismic detection of the martian core. *Science*, 373(6553):443–448, July 2021. doi: 10.1126/science.abi7730.
- [304] Stein, S. and Wysession, M. *An Introduction to Seismology, Earthquakes, and Earth Structure*. John Wiley & Sons, Incorporated, Hoboken, UNITED KINGDOM, 1991. ISBN 978-1-4443-1131-0.
- [305] Stooke, P.J. and Marcus, M. Identification of the Apollo 12 lunar module ascent stage impact site on the moon. *Icarus*, 331:98–102, October 2019. ISSN 00191035. doi: 10.1016/j.icarus.2019.05.002.
- [306] Strachey, R. II. Note on the foregoing paper. *Proceedings of the Royal Society of London*, 36(228-231):143–151, 1883. doi: 10.1098/rspl.1883.0088.
- [307] Stump, B.W. Constraints on explosive sources with spall from near-source waveforms. *Bulletin of the Seismological Society of America*, 75(2):361–377, April 1985. ISSN 0037-1106. doi: 10.1785/BSSA0750020361.
- [308] Stump, B.W. and Johnson, L.R. Higher-degree moment tensors — the importance of source finiteness and rupture propagation on seismograms. *Geophysical Journal International*, 69(3):721–743, June 1982. ISSN 0956-540X. doi: 10.1111/j.1365-246X.1982.tb02772.x.
- [309] Stutzmann, E., Schimmel, M., Lognonné, P., Horleston, A., Ceylan, S. et al. The Polarization of Ambient Noise on Mars. *Journal of Geophysical Research: Planets*, 126(1):e2020JE006545, 2021. ISSN 2169-9100. doi: 10.1029/2020JE006545.
- [310] Supino, M., Poiata, N., Festa, G., Vilotte, J.P., Satriano, C. et al. Self-similarity of low-frequency earthquakes. *Scientific Reports*, 10(1):6523, April 2020. ISSN 2045-2322. doi: 10.1038/s41598-020-63584-6.
- [311] Svetsov, V.V., Nemtchinov, I.V. and Teterev, A.V. Disintegration of Large Meteoroids in Earth’s Atmosphere: Theoretical Models. *Icarus*, 116(1):131–153, July 1995. ISSN 0019-1035. doi: 10.1006/icar.1995.1116.
- [312] Symons, G.J. The Eruption of Krakatoa and Subsequent Phenomena: Report of the Krakatoa Committee of the Royal Society. *Quarterly Journal of the Royal Meteorological Society*, 14(68):301–307, 1888. ISSN 1477-870X. doi: 10.1002/qj.4970146809.
- [313] Tabetah, M.E. and Melosh, H.J. Air penetration enhances fragmentation of entering meteoroids. *Meteoritics & Planetary Science*, 53(3):493–504, 2018. ISSN 1945-5100. doi: 10.1111/maps.13034.
- [314] Takei, Y. and Kumazawa, M. Why have the single force and torque been excluded from seismic source models? *Geophysical Journal International*, 118(1):20–30, 1994.
- [315] Tancredi, G., Ishitsuka, J., Schultz, P.H., Harris, R.S., Brown, P. et al. A meteorite crater on Earth formed on September 15, 2007: The Carancas hypervelocity impact. *Meteoritics & Planetary Science*, 44(12):1967–1984, 2009. ISSN 1945-5100. doi: 10.1111/j.1945-5100.2009.tb02006.x.
- [316] Tanimoto, T. and Wang, J. Theory for deriving shallow elasticity structure from colocated seismic and pressure data. *Journal of Geophysical Research: Solid Earth*, 124(6):5811–5835, 2019.

- [317] Tanimoto, T., Eitzel, M. and Yano, T. The noise cross-correlation approach for Apollo 17 LSPE data: Diurnal change in seismic parameters in shallow lunar crust. *Journal of Geophysical Research: Planets*, 113(E8), 2008. ISSN 2156-2202. doi: 10.1029/2007JE003016.
- [318] Tape, W. and Tape, C. A geometric setting for moment tensors. *Geophysical Journal International*, 190(1):476–498, August 2012. ISSN 0956-540X. doi: 10.1111/j.1365-246X.2012.05491.x.
- [319] Tape, W. and Tape, C. A uniform parametrization of moment tensors. *Geophysical Journal International*, 202(3):2074–2081, September 2015. ISSN 0956-540X. doi: 10.1093/gji/ggv262.
- [320] Tape, W. and Tape, C. The eigenvalue lune as a window on moment tensors. *Geophysical Journal International*, 216(1):19–33, January 2019. ISSN 0956-540X. doi: 10.1093/gji/ggy373.
- [321] Tarantola, A. *Inverse Problem Theory and Methods for Model Parameter Estimation*. Other Titles in Applied Mathematics. Society for Industrial and Applied Mathematics, January 2005. ISBN 978-0-89871-572-9. doi: 10.1137/1.9780898717921.
- [322] Tauzin, B., Debayle, E., Quantin, C. and Coltice, N. Seismoacoustic coupling induced by the breakup of the 15 February 2013 Chelyabinsk meteor. *Geophysical Research Letters*, 40(14):3522–3526, 2013. ISSN 1944-8007. doi: 10.1002/grl.50683.
- [323] Taylor, G.I. The formation of a blast wave by a very intense explosion I. Theoretical discussion. *Proceedings of the Royal Society of London. Series A. Mathematical and Physical Sciences*, 201(1065):159–174, January 1997. doi: 10.1098/rspa.1950.0049.
- [324] Taylor, J., Teanby, N.A. and Wookey, J. Estimates of seismic activity in the Cerberus Fossae region of Mars. *Journal of Geophysical Research: Planets*, 118(12):2570–2581, 2013. ISSN 2169-9100. doi: 10.1002/2013JE004469.
- [325] Teanby, N.A. and Wookey, J. Seismic detection of meteorite impacts on Mars. *Physics of the Earth and Planetary Interiors*, 186(1):70–80, May 2011. ISSN 0031-9201. doi: 10.1016/j.pepi.2011.03.004.
- [326] Teanby, N. Predicted detection rates of regional-scale meteorite impacts on Mars with the InSight short-period seismometer. *Icarus*, 256:49–62, August 2015. ISSN 00191035. doi: 10.1016/j.icarus.2015.04.012.
- [327] Thomas, N., Cremonese, G., Ziethe, R., Gerber, M., Brändli, M. et al. The Colour and Stereo Surface Imaging System (CaSSIS) for the ExoMars Trace Gas Orbiter. *Space Science Reviews*, 212(3):1897–1944, November 2017. ISSN 1572-9672. doi: 10.1007/s11214-017-0421-1.
- [328] Thompson, S. and Lauson, H. Improvements in the CHART D radiation-hydrodynamic code III: Revised analytic equations of state. Technical report, Sandia Labs., United States, 1974.
- [329] Tillotson, J.H. Metallic Equations of State For Hypervelocity Impact. Technical report, General Dynamics San Diego CA General Atomic Div., San Diego, CA, July 1962. Section: Technical Reports.
- [330] Toksöz, M.N., Dainty, A.M., Solomon, S.C. and Anderson, K.R. Structure of the Moon. *Reviews of Geophysics*, 12(4):539–567, 1974. ISSN 1944-9208. doi: 10.1029/RG012i004p00539.

- [331] Tromp, J. Seismic wavefield imaging of Earth's interior across scales. *Nature Reviews Earth & Environment*, 1(1):40–53, January 2020. ISSN 2662-138X. doi: 10.1038/s43017-019-0003-8.
- [332] Tsikulin, MA. Shock waves during the movement of large meteorites in the atmosphere. Technical report, Institute of Earth Physics, USSR Academy of Sciences, Nauka Izadatel'stvo, Moscow, 1969.
- [333] Walker, J.D. Loading sources for seismological investigation of asteroids and comets. *International Journal of Impact Engineering*, 29(1-10):757–769, December 2003. ISSN 0734743X. doi: 10.1016/j.ijimpeng.2003.10.022.
- [334] Wang, W. and Vidale, J.E. Seismological observation of Earth's oscillating inner core. *Science Advances*, 8(23):eabm9916, June 2022. ISSN 2375-2548. doi: 10.1126/sciadv.abm9916.
- [335] Warner, N.H., Golombek, M.P., Sweeney, J., Fergason, R., Kirk, R. et al. Near Surface Stratigraphy and Regolith Production in Southwestern Elysium Planitia, Mars: Implications for Hesperian-Amazonian Terrains and the InSight Lander Mission. *Space Science Reviews*, 211(1):147–190, October 2017. ISSN 1572-9672. doi: 10.1007/s11214-017-0352-x.
- [336] Waxler, R. A vertical eigenfunction expansion for the propagation of sound in a downward-refracting atmosphere over a complex impedance plane. *The Journal of the Acoustical Society of America*, 112(6):2540–2552, December 2002. ISSN 0001-4966, 1520-8524. doi: 10.1121/1.1514930.
- [337] Weber, R.C., Lin, P.Y., Garnero, E.J., Williams, Q. and Lognonné, P. Seismic Detection of the Lunar Core. *Science*, 331(6015):309–312, January 2011. doi: 10.1126/science.1199375.
- [338] Wetherill, G.W. Occurrence of Giant Impacts During the Growth of the Terrestrial Planets. *Science*, 228(4701):877–879, May 1985. doi: 10.1126/science.228.4701.877.
- [339] Whipple, F.J.W. On Phenomena related to the great Siberian meteor. *Quarterly Journal of the Royal Meteorological Society*, 60(257):505–522, 1934. ISSN 1477-870X. doi: 10.1002/qj.49706025709.
- [340] Wiggins, S.E., Johnson, B.C., Bowling, T.J., Melosh, H.J. and Silber, E.A. Impact Fragmentation and the Development of the Deep Lunar Megaregolith. *Journal of Geophysical Research: Planets*, 124(4):941–957, April 2019. ISSN 2169-9097, 2169-9100. doi: 10.1029/2018JE005757.
- [341] Woods, D.C., Bolton, J.S. and Rhoads, J.F. On the use of evanescent plane waves for low-frequency energy transmission across material interfaces. *The Journal of the Acoustical Society of America*, 138(4):2062–2078, October 2015. ISSN 0001-4966. doi: 10.1121/1.4929692.
- [342] Wünnemann, K., Collins, G. and Melosh, H. A strain-based porosity model for use in hydrocode simulations of impacts and implications for transient crater growth in porous targets. *Icarus*, 180(2):514–527, February 2006. ISSN 00191035. doi: 10.1016/j.icarus.2005.10.013.
- [343] Wünnemann, K., Nowka, D., Collins, G.S., Elbeshausen, D. and Bierhaus, M. Scaling of impact crater formation on planetary surfaces – insights from numerical modeling. In *Proceedings of the 11th Hypervelocity Impact Symposium*, pages 1–16, 2011.

- [344] Wójcicka, N., Collins, G.S., Bastow, I.D., Teanby, N.A., Miljković, K. et al. The Seismic Moment and Seismic Efficiency of Small Impacts on Mars. *Journal of Geophysical Research: Planets*, 125(10), October 2020. ISSN 2169-9097, 2169-9100. doi: 10.1029/2020JE006540.
- [345] Xu, Z., Froment, M., Garcia, R.F., Beucler, É., Onodera, K. et al. Modeling Seismic Recordings of High-Frequency Guided Infrasond on Mars. *Journal of Geophysical Research: Planets*, 127(11):e2022JE007483, 2022. doi: 10.1029/2022JE007483.
- [346] Yamamoto, M.y., Ishihara, Y., Hiramatsu, Y., Kitamura, K., Ueda, M. et al. Detection of Acoustic/Infrasonic/Seismic Waves Generated by Hypersonic Re-Entry of the HAYABUSA Capsule and Fragmented Parts of the Spacecraft. *Publications of the Astronomical Society of Japan*, 63(5):971–978, October 2011. ISSN 0004-6264. doi: 10.1093/pasj/63.5.971.
- [347] Yamamuro, J.A., Bopp, P.A. and Lade, P.V. One-Dimensional Compression of Sands at High Pressures. *Journal of Geotechnical Engineering*, 122(2):147–154, February 1996. ISSN 0733-9410, 1944-8368. doi: 10.1061/(ASCE)0733-9410(1996)122:2(147).
- [348] Yan, C., Zheng, H., Sun, G. and Ge, X. Combined Finite-Discrete Element Method for Simulation of Hydraulic Fracturing. *Rock Mechanics and Rock Engineering*, 49(4):1389–1410, April 2016. ISSN 1434-453X. doi: 10.1007/s00603-015-0816-9.
- [349] Zenhäusern, G., Wójcicka, N., Stähler, S., Collins, G., Daubar, I. et al. Are high frequency marsquakes caused by meteoroid impacts? Implications for a seismically determined impact rate on Mars. *Nature Portfolio*, Preprint, 2023. doi: 10.21203/rs.3.rs-2742268/v1.
- [350] Zhao, Q., Lisjak, A., Mahabadi, O., Liu, Q. and Grasselli, G. Numerical simulation of hydraulic fracturing and associated microseismicity using finite-discrete element method. *Journal of Rock Mechanics and Geotechnical Engineering*, 6(6):574–581, December 2014. ISSN 1674-7755. doi: 10.1016/j.jrmge.2014.10.003.



## List of Copyrighted Materials

List of articles removed from the complete version of the thesis due to copyrights.

- Froment, M., Rougier, E., Larmat, C., Lei, Z., Euser, B. et al. Lagrangian-based Simulations of Hypervelocity Impact Experiments on Mars Regolith Proxy. *Geophysical Research Letters*, 47(13), July 2020. doi: 10.1029/2020GL087393. **Pages 113–120.**
- Posiolova, L.V., Lognonné, P., Banerdt, W.B., Clinton, J., Collins, G.S. et al. Largest recent impact craters on Mars: Orbital imaging and surface seismic co-investigation. *Science*, pages 1–5, October 2022. doi: 10.1126/science.abq7704. **Pages 121–125.**

